The Design and Synthesis of a new Biomimetic Code: Squaratides

Maynooth University
National University of Ireland Maynooth

A thesis submitted to Maynooth University in fulfilment of the requirements for the degree of

Doctor of Philosophy

By

Farhad Mohammed, B.Sc.

Department of Chemistry,

Maynooth University,

Maynooth,

Co. Kildare, Ireland.

October 2025

Research Supervisor: Dr. Robert Elmes

Head of Department: Dr. Diego Montagner

Table of Contents

Declaration

I declare that the work presented in this thesis was carried out in accordance with the regulations of Maynooth University. The work is original, except where indicated by reference, and has not been submitted before, in whole or in part, to this or any other university for any other degree.

Signed: *Farhad Mohammed* Date: 14/10/2025

Farhad Mohammed, B.Sc. (Hons)

Acknowledgements

لَا يُكَلِّفُ اللَّهُ نَفْسًا إِلَّا وُسْعَهَا

“Allah does not burden a soul beyond that it can bear.”
- (Qur’an 2:286)

All praise is due to Allah, for granting me the strength and knowledge to complete this work. In moments of difficulty, He granted me patience; in times of doubt, He gave me clarity. Every success I have achieved is by His will and grace.

"And He found you lost and guided you." - *(Qur'an 93:7)*

The PhD journey over the past four years has not only provided me with invaluable knowledge that I will carry with me forever but has also shaped me as a person — teaching me many life lessons and revealing the true meaning of perseverance, patience, and discipline. However, the most important lesson it has taught me is the value and power of having a strong support system around you. With that being said, all of your support has never gone unnoticed, and I'd like to take this opportunity to thank you all for being a part of this journey and for making this possible.

First, I would like to thank my supervisor, Dr. Robert Elmes. Your friendly demeanour and approachable personality were what first encouraged me to speak with you after one of your lectures in my third year of undergraduate studies to express my interest in research. You gave me the opportunity that, over the years, blossomed into an unforgettable mentorship, and you are the reason I've grown into the researcher I am today.

Thanks for always being able to have a laugh with me and for never taking things too seriously. Getting side tracked in our meetings talking about cars and trying to avoid you breaking me up when we played football on Thursdays, which was probably revenge for always texting and annoying you on WhatsApp. Nevertheless, you still always showed support and helped me get through stressful situations, which I will always be grateful for!

I would also like to extend my appreciation to all the admin, technical staff, and academic staff within the department who have helped progress my research along the way. Big shout out to Noel for hitting random broken equipment with his wrench and somehow fixing it with a 100% success rate. I'd also like to thank Barbara for always giving me the keys for the NMR solvent press and telling her I only took one bottle while another bottle was in my pocket. I'm sorry, but it had to be done. And to the health and safety

committee, thanks for not going to hard on me for never wearing my lab coat and glasses.

To the Elmes Group – past and present members, thanks for all the laughs and great memories over the years, and for always keeping the good energy even on bad days in the lab.

To my boy Ste, we got it done bro. we started this journey together and finished together, and no better man to have done it alongside with. Who would have thought we'd finish a PhD by just hitting the weights and playing footy every week (I'm the better baller). Two boys just winging it half the time in the lab and somehow paid off. It's tough at the top bro. Thanks for always keeping it real, and I wish you nothing but the best in the future.

To Xuanyang, thanks for always smiling and keeping a positive attitude no matter what would happen in the lab as a constant reminder not to take things to seriously!

To the rest of the Elmes group, Jordan, Emily and postdocs, Tomas, and Hilal. Best of luck with the rest of your research and studies, don't miss me too much!

To the past members, Gero and Wynner, the golden era back in the day. Thanks for showing me the ropes at the start and teaching me not to take the bad results too seriously. Gero, don't worry, I deleted your search history from your computer when you finished and left your ketchup bottle by your desk as a reminiscent of you. Wynner, since taking over your bench, it's a complete mess now and nothing like how you always kept it. If you see the state of it now, you will malfunction. Sorry about that.

To the other Past members, Hua, Luke M and Luke B, I hope you guys are doing well in life and thanks for sharing your knowledge and expertise with me when I started.

To the CH boys, Barry (Baz), Adam (Adz) and Tom (T dog). If I speak, I'm in trouble, so I'll keep it brief. From being friends and brothers since knee high, you boys have helped me in ways you don't even realise by your own unique personalities. Always turning any situation good or bad into one big joke is what keeps me going throughout the days, and I am blessed to have such an amazing inner circle that aside from the constant insults and mockery, we always look out for each other no matter what.

To my family, you are the reason I've reached this milestone in my life and the person I am today.

To my sisters, Joanne, and Naz, thank you for always showing me love and support, and for constantly cheering me on — celebrating every accomplishment, no matter how big or small. I'm truly grateful to have such amazing sisters who care for me like a mother would, always making sure I'm okay.

To my brothers, Azad and Nuzy, not much to say about you lads, to be honest — apart from arguing over who has the bigger muscles and playing PlayStation together, we don't really do much! All jokes aside, our shared competitiveness as brothers has always been a driving force for me. Trying to fill the shoes of my older brother, Azad, while also striving to be a good role model for my younger brother, Nuzy, has been both challenging and motivating. I hope I've made you both proud — and continue to do so.

To my mother and father, words can't truly describe everything you've done for me. You continue to teach me invaluable life lessons and the true meaning of hard work and humility. You've sacrificed so much and have always provided for me, no matter the circumstances. Your faith in me, even when I doubted myself, made this accomplishment possible. I hope to keep making you both proud.

Finally, to my caring and loving fiancée, Rebecca — I still don't know how you manage to put up with me every day, and for agreeing to do so for the rest of our lives. Your constant support and care never go unnoticed. You always put me ahead of yourself, being my number one fan and cheering me on every step of the way. You always know the right things to say when everything feels overwhelming, and your trust and belief in me drive me every day to be the best version of myself. Thank you for your patience through the long days, late nights, and stressful moments, and for always believing in me even when I doubted myself. Your love, strength, and understanding have meant more to me than words can express. This thesis is as much yours as it is mine.

I'd also like to give a special mention to my secondary school teachers who never believed in me, constantly putting me down, and to the principal who said I shouldn't study chemistry as it "requires a lot of study" and that I was "not that type of student". Thank you for not believing in me – it made proving you all wrong that more satisfying.

Abstract

Anion recognition is a cornerstone of supramolecular chemistry, addressing the selective interaction of host molecules with anionic guests through non-covalent forces. Anions are ubiquitous in biological, environmental, and industrial systems, playing critical roles in processes such as enzymatic regulation, cellular signalling, and environmental remediation. However, their diverse geometries, sizes, and solvation properties present significant challenges for selective recognition.

Since its inception in the 1960s, driven by the groundbreaking contributions of Lehn, Cram, and Pederson, supramolecular chemistry has proven itself to provide a powerful framework for designing host molecules that exploit hydrogen bonding, halogen bonding, ion-dipole interactions, and electrostatic forces to bind specific anions. These interactions are often fine-tuned using macrocyclic, cage-like, or anion-π receptor architectures, allowing for enhanced selectivity and binding strength. Advances in supramolecular design have enabled the detection of environmentally hazardous anions (e.g., nitrate and phosphate) and biologically relevant anions (e.g., chloride, sulfate, and ATP), providing tools for sensing, diagnostics, and pollutant capture.

Moreover, the principles of anion recognition extend to functional applications such as anion transport across lipid bilayers, a process critical for mimicking ion channels and addressing chloride-related diseases like cystic fibrosis. Supramolecular systems that integrate anion recognition and transport highlight the transformative potential of this field in solving contemporary challenges in medicine, environmental science, and materials development. This thesis titled “The Design and Synthesis of a new Biomimetic code: Squaratides” aims to introduce a new class of peptidomimetic receptors – a hybrid mix of squaramides and peptides that we call “squaratides”. This new building block enables the creation of a library of modified amino acid-based biopolymers that can be tailored for improved hydrogen-bond donor and acceptor behaviour, producing a diversity of anion receptor subtypes with readily engineerable cavity size, lipophilicity and charge.

The thesis opens with a literature review (**Chapter 1**) documenting the historical perspective on the supramolecular chemistry of anion recognition, addressing the importance and challenges faced with anion recognition and anion receptors, followed by the unique structural features of macrocyclic receptors, such as their well-defined structures and pre-organised binding sites, that contribute to their exceptional anion-binding and transport capabilities.

Chapter 2 details the design of a new peptidomimetic scaffold that incorporates squaramides into the peptide backbone, utilising all the advantages that squaramides offer including rigidity, aromaticity and strong specific anion binding. This new building block enables the creation of a library of modified amino acid-based biopolymers that can be tailored for improved hydrogen-bond donor and acceptor behaviour. With this new class of receptors at hand, we use a combination of experimental techniques to characterise the solid and solution state behaviour of the squaratides as well as their ability to discriminate specific anions through preferential binding interactions.

Chapter 3 builds upon the data and insights presented in the previous chapter whereby we optimise the synthetic pathway of our previously described squaratides as a means to synthesise what we call 2nd generation squaratides. Developed through a solid support using SPPS, this synthetic approach grants us the flexibility in designing longer squaratide chains as well as larger macrocyclic squaratides with various cavity sizes allowing us to utilize this approach for carrying work out on exploring squaratides as antimicrobials. we have generated a structurally diverse library of receptor subtypes. These synthetic constructs are designed to replicate the membrane-targeting activity and selectivity of natural antimicrobial peptides, while offering enhanced stability and tunability. This work highlights the potential of cyclic and modular frameworks as next-generation platforms for addressing the growing challenge of antimicrobial resistance.

Chapter 4 utilises the new solid phase synthesis approach to squaratides mentioned in Chapter 3, where we set out to synthesise asymmetric squaratides and a fluorinated squaratide as well as taking advantage of the functionalisation capability of these receptors in order to synthesise a family of functionalised squaratides by incorporating anion binding motifs onto the side chains of the squaratide backbones as a means to

further enhance anion recognition as well expanding the application range of squaratides by studying them as potential anion transporters.

Chapter 5 reveals the development and study of a novel fluorescent based squaratide. By integrating a napthalimide based fluorescent amino acid into the peptidomimetic backbone, we give rise to the first fluorescent squaratide; **Sq-2-Lys-Naph,** which functions as a self-reporting anion sensor, providing real-time optical feedback on fluoride binding and displacement. We envisage that this design principle can be expanded to engineer new fluorescent peptidomimetics with tailored selectivity and tuneable optical responses.

Abbreviations

Å Angstrom

AA Amino Acid

AA-Sq.-EDA Amino Acid-Squaratide-Ethylenediamine

AcOEt Ethyl Acetate

AcO^- Acetate

AMP Antimicrobial peptide

Asp Aspartic Acid

Bn Benzyl

Boc tert-Butyloxycarbonyl Group

Cbz BenZyl Chloroformate

$CDCl_3$ Deuterated Chloroform

Cl^- Chloride

COSY Correlation Spectroscopy

DCM Dichloromethane

DeSq Diethyl Squarate

DIPEA N,N-Diisopropylethylamine

DMAP 4-Dimethylaminopyridine

DMF Dimethylformamide

DMSO-d_6 Deuterated Dimethyl Sulfoxide

EDA 1,2-EthyleneDiAmine

e.g. Exempli gratia (Latin for 'for example')

equiv. Equivalence

ESI Electrospray Ionization

TEA Triethylamine

EtOH Ethanol

Fmoc Fluorenylmethyloxycarbonyl

Gly Glycine

h Hour

HCl Hydrochloric Acid

HFIP 1,1,1,3,3,3-HexaFluoroIsoPropanol

HMBC Heteronuclear Multiple Bond Correlation

HRMS High Resolution Mass Spectroscopy

HSQC Heteronuclear Single Quantum Coherence

i.e. id est (Latin for 'that is')

IR Infrared Spectroscopy

K Kelvin

LC-MS Liquid Chromatography-Mass Spectroscopy

Lys Lysine

Me Methyl

MeCN Acetonitrile

MeOH Methanol

µL Microliter

mg Milligram

min Minute

mL Milliliter

mm Millimeter

MRSA Methicillin-resistant *Staphylococcus aureus*

NaH Sodium Hydride

nm Nanometer

NMM N-methylmorpholine

NMR Nuclear Magnetic Resonance

OH Hydroxyl Group

Phe Phenylalanine

PyBoP Benzotriazol-1-yloxytriPyrrolidinophosphonium hexafluoroPhosphate

RPM Round Per Minute

RT/rt Room Temperature

Sq. Squaratide

TBAF Tetrabutylammonium fluoride

tBu tert-butyl

TEA Triethyl amine

TFA Trifluoroacetic acid

UV – vis Ultraviolet-Visible

Chapter 1

Introduction

1: Introduction

1.1: Introduction to Supramolecular Chemistry

The realm of supramolecular chemistry is a fascinating field of research that transcends the traditional boundaries of molecular science by focusing on the interactions and assemblies of molecular entities. Often described as "chemistry beyond the molecule," supramolecular chemistry delves into the formation of complex structures through non-covalent interactions, such as hydrogen bonding, Van der Waals forces, π-π stacking, and coordination interactions. These weak yet highly specific and unique forces enable the self-assembly of molecules into organized structures with distinct properties and functions. [1]

A cornerstone of supramolecular chemistry is host-guest chemistry, a concept central to understanding molecular recognition and interaction. Host-guest chemistry involves the specific binding of a "host" molecule to a complementary "guest" molecule, driven by shape, size, and interactive complementarity. These interactions are highly selective and reversible, relying on weak non-covalent forces for the formation of stable complexes, which will be the fundamental theme of this thesis.

Pioneered by Nobel laureates Jean-Marie Lehn[2], Donald Cram[3], and Charles Pedersen[4], in 1987 "*for their development and use of molecules with structure-specific interactions of high selectivity*". Their pioneering work on cation-selective molecular receptors spurred extensive research and fuelled the rapid growth of the field. Remarkably, within a year of Pedersen's development of crown-ether cation receptors, Park and Simmons synthesized the first abiotic anion receptor, capable of recognizing halides in aqueous trifluoroacetic acid (TFA) (Figure 1.1).[5] Since then, supramolecular chemistry has established itself as an accepted discipline in the field of chemistry which has evolved to include dynamic covalent chemistry and stimuli-responsive systems.

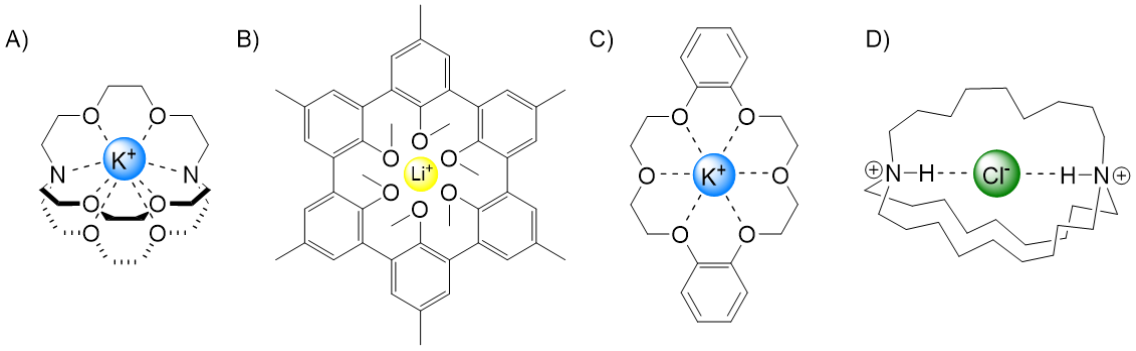

Figure 1.1: Early examples of ion receptors. a) Lehn's [2,2,2] cryptand Potassium receptor; b) Cram's spherands for Lithium recognition; c) Pederson's dibenzo-18-crown-6 that acts as a receptor for Potassium; and d) Park and Simmons's seminal "Katapinate" Chloride receptor.

Supramolecular chemistry acts as a host for a variety of applications in drug delivery, sensors, catalysis, and nanotechnology, offering a platform for the creation of smart and adaptive systems. By leveraging the self-assembly and recognition capabilities of molecules, researchers aim to create innovative solutions for global challenges, including sustainability, medicine, and energy.[6] This interdisciplinary field continues to inspire new ways of thinking about molecular architecture and function, embodying a synergy of fundamental science and practical innovation whereby we plan to with our best efforts, represent the intrinsic beauty of supramolecular chemistry throughout this thesis.

1.1.2: Molecular Recognition

Supramolecular chemistry and molecular recognition are intrinsically interconnected, with molecular recognition forming the foundational principle of supramolecular systems (Figure 1.2).[7] Molecular recognition refers to the ability of one molecule (the receptor or host) to selectively interact with another molecule (the substrate or guest) through non-covalent interactions such as hydrogen bonding, van der Waals forces, electrostatic attractions, and π-π interactions. This selective interaction enables the formation of stable, yet reversible, complexes that are fundamental to the behaviour of supramolecular systems.[8, 9]

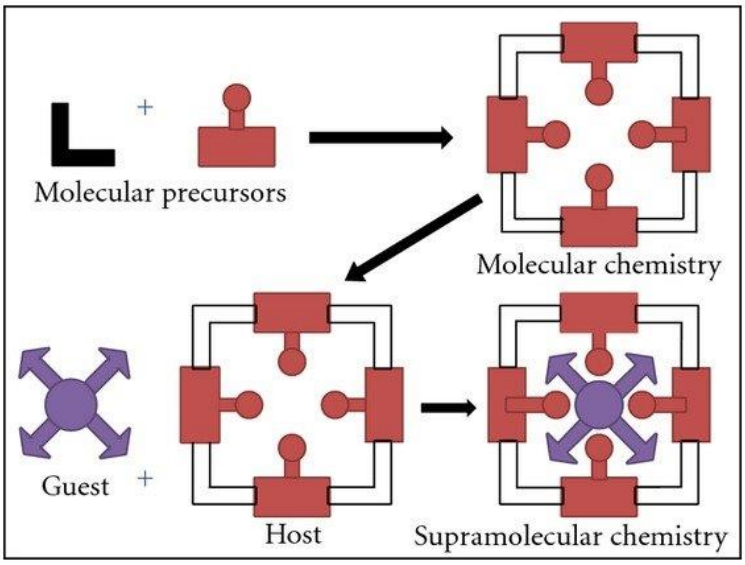

Figure 1.2: Comparison between the scope of molecular and supramolecular chemistry according to Lehn.[7]

Supramolecular chemistry extends this concept by studying how molecular recognition processes can be designed, controlled, and applied in complex systems. Host-guest chemistry, a core aspect of supramolecular chemistry, epitomizes molecular recognition in action. Hosts are typically designed with specific geometric and electronic features that complement the shape, charge, or chemical properties of their guest targets.[9, 10] This complementarity ensures selective binding, mimicking natural systems such as enzyme-substrate interactions or antibody-antigen recognition.[11]

The synergy between supramolecular chemistry and molecular recognition has enabled advancements in various fields [6] such as biological mimicry: Supramolecular systems emulate molecular recognition in biological processes, such as ion transport across membranes or DNA base pairing, providing insights into the fundamental principles of life.[12] Material design: Molecular recognition is used to develop functional materials like molecular sensors, catalysts, and self-healing polymers, where precise interactions dictate material properties.[13] Environmental and industrial applications: Selective molecular recognition is exploited for detecting and binding pollutants, separating mixtures, or catalysing specific chemical reactions with high efficiency.[14-16]

In essence, molecular recognition serves as the "language" through which supramolecular chemistry operates, enabling the design of highly selective and functional systems. This interplay not only deepens our understanding of chemical interactions but also drives innovation in diverse scientific and technological arenas.

1.1.3: Anion Recognition – Physiological Importance

The International Union of Pure and Applied Chemistry (IUPAC) defines an anion as a "monoatomic or polyatomic species possessing one or more elementary charges of the electron." Anionic atoms and molecules play a prevalent role in daily life as part of numerous environmental, chemical, and biological processes.[17-20]

For example, anions are ubiquitous in the environment, appearing in various forms, from the abundance of chloride ions in oceans to sulfates in acid rain and nitrates in soil. These chemically significant entities are utilized in numerous applications, such as fluoride in toothpaste to prevent dental decay and phosphate as a masking agent in prodrug development. In aqueous systems, the ability to bind and sequester anions is of great interest, with applications ranging from enhancing organocatalysis to removing harmful anionic pollutants from industrial or radioactive waste.

From a biological perspective, anions are not only crucial for maintaining cellular pH[21] and volume[22], but they also contribute to the formation of membrane potentials, which facilitate the propagation of electrical signals through our nervous system, as well as numerous cellular and systemic functions that are fundamental to life.

For example, iodide is an essential trace element required for various physiological functions, most notably the production of thyroid hormones. These hormones regulate metabolism, growth, and development, making iodide critical for maintaining overall health as it can serve as an indicator for thyroid cancer.[23] deficiency and low levels of iodide can result in various diseases such as Goitre and Hypothyroidism. In turn, an excess of iodide can result in Hyperthyroidism and autoimmune thyroid diseases like Hashimoto's thyroiditis or Graves' disease. [24]

Chloride anions are among the most abundant ions in biological systems and play a critical role in maintaining physiological and biochemical functions.[25] As a major

extracellular anion, chloride is essential for processes ranging from maintaining osmotic balance and acid-base homeostasis to facilitating signal transmission in the nervous system.[26] For example, chloride channels, such as the cystic fibrosis transmembrane conductance regulator (CFTR), regulate the movement of chloride ions across cell membranes. Dysfunctions in these channels can lead to diseases like cystic fibrosis, characterized by thick mucus secretions due to disrupted ion transport.[27] In addition to this, chloride ions, alongside sodium and potassium ions, are crucial for maintaining the osmotic pressure of extracellular fluids. This regulation is vital for Kidney Function whereby chloride is reabsorbed in the renal tubules to regulate the salt balance, a process essential for fluid homeostasis and waste excretion, an imbalance of chloride can result in Bartter syndrome, *an autosomal recessive disorder of salt reabsorption.*[28, 29]

Sulfate anions are vital components of biological systems, contributing to a diverse range of physiological functions and biochemical processes.[30] As the oxidized form of sulfur, an essential element for life, sulfate plays a crucial role in cellular structure, metabolism, and detoxification. Its versatility stems from its ability to form stable bonds and participate in various chemical reactions essential for maintaining health and homeostasis.[31] Sulfate is a key structural component of biomolecules such as glycosaminoglycans, including heparan sulfate and chondroitin sulfate, which provide mechanical support to tissues, mediate cell signalling, and regulate enzymatic activity.[32, 33] It also serves as a detoxification agent in the liver, where it conjugates with drugs and toxins to enhance their water solubility for excretion.[34] Additionally, sulfate contributes to the formation of connective tissues, bone mineralization, and cartilage development, underscoring its importance in skeletal health.[35] Disruptions in sulfate levels can result in several health issues such as Impaired detoxification, leading to toxin accumulation. Abnormal cartilage and connective tissue development and increased susceptibility to oxidative stress due to reduced synthesis of sulfur-containing antioxidants like glutathione; all of which can cause diseases such as Diastrophic Dysplasia: A genetic disorder caused by mutations in sulfate transporters, leading to abnormal skeletal development, and oxalate imbalance: Defective sulfate transport resulting in excessive oxalate, contributing to kidney stone formation.[36-38]

Phosphate anions are indispensable to life, serving as critical components in energy transfer, cellular signalling, and structural integrity[39]. As one of the most versatile and reactive ions in biological systems, phosphate plays a central role in maintaining cellular function and homeostasis. Its ability to form stable bonds while participating in dynamic processes makes it a cornerstone of metabolic and biochemical pathways.[40, 41]

Phosphate is perhaps best known for its role in energy metabolism, as it forms part of adenosine triphosphate (ATP), the universal energy currency of cells.[42] Consisting of an adenosine molecule (adenine attached to ribose) bonded to three phosphate groups. These phosphate groups are linked by high-energy phosphoanhydride bonds. The hydrolysis of ATP, where a terminal phosphate group is cleaved to form adenosine diphosphate (ADP) or adenosine monophosphate (AMP), releases a significant amount of free energy (Figure 1.3). This energy powers numerous cellular processes, such as, muscle contraction, active transport of ions and molecules across membranes, biosynthesis of macromolecules (proteins, nucleotides, and polysaccharides) and signal transduction pathways. [43, 44]

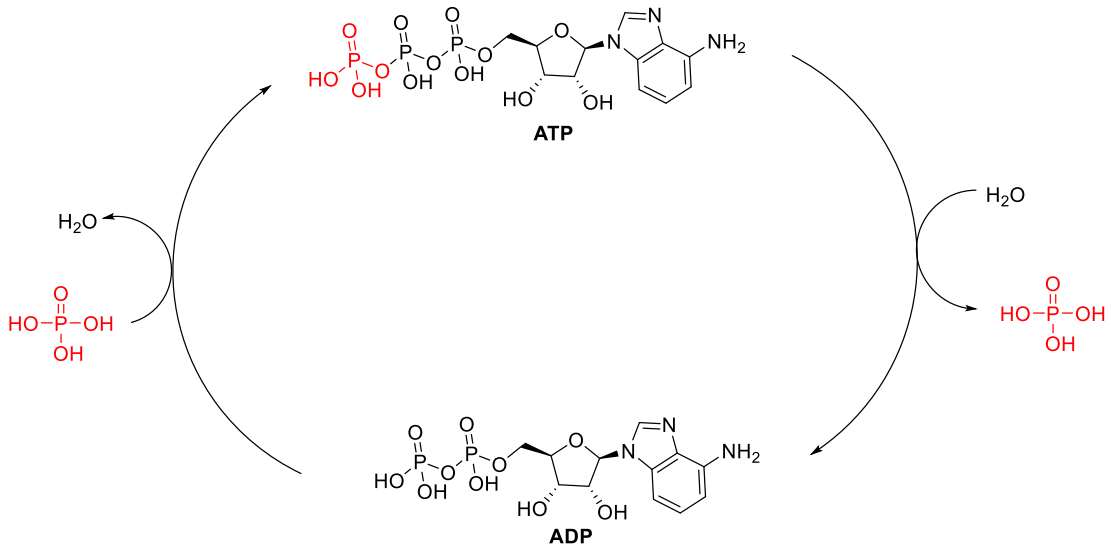

Figure 1.3: ATP Hydrolysis cycle.

Phosphate is the fundamental structural component of Deoxyribonucleic acid (DNA) and ribonucleic acid (RNA), which are nucleic acids responsible for storing and transmitting the genetic instructions essential for the development, growth, and reproduction of all living organisms.[45] Both DNA and RNA are composed of nucleotides, which are repetitive

units consisting of a nitrogenous base covalently attached to a ribose or deoxyribose sugar, further linked to a phosphate group. The ribose/deoxyribose sugar and phosphate form the structural backbone of DNA and RNA, with each phosphate serving as a bridge between adjacent sugar units and their associated nitrogenous bases through phosphodiester bonds. (Figure 1.4). The negative charge on phosphate groups repels nucleophiles and protects the DNA and RNA backbone from hydrolytic cleavage, ensuring the durability of genetic material. In RNA molecules, phosphate groups facilitate folding into complex structures required for functions such as catalysis (ribozymes) and protein synthesis (ribosomal RNA).[46] It also relies on the phosphate backbone for maintaining stability in cellular environments.[47]

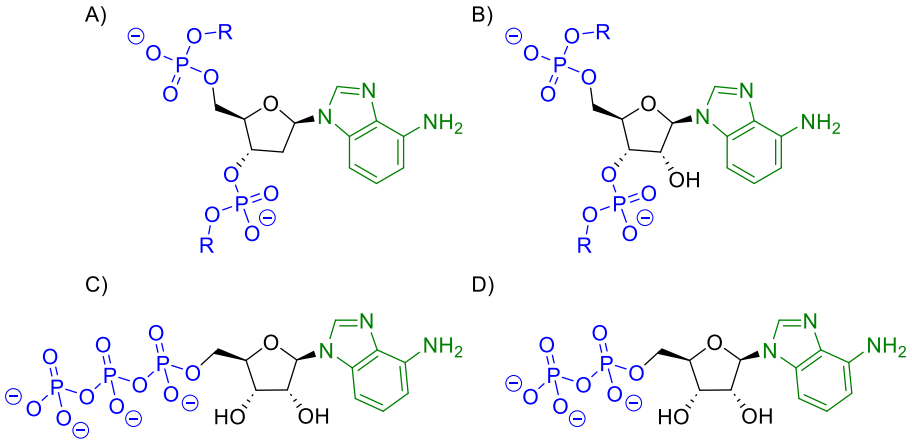

Figure 1.4: The structures of adenine-derived DNA, and RNA, ATP, and ADP (counterions omitted for clarity); a) Structure of one adenosine DNA subunit (R = additional DNA subunits), b) Structure of one adenosine RNA subunit (R = additional RNA subunits), c) Adenosine tri-phosphate (ATP), d) Adenosine di-phosphate (ADP).

The examples above highlight the breadth and diversity of anionic species that play essential roles in biological systems. From energy production to membrane construction, anions are indispensable for life. The subsequent section will explore the intricate challenges associated with anion binding, strategies employed by nature to bind and recognize anions, and examples of early anion binding receptors.

1.2: Challenges Associated with Anion Binding

The molecular recognition and transport of anions have garnered significant interest among supramolecular chemists, particularly in the field of medicinal chemistry.

Designing receptors capable of selectively binding and facilitating anion transport across biological membranes holds therapeutic potential, particularly for treating channelopathies and cancer. However, creating selective anion receptors and transporters presents numerous challenges due to the structural and chemical diversity of anions.

Unlike cations, which are generally spherical, anions exhibit a wide range of geometries, such as spherical (halides), linear (azide), bent (nitrite), trigonal-planar (carbonate, nitrate), tetrahedral (phosphate, sulfate), and octahedral (hexafluorophosphate) (Figure 1.5).[48] This structural complexity increases the difficulty of designing effective receptors. Furthermore, anions are typically larger than cations, leading to a lower charge-to-radius ratio, which weakens the electrostatic and hydrogen-bonding interactions between the host receptor and the anion guest.[19] These factors necessitate a rational design approach, wherein chemists create preorganized binding pockets specifically tailored to the target anion.

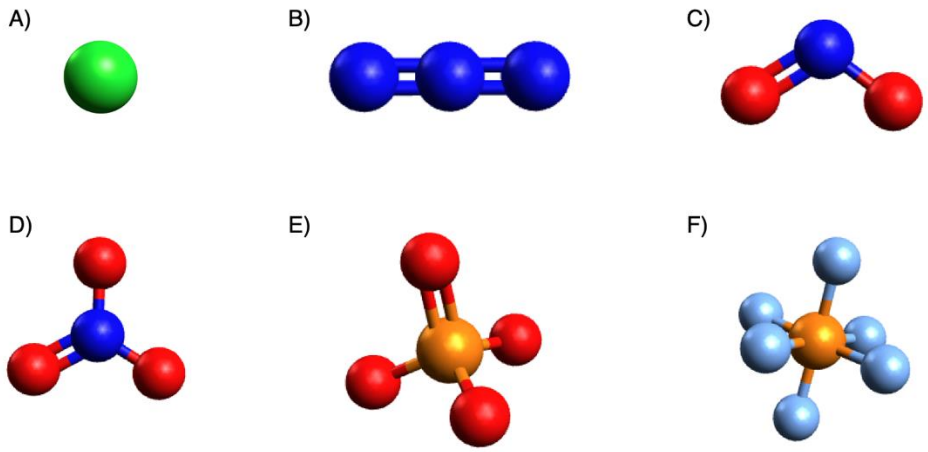

Figure 1.5: The various adopted geometries of common anionic species; a) Spherical, b) Linear, c) Bent, d) Trigonal-planar, e) Tetrahedral, f) Octahedral.

The pH-dependence of anion recognition adds another layer of complexity. Anions often exist in multiple protonation states and can undergo protonation when the pH decreases. For receptors that rely on positively charged hydrogen-bond donors, such as ammonium or guanidinium groups, effective recognition is contingent on both the anion being deprotonated and the receptor being protonated within a specific pH range (Figure 1.6). Outside this "pH window," the interaction is significantly weakened or

entirely disrupted. Additionally, basic anions such as acetate, phosphate, and fluoride can deprotonate receptors if the receptor's hydrogen-bond donors are sufficiently acidic.[49] For example, thiosquaramide-based receptors exhibit pH-dependent transport across phospholipid bilayers; their ability to transport anions "switches off" above pH 7 when the receptor is deprotonated and "switches on" at lower pH values, where the receptor regains its protonated and functional form.[50]

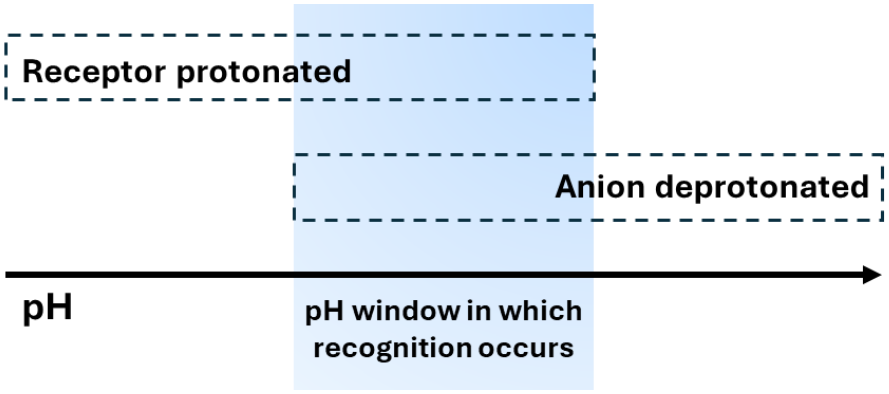

Figure 1.6: Schematic representation of the narrow pH window in which an anion recognition process occurs for a pH-dependent receptor

Another critical factor in anion recognition is the impact of solvation.[51] In aqueous environments, Interactions between anions and dissolved anion receptors are predominantly influenced by the anion's charge density and hydration enthalpy. Strongly hydrated anions, such as F^- and SO_4^{2-}, disrupt hydrogen bonding between organic solutes and water by polarizing adjacent water molecules, which promotes solute aggregation resulting in significant dehydration energy penalties during binding.[19, 52] This solvation effect is strongly correlated with the Hofmeister series, where anions with higher charge density exhibit stronger hydration and lower lipophilicity (Figure 1.7).[53] Consequently, for effective recognition, receptors must overcome these thermodynamic barriers and possess sufficient affinity to offset the large energy cost of dehydration. While Receptors with buried, hydrophobic binding sites are optimal for weakly hydrated anions, those with exposed binding sites can better accommodate strongly hydrated anions.[54]

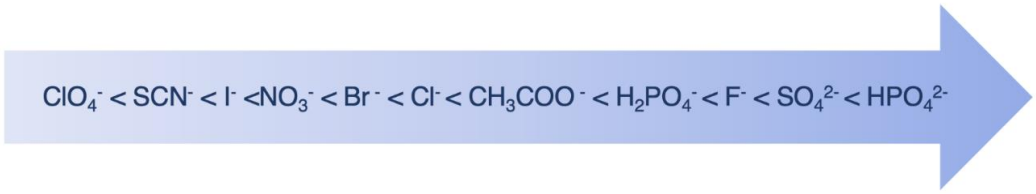

Figure 1.7: The Hofmeister series of anion hydrophobicity in order of increasing hydration.

Together, these challenges underscore the complexity of designing anion receptors and transporters. By addressing issues such as geometric diversity, solvation, pH sensitivity, and binding energy, supramolecular chemists continue to advance the field, with potential applications in medicine, environmental remediation, and molecular sensing.

1.3: Natural Anion Binding Receptors

When designing receptors for anions, supramolecular chemists frequently draw inspiration from nature. Biological anion receptors are known for their exceptional binding strength and selectivity, prompting efforts to replicate these intricate architectures using synthetic host systems. Notable examples of natural anion receptors include sulfate-binding proteins (SBP), phosphate-binding proteins (PBP), apotransferrin, and chloride ion-channel proteins (CIC), which showcase nature's sophisticated strategies for anion recognition and transport.

1.3.1 Anion Binding Proteins

Anion-binding sites within proteins leverage various non-covalent interactions to target specific anions. A common strategy involves electrostatic interactions between negatively charged anions and cationic residues in the protein. For instance, arginine residues bind to phosphate and guanine in TAR RNA through a mechanism known as the "arginine fork," (Figure 1.8) where the guanidinium NH groups serve as dual hydrogen bond donors, interacting with both the phosphate and guanine.[55, 56]

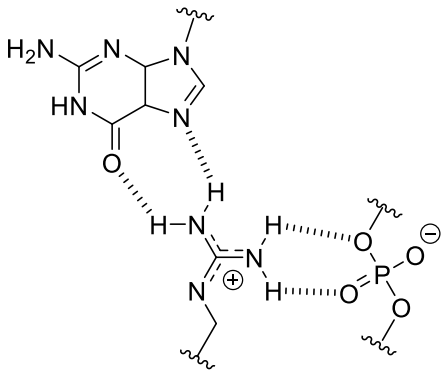

Figure 1.8: Arginine binding to phosphate and guanine of TAR RNA.24.

Amino acids such as arginine, lysine, histidine, and serine (Figure 1.9) are frequently utilized in binding regions due to their side chains, which feature functional groups like hydroxyl, amino, and imidazole capable of forming hydrogen bonds with anionic species.[57]

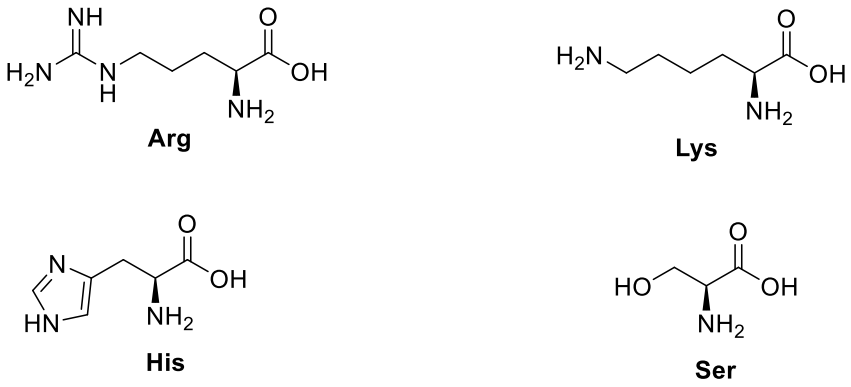

Figure 1.9: Arginine, lysine, histidine and serine – the most common amino acids that use their side chain for anionic binding.

In many cases, the peptide backbone itself forms the binding site, with amide NH groups participating in hydrogen bonding with the substrate. For example, apotransferrin, a specialized iron transport protein, plays a crucial role in the cellular uptake and distribution of Fe(III) through a unique anion-mediated cation binding process. Spectroscopic and kinetic studies indicate that the initial step involves the binding of a carbonate anion (CO_3^{2-}) to its anion-binding site, which exhibits high affinity for this substrate.[58] The carbonate-binding site is composed of a positively charged arginine residue (Arg-121) and amide NH groups from the peptide backbone, enabling hydrogen

bonding with the carbonate anion. This initial interaction facilitates subsequent cooperative binding of Fe(III), as the carbonate neutralizes positive charges that might otherwise repel the cationic iron.[59] Additionally, the carbonate provides two oxygen atoms that act as ligands, further enhancing iron coordination and transport. It is also hypothesized that protonation of the bound carbonate may be the trigger for iron release from the binding site, underscoring the dynamic and cooperative nature of this anion-cation binding mechanism.[60]

The sulfate-binding protein (SBP) (Figure 1.10), one of the most well-known anion-binding proteins, is found in the gram-negative bacterium *Salmonella typhimurium*.[61] First characterized structurally by Pflugrath and Quiocho in 1988, SBP exemplifies highly selective anion recognition.[62] Sulfate is bound approximately 8 Å deep within a cavity formed at the intersection of two globular protein domains, effectively shielding it from bulk solvent. Notably, the binding pocket lacks positively charged residues, relying solely on a network of seven neutral hydrogen bonds for sulfate recognition. These bonds include five from the main chain peptide NH groups, one from the hydroxyl group of a serine residue, and one from the indole NH group of a tryptophan side chain. This precise arrangement, maintained by the rigid folding of the polypeptide backbone, ensures geometric fidelity, and confers an impressive association constant of approximately 10^6 M^{-1} in aqueous environments at pH 5–8.1.

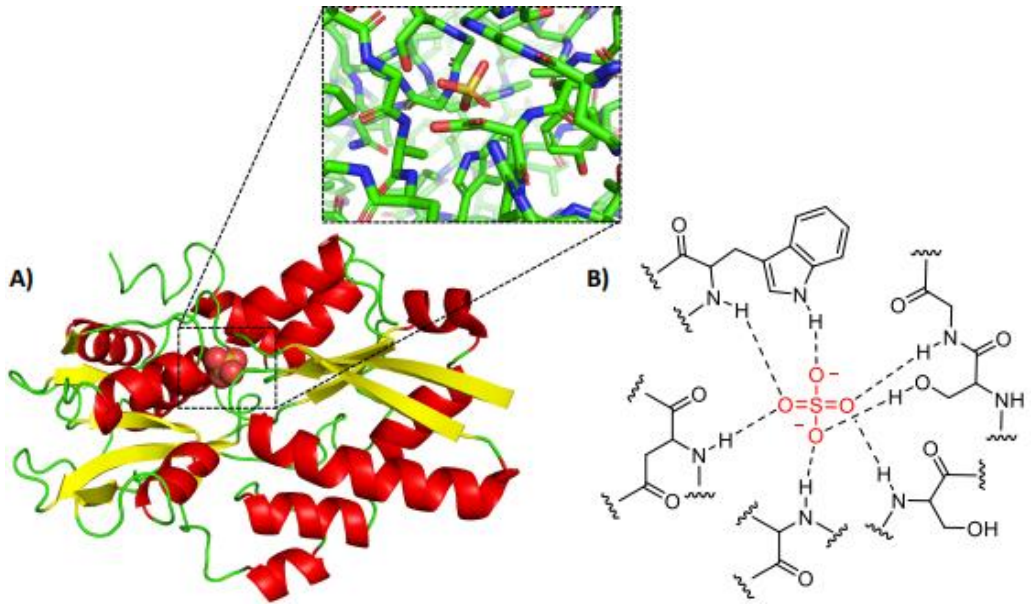

Figure 1.10: The Structure and binding pocket of bacterial SBP. A) X-ray crystal structure of SBP from *S. typhimurium,* showing secondary structure and a magnified view of the relevant SO_4^- binding cleft. B) Schematic representation of key H-bonds between SO_4^- and SBP binding cleft.

The selective binding of sulfate by SBP contrasts with other bacterial anion-binding proteins, such as phosphate-binding protein (PBP), which exhibits a similarly high affinity for hydrogen phosphate with an association constant of $3.2 \times 10^6\ M^{-1}$. PBP uses a more complex network of 12 hydrogen bonds, including nine neutral donors, two derived from the positively charged Arg-135 residue, and one acceptor from Asp-56 (Figure 1.11). This unique acceptor motif contributes significantly to PBP's exceptional selectivity for hydrogen phosphate. Unlike PBP, SBP's neutral hydrogen bond network effectively minimizes unfavourable electrostatic repulsion, enabling the efficient binding of the fully deprotonated, tetrahedral sulfate anion within its solvent-inaccessible pocket.[63]

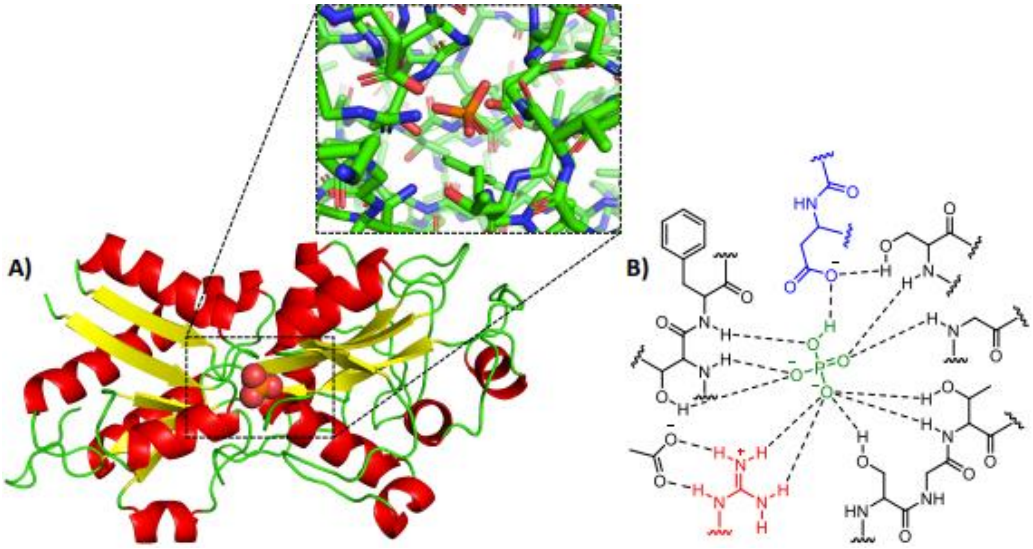

Figure 1.11: The Structure and binding pocket of bacterial PBP.[30] A) X-ray crystal structure of PBP (p.Ala197Trp) from *E. coli,* showing secondary structure and a magnified view of the relevant SO_4^- binding cleft. B) Schematic representation of key H-bonds between $H_2PO_4^-$ and PBP binding cleft.

Chloride ion channel (CIC) proteins in *Escherichia coli* (*E. coli*) and *Salmonella typhimurium* are specialized for the selective transport of chloride ions (Cl^-) across the cell membrane. The binding site within these channels forms a narrow pore that facilitates chloride movement while ensuring specificity.[64] The coordination of Cl^- involves four hydrogen bond donors: two NH groups from the amide backbone of Phe-3 and Ile-356, and two OH groups from the side chains of Tyr-445 and Ser-107. These interactions tightly encapsulate the chloride ion, stabilizing it within the channel. Additionally, hydrophobic contacts between the chloride and the surrounding protein structure further enhance binding stability.[21] This precise arrangement of hydrogen bonding and hydrophobic interactions allows CIC proteins to selectively and efficiently transport chloride ions, playing a critical role in maintaining cellular ionic balance and supporting cellular functions.

As demonstrated in the examples above, nature utilizes hydrogen bonds to recognize and bind anionic species. The precise arrangement of binding motifs is crucial for achieving both strong and selective binding. These principles serve as key considerations in the design of synthetic anion receptors.

1.4: Synthetic Anion Receptors

Synthetic supramolecular chemists have long sought inspiration from nature in designing anion recognition receptors. However, recent advancements have marked a decisive shift toward fully synthetic systems with entirely abiotic motifs. These innovative receptors are equipped with structural features tailored to enhance their ability to recognize and bind anions efficiently across diverse environments.

Anion receptors are highly specialized molecules that selectively interact with anionic species through non-covalent interactions, such as hydrogen bonding, electrostatic forces, π-stacking, and coordination bonds.[65] Over the past two decades, the field has seen dramatic progress, with the development of a vast array of selective receptors and sensors. These advances have been driven by the critical applications of anion receptors in environmental science, biology, and materials technology.[66] This continuous pursuit has spurred significant innovation in receptor design and synthesis.

Current research focuses on enhancing the selectivity of anion receptors in challenging environments, such as highly competitive aqueous solutions, and designing multifunctional receptors that can perform dual roles, such as simultaneous anion binding and catalytic activity.[67-69] Additionally, the integration of anion receptors into smart materials and nanodevices has opened exciting new frontiers in areas like advanced sensing, environmental remediation, and therapeutic applications.[70, 71] These developments highlight the transformative potential of synthetic anion receptors in both fundamental science and practical applications.

1.4.1: Early Examples of Abiotic Anion Receptors

The development of anion receptors marked a significant milestone in supramolecular chemistry, driven by the challenge of designing molecules capable of selectively binding negatively charged species. Early examples laid the foundation for the field by demonstrating the principles of anion recognition and providing the first abiotic systems to achieve this feat. These pioneering receptors showcased the ability to bind anions using non-covalent interactions, such as hydrogen bonding and electrostatic forces, often inspired by biological systems.

One of the earliest milestones in anion receptor chemistry was achieved by Park and Simmons in 1968, by which they developed an ammonium-based macrobicyclic receptor, noted as the first synthetic anion receptor (Figure 1.12).[5] This receptor was specifically designed for halide recognition whereby the protonated amines of these receptors pointing into the cavity in addition to the cationic ammoniums forms a binding pocket, in which chloride binds with K_a = 4 M^{-1}. Inspired by the emerging success of crown ethers for cation recognition, this system demonstrated the feasibility of binding negatively charged species using a complementary host structure. The receptor utilized hydrogen bonding interactions, which became a cornerstone of anion receptor design.

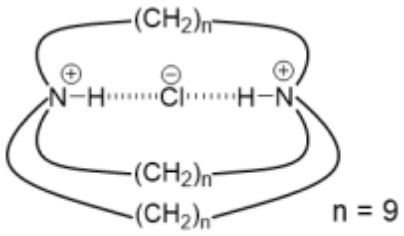

1.1

Figure 1.12: Structure of ammonium-based macrobicyclic receptor synthesised by Simmons and Park.

In 1976, Eight years after the work published by Park and Simmons, Graf and Lehn expanded the range of ammonium-based anion receptors by synthesizing **1.2** (Figure 1.13), a cryptand composed of four fused triaza[18]crown-6 rings.[72] In its tetraprotonated state, **1.2** forms four hydrogen bonds with chloride ions (Cl^-), further stabilized by electrostatic interactions with the ammonium groups. This receptor demonstrated selectivity for Cl^- over bromide (Br^-), as the larger size of bromide creates a poor fit for the macrotricycle's cavity. While receptor **1.2** is perfectly spherical, offering excellent complementarity for spherical anions, in 1982 Graf and Lehn synthesised a hexaprotonated macrobicyclic ligand (**1.3**) , which has an elliptical geometry optimized for linear anions (Figure 1.13).[73, 74] As a result, **1.3** exhibits significantly lower binding affinity for Cl^- (log K_a < 1.0) compared to linear azide (N_3^-) (log K_a = 4.6), reflecting the geometric compatibility between the receptor and the respective anions.

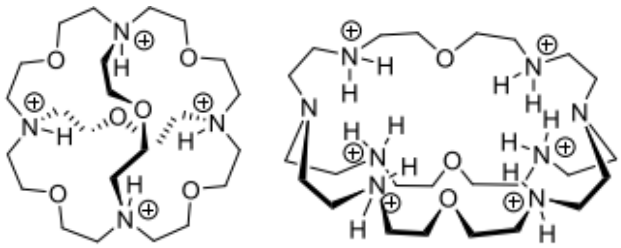

1.2 1.3

Figure 1.13: Structure of cryptand 1.2 and 1.3 synthesised by Graf et al.

In his early work, Schmidtchen synthesized the macrotricyclic quaternary ammonium hosts **1.4** and **1.5**, demonstrating their ability to form complexes with a variety of anions in aqueous environments (Figure 1.14).[75, 76] Receptor **1.4**, with an internal cavity diameter of 4.6 Å, strongly binds iodide ions (diameter: 4.12 Å) that showed to be fully encapsulated within the macrotricycle , as evidenced by the X ray crystallography. By varying the length of the alkyl chain between the quaternary ammonium groups, the size of the cage could be tuned to accommodate halide anions of different sizes. This was shown by the larger receptor **1.5** as it could accommodate anions such as p-nitrophenolate, which are too large to bind within receptor **1.4**.

Both receptors **1.4** and **1.5** are positively charged, necessitating the presence of counterions that can compete with the anionic guests for binding. To address this, Schmidtchen developed zwitterionic receptors, such as **1.6** and **1.7**, which are neutral and mitigate counterion competition.[77, 78] NMR studies in water revealed that receptor **1.7** forms stronger complexes with chloride, bromide, and iodide ions compared to receptor **1.4**, highlighting its enhanced binding capabilities.

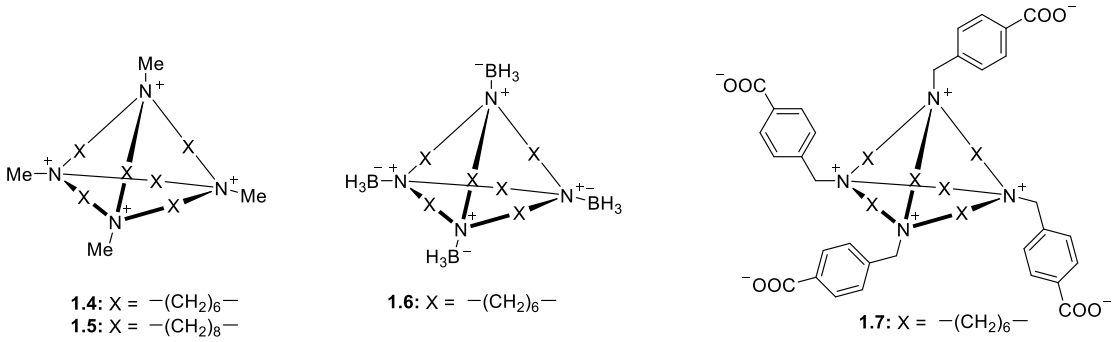

Figure 1.14: The macrotricyclic quaternary ammonium receptors 1.4 - 1.7 reported by Schmidtchen and co-workers.

1.5: Design Considerations for Synthetic Anion Receptors

Association constants (K_a) are a critical parameter for synthetic anion receptors in evaluating the efficiency and strength of anion binding by synthetic receptors. These constants quantify the equilibrium between free and bound anions, providing insight into the receptor's affinity for specific anions under a given solvent.[79] A high association constant indicates a strong interaction between the receptor and the anion, which is essential for applications such as sensing, catalysis, environmental remediation, and drug delivery. The relationship between the rates of association (K_1) and dissociation (K_{-1}) and the binding constant (K_a) can be described by several key equations.

$$K_a = \frac{1}{K_d} = \frac{K_1}{K_{-1}} \qquad K_1 = \frac{[HG]}{[H][G]} \qquad K_2 = \frac{[HG_2]}{[H][HG]}$$

These equations account for different binding scenarios, such as primary (1:1) binding events, where a single receptor binds a single anion (K_1), and secondary (1:2) binding events, where one receptor binds two anions (K_2). In these models, Ka represents the equilibrium constant for association, K_d is the dissociation constant, H and G represent the host and guest respectively, and HG or HG2 denote the formed host-guest complexes. Comparison of K_a values across different anions provides insight into the receptor's selectivity. Receptors with significant differences in K_a for competing anions

can differentiate between targets in complex mixtures, a crucial feature for applications like sensing and therapeutic agents.

Association constants serve as a clear thermodynamic measure of anion binding reflecting the delicate balance between energetic contributions that drive and opposed binding. Analysing the thermodynamic parameters—enthalpy (ΔH), and entropy (ΔS), provides deeper insights into the anion recognition process and guides the design of an effective anion receptor.[80] With that being said, these receptors must be tailored to achieve high affinity and selectivity for target anions, often under challenging conditions such as competitive aqueous environments, and so several structural and functional factors can influence the binding process, affecting the balance between enthalpic and entropic contributions that determine the overall K_a.

Preorganization is a fundamental design strategy in supramolecular chemistry that aims to enhance the binding affinity of anion receptors by reducing the structural and energetic penalties associated with the binding process.[81] In the context of anion receptors, preorganization refers to designing receptors with rigid, prearranged binding sites that complement the size, shape, and charge distribution of the target anion ensuring that the receptor is "ready" to bind the target anion without requiring significant conformational changes. This principle, introduced by Donald J. Cram, contrasts with "induced fit," where the receptor adapts its structure upon binding.[82] This approach minimizes the entropic and enthalpic costs of binding, leading to higher association constants (Ka) and improved efficiency in anion recognition.

An example of effective preorganisation by an anion receptor can be seen by S. Kaabel et. al. where they reported a comprehensive study on the anion binding properties of a hemicucbit[b]uril derivative, a chiral (all-R)-cyclohexanohemicucurbit[8]uril (**1.8**) in protic solvents with exceptional selectivity (Figure 1.15).[83] The binding selectivity of **1.8** towards different anions tested in methanol is governed by their size, shape, and charge distribution. The association constants for anion binding vary over five orders of magnitude, with the strongest binding observed for the largest tested octahedral anion SbF_6^- (K_a = 2.5 x 10^5 M^{-1}) and weakest binding observed for the smallest octahedral anion BF_4^- (K_a = 4.8 x 10 M^{-1}). Halides on the other hand showed very weak complexation

presumably due to a mismatch in size with the cavity. These results demonstrate the strong size dependency of their anion binding properties. Also, the symmetric, receptor cavity-matching charge distribution of the anions leads to significantly stronger binding compared to anions with asymmetric charge distribution. This is because symmetric charge distribution enables the formation of a greater number of hydrogen bonds simultaneously, resulting in stronger binding.

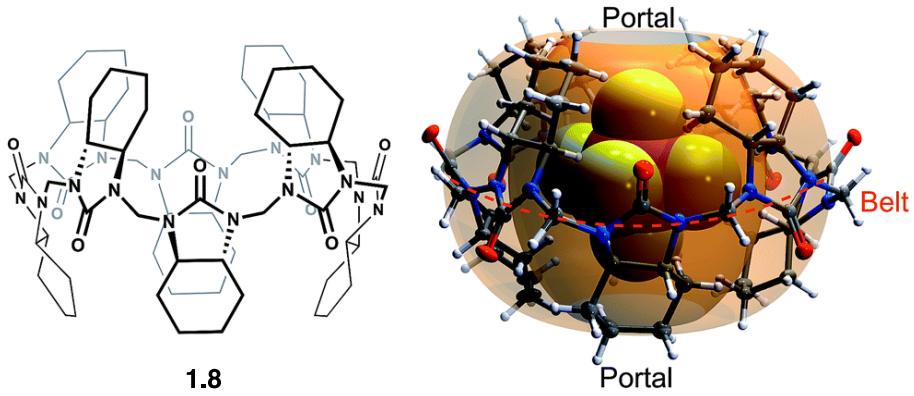

1.8

Figure 1.15: Molecular structure of (all-R)-cyclohexanohemicucurbit[8]uril, **1.8** (left), and the X-ray structure of an inclusion complex with SbF_6^- (right) reported by S. Kaabel et. al.

Another important design consideration for anion receptors is the incorporation of anion binding units (ABUs) which are functional groups or molecular motifs within synthetic receptors that directly interact with anions, forming the basis of anion recognition. These units play a pivotal role in determining the strength, selectivity, and efficiency of binding, as reflected in the association constant (K_a). Careful selection and arrangement of ABUs are crucial for optimizing anion receptors to achieve high K_a values. ABUs facilitate binding through non-covalent interactions, such as hydrogen bonding, electrostatic interactions, anion-π interactions, and coordination with metal centres. Their effectiveness depends on their strength, geometry, and complementarity to the target anion. The arrangement of ABUs determines how well the receptor complements the anion's shape and size. Poor alignment leads to weak binding and lower K_a. Hydrogen bonding being the most widely used interaction in anion recognition has led to a plethora of ABUs that have been incorporated into anion receptors such as Amide, urea, thiourea, pyrrole, squaramides, and guanidinium groups.

An example of incorporating ABUs with careful arrangement to achieve high selectivity and sensitivity towards anions can be can be seen by Wang and co-workers, where they reported the assembly of a novel calix[4]arene based chemosensor **1.9,** comprising of a coumarin as a reporter and thiourea groups as the anion-binding site on the calix[4]arene framework for the recognition of fluoride via hydrogen bonding (Figure 1.16).[84] The sensor's selective and sensitive response to fluoride ions was assessed using fluorescence spectroscopy, UV–vis spectroscopy and ^{1}H NMR titrations. Chemosensor **1.9** exhibited remarkable sensitivity and selectivity towards F^- ions. The other anions tested (I^-, Br^-, CN^-, Cl^-, HSO_4^-, $H_2PO_4^-$, and CH_3COO^-) did not induce any significant changes in the absorption spectra, underscoring the sensor's selectivity for fluoride ions. ^{1}H NMR titrations conducted revealed that **1.9** forms a 1:1 complex with F^-, featuring an association constant of 2.1×10^4 M^{-1}

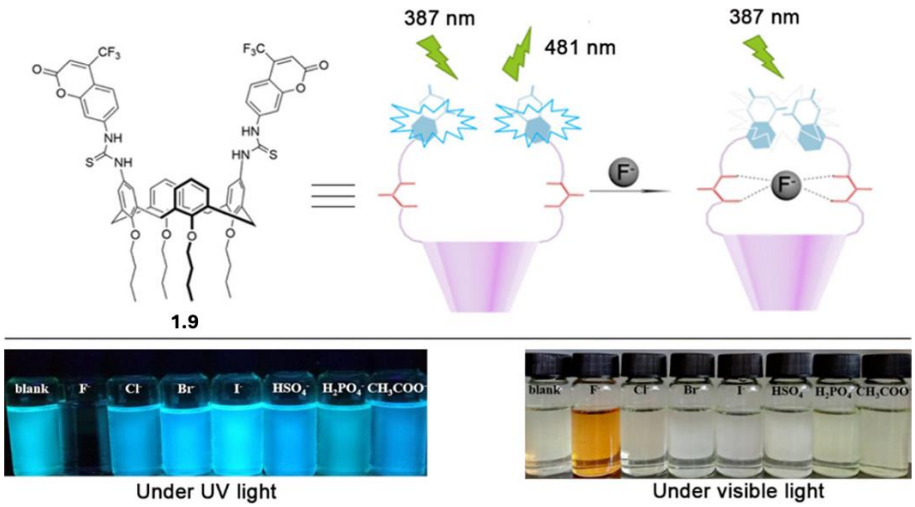

Figure 1.16: a). Schematic representation of **1.9** b). Photograph of visible fluorescence emission responses of **1.9** in the presence of various anions (indicated) under UV lamp (365 nm) and visible light, reported by Wang and Colleagues.

As from the examples mentioned above, the combination of preorganization and well-designed ABUs are important design considerations which results in receptors with significantly enhanced K_a. Preorganization ensures that ABUs are optimally positioned to interact with the anion, while ABUs provide the necessary functional interactions for strong and selective binding.

1.6: Macrocyclic Anion Receptors – Advantages

macrocyclic receptors in particular have emerged as promising scaffolds in this domain of supramolecular chemistry.[85, 86, 87] Already recognised for their applications in drug-delivery systems, supramolecular polymers and molecular machines and devices, their role in anion recognition stands out prominently,[88] where their ability to bind selectively to specific anions through size and shape complementarity has led to their application in various fields, including environmental monitoring for the detection of environmentally relevant anions, such as nitrate, phosphate, and chloride, to monitor water quality and pollution levels. [89-91] The field of biomedical diagnostics has also exploited anion binding macrocyclic scaffolds for the recognition of biologically important anions, such as chloride, bicarbonate, and phosphate, for disease diagnosis and monitoring of physiological conditions.[92-94] Even industrial processes have begun to exploit these versatile molecules for monitoring levels of anions in chemical manufacturing and waste treatment, to ensure process efficiency and compliance with regulations.[95-97] Considering their demonstrated and potential uses, it is unsurprising that research in this area has been so pronounced in recent years.

Macrocyclic receptors possess several key features to make them highly effective for anion recognition. Most importantly, macrocyclic receptors have a preorganised structure that minimizes the entropic cost of binding. This preorganisation aligns the binding sites in a favourable conformation for interaction with the anion, enhancing binding affinity and selectivity.[98] Additionally, macrocycles contain a degree of rigidity within the framework that reduces the flexibility of the binding sites, maintaining an optimal geometry for anion interaction. This rigidity helps maintain high binding constants and reduces non-specific interactions.[99] Size matching is another key feature in the synthesis of macrocycles whereby the cavity size of the macrocycle can be tailored to match the size of the target anion. Effective size matching coupled with the three-dimensional shape of the macrocyclic cavity can be designed to complement the shape of the target anion, ensuring that the anion fits snugly within the binding cavity, maximizing interaction strength and selectivity as well as enhancing the specificity of the interaction.[100] Furthermore, multivalency is another key feature in macrocyclic receptors. The ability for macrocycles to occupy multiple binding sites within their cavity

allows for cooperative binding through exhibiting various binding interactions with anions, including electrostatic interactions, hydrogen bond formation, anion-π interactions, and halogen bonding to name but a few.[74, 101-103] Such interactions can be exploited in tandem with unique structural features together with chemical modifiability and tailored functionalisation with a vast array of functional groups to achieve exquisite selectivity.[51, 104, 105] Understanding the key features mentioned above and the nuanced interplay of binding interactions allows the design and optimisation of macrocyclic receptors for precise anion recognition, making macrocyclic receptors a valuable tool for the supramolecular chemist.

The following section will provide a review of the recent advances in the design, synthesis, and applications of macrocyclic receptors specifically tailored for anion recognition a long with various anion interactions that they possess. The unique structural features of macrocycles, such as their well-defined structures and pre-organised binding sites, contribute to their exceptional anion-binding capabilities that have led to their application across a broad range of the chemical and biological sciences.

1.7: Non-covalent Interactions via Macrocyclic Receptors

Non-covalent interactions are essential for the recognition and binding of anions by macrocyclic receptors, serving as the driving forces behind the formation of receptor-anion complexes and enabling high binding affinity and selectivity across diverse environments. As previously mentioned, macrocyclic receptors, are particularly effective platforms for anion recognition due to their preorganized structures, which allow for the incorporation of functional groups that facilitate a wide range of non-covalent interactions. These systems rely on a myriad of forces such as hydrogen bonding, electrostatics, anion-π interactions, CH hydrogen bonding, Halogen bonding and hydrophobic effects, in order to achieve precise complementarity with target anions. This discussion explores ta number of non-covalent interactions utilized by macrocyclic receptors and their implications for receptor design.

1.7.1: Hydrogen Bonding Macrocycles

Hydrogen bonding macrocycles are a class of supramolecular compounds that are designed to selectively bind and recognise specific guest molecules through hydrogen bonding interactions. These macrocycles typically consist of a cyclic array of hydrogen bond donor and acceptor groups that are arranged in a specific geometry to create a binding pocket for the guest molecule.[106, 107] Hydrogen bonds are often viewed as a dipole-dipole interaction, whereby a hydrogen atom, bonded to an electronegative atom (referred to as the donor), is attracted to the dipole of an adjacent electronegative atom (referred to as the acceptor). The strength of a hydrogen bond can vary significantly, but generally, the greater the electronegativity of the atoms on either side of the hydrogen, the stronger the bond.[108] Typically, the most common hydrogen bond donor is the N-H group, found in anion-binding units such as amides, sulfonamides, ureas, thioureas, squaramides, pyrroles, and indoles. Ureas, thioureas, and squaramides are particularly valued as anion receptors due to their dual hydrogen bond donor capabilities, which are advantageous for strong anion complexation (Figure 1.17). [109-112]

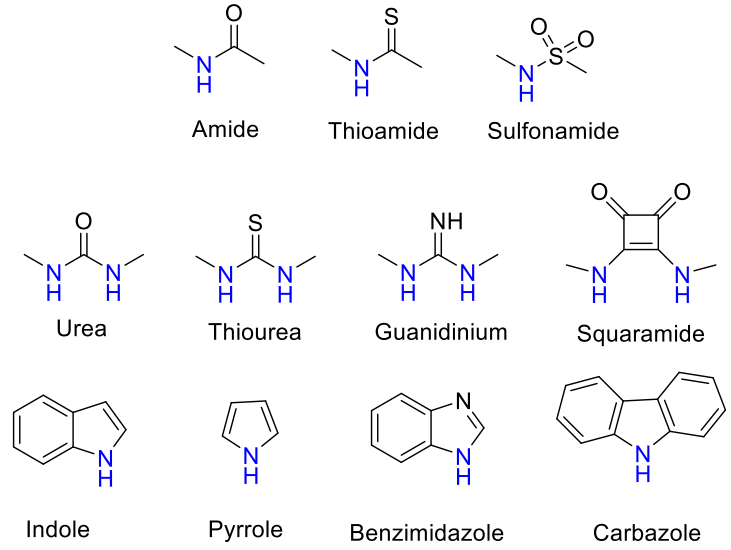

Figure 1.17: An overview of the most common NH H-bond donors utilised in anion receptor Design.

1.7.1.1: Amide – and Urea – based Macrocycles

Utilising H-bond donors for the synthesis of successful macrocyclic receptors can be seen in the work of Jolliffe and co-workers, whereby they reported a fluorescent macrocyclic receptor (**1.10**) with selective binding towards citrate via hydrogen bonding interactions in aqueous media (Figure 1.18).[113] The macrocyclic receptor comprises of a carbazole-based unit featuring three hydrogen bonding thiourea units with highly preorganization for citrate binding. ^{1}H NMR titrations carried out in 1% H_2O/DMSO-d_6 with TBA citrate revealed diverse species formation in solution. Attempts to fit the data to 1:1, 1:2, or 2:1 binding model proved unsatisfactory, yet the absence of further chemical shift changes after adding 1.6 equivalents of citrate strongly indicated robust binding. Throughout the titration, the signals associated with the receptor displayed broadness, and the resonances linked to the thiourea and carbazole NH groups exhibited downfield shifts, indicative of hydrogen-bonding interactions with citrate. A similar shift was noted for the inward-facing aromatic hydrogens of the xylyl linkers, suggesting a conformational change during citrate binding. A fluorescent screen with **1.10** along a range of dicarboxylates was carried out. Fluorescence quenching, ranging from -20% to -48%, was noted upon introducing terephthalate and various monovalent anions like benzoate, acetate, bicarbonate, nitrate, and halides. Alkyl dicarboxylates of varying lengths from oxalate (C2) to adipate (C6) and dihydrogen phosphate elicited minimal changes in fluorescence response. However, a distinct and significant fluorescence enhancement of over 90% was observed with the addition of citrate. The fluorescence maximum wavelength remained unchanged at 385 nm, while a new shoulder emerged around ~405 nm, implying the formation of a second, associated excited state complex. These studies provided insights into the selectivity of the probe for citrate over other biologically relevant dicarboxylate species and common anions.

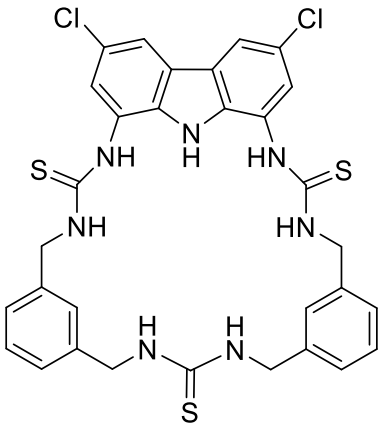

1.10

Figure 1.18: Chemical structure of macrocycle **1.10** reported by Jolliffe and co-workers.

Another example of utilising H-bond donors into macrocyclic receptors comes from Bao and colleagues whereby they reported the anion binding properties of two macrocycles containing a carbazole and two sulfonamide units that exhibit a strong propensity towards F^- binding (Figure 1.19).[114] Macrocycle **1.11** contains a 1,3-xylyl linker, while macrocycle **1.12** features a 2,6-lutidinyl linker. This difference in the linker structure leads to distinct effects on the anion affinity. ^{1}H NMR titrations demonstrated that compound **1.11**, with a 1,3-xylyl bridging unit, exhibits remarkable selectivity and binding strength for F^- in CD_3CN, outperforming competing anions such as AcO^-, Cl^-, Br^-, NO_3^-, ClO_4^-, and $H_2PO_4^-$. It showed a large binding constant (K_a) of 50,878 ± 4,721 M^{-1} in a 1:1 binding model. This could be rationalized by the cooperative binding of fluoride through the strong downfield shifts observed from the sulfonamide NHs, and carbazole NH in **1.11**. Noteworthily, this fluoride complexation was dominated by hydrogen bonding interactions under low F^- concentrations (< 2.8 equivalents). UV-vis studies were carried out for the macrocycles to confirm the binding affinities with the macrocycle for fluoride. with increasing concentrations of TBA F^-, a progressive increase in the absorption peak at 294 nm was observed for **1.11** simultaneously, two pseudo-isosbestic points were identified at 305 and 355 nm, confirming the formation of a 1:1 complex between **1.11** and F^-. The UV-vis study provided complementary evidence to the ^{1}H NMR titration study, confirming the strong and selective binding of **1.11** towards fluoride in acetonitrile solution. A decrease in the affinity was observed for **1.12** with anions F^-, H_2PO_4, and Br^-, with respective decreases of approximately 3.9-fold, 2.0-fold, and more than 2.4-fold.

Conversely **1.12** exhibited a higher affinity compared to **1.11** towards other anions such as $PhCOO^-$, CH_3COO^-, Cl^-, and HSO_4^-, with enhancements ranging from approximately 2.0-fold to over 4.2-fold. **1.11**, featuring a 1,3-xylyl linker, benefitted from the presence of an additional aromatic CH group, which served as a potential anion-binding site. Replacing the 1,3-xylyl linker with a 2,6-lutidinyl spacer in compound **1.12** likely induced some degree of preorganization for its SO_2NH protons in solution, enabled by intramolecular hydrogen-bonding interactions with the pyridine nitrogen atom. However, this replacement also led to the loss of an additional anion-binding site. Consequently, distinct changes in affinity towards various anions were observed between the two macrocycles.

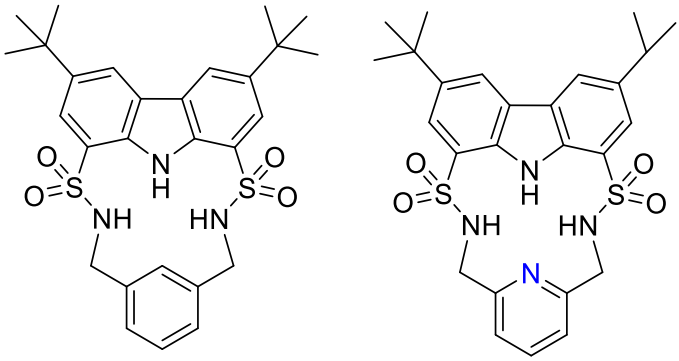

Figure 1.19: Chemical structures of macrocycles **1.11** and **1.12**. Reported by Bao and colleagues.

An example of using hydrogen bond donors for dicarboxylate binding can be seen by work carried out by Jolliffe and co-workers, where they set out to synthesise conformationally adaptable tetra thiourea macrocyclic receptors consisting of bis-carbazole units that are linked by either 1,3-xylyl (**1.16**) or 1,4-xylyl (**1.17**) groups in order to vary the macrocycles cavity shape and size as well as providing some flexibility within the structure (Figure 1.20). [115] This work gains insight into chelate cooperativity as well as exploring how these semi-flexible receptors interact with various dicarboxylate anions (Mal^{2-}, Suc^{2-}, Glu^{2-}, Adi^{2-}, Pim^{2-}, Sub^{2-}, Aze^{2-}, Ter^{2-}, ttM^{2-} and aKG^{2-}) in a competitive solvent mixture. Initially, fluorescence spectroscopy was carried out in H_2O: DMSO (1 : 9 v/v) in order to explore the spectroscopic responses of **1.16** and **1.17** whereby a quenching of fluorescence as a result of PET inhibition was observed for all dicarboxylate anions. Further investigation to measure the binding interactions and affinities between the

receptors and the dicarboxylates was carried out via UV-vis titrations. It was found that for saturated linear dicarboxylate species (Mal–Aze), **6** and **7** exhibited minor differences in binding affinity, both showing the highest affinity for the guest Adi (n = 4) with strong 1:1 binding in a competitive aqueous solvent mixture (**1.16**: K_a = 7.5 x 10^4 M^{-1}) (**1.17**: K_a = 8.7 x 10^4 M^{-1}). Despite their differing pore shapes, both macrocycles displayed similar selectivity patterns across the linear dicarboxylate series, attributed to the flexibility of the receptors. However, binding strength decreased sharply for anions larger than Adi, as they became too large to fit within the macrocyclic pores. In contrast, when binding to rigid dicarboxylates, the macrocycles differed significantly in their affinities. **1.17** bound the rigid guest Ter with a high affinity (K_a = 8.7 x 10^4 M^{-1}), while **1.16** was three times weaker (K_a = 3 x 10^4 M^{-1}), indicating that Ter is a better geometric match for **7**. A similar trend was observed with ttM, where **1.17** (K_a = 5.8 x 10^4 M^{-1}) bound more strongly than **1.16** (K_a = 2.8 x 10^4 M^{-1}). To confirm the binding mechanism, ^{1}H NMR titration experiments were conducted in DMSO-d_6 with 0.5% H_2O. **1.16** and **1.17** showed slow exchange up to 1 equivalent of the Adi after which no further changes in the NMR spectra were observed. A notable sharpening of the methylene protons indicated a conformational change upon binding, resulting in all 8 methylene protons becoming chemically equivalent in the 1:1 complex. when **1.16** and **1.17** was tested with the smallest anion, Mal, intermediate exchange was observed, aligning with UV-vis titration results, with further peak splitting at higher guest concentrations, indicating potential formation of higher-order complexes (oligomers). Finally, a double mutant cycle analysis was carried out to evaluate the cooperativity effects of the macrocycles with their respective guests. Negative cooperativity (log (K_{intra})< 0) was observed for Mal, Sub, and Aze towards both receptors, as the guest is either too short (mal) to span the macrocycle pore or too large (Sub, Aze) to favour a 1:1 binding complex implying favourable oligomer formation, despite the guest's ability to flex and bind both parts of the ditopic host in the solid state. In contrast, moderate positive cooperativity (log (K_{intra}) > 0) was observed for Suc, Glu, and Pim, and the strongest binding linear dicarboxylate, Adi, showed the highest log (K_{intra}) value, reflecting strong positive cooperativity for both **1.16** and **1.17**, indicating that Adi can fully span and fit within the macrocyclic pore. Notable differences in cooperativity were observed between **1.16** and **1.17** when interacting with rigid anions. For the anion ttM, **1.17** demonstrated strong positive cooperativity than that for

1.16. The same discrepancies were seen with Ter. The strong cooperativity of Ter can be attributed to a combination of π-π interactions between the central aromatic rings of the macrocycle and the aromatic guest, and Ter being a suitable geometric fit for the macrocycles. This work underscores the intricacies anion recognition and emphasizes the significance of geometric compatibility in improving binding strength and selectivity of macrocycles, offering valuable insights for the development of future macrocyclic receptors.

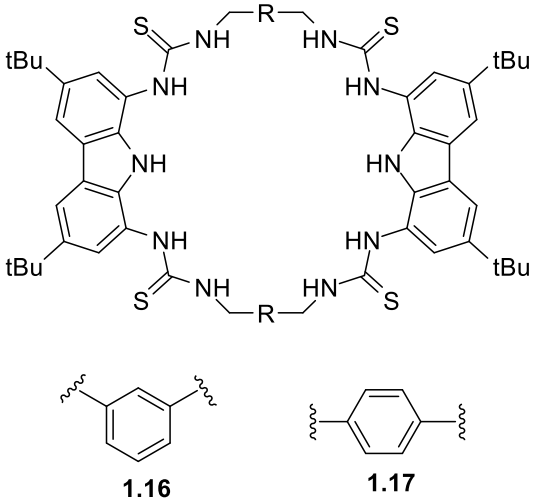

Figure 1.20: Chemical structures of macrocycles **1.16** and **1.17**. Reported by Jolliffe and colleagues.

1.7.1.2: Cyclic Peptides

The interaction between peptides and proteins with anionic species constitutes a vital recognition event in biological systems, imparting diverse downstream effects encompassing structural stabilization and catalysis.[58, 61, 116] Various binding modalities have been discerned in the interaction between peptides/proteins and anions. These interactions include those facilitated by bridging metal ions, electrostatic interactions involving amino acid side chains like lysine and arginine, and hydrogen bonding with side-chain donors such as serine, threonine, and asparagine, as well as the NH groups of the peptide backbone.[55, 64, 117, 118] This multifaceted spectrum of binding interactions underscores the intricate nature of anion recognition by peptides and proteins in biological contexts. Taking inspiration from natural binding abilities that amino acids possess, cyclic peptides have emerged as suitable macrocyclic receptors.[119-121]

Mimicking natural subunits, cyclic peptide receptors can provide a rigid and preorganized cavity with multiple directional hydrogen bond donors pointing into a central core. Selectivity can be tuned through backbone modification using different spacers to achieve preference to anions of a variety of shapes and sizes[118]. The rest of this section will outline some recent examples of anion recognition achieved through cyclic peptides.

Jolliffe and co-workers have made substantial contributions to synthesis of cyclic peptides and peptidomimetics as receptors for molecular recognition.[118, 122, 123] One example is the monocyclic peptide [cyclo(Val-Thr)$_3$] **1.18** which was shown to bind to Cl^-, $H_2PO_4^-$, SO_4^{2-} and SeO_4^{2-} in ^{1}H NMR spectroscopic titration experiments (Figure 1.21). SO_4^{2-} and SeO_4^{2-} gave the best fit to a 1:1 binding model and under these conditions (H_2O: DMSO, 2:8), SO_4^{2-} (K_a = 500 M^{-1}) is more favoured than SeO_4^{2-} (K_a = 90 M^{-1}). The authors hypothesized that it could be a result of increased water coordination of the anions which prevented the association of a second peptide, as inferred from density functional theory (DFT) calculations. When sulfate was present, compound **1.18** assumed a conformation where all six NH protons pointed towards the centre of the macrocycle, forming six hydrogen bonds with the sulfate ion. The intramolecular hydrogen-bonding interactions between Thr-OH groups also contributed to the stabilization of the structure, which was consistent with the observed downfield shifts of the signals attributable to these protons in the ^{1}H NMR spectra.[124]

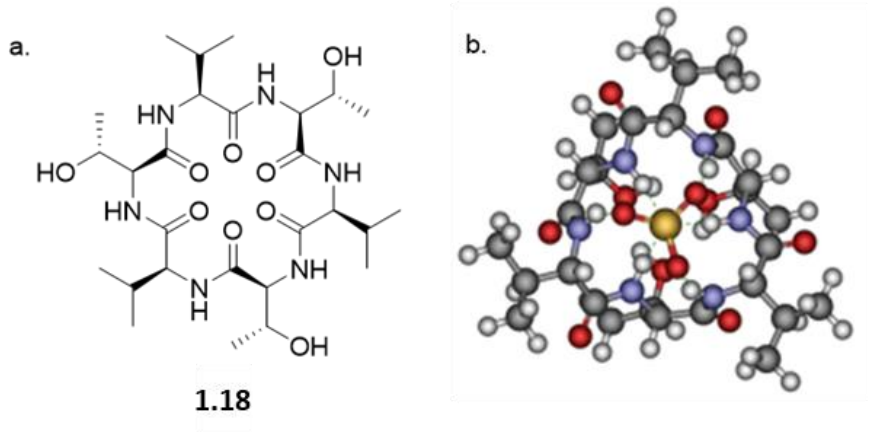

Figure 1.21: **a).** Structure of [cyclo(Val-Thr)$_3$] **1.18** reported by Jolliffe and colleagues. **b).** DFT optimised structure of 1:1 complex of **1.18** and sulphate indicating hydrogen bonds to the sulphate.

Kubik and co-workers have reported several examples of cyclic peptide receptors ranging from monocyclic receptors to sandwich-like ditopic receptors over two decades.[125, 126, 127, 128] In a more recent study Kubik et al. synthesized a series of palladium(II)-mediated assemblies consisting of one M_2L_2 (**1.20**) macrocycle and one M_3L_6 cage made up of a cyclic tetrapeptide ligands **1.19** (Figure 1.22).[129] During the titrations of **1.20** with dicarboxylates and disulfonates, upfield shifts of anion protons were observed, indicating that the anions were encapsuled within the macrocycle's cavity thus the protons were shielded by the aromatic rings. The binding constant of **1.20** to 1,3-benzenedisulfonate was found to be log K_a = 4.8 while that to 2,6-naphthalenedisulfonate could not be accurately calculated due to the complexity of equilibrium of the 1:2 binding complex. Such complex equilibria can be a difficulty when trying to assess anion affinity with larger macrocyclic structures.

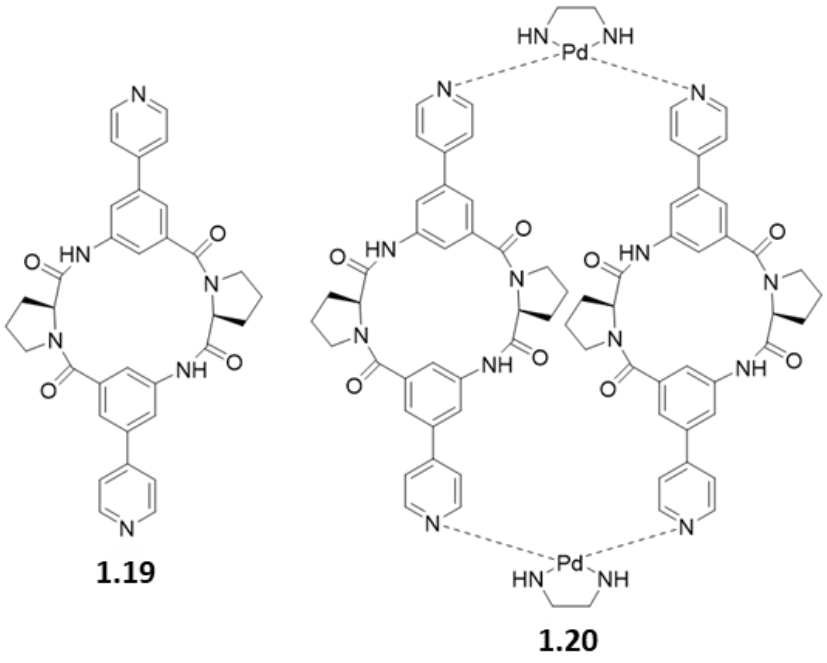

Figure 1.22: General structure of the ligand **L** (**1.19**), and macrocycle **M_2L_2** (**1.20**), reported by Kubik *et al*.

Tomišić and co-workers have recently reported the synthesis of cyclic pentaphenylalanine **1.21** as an efficient macrocyclic receptor for a variety of anions in acetonitrile and methanol (Figure 1.23). Using a range of experimental techniques and computational methods such as fluorimetry, spectrophotometry, ^{1}H NMR,

microcalorimetric titrations and molecular dynamics (MD) simulations, stability constants and anion binding ability of the corresponding complexes were determined.[130] The receptor **1.21** exhibited the strongest affinity towards Cl^- with a stability constant of 6.06, followed by that for Br^- (4.97), HSO_4^- (4.18), and $H_2PO_4^-$ (4.31). The stability constants of **1.21** -halogen anion complexes are strongly correlated with anion size, with **1.21** showing a weaker affinity for larger anions. In MeCN, receptor **1.21** primarily formed 1:1 complexes, except with $H_2PO_4^-$, where ^{1}H NMR titrations suggested the likely formation of 1:2 species. Anion coordination was investigated using molecular dynamics simulations, which revealed the binding of nearly all amide protons. This was further supported by circular dichroism titrations in MeCN, showing a significant change in the 220 nm region upon anion complexation. When MeOH was used as a solvent, a moderate to high loss of affinity and selectivity was observed. The main factor contributing to the decreased stability of **1.21**-anion complexes was predicted to be the strong anion solvation properties of the solvent compared to MeCN. The observed difference in overall complex stability is primarily due to the significantly stronger solvation of free anions in methanol than in acetonitrile. The overall results showed that **1.21** can be a possible candidate as versatile anion binding receptor in protic and aprotic solvents for anion sensing and transport.

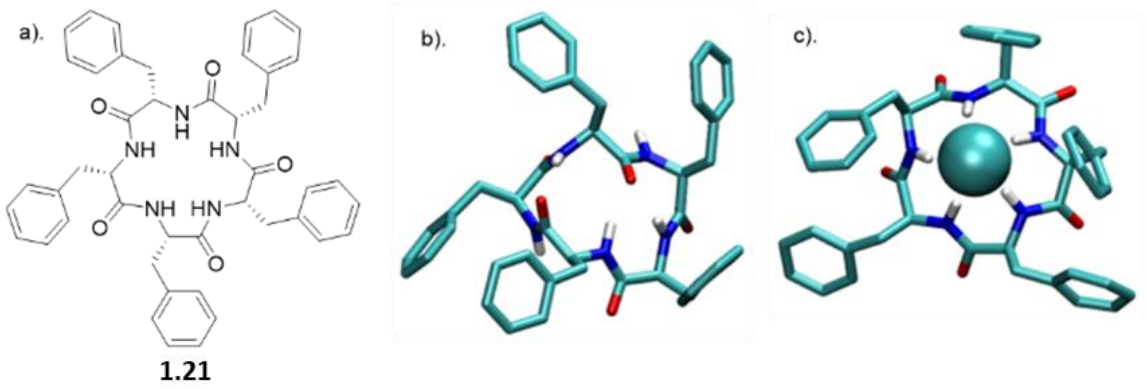

1.21

Figure 1.23: a). Chemical Structure of **1.21. b).** MD simulation of free **1.21 c).** MD simulation of anion complexes of **1.21** with chloride reported by Tomišić and co-workers.

1.7.1.3: Squaramide-based Macrocycles

Squaramides are a relatively recent addition to supramolecular chemistry and have attracted significant attention due to their diverse applications in biological and chemical sciences. Comprising a cyclobutene ring with two carbonyl groups adjacent to two NH groups, squaramides feature hydrogen bond acceptors and donors in close proximity. This unique arrangement makes them particularly useful in molecular recognition and transport.[112] Many researchers have focused their attention towards squaramides, such as Caltagirone and co-workers who have worked on squaramide based receptors and ionophores [131-133], Gale and co-workers who have shown squaramides to be successful anion transporters [134-136] , and many others in the field of supramolecular chemistry and beyond.

An example of the utilisation of squaramides for anion recognition was reported by Jolliffe and co-workers where they synthesised a series of squaramide based macrocycles (**1.22** and **1.23**) comprising of alternating squaramide and benzylic groups tethered with the triethylene glycol monomethyl groups that displays high affinity and selectivity towards SO_4^{2-} in aqueous media (Figure 1.24).[137] The binding studies of TEG-MSQs **1.22** and **1.23** involved quantitative NMR binding experiments for a range of anions in a 1:2 (v/v) H_2O/DMSO-d_6 solvent The binding affinities were calculated by fitting to a 1:1 binding model. **1.22** showed affinity for SO_4^{2-} in the competitive solvent mixture, however, **1.23** exhibited a much greater affinity for SO_4^{2-} that was too high to quantify in these very competitive conditions (K_a = < 10^4 M^{-1}). The high binding affinity of **1.23** for SO_4^{2-} was attributed to having an additional squaramide binding site compared to **1.22**, together with additional hydrogen bonding interactions to the anion. Selectivity studies carried out for **1.23** exhibited notable selectivity for SO_4^{2-} over other tetrahedral anions, demonstrating a binding affinity for sulfate that is at least three orders of magnitude higher than that observed for phosphate species presenting itself as an extremely potent and selective binding macrocycle for SO_4^{2-} ions, outperforming the sulfate binding protein (SBP). In 2019 Jolliffe and colleagues showed MSQ **1.23** proved to be a highly selective ligand for SO_4^{2-}, even in the presence of various interferents in aqueous mixtures and across a pH range from 3.2 to 14.1. This enables potential SO_4^{2-} separation by the MSQs in a variety of applications from nuclear waste and in plasma sulfate assays.[138] In 2020 Jolliffe and colleagues showed that by functionalising **1.23** with

aliphatic chains to produce macrocycles **1.24** and **1.25**, they could efficiently extract SO_4^{2-} from an aqueous Na_2SO_4 solution into organic solution, via an anion exchange mechanism with nitrate ions, as well as transport SO_4^{2-} across a bulk chloroform layer via an anion exchange mechanism with NO_3^-, allowing the extraction of SO_4^{2-} from Na_2SO_4 solutions.[139]

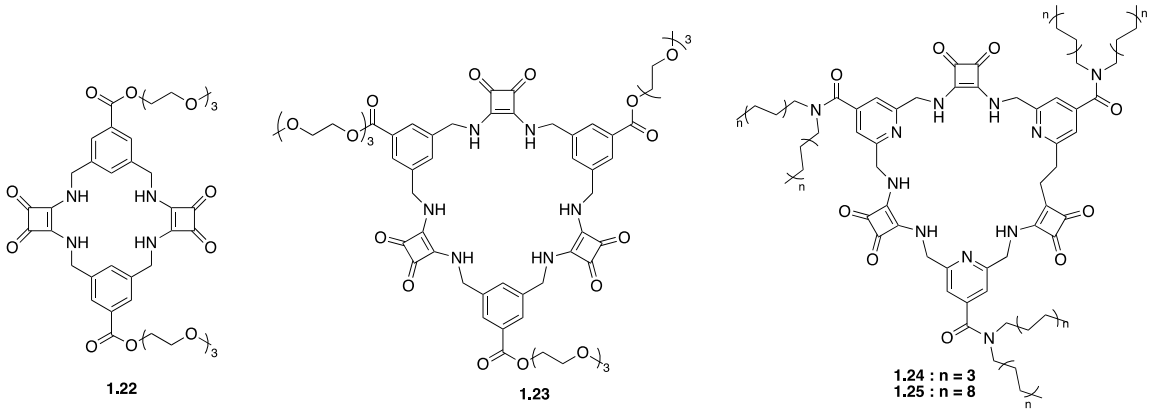

Figure 1.24: General structures of MSQ's **1.22 – 1.25** reported by Jollife and colleagues.

The utilisation of squaramides as effective ion - pair receptors have been reported by a number of studies carried out by Jan Romanski and colleagues [140-142]. An example of a macrocyclic squaramide ion-pair receptor and fluorescent sensor with selectivity towards sulfates was reported by Romanski and colleagues whereby using a combination of specific diamines and methyl squarates under high dilution conditions they synthesised a multi-macrocyclic ion pair receptors **1.26** and **1.27** based on a squaramide recognition moiety appended to benzo-18-crown-6. An analogous anion receptor **1.28**, and a fluorescent sensor by incorporating a simple naphthalene unit into the structure of the receptor **1.29** (Figure 1.25) [143]. ^{1}H NMR titrations were carried out in order to measure binding constants for a variety of anions such as Cl^-, Br^-, NO_2^-, NO_3^-, $PhCOO^-$, CH_3COO^- and SO_4^{2-} against each receptor except for **1.27** due to insolubility issues. **1.26** displayed an increase in affinity for Cl^- (K_{TBACl} = 61 M^{-1}) anions in the presence of one equivalent of Na^+ (K_{NaCl} = 78 M^{-1}) and K^+ (K_{KCl} = 95 M^{-1}). Interestingly, further strength of Cl^- binding was achieved by the addition of 3 equivalents of K^+ producing a stability constant of (K_{KCl} = 120 M^{-1}). In order to verify the role of the cation binding domain in the structure of **1.26**, **1.28** lacking the crown ether unit was tested towards the same range of anions which showed increased anion recognition compared to **1.26**. This is

attributed to the absence of two electron-donating alkoxy substituents in the structure of anion receptor **1.28**. Compared to **1.26**, this decreases the electron density on the phenyl ring, facilitating a more rigid interaction with the anion. However, **1.28** could not recognize Cl^- in an enhanced manner in the presence of K^+ due to the lack of the cation binding domain in the structure (K_{KCl} = 71 M^{-1} vs. K_{TBACl} = 76 M^{-1}). Finally, **1.29** resulted in an optical ion pair sensor selective towards SO_4^{2-}, where upon the addition of SO_4^{2-}, a change in optical properties were observed including a including a bathochromic shift in the maximum absorption, an increase in fluorescence intensity, and the appearance of a new band at 420 nm. All receptors were found to interact with anions by utilizing the squaramide and amide functions of the receptors further supporting the efficiency of squaramides as hydrogen bonding motifs for anion recognition.

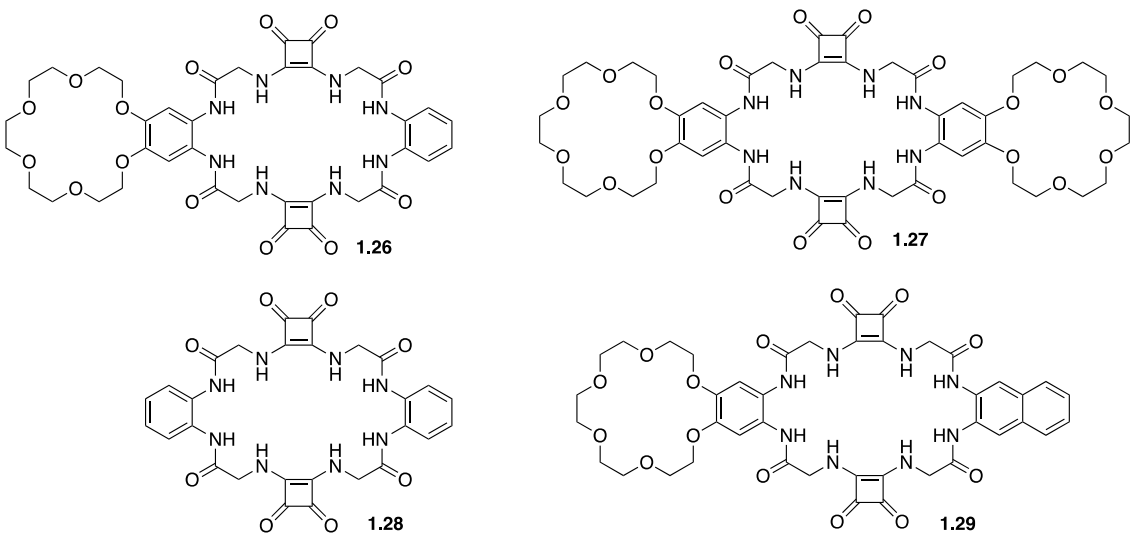

Figure 1.25: General structures of Squaramide based ion – pair receptors **1.26 – 1.29** reported by Jan Romanski and colleagues,

1.7.1.4: Calix[4]pyrrole – based macrocycles

Pyrrole- and calix[4]pyrrole-based anion receptors differ from the previously discussed macrocyclic receptors. They can only function as hydrogen bond donors as a result of their absence of hydrogen bond acceptor functional groups. However, calix[4]pyrrole-based receptors, adopt a non-planar tetrapyrrolic macrocyclic conformation, enabling them to capably bind to Lewis basic anions such as halides.[144] Since Sessler et al. first introduced calix[4]pyrrole into the design of anion receptors in the mid-1990s,

calix[4]pyrrole-based receptors have demonstrated high affinity and selectivity for various anions. This has been achieved by adding straps to one side of the calix[4]pyrrole or by incorporating probe units at the periphery of the macrocycle.[144, 145]

In 2023, Wezenberg and colleagues reported a dithienylethene-strapped calix[4]pyrrole whereby the dithienylethene (DTE) unit that serves as a photo switch. The DTE unit allows the molecule to isomerize between a ring-open (**1.30**) and a ring-closed (**1.31)** form upon exposure to 300/630 nm light (Figure 1.26).[146] This photo switching process brings about a subtle change in the size of the binding pocket, enabling the receptor to selectively bind different halide ions based on their size, thus functioning as an artificial anion receptor with tunable selectivity. ^{1}H NMR titrations were carried out for the receptor in its open-ring isomer **1.30** in MeCN-d_3. Addition of Cl^-, Br^-, and I^- to led to substantial downfield shifts of the pyrrole-NH as a result of strong hydrogen bonding. Isothermal titration calorimetry (ITC) was carried out to quantify the binding affinities which showed a 1:1 binding model with strong affinity for Cl^- (K_a = 2.6 x 10^5 M^{-1}) and Br^- (K_a = 8.8 x 10^3 M^{-1}) however a much lower binding affinity was observed for I^- (K_a = 23 M^{-1}). Upon 300nm irradiation where the receptor now presented itself as its closed-ring isomer **1.31**. ^{1}H NMR titrations revealed similar downfield shifts of the pyrrole-NH. When the DTE unit is in the ring-closed form, the binding pocket is smaller, which reduces the binding affinity for larger halide ions, this was seen from the association constants where little change was observed for Cl^- (K_a = 1.2 x 10^5 M^{-1}). As for Br^- a significant decrease was observed (K_a = 54 M^{-1}) and the same for I^- (K_a = < 1 M^{-1}). This shows that the binding affinity is highly dependent on the photo switching process even though the process brings about a subtle change in the size of the binding pocket, it affects the binding affinity and selectivity of different halide ions.

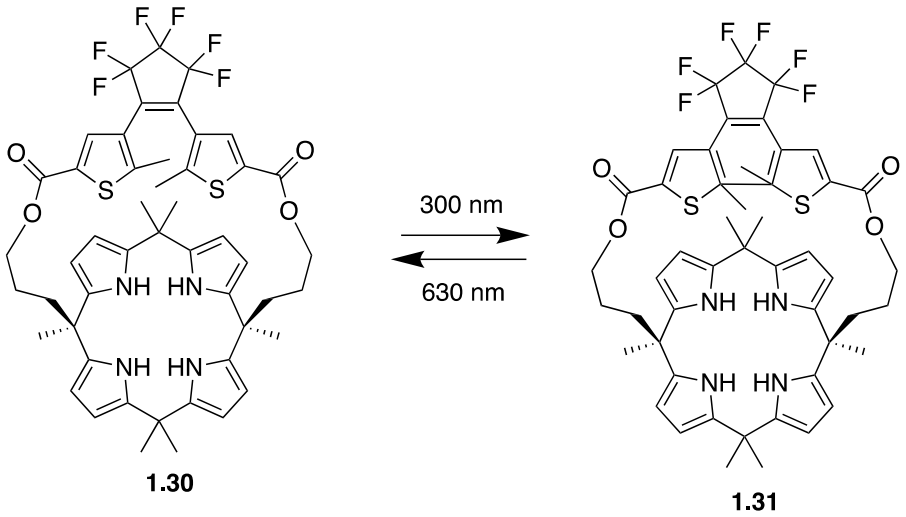

1.30 **1.31**

Figure 1.26: General structure of dithienylethene-strapped calix[4]pyrrole macrocycles in its ring open **1.30** and ring closed **1.31** form reported by Wezenberg and colleagues.

Sessler and co-workers set out to synthesise the smallest bis-calix[4]pyrrole (**1.32**) comprised of small two-wall bis-calix[4]pyrrole formally linked by two single oxygen atom bridges which proved capable of trapping F^- exclusively relative to other anions (Figure 1.27). [147] The small size of the cavity in bis-calix[4]pyrrole (**1.32**) is significant for its selectivity towards F^- because it restricts the conformation of the receptor, preventing it from accessing the cone conformation that is most favourable for anion binding. This restriction results in a three-dimensional cavity that is slightly larger than the volume of F^-, capable of supporting hydrogen-bonding interactions. As a result, the receptor can reject anions larger than F^-, resulting in exclusive selectivity for F^-. The results of this study were confirmed through various analytical techniques, including X-ray diffraction analysis, DFT calculations, and molecular dynamics simulations. In the solid state, bis-calix[4]pyrrole **1.32** was found to be capable of binding F^-in a 1:2 stoichiometry , with the association constants of K_{11} = (5.2 ± 0.4) x 10^3 and K_{12} = (4.4 ± 1.4) x 10^2 M^{-1} where each F^- atom trapped itself inside the cavity of the calix[4]pyrrole ring, as evidenced by a single crystal structural analysis. The expected electrostatic repulsion between the two F^- atoms was said to be stabilised by multiple cooperative hydrogen bonding interactions. In solution, **1.32** was found to have favourable binding towards F^- but not interact appreciably with other anions, e.g. Cl^-, Br^-, SCN^-, NO_3^-, HSO_4^-, $H_2PO_4^-$, and SO_4^{2-} as inferred from ^{1}H NMR spectroscopic analyses showing no noticeable changes in the proton

signals. DFT calculations and molecular dynamics studies were conducted in the gas phase in order to support the hypothesis that the exclusive selectivity for F^- is due to the limited three-dimensional space within receptor **1.32**.

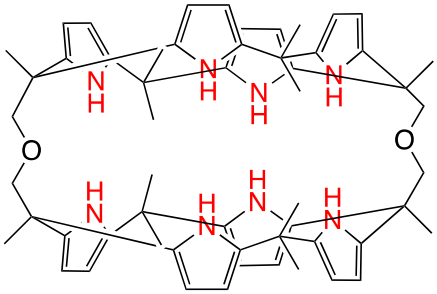

1.32

Figure 1.27: General structure of bis-calix[4]pyrrole (**1.32**) reported by Sessler et al.

1.7.2: C-H Hydrogen Bonding Macrocycles

C-H hydrogen bonding macrocycles, a class of supramolecular compounds, have captured considerable attention in recent years owing to their unique properties and potential applications in various fields particularly in anion recognition. These macrocycles feature C-H groups that serve as hydrogen bond donors, enabling them to selectively bind to a variety of guest molecules. [148] Unlike traditional hydrogen bonding, where hydrogen bridges between a donor and acceptor, C-H hydrogen bonding involves direct interactions between a carbon-hydrogen bond and a suitable acceptor, offering diverse possibilities for designing and synthesizing macrocyclic structures with intriguing properties in the field of supramolecular chemistry.[149] Flood and colleagues pioneered the work for C-H Hydrogen bonding macrocycles in 2008, where they introduced a [3_4]triazolophane macrocycle **1.33** comprising of four triazoles and four phenylene CH groups orientated directly into the cavity with rigidity and preorganisation (Figure 1.28) [150]. Through multiple triazole C–H-anion and phenyl C–H - anion hydrogen bonding interactions the triazolophane **1.33** displayed a pronounced affinity for chloride followed by Br^- >> F^- >> I^-, with an association constant of K_a = (130,000 ± 30,000) L/mol for Cl^-.

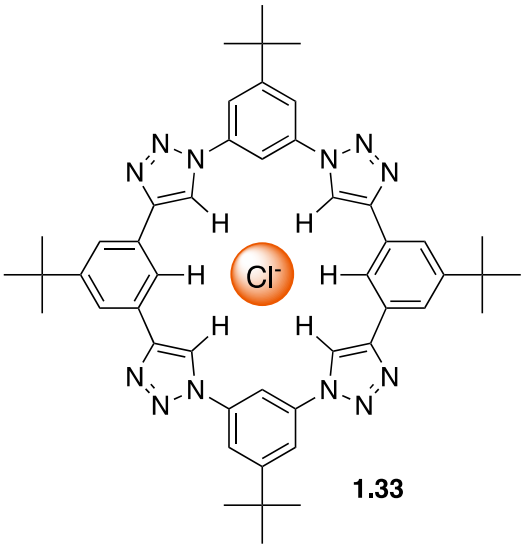

Figure 1.28: Schematic representation of a [3_4] triazolophane macrocycle **(1.33)** binding to Chloride via C-H Hydrogen bonding, reported by Flood and colleagues.

Through garnering the information acquired, Flood and colleagues used their understanding of receptor design and CH based hydrogen bonding to explore untapped and uncharted opportunities. From this they set out to create a whole new class of cyano stilbene based macrocyclic receptors, called cyanostars.[151] In this section we will discuss examples of C-H Hydrogen bonding macrocycles reported in recent years.

In 2021 G. Bachas, Flood and colleagues set out to design a clamshell-shaped anion-binding ionophore, **1.35**, to analyse its performance in ion-selective electrodes (ISE). This ionophore consisted of two cyanostar (**1.34**) macrocycles with prearranged cavities connected by a 12-carbon chain (Figure 1.29) and plays a crucial role in anion recognition and detection due to its capacity to prearrange cavities and selectively identify anions through CH-hydrogen bonding.[152] This distinctive structure and composition facilitate the selective transfer of anions from the solution to the membrane phase, resulting in enhanced selectivity and sensitivity in anion detection, potentiometric performance of the clamshell ionophore in ISEs was evaluated by measuring its response to different anions (e.g. Cl^-, Br^-, NO_3^-, salicylate, I^-, SCN^-, and ClO_4^-) and assessing its selectivity and sensitivity. Membrane compositions containing the clamshell ionophore were prepared, and the resulting electrodes were subjected to potentiometric measurements to determine their response characteristics. The electrode based on **1.35** showed the greatest potentiometric response and excellent selectivity towards I^- over various anions,

with a selectivity coefficient of $10^{-2.13}$. In contrast to the Hofmesiter series, salicylate showed the lowest response. ESI-MS was utilised to evaluate the selectivity of the clamshell ionophore (**1.35**) and its parent CNstar (**1.34**) towards various anions. Through conducting ESI-MS experiments, observations and analysis the formation of complexes between the ionophores and specific anions were measured. The results revealed the formation of a 1:1 complex between **1.34** and Cl^-, NO_3^-, Br^-, ClO_4^-, I^-, and salicylate, each with intensities less than 4%. Higher stoichiometry complexes, such as [3(**1.34**) + $2ClO_4$] $^{2-}$, [3(**1.34**) + I + ClO_4]$^{2-}$, and [3(**1.34**) + 2I] $^{2-}$, were also observed, with relative abundances of 21.7%, 9.7%, and 1.2%, respectively. The most intense peak observed, corresponded to the 2:1 complex [2(**1.34**) + ClO_4]$^-$. Interestingly, another peak representing the 4:2 heterocomplex [4(**1.34**) + I + ClO_4]$^{2-}$, followed by the 2:1 complex [2(**1.34**) + I]$^-$ were observed with both relative intensities below 10%. Additionally, a peak attributed to a 3:1 complex [3(**1.34**) + ClO_4]$^-$ was also found. Upon increasing the clamshell concentration to 5 µM, ESI-MS analysis revealed predominant peaks at m/z 2147.6 corresponding to 1:1 and 2:2 multimers [(**1.35**) + I]$^-$ and [2(**1.35**) + 2I] $^{2-}$. However, increasing the ionophore concentration to 10 µM caused a shift in the prominent peak of the ESI-MS spectra from iodide to perchlorate with relative contributions of the 1:1 and 2:2 (**1.35**) and ClO_4^- complexes. The findings from Ionophore Selectivity by ESI-MS provided significant insights into the complexation behaviour of the ionophores, enabling a thorough evaluation of their selectivity towards particular anions and their potential impact on ion detection and quantification in Ion-Selective Electrodes.

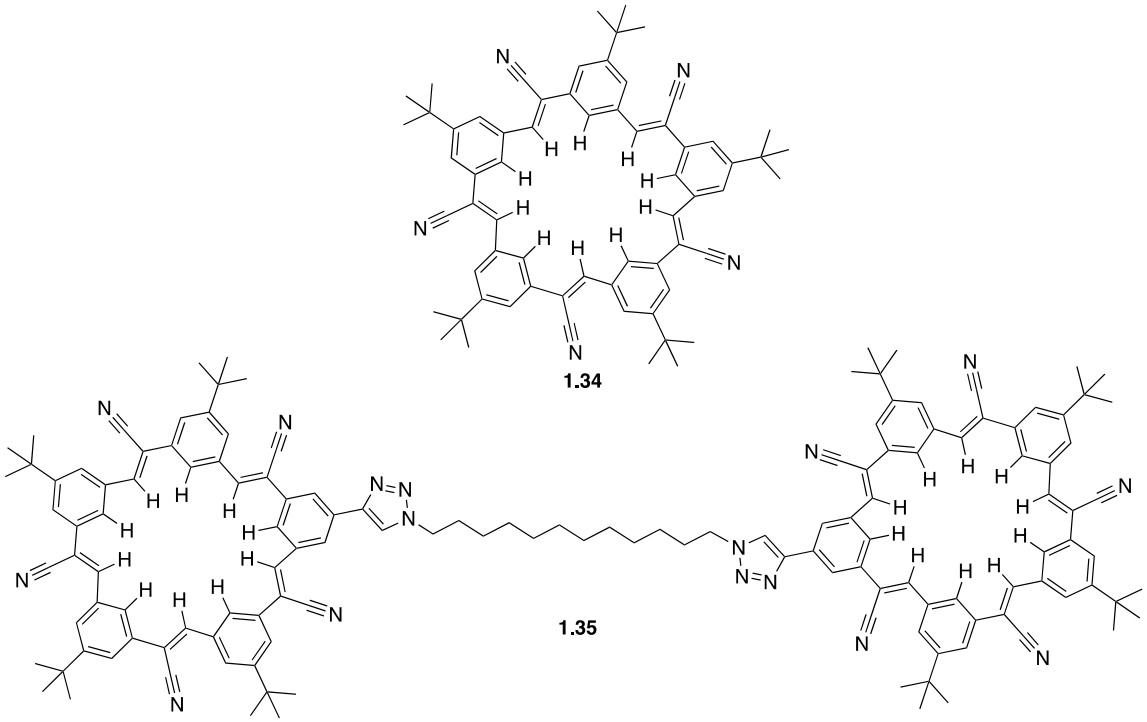

Figure 1.29: General structure of Cyanostar (**1.34**) and the Clamshell ionophore (**1.35**) reported by G. Bachas, Flood and colleagues.

In 2022, Flood and colleagues reported the binding of a series of Organotrifluoroborate Anions (R-BF3$^-$) e.g. small (methyl, $MeBF_3^-$), medium (vinyl, $VinBF_3^-$), and large (thiophene, $ThBF_3^-$ and phenyl, $PhBF_3^-$) to Cyanostar macrocycles (**1.34**) (Figure 1.30.).[153] X-ray crystallography revealed 2 : 1 complex between **1.34** and the $ThBF_3^-$ and $PhBF_3^-$ anions. As a result of steric interactions taking place between the macrocycle and the ortho hydrogen atoms of the anion (one for thiophene and two for phenyl), both substituents are prevented from ideally fitting into the binding cavity defined by the center of the two π-stacked macrocycles. Additionally, they are kept further from the bottom macrocycle, which disengages the CH hydrogen bond donors of the second macrocycle, likely reducing stability. From this a combination of techniques, including ^{1}H NMR and UV-vis titrations were carried out to quantify the impact of sterics on the binding affinity of the anions. ^{1}H NMR titrations revealed that the shifts in the peaks of the macrocycle reach a plateau at approximately 0.5 equivalents of the guest. This saturation is accompanied by subtle downfield shifts in the interior protons, which are indicative of the CH···anion hydrogen bonding of cyanostars. $MeBF_3^-$ and $VinBF_3^-$, characterized by small steric profiles, exhibited positive cooperativity, favouring the formation of the 2:1 species with association constants of logK_2 = > 6.5 and > 6.4

respectively. Conversely, the addition of further guest molecules to the larger $PhBF_3^-$ and $ThBF_3^-$ anions results in downfield shifts consistent with the conversion to a 1:1 complex and less cooperativity due to greater steric demand. Consequently, the $PhBF_3^-$ anion forms mixtures that are not suitable for use as designer anions which according to the crystal data, aligns with the hypothesis, that 2: 1 anion binding weakens upon disengaging the bottom macrocycle from binding.

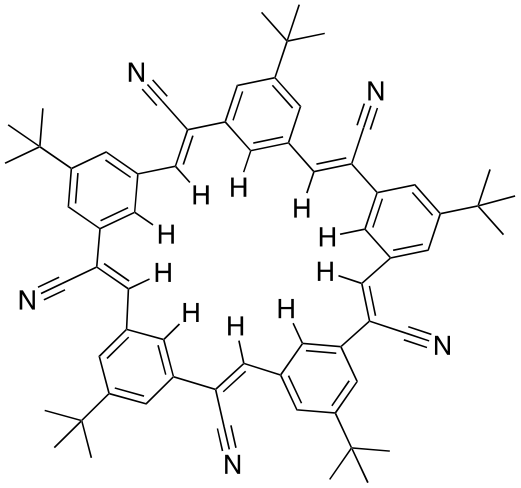

1.34

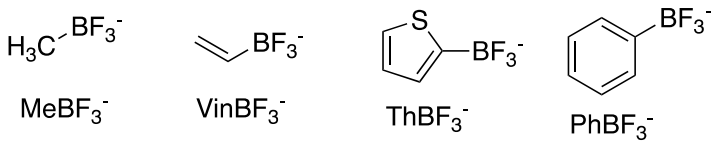

Figure 1.30: General structure of Cyanostar macrocycle (**1.34**) and of Organotrifluoroborate Anions reported by Flood et al.

1.7.3: Halogen Bonding Macrocycles

Halogen bonding macrocycles represent a compelling and rapidly evolving area of supramolecular chemistry, characterized by the utilization of halogen bonding interactions within the confines of macrocyclic structures. Halogen bonding, an emerging non-covalent interaction akin to hydrogen bonding, has garnered significant attention due to its unique directional and tuneable nature, offering diverse opportunities for the design of functional macrocyclic systems.[154] The interaction is usually represented in literature as R—X·····Y, where the halogen atom X, acting as the halogen bonding (XB) donor or Lewis acid, is covalently bonded to an electron-

withdrawing group R. The entity Y serves as the XB acceptor, functioning as a Lewis base or anion. [155] The incorporation of halogen bonding motifs into macrocyclic architectures has opened new avenues for the construction of sophisticated host molecules with tailored binding cavities and selective recognition properties. These halogen bonding receptors often exhibit contrasting, and in many cases, superior anion binding affinities and properties compared to their counterparts based on hydrogen bonding. [99, 156]

In 2021 Beer and co-workers set out to study lithium halide ion-pair recognition through halogen and chalogen bonding heteroditopic macrocycles. They achieved this by assembling a series of 1,10-phenanthroline-based macrocycles involving XB (**1.36**), ChB (**1.37**), and HB (**1.38**) interactions. These macrocycles act as heteroditopic ion-pair hosts, facilitating the cooperative recognition and solid–liquid extraction of lithium halide salts, where the co-bound lithium cation activates the binding of the halide anion (Figure 1.31).[157] To investigate the ion-pair binding properties of the macrocycles, initial qualitative ^{1}H NMR binding studies were conducted in a 1:1 $CDCl_3$:CD_3CN solvent mixture. Titration experiments with halide anions on **1.36** revealed no observable halide binding. However, when one equivalent of $LiClO_4$ was added, followed by sequential additions of one, two, and five equivalents of TBA halide salts, evidence was observed indicating that the macrocycle's phenanthroline-bound Li^+ participated in the binding of halide anions. Bind-fit analysis of the titration binding isotherm data determined 1:1 stoichiometric anion association constant. Comparing the halide anion association constant data, compound **1.36** is the most effective ion-pair receptor for all halides tested, demonstrating two- to seven-fold increases in affinity for Br^- (K_a = 1214 M^{-1}) and I^- (K_a = 1236 M^{-1}) compared to the ChB and HB analogues. Notably, the effectiveness of the halogen bonding donor motif is further highlighted by **1.36**'s ability to simultaneously complex with the "hard" LiCl ion-pair, whereas similar experiments with **1.37** and **1.38** led to the precipitation of LiCl salt. Overall, the anion binding studies demonstrate the significant impact of the sigma-hole donor motifs on the binding affinity and selectivity of the heteroditopic macrocycles for lithium halide ion-pairs.

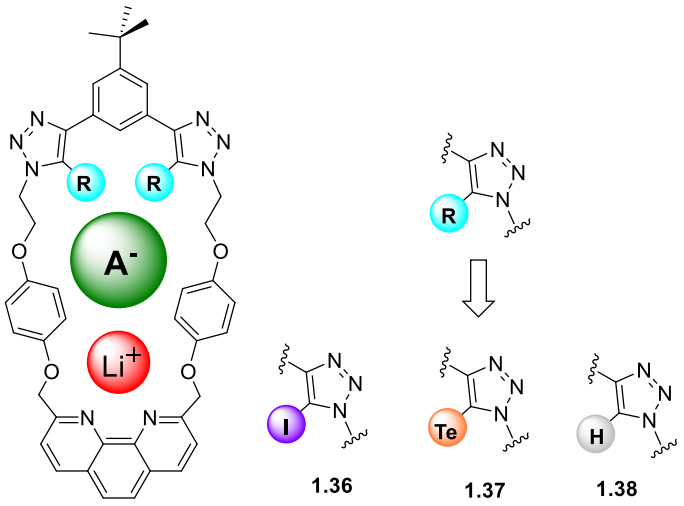

Figure 1.31: Structure of phenanthroline-based heteroditopic macrocycles incorporated with sigma–hole donors designed for ion-pair recognition of lithium salts. A = anion, reported by Beer et. al.

In the same year Beer and co-workers reported a series of neutral tetradentate halogen bonding (XB) macrocycles, comprising of two bis-iodotriazole XB donors with varying ring sizes through the integration of meta- and para-substituted xylyl spacer units as well as a naphthyl spacer unit, capable of anion recognition in highly competitive aqueous media (Figure 1.32).[158] A qualitative ^{1}H-NMR binding study with the meta – xylyl spacer macrocycle (**1.39**) with TBA Cl^- in 5% D_2O/ Acetone-d_6 revealed that, upon adding 0–1 equivalents of Cl^-, the resonances gradually became more resolved, possibly indicating increased macrocycle rigidity due to Cl^- complexation. Significant downfield shifts in the macrocycle's internal aromatic protons surrounding the binding site were observed. Importantly, no further proton perturbations occurred after the addition of one equivalent of Cl^-, suggesting robust binding in this competitive aqueous-organic solvent mixture. Similar proton signal perturbations were observed in. By monitoring the shifts in aromatic proton signals, binding isotherms were generated. Non-linear regression analysis using Bindfit yielded 1:1 stoichiometric host–guest association constants for compound **1.39**, with association constants exceeding 10^5 M^{-1} for all halides. The substitution of the m-xylyl spacer unit with p-xylyl and naphthyl groups in XB macrocycles **1.40** and **1.41**, respectively, was envisioned to yield enlarged cavities with the ability to accommodate larger anionic guest species. Notably, the Bindfit analysis of

the ^{1}H NMR halide titration data with compound **1.40** showed 1:1 stoichiometric host–guest association constants for Cl^- and Br^-, both approximately 335 M^{-1}. In contrast, the larger iodide demonstrated a 1:2 host–guest binding stoichiometry, with a slightly higher K_{11} value of 585 M^{-1}. In comparison, the naphthyl macrocycle **1.41**, featuring the most capacious cavity, formed relatively weaker halide complexes, showcasing the Hofmeister selectivity trend. ^{1}H-NMR anion binding studies were extended to dicarboxylate anions, showing that compounds **1.40** and **54** bind these anions in a 1:1 stoichiometric host–guest manner. The selectivity for dicarboxylate binding was observed as oxalate > malonate > succinate, with compound **1.39** forming much stronger complexes with higher association constants compared to **1.41**. Fluorescence spectroscopy carried out for **1.41** in the presence of 10 mM TBA malonate, whereby a notable 38% enhancement in the emission intensity of the naphthyl bands was observed. In contrast, oxalate and succinate induced comparatively smaller enhancements in emission intensity, measuring 6% and 18%, respectively. This trend of heightened emission intensity aligns with the increased length of the dicarboxylate guests, despite the similarity in the magnitude of K_a values determined through NMR titration. This paper illustrates the capability of charge-neutral bis-iodotriazole macrocycles, utilizing halogen bonding, to effectively serve as robust and selective hosts for anion recognition in challenging aqueous environments.

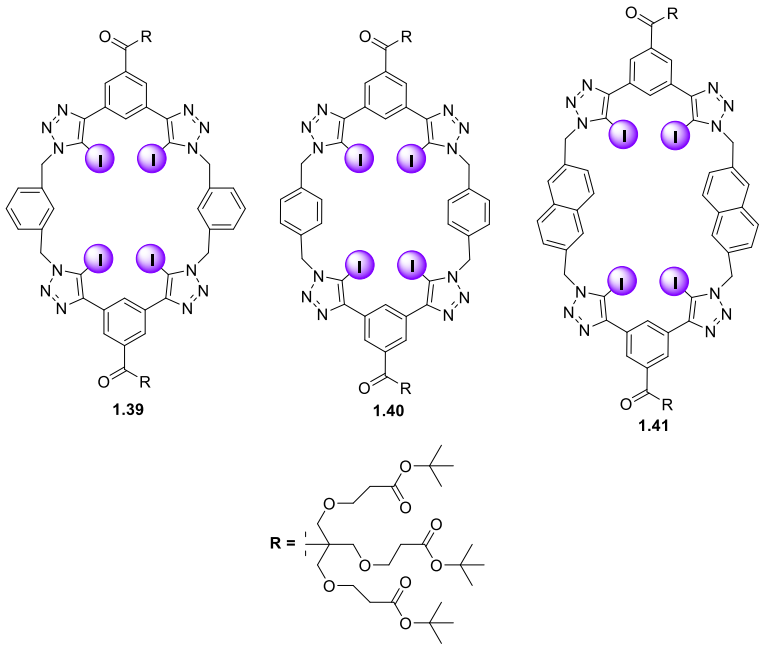

Figure 1.32: General Structure of the XB macrocycle series (**1.39 – 1.41**) reported by Beer et. al.

In 2022 Sessler and colleagues reported the preparation of tetra iodotriazole halogen bonding macrocycle known as the Ibox (**1.43**) through copper(I)-catalyzed azide-alkyne cycloaddition (CuAAC)[159], which was inspired from the "Texas-sized" molecular box (**1.42**), a tetracationic macrocycle that bound to anions through Hydrogen bonding and electrostatic interaction first reported by Sessler et. al in 2010 (Figure 1.33).[160] The anion binding properties of **1.43** was measured through ^{1}H NMR spectroscopic studies carried out in $CDCl_3$ and was found to recognise Cl^-, Br^- and I^-. The signals corresponding to the pyridyl proton were seen to shift in an anion and concentration-dependent manner upon the addition of increasing quantities (up to 13 equiv.) of F^-, Cl^-, Br^-, and I^- to a 1.25 mM $CDCl_3$ solution of **1.43**. The pyridyl proton signal exhibited an upfield shift, moving from 8.56 ppm to 8.40 ppm for F^-, Cl^-, Br^-, and I^-, respectively. Further studies revealed a higher affinity for the heavier halide anions and provided support for a preferred 1:2 binding stoichiometry. The ^{1}H NMR spectral titration data were fitted to a 1:2 binding model and showed a clear binding preference for iodide ($I^- > Br^- > Cl^-$). The binding mode is thought to involve a pair of iodotriazole subunits within the macrocycle, with each subunit binding one halide anion. This tends to be the opposite of what is typically seen in classic hydrogen bonding anion recognition systems. Additionally, this preference differs significantly from the binding abilities of the "Texas-sized" molecular box **1.42**, which was noted for its capacity to bind both Cl^- and NO_3^- anions.

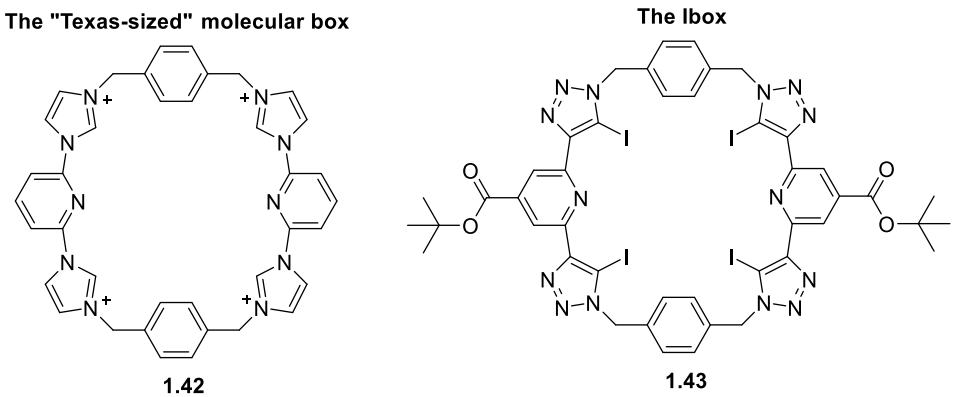

Figure 1.33: Comparison between the structure of the "Texas-sized" molecular box **1.42** and the Ibox **1.43**. Reported by Sessler and colleagues.

1.7.4: Anion-π Bonding Macrocycles

As previously mentioned, macrocycles are a versatile class of supramolecular structures for anion recognition, owing to their capacity to host diverse non-covalent interactions. Among these interactions, anion-π interactions have gained significant attention as a unique and powerful mechanism for stabilizing anions. Unlike traditional strategies that rely on hydrogen bonding or electrostatic forces, anion-π interactions exploit the attractive forces between anions and electron-deficient aromatic systems. These interactions occur when the negative charge of an anion is attracted to the partially positive π-system of an aromatic ring, such as triazine, perfluorinated benzene, or other electron-deficient moieties.

An example of an Organic-based cage that binds anions via anion-pi interactions can be seen by Wang and colleagues whereby they reported the design and synthesis of a triangular prism like cage (**1.44)** bearing benzene triimide as its base, and 2,7 naphthalene dimethylene acting as supporting pillars (Figure 1.34). [161] The articulate structure of **1.44** possesses a cavity size of 7.6 Å, capable of accommodating and exhibiting strong anion-π binding properties towards a variety of polyhedral anions. The electron-deficient Benzene triimide and electron-rich naphthalene moieties engage in intermolecular π–π stacking interactions, leading to an ordered self-assembly in the solid state. The anion binding ability of **1.44** towards a variety of anions including Cl^-, Br^-, I^-, N_3^- , SCN^-, NO_3^-, AcO^-, BF_4^- , ClO_4^- , $HSO4^-$, $CH_3SO_3^-$, and PF_6^- , were investigated via UV-Vis Spectrometry. For anions such as I^-, N_3^-, SCN^-, and AcO^-, a new charge transfer (CT) band was detected in the range of 400–500 nm, accompanied by a noticeable colour change in the solution. In contrast, for Br^-, only a weak charge transfer band was observed, with no accompanying colour change. For the other anions, including Cl^-, NO_3^-, BF_4^-, ClO_4^-, HSO_4^-, $CH_3SO_3^-$, and PF_6^-, the charge transfer band was absent; instead, a hypochromic effect was noted in the range of 360–450 nm. These varying spectral responses likely indicate different positions of the anions on the surface of **1.44**. Binding affinity constants were measured by fitting UV–vis spectrometric titration data to a 1:1 stoichiometry model as revealed via Job's plot. **1.44** demonstrates a notably high binding affinity for polyhedral anions (BF_4^- , ClO_4^- , $HSO4^-$, $CH_3SO_3^-$, and PF_6^-), despite their large size and relatively low electron density. The binding constants range from 24,651 M^{-1} for PF_6^- to 84,623 M^{-1} for HSO_4^-, indicating the strongest anion-π

complexation observed for a single polyhedral anion. The binding strength for SCN^- and N_3^- varies considerably with SCN^- demonstrating strong binding at 14,878 M^{-1}, whereas N_3^- shows only moderate binding at 599 M^{-1}. For spherical halides, size has a clear impact on binding: I^- is strongly complexed at 2,220 M^{-1}, Br^- exhibits moderate binding at 58 M^{-1}, and no significant binding was observed for Cl^-. As for AcO^- and NO_3^-, weak to moderate binding was observed with binding constants of 73 and 604 M^{-1}, respectively. Wang and colleagues have demonstrated an efficient host (**1.44**) for polyhedral anions. The binding constants, ranging from 24,651 to 84,623 M^{-1}, reflect the strongest anion-π binding recorded for charge-neutral π receptors interacting with individual polyhedral anions.

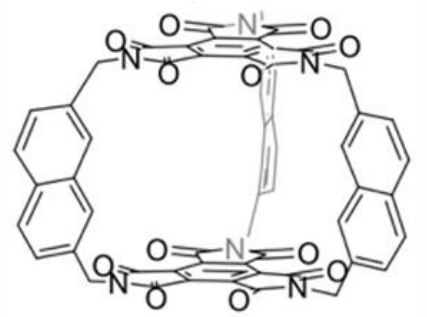

1.44

Figure 1.34: General structure of cage-based receptor **1.44** reported by Wang et al.

In 2022 Shi, Liu and colleagues reported the synthesis of an electron deficient fluorinated leaning pillar[6]arene **1.45** consisting of two tetrafluoro-benzene units with a preorganised structure and suitable cavity size capable of forming a 1:1 binding complex with strong selectivity and binding toward Iodine ion driven by anion–π interactions (Figure 1.35).[162] Initially, UV-vis experiments were conducted to confirm the binding interaction between **1.45** and I^- . The UV-vis spectra of **1.45** in $CHCl_3$ showed a single maximum absorption band at 295 nm. When 5.00 equivalents of TBA I^- were introduced, a new absorption band appeared at 246 nm, indicating the formation of a new species in the solution. Importantly, the addition of 5.00 equivalents of F^-, Cl^-, and Br^- did not disrupt the absorption band of **1.45**, demonstrating its specific recognition of iodide anions in chloroform. Furthermore, controlled experiments under competing conditions confirmed the unique selectivity of **1.45** for I^-, unaffected by competing anions such as F^-, Cl^-, and Br^-, thus affirming its selective recognition of iodide anions. ^1H NMR and ^{19}F

NMR experiments were conducted to further explore the host–guest complexation between **1.45** and I^-. Upon the addition of 5 equivalents of TBA I^- to **1.45**, the peaks corresponding to the proton signals on **1.45** experienced up field shifts, similarly the ^{19}F NMR spectrum of **1.45** exhibited an upfield shift after the introduction of 5.00 equivalents of TBA I^- to **1.45.** These observations are indicative of the heightened electron density of the host molecule **1.45** resulting from the encapsulation of electron-rich iodide anions within its cavity. The binding data was fitted to a 1:1 binding stoichiometry with an association constant for iodide to be 3.18×10^3 M^{-1}. This study introduced a novel and selective pillar[n]arene receptor for I^- via anion-pi interactions.

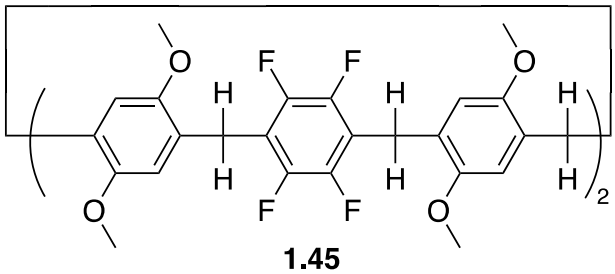

1.45

Figure 1.35: General Structure of fluorinated leaning pillar[6]arene **1.45** reported by Shi, Liu and colleagues.

1.8: Project Aims

Anion recognition and transport is a rapidly advancing field in supramolecular chemistry due to the ubiquitous nature of anions, their critical role in human biology, and the impact of channelopathies on patient outcomes. Despite significant progress, including the development of potent anionophores with clinical applications, many opportunities remain unexplored, particularly in creating robust methods to apply these supramolecular motifs in biological contexts and study their *in-cellulo* activity. This research focuses on squaramides as versatile anion-binding motifs, exploring their potential in developing novel strategies for anion recognition, sensing, transport, and antimicrobial properties. By conjugating squaramides to biomolecules such as amino acids and peptides (Figure 1.36); an area that remains underexplored despite its potential applications, this study aims to enhance their sensing capabilities, achieve spatiotemporal control over anionophoric activity, and further integrate these systems into medicinal chemistry, as biologically relevant anionophores continue to emerge.

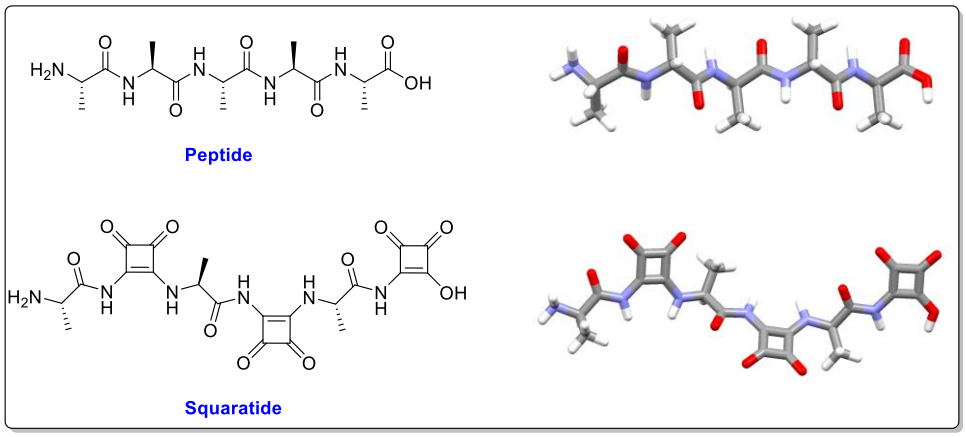

Figure 1.36: Schematic structural comparison of peptides vs. squaratides.

Chapter 2 focuses on the introduction and development of a novel class of peptidomimetic structures, termed squaratides—hybrid molecules combining the unique anion-binding properties of squaramides with the structural versatility of peptides (Figure 1.37). This chapter details the systematic exploration of these innovative structures, including the design and synthesis of a library of cyclic squaramides with varying amino acid side chains as a means to evaluate their efficacy in anion recognition. By integrating the distinct advantages of squaramides and amino

acids, this work aims to contribute a significant advancement to the field of anion receptor chemistry.

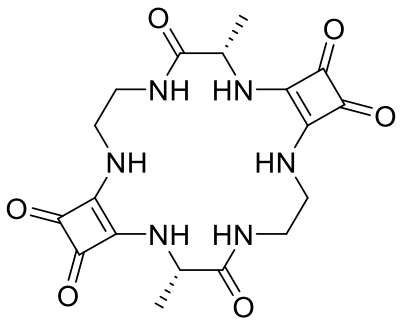

Figure 1.37: Chemical structure of 2.14 (Sq-2-Ala).

Building upon the work presented in Chapter 2, which focused on the solution-phase synthesis of squaramide-based receptors for anion recognition, **Chapter 3** chapter aims to expand the chemical space and functional application of squaramides through the development of solid-phase synthetic methodologies. By utilising solid-phase peptide synthesis (SPPS), a series of lysine based squaratides with enlarged cavity architectures were constructed, allowing for greater structural diversity and enhanced molecular interaction potential (Figure 1.38). With our compounds at hand, we aimed to evaluate the antimicrobial activity of these newly synthesised squaratides, particularly against methicillin-resistant *Staphylococcus aureus* (MRSA), through both phenotypic susceptibility testing and in-depth proteomic profiling. This approach seeks to explore the therapeutic potential of cavity-expanded squaramides as a new class of antimicrobial agents and to provide insight into their modes of action at the molecular level.

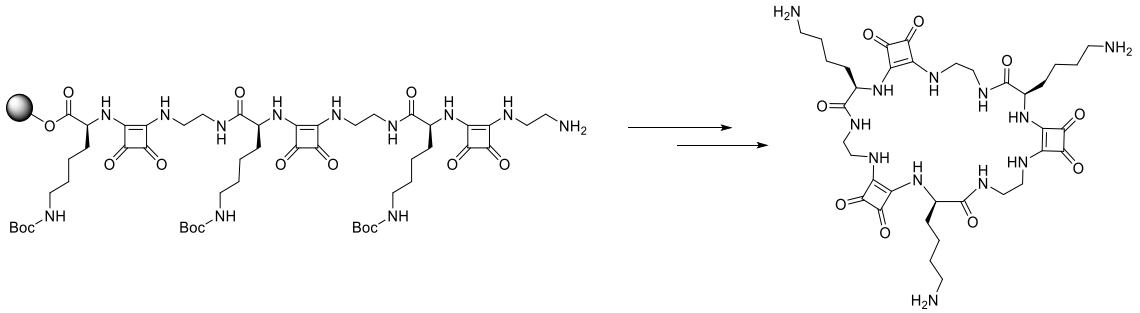

Figure 1.38: General schematic approach towards 3.5 (Sq-3-Lys).

Chapter 4 explores the functional diversification of squaratides by leveraging the side chain functionalities of amino acids (Figure 1.39). This includes the incorporation of

anion-transporting motifs onto the squaratide framework and the integration of fluorinated amino acids into their backbone. These modifications aim to expand the chemical space, enabling the development of not only innovative anion-binding receptors but also systems exhibiting efficient anion transport properties, thereby broadening the potential applications of squaratides in supramolecular and medicinal chemistry.

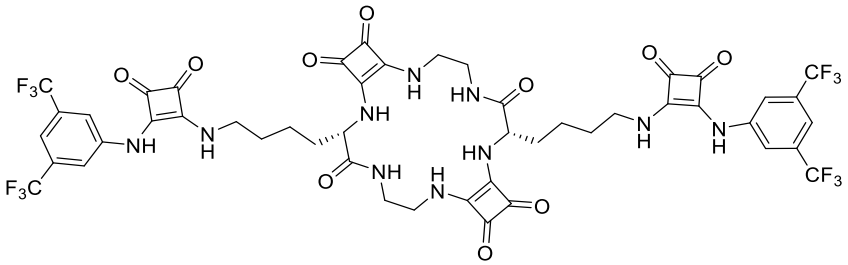

Figure 1.39: Chemical structure of 4.18 (Sq-2-Lys(SqBisCF_3).

Chapter 5 aims to utilise the Solid phase synthesis approach of squaratides to design, synthesise, and characterise a structurally novel fluorescent based squaratide for the selective recognition and sensing of fluoride anions. By implementing a naphthalimide based fluorescent amino acid into the backbone of the squaratide structure (Figure 1.40), it enables the receptor to operate as both a high-affinity anion binder and a real-time optical sensor. through a suite of spectroscopic techniques such as fluorescence emission, UV-visible absorption, and ^{1}H NMR titration studies, which together provide mechanistic insights into fluoride binding, hydrogen bonding interactions, deprotonation events, we set out to Investigate the anion-binding properties of the receptor as a means to advancing the development of dynamic, selective, and optically responsive supramolecular systems for practical applications in anion sensing, environmental analysis, and molecular diagnostics.

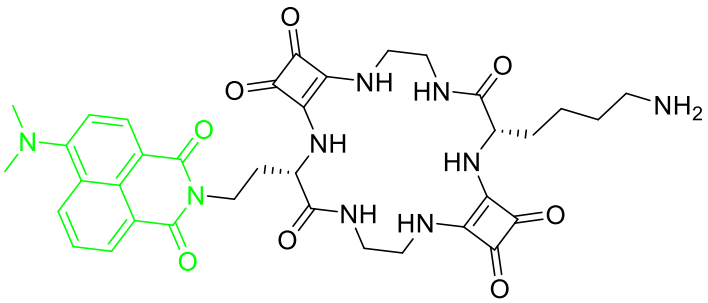

Figure 1.40: Chemical structure of 5.12 (Sq-2-Lys-Naph).

Chapter 2

Squaratides: A New Peptidomimetic code in Anion Recognition

2: Squaratides: A New Peptidomimetic code in Anion Recognition

2.1: Introduction

Molecular recognition plays an important role in a variety of biological systems such as, ion detection and environmental pollution control, as previously mentioned in chapter 1. The ability of researchers to develop host molecules that display excellent molecular recognition properties has been an expanding area of research since the birth of the field of supramolecular chemistry.[163, 164] Among the various molecular architectures employed for molecular recognition, artificially designed receptors that emulate natural systems in their ability to selectively bind target ions have emerged as powerful tools for advancing supramolecular chemistry.[66, 69, 165] These receptors play a crucial role in promoting intermolecular interactions and enhancing the stability of supramolecular assemblies, with applications spanning diverse fields such as sustainable electronics, advanced material science, and molecular medicine.[166-168] Their design draws inspiration from nature's remarkable modularity and structural diversity, particularly evident in the biosynthesis of anion-binding proteins. Nature employs well-defined design principles, where complementary hydrogen-bond interactions between amino acid side chains (e.g., the hydroxymethyl group of serine and the guanidino group of arginine) are coupled with stabilizing contributions from backbone amides to achieve specificity and strength in anion binding. [55, 169] Proteins with pre-organized secondary structures exemplify these principles, demonstrating ultra-high affinity and selectivity for their target anions.[118, 170] These insights serve as a blueprint for developing next-generation artificial receptors, with immense potential for innovation across multidisciplinary scientific and technological domains.[171-173]

Several groups have reported sequence-defined scaffolds that incorporate abiotic elements to enhance molecular recognition. For example, Kubik and co-workers synthesised a macrocyclic pseudopeptide **2.1**, incorporating three amide groups and three 1,4-disubstituted 1,2,3-triazole units arranged around the ring (Figure 2.1). [174] This pseudopeptide was specifically designed with amide NH groups and triazole CH groups oriented toward the central cavity, creating an optimal environment for effective anion recognition. Binding studies using ^{1}H NMR titrations in 2.5 and 5 vol% H_2O/DMSO-d_6

were conducted with various anions, including chloride, nitrate, sulfate, and dihydrogen phosphate. The results demonstrated that the pseudopeptide exhibited a stronger affinity for larger oxoanions anions, such as sulfate and dihydrogen phosphate, compared to smaller anions like chloride and nitrate, which is attributed to the structural features of the pseudopeptide that facilitate effective interactions with these larger oxoanions. Notably, while the pseudopeptide primarily forms a 1:1 complex with anions, binding studies revealed a more complex scenario for sulfate and dihydrogen phosphate, where a 2:1 (pseudopeptide-to-anion) complex is formed, highlighting the pseudopeptide's multiple binding sites and its capacity to accommodate larger anionic guests, thus showcasing its versatility in molecular recognition. Following this study, Kubik and colleagues enhanced the macrocyclic pseudopeptide framework (**2.1**) by incorporating three 5-iodo-1,2,3-triazole subunits. These subunits act as halogen bond donors, significantly improving the receptor's ability to interact with anions, particularly halides like chloride. The iodine atoms in the triazole units facilitate the formation of halogen bonds, which are distinguished by their high directionality and strength, offering superior anion-binding efficiency compared to hydrogen-bonding analogues. Qualitative ^{1}H-NMR spectroscopic studies were conducted to evaluate the receptor's affinity for various anions. The findings revealed substantial differences between the halogenated receptor **2.2** and its non-halogenated counterpart (**2.1**). While **2.1** primarily binds oxoanions such as dihydrogen phosphate (DHP) and sulfate through hydrogen bonding, the introduction of iodine in **2.2** alters the binding behaviour. The halogenated receptor's iodine atoms create a more confined cavity, reducing its interaction strength with oxoanions but significantly enhancing its affinity for halides.

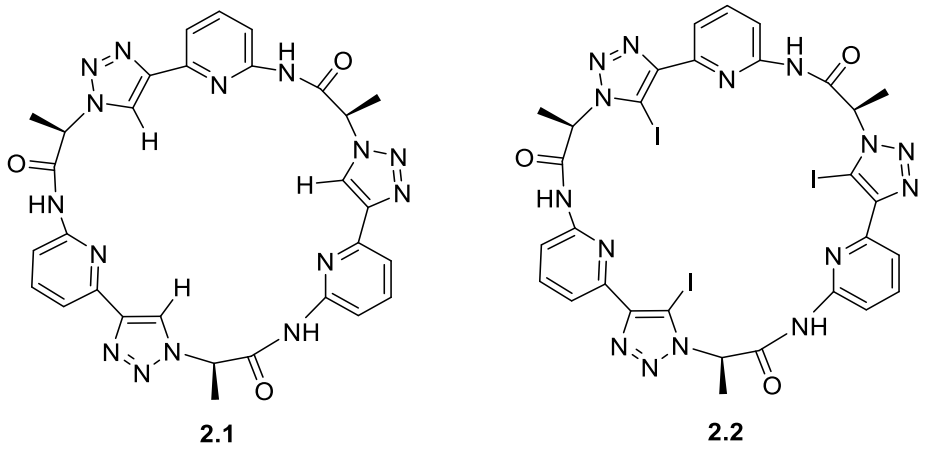

2.1 **2.2**

Figure 2.1: Chemical structures of cyclic pseudopeptides **2.1** and **2.2**. Reported by Kubik and colleagues.

The Haberhauer group has synthesized a series of cyclic peptide scaffolds inspired by the Lissoclinum family of natural hexapeptides, demonstrating their potential applications in molecular recognition and combinatorial chemistry.[175-178] They set out to synthesis a set of C2-symmetric azole-containing macrocyclic peptides (**2.3 – 2.6**) (Figure 2.2). Using ^{1}H-NMR titrations in DMSO-d_6/5% $CDCl_3$, the binding capabilities of these macrocycles were evaluated with various anions, including dihydrogen phosphate, acetate, fluoride, hydrogen sulfate, toluene sulfonate, methyl sulfonate, chloride, nitrate, bromide, iodide, and perchlorate.[179] Job's plot analyses confirmed 1:1 binding stoichiometry for all tested anions, with dihydrogen phosphate consistently exhibiting the strongest binding affinity. Among the macrocycles, the thiazole-containing receptor **2.5** displayed the highest affinity for $H_2PO_4^-$ (K_a = 3 × 10^4 M^{-1}), followed by the oxazole receptor **2.4** (K_a = 2.47 × 10^4 M^{-1}) and the imidazole receptor **2.3** (K_a = 2.64 × 10^3 M^{-1}). In contrast, receptor **2.6** exhibited the lowest binding affinities, likely due to the larger size of its macrocyclic cavity. Interestingly, while thiazole receptor **2.5** showed the highest overall binding affinities, the imidazole receptor **2.3** demonstrated the best selectivity for $H_2PO_4^-$ (10-fold selectivity). This enhanced selectivity was attributed to the higher basicity of the imidazole nitrogen atom, which allows the protons of $H_2PO_4^-$ to form additional hydrogen bonds, underscoring the role of azole functionality in fine-tuning binding behaviour.

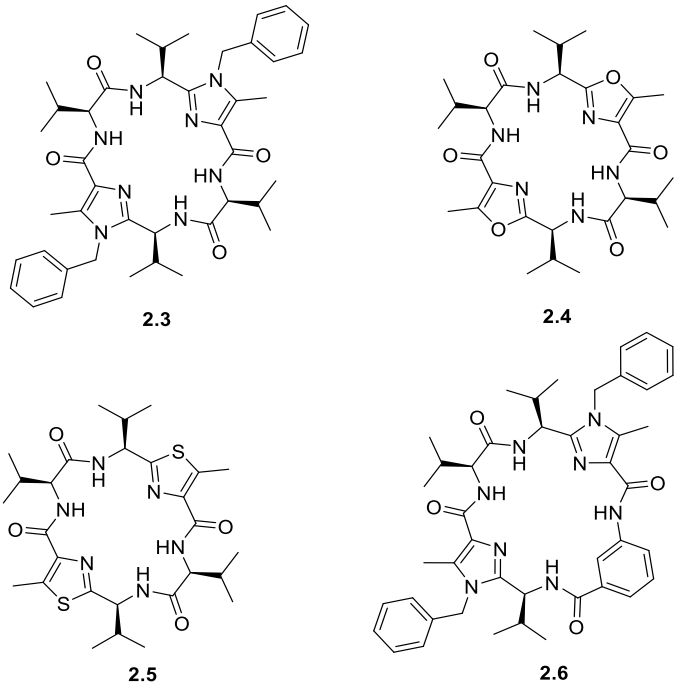

Figure 2.2: Chemical structure of a series of cyclic peptide scaffolds reported by Haberhauer and colleagues.

While we have discussed some examples above, some other work worth mentioning include the group of Flood, whereby they encapsulated Cl^- with attomolar affinity in a triazolo cryptand-like cage stabilized by unusual, polarized C-H bonds.[180,] Knipe and co-workers synthesised alpha-helical and beta-strand peptidomimetics based on pyrimidines while Meisel and Hamilton reported cavitand-like molecular containers based on 2,4-dialkoxy-meta-aminomethylbenzoic acid (MAMBA) monomers.[181] Alfonso and co-workers synthesised a family of tris-pyridine decorated cyclic peptides capable of self-assembly to carry out chloride recognition and transport.[182, 183]

The common theme among these examples is the judicious use of receptor design to incorporate abiotic elements into peptidomimetic scaffolds to produce a wide variety of potential compound designs.[118, 184] However, there are scarce examples of sequence-based scaffolds that incorporate additional binding units within the peptide backbone, even though the incorporation of additional H-bonding capacity within the peptide backbone can improve anion affinity and selectivity without damaging the helical folding.[185, 186] Although synthetic receptors generally rely on the same non-covalent interactions nature uses for anion binding, many use diverse recognition motifs based on amides, ureas, thioureas and, more recently, squaramides to provide the required hydrogen-bond donor sites.[111, 187-189] Squaramides offer a host of advantages, including rigidity, aromaticity and strong specific anion binding. We have reported several examples of squaramides as anion recognition units[112, 190] and squaramide-peptide conjugates as highly discriminating sulfate binders.[191] Incorporation of squaramides within a macrocyclic structure enables sulfate binding in highly competitive environments, with the ability to extract this hydrophilic anion into both water and organic solvents.[137, 138].

An example of macrocyclic squaramides can be seen in work carried out by Elmes, Jolliffe, and co-workers where they synthesized a series of macrocyclic squaramides as anion receptors (Figure 2.3), demonstrating their potential in anion recognition.[137] Receptors **2.7** and **2.8** exhibited strong binding affinities for SO_4^{2-}, with association constants (K_a) exceeding 10^4 M^{-1}. Additionally, receptor **2.7** displayed notable selectivity for $H_2PO_4^-$ and AcO^-, with $K_a > 10^4$ M^{-1} and $K_a = 7530$ M^{-1}, respectively. Although receptors **2.9** and **2.10** exhibited low solubility in DMSO-d_6, their interaction with anions

provided valuable insights. The addition of 1 equivalent of AcO^- or SO_4^{2-} induced significant changes and simplification in their ^1H NMR spectra, indicating strong binding. Furthermore, the introduction of 1.2 equivalents of SO_4^{2-} completely dissolved **2.9** and **2.10** in DMSO-d_6, further supporting their high affinity for SO_4^{2-}. These observations highlight the effectiveness of these macrocyclic squaramides as selective anion receptors. However, one of the drawbacks is the relative insolubility of these receptors and the difficulty in incorporating additional functionality. Therefore, there is a significant unmet need for programmable receptors that are easily modified but retain high anion binding affinity and specificity across a range of solvents.

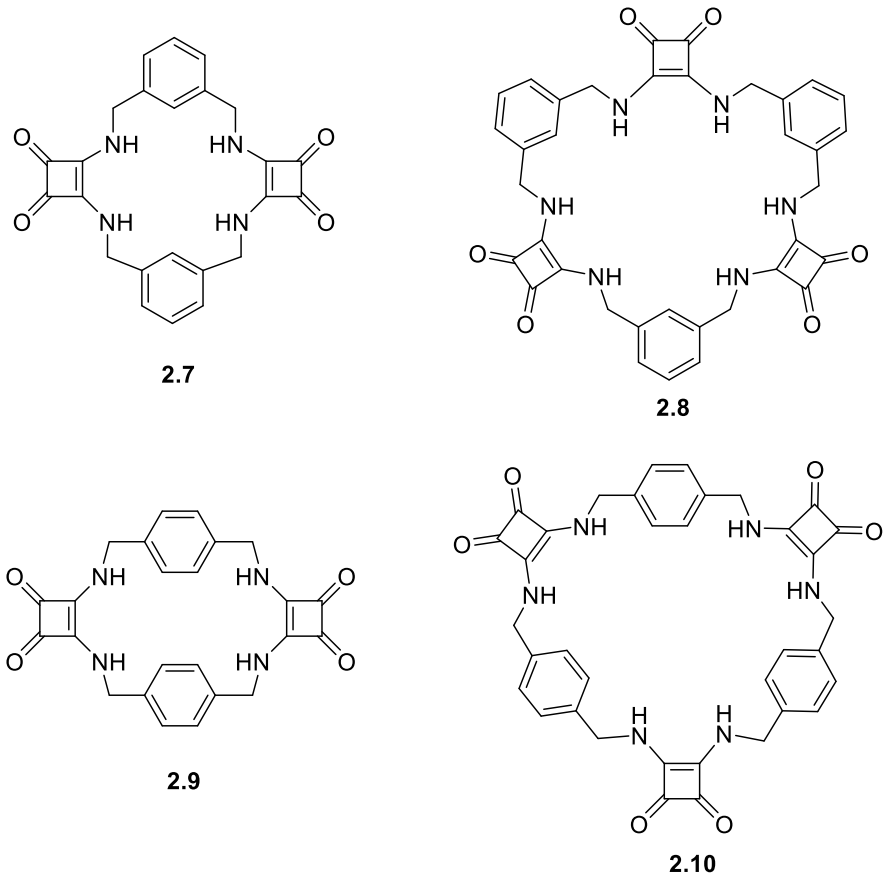

Figure 2.3: Chemical structures of squaramide based macrocycles reported by Jolliffe and co-workers.

The aforementioned examples highlight the utility of cyclic pseudopeptides and cyclic squaramides while underscoring their limited representation in the current literature. These compounds exhibit significant potential in anion recognition, particularly for oxoanions such SO_4^{2-} and various phosphate species. However, as a recently introduced class of receptors, the number of reported cyclic squaramides remains relatively small. Moreover, a hybrid structure combining the squaramide moiety within cyclic peptide frameworks—has yet to be explored. To address this gap, this study takes the initial steps into this uncharted territory, aiming to design and synthesise such a hybrid structure - termed 'squaratides' and uncover their potential as a new programable anion recognition motif.

2.2: Chapter Objective

The objective of this chapter can be split into two parts. Our first aim is to introduce the design of a sequence-defined material that could be used to create a diverse set of receptor molecules. This new class of molecules we call “squaratides”, a portmanteau of the words squaramide and peptide (Figure 2.4). The initial generation of cyclic squaratides would be synthesized using a solution-phase approach, which to synthesise the 1st generation of receptors and gain important insights into their structural and functional properties. We believed that this information would pave the way for the construction of intriguing supramolecular systems; a series of readily accessible and modifiable squaratides, enhancing the availability of efficient anion recognition systems.

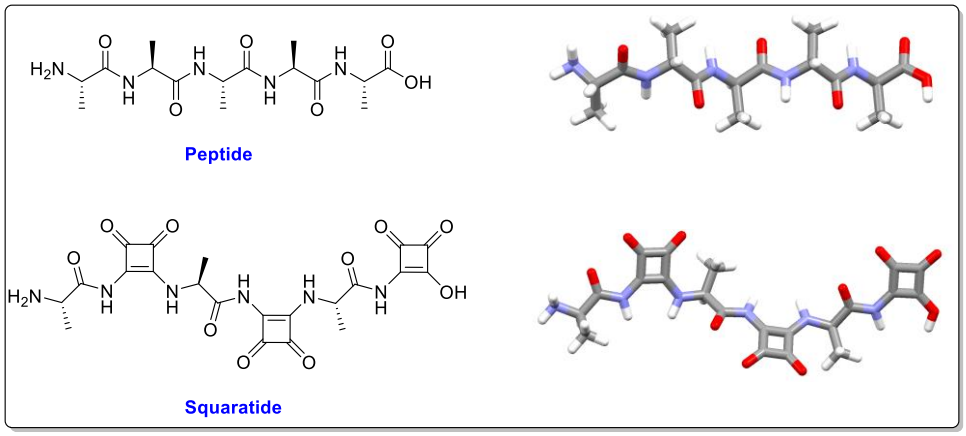

Figure 2.4: Design comparison between peptides and ‘Squaratides’.

The second aim of this chapter is to leverage these macrocyclic scaffolds as a tool for anion recognition in solution. As of yet, there are no reports of macrocyclic squaratides that bear squaramide moieties into a peptide backbone. We believe that combining all the advantages that squaramides offer including rigidity, aromaticity and strong specific anion binding with the structural versatility of peptides will result in useful binding properties. The incorporation of natural and protected amino acid residues introduces diversity in steric, electronic, and hydrophobic character. Through this approach, we hope to discover a versatile and innovative platform for probing anion–host interactions in a controlled and systematic manner adding to the field of molecular recognition and supramolecular chemistry.

2.3: Synthesis and Characterisation

2.3.1: Design Strategy towards the synthesis of Squaratides

The initial synthetic design of our squaratides can be seen in scheme 2.1. diethyl squarate with N-Boc-AA to yield intermediate **A** that could subsequently be reacted with the desired amino acid to provide the disubstituted squaramide derivative **B**. Boc deprotection would yield monomer **C** that could then undergo dimerization in the presence of a coupling reagent to afford the desired cyclic squaratide **D**. However, before carrying out our synthesis, our research group discovered and confirmed the occurrence of a Smiles rearrangement that, to the best of our knowledge, has not been previously reported in the context of squaramides. This transformation appears to involve intramolecular nucleophilic attack by a free primary amine on the electron-deficient cyclobutene ring, leading to the displacement of a terminal amide moiety.[192, 193] A plausible mechanistic pathway is proposed in Scheme 2.1. It is hypothesized that the presence of multiple electron-withdrawing substituents significantly enhances the electrophilicity of the cyclobutene carbon, thereby facilitating nucleophilic substitution by the adjacent amine functionality.

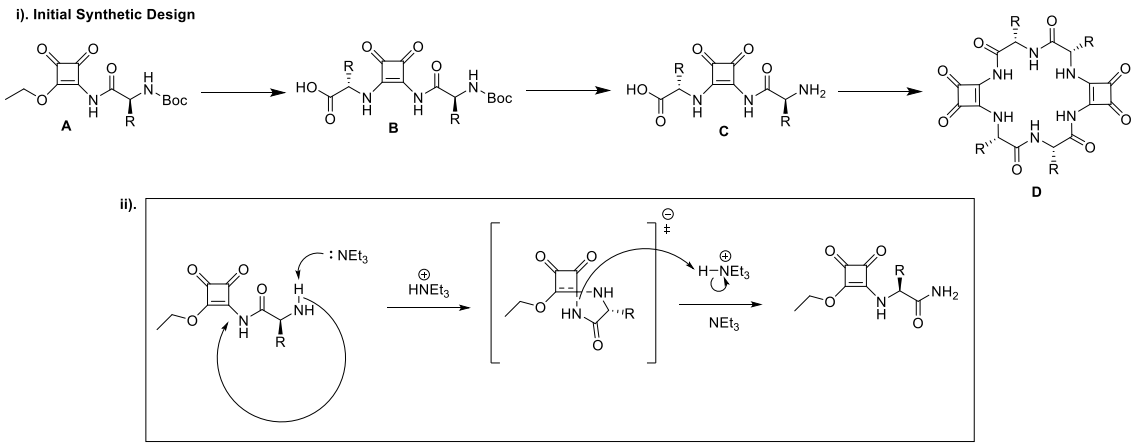

Scheme 2.1: **i).** Initial design strategy towards the synthesis of squaratides. **ii).** The speculated Smiles rearrangement mechanism of squaratide monomer, under basic condition to form the rearranged product.

As a result, our initial design strategy was not plausible. We hypothesized that eliminating the adjacent carbonyl moiety could mitigate the observed instability and facilitate successful macrocyclization. Specifically, the substitution of one amino acid

residue with 1,2-ethylenediamine (EDA) was proposed as a strategic modification. This substitution was expected to preserve the overall cavity geometry of the macrocycle while reducing the likelihood of undesired side reactions such as rearrangement or hydrolytic cleavage. Structurally, EDA may be viewed as a minimalistic analogue of glycine, retaining backbone flexibility without introducing a carbonyl group adjacent to the squaramide core. In this revised design (Scheme 2.2), the original amide linkage between the cyclobutene ring and the amino acid is replaced, yet macrocyclization remains feasible through the formation of two new amide bonds—linking the EDA spacer with the opposing amino acid residue. Briefly, diethyl squarate is first reacted with N-Boc-protected EDA to generate the mono-substituted intermediate **2.11**. This intermediate is subsequently coupled with the desired amino acid to furnish the disubstituted squaramide derivative **2.12 (AA)**. Removal of the Boc protecting group yields the free amine monomer **2.13 (AA)**, which is then subjected to dimerization using standard peptide coupling conditions to afford the target macrocyclic squaratide **Sq-2-AA**.

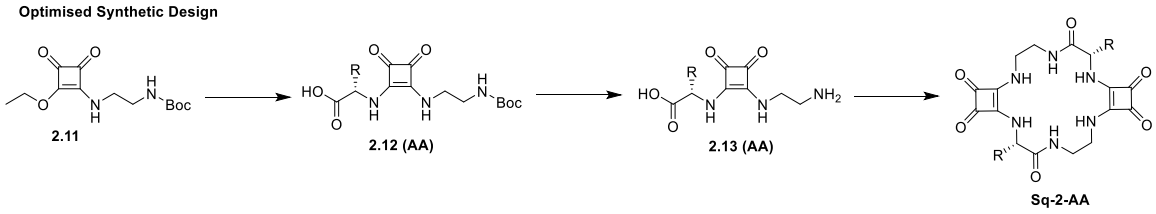

Scheme 2.2: Optimised design strategy towards the synthesis of squaratides

2.3.2: General Synthesis of 1st Generation Squaratides

The initial step involved synthesising 3,4-diethoxy-3-cyclobutene-1,2-dione, commonly known as diethyl squarate (DeSq). Diethyl squarate is one of the most prevalent alkoxy derivatives of squaric acid and serves as a primary component for synthesising the squaratides. **DeSq** was synthesized using a method adapted from the one originally reported by Liu *et al*.[194] In this process, 3,4-diethoxy-3-cyclobutene-1,2-dione – squaric acid – was reacted with triethyl orthoformate to afford **DeSq** with a yield of 85%, allowing us to proceed with the synthesis of cyclic squaratides as outlined in Scheme 2.3. Briefly, to a stirring solution of diethyl squarate in EtOH. N-Boc-ethylenediamine was added dropwise and stirred overnight to yield intermediate **2.11,** that was subsequently reacted in EtOH under basic refluxing conditions to yield the corresponding monomers

with a variety of amino acids including Ala, Phe, Leu, Lys and Bn-Asp to provide disubstituted squaramide derivatives **2.12 (AA)** in 86 %, 52 %, 91%, 91% and 92%, respectively. Boc deprotection in the presence of TFA: DCM (1:1) yielded all desired monomers **2.13 (AA)** in quantitative yields. With the monomers in hand, the next step was dimerization of each of the **2.13 (AA)** building blocks to create the proposed cyclic dimers **2.14 – 2.18 (Sq-2-AA).** This was carried out in DMF at low concentration (approx. 7.5 x 10^{-5} mM) in the presence of N-methylmorpholine (NMM) and benzotriazol-1 yloxytripyrrolidinophosphonium hexafluorophosphate (PyBOP), whereby LC-MS analysis of each reaction mixture confirmed the formation of the desired cyclic dimers **2.14 – 2.18 (Sq-2-AA)** in all cases. Using these conditions, the cyclic dimers were isolated in yields varying from 25% to 54% (See Scheme 2.3). **2.17** was subsequently deprotected using 33% HBr in AcOH solution in a yield of 90%. Attempts to deprotect **2.18** under standard reducing conditions (*e.g.*, $NaBH_4$ or H_2/Pd/C) were unsuccessful, which we believe is likely due to the vulnerability of the squaramide motif to hydrogenation.

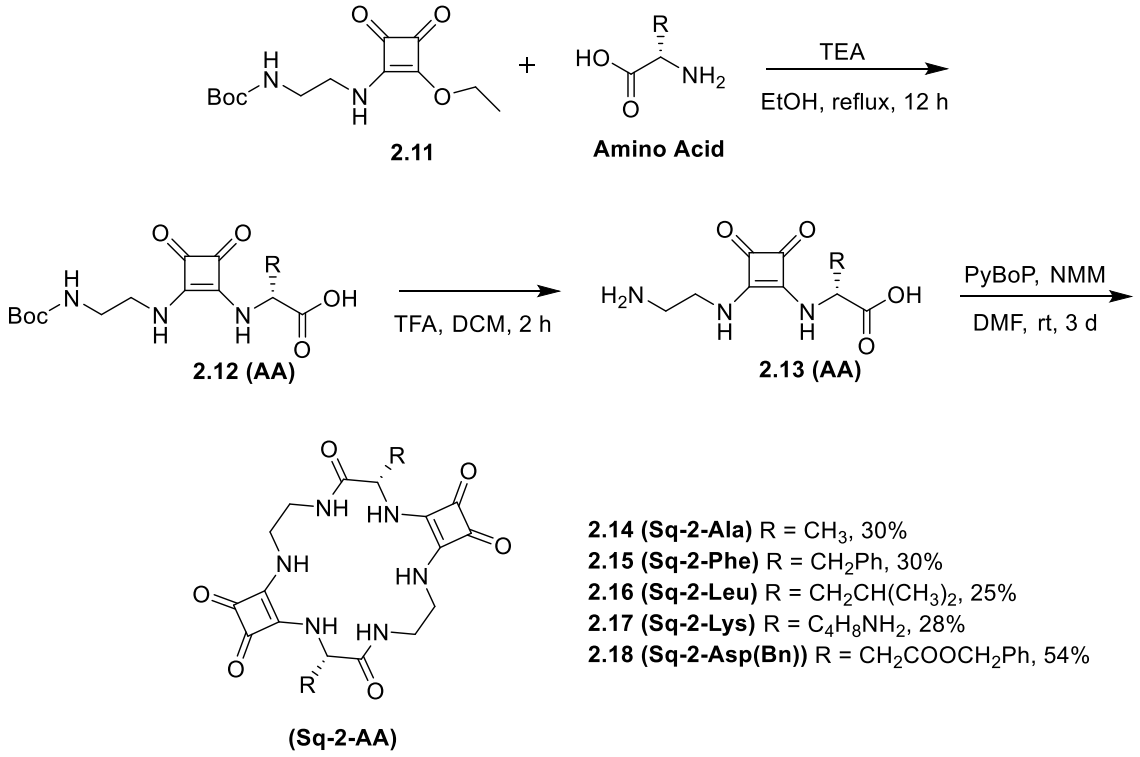

Scheme 2.3: General synthetic strategy towards 1st Generation cyclic Squaratides.

During NMR characterisation, it was noted that the ^{1}H NMR spectra of these compounds gave rise to complex behaviour where several sets of significantly broadened peaks were observed even though LC-MS analysis confirmed a high degree of purity. Data for (**2.15 (Sq-2-Phe)**) is shown as an example in Figure 2.5, where the α-proton of the amino acid exhibited splitting into two distinct signals at 4.6 and 4.8 ppm, while the methylene protons of the phenylalanine (Phe) moiety appeared as two poorly resolved doublets at 2.75 and 2.9 ppm. Assignment of the two methylene protons within the ethylenediamine (EDA) linker necessitated the use of two-dimensional NMR techniques, specifically COSY and HSQC spectroscopy. The methylene protons appeared at approximately 2.8 ppm, 3.2 ppm, while significant signal overlap was present in the 3.6 – 3.8 ppm region. Detailed analysis revealed this region to comprise two closely spaced but distinct signals at 3.76 and 3.77 ppm. Although these proton resonances were split across different chemical shifts, HSQC analysis showed that each pair remains coupled to the same respective carbon atom. Supporting this, the resonances at 2.8 and 3.76 ppm were assigned based on their correlation with a ^{13}C signal at 38.9 ppm, while the resonances at 3.2 and 3.77 ppm, correlated with a ^{13}C resonance at 44.05 ppm (See Appendix). The aromatic region displayed characteristic signals between 7.1 and 7.3 ppm, corresponding to ortho (7.2 ppm), meta (7.3 ppm), and para (7.1 ppm) protons of the phenyl ring. The amide NH proton of Phe appeared as a doublet at 7.5 ppm, whereas the NH proton of the EDA moiety linking the cyclobutene ring appeared as a poorly resolved triplet at 7.05 ppm. The amide NH proton was observed as a similarly unresolved triplet at 8.1 ppm. In addition to these assignments, several broad and overlapping resonances in the region of 7.5–8.45 ppm were observed, thought to arise from conformational isomerism, leading to multiple NH-related signals. This is seen at 8.45ppm whereby a small peak is observed because of an alternate secondary conformation of the receptor, and that the larger peak at 8.1 ppm represents the same amide proton in its primary conformation.

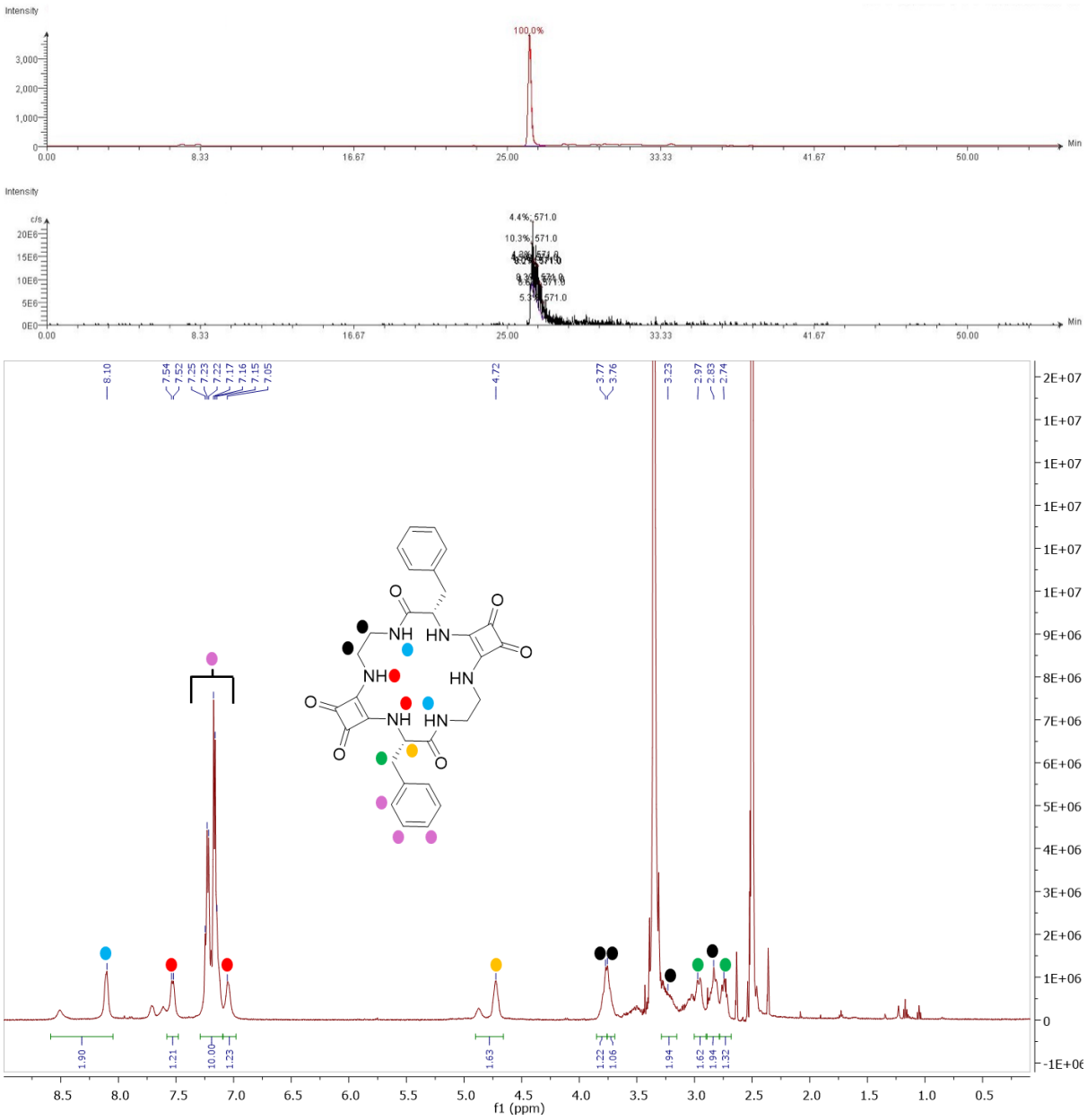

Figure 2.5: (**Top**) LCMS Characterisation of **2.15 (Sq-2-Phe)** (red) Analytical HPLC trace of purified **2.15 Sq-2-Phe**; t_R = 27 mins (0 – 100% MeCN over 55 mins, λ = 254 nm). (black) Extracted Ion Chromatogram for 571 $[M + H]^+$. (**bottom**) ^{1}H NMR spectrum of **2.15 (Sq-2-Phe)** (500 MHz, DMSO-*d*$_6$, 298K).

To clarify this, variable temperature (VT) NMR was conducted on Sq-2-Phe in DMSO-d_6 (19 mM) from 298K to 348K. As shown in Figure 2.6(a) and 2.6(b), significant changes were observed over that temperature range where the signals associated with squaramide and amide NHs undergo changes in their chemical shift as a function of increasing temperature, further suggesting the presence of conformational isomers in solution. Previously reported squaramide macrocycles also exhibited conformational

isomers that underwent slow interconversion on the NMR time scale.[137] Small cyclic peptides[195] and peptoids[196] also exhibit conformation isomerism. This is likely due to the formation of intramolecular hydrogen bonds which reduces conformational flexibility. To test this further, we introduced tetrabutylammonium acetate (TBAAcO) to a solution of **2.15 (Sq-2-Phe)** in a bid to reduce conformational flexibility through the formation of a supramolecular host: guest complex. In this instance, a clear increase in spectral resolution was observed in the ^{1}H NMR spectrum with increased resolution and a reduced number of peaks. This was particularly evident in the NH region of the spectra where six signals were reduced to three and the peptide CH resolved to a single peak (Figure 2.6(c)). It is also worth noting that the previously mentioned peak at 8.45 ppm disappeared upon increasing temperature and addition of Acetate. This suggests that the conformation of the receptor upon anion binding results in the formation of a single conformational isomer, which is herein defined as a 'conformational unification', where a significant increase in rigidity is observed.

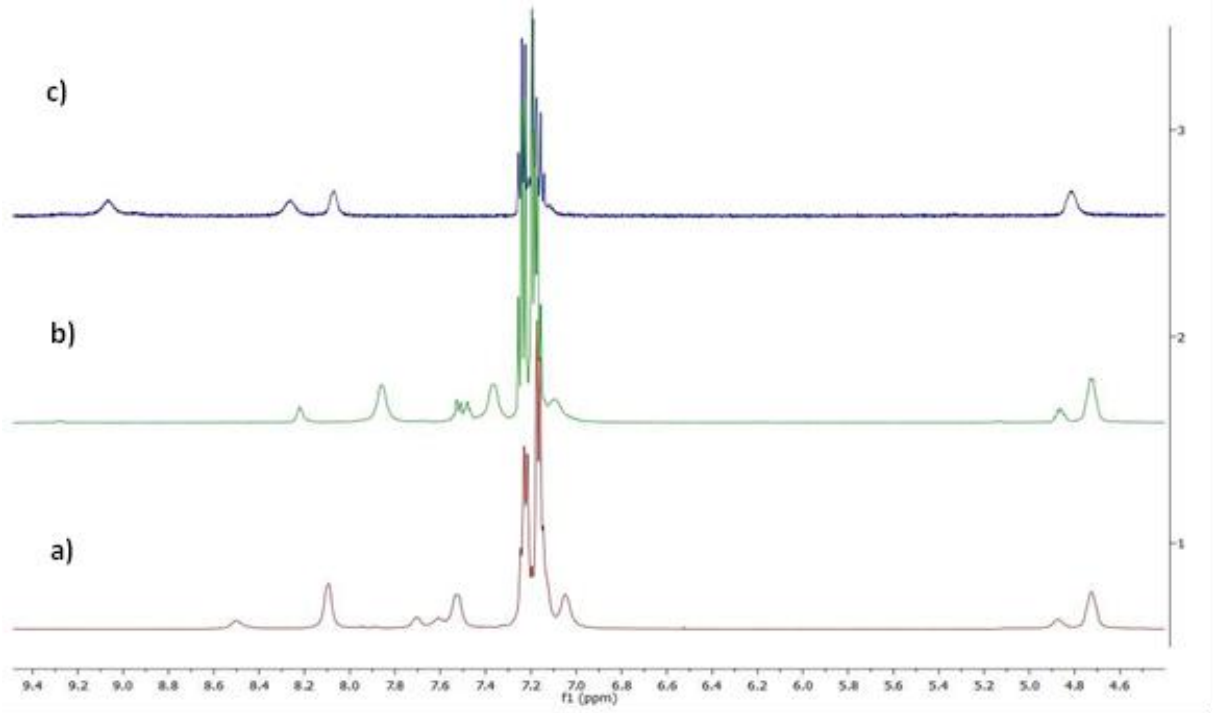

Figure 2.6: a) ^{1}H NMR Spectrum of **2.15 (Sq-2-Phe)** in DMSO-d_6 at 298 K. **b)** at 348 K. **c)** at 298 K after addition of TBA AcO (8eq).

As further characterisation of the solution behaviour, the absorption spectrum of **2.15 (Sq-2-Phe)** was recorded in DMSO (10 µM) and was shown to consist of a single broad band centred at 290 nm likely a result of a $\pi \rightarrow \pi^*$ HOMO→LUMO transitions. Furthermore, circular dichroism (CD) analysis confirmed the chiral nature of the macrocycles where the CD spectrum of **2.15 (Sq-2-Phe)** had a similar shape to the absorption spectrum albeit with both positive and negative regions of the spectrum with maxima being observed at 305 nm (negative) and at 280 nm (positive) (Figure 2.7).

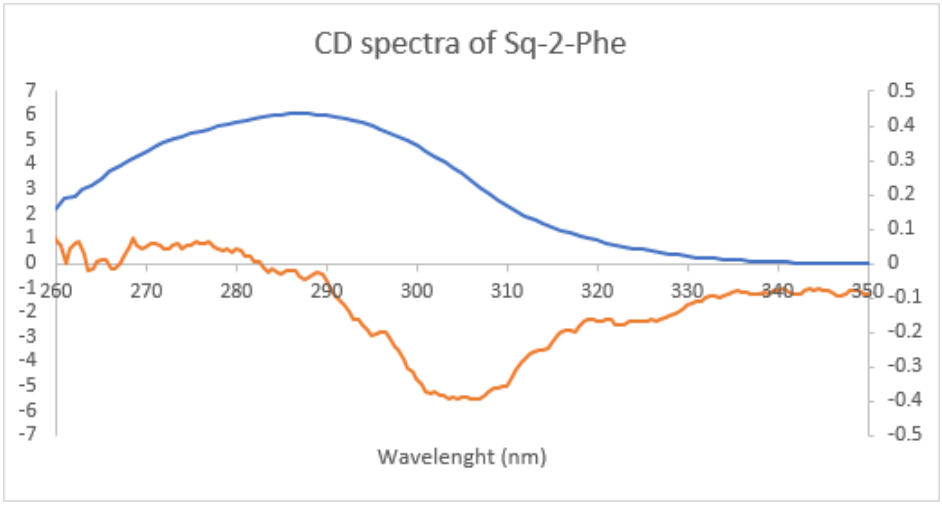

Figure 2.7: Absorption (Blue) and circular dichroism (orange) spectra of Sq-2-Phe.

2.4: X-ray crystallography and DFT analysis

Single crystals of **2.14 (Sq-2-Ala)** were obtained (by Dr Hua Tong) from a dilute solution of the receptor in DMSO-d_6 and X-ray crystallography analysis conducted by Dr. Chris Hawes at Keele University allowed detailed examination of the receptor conformation in the solid state. The diffraction data were solved and refined in the chiral monoclinic space group $P2_1$ and revealed a bis-DMSO solvate of the macrocycle. As shown in Figure 2.8(a), the two squaramide units adopt a *syn* conformation with both pairs of squaramide N-H hydrogen bond donors (N1, N2 and N4, N5) oriented in the same direction. However, puckering of the macrocycle offsets the two cyclobutene rings; the centroid of each ring being slipped by between 1.4 and 2.2 Å from the normal vector of the other, with their mean planes offset by 15.9° to each other. As such, each interacts independently as a bis-bidentate (rather than tetradentate) hydrogen bond donor, at

least when hydrogen bond acceptor character is limited to a single oxygen atom. One of the two squaramides donates hydrogen bonds to the squaramide carbonyl of an adjacent macrocycle, while the other binds a lattice DMSO molecule (Figure 2.8(b)). The peptide N-H groups both donate hydrogen bonds to the second lattice DMSO molecule. The amino acid sidechains point towards the periphery of the macrocycle, suggesting that they may not sterically interfere with anion recognition.

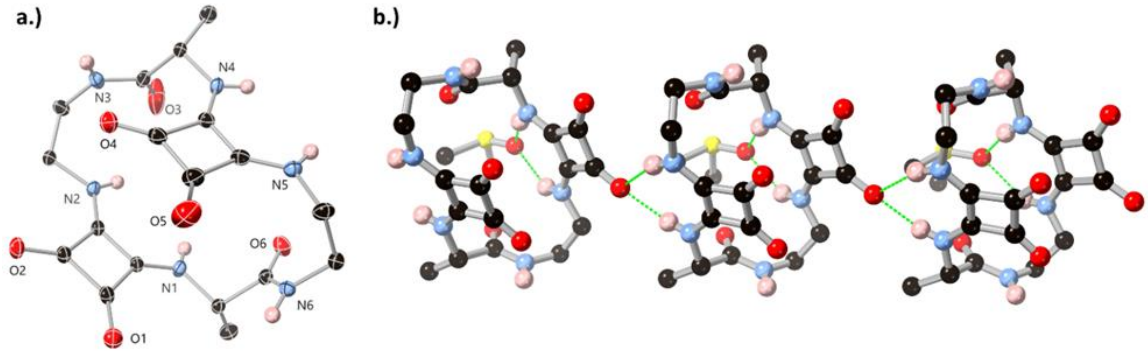

Figure 2.8: a.) Structure of the asymmetric unit of **2.14 (Sq-2-Ala)** ·2DMSO with heteroatom labelling scheme. Anisotropic displacement parameters ADP are rendered at the 50% probability level. Non N-H hydrogen atoms and DMSO molecules omitted for clarity. **b.)** The Hydrogen bonds between adjacent **Sq-2-Ala** including the hydrogen bond between the amide NH with the adjacent cyclobutene ring carbonyl, and the hydrogen bonds between the squaramide NHs with DMSO-d_6 molecules.

To help predict the anion recognition capability of the cyclic **Sq-2-Ala** receptor, computational modelling of the binding affinity of both Cl^- and AcO^- ions to **2.14 (Sq-2-Ala)** was conducted using density functional theory (DFT) by Dr. Shayon Bhattacharya at the University of Limerick. Calculations were conducted using a continuum implicit aqueous model[197] with D2 empirical dispersion corrections[198] using the Gaussian 16[199] code. The predicted binding energy (ΔE_{bind}) revealed that **2.14 (Sq-2-Ala)** discriminates between AcO^- and Cl^- (Figure 2.9) with a computed binding energy difference $\Delta\Delta E$ of -0.77 eV for preferential AcO^- binding. The squaramide-directed recognition is evident from the tight contacts and the alignment between the anion and the squaramide NH (H1, H2, H4 and H5 marked in bold in Figure 2.9). This predicted behaviour suggested

that squaratides may have high affinity for carboxylate anions and potentially show selectivity over smaller inorganic anions.

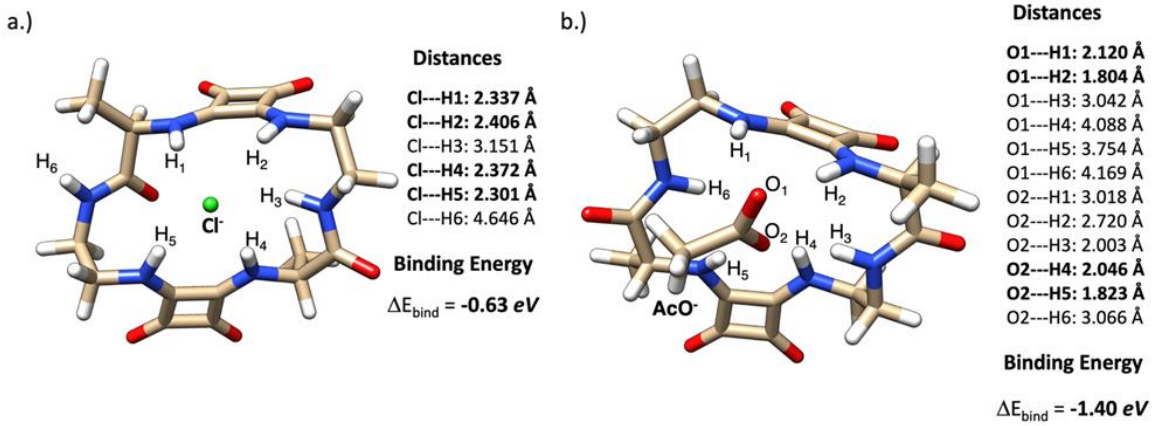

Figure 2.9: DFT-optimized structures of receptor **2.14 (Sq-2-Ala)** in complex with chloride (**a**) and acetate (**b**).

2.5: ^{1}H NMR anion binding analysis

With the insight gained from the structural analysis and predictive modelling (Figure. 2.8, 2.9) and given the observation that AcO^- significantly affects the conformation of the receptors in solution (Figure 2.6(b)), ^{1}H NMR spectroscopic measurements were performed to confirm the ability of squaratides to bind to anionic species in solution. Screening experiments were performed in the presence of eight tetrabutylammonium (TBA) salts of halides and oxoanions; F^-, Cl^-, Br^-, I^-, SO_4^{2-}, AcO^-, $H_2PO_4^-$, NO_3^- where the shifts of several proton signals within the ^{1}H NMR spectrum were measured as a function of anion concentration. Each experiment was carried out in DMSO-d_6 in order to allow observation for the change in ppm of the NH protons within the receptors' cavity.

F^- appeared to undergo deprotonation, and no binding behaviour was observed. For I^-, Br^- and NO_3^-, there was no evident shift for any peaks, suggesting that there was little or no interaction taking place. This aligns with other literature examples whereby several reports confirm that affinity for I^- and NO_3^- with squaramides is low.[49, 200] Interestingly, very minor changes were observed in the presence of SO_4^{2-}. This result is at odds with previously reported cyclic squaramide anion receptors which all showed a high degree of selectivity for this anion.[137] We suspect that this is a result of steric constraints within the squaratides framework that hinders optimal sulfate coordination resulting in an unfavourable binding geometry.

The squaratides displayed distinct behaviour upon the addition of AcO^-. The amide NH peak shifted first upfield and then downfield, while the squaramide NH peaks shifted downfield to a large extent (Δ ppm ≈ 1.5 for both). This unusual binding behaviour from the amide NH suggests a complex, multi-stage binding process where, at low acetate concentrations, weak transient interactions and conformational effects cause initial upfield shifts. As anion concentration increases, the amide NH eventually participates in direct hydrogen bonding with the anion, resulting in a downfield shift. With Cl^-, the NH peaks experienced a similar trend as for AcO^-, yet the Δ ppm was not as large (Δ ppm ≈ 0.6 and 0.9). From this titration data, affinity constants were determined for Cl- and AcO- by plotting the changes in chemical shift of the NH peaks against anion concentration and the resulting plots were analysed using the open-access software BindFit.[201]

Each receptor exhibited distinct chloride and acetate binding characteristics influenced by its amino acid side chain. **2.14 (Sq-2-Ala)**, used as a reference system, displayed straightforward 1:1 binding stoichiometry for both chloride (K_a = 692 M^{-1}) and acetate (K_a = 227 M^{-1}) (Figure 2.10). This behaviour is consistent with its structural simplicity (namely, the absence of bulky or charged side chains) resulting in minimal steric hindrance or electrostatic contributions. The small, nonpolar methyl group of alanine does not participate in secondary interactions, allowing the squaramide NH groups to dominate binding through directional hydrogen bonding. The higher affinity for chloride over acetate can be attributed to better size and shape complementarity between the spherical chloride ion and the preorganized squaramide cavity. Supporting this interpretation Job plot analyses for both anions revealed maxima at a 0.5 mole fraction, confirming a 1:1 binding stoichiometry and reinforcing the discrete, single-site nature of the host–guest interaction (Figure 2.11). Furthermore, speciation analysis (Figure 2.18) carried out on **2.14 (Sq-2-Ala)** revealed a clean and unambiguous transition between free and bound states, providing additional support for a simple non-cooperative binding mode. Taken together, the titration, Job plot, and speciation data all point toward a monomeric, preorganized receptor that binds anions in a predictable and well-behaved manner, making **2.14 (Sq-2-Ala)** an ideal benchmark for comparison with more complex or self-associating squaratides.

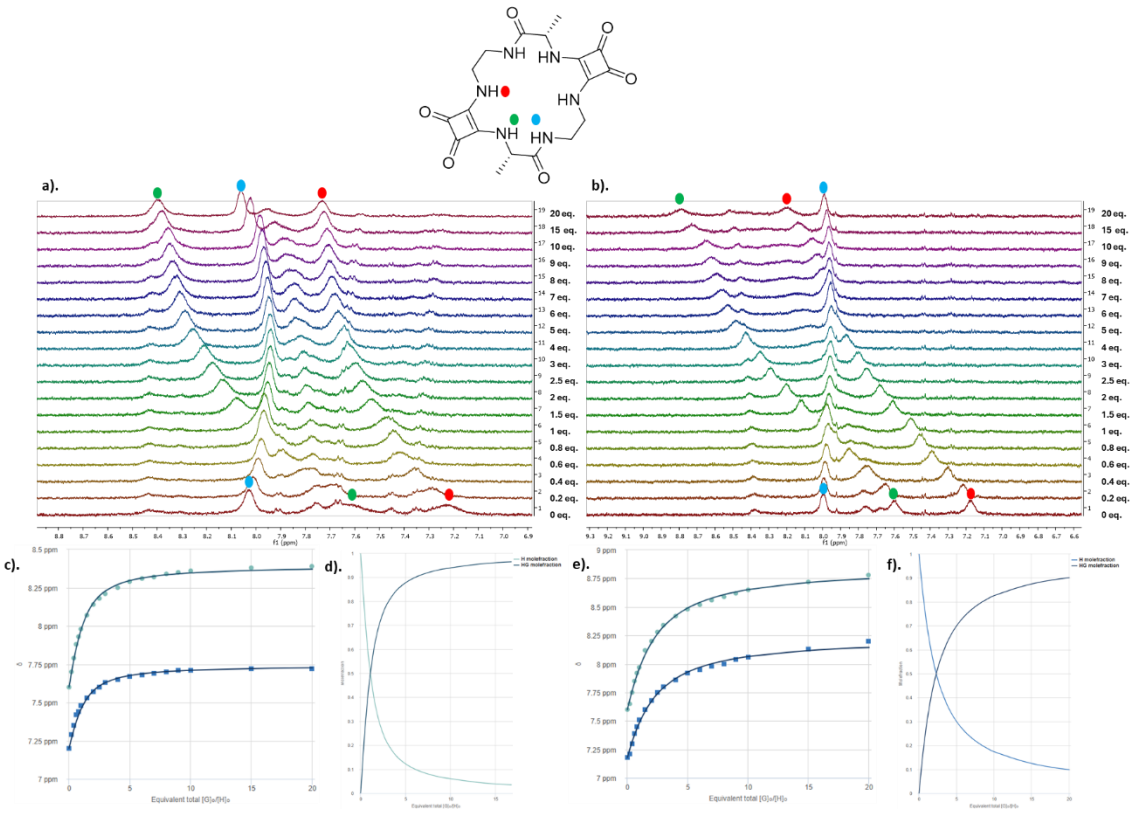

Figure 2.10: ^{1}H NMR Titration of **2.14 (Sq-2-Ala)** against (**a**) TBACl and (**b**) TBAAcO. Fitted data of the chemical shift change of the squaramide NH's of **2.14** against molar equivalents of (**c**) TBACl and TBAAcO. Speciation plot of **2.14** against **d**) TBACl and (**f**) TBAAcO.

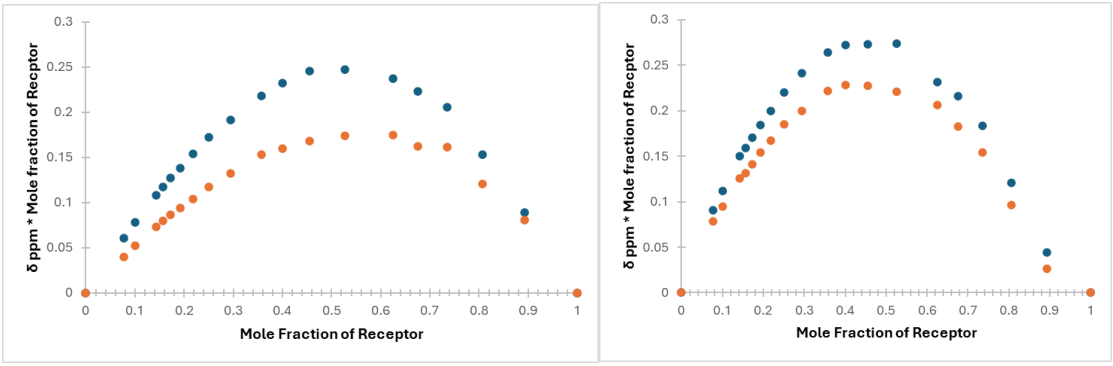

Figure 2.11: Jobs plot analysis of **2.14 (Sq-2-Ala)** against (**left**) TBACl and (**Right**) TBAAcO.

2.17 (Sq-2-Lys) on the other hand, with the presence of a positively charged ammonium group (-NH_3^+) on lysine engaged in secondary interactions resulting in enhanced chloride affinity, leading to a strong first binding event (K_{11} = 1.8 × 10^3 M^{-1}) through charge-assisted hydrogen bonding followed by a weaker second binding (K_{21} = 703 M^{-1}) which can be attributed to conformational rearrangement influencing the binding sites accessibility and electronics, resulting in repulsion from the first bound anion or decreased hydrogen bonding efficiency. This behaviour suggests cooperative 2:1 binding, where the initial chloride binding reorganizes the macrocyclic framework, making a second binding event less favourable but still possible due to electrostatic stabilisation.

During acetate titration with **2.17 (Sq-2-Lys)** partial deprotonation was observed on both the lysine side chain NH_3^+ group as a result of acetate's basicity, as well as large peak broadening on one of the squaramide NHs, which resulted in difficulty to discern and track its downfield shift throughout the titration. This reduced the number of available hydrogen bond donors losing effectively 50% of the squaramides hydrogen bonding donor ability and removing any additional potential stabilising interaction from the lysine side-chain ammonium (-NH_3^+), led to a 1:1 binding mode with a significantly lower association constant (K_a = 710 M^{-1}) compared to other squaratides where both squaramide NHs remained protonated, participating in binding and exhibiting a 2:1 binding mode with acetate (Figure 2.12).

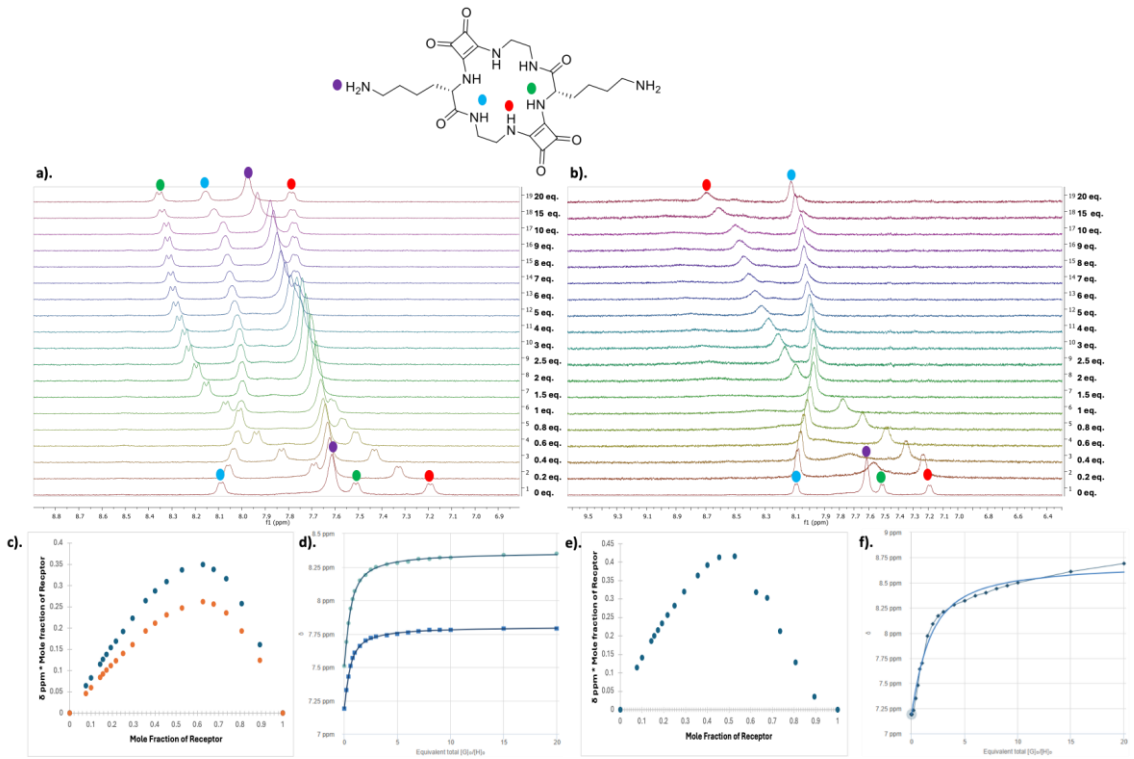

Figure 2.12: ^{1}H NMR Titration of **2.17 (Sq-2-Lys)** against (**a**) TBACl and (**b**) TBAAcO. Jobs plot analysis of **2.17** against (**c**) TBACl and (**e**) TBAAcO. Fitted data of the chemical shift change of the squaramide NHs of **2.17** against molar equivalents of (**d**) TBACl and (**f**) TBAAcO.

2.15 (Sq-2-Phe) resulted in a moderate chloride binding constant (K_a = *366* M^{-1}) best fitted to a 1:1 binding mode (Figure 2.13). The Job plot analysis further confirmed this stoichiometry, displaying a maximum at a 0.5 mole fraction, consistent with discrete 1:1 host–guest binding (Figure 2.14). The reduced affinity relative to **2.14 (Sq-2-Ala)** suggests that the bulky, hydrophobic phenyl ring may sterically hinder chlorides accessibility to the binding site or introduce competing weak π-interactions that do not significantly stabilize chloride binding. Thus, chloride binding is predominantly governed by squaramide NH···Cl^- hydrogen bonding. In contrast to **2.17 (Sq-2-Lys)**, which benefits from charge-assisted binding, **2.15 (Sq-2-Phe)** lacks additional electrostatic stabilization, limiting its binding strength and leading to weaker overall chloride affinity.

However, unlike chloride, acetate binding to **2.15 (Sq-2-Phe)** was significantly enhanced, exhibiting a strong 2:1 binding mode with binding constants K_{11} = 8.3 × 10^3 M^{-1} and K_{21} = 3 × 10^3 M^{-1}. The Job plot revealed a maximum near a mole fraction of 0.66, consistent with the proposed 2:1 stoichiometry (Figure 2.14). This cooperative behaviour is further

supported by the concentration-dependent ^{1}H NMR study, which revealed evidence of self-association in **2.15 (Sq-2-Phe)**. At increasing concentrations (0.1–20 mM) whereby notable peak changes were observed (figure 2.17). This aggregation behaviour has significant implications for anion binding, as the introduction of acetate may disrupt these higher-order assemblies, releasing monomeric units or partially dissociated oligomers that contribute to complex binding stoichiometries. Thus, the strong 2:1 binding observed for acetate may reflect not only direct hydrogen bonding and stabilizing π-interactions but also a dynamic interplay between guest-induced disaggregation and cooperative recognition. In contrast to the predictable 1:1, monomeric binding observed in **2.14 (Sq-2-Ala)**, the acetate binding in **2.15 (Sq-2-Phe)** underlines the profound influence of the amino acid side chain on the receptor's supramolecular behaviour and its resultant host–guest properties.

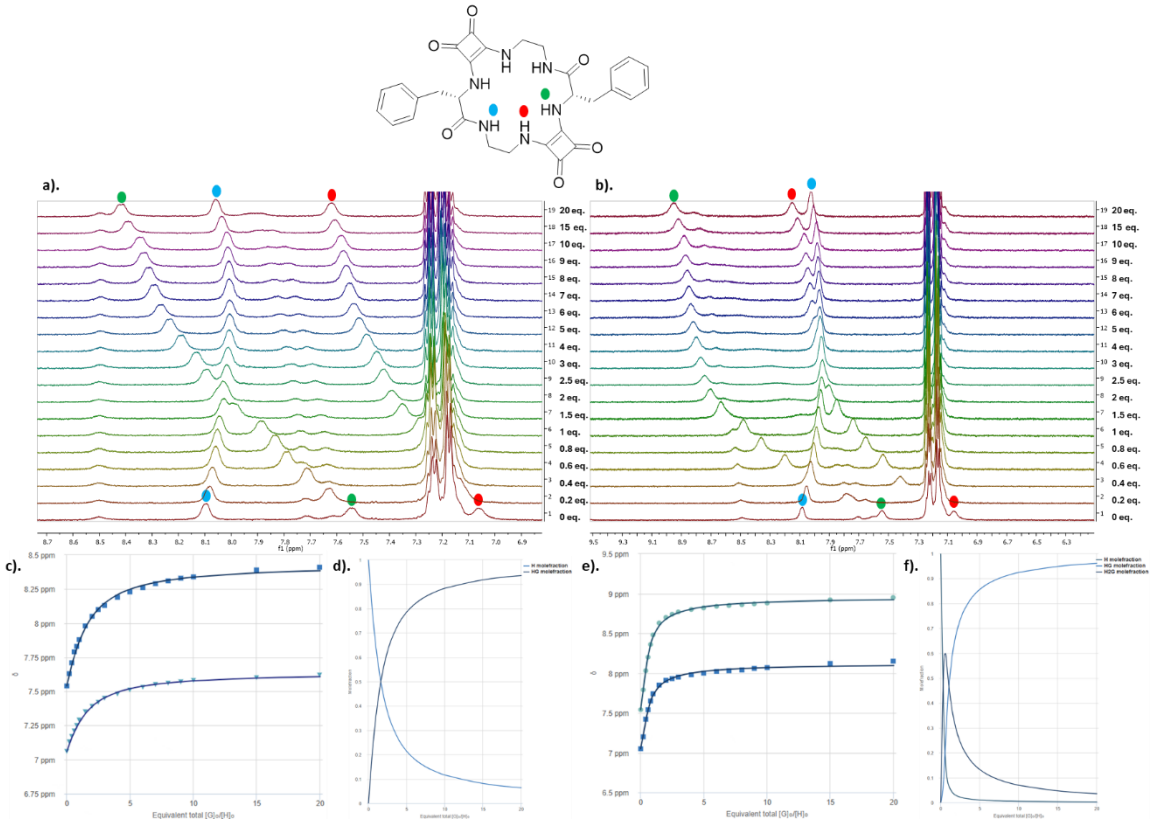

Figure 2.13: ^{1}H NMR Titration of **2.15 (Sq-2-Phe)** against (**a**) TBACl and (**b**) TBAAcO. Fitted data of the chemical shift change of the squaramide NHs of **2.15** against molar equivalents of (**c**) TBACl and (**e**) TBAAcO. speciation plot of **2.15** against **d**) TBACl and (**f**) TBAAcO.

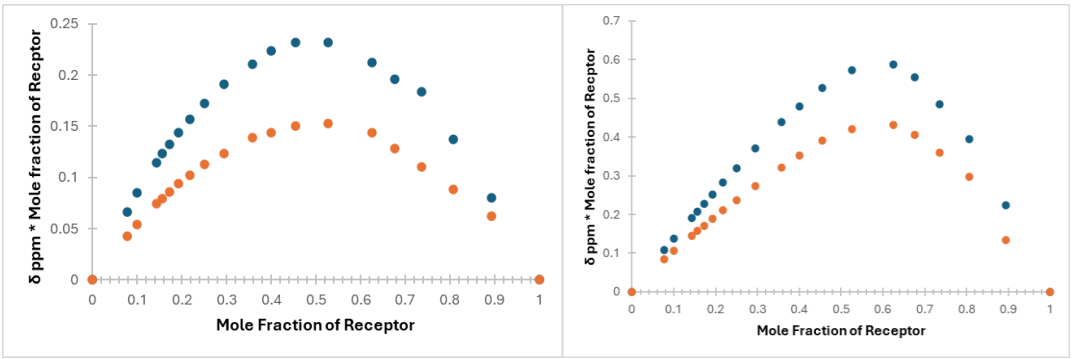

Figure 2.14: Jobs plot analysis of **2.15 (Sq-2-Phe)** against (**left**) TBACl and (**Right**) TBAAcO.

2.18 (Sq-2-Asp(Bn)) exhibited the strongest binding affinity for both Cl^- and AcO^- among the five studied squaratides (Figure 2.15). This enhanced affinity arises from a combination of steric preorganization, hydrogen bonding, and cooperative binding effects, which distinguish this receptor from the others. **2.18 (Sq-2-Asp(Bn))** demonstrated exceptional chloride affinity, with a binding constant of K_{21}= > 10^4 M^{-1}. This exceptionally strong chloride interaction can be attributed to the benzyl-protected aspartic acid introducing steric bulk near the binding pocket, locking the squaratide into a conformation that favours anion recognition. This preorganization minimizes entropic penalties upon anion binding, leading to higher affinity compared to the other semi flexible squaratides. The data was best fitted to a 2:1 binding mode suggesting cooperative binding, unlike **2.17 (Sq-2-Lys)** which predominantly favoured the 1:1 over the 2:1.

Similarly, **2.18 (Sq-2-Asp(Bn))** also displayed the highest affinity for acetate. Although the binding data were best fitted using a 2:1 host : guest model, the interaction is predominantly driven by a strong initial 1:1 binding event, with an association constant of K_{11} > 10^4 M^{-1}. This behaviour can be attributed to the conformational preorganisation imposed by the benzyl-protected aspartic acid side chains, which optimally position the squaramide NH donors for acetate recognition, thereby enhancing anion stabilisation. Additional π–π interactions between the benzyl groups may further support higher-order complex formation. In contrast, **2.17 (Sq-2-Lys)** exhibited significantly weaker acetate binding, as deprotonation of the lysine side chain NH_3^+ group, as well as peak broadening on the squaramide NH disrupted the hydrogen-bonding interactions required for effective anion binding.

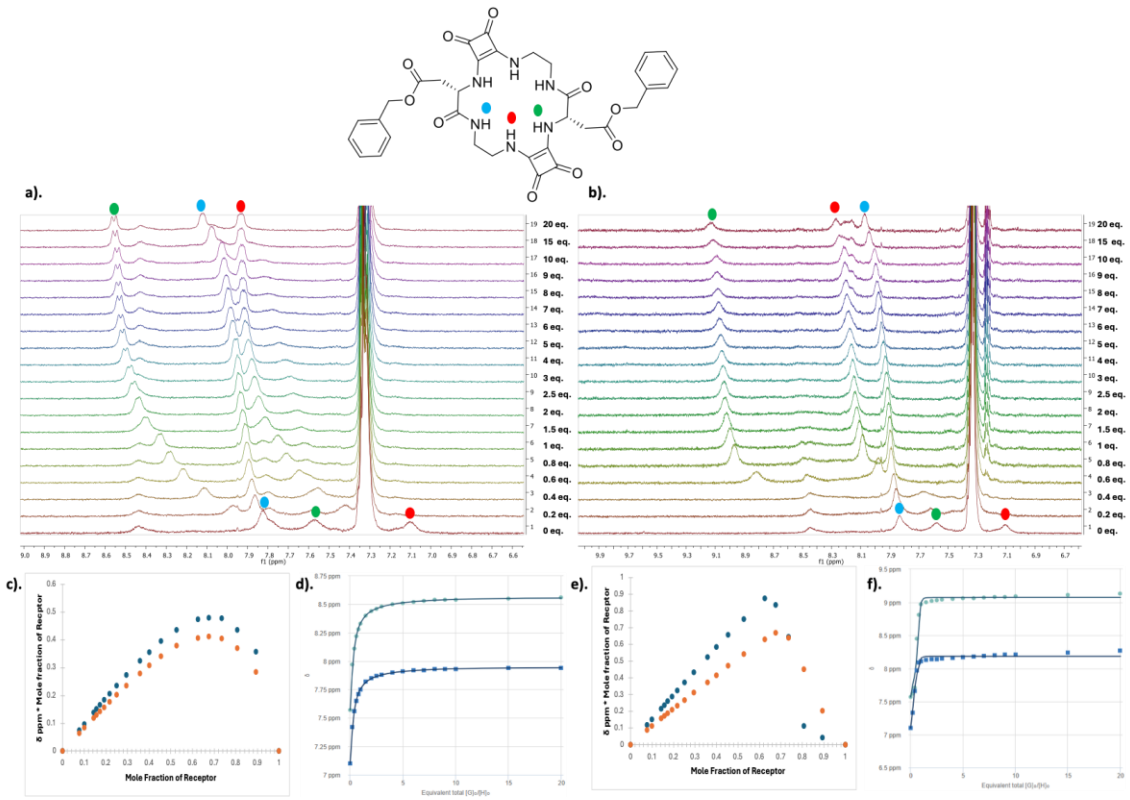

Figure 2.15: ^{1}H NMR Titration of **2.18 (Sq-2-Asp(Bn))** against (**a**) TBACl and (**b**) TBAAcO. Jobs plot analysis of **2.18** against (**c**) TBACl and (**e**) TBAAcO. Fitted data of the chemical shift change of the squaramide NHs of **2.18** against molar equivalents of (**d**) TBACl and (**f**) TBAAcO.

2.16 (Sq-2-Leu) displayed a weak chloride binding affinitiy, with a 1:1 binding mode and an association constant of K_a = 588 M^{-1}. This can be attributed to the the lack of Charge-Assisted Interactions. Unlike **2.17 (Sq-2-Lys)**, which benefits from charge-assisted chloride stabilization via the ammonium group, the hydrophobic nature of leucine's isobutyl side chain does not contribute to direct anion stabilisation, making chloride binding relatively weak towards **2.16 (Sq-2-Leu)**. Furthermore, steric considerations may be accounted for, as the isobutyl group of leucine introduces steric hindrance, which may reduce the accessibility of chloride to the binding site, in comparison to **2.14 (Sq-2-Ala),** which contains a small methyl side chain and no steric bulk.

Although the isobutyl groups orientate the squaratide in such a way that induces steric hinderance and an unfavourable conformation that limits chloride binding, the opposite is true for acetate, as **2.16 (Sq-2-Leu)** displayed highly enhanced binding affinity for acetate (K_{21} = 10^4 M^{-1}), best fitted to a 2:1 binding mode (Figure 2.16). The isobutyl side

chain of leucine introduces a hydrophobic pocket, which can stabilize the nonpolar methyl end of acetate providing additional stabilization compared to more polar or rigid side chains.

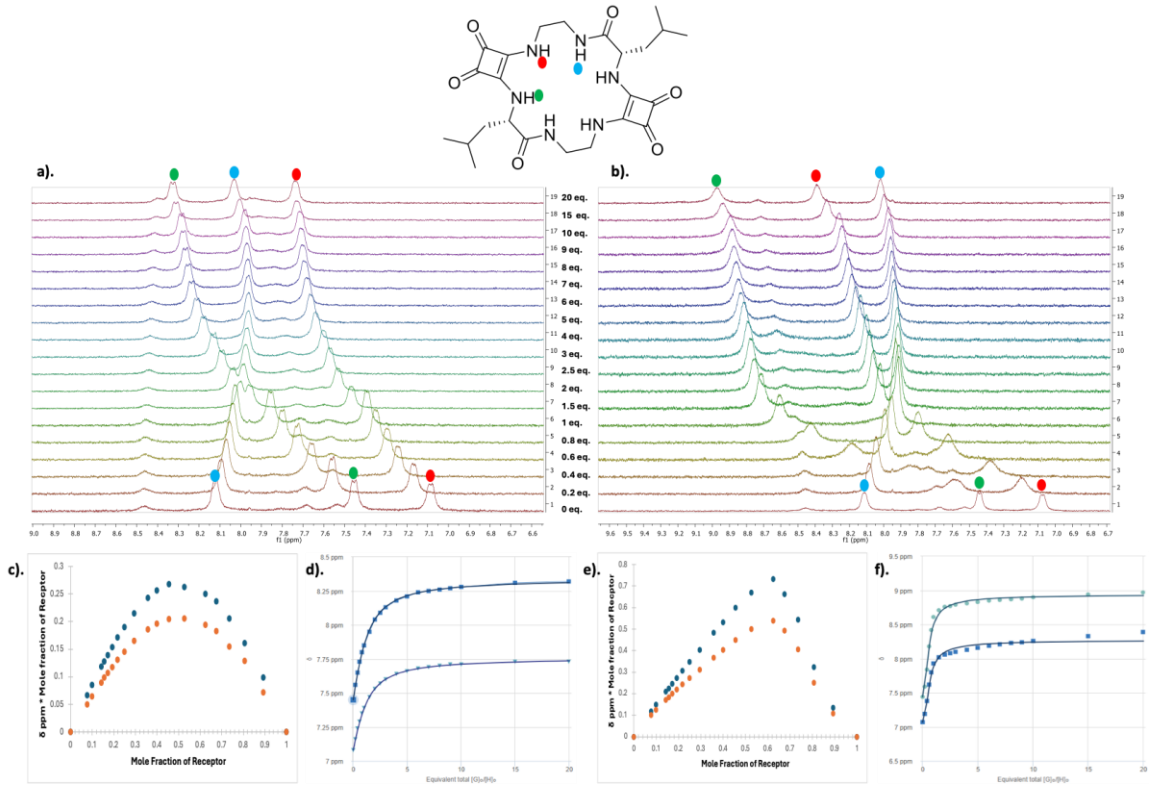

Figure 2.16: ^{1}H NMR Titration of **2.16 (Sq-2-Leu)** against against (**a**) TBACl and (**b**) TBAAcO. Jobs plot analysis of **2.16** against (**c**) TBACl and (**e**) TBAAcO. Fitted data of the chemical shift change of the squaramide NHs of **2.16** against molar equivalents of (**d**) TBACl and (**f**) TBAAcO.

In summary, the detailed analysis of each squaratide's anion-binding behaviour has allowed for the determination of association constants, the elucidation of preferred binding modes, and the evaluation of binding stoichiometries through Job's plot analysis. Although Job's plots were used in this work to assist in identifying the most likely stoichiometries, it is important to acknowledge that the method carries inherent limitations. In particular, Job's analysis assumes the formation of a single dominant complex, relies on linearity of the analytical signal, and can be distorted by weak binding or the presence of multiple equilibrating species—factors that may affect the precision of stoichiometric assignments. Accordingly, the Job's plots presented here should be interpreted as supportive evidence rather than definitive proof, and their conclusions

are considered in conjunction with the more quantitative titration data. While the preceding discussion has addressed these aspects individually for each squaratide, a consolidated comparison of the binding behaviour can be seen in Table 2.1, which provides a comprehensive overview of the anion-binding outcomes for the squaratides investigated.

Receptor	Cl^-	Jobs Plot	AcO^-	Jobs Plot
2.14 (Sq-2-Ala)	K_a = 692 (± 6) M^{-1}	1:1 Binding	K_a = 227 (± 3) M^{-1}	1:1 Binding
2.15 (Sq-2-Phe)	K_a = 366 (± 4) M^{-1}	1:1 Binding	K_{11} = 8.3 x 10^3 (± 69) M^{-1} K_{21} = 3 x 10^3 (± 86) M^{-1}	2:1 Binding
2.16 (Sq-2-Leu)	K_a = 588 (± 2) M^{-1}	1:1 Binding	$K_{21} > 10^4$ M^{-1}	2:1 Binding
2.17 (Sq-2-Lys)	K_{11} = 1.8 x 10^3 (± 3) M^{-1} K_{21} = 703 (± 9) M^{-1}	2:1 Binding	K_a = 333 (± 12) M^{-1}	1:1 Binding
2.18 (Sq-2-Asp(Bn))	$K_{21} > 10^4$ M^{-1}	2:1 Binding	$K_{11} > 10^4$ M^{-1}	2:1 Binding

Table 2.1: Summary of Chloride and Acetate binding of compounds **2.14 – 2.18**.

2.6: Concentration Dependent Study

To investigate the underlying reasons behind the complex binding behaviour observed during anion titrations with **2.15 (Sq-2-Phe)**, a concentration-dependent ^{1}H NMR study was conducted over a range of 0.1 mM to 20 mM (Figure 2.17). The resulting spectra revealed substantial changes across the concentration gradient, particularly within the aromatic and squaramide NH proton regions. As the concentration increased, several notable features emerged: chemical shift changes indicative of altered proton environments, broadening of signals, especially for NH resonances, and the appearance of new peaks present at lower concentrations. These spectral changes are characteristic of concentration-dependent self-association phenomena and may also go some way to explaining the complicated ^{1}H NMR spectra.

Such behaviour is consistent with the formation of aggregated species, likely stabilized via a combination of intermolecular hydrogen bonding between squaramide units and π–π stacking interactions between adjacent phenylalanine side chains. The phenyl moieties in **2.15 (Sq-2-Phe)** provide a conjugated surface capable of engaging in face-to-face or edge-to-face aromatic interactions, facilitating the formation of dimers or higher-order oligomers in solution. These aggregates may adopt dynamic conformations, with equilibria shifting based on concentration, temperature, and solvent conditions.

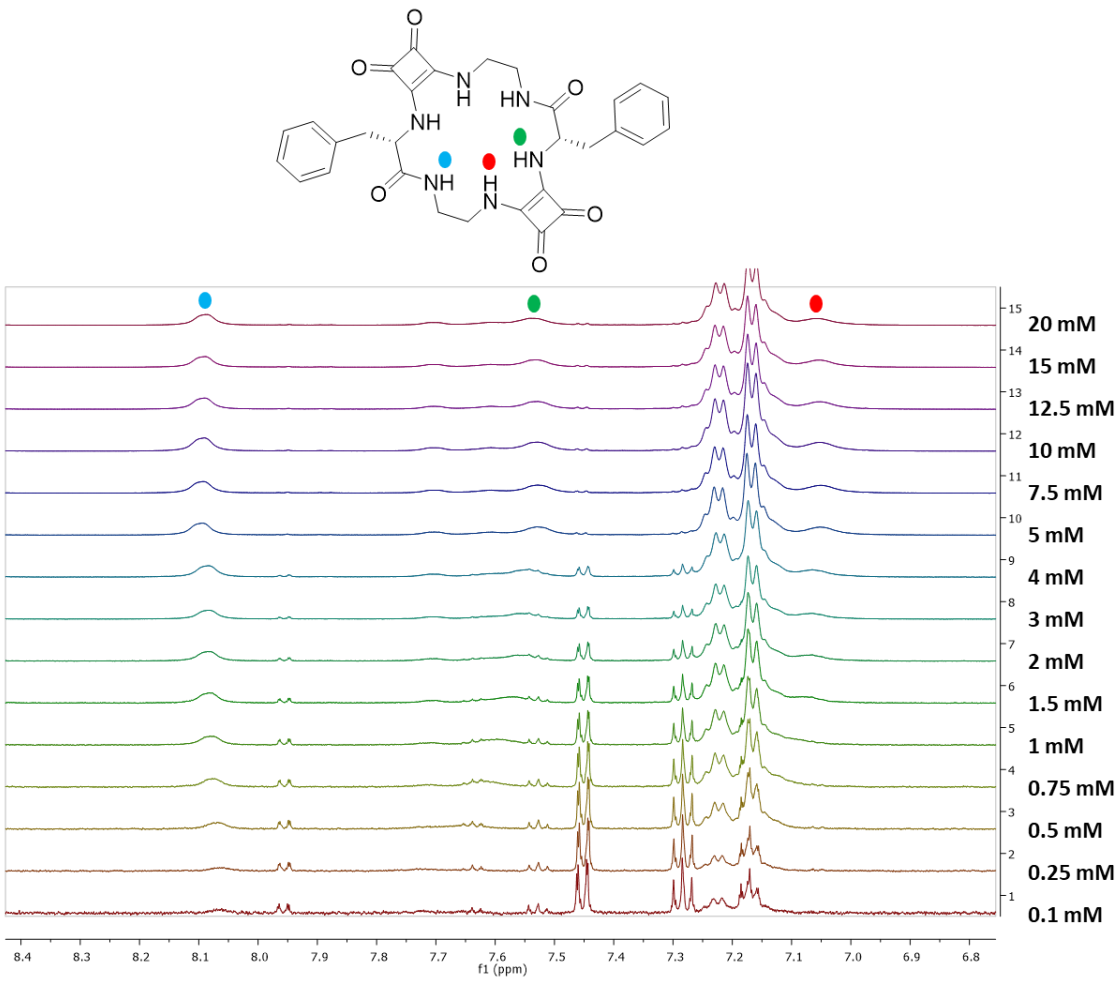

Figure 2.17 Concentration dependent ^{1}H NMR Spectra of **2.15 (Sq-2-Phe).**

To compare and analyse the effects of varying the amino acids into the squaratide backbone, we conducted a similar NMR concentration study with **2.14 (Sq-2-Ala)**. In contrast, the stacked spectra show a clear, consistent set of peaks across the examined concentration range (from low to high). The chemical shifts of the signals remain relatively unchanged, and no broadening or splitting of peaks is observed (Figure 2.18). This spectral stability suggests that **2.14 (Sq-2-Ala)** does not engage in significant self-association in the examined concentration window. The receptor likely exists as a monomeric species throughout, with minimal intermolecular interactions.

This contrasting behaviour is likely due to the small, non-polar methyl side chain of alanine, which neither promotes π–π stacking nor contributes to significant hydrophobic interactions. The absence of these intermolecular forces results in a system that remains monomeric and structurally consistent in solution, even at higher concentrations.

These concentration-dependent studies of the squaramide-based receptors underscore the critical role that amino acid side chains play in modulating both self-association and anion binding behaviour; an important design consideration going forward, where the side chains, though peripheral to the core squaramide binding motif, exert significant influence on the receptor's supramolecular properties by altering both conformational flexibility and anion binding.

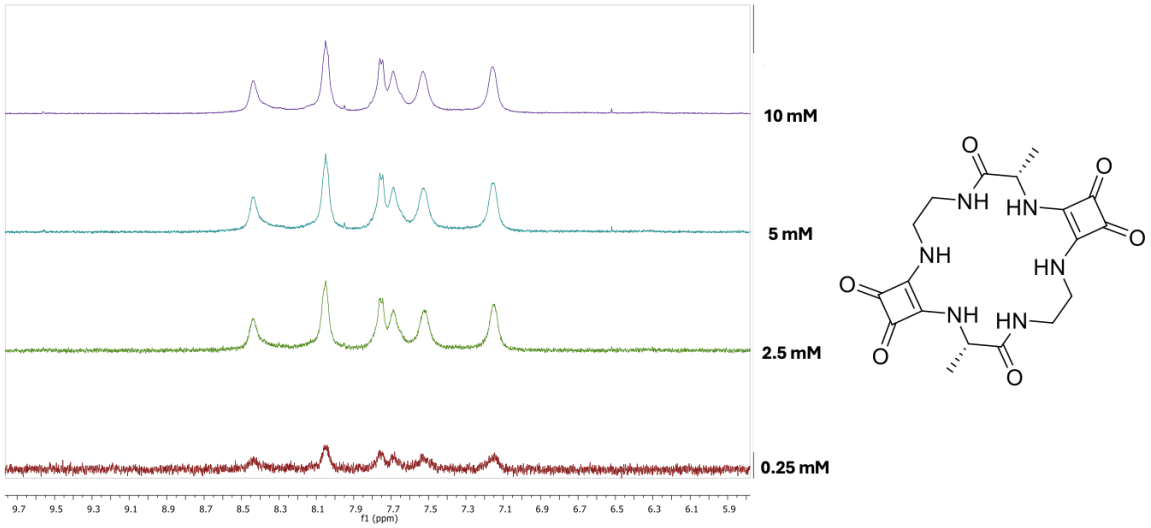

Figure 2.18: Concentration dependent ^{1}H NMR Spectra of **2.14 (Sq-2-Ala).**

The implications of this self-association observed for **2.15 (Sq-2-Phe)** are significant for interpreting anion binding data for all the squaratides. If anion binding competes with self-assembly or induces disaggregation of higher-order structures, the apparent binding stoichiometry and constants may be convoluted by these additional equilibria. For instance, a 2:1 binding model may not solely reflect two anions binding to one receptor molecule but could also arise from binding to two monomeric receptor units released upon aggregate dissociation. Additionally, binding may be entropically penalized if it disrupts favourable aggregation, or alternatively, enthalpically favoured if it stabilizes specific oligomeric forms. Therefore, the complex binding behaviour observed for acetate and chloride with **2.15 (Sq-2-Phe)** particularly the cooperative 2:1 stoichiometry seen with acetate may in part be a consequence of the interplay between receptor aggregation and guest recognition.

In contrast, **2.14 (Sq-2-Ala)**, which lacks bulky or aromatic side chains, displayed sharp and consistent peaks across the entire concentration range, indicative of a

predominantly monomeric species in solution without significant intermolecular interactions or conformational rearrangement. This simplified aggregation behaviour enables a clearer interpretation of binding events, with **2.14 (Sq-2-Ala)** exhibiting straightforward, non-cooperative 1:1 binding with anions. The data suggest a well-defined and preorganized binding site, free from dynamic self-association or steric interference by side chains. This highlights how the nature of the amino acid residue can strongly influence both the stoichiometry and thermodynamics of anion binding.

2.7: Conclusion

In this Chapter, we have successfully set out to design a sequence-defined material that could be used to create a diverse set of anion receptor molecules. Through a hybrid mix of squaramides and amino acids, we reveal the synthesis of this new class of molecules we call “squaratides”. A robust synthetic procedure has been developed for the assembly and cyclisation of several candidate macrocycles with varied sidechain functionality with a focus on comparing them for their anion capture and discrimination abilities.

Our results demonstrate how strategic modifications to macrocycle side chains profoundly impact anion binding affinities and stoichiometries. Hydrogen bonding, electrostatic interactions, π-effects, and hydrophobic stabilization collectively modulate anion selectivity. While the binding affinities provide valuable insights into the interactions between each squaratide, accurately determining the association constants (K_a) was challenging as a result of the complexity of these systems. Due to the complexity and conformational rearrangements in solution, multiple binding interactions and complex stoichiometries appear to take place. Nevertheless, the analysis confirms squaratides to be excellent hosts with a high degree of selectivity towards AcO^- in most cases, and surprisingly high affinity towards Cl^- with the exception of **2.18 (Sq-2-Asp(Bn))**, which showed exceptional binding toward both tested anions. The concentration dependent study gave us valuable insight into the squaratides solution state behaviour whereby we noticed receptor aggregation for **2.15 (Sq-2-Phe)**. This tendency toward self-association has important consequences for the interpretation of anion binding data. If anion binding disrupts or competes with receptor aggregation, the observed binding stoichiometry and affinity constants may be influenced by overlapping equilibria, complicating accurate analysis. Overall, this represents the first insights into utilising the advantages of squaramides and amino acids in order to developed novel peptidomimetics as suitable hosts for molecular recognition. The next chapter of this thesis will further explore the synthetic versatility of this peptidomimetic with a view to designing larger macrocycles with varied binding cavity sizes and testing potential applications in medicinal chemistry.

Chapter 3

Increasing Cavity size for Lysine based Squaratides as Antimicrobials

3: Increasing Cavity size for Lysine based Squaratides as Antimicrobials

3.1: Introduction

The relentless rise of antimicrobial resistance (AMR) represents a profound and multifaceted threat to global public health, one that jeopardizes the efficacy of modern medicine and undermines our capacity to manage infectious diseases.[202, 203] Over the past several decades, the widespread and often indiscriminate use of conventional antibiotics has accelerated the emergence of multidrug-resistant (MDR) and extensively drug-resistant (XDR) bacterial strains.[204-206] These resistant pathogens are now responsible for a growing proportion of hospital- and community-acquired infections, with the World Health Organization designating AMR as one of the top ten global public health threats facing humanity.[207, 208] As existing antibiotics lose their potency and the pipeline of novel agents remains alarmingly sparse, there is an urgent imperative to explore and develop alternative therapeutic strategies that bypass conventional resistance mechanisms.[209-212]

Among the most promising candidates in the search for novel antimicrobial agents are antimicrobial peptides (AMPs)—evolutionarily conserved components of the innate immune system such as lactoferricin, nisin, cecropins and defensins, found in virtually all living organisms, from bacteria to humans.[213-216] AMPs typically exhibit broad-spectrum activity against bacteria, fungi, viruses, and even certain cancer cells.[217-219] Unlike conventional antibiotics that often target specific bacterial enzymes or biosynthetic pathways. AMPs exert their antimicrobial effects primarily through the disruption of microbial membranes, a mechanism that is both rapid and difficult for pathogens to evade through classical genetic mutations.[220, 221] This mode of action, coupled with their immunomodulatory properties, positions AMPs as attractive alternatives or adjuncts to existing antibiotic therapies.[222] However, despite their therapeutic potential, the clinical application of natural AMPs has been hindered by several significant limitations. These include their susceptibility to proteolytic degradation, short plasma half-lives, potential cytotoxicity to host tissues, poor bioavailability, and high production costs associated with peptide synthesis and purification.[223-225] These pharmacokinetic and pharmacodynamic challenges have necessitated the exploration of novel approaches to

harness the benefits of AMP-based therapeutics while mitigating their drawbacks. In this context, antimicrobial peptide mimetics have emerged as a promising and innovative class of compounds designed to replicate the structural and functional characteristics of natural AMPs while offering improved stability, reduced toxicity, and enhanced therapeutic profiles. [226, 227]

To overcome the inherent limitations of natural AMPs, Researchers have developed a variety of design strategies that are carried out to engineer antimicrobial peptide mimetics with improved therapeutic profiles.[228] These strategies aim to preserve the essential physicochemical features of AMPs, including cationic charge and amphipathicity, while introducing structural modifications that enhance stability and selectivity.[229, 230] Among the most prominent approaches are peptidomimetics, which replace natural peptide backbones with non-natural scaffolds to resist enzymatic degradation and prolong bioactivity.[231, 232]

Peptoids offer enhanced metabolic stability and reduced immunogenicity due to their unnatural backbone configuration.[233] They are composed of N-substituted glycine, where the side chains are attached to the nitrogen atom of the amide bond, rather than to the α-carbon as seen in peptides [234] (Figure 3.1). This alteration confers greater stability against proteolytic degradation, making peptoids less susceptible to enzymatic breakdown in biological environments.[235-237] This can be seen by work carried out by H. Jenssen and colleagues whereby they set out to create a library of peptoids consisting of 8 to 9 residues, all with an overall net charge of -4.[238] The peptoids utilized a range of functional side chains designed to mimic traditional amino acids, including bulky hydrophobic residues. This modification aimed to not only improve their antimicrobial efficacy but also provide insights into the effect of specific side chain properties on overall activity The peptoids exhibited a broad spectrum of antimicrobial activity against various bacterial strains including *Escherichia coli, Staphylococcus aureus, and Pseudomonas aeruginosa*, with minimal inhibitory concentrations (MICs) ranging significantly depending on their structure from 2 to 64 μg/mL, indicating overall good antimicrobial activity in the majority of the peptoids. This suggests that by tweaking the structural elements, peptoids can be optimized for specific targets, similar to how antimicrobial peptides are selected for their activity.

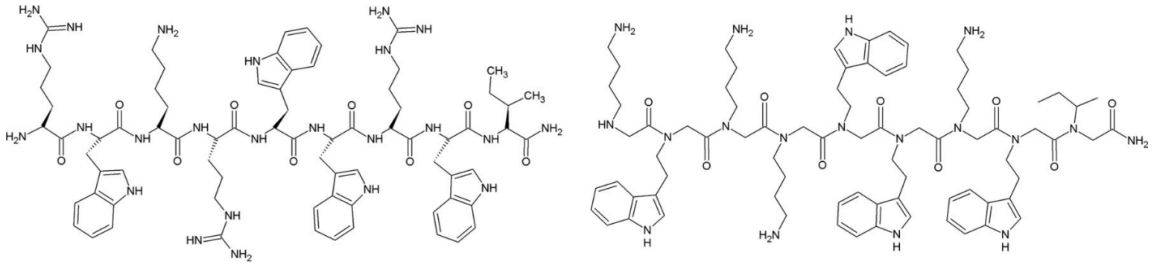

Figure 3.1: Chemical structures of (left) GN-2 peptide (**3.1**) and (right) GN-2 peptoid (**3.2**).

Other efforts have focused on the development of arylamide foldamers, rigid synthetic oligomers that mimic the spatial arrangement of AMPs and demonstrate potent membrane-disruptive activity.[239, 240] Arylamide foldamers possess an arylamide backbone that includes charged and hydrophobic groups, resulting in a topographically amphiphilic structure.[241] This amphiphilicity is crucial because it allows the foldamers to interact favourably with the negatively charged bacterial membranes, promoting insertion and destabilization of these membranes. Such an example can be seen by DeGrado and coworkers where they reported two arylamide foldamers consisting of 2-ethyl guanidinium and 2-ethyl amine substituted to an arylamide backbone (Figure 3.2).[242] These modifications can increase their affinity for microbial membranes while minimizing toxicity towards mammalian cells. Arylamide foldamers demonstrated potent bactericidal activity against *E. coli* at low concentrations 12.5 μg/mL, 6.25 μg/mL). The antimicrobial action of arylamide foldamers primarily hinges on their ability to permeabilize bacterial membranes. They induce structural changes in membranes, leading to leakage of intracellular contents and ultimately cell lysis. The mechanism resembles that of natural AMPs but is tuned to reduce collateral damage to host cells, thus offering a therapeutic advantage.

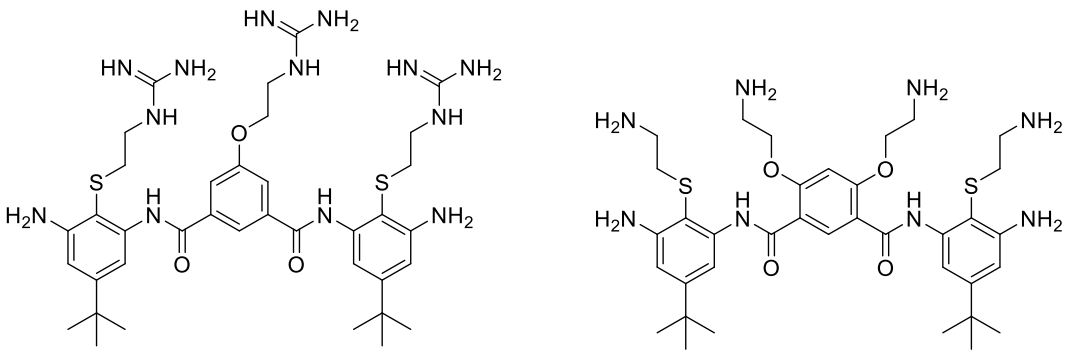

Figure 3.2: Chemical structures of arylamide foldamers **3.3** and **3.4**.

Additional strategies such as cyclization and hydrocarbon stapling further enhance the structural rigidity and protease resistance of AMP mimetics.[243, 244] An example can be seen by Daly and colleagues, where they successfully achieved the backbone cyclization of the antimicrobial peptide Gomesin, an 18-residue cysteine-rich antimicrobial peptide produced by hemocytes of the spider *Acanthoscurria gomesiana*.[245] This structural modification significantly enhanced gomesin's biological potency, leading to increased cytotoxic activity against melanoma and cervical cancer cell lines, as well as improved antimalarial efficacy against *Plasmodium falciparum* W2 and antimicrobial activity against *Escherichia coli* DH5α. Notably, the cyclic analogue retained a hemolytic and cytotoxic profile comparable to that of native gomesin when tested against noncancerous foreskin fibroblast cells, indicating preserved selectivity and safety. Most importantly, cyclic gomesin demonstrated superior proteolytic stability in human serum relative to its linear counterpart, underscoring the advantages of backbone cyclization in enhancing peptide durability and therapeutic potential.

Other strategies such as D-amino acid substitution, and conjugation to nanocarriers or polymeric systems can also improve limitations associated with AMPs.[246-248]

Collectively, these approaches have expanded the chemical space of AMP-like molecules and hold significant promise for the development of next-generation antimicrobials capable of combating multidrug-resistant pathogens. The rational design and optimization of AMP mimetics represent a frontier in antimicrobial drug discovery, offering a versatile platform for the development of next-generation therapeutics capable of combating MDR pathogens. As research in this field advances, the integration of computational modelling, high-throughput screening, and structure–activity relationship (SAR) studies will further refine these compounds and accelerate their translation from bench to bedside.

3.2: Chapter Objective

The objective of this chapter can be split into two parts. Our first aim is to further investigate the design of our previously mentioned new peptidomimetic scaffold called squaratides, introducing a more feasible synthetic pathway, overcoming some of the limitations from our previous synthesis. The initial generation of cyclic squaratides was synthesized using a solution-phase approach, which provided valuable insights into their structural and functional properties. Building upon this foundation, we will discuss the second generation of cyclic squaratides which is developed using a solid-phase synthetic strategy. This transition to solid-phase synthesis significantly streamlined the process, enabling a more efficient and modular approach to receptor construction. Furthermore, the solid-phase methodology allowed for systematic modifications to the squaratide structure, including the ability to increase the cavity size of the macrocycles (Figure 3.3). This feature provides an opportunity to fine-tune squaratides, enhancing the versatility and efficacy of these receptors. By combining innovative synthetic strategies with structural optimization. These unique attributes not only pave the way for the construction of intriguing supramolecular systems but also render Squaratides readily accessible and modifiable, thus enhancing the flexibility in designing efficient supramolecular systems.

The second aim of this chapter is to showcase one of the many potential applications of squaratides by investigating their potential as AMP mimics. We expect that the advantages that squaramides offer including rigidity, aromaticity and strong specific anion binding with the structural versatility of peptides may enable the precise spatial arrangement of functional groups critical for mimicking the membrane-disruptive and selective binding properties of natural antimicrobial peptides Through this approach, we hope to pave the way for a versatile and innovative platform for the design of next-generation antimicrobial peptide mimetics, with potential applications in targeting drug-resistant pathogens through selective membrane interaction or molecular recognition. If successful, this work would position squaratides as promising candidates in the ongoing development of peptidomimetics as antimicrobial agents.

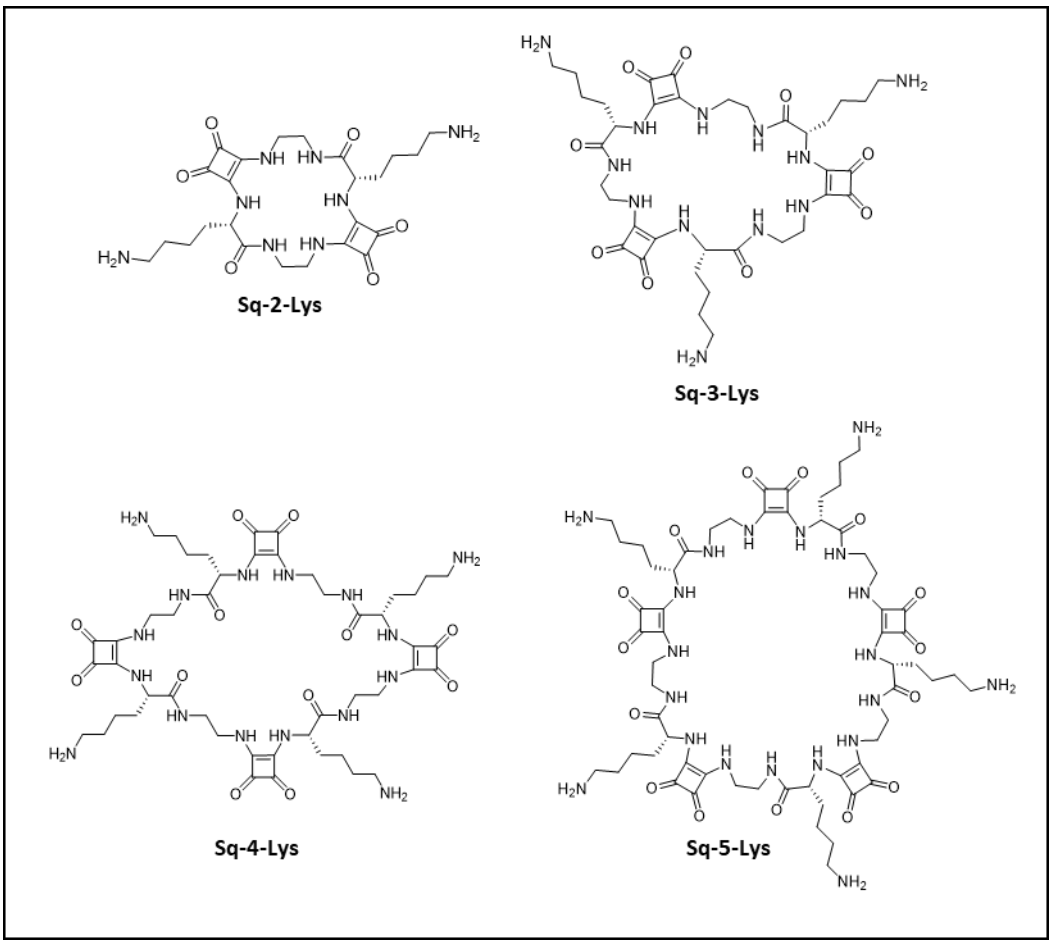

Figure 3.3: Chemical structures of expanded squaratides **Sq-2-Lys – Sq-5-Lys.**

3.3 Rational Design of 2nd Generation Squaratides

In the previously discussed chapter, we introduced a novel class of peptidomimetics termed Squaratides, which exhibited strong anion-binding affinities with particularly strong and selective interactions observed for acetate and chloride. While these early studies established squaratides as potent molecular recognition systems, the synthetic route, which was carried out in solution phase, posed considerable challenges, notably in terms of purification, solubility, and scalability. Furthermore, our synthetic capabilities at the time were constrained to the assembly of monomeric units and their subsequent dimerization, thereby limiting both structural diversity and functional exploration.

With these limitations in mind, we will transition to a solid-phase synthesis (SPS) with Fmoc-Chemistry using 2-chlorotrirtly chloride resin, composed of iterative deprotection

and coupling steps as outlined in Scheme 3.1. This approach is expected to significantly streamline the purification process, as the immobilisation of the growing squaratide chain on a resin support will allow for facile removal of excess reagents and by-products, ultimately yielding higher-purity final products. More importantly, the solid-phase method will provide a greater degree of architectural freedom, enabling the site-specific incorporation of diverse building blocks, including non-natural amino acids and functional moieties, to enhance the structural stability and biological potential of the resulting molecules.

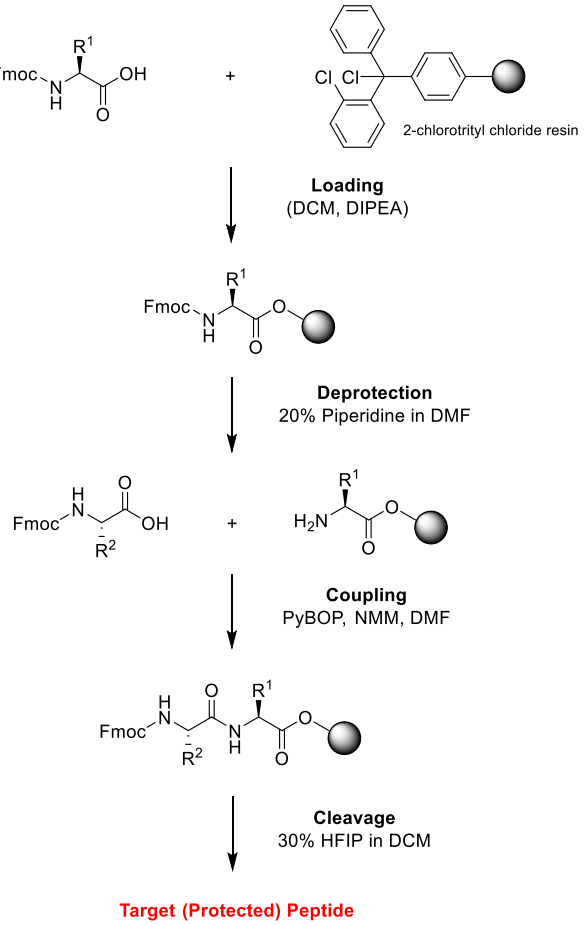

Scheme 3.1: General SPPS steps with Fmoc-chemistry and chlorotrityl resin.

This methodological advancement would not only address the shortcomings of our initial synthetic strategy but also open the door to expanding the squaratide scaffold well beyond dimers. In this chapter, we will outline the successful synthesis of higher-order oligomers, such as trimers, tetramers, and pentamers, and their macrocyclization as confirmed via LC-MS and high-resolution mass spectrometry (HRMS) of **3.5 (Sq-3-Lys),** **3.6 (Sq-4-Lys),** and **3.7 (Sq-5-Lys)**. These larger, cyclic Squaratides would possess increased cavity sizes, offering new opportunities for guest molecule encapsulation

while also providing potential for additional biological interaction. Motivated by these enhanced structural capabilities, we expected to broaden the functional scope of Squaratides, leveraging their unique architecture to develop a new class of antimicrobial agents. The second-generation Squaratides outlined in this chapter thus represent not only a synthetic innovation but also a strategic evolution toward bioactive peptidomimetic systems with promising applications in combating antimicrobial resistance.

The selection of lysine as the amino acid in the synthesis of second-generation Squaratides was a strategic decision, grounded in both its structural versatility and its biological relevance. Lysine is a positively charged, basic amino acid that plays a critical role in the function of many AMPs. From a design perspective, lysine introduces cationic character into the Squaratide backbone, which is essential for mimicking electrostatic interactions with negatively charged bacterial membranes, which are typically composed of phospholipids such as phosphatidylglycerol and cardiolipin. These interactions are crucial for the initial binding and subsequent disruption of the bacterial membrane, a common and effective mechanism of action employed by host-defence peptides.[249, 250] Furthermore, the incorporation of lysine enhances amphiphilicity, especially when alternated with hydrophobic residues, promoting membrane insertion and pore formation. Unlike conventional antibiotics that often target specific intracellular processes and are thus susceptible to resistance mechanisms, lysine-containing antimicrobial peptides act through non-specific, physical interactions with the membrane, significantly reducing the likelihood of resistance development. Additionally, lysine residues contribute to the solubility and structural flexibility of antimicrobial peptides, enabling them to adopt conformations necessary for effective membrane interaction.

3.4: Synthesis and Characterisation

3.4.1: Synthesis of 2nd Generation Squaratides

The synthesis of our 2nd generation squaratides was carried out via solid phase synthesis (Scheme 3.2) as we believed it would streamline our synthesis, surmounting many difficulties including fewer purification steps and higher yields compared to our 1st generation squaratide synthesis discussed in Chapter 2.

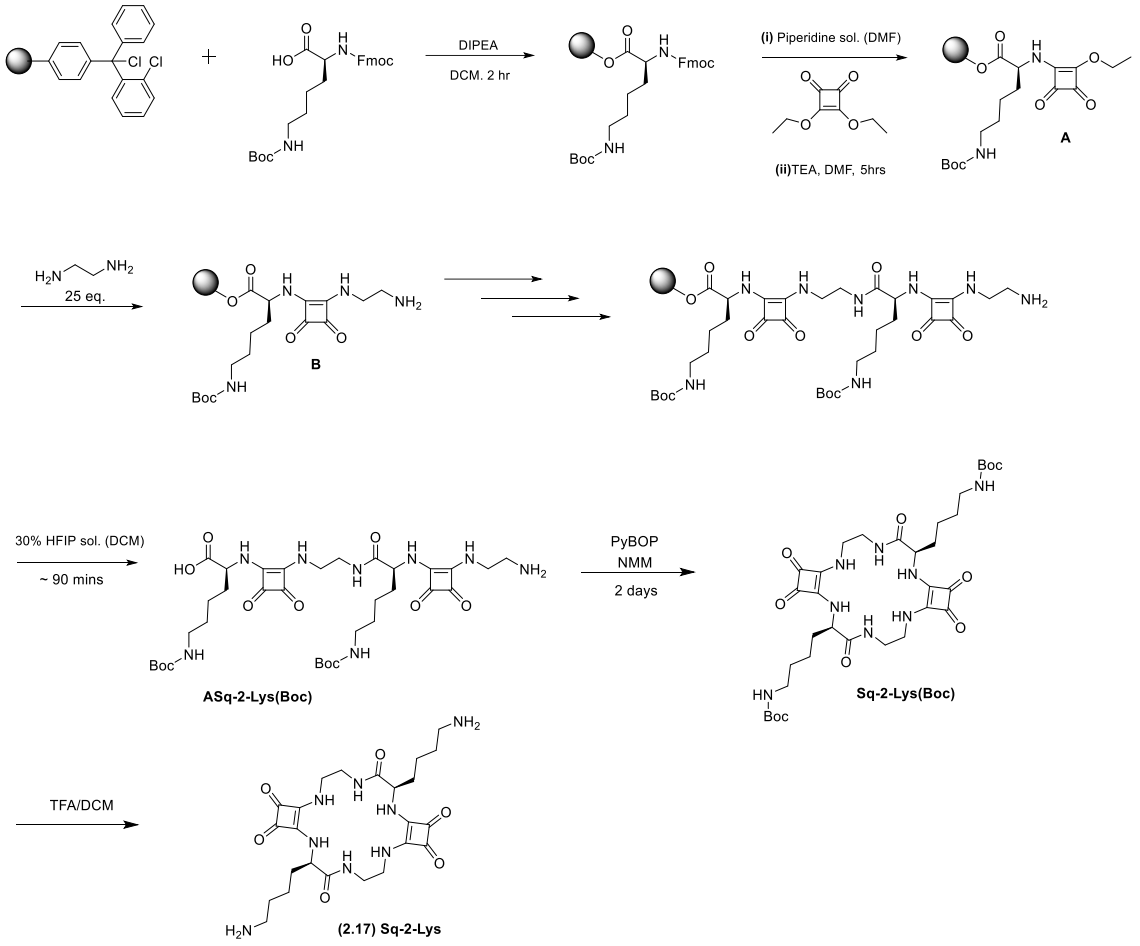

Scheme 3.2: SPPS synthetic pathway for **2.17 (Sq-2-Lys).**

The first step was to assemble the squaratide monomer. This was carried out using 2-chlorotrityl chloride resin via Fmoc/tBu SPPS, whereby Fmoc-Lys(Boc) was initially loaded onto the resin, it was then washed with a solution of DCM/MeOH/DIPEA to endcap any remaining reactive trityl groups. Estimation of the first residue attachment was achieved spectroscopically through the release of Fmoc as described in the Experimental Section which was calculated to be 0.345 mmol (Figure 3.4).

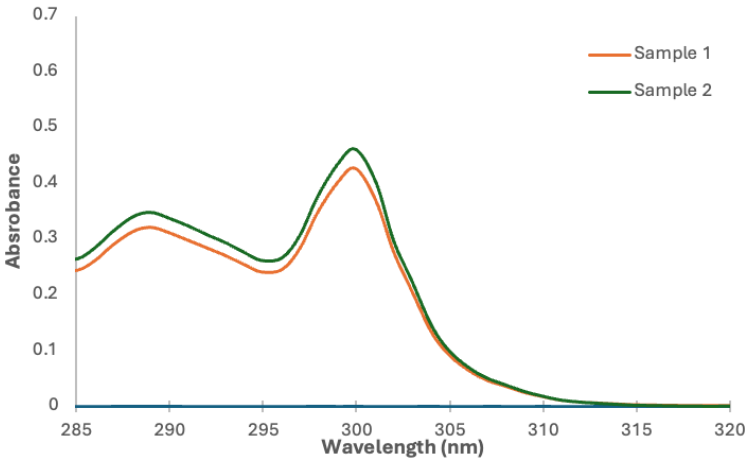

	Reference	Sample 1	Sample 2	Average
Abs @ 304 nm	-0.00015762	0.425977	0.461238	0.443608

Loading Calc (mmol/g)	0.630108312
µmol/g	630.1083117
µmol/0.5473g	344.858279

Figure 3.4: UV spectrum of Fmoc from Fmoc-Lys(Boc)-OH.

The Fmoc group was removed by a 20% piperidine in DMF solution whereby the next step involving substitution of diethyl squarate using 5 equiv of triethylamine in DMF was carried out to afford **A**. As shown in Figure 3.5, the HPLC trace of a test cleavage sample displayed one sharp UV peak with a t_R = 28 min. Strong ionisation was observed for the target mass of $[M+H]^+$ = 371.2 $gmol^{-1}$ in positive mode confirming successful formation of the desired intermediate.

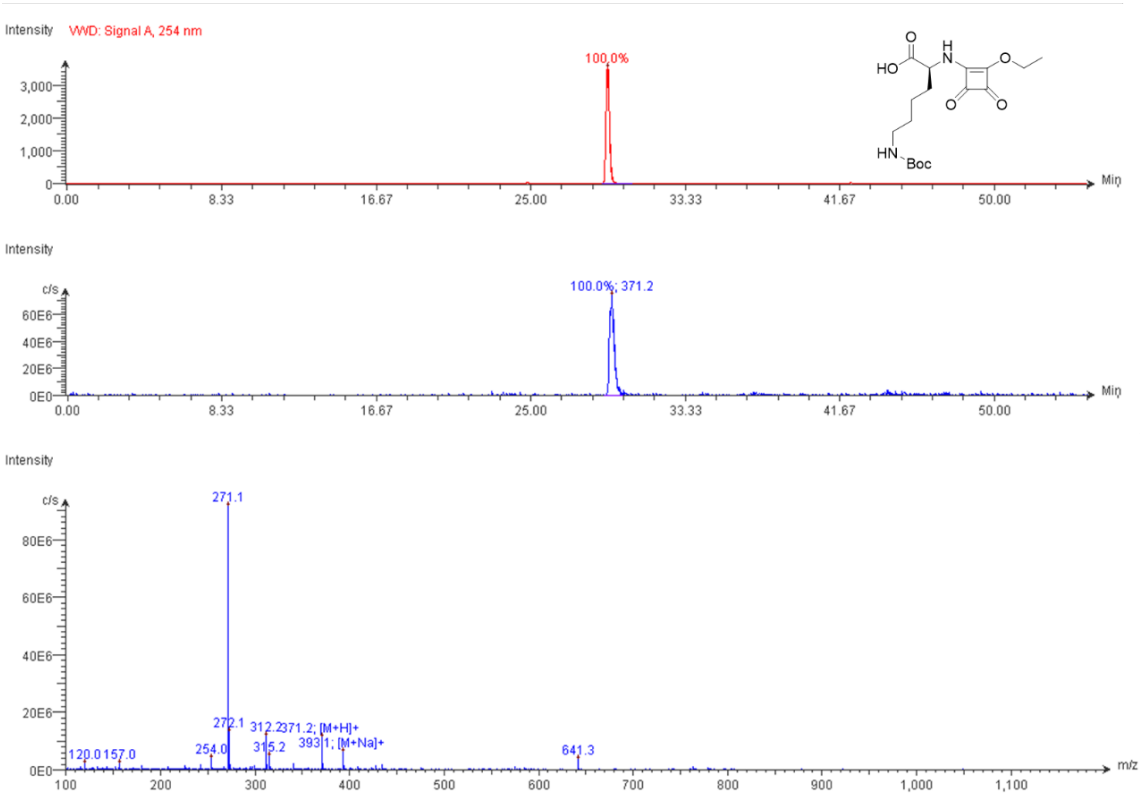

Figure 3.5: LC-MS data for **A.**

The next step was to functionalise the sequence with ethylene diamine (EDA) to yield the squaratide monomer. EDA was found to act as its own base; thus, the use of additional organic bases was unnecessary for complete reaction. Confirmation of the formation of **Lys-Sq-EDA** (**B**) was afforded through LC-MS analysis of a test sample where the HPLC trace displayed one sharp UV peak with a t_R = 24 min, and strong ionisation was observed for the target mass of $[M+H]^+$ = 385.3 $gmol^{-1}$ in positive mode (Figure 3.6).

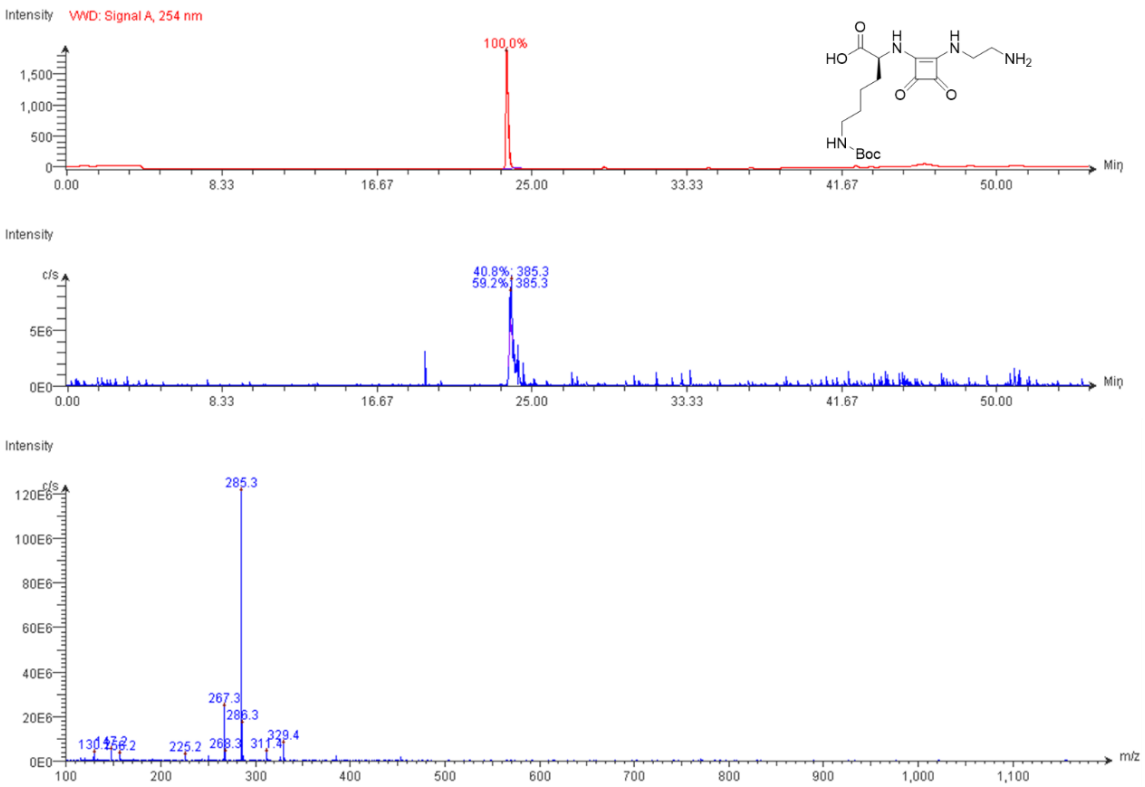

Figure 3.6: LC-MS data for **B.**

Upon synthesising the monomer on solid support, subsequent successful coupling of Fmoc-Lys(Boc) was carried out with PyBOP – as the coupling reagent – in the presence of N-methyl morpholine (NMM), before the second squaramide functionalisation was added, followed by the addition of the second EDA moiety. The linear squaratide dimer **ASq-2-Lys(Boc)** was then cleaved from the resin with a mixture of HFIP/DCM and lyophilized. Characterisation of **ASq-2-Lys(Boc)** was completed using LC-MS (Figure 3.7), HRMS data (Appendix), and ^{1}H NMR spectroscopy (Figure 3.8). The HPLC trace displayed a sharp UV peak with a t_R = 26 min, and strong ionisation was observed for the target mass of $[M+H]^+$ = 825.9 g mol $^{-1}$ in positive mode, confirming the successful synthesis of the desired linear squaratide dimer.

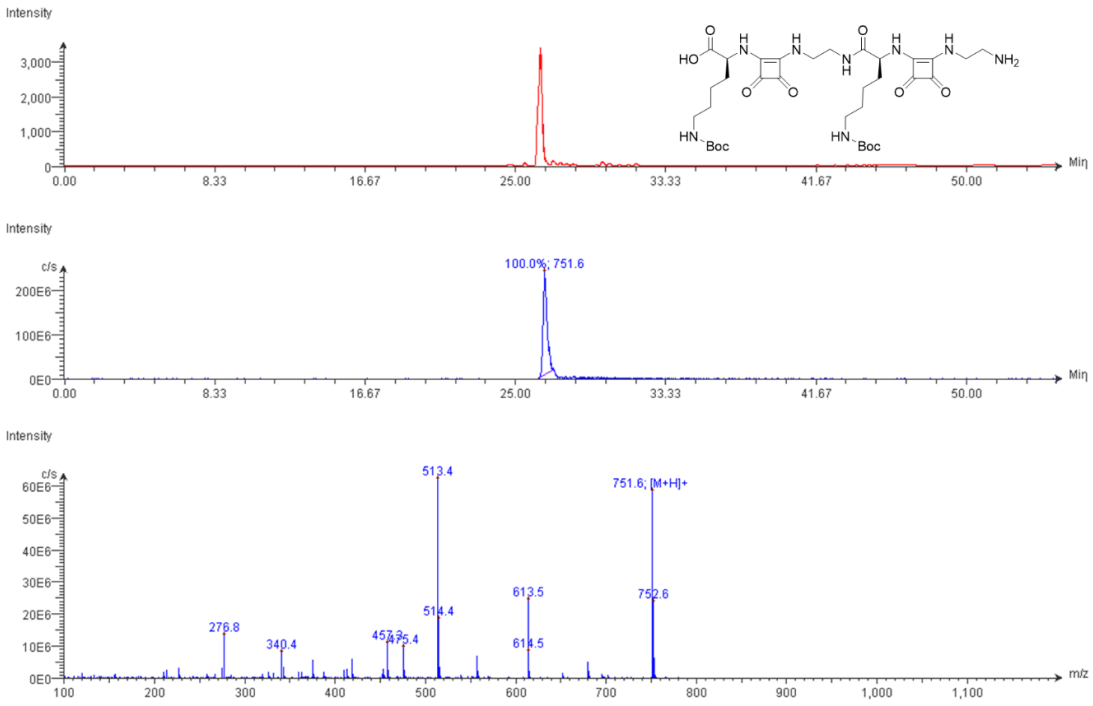

Figure 3.7: LC-MS data for **ASq-2-Lys(Boc).**

The ^{1}H NMR spectrum of **ASq-2-Lys(Boc)** was inherently complex due to the flexible linear architecture of the squaratide giving rise to multiple conformational isomers (Figure 3.8). this behaviour is often seen with acyclic peptidomimetics, where increased mobility and multiple conformations give rise to poorly resolved peaks.[251, 252] Despite this complexity, the spectrum exhibits broad signals arising in the NH region from 7.5 – 9 ppm, which corresponds from the squaramide, amide and lysine NH signals, as well as a sharp singlet amongst the amalgamated signals correlating with the carboxylic acid Hydrogen from the C-terminus. In the aliphatic region (1.2 – 2.0 ppm), multiples attributable to the lysine sidechain methylene's were evident, while a sharp singlet at approximately 1.4 ppm confirmed the presence of the tert-butyl groups from the Boc protecting groups. Although spectral overlap limits the extent of unambiguous assignments, the observed chemical shifts are consistent with the expected structural features of the acyclic squaratide and provided an additional layer of structural confirmation. Together with LC-MS and HRMS analysis, the NMR data support the successful synthesis of **ASq-2-Lys(Boc),** providing a basis for subsequent cyclisation to yield **Sq-2-Lys(Boc)**. It's worth mentioning that the spectral congestion highlights the challenges of characterising flexible linear squaratides by NMR spectroscopy. As such, further insight was gained upon cyclisation of this intermediate to form **Sq-2-Lys(Boc)**,

where the increased conformational restriction was expected to afford a more resolved and interpretable NMR spectrum.

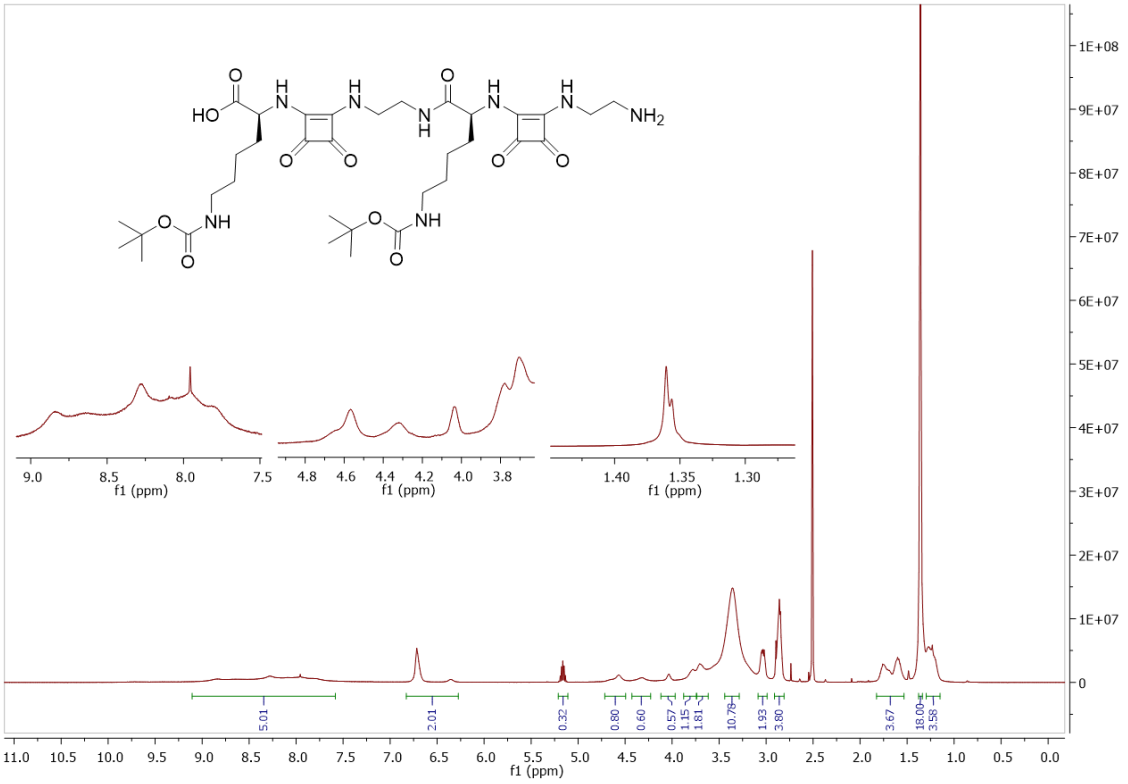

Figure 3.8: ^{1}H NMR spectrum of **ASq-2-Lys(Boc).**

With the linear dimer in hand, the next step was to attempt intramolecular cyclisation to yield the squaratide dimer **Sq-2-Lys(Boc)**. This step was carried out under high-dilution conditions in the presence of PyBOP and NMM in DMF, to successfully afford the desired protected cyclised product as an off-white solid with a yield of 55%. Evidence for this successful cyclisation reaction was obtained from LC-MS (Figure 3.9) and HRMS experiments. The cyclic **Sq-2-Lys(Boc)** possessed a larger retention time of t_R = 29 min compared to its acyclic derivative, indicating that the previously free C-terminus and -NH_2 group (**ASq-2-Lys(Boc)**) are no longer present and have likely been (intramolecularly) coupled together. The HPLC trace displayed one sharp UV peak, however, as a result of the solvent system of the HPLC being 0.1% TFA ACN / H_2O, the ionisation observed for the target mass was $[M - Boc + H]^+$ = 634 gmol^{-1} in positive mode indicating fragmentation of the compound with a Boc removal in the presence of TFA, however HRMS confirmed this target mass $[M+H]^+$ = 733.38 gmol^{-1} possessing a mass error of -2.32 ppm.

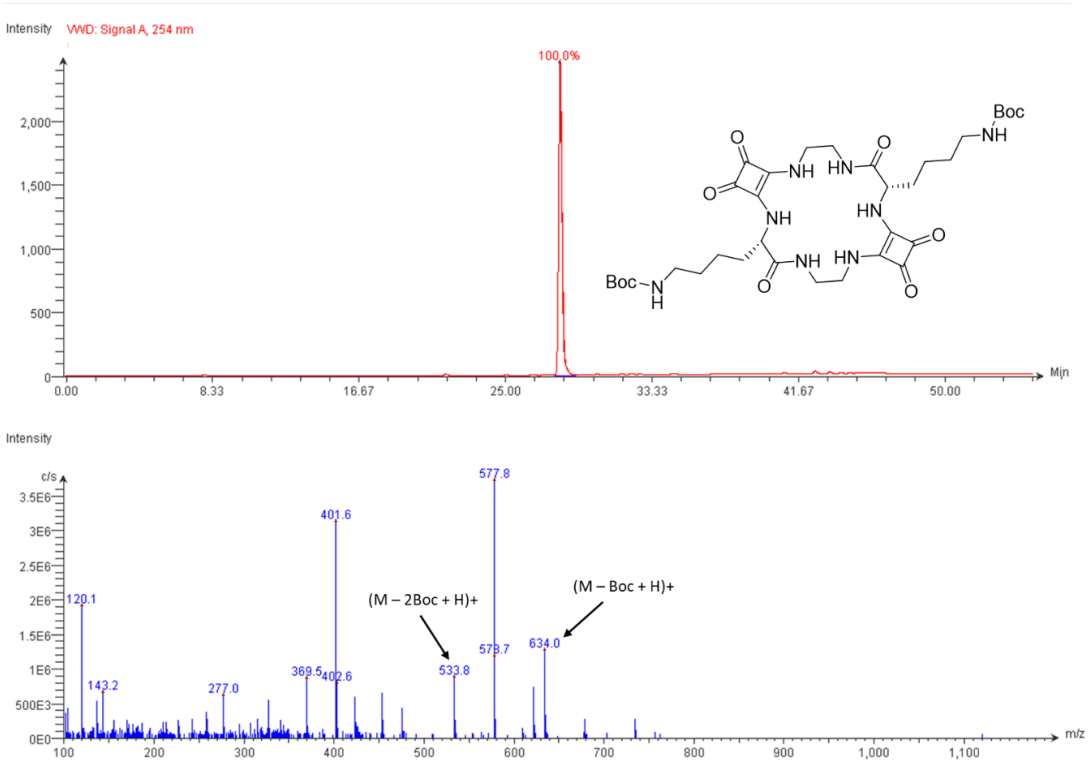

Figure 3.9: LC-MS data for **Sq-2-Lys(Boc).**

The final step was to deprotect the Boc protecting group on the Lysine residue. This was carried out in 50% TFA/DCM which was then evaporated and dissolved in a minimal amount of MeOH before being precipitated out in cold Diethyl Ether and lyophilized to afford the deprotected final product **2.17 (Sq-2-Lys)** as a white solid with a yield of 87%. **Sq-2-Lys** possessed a much lower retention time t_R = 8.33 min in comparison to **Sq-2-Lys(Boc)** indicating that the boc protecting groups have been successfully removed and we have the free NH_2 on the side chain of the Lysine residues. The UV peak on the HPLC trace corresponded to the product with a strong ionisation observed for the target mass of $[M+H]^+$ = 533.7 $gmol^{-1}$ in positive mode (Figure 3.10).

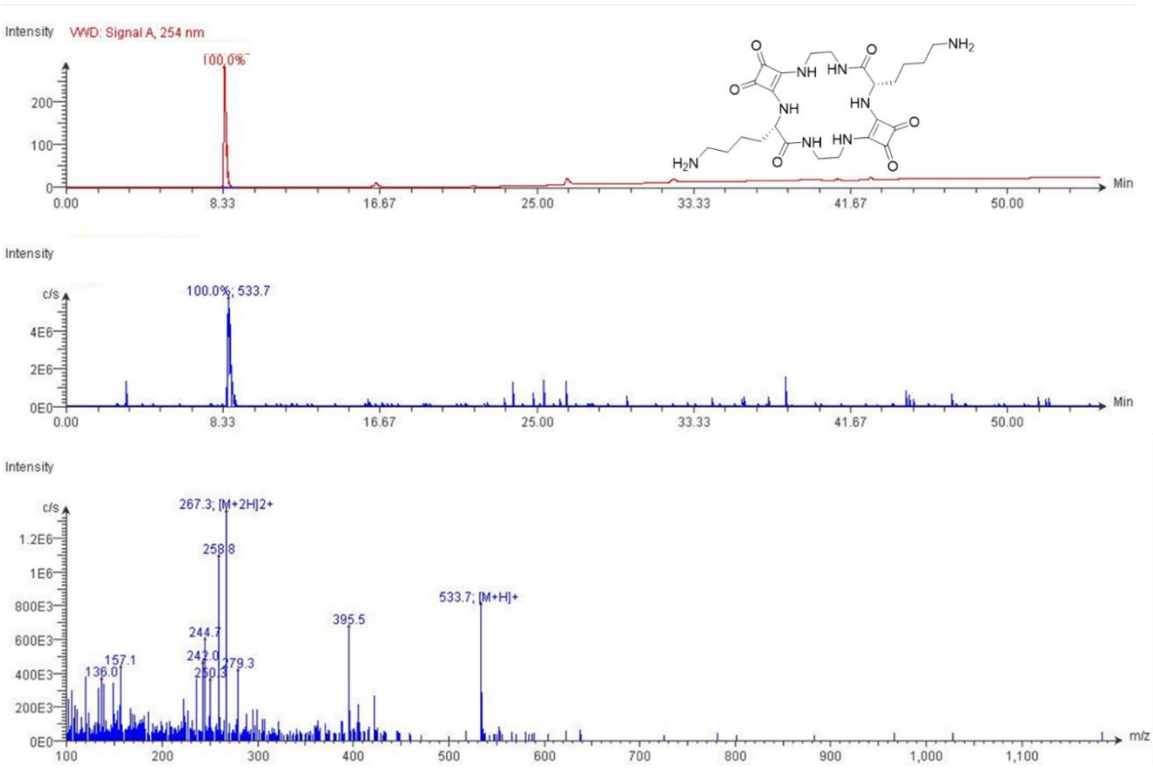

Figure 3.10: LC-MS data for **2.17 (Sq-2-Lys).**

Finally, HRMS was also used as a complimentary analysis to affirm the molecular formula of **Sq-2-Lys**, with confirmation of the target mass $[M+H]^+$ = 533.2828 $gmol^{-1}$ possessing a low mass error value of - 0.33 ppm (Figure 3.11).

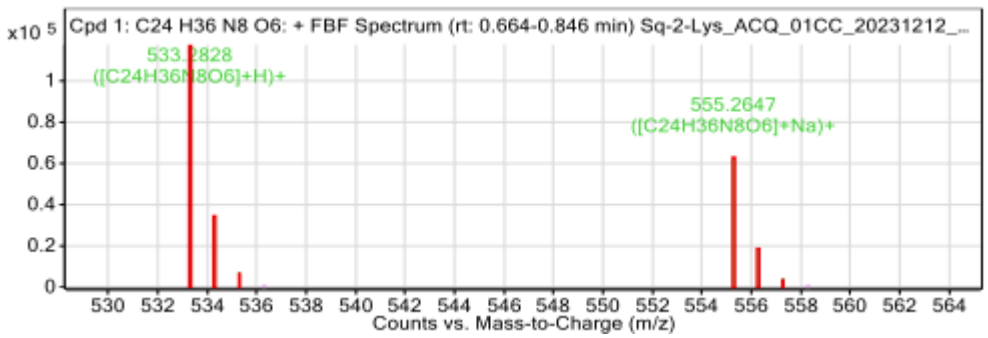

Figure 3.11: HRMS data for **2.17 (Sq-2-Lys)**.

Further structural confirmation of **2.17 (Sq-2-Lys)** was obtained via ^{1}H NMR spectroscopy. (Figure 3.12). in contrast to its linear precursor **ASq-2-Lys(Boc)**, which was notably congested, with extensive signal overlap due to the conformational heterogeneity of the flexibly backbone, the spectrum of **2.17 (Sq-2-Lys)** is far more resolved, reflecting the more induced conformational restriction imposed by cyclisation, which reduces structural flexibility and gives rise to more distinguishable resonances consistent with the proposed structure. The NH region between 7.1 – 8.2 ppm displayed multiple peaks assigned to the squaramide and amide protons as well as the free NH_3^+ on the lysine side chain. The lysine α-proton was observed at approximately 4.5 ppm followed by the methylene protons on the lysine side chain appearing at ~ 2.7 ppm and from 1.2 – 1.8 ppm. Interestingly with the methylene protons from the ethylenediamine bridge, a similar observation was seen with **2.15 (Sq-2-Phe)** as discussed in chapter 2, whereby these proton resonances were split across different chemical shifts at approximately 3.9, 3.8, 3.4.and 2.9 ppm. HSQC analysis showed that each pair remains coupled to the same respective carbon atom. Specifically, the resonances at 3.8 and 3.4 ppm were correlate with a ^{13}C signal at 43.9 ppm, while the resonances at 3.8 and 2.9 ppm, correlate with a ^{13}C resonance at 38.6 ppm (See Appendix). This suggests that the cyclic squaratide environment gives rise to diastereotopic environments for these methylene protons, which manifest as dispersed resonances across different chemical shifts. Overall, the NMR spectrum, combined with the LC-MS and HRMS analysis provided strong evidence that the target squaratide **2.17 (Sq-2-Lys)**, had been successfully synthesized.

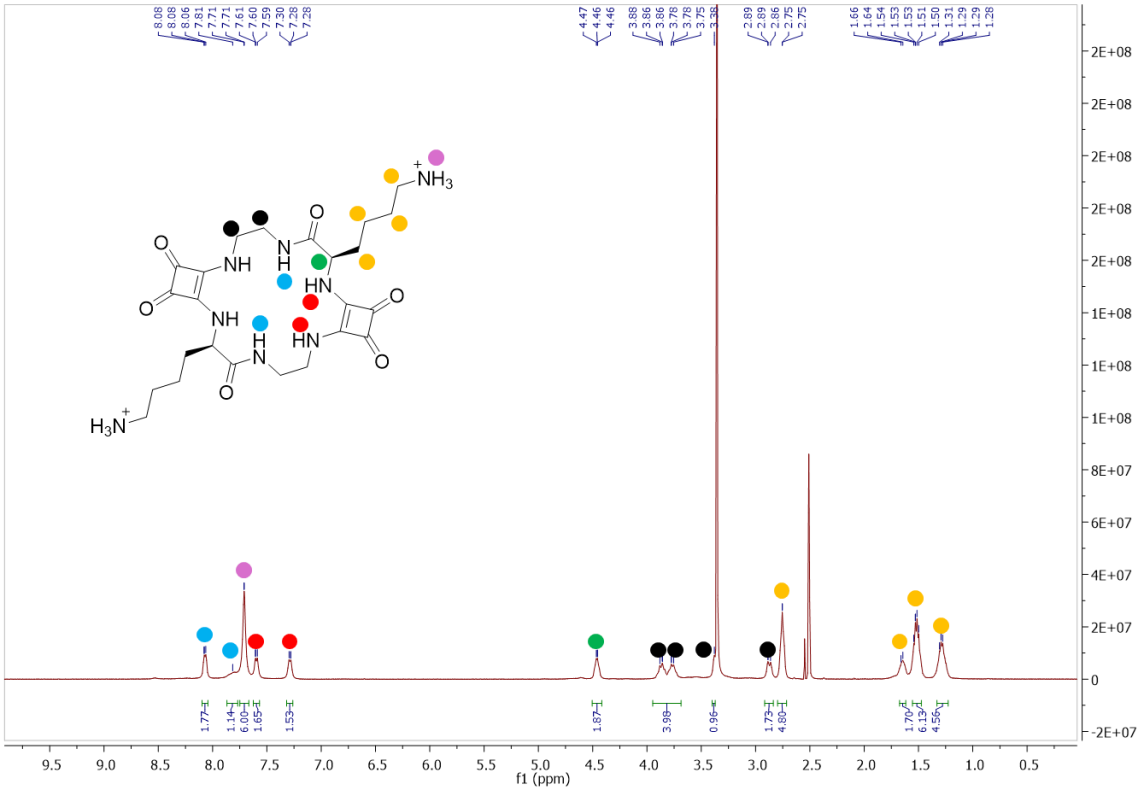

Figure 3.12: ^{1}H NMR spectrum of **2.17 (Sq-2-Lys)**.

The next step was to attempt the synthesis of higher order squaratide oligomers. Using the same iterative deprotection and coupling procedures described earlier, the linear sequences were successfully elongated on solid support to generate the trimer, tetramer, and pentamer analogues **(ASq-3-Lys(Boc)**, **ASq-4-Lys(Boc)**, and **ASq-5-Lys(Boc))**. Prior to macrocyclization, each of these intermediates was subjected to a test cleavage using HFIP/DCM in order to assess the quality of the growing chain. LC-MS and HRMS analysis (Figure 3.13) confirmed the expected molecular ions for each of the acyclic oligomers, validating the successful assembly of the longer linear squaratide chains.

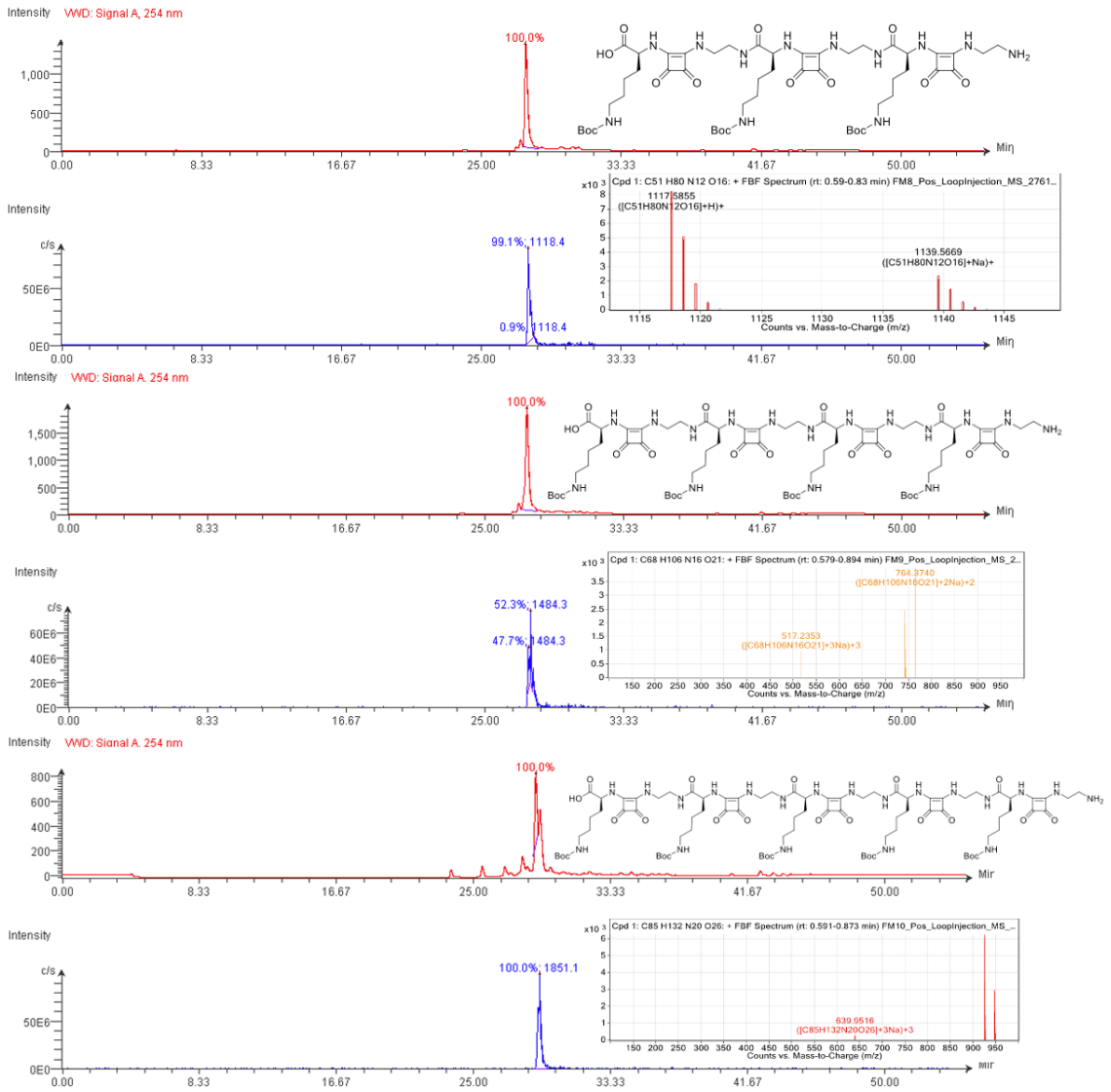

Figure 3.13: LC-MS and HRMS data for (top) **ASq-3-Lys(Boc)**, (middle) **ASq-4-Lys(Boc)**, and (bottom) **ASq-5-Lys(Boc)**.

With the linear oligomers in hand, the squaratides were then subjected to macrocyclization using the same procedure as for **Sq-2-Lys(Boc)**; under high-dilution conditions in the presence of PyBOP and NMM in DMF, to afford the corresponding cyclic derivatives **(Sq-3-Lys(Boc)**, **Sq-4-Lys(Boc)**, and **Sq-5-Lys(Boc))** in a 61%, 49%, and 48% respectively. The protected cyclic squaratides were subjected to Boc deprotection using TFA/DCM to afford our final compounds, **3.5 (Sq-3-Lys)**, **3.6 (Sq-4-Lys)**, and **3.7 (Sq-5-Lys)** in yields all above 80%. Although characterisation of these larger squaratides was complicated by spectral congestion and conformational heterogeneity, the combined LC-MS and HRMS analysis (Figure 3.14) confirmed the expected molecular ions for each of the cyclic squaratides while ^{1}H NMR data (see Appendix) further validated their

successful formation. Notably, with the larger macrocycles, **3.6 (Sq-4-Lys)** displayed distinct peak splitting on the LC-MS trace, consistent with slow conformational exchange processes on the NMR timescale, while **3.7 (Sq-5-Lys)** exhibited peak tailing, suggestive of dynamic conformer interconversion and potential aggregation behaviour. These phenomena reflect the increased structural complexity of higher-order macrocyclic squaratides and highlight the conformational diversity introduced by expanding ring size.

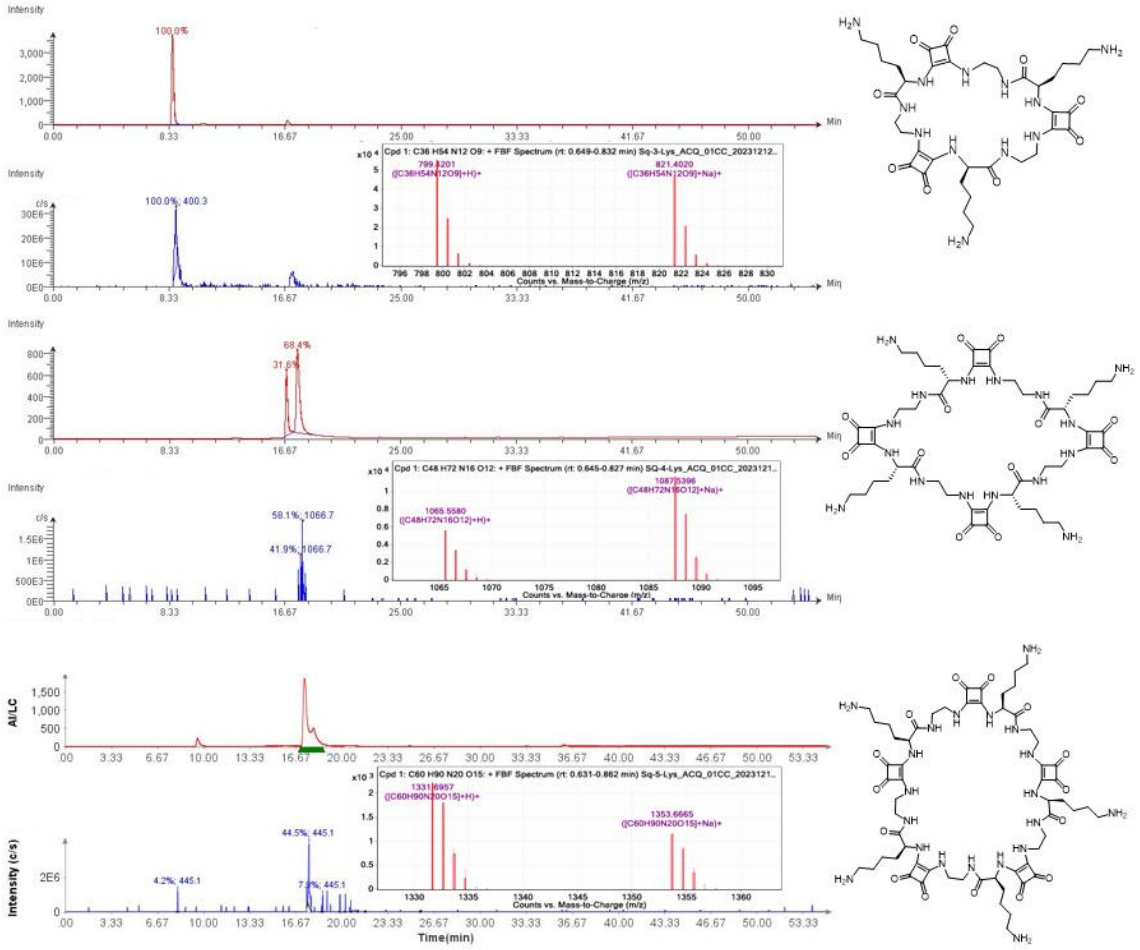

Figure 3.14: LC-MS and HRMS data for (top) **Sq-3-Lys**, (middle) **Sq-4-Lys**, and (bottom) **Sq-5-Lys**.

Remarkably, efficient cyclisation was observed even for the **3.7 (Sq-5-Lys)**, which at the outset we had anticipated would be significantly disfavoured due to the entropic penalty associated with closing longer chains. Upon further investigation, we hypothesise that the embedded squaramide linkages provide an element of structural preorganisation, biasing the acyclic intermediates into conformations conducive to head-to-tail cyclisation. This intrinsic preorganisation is likely to mitigate the expected entropic cost of macrocyclization and represents a valuable feature of the squaramide backbone for

the construction of medium- to large-cavity sizes. Advancing our synthetic approach towards solid-phase methods has greatly enhanced the versatility of squaratide synthesis, enabling the controlled construction and cyclisation of longer squaratides in a stepwise and reproducible manner. This strategy significantly expands the accessible chemical space of squaratides, yielding macrocyclic architectures with customisable cavity dimensions, multiple cationic side chains, and enhanced conformational rigidity. The preorganised nature of these cyclic structures produces well-defined cavities that are highly relevant to their potential as antimicrobial peptide mimetics, as the positively charged side chains promote electrostatic interactions with negatively charged bacterial membranes, while the squaramide backbone contributes hydrophobic and hydrogen-bonding elements capable of driving membrane disruption or translocation. Taken together, the successful synthesis and cyclisation of higher-order squaratides highlight both the robustness of the solid-phase methodology and the promise of these macrocycles as scaffolds for future functional applications.

3.5 Antimicrobial Activity of Squaratides

Author Contribution: *The antimicrobial activity of squaratides including all proteomic studies described in Section 3.5 were conducted by Dr. Poonam Ratrey in Prof. Kevin Kavanagh's Mycology lab at Maynooth University.*

With the successfully synthesised squaratides in hand, we next sought to evaluate their antimicrobial properties. A panel of compounds was selected to probe the structural features most critical for activity: (i) cyclic squaratides (**Sq-2-Lys** to **Sq-5-Lys**) of varying ring size, to test the effect of macrocyclic topology; (ii) linear squaratides (**ASq-2-Lys** to **ASq-5-Lys**), to assess whether conformational preorganisation is necessary; and (iii) Boc-protected cyclic squaratides (**Sq-2-Lys(Boc)** to **Sq-5-Lys(Boc)**), to examine the importance of free cationic lysine side chains. Antimicrobial activity was assessed using agar diffusion assays against Staphylococcus aureus as a representative Gram-positive pathogen. Compound solutions prepared in both DMSO and sterile water to evaluate solubility effects. To do so, 5 µL of a 1 mM stock of the respective compound was pipetted atop nutrient agar which was previously spread with *Staphylococcus aureus*. Following incubation at 37 °C for 24 hr, zones of inhibition were measured and recorded for each

compound.[253] Zones with a radius < 2 mm were deemed as not active and thus eliminated from further study. Strikingly, a pronounced difference in activity was observed between the cyclic and linear Squaratides. Cyclic squaratides (**Sq-2-Lys** to **Sq-5-Lys**) exhibited clear zones of inhibition under both DMSO and aqueous solubilisation conditions, confirming that these macrocycles possess intrinsic antibacterial properties (Figure 3.15). In contrast, the linear squaratides (**ASq-2-Lys** to **ASq-5-Lys**) did not produce detectable inhibition zones, even at comparable concentrations, suggesting that conformational pre-organisation is a critical factor in enabling effective bacterial killing. The absence of activity in the Boc-protected cyclic squaratides (**Sq-2-Lys(Boc)** to **Sq-5-Lys(Boc)**) further supports this interpretation and suggests that the charge state of the side chain is another important factor. Protection of the lysine side chains abolishes their cationic charge, preventing electrostatic attraction to the negatively charged bacterial cell envelope. This highlights the central role of free cationic amines in mediating antimicrobial activity and establishes that the squaramide backbone alone is insufficient to drive bacterial inhibition without complementary charge presentation. The observed activity is consistent with a model in which macrocyclic topology provides conformational preorganisation that favours membrane binding, while accessible cationic residues enhance electrostatic interactions with the negatively charged bacterial surface.

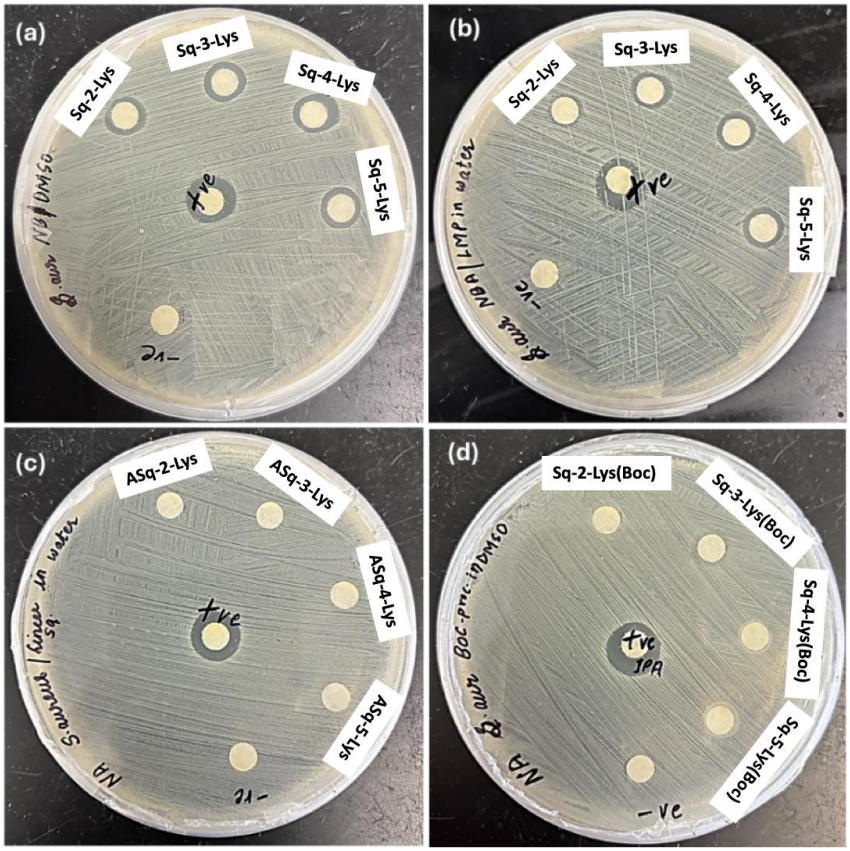

Figure 3.15: Agar plates showing zones of inhibition of *S. aureus* bacteria when treated with Sq-2-Lys to Sq-5-Lys in **(a)** - when compounds are dissolved in DMSO and **(b)** - when compounds are dissolved in a sterile water. The lower panel images display no zones of inhibition **(c)** – linear squaratides, ASq-2-Lys to ASq-5-Lys in DMSO and **(d)** – cyclic protected squaratides, Sq-2-Lys(Boc) to Sq-5-Lys(Boc) in DMSO.

3.5.1: Minimum Inhibitory Concentration (MIC) Studies

To further quantify the antimicrobial activity observed in the agar diffusion assays, minimum inhibitory concentration (MIC) determinations were carried out against *S. aureus* using the cyclic squaratides **Sq-2-Lys** to **Sq-5-Lys** (Figure 3.16). The inhibition curves provide valuable insight into both potency trends across the squaratide series and the influence of solvent environment on activity. When dissolved in DMSO (Figure 3.16a), all four cyclic squaratides demonstrated significant antibacterial activity, with **3.5 (Sq-3-Lys)** emerging as the most potent analogue. At concentrations as low as 250–300 µg/mL, **3.5 (Sq-3-Lys)** maintained >50% inhibition, whereas **3.6 (Sq-4-Lys)** and **3.7 (Sq-5-Lys)** showed a more rapid decline in activity over the same concentration range. Interestingly, **2.17 (Sq-2-Lys)** displayed a markedly different profile: although initial inhibition was moderate (~55–60%), its activity plateaued and remained largely

unchanged across the tested concentration range, suggesting a possible difference in its mode of interaction with bacterial membranes compared to the larger macrocycles.

A similar trend was observed when the compounds were dissolved in sterile water (Figure 3.16b). Again, **3.5 (Sq-3-Lys)** consistently outperformed the other analogues, achieving the greatest inhibition at intermediate concentrations and retaining significant potency down to lower doses. By contrast, **3.6 (Sq-4-Lys)** and **3.7 (Sq-5-Lys)** exhibited progressively weaker inhibition as concentration decreased, while **2.17 (Sq-2-Lys)** remained largely flat with only modest inhibition across all concentrations tested. The fact that the activity profiles are broadly consistent in both solvents indicates that the antimicrobial properties are inherent to the squaratide scaffolds and not solely a consequence of solvent-assisted solubilisation.

Taken together, these MIC results reinforce the conclusion from the agar diffusion assays that macrocyclisation is essential for antibacterial function and further reveal that **3.5 (Sq-3-Lys)** represents the optimal balance of ring size, charge density, and conformational preorganisation within the series. The reduced activity of **3.6 (Sq-4-Lys)** and **3.7 (Sq-5-Lys)** may reflect increased conformational flexibility in larger macrocycles, which could disperse cationic charge density and weaken electrostatic interactions with the bacterial membrane. Conversely, the smaller **2.17 (Sq-2-Lys)**, while active, may present its charges in a less favourable geometry for membrane insertion, leading to its atypical flat inhibition profile. Overall, these findings establish that ring size critically governs antimicrobial potency, with **3.5 (Sq-3-Lys)** emerging as the lead candidate within this class of antimicrobial peptide mimetics.

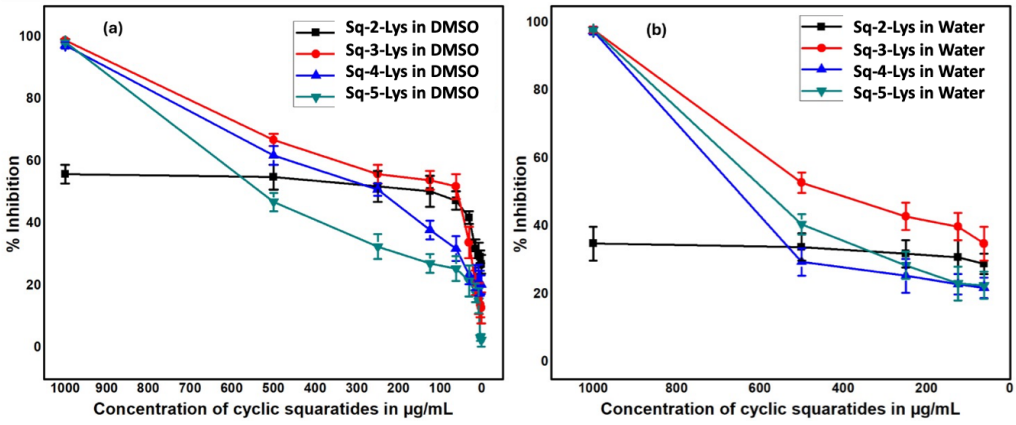

Figure 3.16: Minimum inhibitory concentration plots against *S. aureus* bacteria when treated with Sq-2-Lys to Sq-5-Lys in (a) DMSO and (b) in a sterile water.

3.5.2: Proteomic Profiling of *S. aureus* in Response to Sq-3-Lys

To further probe the mode of action of the squaratides, global proteomic analysis was performed on *S. aureus* cultures treated with **3.5 (Sq-3-Lys)** at 500 μg/mL for 6 hours, compared to untreated controls (Figure 3.17). Principal component analysis (PCA) revealed a clear separation between the proteomes of the treated and control groups, confirming that **3.5 (Sq-3-Lys)** induces a pronounced shift in bacterial protein abundances. This separation demonstrates that **3.5 (Sq-3-Lys)** elicits a distinct and reproducible perturbation of cellular physiology, consistent with a targeted antimicrobial effect rather than nonspecific cytotoxicity. Hierarchical clustering and heatmap analysis of differentially abundant proteins further highlighted the breadth of the response. Numerous proteins were significantly up- or down-regulated upon treatment, reflecting disruption of multiple cellular processes. The predominance of changes in proteins associated with membrane integrity, stress response, and metabolic regulation suggests that **3.5 (Sq-3-Lys)** exerts its activity, at least in part, through membrane-targeted mechanisms, akin to natural cationic antimicrobial peptides. Importantly, the clustering analysis demonstrated a tight grouping of **Sq-3-Lys**–treated replicates, underscoring the reproducibility of the observed proteomic response. These findings strengthen the conclusion that **3.5 (Sq-3-Lys)** operates as an antimicrobial peptide mimetic, disrupting bacterial survival pathways in a manner reminiscent of host defence peptides[254, 255], but with the added advantages of synthetic stability and tunability afforded by the squaramide backbone.[112] The proteomic data therefore provide molecular-level validation of the phenotypic antimicrobial assays, confirming that the observed bacterial growth inhibition reflects a substantive and multifaceted biological effect.

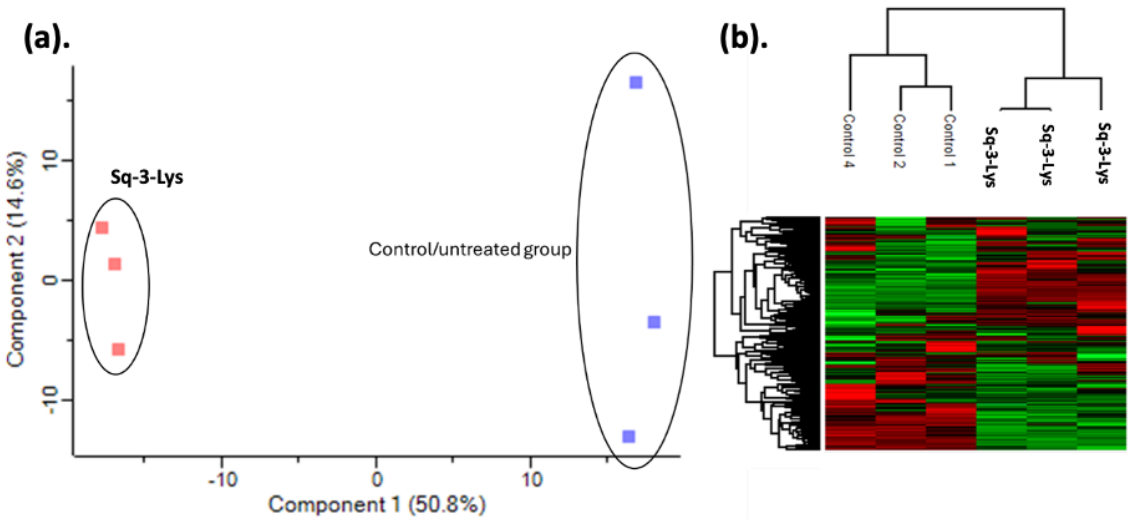

Figure 3.17: (a) Principal component analysis of *S. aureus* proteins after 6 hours of treatment with Sq-3-Lys drug at 500 µg/mL, demonstrating good separation in the proteome as compared to the untreated control group. **(b)** Heatmap generated through two-way unsupervised hierarchical clustering of the median protein expression values of all statistically significant differentially abundant proteins.

3.5.3: Differential Protein Expression Analysis

To identify specific cellular pathways affected by **3.5 (Sq-3-Lys)**, a volcano plot of statistically significant and differentially abundant (SSDA) proteins was generated (Figure 3.18). Using a significance threshold of $-\log10(\text{p-value}) > 1.3$ ($p < 0.05$), several proteins were found to be either markedly increased (green) or decreased (red) in abundance relative to the untreated control. These findings provide insight into the molecular basis of **3.5 (Sq-3-Lys)** activity. Proteins increased in abundance included key enzymes associated with cell wall organisation and metabolism, such as the probable cell wall hydrolase LytN (Q9ZNI1), N-acetylmuramoyl-L-alanine amidase Sle1 (Q2G0U9), and a LysM domain protein (Q2FV81). The induction of these proteins suggests that **3.5 (Sq-3-Lys)** triggers compensatory stress responses related to cell wall turnover and peptidoglycan remodelling, consistent with a membrane- or envelope-targeted mechanism of action. Additionally, metabolic enzymes such as ATP-dependent 6-phosphofructokinase (Q2FXM8) and a phosphatidic acid biosynthetic protein (Q2FXJ7) were also upregulated, pointing to broader perturbations of energy metabolism and lipid biosynthesis in response to treatment. In contrast, several proteins were found to be downregulated. These included the delta subunit of RNA polymerase (Q2FWD0), a

NAD(P)-binding domain protein (Q2FWB1), and ribosomal protein S1 (Q2FY9), along with the DNA-binding protein HU (Q2FYG2) and PurS formylglycinamide synthase (Q2FZJ2). Proteins decreased in abundance were involved in processes such as transcription, translation, and nucleotide biosynthesis suggests that **3.5 (Sq-3-Lys)** disrupts fundamental processes of gene expression and DNA/RNA metabolism, potentially as a downstream consequence of membrane perturbation and energy depletion.

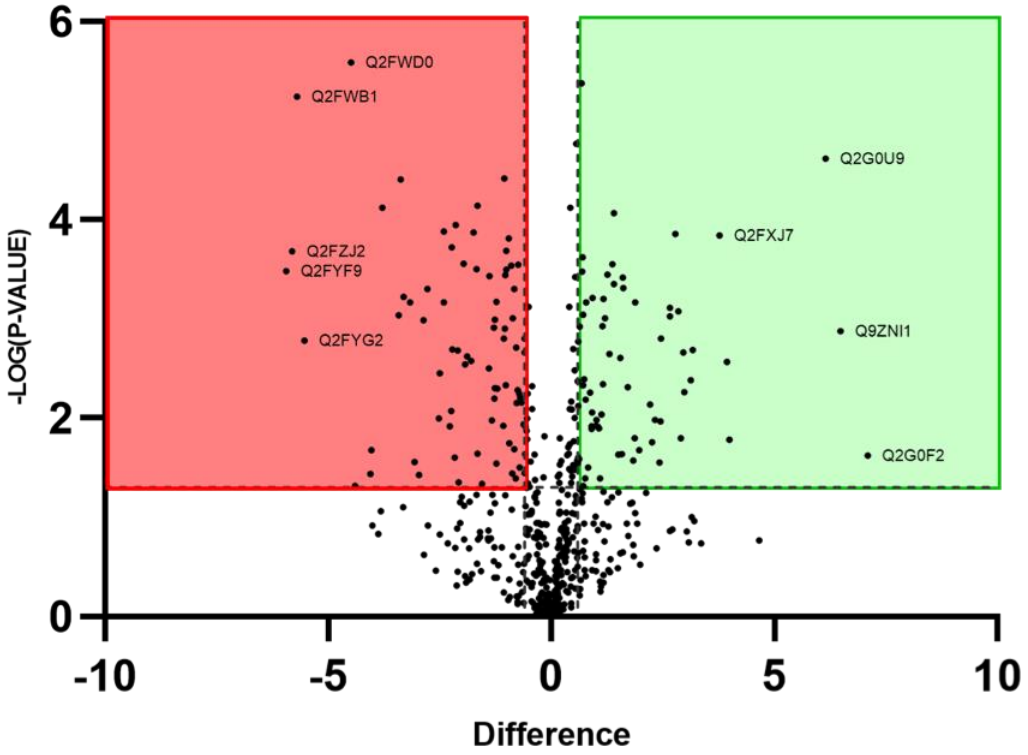

Figure 3.18: Volcano plots showing the distribution of statistically significant and differentially abundant (SSDA) proteins which have a −log (p-value) > 1.3 compared to the untreated control group. Green shows all the proteins increased in abundance, while red shows all the proteins decreased in abundance. A threshold of -log10(p-value) of 1.3 (p-value 0.05) was chosen to consider differences statistically significant.

This provided a mechanistic fingerprint for **3.5 (Sq-3-Lys)** action: initial membrane disruption leads to cell envelope stress and metabolic compensation, while simultaneously suppressing central processes of transcription, translation, and nucleotide synthesis. This dual effect mirrors the multifaceted action of natural cationic antimicrobial peptides, which destabilise bacterial membranes while also exerting downstream effects on macromolecular biosynthesis.

S.No	Protein ID	Protein name	Function of protein	Difference
1	**Q9ZNI1**	Probable cell wall hydrolase LytN (EC 3.-.	cell wall organization	6.47
2	**Q2G0U9**	N-acetylmuramoyl-L-alanine amidase sle1 (EC 3.5.1.28)	cell wall organization	6.14
3	**Q2FV81**	LysM domain protein (EC 3.5.1.28)	N-acetylmuramoyl-L-alanine amidase activity [GO:0008745]	3.99
4	**Q2FXM8**	ATP-dependent 6-phosphofructokinase (ATP-PFK) (Phosphofructokinase) (EC 2.7.1.11) (Phosphohexokinase)	canonical glycolysis [GO:0061621]; fructose 1,6-bisphosphate metabolic process [GO:0030388]; fructose 6-phosphate metabolic process [GO:0006002]	3.94
5	**Q2FXJ7**	1-acyl-sn-glycerol-3-phosphate acyltransferases domain protein (EC 2.3.1.51)	phosphatidic acid biosynthetic process	3.77
6	**Q2FYM2**	Dihydrolipoyllysine-residue succinyltransferase component of 2-oxoglutarate dehydrogenase complex (EC 2.3.1.61) (2-oxoglutarate dehydrogenase complex component E2) (OGDC-E2) (Dihydrolipoamide succinyltransferase component of 2-oxoglutarate dehydrogenase complex)	L-lysine catabolic process to acetyl-CoA via saccharopine [GO:0033512]; tricarboxylic acid cycle [GO:0006099]	3.17
7	**Q2FWD0**	Probable DNA-directed RNA polymerase subunit delta (RNAP delta factor)	DNA-templated transcription [GO:0006351]; regulation of DNA-templated transcription [GO:0006355]	-4.48
8	**Q2FWB1**	NAD(P)-binding domain-containing protein	-	-5.69
9	**Q2FYF9**	30S ribosomal protein S1, putative	translation [GO:0006412]	-5.93
10	**Q2FYG2**	DNA-binding protein HU, putative	chromosome condensation [GO:0030261]	-5.52
11	**Q2FZJ2**	Phosphoribosylformylglycinamidine synthase subunit PurS (FGAM synthase) (EC 6.3.5.3) (Formylglycinamide	IMP biosynthetic process [GO:0006189]	-5.80

Table 3.1: List of statistically significant and differentially abundant proteins.

3.5.4: Protein–Protein Interaction Network Analysis

To contextualise the proteomic changes induced by **3.5 (Sq-3-Lys)**, protein–protein interaction (PPI) networks were generated for differentially abundant proteins via the STRING database. This analysis compiled and provided a systems-level view of how **3.5 (Sq-3-Lys)** perturbs bacterial physiology by clustering affected proteins into coherent functional modules (Figure 3.19). Proteins increased in abundance clustered into pathways linked to cell envelope integrity and carbon metabolism. Proteins involved in peptidoglycan biosynthesis and cell wall organisation (e.g., Sle1, LytN, MurF) were enriched, consistent with an adaptive response to envelope stress. Additionally, metabolic enzymes associated with glycolysis and energy production (e.g., PfkA, Zwf) were significantly upregulated, suggesting that **3.5 (Sq-3-Lys)** treatment drives compensatory metabolic reprogramming to sustain energy-demanding stress responses. Together, these findings indicate that S. aureus attempts to bolster both structural defences and metabolic capacity in response to **3.5 (Sq-3-Lys)** challenge. Conversely, proteins decreased in abundance formed dense clusters related to central information-processing pathways. These included proteins involved in RNA biosynthesis (e.g., PurS, folD), transcriptional regulation (RNA polymerase subunits RpoA, RpoB, RpoE), and core metabolic enzymes (e.g., Pgk, Eno). The suppression of ribosomal and transcriptional machinery points towards a collapse in biosynthetic capacity, consistent with the antimicrobial phenotype observed. Importantly, the clustering analysis highlights that **3.5 (Sq-3-Lys)** does not affect isolated targets, but rather orchestrates a coordinated disruption of essential transcriptional, translational, and metabolic hubs. These systems-level insights reinforce the conclusion that **3.5 (Sq-3-Lys)** exerts a multifaceted mode of action: Primary membrane perturbation, leading to activation of cell wall stress and repair pathways; secondary metabolic reprogramming, attempting to meet elevated energy demands under stress; and suppression of transcriptional and translational processes, resulting in impaired growth and survival. This network-level disruption mirrors the complex activity of natural antimicrobial peptides but is here achieved using a synthetic, novel class of peptidomimetics that incorporates a squaramide backbone. The data therefore provide compelling evidence that **3.5 (Sq-3-Lys)** is not merely bacteriostatic but induces a global collapse of bacterial homeostasis through simultaneous pressure on multiple essential pathways.

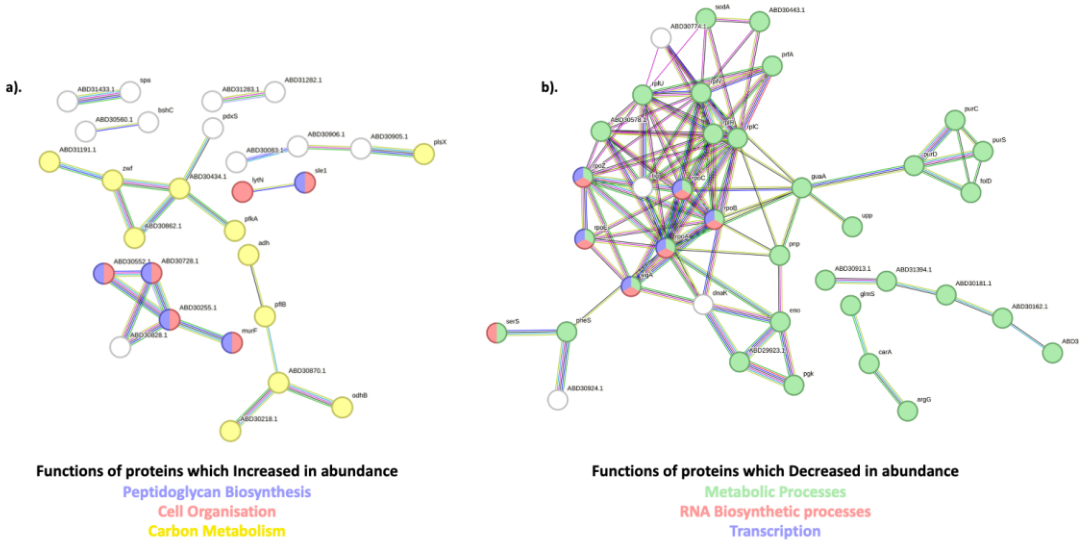

Figure 3.19: STRING analysis of protein networks increased **(a)** & decreased **(b)** in abundance in *S. aureus* treated with Sq-3-Lys at 500 µg/mL for 6 hours Vs. untreated controls. Data accrued from the STRING database using UniProt IDs from SSDA proteins from multiple sample t tests ($p < 0.05$) details the interactions between individual proteins, or corresponding pathways (highlighted in distinct colours & labelled). **(a)** Protein pathways observed in increased abundance **(b)** Protein pathways observed to be downregulated in response upon treatment with Sq-3-Lys.

3.6: Conclusion

This chapter has demonstrated how methodological advances in synthesis can directly enable the discovery of new biological function within the squaratide family. In Chapter 2, squaratide derivatives were prepared using a solution-phase synthetic pathway. While this approach provided access to the first generation of squaratide receptors and proved invaluable for establishing their anion binding capabilities, it was inherently limited in scope. The solution-phase strategy often required lengthy purification steps, restricted the accessible molecular complexity, and placed practical limitations on the size and diversity of compounds that could be obtained. These challenges constrained the development of more elaborate squaratide frameworks, particularly those requiring higher order architectures or precise side-chain modifications. In the present chapter, these limitations were overcome through the adaptation of solid-phase synthesis, which transformed the squaratide platform into a more versatile and scalable methodology. By harnessing the efficiency of resin-bound chemistry and the iterative protection–deprotection cycles characteristic of peptide synthesis, it became possible to extend squaratide chains systematically, incorporate multiple functional residues, and achieve on-resin macrocyclisation. This streamlined route significantly reduced synthetic bottlenecks while increasing structural precision. Importantly, the solid-phase pathway enabled the preparation of larger cyclic squaratides that would have been impractical to obtain by solution-phase methods and provided the synthetic flexibility to introduce tailored side-chain functionalities. As a result, a diverse library of squaratide receptors was generated, encompassing both linear and cyclic architectures with tuneable charge density, ring size, and substitution patterns. This methodological leap not only demonstrates the adaptability of squaramide chemistry but also underscores its potential as a general platform for the design of customisable, functionally diverse peptidomimetics.

The biological evaluation of these compounds further illustrates the impact of synthetic innovation on molecular function. Antimicrobial assays revealed a striking structure–activity relationship: only cyclic, deprotected squaratides exhibited antibacterial activity, whereas their linear or Boc-protected analogues were inactive. This finding highlights the dual requirement of macrocyclic preorganisation and cationic charge accessibility for effective antimicrobial function. Within the cyclic series, **3.5 (Sq-3-Lys)** emerged as the most potent analogue, producing pronounced zones of inhibition and the lowest MIC

values against S. aureus. The optimal activity of this intermediate-sized macrocycle reflects a balance between structural rigidity and charge distribution, with smaller or larger rings displaying diminished potency. Mechanistic insights gained from proteomic and network analyses provided molecular-level evidence of the multifaceted action of **3.5 (Sq-3-Lys)**. Treatment of *S. aureus* resulted in significant proteomic shifts, with upregulation of cell wall–associated hydrolases and metabolic enzymes indicative of envelope stress responses, alongside downregulation of transcriptional and translational machinery essential for growth and survival. Protein–protein interaction networks revealed that these changes are not isolated but occur within coordinated functional clusters, suggesting that **3.5 (Sq-3-Lys)** induces a global reprogramming of bacterial physiology. This dual mechanism of primary membrane disruption and secondary intracellular suppression strongly parallels the behaviour of natural antimicrobial peptides. However, unlike natural AMPs, the squaramide backbone offers enhanced chemical stability, protease resistance, and structural tunability, making squaratides a promising class of synthetic AMP mimetics.

Collectively, the results of this chapter highlight the direct relationship between synthetic design and biological function. The transition from solution-phase to solid-phase synthesis not only expanded the structural repertoire of squaratides but also uncovered a new biological application for these molecules as antimicrobial agents. By combining the structural principles of natural host-defence peptides with the synthetic versatility of squaramide chemistry, squaratides emerge as a robust and adaptable platform that can bridge the gap between fundamental molecular recognition and biologically relevant function. This work thus lays the foundation for subsequent chapters, where the squaratide scaffold will be further exploited in the context of anion transport and sensing, broadening their utility as multifunctional peptidomimetic systems.

Chapter 4

Modified Squaratides: Potential Anion Transporters

4: Modified Squaratides: Potential Anion Transporters

4.1: Introduction

Anion transport across cellular membranes is a fundamental physiological process, orchestrated with high specificity and regulation by membrane-bound anion channels and transporters.[256, 257] These specialized proteins maintain the delicate equilibrium of intra- and extracellular anionic species such as chloride, bicarbonate, and phosphate, which are crucial for processes ranging from cell volume regulation to pH balance and signal transduction.[258-261] Dysfunction or absence of these transport proteins can lead to a class of disorders known as channelopathies—diseases characterized by aberrant ion flux—of which cystic fibrosis is a well-documented example (as discussed in Chapter 1).[262-264]

Given the centrality of anion homeostasis in cellular health, the design and development of synthetic systems capable of mediating anion transport has emerged as a vibrant subfield within supramolecular chemistry. In recent years, considerable effort has been devoted to the creation of low-molecular-weight, drug-like molecules that mimic the function of natural ion transporters.[265-268] These artificial anionophores are engineered to bind selectively to target anions and facilitate their transmembrane transport, either via carrier or channel-like mechanisms.[269, 270]

The biomedical implications of such systems are profound. On one hand, synthetic anion transporters offer a promising therapeutic avenue for restoring ion flux in cells where native transporters are defective or absent, as in the case of certain genetic channelopathies.[271, 272] On the other hand, deliberate disruption of anion gradients by these synthetic constructs can lead to intracellular acidification, osmotic imbalance, and ultimately apoptosis—an approach being explored as a novel anticancer strategy.[273, 274]

An example of one of many applications of anion transport can be seen by Sessler and Shin whereby they demonstrated the pro-apoptotic capabilities of ionophores **4.1** and **4.2**, which facilitated chloride transport across the membranes of various cell lines (Figure 4.1).[275] Their study revealed that these ionophores promote the influx of Cl^- in conjunction with Na^+ into the intracellular environment. This ionic imbalance leads to an increase in intracellular chloride and sodium concentrations, triggering elevated reactive oxygen species (ROS) levels. Consequently, cytochrome c is released from the

mitochondria, activating caspase-dependent apoptotic pathways. This discovery further advanced the field of anion transport, highlighting the clinical potential of ionophores for therapeutic applications.

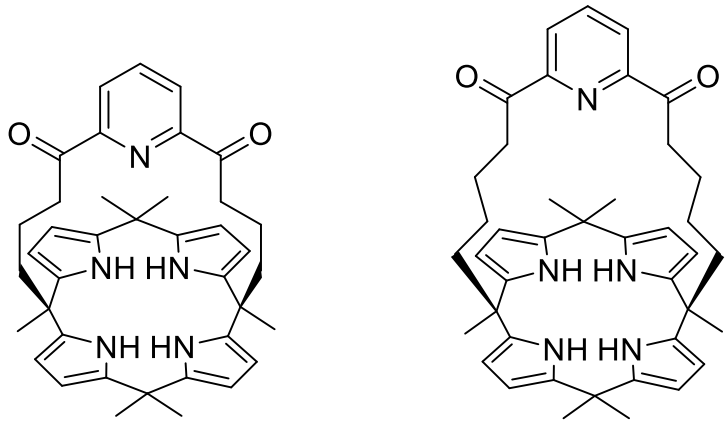

4.1 **4.2**

Figure 4.1. Structures of two pyridine diamide-strapped calix[4]pyrroles capable of inducing apoptosis in cells.

Fluorination of anionophores is widely recognized as a powerful and versatile strategy for enhancing molecular recognition and transport performance in various applications including medicinal chemistry, supramolecular chemistry and chemical biology.[265, 276, 277] The incorporation of fluorine atoms into anion transporters confers several advantageous characteristics. Due to the strong electron-withdrawing nature of fluorine atoms and their capacity to increase lipophilicity, fluorination can alter hydrogen bonding strength, and enhance chemical and thermal stability which in turn, improves anion-binding affinity and facilitate membrane partitioning. As a result, this modification has been shown to significantly enhance transport rates across various synthetic systems.[278] Additionally, fluorinated scaffolds often display enhanced membrane permeability, facilitating their function as efficient anion carriers or channels in both synthetic and biological membranes.[279, 280] The ability to fine-tune the properties of fluorinated compounds through strategic molecular design further expands their applicability, giving rise to next-generation anion transporters with optimized efficacy and selectivity.

An example of utilising fluorination can be seen by Sindelar and co-workers focused on synthesising a series of fluorinated bambusurils to act as highly effective and selective transmembrane Cl^-/HCO_3^- antiporters.[281] By introducing electron-withdrawing substituents connected via aryl groups to H-bond donors, the acidity of the H-bond donors generally increases leading to stronger binding properties. It also leads to an increase in lipophilicity which is advantageous for transmembrane transport. In this study, Sindelar set out to investigate the effects on anion binding and transport by designing fluorinated derivatives of bambusuril **4.3** through various numbers and positions of fluorine atoms or fluourine-containing groups on the benzyl substituents (Figure. 4.2).

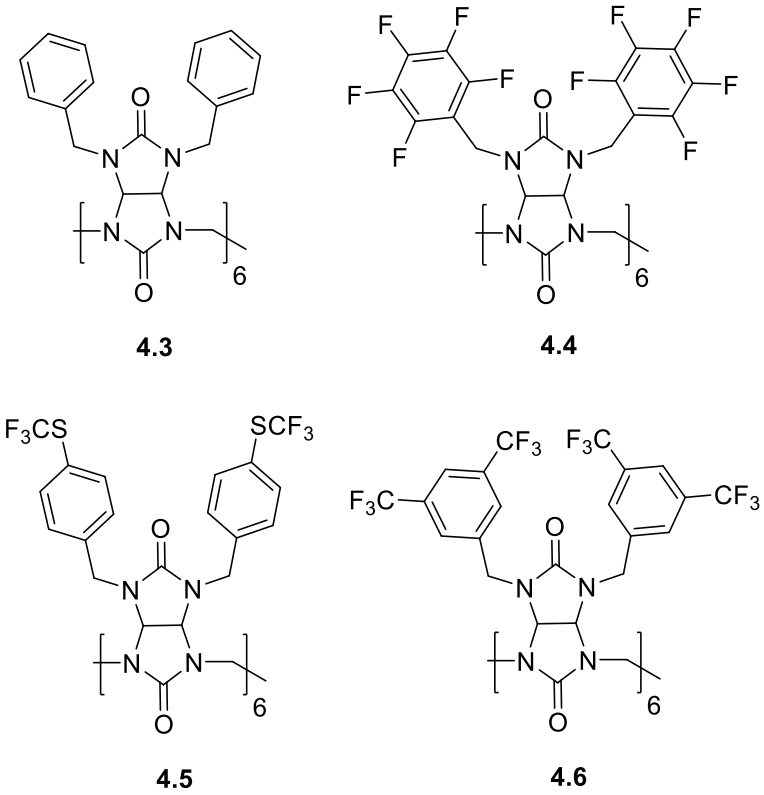

Figure. 4.2 Structures of bambus[6]urils **4.3** – **4.6** reported by Sindelar and coworkers.

^{1}H NMR spectroscopy was carried out in MeCN to study the binding properties and formation of host–guest complexes between bambusurils **4.4**, **4.5**, and **4.6** and Cl^-, NO_3^-, and HCO_3^- Association constants were calculated which showed **4.6** to be the strongest receptor with the highest affinity for NO_3^- (K_a = 5 x 10^{11} M^{-1}) followed by Cl^- (K_a = 6 x 10^{10} M^{-1}), and HCO_3^- (K_a = 2 x 10^9 M^{-1}). The evaluation of bambusurils as anion carriers involved the use of liposomes in the fluorescence-based lucigenin assay, where they demonstrated exceptional transport properties. Among these, receptor **4.6**, with the

highest affinities, stands out to the authors knowledge, as the most potent Cl^-/HCO_3^- carrier reported to date. It was noted that the Cl^-/NO_3^- antiport exhibited orders of magnitude slower kinetics compared to the Cl^-/HCO_3^- antiport. This disparity can be attributed to the strong affinities towards NO_3^- as well as its binding selectivity over Cl^- which disfavours decomplexation. This work demonstrates the potential of bambusurlis for applications in anion transport and drug delivery through successful incorporation of bambusuril molecules in the bilayers of liposomes followed by membrane fusion.

As discussed in Chapter 1, the most widely utilized anion-binding motifs predominantly rely on hydrogen bonding interactions, particularly those involving H-bond donor systems derived from acidic NH bonds. The acidity of these functional groups contributes to their strong binding affinity for biologically relevant anions such as chloride (Cl^-) and bicarbonate (HCO_3^-). This has been largely achieved through the incorporation of various structural motifs, including ureas, thioureas, pyrroles, thioamides, and squaramides, among others.[165, 282] These systems have been extensively explored for their efficacy in anion recognition and transport, owing to their versatile and tunable binding properties.[283, 284]

Gale et al. demonstrated that squaramides not only exhibit significantly higher anion binding association constants than their urea analogues but also possess superior anion transport capabilities (Figure 4.3).[285] Binding constants were determined using ^1H NMR spectroscopy, while anion transport efficiency was evaluated using POPC liposomes in conjunction with a chloride-selective electrode.

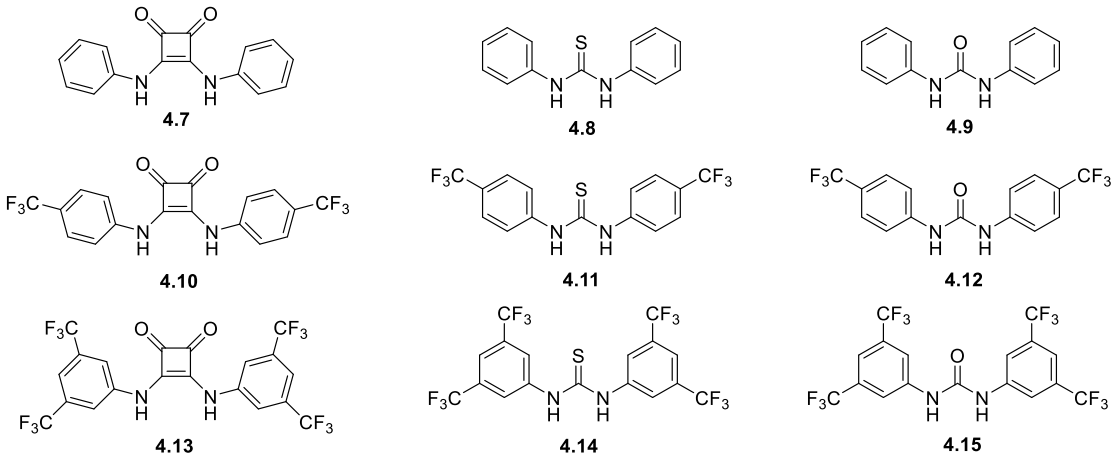

Figure 4.3. Structures of squaramide, thiourea and urea analogues Busschaert et al. used to compare anion binding and anionophoric activity.

The squaramide analogues displayed anion binding affinities an order of magnitude greater than those of their urea and thiourea counterparts, along with substantially lower EC_{50} values in Cl^-/NO_3^- exchange assays (Table 4.1). The authors attributed this enhanced binding ability to the increased thermodynamic stability conferred upon squaramides upon anion complexation.

Compound	K_a [M^{-1}] [a]	EC_{50} [mol%] [b]
4.7	260	1.38
4.8	15	-[c]
4.9	31	-[c]
4.10	458	0.06
4.11	43	0.22
4.12	75	0.42
4.13	643	0.01
4.14	41	0.16
4.15	88	0.30

Table 4.1: Summary of chloride binding (K_a) and anion transport (EC_{50}) abilities of compounds **4.7 – 4.15**. [(a)] Association constant with receptors and Bu4NCl in DMSO-d_6/0.5% H_2O at 298 K. [(b)] Concentration of transport (mol% carrier with respect to lipid) required to obtains 50% chloride efflux in 270s during Cl^-/NO_3^- assays. [(c)] Compound was not active enough to perform Hill analysis.

Our group has extensively utilized the squaramide motif in the design of molecular receptors, sensors, and anion transporters.[57, 286, 287] Squaramides are particularly well-suited for these applications due to their strong hydrogen-bond donating capability, facilitated by dual-directional NH bonds, as well as their planar aromatic structure, which experiences enhanced aromaticity upon guest binding.[288] This distinctive cyclobutene-dione framework has garnered significant interest across the chemical sciences in recent years, owing to its advantageous properties. As a result, squaramides have demonstrated potential for applications across multiple branches of chemical science, including supramolecular chemistry, medicinal chemistry, and materials science.[112, 289, 290]

4.2: Chapter Objective

The aims of this chapter can be divided into two sections, but both are primarily concerned with the synthesis of squaratides for exploration as potential anion transporters. The first objective of this chapter focuses on the rational design and synthesis of novel anion transport squaratides by incorporating a squaramide scaffold onto our squaratide framework. We aim to exploit the lysine side chains by covalently attaching a squaramide motif, in order to enhance their anion transport properties while maintaining a structurally robust and tuneable framework. We intend to investigate the impact of the squaramide motifs positioning within the squaratide scaffold to assess how hydrogen bonding interactions of the additional squaramide motifs influence anion recognition and transport particularly with chloride in comparison to its non-functionalised counterparts (Scheme 4.1).

The second objective is to utilise our versatile synthesis of squaratides via solid phase synthesis in order to incorporate fluorinated amino acids into the squaratide backbone ensuring precision in sequence design and structural consistency giving rise to novel fluorinated squaratides. We hypothesised that fluorination is expected to modulate the physicochemical properties of the transporters by increasing lipophilicity, improving membrane permeability, and fine-tuning anion-binding affinities of our squaratides.

With the synthesis of both novel classes of potential squaratide based anion transporters at hand, We intend to systematically compare the anion-binding affinities of squaramide-functionalized and fluorinated squaratides as well as their non functionalised and fluorinated counterparts using NMR spectroscopy, and to further assess the anion binding and transport capabilities across lipid bilayers using lucigenin assays, with further investigation in determining the structure–activity relationships governing anion transport efficiency, focusing on how squaramide hydrogen bonding and fluorine-induced lipophilicity contribute to enhanced function. We hoped that these findings will provide critical insights into the molecular mechanisms underlying synthetic anion transport and offer potential applications in supramolecular chemistry, medicinal chemistry, and the development of biomimetic membrane transport systems.

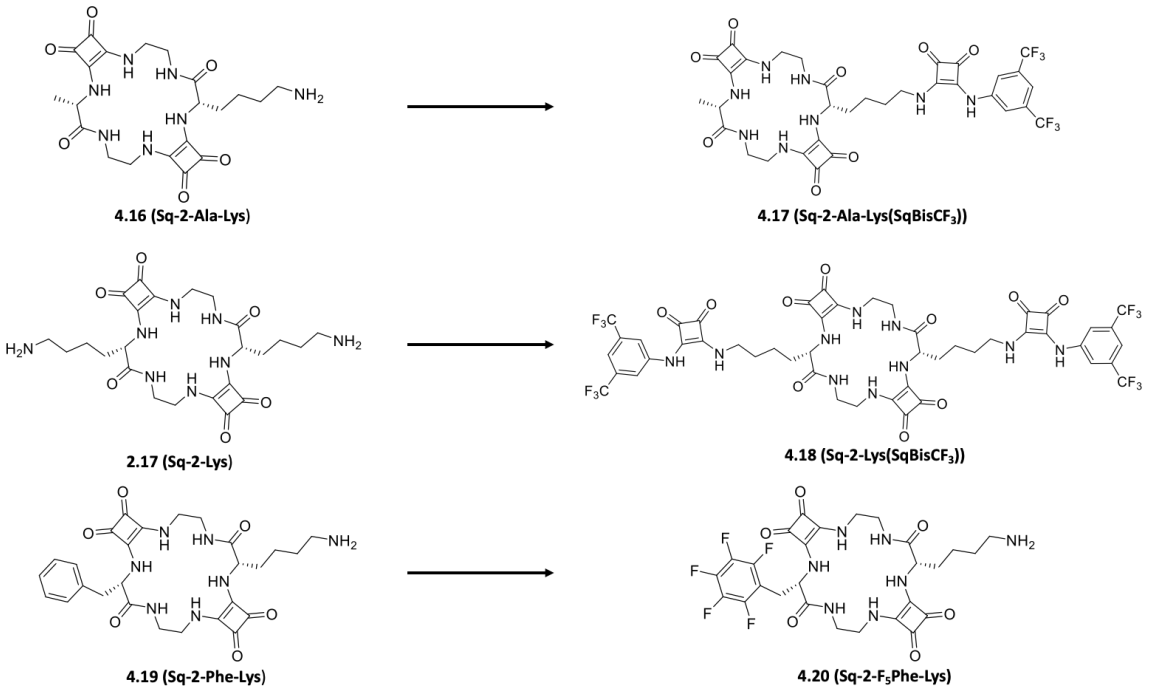

Scheme 4.1: Chemical Structures of target compounds **2.17**, and **4.16 - 4.20.**

4.3: Synthesis and Characterisation

Following a similar approach to the peptide synthesis described in Chapter 3, the initial step involved assembling the linear sequence through solid-phase peptide synthesis (SPPS). This was carried out using 2-chlorotrityl chloride resin and sequential coupling based on the Fmoc/Boc strategy as outlined in Scheme 4.2.

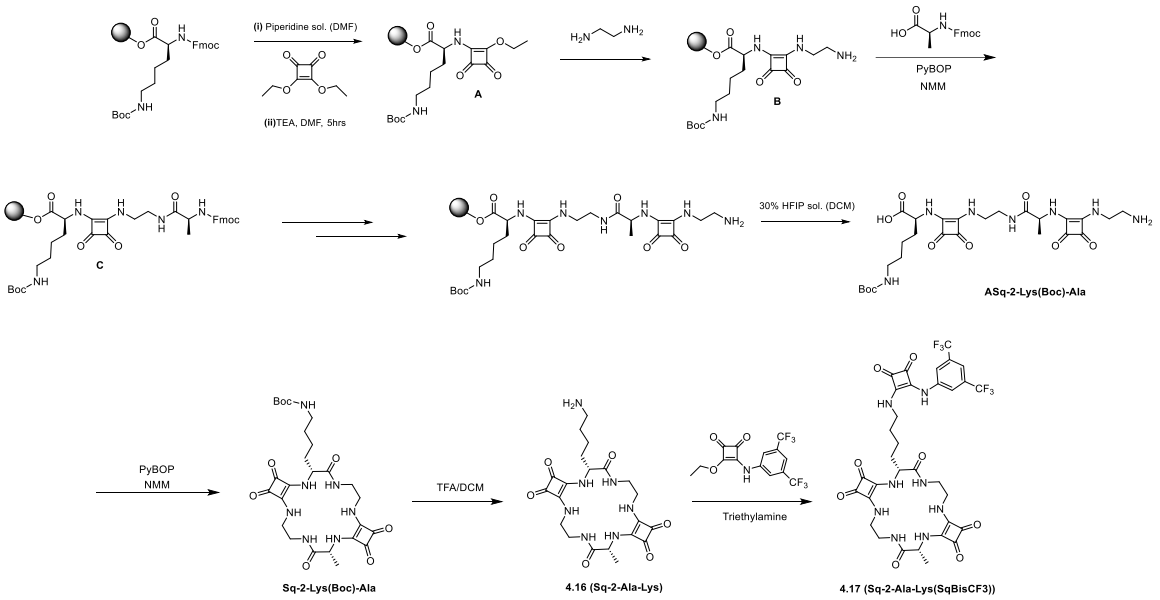

Scheme 4.2: Synthetic Scheme towards the Synthesis of **4.17 (Sq-2-Ala-Lys(SqBisCF$_3$)).**

The first step was to assemble the squaratide monomer (**B**) whereby Fmoc-Lys (Boc) was initially loaded onto the resin. To cap any unreacted trityl chloride groups, the resin was treated with a capping solution consisting of DCM/methanol/DIPEA. To functionalize the amine of lysine with a squarate moiety, the resin was treated with 20% piperidine in order to deprotect the Fmoc. Once deprotected, the resin was treated with diethyl squarate and triethylamine in DMF, affording the resin-bound squarate-conjugated lysine (**A**). The HPLC trace displayed one sharp UV peak with a t_R = 28 min. Strong ionisation was observed for the target mass of $[M+H]^+$ = 371.2 $gmol^{-1}$ in positive mode (Figure 4.4).

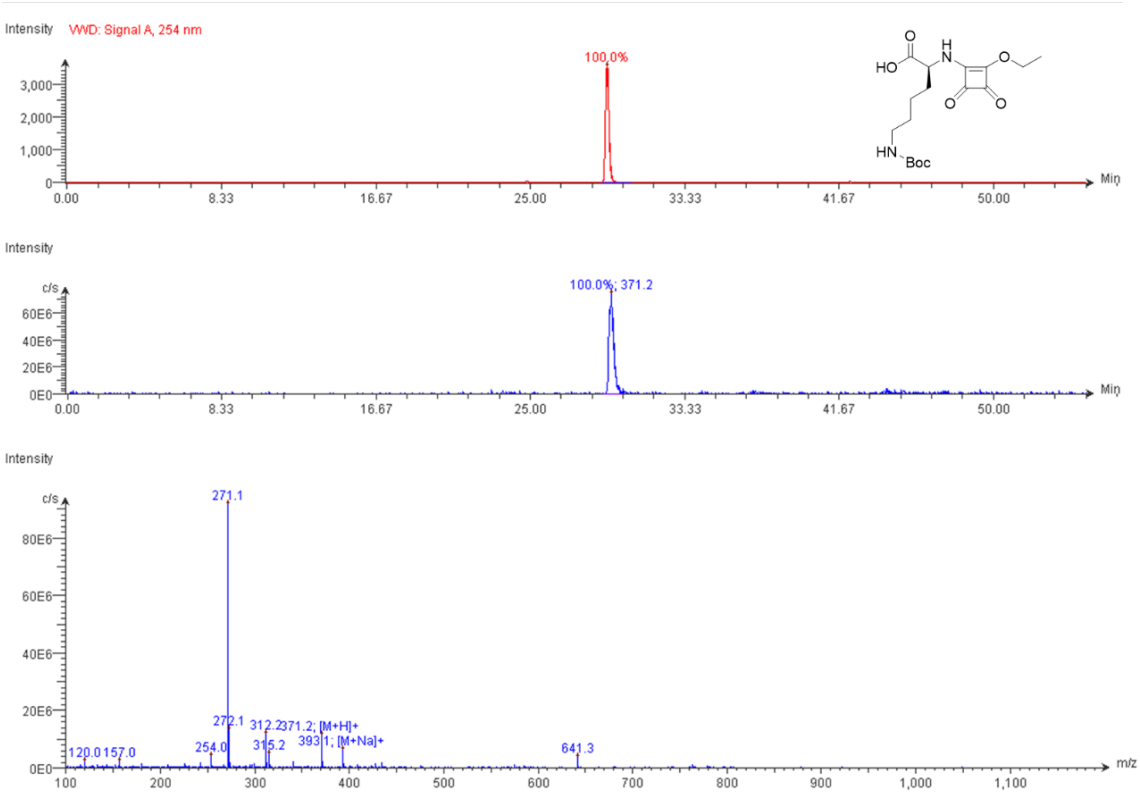

Figure 4.4: LC-MS data for **A.**

The subsequent step involved functionalizing the resin-bound intermediate with ethylenediamine (EDA) to obtain the desired squaratide monomer (**B**). Due to its high nucleophilicity and basicity, EDA can act as both a nucleophile and a base, eliminating the need for additional organic bases to drive the reaction to completion. The resulting Lys-Sq-EDA conjugate was characterized by liquid chromatography–mass spectrometry (LC-MS) (Figure 4.5). The HPLC trace displayed one sharp UV peak with a t_R = 24 min, and

strong ionisation was observed for the target mass of $[M+H]^+$ = 385.3 $gmol^{-1}$ in positive mode.

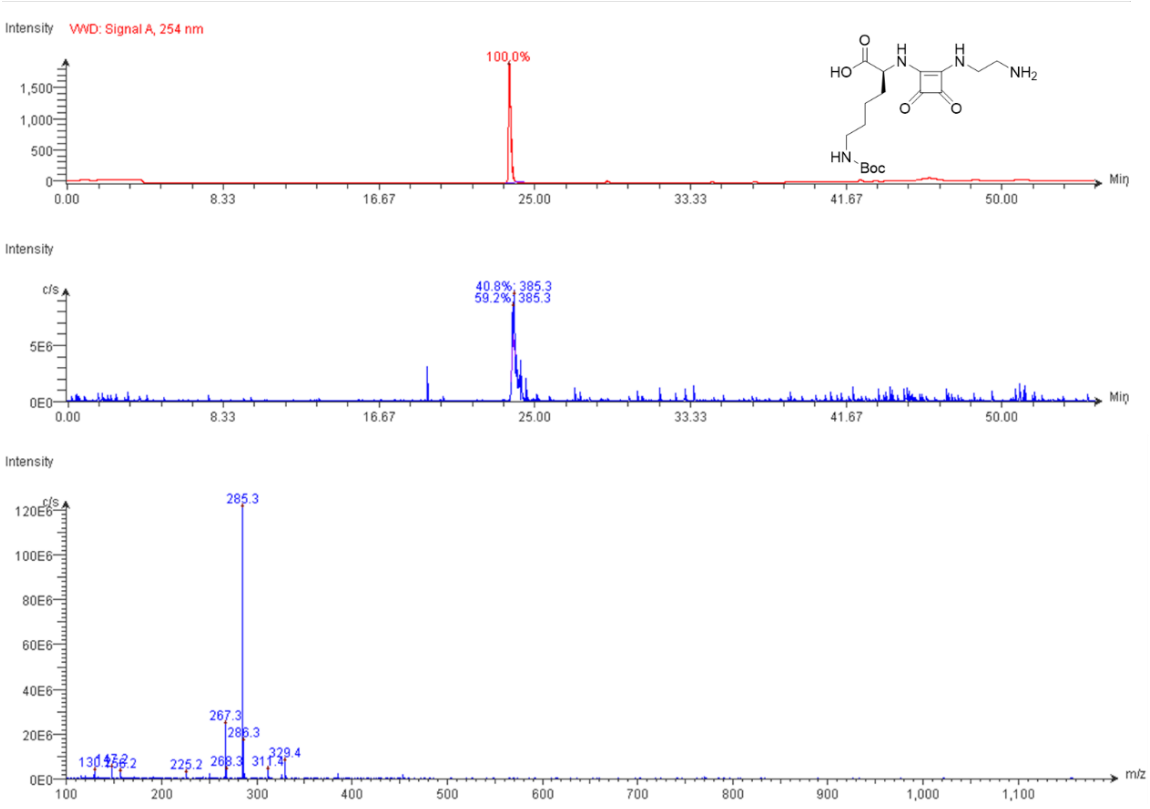

Figure 4.5: LC-MS data for **B**

Following the successful synthesis of the monomer on solid support, Fmoc-Ala-OH was coupled to the intermediate using PyBOP as the coupling reagent in the presence of N-methylmorpholine (NMM) to afford (**C**). This was followed by a second squaramide functionalization and subsequent addition of ethylenediamine (EDA), affording the linear squaratide dimer, **ASq-2-Lys(Boc)-Ala**. The product was then cleaved from the resin using a mixture of hexafluoroisopropanol (HFIP) and dichloromethane (DCM), followed by lyophilization. The resulting acyclic squaratide was characterized by liquid chromatography–mass spectrometry (LC-MS) (Figure 4.6). The HPLC trace displayed one sharp UV peak with a t_R = 23 min, and strong ionisation was observed for the target mass of $[M+H]^+$ = 594.2 $gmol^{-1}$ in positive mode.

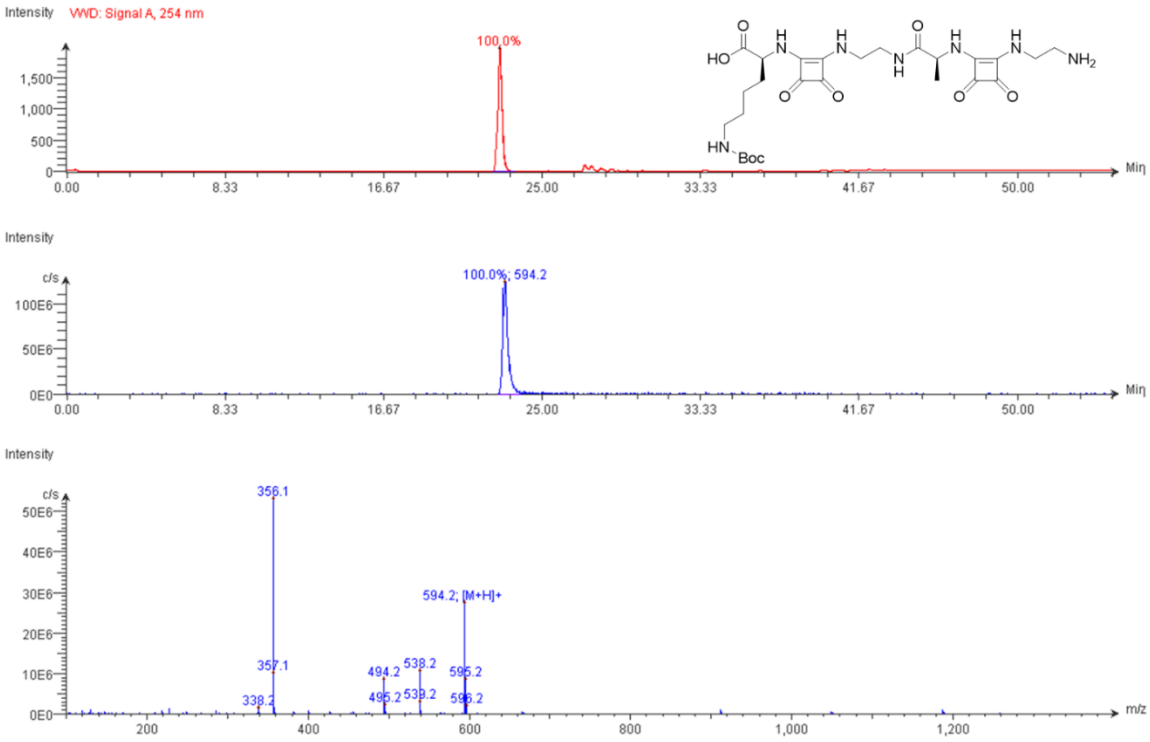

Figure 4.6: LC-MS data for **ASq-2-Lys(Boc)-Ala**

Intramolecular cyclization was performed under high-dilution conditions using PyBOP as the coupling reagent and N-methylmorpholine (NMM) as the base in DMF, yielding the protected cyclic product **Sq-2-Lys(Boc)-Ala** as an off-white solid with an isolated yield of 61%. Confirmation of successful cyclization was obtained through LC-MS (Figure 4.7). The product exhibited a longer HPLC retention time (tR = 28 minutes) compared to the linear precursor **ASq-2-Lys(Boc)-Ala**, consistent with the loss of the free C-terminal carboxyl and amino groups, suggesting successful intramolecular coupling.

The HPLC trace revealed a single, sharp UV-absorbing peak. However, due to the acidic conditions of the HPLC solvent system (0.1% TFA in acetonitrile/water), partial deprotection of the Boc group occurred, leading to fragmentation. This was evidenced by a strong signal at $[M - Boc + H]^+ = 476.1\ gmol^{-1}$ in positive ion mode, indicative of Boc group loss in the presence of trifluoroacetic acid (TFA).

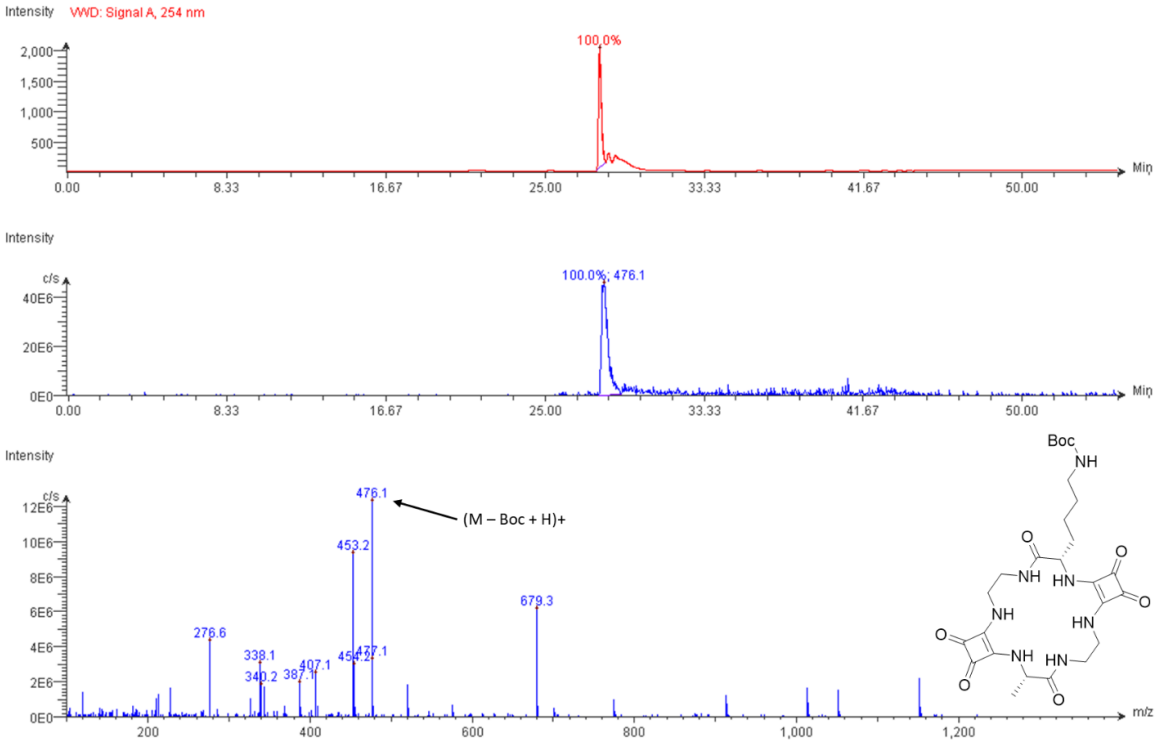

Figure 4.7: LC-MS data for **Sq-2-Lys(Boc)-Ala.**

Before the functionalisation of our squaramide motif onto the free amine lysine side chain, Boc deprotection was achieved using a 50:50 (v/v) mixture of trifluoroacetic acid (TFA) and dichloromethane (DCM). Following reaction completion, the solvent was evaporated under reduced pressure, and the residue was redissolved in a minimal volume of methanol. The product was subsequently precipitated by addition to cold diethyl ether and lyophilized to yield the deprotected final product, **4.16 (Sq-2-Ala-Lys**), as a white solid with an isolated yield of 90%.

Analytical HPLC revealed a significantly shorter retention time (t_R = 18.33 minutes) for **4.16** compared to its Boc-protected precursor (**Sq-2-Lys(Boc)-Ala**), consistent with the removal of the Boc groups and the presence of free primary amines on the lysine side chains. The chromatogram displayed a sharp UV-absorbing peak corresponding to the desired product; however, a slight shoulder was observed on the main peak, which may suggest minor tailing effects during elution. Furthermore, strong ionization was observed in the LC-MS analysis, with a prominent signal at $[M+H]^+$ = 476.4 $gmol^{-1}$ in positive ion mode, confirming the successful deprotection and formation of the desired compound.

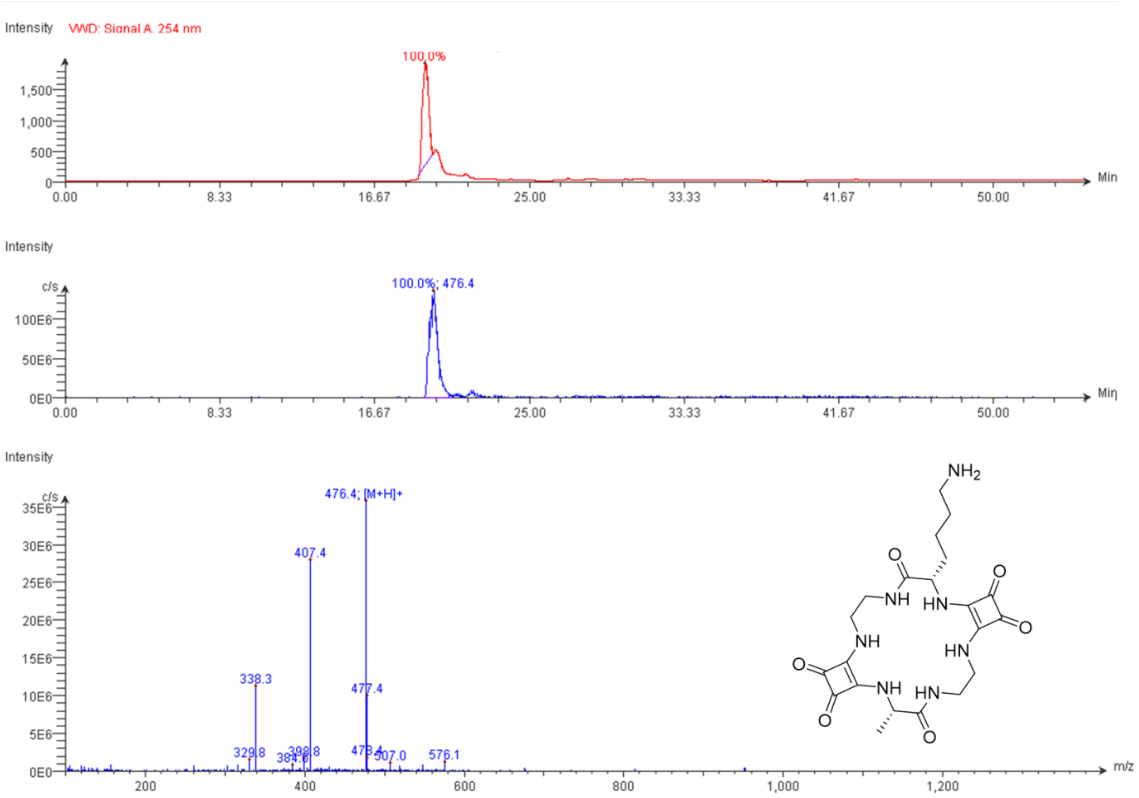

Figure 4.8: LC-MS data for **4.16 (Sq-2-Ala-Lys**).

The final step of the synthetic pathway was to functionalise Sq-BisCF_3 onto the free amine lysine side chain of our squaratide. This was carried out in the presence of triethylamine acting as the base in DMF to afford our final compound, **4.17 (Sq-2-Ala-Lys(SqBisCF_3))** in an 80% yield. The UV peak on the HPLC trace corresponded to the product with a strong ionisation was also observed for the target mass of $[M+H]^+$ = 783.4 $gmol^{-1}$ in positive mode.

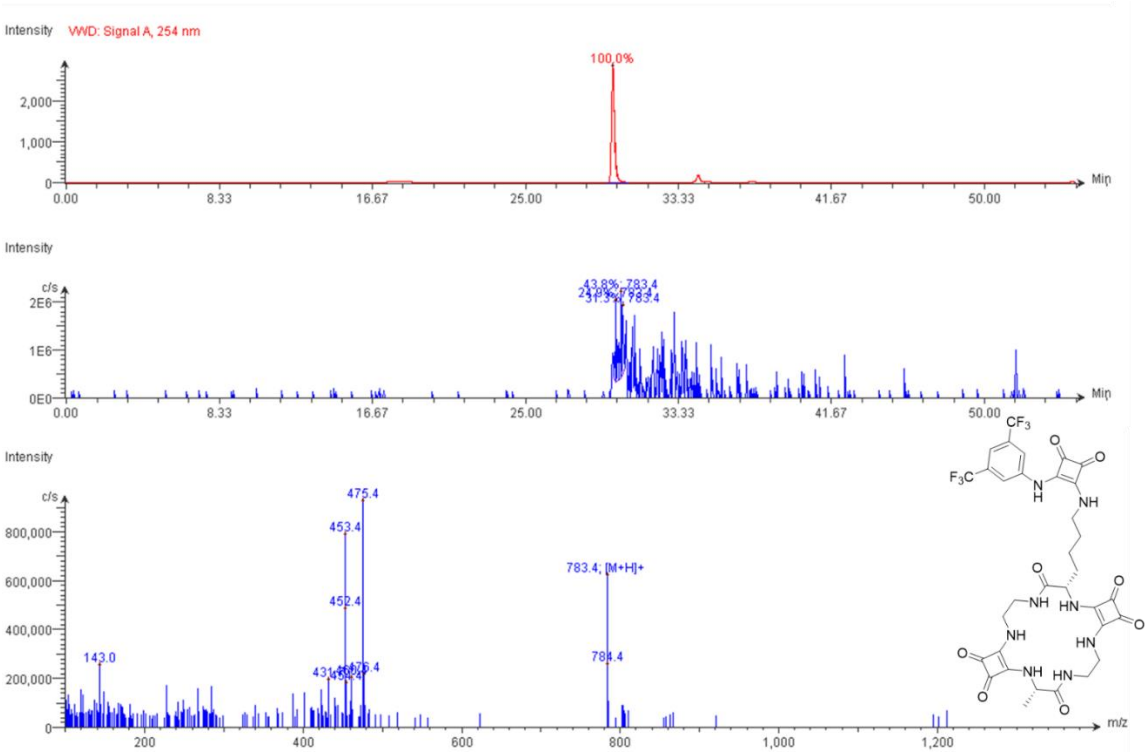

Figure 4.9: LC-MS data for **4.17 (Sq-2-Ala-Lys(SqBisCF$_3$)).**

HRMS was also used as a complimentary analysis to confirm the molecular formula of **4.17 (Sq-2-Ala-Lys(SqBisCF$_3$))**, with confirmation of the target mass $[M+H]^+$ = 783.2313 gmol^{-1} possessing a low mass error value of - 0.89 ppm.

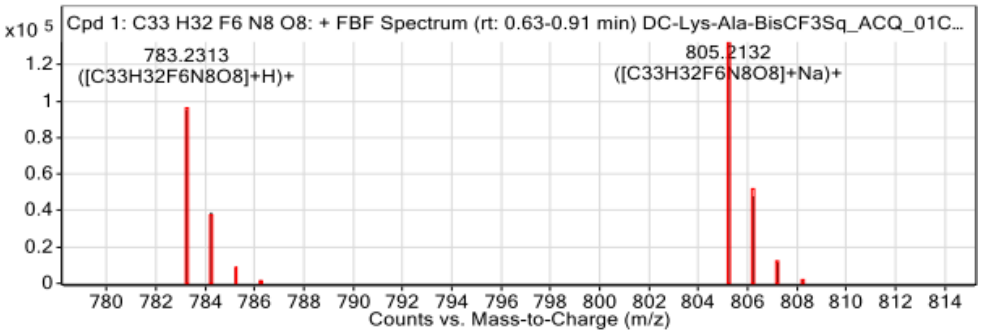

Figure 4.10: HRMS data for **4.17 (Sq-2-Ala-Lys(SqBisCF$_3$)).**

Similarly to the compounds synthesised in Chapter 2 and Chapter 3, It was noted that the ^{1}H NMR spectra of these compounds during NMR characterisation, gave rise to complex behaviour where several sets of significantly broadened peaks were observed despite LC-MS and HRMS analyses confirming the presence of the expected molecular ions. However, through comparative spectra of the functionalised and unfunctionalized analogues presented in Figure 4.11, the successful functionalisation of the squaramide-Bis(CF_3) unit for **4.17 (Sq-2-Ala-Lys(SqBisCF_3))** was confirmed. Notably, a distinct singlet at δ ≈ 10.25 ppm (highlighted in red) is observed in the functionalised derivative, corresponding to the highly deshielded squaramide NH proton adjacent to the electron-withdrawing aryl ring. Additionally, the presence of two characteristic aromatic doublets at δ ≈ 7.85 and 7.75 ppm (red markers) further confirms the incorporation of the 3,5-bis(trifluoromethyl)phenyl group. In contrast, the unfunctionalized **4.16 (Sq-2-Ala-Lys)** spectrum lacks these downfield squaramide NH and aromatic resonances, displaying only a single α-NH resonance at δ ≈ 7.75 ppm (purple marker) assigned to the free ε-amino group of lysine. The clear spectral differences, particularly the emergence of new, well-defined signals in the functionalised spectrum, provide conclusive evidence for the successful derivatization of the lysine side chain. These spectral assignments are fully consistent with the expected electronic effects of the CF_3 groups and the hydrogen-bond-donating nature of the squaramide scaffold further validating that the final product was obtained.

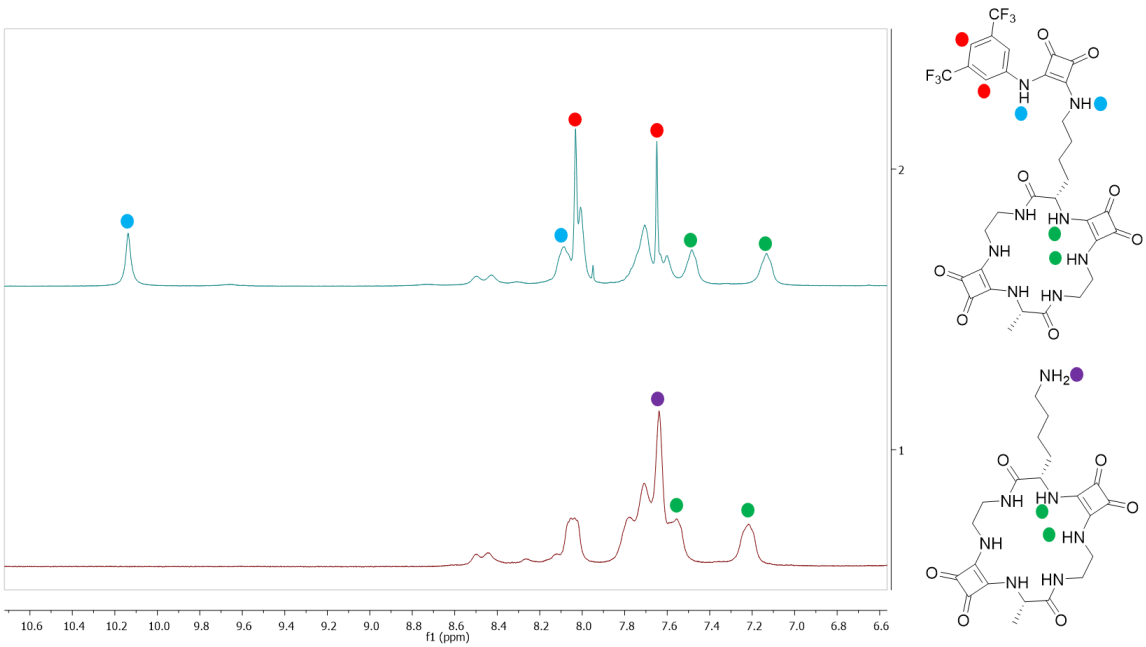

Figure 4.11: Partial ^{1}H NMR spectrum, of **4.16** and **4.17.**

Further confirmation of successful derivatisation was obtained from the ^{19}F NMR spectrum of **4.17 (Sq-2-Ala-Lys(SqBisCF₃))** which displayed a single sharp resonance at δ ≈ – 61.7 ppm (Figure 4.12). The chemical shift ppm lies within the expected region for aryl-CF_3 substituents adjacent to an electron-withdrawing group such as a squaramide.[291] This signal is fully consistent with the presence of two chemically equivalent CF_3 groups located at the 3' and 5' positions of the aryl ring, whose environments are magnetically indistinguishable on the NMR timescale. The unique CF_3 signal at – 61.7 ppm, coupled with diagnostic downfield squaramide NH resonances observed in the ^1H NMR spectrum, establishes the identity and integrity of the functionalised receptor. This cross-validation across multiple NMR nuclei (H, C, and F), alongside HRMS data, gives robust evidence for the structural assignment of (**4.17**) **Sq-2-Ala-Lys(SqBisCF₃)**.

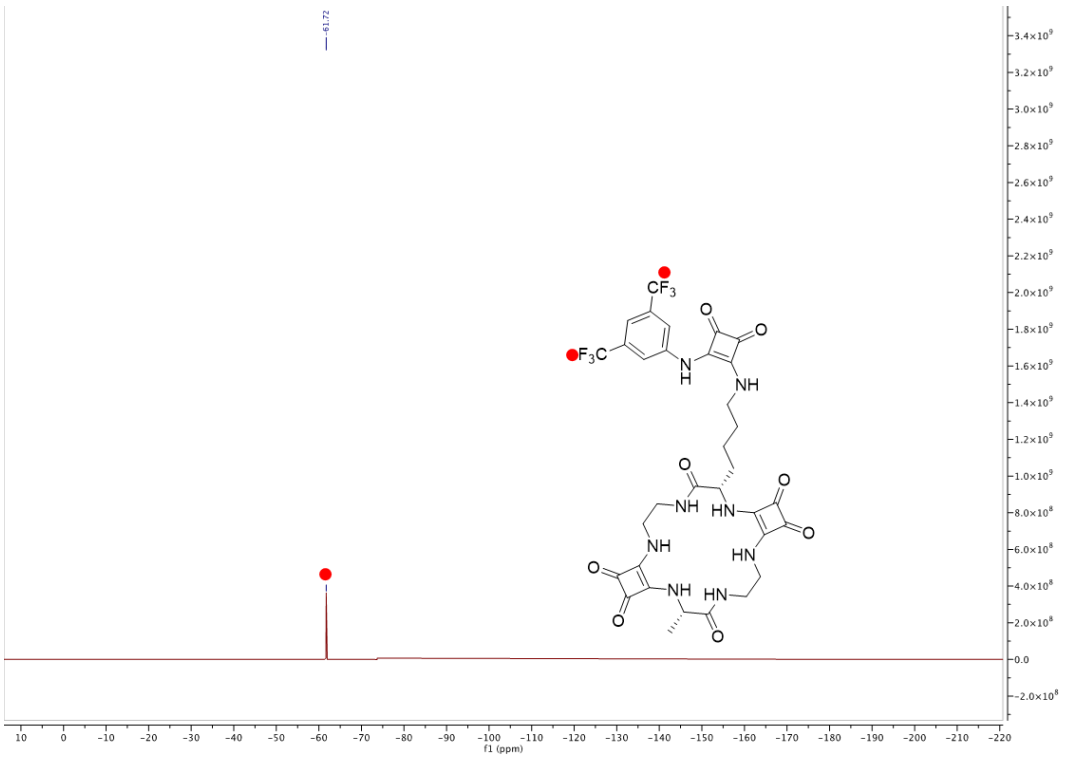

Figure 4.12: ^{19}F NMR spectrum of **4.17**.

In parallel, the successful functionalisation of **4.18 (Sq-2-Lys(SqBisCF$_3$))** could be confirmed through analogous spectral analysis (Figure 4.13). When compared to its unfunctionalized precursor **2.17 (Sq-2-Lys)**, the disappearance of the broad ε-NH$_2$ resonance at δ ≈ 7.75 ppm (purple marker) provides immediate evidence of side-chain derivatisation. Concomitantly, two new downfield resonances emerge: a strongly deshielded singlet at δ ≈ 10.15 ppm, characteristic of the aryl-squaramide NH, and a second squaramide NH resonance at δ ≈ 8.20 ppm (blue marker), both diagnostic of successful coupling to the 3,5-bis(trifluoromethyl)phenyl squarate. Moreover, a distinct set of aromatic resonances between δ ≈ 7.40–7.80 ppm (red markers) corresponds precisely to the expected pattern for the bis-CF$_3$ substituted phenyl moiety. These spectral signatures, absent in the parent **2.17**, not only confirm incorporation of the electron-deficient aryl squaramide unit but also align with the electronic deshielding trends observed for **4.18**. Together, the comparative NMR data across both **4.17** and **4.18** establish unambiguously that side-chain functionalisation with the bis(trifluoromethyl)aryl squarate motif has been achieved in both cases, furnishing the desired squaratide-based receptors.

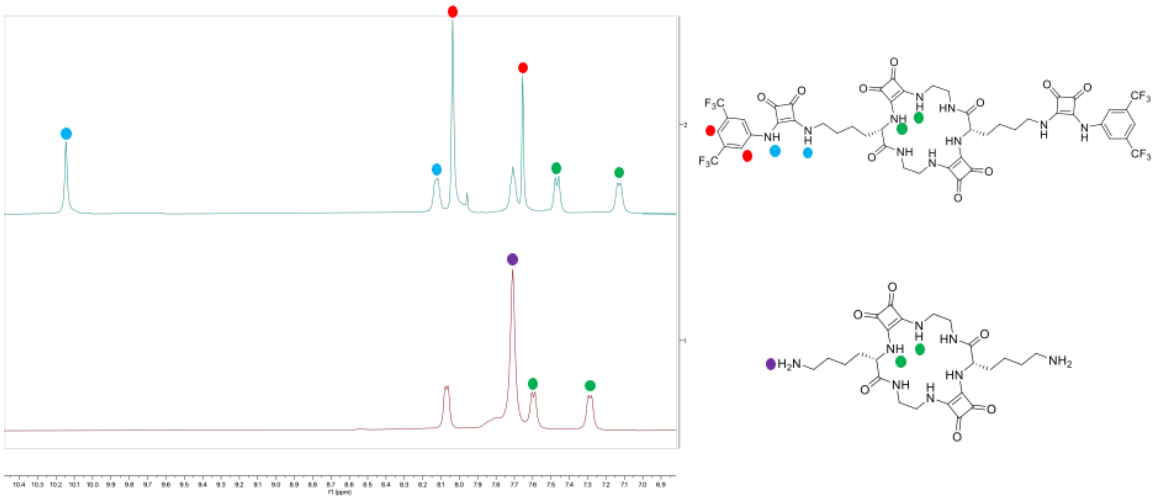

Figure 4.13: Partial ^{1}H NMR spectrum, of **2.17** and **4.18.**

As noted previously, the ^{1}H NMR spectra of squaratide derivatives are often complex and can be difficult to analyse, particularly in Chapter 2 where the self-association behaviour of **(4.19) Sq-2-Phe** gave rise to significant peak broadening. Nevertheless, comparison of the spectra for **(4.20) Sq-2-F$_5$Phe-Lys** and **(4.19) Sq-2-Phe-Lys** (Figure 4.14) allows us to

confidently assign key resonances and confirm the successful synthesis of both analogues. In **4.19** (lower spectrum), the characteristic aromatic multiplets of the phenylalanine residue are observed between δ 7.0–7.3 ppm (highlighted in yellow), consistent with the presence of a monosubstituted benzene ring. In contrast, **4.20** (upper trace) lacks these aromatic proton signals entirely, as anticipated for a pentafluorophenyl unit (no aryl protons). The disappearance of the phenylalanine multiplet set, together with retention of the lysine ε-NH_2 signal at δ ≈ 7.75 ppm (purple) and the overall macrocyclic NH envelope, provides clear spectral evidence that phenylalanine has been replaced by the perfluoroaryl analogue. Although some features are broadened—consistent with the aggregation behaviour noted for **(2.15) Sq-2-Phe** in Chapter 2, the clear distinction between the phenylalanine-derived multiplets in **4.19** and the simplified, deshielded aromatic profile of **4.20** provides conclusive spectral evidence for the expected structural differences which is further supported by HRMS/LC-MS, confirming that both targets have been obtained in their intended forms despite the challenges posed by aggregation and conformational heterogeneity in solution.

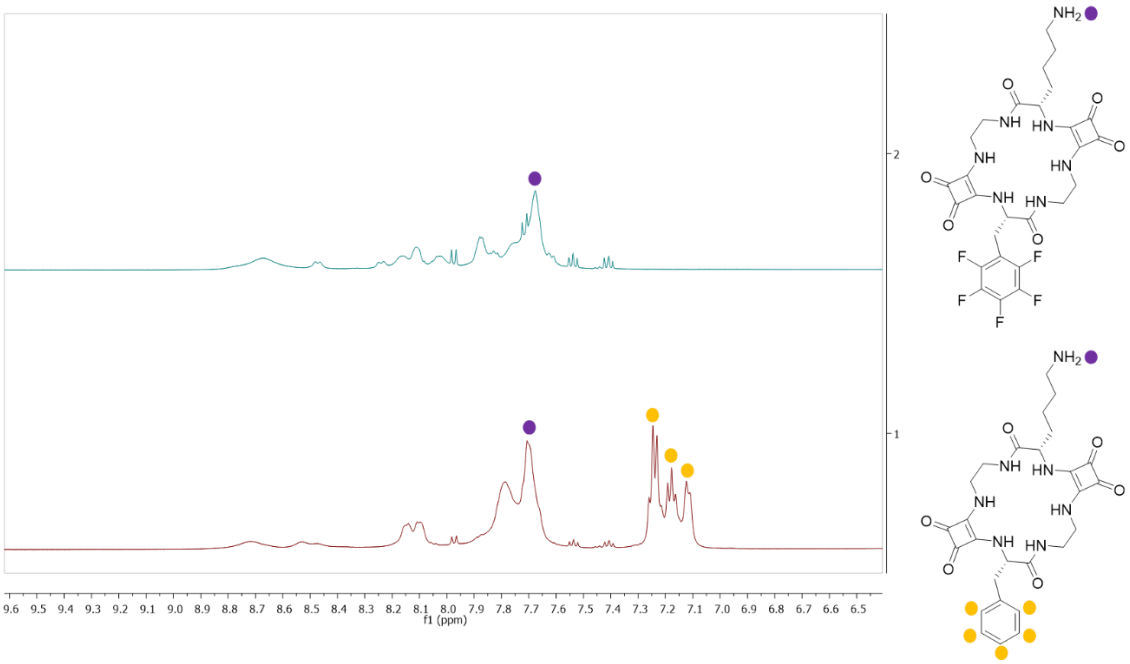

Figure 4.14: Partial ^{1}H NMR spectrum, of **4.19** and **4.20**.

In addition to the ^{1}H NMR analysis, further confirmation of the structural integrity of **(4.20) Sq-2-F_5Phe-Lys** was obtained by ^{19}F NMR spectroscopy. The ^{19}F NMR spectrum of **4.20** (Figure 4.15, top trace) exhibits three well-resolved sets of resonances, consistent with the presence of chemically distinct fluorine environments within the pentafluorophenyl unit. The most deshielded resonance appears at approximately ~ 73 ppm (green, assigned to the pair of ortho-fluorine atoms), while the central peak at ~ 77 ppm (red) corresponds to the para-fluorine, and the slightly more shielded resonance at ~ 79 ppm (blue) is attributable to the two meta-fluorine's. This pattern precisely matches the expected substitution profile of a C_6F_5 ring, in which symmetry renders the ortho and meta positions equivalent in pairs, while the para site remains unique. the ^{19}F data not only corroborate the absence of aromatic protons in the ^{1}H NMR but also provide a more resolved spectroscopic fingerprint for **4.20**.

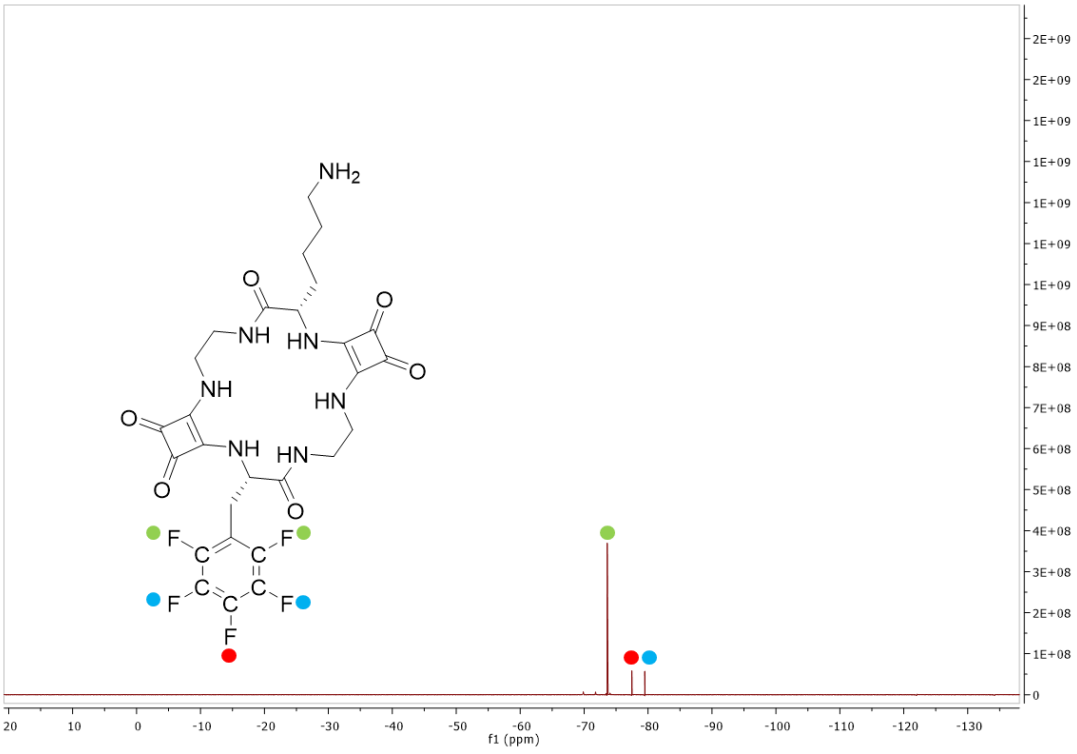

Figure 4.15: ^{19}F NMR spectrum of **4.20.**

4.4: ^{1}H NMR anion binding studies

To evaluate the chloride-binding capabilities of the compounds under investigation, a series of ^{1}H NMR titration experiments were conducted. Each receptor was dissolved in DMSO-d_6 at a fixed concentration of 2.5 mM and titrated with successive additions of tetrabutylammonium chloride (TBA Cl) ranging from 0.2 – 20 equivalents. The resulting changes in chemical shift—particularly of the hydrogen-bond donating NH resonances—were monitored after each addition. These shifts were plotted against the chloride concentration and quantitatively analysed using the BindFit software suite. Binding isotherms were fitted to the most suitable host–guest model, enabling the extraction of the corresponding association constants (K_a) for each compound with chloride.

Taking **4.18 (Sq-2-Lys(SqBisCF_3))** as an example, represents a rationally designed receptor that integrates both macrocyclic preorganization and side-chain electronic activation to achieve high-affinity and structured chloride recognition. The key feature of this molecule is the functionalization of the lysine side chain with a 3,5-bis(trifluoromethyl)phenyl squarate, effectively converting the terminal ε-amino group into a highly acidic squaramide hydrogen bond donor. This transformation not only increases the total number of hydrogen bonding sites available for anion binding but also introduces a geometrically and electronically distinct motif—one that is widely recognized in supramolecular chemistry for its ability to bind anions such as chloride through bidentate hydrogen bonding. The incorporation of two electron-withdrawing CF_3 groups onto the aromatic ring significantly enhances the acidity of the squaramide NHs, promoting stronger interactions with anionic guests.

Upon titration with chloride, the ^{1}H NMR spectrum of **4.18 (Sq-2-Lys(SqBisCF_3))** reveals pronounced downfield shifts in the squaramide NH resonances, especially those associated with the aryl squaramide unit, which shifts from ~ 10.1 to beyond 11.5 ppm (Figure 4.16(a)). These large deshielding effects are consistent with the formation of strong, directional hydrogen bonds between chloride and the aryl squaramide, confirming that this side chain motif acts as the primary binding site. Shifts in other NH environments, particularly the squaramides within the macrocyclic scaffold, are also observed, though to a lesser extent, suggesting partial or secondary involvement in the binding event. Fitting of the titration data (Figure 4.16(c)) reveals a 1:2 host: guest binding model, with a notably high first association constant (K_{11} = 4035 M^{-1}) and a much

weaker second constant (K_{12} = 65 M^{-1}). Further evidence for multi-site interaction is provided by the Job plot analysis (Figure 4.16(b)), which displays a maximum at a mole fraction of approximately 0.33, indicative of a 1:2 host–guest binding stoichiometry. This stepwise profile indicates negative cooperativity, wherein the strong initial binding event—presumably localized at the aryl squaramide—either sterically or electrostatically hinders the subsequent complexation of a second chloride anion by the macrocyclic NHs.

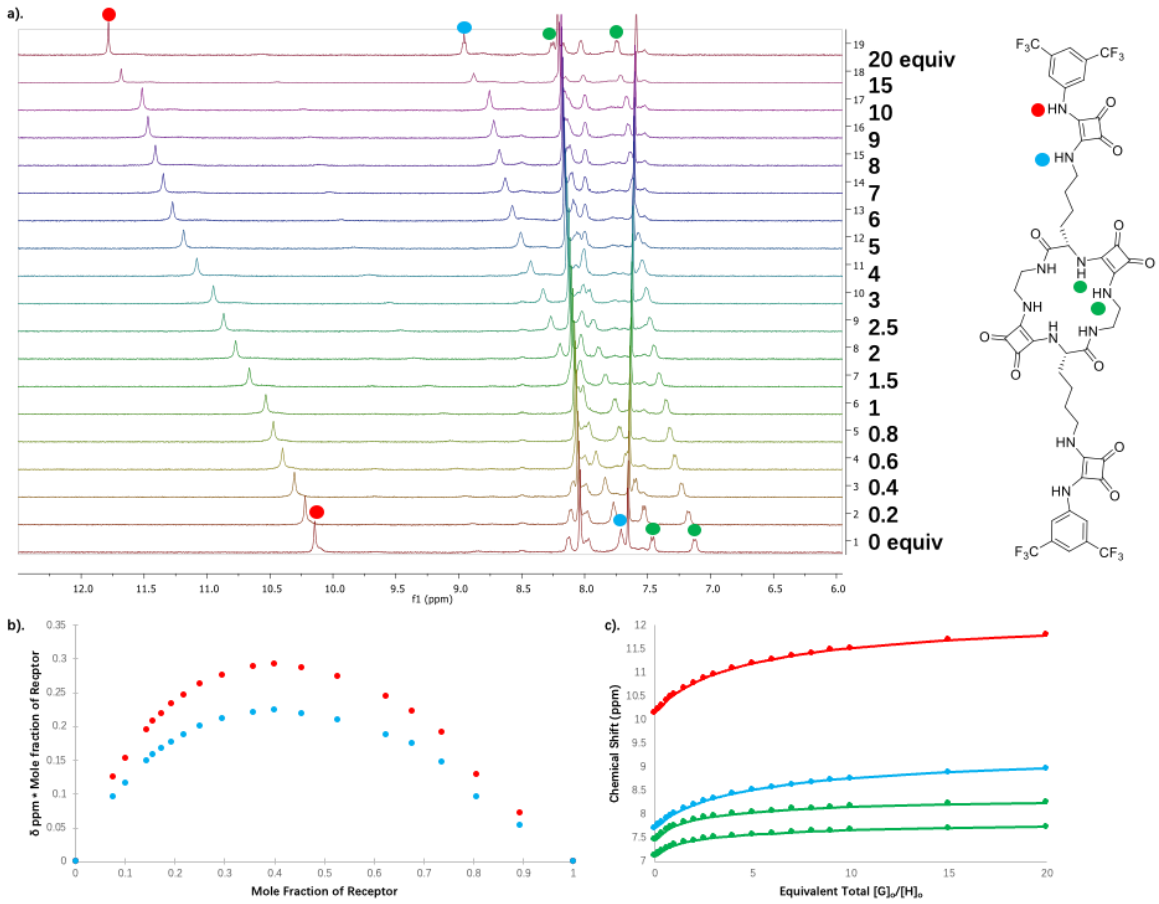

Figure 4.16: (a). ^{1}H NMR Titration of **4.18 (Sq-2-Lys(SqBisCF$_3$))** against TBACl **(b)**. Jobs plot analysis of **4.18** against TBACl **(c).** Fitted data of the chemical shift change of **4.18** against molar equivalents of TBACl.

This binding behaviour illustrates the functional asymmetry introduced by the aryl squaramide moiety: while it significantly enhances the receptor's overall anion affinity, it also imposes a hierarchy of binding sites that limits the simultaneous engagement of two anions. The receptor architecture thus favours a high-affinity first binding event, which likely drives conformational locking, making the second site less accessible or less favourable for anion coordination. Such negative cooperativity is not uncommon in systems with a strong preorganized binding site paired with a more flexible or weaker secondary site.

A direct comparison can be made with **4.17 (Sq-2-Ala-Lys(SqBisCF$_3$))**, which features the same electronically activated aryl squaramide functionality but differs in the substitution at the macrocyclic backbone, where an alanine residue replaces the lysine. This seemingly minor alteration introduces a sterically modest methyl group in place of the longer, more flexible lysine side chain, yet the consequences for chloride binding are significant. Like its lysine analogue, **4.17 (Sq-2-Ala-Lys(SqBisCF$_3$))** displays substantial downfield shifts in the ^{1}H NMR spectrum upon titration with chloride, particularly at the NH resonances associated with the aryl squaramide motif (Figure 4.17(a)). This indicates that the appended squaramide unit remains the dominant binding site, functioning as the primary locus of anion recognition. However, unlike **4.18 (Sq-2-Lys(SqBisCF$_3$))**, where the macrocycle contributes a secondary, albeit weaker, binding site to support a 1:2 host–guest interaction, the chloride binding behaviour of **4.17 (Sq-2-Ala-Lys(SqBisCF$_3$))** conforms more precisely to a 1:1 binding model (figure 4.17(c)), with an association constant of K_a = 217 M^{-1}. This stoichiometry is further supported by the Job plot shown in Figure 4.17(b), where the maximum occurs at a mole fraction of 0.5, consistent with a 1:1 complex formation.

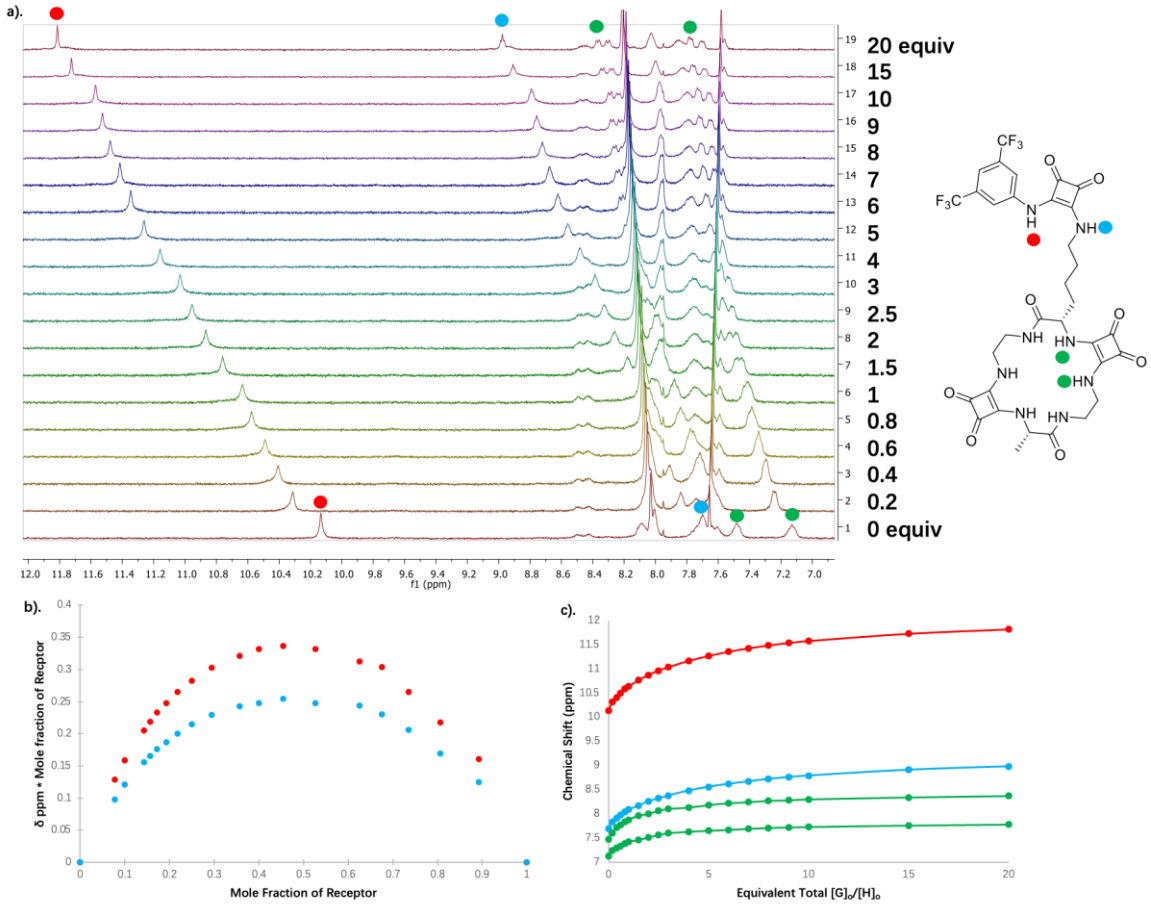

Figure 4.17: (a). ^{1}H NMR Titration of **4.17 (Sq-2-Ala-Lys(SqBisCF$_3$))** against TBACl **(b)**. Jobs plot analysis of **4.17** against TBACl **(c).** Fitted data of the chemical shift change of **4.17** against molar equivalents of TBACl.

The reduced binding affinity and simplified 1:1 stoichiometry observed for **4.17 (Sq-2-Ala-Lys(SqBisCF$_3$))** can be attributed to the absence of a second lysine residue, which in **4.18 (Sq-2-Lys(SqBisCF$_3$))** contributes additional flexibility and extra reach inside the macrocycle. This can help the macrocycle adopt conformations that bring its internal squaramide NHs into alignment to bind a second chloride after the first has been captured at the aryl squaramide site. The substitution with alanine reduces conformational flexibility of the squaratide and removes a potential secondary binding element within the backbone NH's, limiting preorganization and preventing efficient engagement of a second chloride ion. As a result, binding is dominated by the aryl squaramide, and the receptor behaves as a monotopic binder under the conditions studied.

In stark contrast, **4.16 (Sq-2-Ala-Lys)**, **4.19 (Sq-2-Lys-Phe) and 4.20 (Sq-2-Lys-F_5Phe)** displayed complex and unresolved binding behaviour upon titration with chloride. The ^{1}H NMR spectra reveal significant line broadening, overlapping NH signals, and a lack of clean saturation points, all of which indicate the occurrence of slow exchange processes on the NMR timescale as well as conformational heterogeneity. These spectral complexities prevented reliable fitting to any standard binding model, and no meaningful association constant could be determined. The origin of this behaviour can be rationalised by comparison with the symmetric squaratides studied in Chapter 2, where both side chains were identical and produced relatively well-defined binding isotherms. In those cases, the presence of structural redundancy simplified the binding event, allowing for straightforward quantification. By contrast, in the asymmetric squaratides described here, incorporation of two different amino acid side chains, breaks the line of symmetry within the macrocyclic scaffold. This asymmetry introduces non-equivalent hydrogen-bond donor environments, alters local electronic effects, and likely generates multiple, overlapping binding modes for chloride. As a result, the ^{1}H NMR titrations of these systems (Figure 4.18) do not conform to simple host–guest models, instead giving rise to broadened signals, irregular chemical shift progressions, and binding profiles that cannot be satisfactorily fitted to single stoichiometric models. Taken together, these observations underscore how subtle modifications in side-chain architecture can dramatically alter not only the strength but also the stoichiometry and cooperativity of chloride recognition. While symmetry promotes clarity and predictable behaviour, asymmetry appears to induce additional complexity, not by eliminating binding, but by dispersing it across multiple sites and conformations. This duality illustrates the delicate balance between molecular recognition and structural design in squaratide chemistry and provides a crucial rationale for extending the scope of these receptors beyond binding studies. With these insights into binding complexity, the next stage of this investigation sought to determine whether such structural modifications could be harnessed to promote functional membrane transport activity, as explored in the following section through lucigenin-based transport assays.

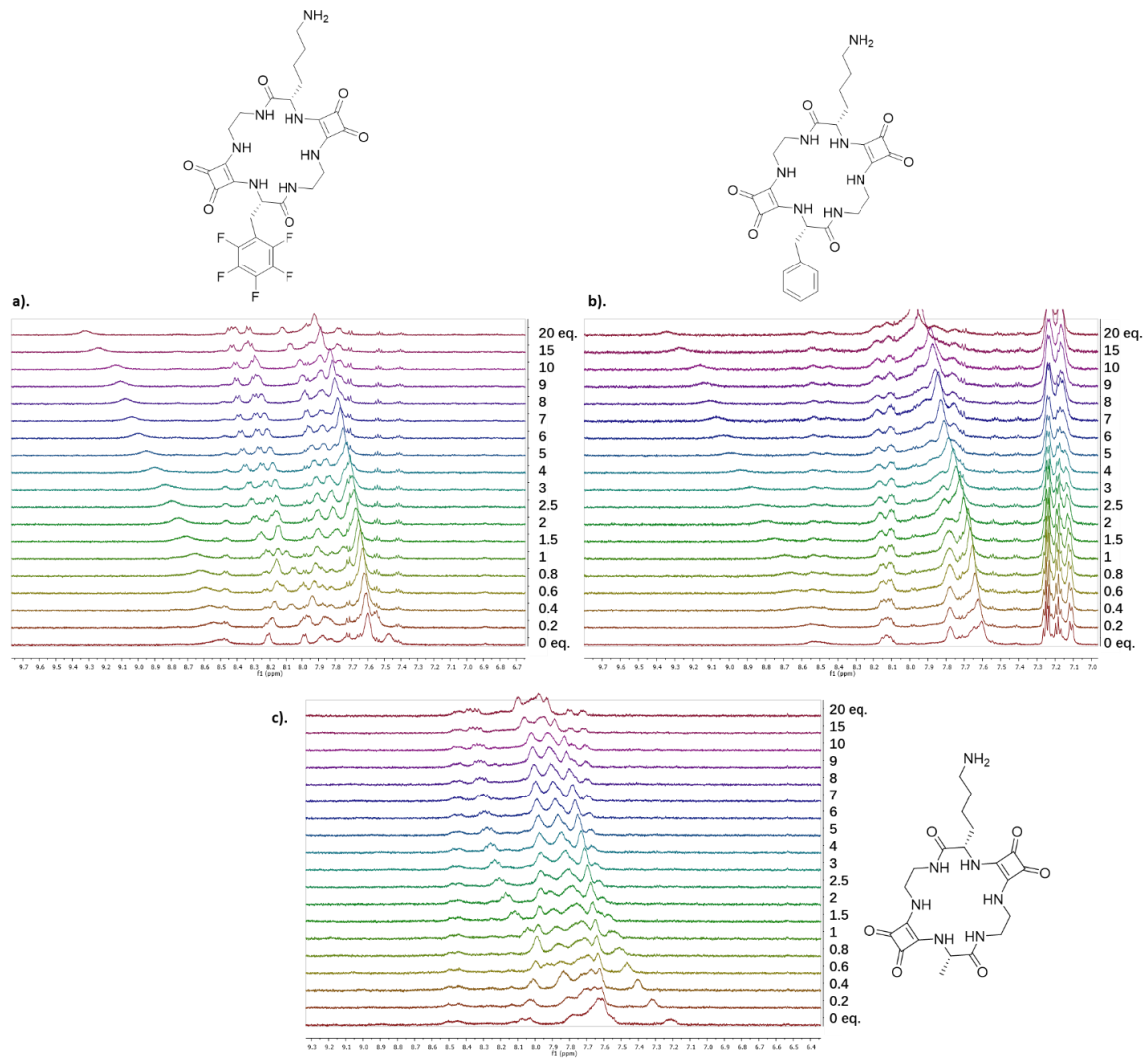

Figure 4.18: ^{1}H NMR Titration of (**a**) **4.20 (Sq-2-F$_5$Phe), (b**) **4.19 (Sq-2-Phe)** and (**c**) **4.16 (Sq-2-Ala-Lys)** against TBACl

4.5: Anion Transport Studies

As a result of the complexity of our designed squaratides affording ambiguous Cl- binding propensities, we expected that the unmodified squaratides, **4.16 (Sq-2-Ala-Lys)**, **2.17 (Sq-2-Lys)** and **4.19 (Sq-2-Lys-Phe)** may not exhibit efficient anion transport as we had initially envisaged. However, the anion recognition profiles for the series of functionalised squaratides **4.17 (Sq-2-Ala-Lys(SqBisCF_3))** and **4.18 (Sq-2-Lys(SqBisCF_3))** gave us hope. Thus, we sought to ascertain the level of anionophoric ability of all our squaratide receptors via Lucigenin assays previously reported by Prof. Vladimír Šindelář, Dr. Hennie Valkenier and co-workers (Figure 4.19).[292] Liposomes consisting of a 7:3 molar ratio of 1-palmitoyl-2-oleoyl-sn-glycero-3-phosphocholine (POPC) and cholesterol were prepared in a 225 mM $NaNO_3$ solution, ensuring that both the interior and exterior environments initially contain only nitrate as the counterion. Prior to initiating the transport experiment, a solution of the squaratide (anionophore) was added to the liposome suspension, allowing post-insertion of the transporter into the lipid bilayer. A chloride pulse of 25 mM NaCl is then introduced to the external medium (75 µL of 1 M NaCl in 225 mM $NaNO_3$) at 30 seconds, thereby establishing a chloride gradient across the membrane. The subsequent dissipation of this gradient, facilitated by the anionophore, was monitored by recording the time-dependent decrease in lucigenin fluorescence, which occurs via collisional quenching of the dye by chloride ions. The rate and extent of fluorescence quenching over time served as indicators of chloride influx, from which concentration–response relationships and EC_{50} values were determined.

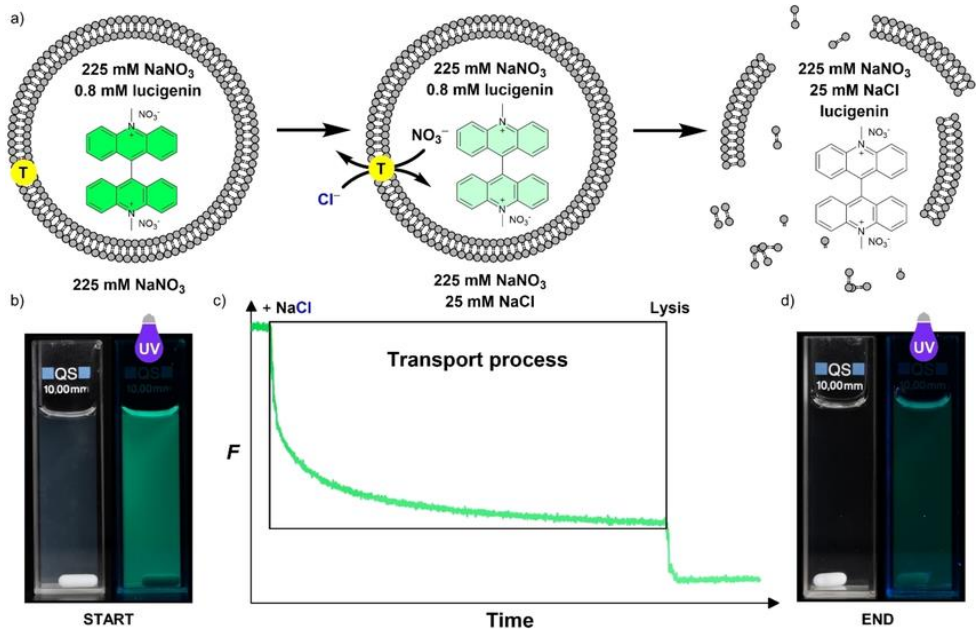

Figure 4.19: a) Schematic illustration of the standard lucigenin assay used to investigate Cl^-/NO_3^- antiport mediated by a transporter (T). The accompanying images show: b) the liposome suspension at the beginning of the transport experiment, and c) the sample following NaCl addition and subsequent lysis (left: visible light image; right: under 365 nm UV illumination). Reported by Šindelář, Valkenier and colleagues.[292]

Under the conditions studied, **4.18 (Sq-2-Lys(SqBisCF$_3$))** displayed the highest chloride transport efficiency amongst all squaratides analysed (Figure 4.20). In the lucigenin Cl^-/NO_3^- antiport assay, the addition of NaCl resulted in a rapid and pronounced decrease in fluorescence intensity, consistent with efficient chloride influx and nitrate efflux through the bilayer, followed by a slower decay to equilibrium.

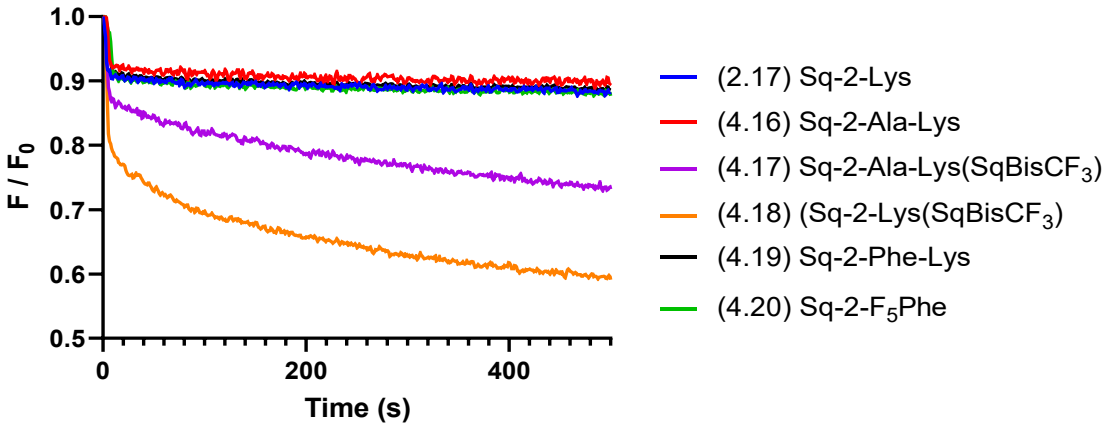

Figure 4.20: Normalised lucigenin fluorescence (F/F_0) as a function of time for liposomes subjected to external NaCl addition in the presence of receptors **2.17**, and **4.16 - 4.20** at 30μM.

The corresponding dose–response curve (Figure 4.21) fitted to a four-parameter logistic model, yielded an EC_{50} value of 4 mol%, indicative of transport ability. This activity is consistent with its strong and well-defined chloride-binding profile in solution, as revealed by ^{1}H NMR titration experiments, by which the functionalised aryl squaramide motif on the lysine side chain acted as the dominant high-affinity binding site, further supplemented by a secondary, weaker binding event involving the squaramide NH donors on the macrocyclic backbone. The flexible lysine side chain likely plays a dual role, assisting in the initial capture of chloride at the membrane interface and facilitating its release on the opposite side, hereby optimising the receptor for a carrier-mediated transport mechanism. The combination of strong binding, negative cooperativity preventing over-saturation, and a conformationally adaptable macrocyclic scaffold appears to underpin the rapid chloride pick-up and release observed, ultimately translating into the transport efficiency measured in the lucigenin assay.

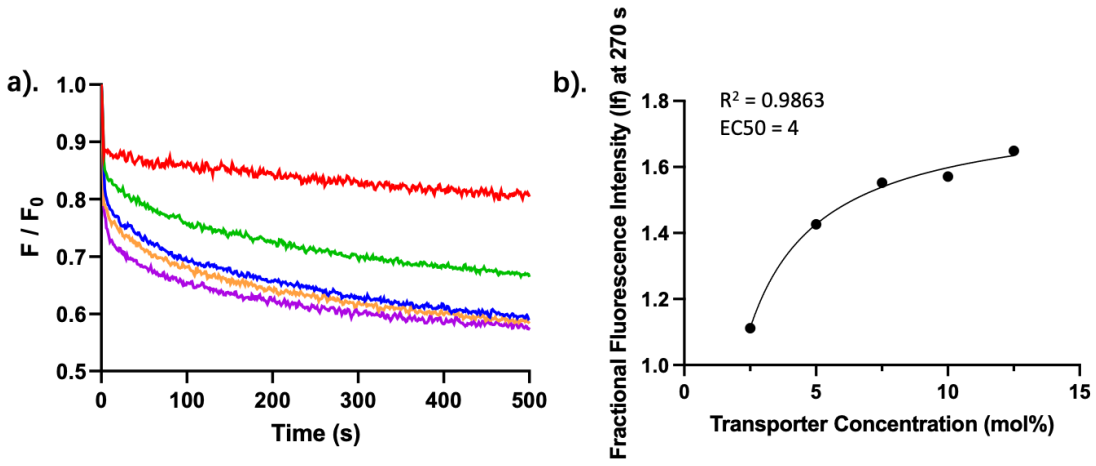

Figure 4.21: (a). Normalised lucigenin fluorescence (F/F_0) as a function of time for liposomes (225 mM $NaNO_3$, 0.8 mM lucigenin) subjected to external NaCl addition in the presence of **(4.18) Sq-2-Lys(SqBisCF$_3$)** at varying concentrations. **(b).** Dose–response plot of fractional fluorescence intensity at 270 s versus transporter concentration.

In contrast, **4.17 (Sq-2-Ala-Lys(SqBisCF$_3$))** although displaying clear chloride transport activity, demonstrated significantly weaker transport activity under identical conditions. While fluorescence quenching was still observed upon NaCl addition (Figure 4.22(a)), the rate and extent of transport were markedly reduced, with the corresponding dose–response curve (Figure 4.22(b)) yielded an EC_{50} value of 8.10 mol%, double the value than for **4.19 (Sq-2-Lys(SqBisCF$_3$))**. These results align with its simpler 1:1 binding stoichiometry in solution, which suggests that only the aryl squaramide site on the lysine side chain is significantly involved in chloride coordination. The substitution of lysine for alanine in the macrocyclic backbone likely removes a flexible, auxiliary binding element, diminishing the receptor's ability to adapt conformationally during the translocation process. Consequently, although capable of binding chloride strongly at one site, this receptor appears less adept at the dynamic binding and release cycles necessary for high transport efficiency.

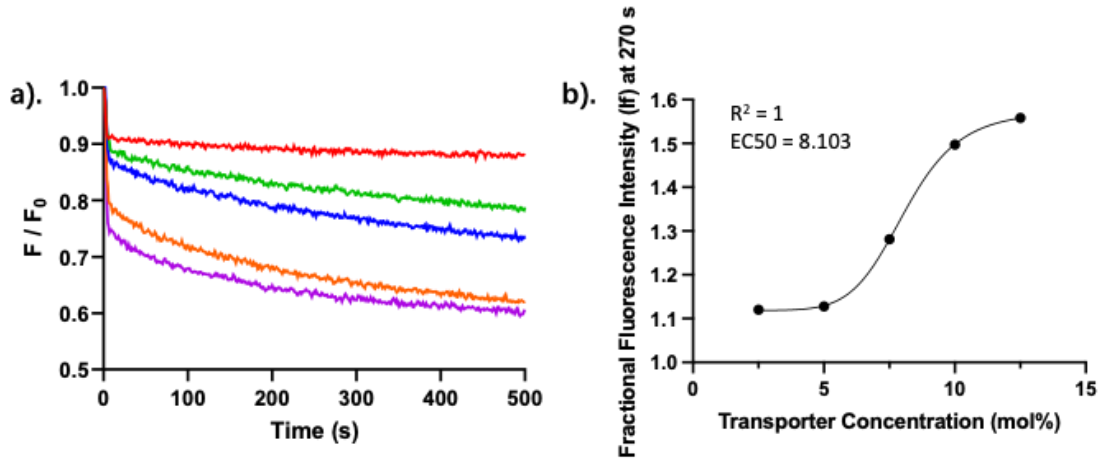

Figure 4.22: (a). Normalised lucigenin fluorescence (F/F_0) as a function of time for liposomes (225 mM $NaNO_3$, 0.8 mM lucigenin) subjected to external NaCl addition in the presence of **(4.17) Sq-2-Ala-Lys(SqBisCF_3)** at varying concentrations. **(b).** Dose–response plot of fractional fluorescence intensity at 270 s versus transporter concentration.

The parent macrocycles **4.16 (Sq-2-Ala-Lys), 4.19 (Sq-2-Phe-Lys)** and **2.17 (Sq-2-Lys)** exhibited no detectable chloride transport activity in the lucigenin assay, indicating that high-affinity binding alone is insufficient to drive membrane translocation in this system (Figure 4.23). A key structural distinction from their active analogues is the absence of the 3,5-bis(trifluoromethyl)phenyl squarate moiety. This substituent not only introduces an electronically powerful aryl squaramide binding site but also significantly increases the overall lipophilicity of the receptor through the presence of multiple CF_3 groups. Enhanced lipophilicity is known to facilitate membrane partitioning, a prerequisite for efficient carrier-mediated transport.[278, 293, 294] The lack of these CF_3-containing aromatic groups in the parent compounds likely reduces their membrane affinity, preventing them from attaining the bilayer residence time or orientation necessary to complete the chloride exchange cycle, and thereby accounting for their complete lack of transport activity under the experimental conditions employed.

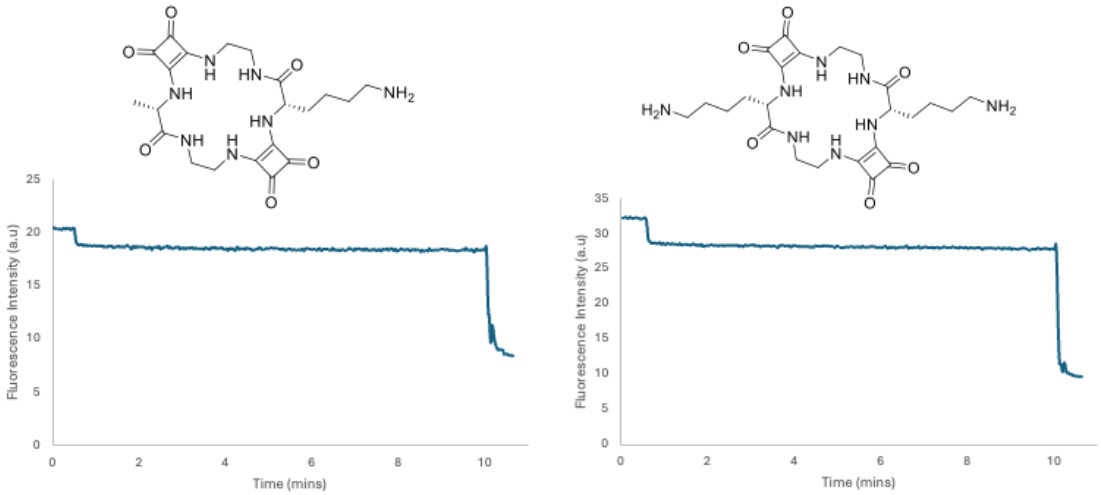

Fgiure 4.23: Raw data obtained from transport measurements of compounds **4.16** and **2.17**

Interestingly, the para-fluorophenyl analogue **4.20 (Sq-2-Lys-F$_5$Phe)** also exhibited no transport activity. We initially hypothesised that the fluorinated phenyl group could increase overall lipophilicity, potentially bolstering bilayer partitioning and supporting transport activity. However, we believe that the pentafluorophenyl substituent is less electron-withdrawing than the bis-CF_3 analogue, leading to reduced NH acidity and consequently weaker anion binding. Moreover, the smaller hydrophobic contribution compared to two CF_3 groups likely results in only modest lipophilicity gains, insufficient to offset the loss in binding strength. The combined effects of weaker binding and limited enhancement in bilayer affinity provide a compelling explanation for the complete absence of transport activity, underscoring that both strong anion recognition and membrane partitioning must act in concert to achieve functional transport in this system.

4.6 Conclusion

This Chapter set out to explore the potential of our squaratides as functional anion transporters, building upon their demonstrated anion binding capabilities in Chapter 2. The parent macrocycles **4.16 (Sq-2-Ala-Lys)** and **2.17 (Sq-2-Lys)** were selected as versatile scaffolds for targeted functionalisation by utilising the free amine group on the lysine side chain, with the aim of enhancing both their binding affinity and membrane compatibility. A key design strategy was the incorporation of a 3,5-bis(trifluoromethyl)phenyl squarate unit onto the lysine side chain, generating **4.17 (Sq-2-Ala-Lys(SqBisCF$_3$))** and **4.18 (Sq-2-Lys(SqBisCF$_3$))**. This modification was envisaged to achieve a dual effect: the introduction of a highly electron-deficient aryl squaramide to provide a strongly acidic, bidentate hydrogen-bond donor site for anion recognition, and the inclusion of multiple CF_3 groups to substantially increase the overall lipophilicity of the receptor, thereby improving bilayer partitioning. In parallel, we sought to probe an alternative structural tuning approach by incorporating a fluorinated amino acid into the macrocyclic backbone, producing **4.20 (Sq-2-Lys-F$_5$Phe)**, with the hypothesis that the para-fluorophenyl substituent might similarly enhance lipophilicity and membrane association.

^{1}H NMR titration studies in DMSO-d$_6$ confirmed that functionalisation with the 3,5-bis(trifluoromethyl)phenyl squarate motif profoundly increased chloride-binding affinity relative to the parent compounds. In **4.18 (Sq-2-Lys(SqBisCF$_3$))**, the aryl squaramide side chain acted as a dominant high-affinity binding site (K_{11} = 4035 M^{-1}), supported by secondary interactions from the squaramide NH donors within the macrocyclic backbone, and displayed a stepwise 1:2 binding profile indicative of negative cooperativity. In **4.17 (Sq-2-Ala-Lys(SqBisCF$_3$))**, the same motif retained strong chloride recognition but operated predominantly via a 1:1 stoichiometry, a consequence of the functionalised aryl squaramide lysine with a shortened alanine side chain resulting in reduced macrocyclic flexibility.

Lucigenin Cl^-/NO_3^- antiport assays translated these binding observations into functional membrane transport data. **4.18 (Sq-2-Lys(SqBisCF$_3$))** emerged as an effective transporter, with an EC_{50} value of 4 mol% and largely non-cooperative transport kinetics. Its activity can be attributed to the synergy between strong, electronically activated binding at the aryl squaramide site and the conformational adaptability of the lysine-

based macrocycle. **4.17 (Sq-2-Ala-Lys(SqBisCF$_3$))** also facilitated chloride transport but with reduced efficiency, exhibiting an EC_{50} of 8.10 mol% and pronounced cooperative behaviour, consistent with a threshold requirement for activity at higher loadings. Although these squaratides are not the strongest transporters reported in the literature, their performance demonstrates that targeted functionalisation with the 3,5-bis(trifluoromethyl)phenyl squarate motif can successfully expand the utility of this receptor platform. What were originally designed as anion-binding hosts, described in Chapter 2, have thus been re-engineered into functional anion transporters, establishing a foundation for future optimisation of squaratide scaffolds in membrane transport applications. The parent macrocycles **4.16 (Sq-2-Ala-Lys), 2.17 (Sq-2-Lys)**, as **4.19 (Sq-2-Lys-Phe)** and **4.20 (Sq-2-Lys-F$_5$Phe)** were completely inactive under identical conditions. For the former, the lack of the bis-CF_3 aryl squaramide eliminated both the enhanced binding site and the lipophilicity boost necessary for bilayer engagement. For **4.20 (Sq-2-Lys-F$_5$Phe)**, the absence of strong electronic activation from the pentafluoro phenyl ring, combined with only modest lipophilicity, failed to deliver the anticipated transport capability, underscoring that fluorination alone is insufficient without concomitant binding-site strengthening.

Collectively, these findings establish that in this class of squaratide receptors, successful anion transport requires the deliberate co-optimisation of binding-site electronics, macrocyclic architecture, and lipophilicity. The 3,5-bis(trifluoromethyl)phenyl squarate unit proved uniquely effective in meeting these criteria, producing receptors that are not only strong and selective chloride binders in solution but also capable of operating as efficient anion carriers in lipid bilayers. This work therefore represents a significant step in the rational design of squaratide-based anion transporters and highlights the broader principle that supramolecular function at the membrane interface emerges from a finely tuned interplay between molecular recognition and membrane compatibility.

Chapter 5

Fluorescent Squaratide for Selective Fluoride Recognition and Anion Exchange

5: Fluorescent Squaratide for Selective Fluoride Recognition and Anion Exchange

5.1: Introduction

Fluoride anions (F^-) are chemically distinctive species that play critical roles in diverse biological, environmental, and industrial settings.[295, 296] In biological systems, fluoride at trace levels is essential for bone and dental health and is widely incorporated into municipal water supplies to prevent tooth decay.[297] However, prolonged exposure to elevated concentrations of fluoride can result in dental and skeletal fluorosis, posing significant public health concerns.[298, 299] Industrially, fluoride is used in aluminium production, uranium processing, and the manufacturing of fluorinated pharmaceuticals and agrochemicals.[300, 301] Consequently, the selective and sensitive detection of fluoride in complex environments remains an important analytical challenge.[302] From a chemical standpoint, fluoride is the most electronegative element and possesses a uniquely high hydration energy, rendering it highly solvated and challenging to extract or bind selectively in aqueous and competitive solvent systems.[303, 304] Its small ionic radius, high charge density, and strong basicity distinguish it from other halide anions and make it a particularly demanding target for selective molecular recognition.[165, 305]

Among the diverse molecular architectures developed for molecular recognition, fluorescent macrocyclic receptors have emerged as particularly powerful tools due to their unique combination of structural preorganization and optical responsiveness.[306] The cyclic nature of macrocycles confers a well-defined cavity with inherent conformational rigidity, enabling the selective accommodation and stabilization of specific anions through geometrically and chemically complementary interactions.[69, 307, 308] The size, shape, and electronic characteristics of the macrocyclic binding pocket play a critical role in determining the strength and selectivity of anion recognition.[98, 309] This high degree of molecular specificity, reminiscent of natural receptors, makes macrocycles indispensable platforms in both biological and synthetic systems.[85, 310]

What further elevates their utility is the integration of fluorogenic or chromogenic units, which transform these receptors into dual-function systems capable of not only binding but also transducing molecular interactions into measurable optical signals.[311, 312] Fluorescence spectroscopy, in particular, offers a highly sensitive, and real-time method

for monitoring anion binding.[313] By embedding fluorophores such as naphthalimides, coumarins, or other π-conjugated systems into macrocyclic frameworks, these receptors can exhibit distinct spectral changes—such as intensity modulation or wavelength shifts—in response to guest binding.[314-316] As a result, many research groups have explored various macrocyclic architectures and have utilised their anion binding capabilities and tuneable functionality by modifying the macrocyclic structure with a suitable fluorophore for anion detection and binding.[88, 302, 317-319]

Kim and Cho recently synthesized receptor **5.1**, a calix[4]triazole framework, where pyrene is chemically linked to the calix[4]triazole via an ester linker (Figure 5.1).[320] This receptor demonstrated selective fluoride binding resulting in fluorescence quenching via photoinduced electron transfer (PET) whereby the presence of fluoride enhances the electron density on the calix[4]triazole, facilitating the transfer of electrons to the excited state of pyrene, thereby reducing its fluorescence. Fluorescence titration experiments revealed a 1:1 binding stoichiometry between **5.1** and fluoride ions, with an association constant calculated to be 74.30 ± 12 M^{-1}. This quantitative analysis supports the formation of a stable complex between the receptor and the anion. When tested against various competing anions (such as Cl^-, Br^-, I^-, $H_2PO_4^-$, NO_3^-, HSO_4^-, and $CH_3CO_2^-$), **5.1** demonstrated remarkable selectivity for fluoride ions; the presence of these anions did not significantly affect the fluorescence response. ^{1}H NMR titration revealed changes in the triazole proton signals, confirming the formation of hydrogen bonds with fluoride ions at low concentrations. At higher fluoride concentrations, deprotonation of the triazole occurred, indicating the dynamic nature of the binding interaction.

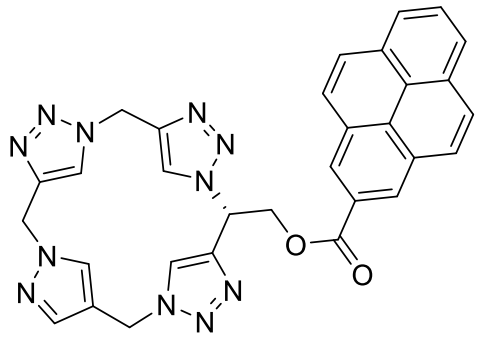

5.1

Figure 5.1: Chemical structure of calix[4]triazole based receptor **5.1**, reported by Cho and colleagues.

Hosseinzadeh and collaborators reported the design and synthesis of a highly selective colorimetric and fluorescent chemosensor, designated as compound **5.2**, for the detection of fluoride ions (Figure 5.2(b)).[321] This sensor was constructed by appending fluorene moieties to the lower rim of a calix[4]arene scaffold. Spectroscopic investigations—specifically UV–vis absorption and fluorescence emission studies conducted in acetonitrile—demonstrated that **5.2** exhibits exceptional affinity and selectivity for fluoride over other anions examined. The association constant (K_a) for the fluoride–**5.2** complex, as derived from fluorescence titration data, was determined to be 1.18×10^6 M^{-1}. Moreover, the sensor exhibited a remarkably low detection limit of 3.20×10^{-8} M, calculated using the 3σ/S method. The high sensitivity is primarily attributed to favourable host–guest interactions, mediated by strong hydrogen bonding between fluoride ions and the sensor's amido and phenolic hydroxyl groups, which act as hydrogen bond donors. Notably, the introduction of fluoride to the system induced distinct and observable fluorescence and colorimetric changes (Figure 5.2(c)), attributed to a photoinduced electron transfer (PET) mechanism. This phenomenon likely arises from deprotonation of the amide NH and phenolic OH functionalities, facilitating electron transfer from the bound anion to the fluorenone moiety.

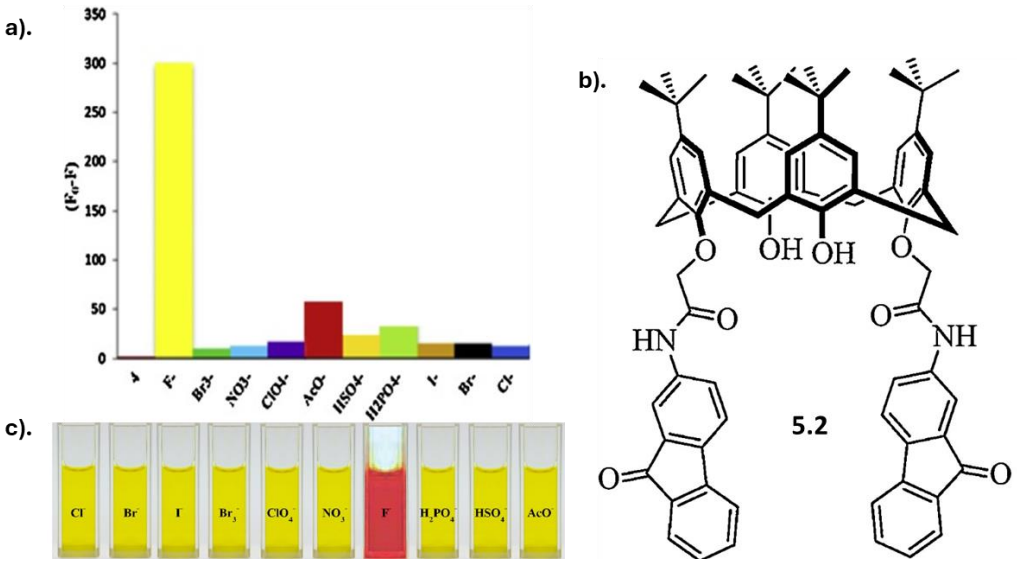

Figure 5.2: a). Fluorescent intensity changes of **5.2** upon the addition of various anions. **b).** Chemical structure of **5.2**. Reported Hosseinzadeh and co-workers. **c).** Visual changes of **5.2** upon the addition of various anions.

Kataev and colleagues designed macrocyclic receptors (**5.3, 5.4** and **5.5**) consisting of a tren subunit and hydrogen bond donor amide groups for recognition and a naphthalimide fluorophore as a reporting unit sensitive to F^- binding in aqueous solutions (Figure 5.3). [322] Receptor **5.3** shows the strongest binding of F^- with 100-fold selectivity over other anions in aqueous solution with a remarkable binding constant of 10^5 M^{-1} as evidenced by ^1H NMR titrations, highlighting its strong interaction with F^-. Unlike **5.4** and **5.5**, receptor **5.3** exhibited a unique turn-on fluorescence response upon binding with F^-, making it a promising visual probe for F^- detection. One key feature of receptor **5.3** is its ability to accommodate multiple F^- ions, forming stable complexes with 1:1, 1:2, and 1:3 stoichiometries as inferred from the fitting analysis of the fluorescence titration of **5.3** with F^-. This multiple anion coordination led to the protonation of the tertiary amine group within the receptor, hindering the photoinduced electron transfer process and resulting in a fluorescence enhancement. The size selectivity of receptor **5.3** allows it to selectively bind F^- ions while preventing aggregation, further enhancing its fluorescence response specifically for F^- detection. Moreover, the positively charged ammonium groups in receptor **5.3** play a crucial role in compensating the negative charge of fluoride ions, enhancing the electrostatic interactions and binding affinity.

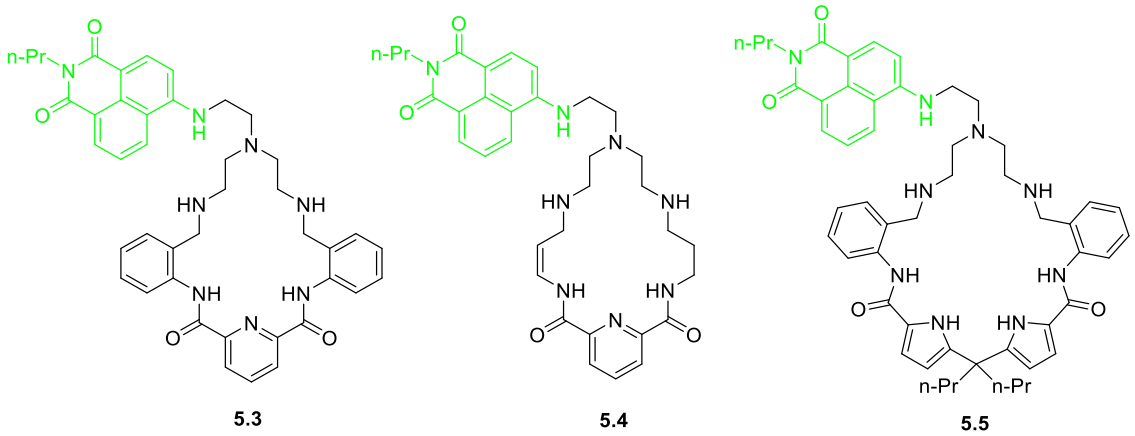

Figure 5.3: Chemical structures of macrocycles **5.3**- **5.5**. Reported by EA. Kataev et al.

The examples mentioned above highlight the value of integrating macrocyclic scaffolds such as calix[4]triazole, calix[4]arene, and intrinsic preorganization via urea-based macrocycles with responsive fluorescence signalling in the ongoing pursuit of selective anion recognition systems. The continued development of these systems not only

enhances our understanding of anion–receptor interactions but also shows the significant potential for real-time sensing applications, expanding the capabilities of supramolecular chemistry in addressing critical challenges in anion detection and monitoring. However, designing receptors that exhibit both selectivity and reversibility remains a challenge.

5.2: Chapter Objective

So far, we have shown the versatility of squaratides for anion recognition (Chapter 2), antimicrobials (Chapter 3), and anion transporters (Chapter 4). The aim of this chapter is to further develop and explore the possible applications that squaratides can possess. By utilizing our new synthetic approach of squaratides via SPPS, we aim to synthesise a naphthalimide based amino acid and integrate it into the squaramide backbone, to exemplify the first fluorescent squaratide; (**5.12**) **Sq-2-Lys-Naph,** as an anion sensor (Figure 5.4). We envisaged that the naphthalimide based amino acid would act as both a structure and a signalling unit of the receptor that provides site-specific functionality while preserving the receptor's overall conformational integrity and binding preorganization.

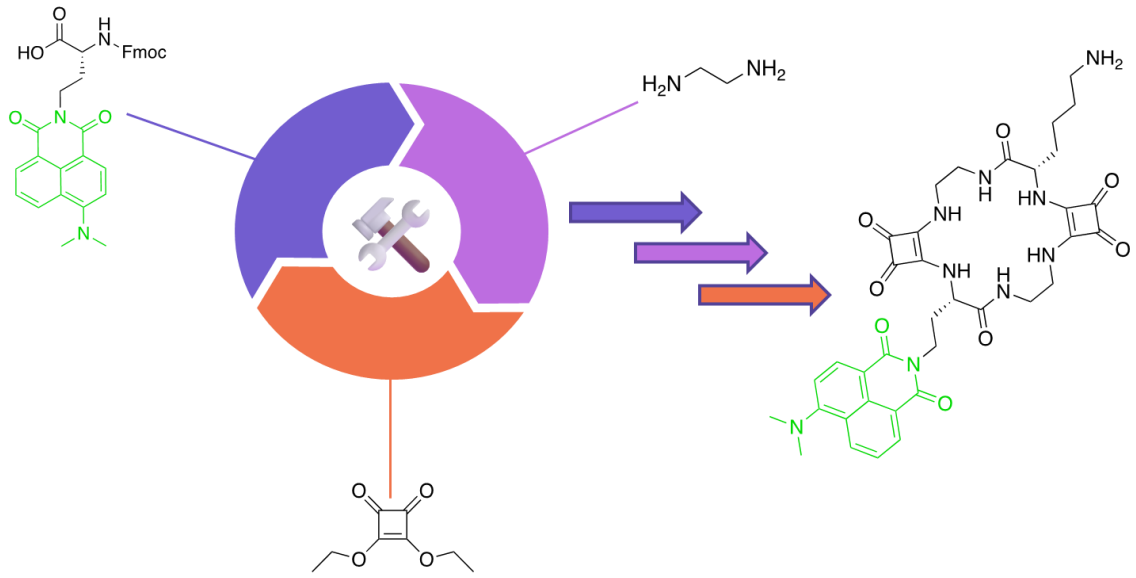

Figure 5.4: Schematic overview of the modular design strategy for (**5.12**) **Sq-2-Lys-Naph**.

With our fluorescent squaratide design in hand, this chapter aims to exemplify the use of squaratides as molecular sensors, taking advantage of their modular design , enabling the receptor to function as a dual-purpose system: facilitating selective anion binding through directional hydrogen bonding, while simultaneously providing real-time optical output via fluorescence modulation. As of yet, there are no reports of fluorescent peptidomimetics for molecular sensing that are used to selectively bind and discriminate against anions. We envisage that this design principle which offers a promising alternative due to their modularity, synthetic accessibility, and ability to display

hydrogen-bond donors in defined spatial arrangements, can be expanded to engineer new fluorescent peptidomimetics with tailored selectivity and tuneable optical responses.

The chapter sets the stage for the synthesis and comprehensive analytical evaluation of a structurally novel and functionally responsive macrocyclic peptidomimetic receptor with relevance to the fields of molecular sensing, supramolecular chemistry, and anion recognition. Herein we report the design and study of **5.12 (Sq-2-Lys-Naph)**, encompassing the receptor's synthesis, detailed photophysical characterization, and systematic binding evaluation using a suite of spectroscopic techniques, including fluorescence emission, UV-Vis absorption, and ^{1}H NMR spectroscopy, to elucidate its anion recognition properties—particularly toward fluoride.

5.3: Synthesis and Characterisation

5.3.1: Design rationale

The goal of this chapter was to integrate an optical reporter into the squaratide receptor framework so that anion binding would be translated into a measurable change in emission. We selected a 4-dimethylamino-1,8-naphthalimide chromophore because (i) it offers bright emission in the green region, (ii) its charge-transfer character is exquisitely sensitive to local polarity/acid–base events, and (iii) it tolerates peptide-style protecting groups, allowing installation as an amino-acid-like building block (Naph-aa). Embedding the fluorophore as an amide-linked side chain next to the squaramide array was intended to preserve recognition while maximizing electronic communication between the binding site and reporter.

5.3.2: Synthesis of a Napthalimide based amino acid (5.11)

A key component in the design of **Sq-2-Lys-Naph** is the incorporation of a naphthalimide-based fluorescent amino acid, **5.11**, in its Fmoc-protected form, making it suitable for incorporation into the squaratide sequence using the solid phase peptide synthesis (SPPS) Fmoc-strategy. When strategically tethered to an amino acid side chain, the resulting fluorescent amino acid preserves both the α-amino acid functionality necessary for our squaratide synthesis and the fluorogenic capacity required for real-time signal transduction.

The synthesis of **5.11** was carried out using a procedure adapted from Strömberg and colleagues[323] as outlined in Scheme 5.1. Initially, A mixture of 4-bromo-1,8-naphthalic anhydride (**5.6**), dimethylamine hydrochloride, and $CuSO_4 \cdot 5H_2O$ in DMF was treated with triethylamine and heated under microwave irradiation at 130 °C for 40 minutes. The reaction was quenched with water, and the resulting solid was collected by filtration. The crude product was purified by dissolution in chloroform, filtration, and precipitation with hexane, followed by short silica gel filtration to afford intermediate **5.7**. The corresponding 4-dimethylamino-1,8-naphthalic anhydride (**5.7**) and Boc-D-Dab-OH (**5.8**) were reacted under a nitrogen atmosphere in refluxing dioxane with aqueous $NaHCO_3$ as a base. After 1 hour, the reaction was concentrated, diluted with water, washed with diethyl ether, and acidified to pH 3, yielding a yellow precipitate. The aqueous layer was extracted with DCM, and the combined organics were dried over Na_2SO_4 and concentrated. The crude product was purified by column chromatography (40–50% EtOAc in hexane with 0.1% AcOH) to afford intermediate **5.9**, which was then treated with a 1:1 mixture of DCM and TFA and stirred for 2 hours. The reaction was concentrated under reduced pressure, and the resulting residue was redissolved in methanol and precipitated by dropwise addition into diethyl ether. The mixture was filtered to yield **5.10** which was subsequently dissolved in aqueous $NaHCO_3$, and dioxane was added followed by Fmoc-OSu. The reaction was stirred at 0 °C for 2 hours. The mixture was diluted with water, washed with diethyl ether, and acidified to pH 6 with 6 N HCl. The product was extracted with DCM and purified by column chromatography (0.5–1% MeOH in DCM with 0.1% AcOH) to afford our desired final compound **5.11**, in a 69% yield. All characterisation data aligned with the reported literature[323], with LC-MS analysis displaying one sharp UV peak with a t_R = 41 min, and strong ionisation was observed for the target mass of $[M+H]^+$ = 564.7 $gmol^{-1}$ in positive mode (Figure 5.4).

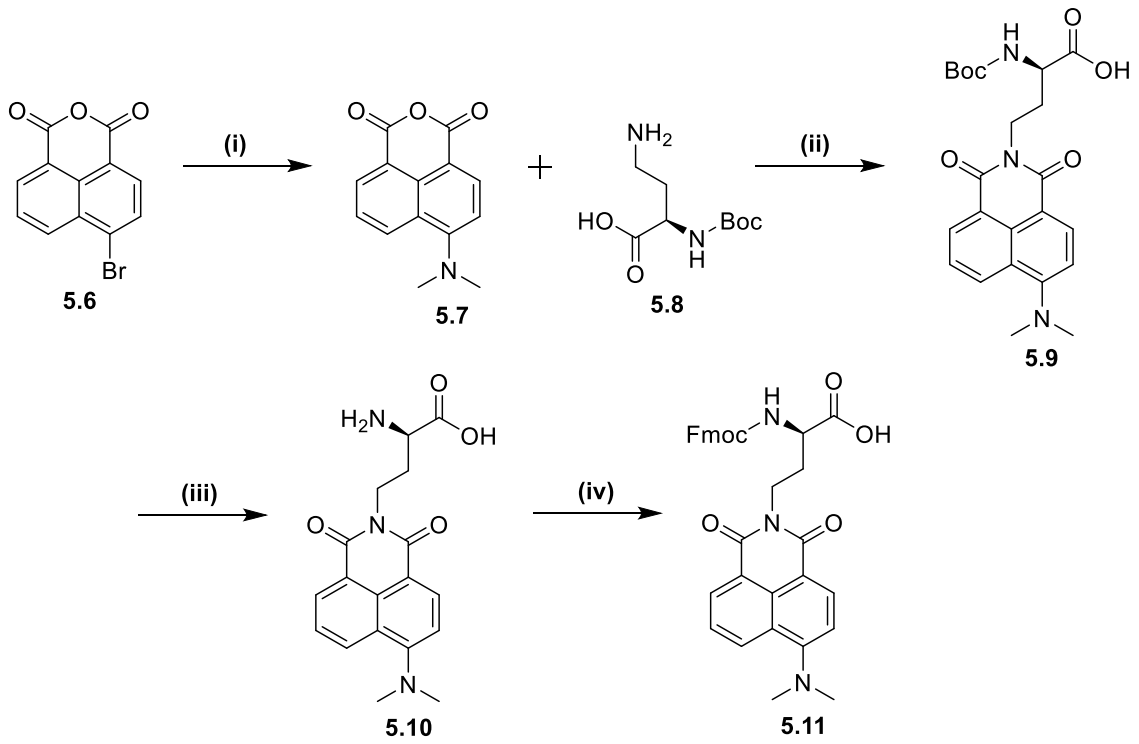

Scheme 5.1: The synthesis of naphthalimide based amino acid **5.11**. *Reagents and conditions:* i) $CH_3NHCH_3 \cdot HCl$, $CuSO_4 \cdot 5H_2O$, Triethylamine, DMF, m.w: 130 °C, 1 h, 85%; ii) **5.8**, aq NaHCO3, dioxane, reflux, 1 h, 65%; iii) Trifluoroacetic acid, DCM, 0 C, 2 h; (iv) Fmoc-OSu, water–dioxane (1:1), $NaHCO_3$, 0 C, 2 h, 68% (over two steps).

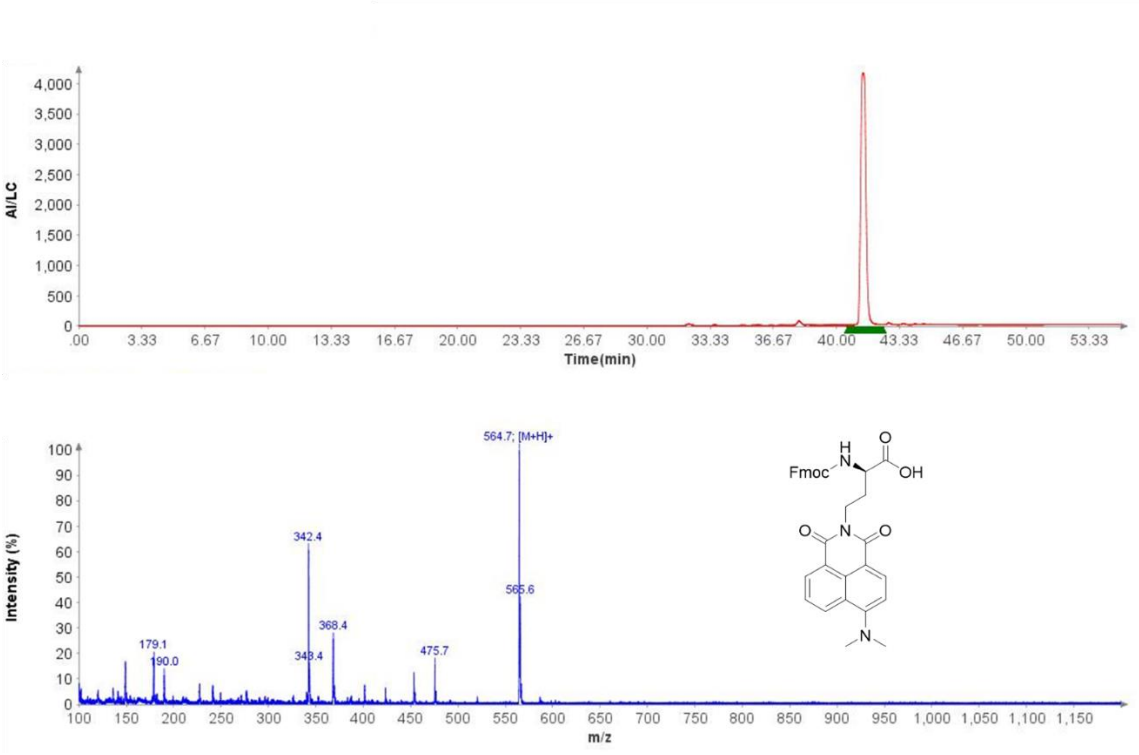

Figure 5.4: LC-MS data for Naphthalimide amino acid **5.11**.

5.3.3: Synthesis of (5.12) Sq-2-Lys-Naph

With the successful synthesis of the desired naphthalimide-functionalized amino acid in hand, we proceeded to construct the target receptor **5.12 (Sq-2-Lys-Naph)** as outlined in scheme 5.2. Through stepwise solid-phase synthesis, followed by macrocyclization as outlined below, the receptor was assembled and purified. The resulting structure integrates hydrogen bond donor sites with a conjugated emissive core, thus positioning **5.12 (Sq-2-Lys-Naph)** as a novel platform for anion sensing via fluorescence modulation. This synthetic milestone laid the foundation for further spectroscopic and binding studies to elucidate the receptor's anion recognition properties.

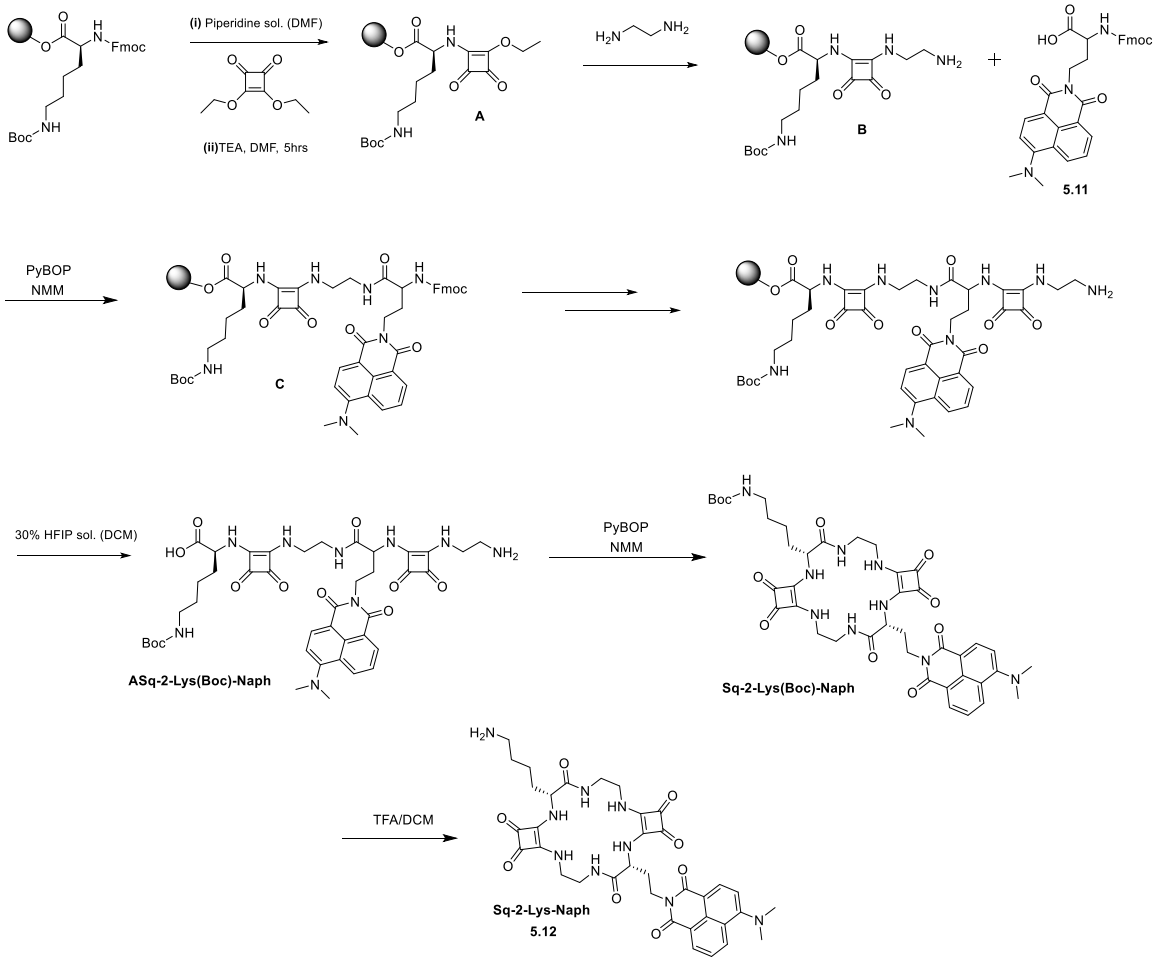

Scheme 5.2: Synthetic pathway towards the synthesis of **5.12 (Sq-2-Lys-Naph).**

The synthesis of **5.12 (Sq-2-Lys-Naph)** is carried out using the same stepwise procedures as described in chapters 3 and 4. Briefly, Fmoc-Lys(Boc) was attached to 2-chlorotrityl resin, followed by the coupling of diethyl squarate in triethylamine in DMF that was then

subsequently reacted with EDA to provide the monomer **B**. **5.11** which was synthesised beforehand, was coupled to monomer **B** using PyBOP/NMM to give monomer **C**. The same sequence of reaction steps was carried out until the desired linear squaratide was achieved, whereby the resin was treated with a mixture of HFIP / DCM in order to cleave and obtain **ASq-2-Lys(Boc)-Naph**. The HPLC trace (Figure 5.5) displayed a sharp UV peak with a t_R = 27 min, and strong ionisation was observed for the target mass of $[M+H]^+$ = 847.4 g mol $^{-1}$ in positive mode, confirming the successful synthesis of the desired linear squaratide dimer.

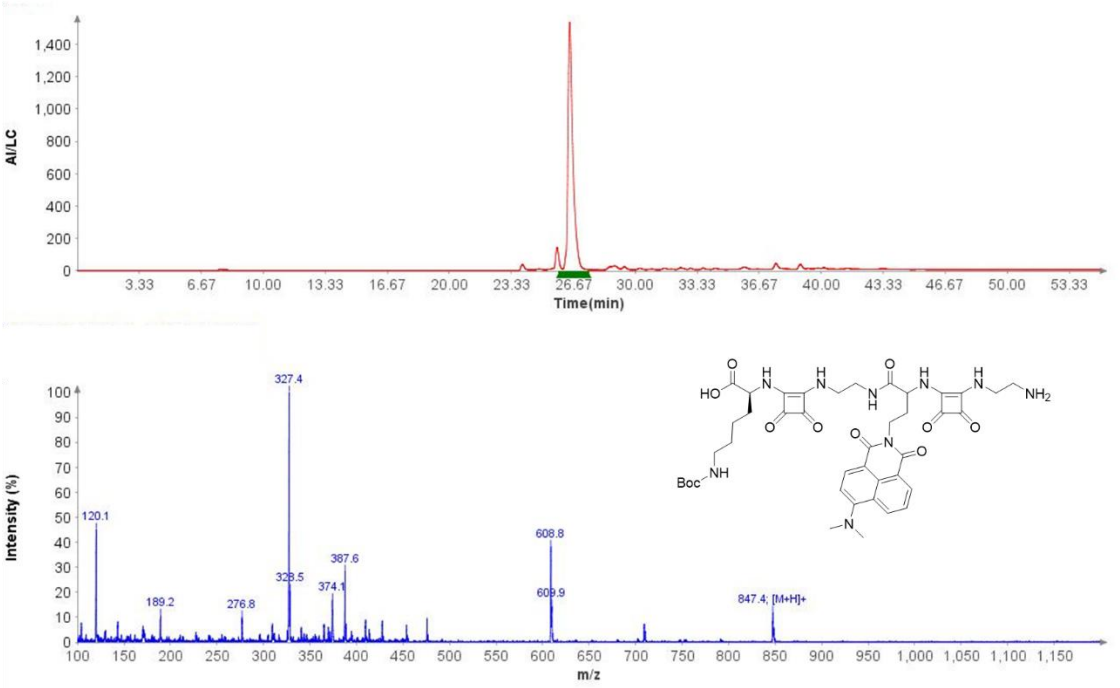

Figure 5.5: LC-MS data for **Asq-2-Lys(Boc)-Naph.**

ASq-2-Lys(Boc)-Naph was subjected to Intramolecular cyclization under high-dilution conditions in DMF using PyBOP and NMM, affording the protected cyclic product **Sq-2-Lys(Boc)-Naph** as a yellow solid in 62% isolated yield. LC-MS analysis (Figure 5.6) confirmed the expected mass for the cyclic product, and HPLC showed a longer retention time (t_R = 41 min) relative to the corresponding linear precursor, consistent with successful macrocyclization. A single sharp peak was observed in the chromatogram, although partial Boc deprotection was detected under the acidic HPLC conditions (0.1% TFA in acetonitrile/water), giving rise to a fragment ion at $[M – Boc +H]^+$ = 728.9 gmol^{-1} in positive ion mode.

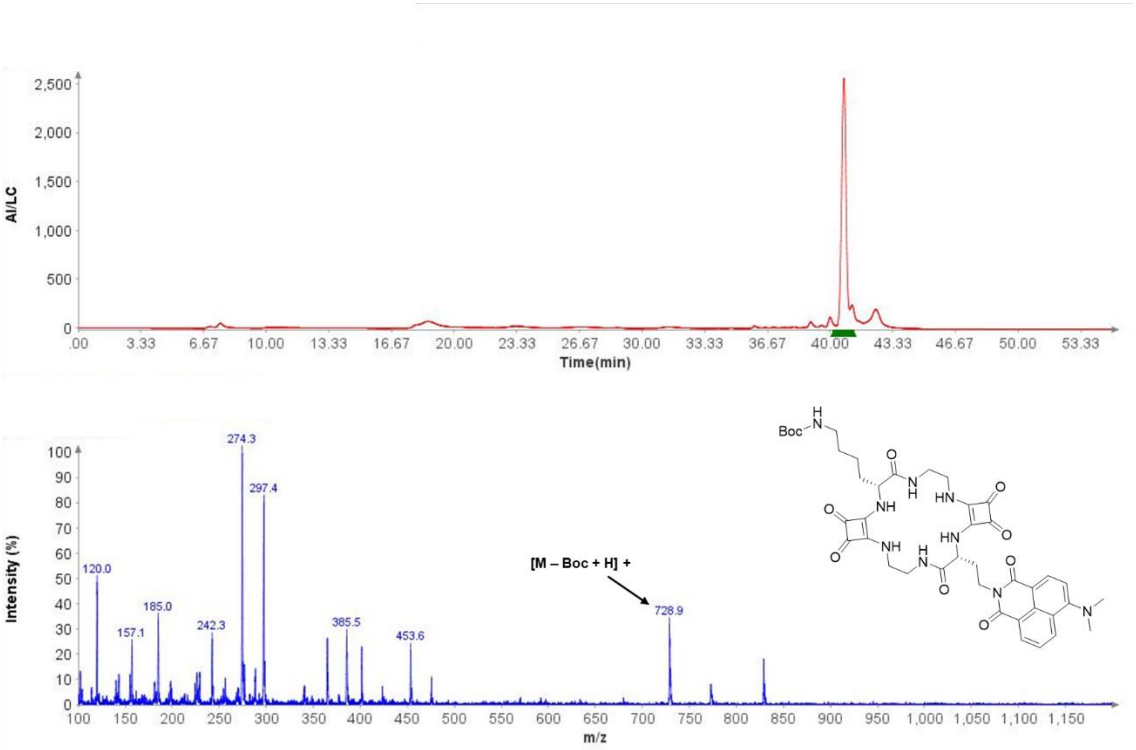

Figure 5.6: LC-MS data for **Sq-2-Lys(Boc)-Naph.**

Boc deprotection of **Sq-2-Lys(Boc)-Naph** was carried out using a 1:1 (v/v) mixture of trifluoroacetic acid (TFA) and dichloromethane (DCM). After completion, the solvent was removed under reduced pressure, and the residue was dissolved in minimal methanol before precipitation with cold diethyl ether. The crude material was lyophilized to afford the deprotected product **5.12 (Sq-2-Lys-Naph)** as a yellow solid in 89% isolated yield. Analytical HPLC (Figure 5.7) showed a shorter retention time (t_R = 27 min) relative to the Boc-protected precursor, consistent with removal of the protecting groups. The chromatogram displayed a sharp UV-absorbing peak corresponding to the desired compound with the expected molecular ion showing a strong signal at $[M+H]^+$ = 728.1 in positive ion mode.

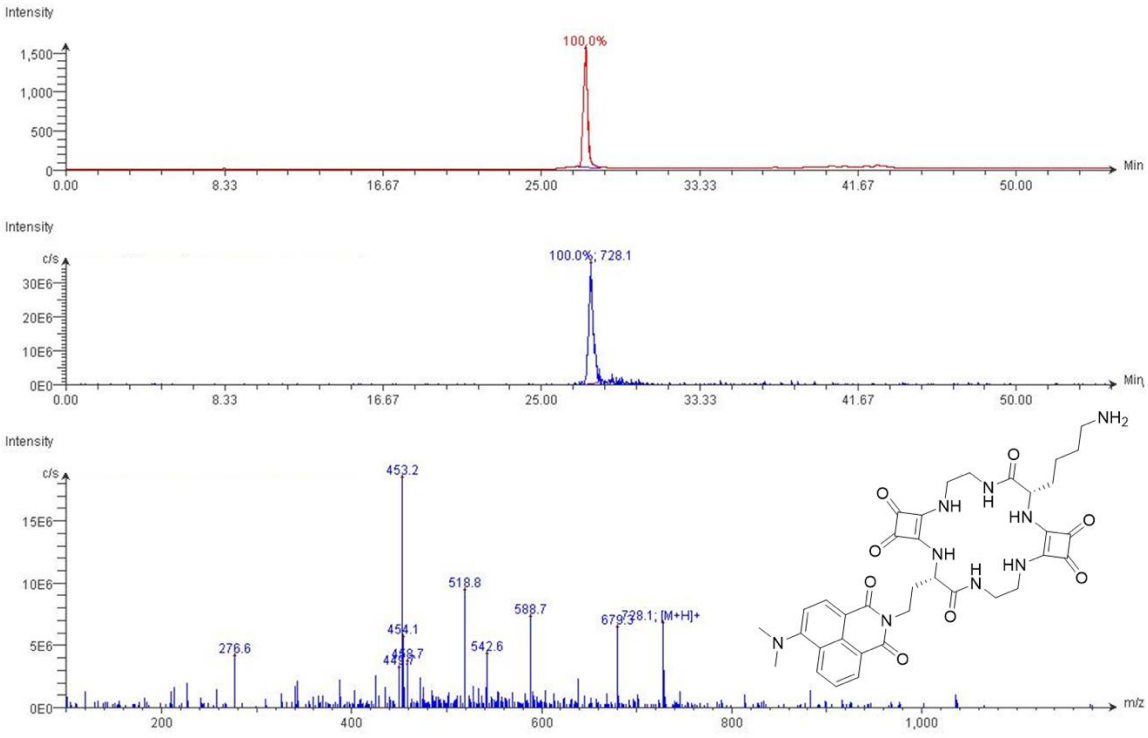

Figure 5.7: LC-MS data for **5.12 (Sq-2-Lys-Naph).**

Finally, HRMS was also used as a complimentary analysis to confirm the molecular formula of **5.12 (Sq-2-Lys-Naph)**, with confirmation of the target mass through detection of the protonated ions: $[M+H]^+$ = 728.3151 $gmol^{-1}$ possessed a low mass error value of -0.27 ppm (Figure 5.8).

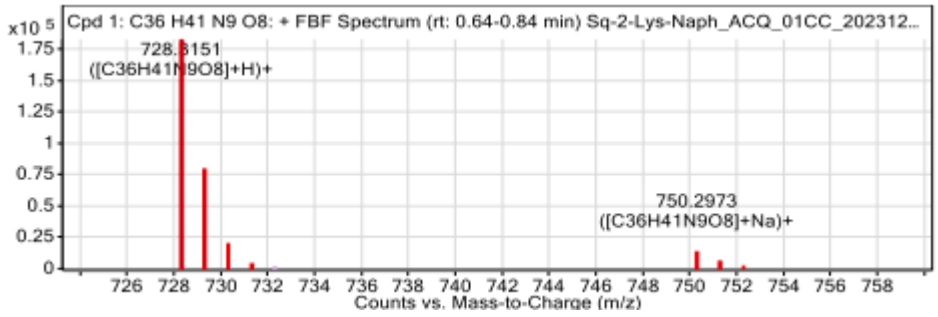

Figure 5.8: HRMS data for the deprotected cyclic squaratide **5.12 (Sq-2-Lys-Naph).**

The ^{1}H NMR spectra obtained for **5.12 (Sq-2-Lys-Naph)**, revealed notable spectral complexity and peak broadening, as illustrated in Figure 5.9, despite obtaining high-purity material—as verified by both LC-MS and HRMS. This observation is consistent with our earlier NMR analyses of squaratides; thought to be a result of both self-assembly and the existence of several conformational isomers in. The increased conformational rigidity and restricted rotational freedom imposed by macrocyclisation often lead to the presence of multiple slowly interconverting conformers on the NMR timescale.[324-326] These conformational isomers give rise to broadened or duplicated resonances, especially in the amide and aromatic regions, as seen in the inset expansion of the aromatic domain. In particular, the squaramide and amide NHs, which participate in extensive intramolecular hydrogen bonding networks, are highly sensitive to the conformational environment and dynamic exchange, contributing significantly to spectral complexity.[112, 327] Furthermore, the macrocycle's rich hydrogen-bonding topology, combined with its relatively high density of polar and aromatic functionalities, likely promotes intramolecular aggregation in solution. These interactions result in deshielding effects and dynamic line broadening that further complicate spectral resolution. However, upon Boc deprotection, a clear shift in the chemical environment is observed, as indicated by diagnostic signals such as the disappearance of the tert-butyl singlet (δ ~1.4 ppm) and the appearance of the NH_2 from the lysine side chain in the aromatic region. Taken together, these data are consistent with the successful synthesis of **Sq-2-Lys-Naph**, albeit accompanied by the expected conformational heterogeneity typical of these cyclic peptidomimetics.

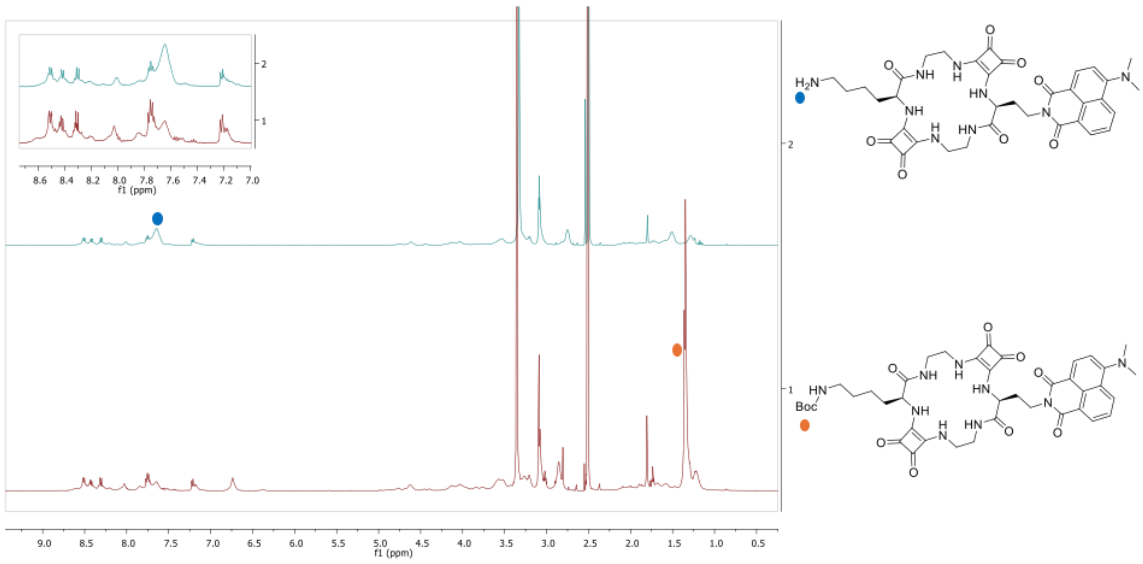

Figure 5.9: ^{1}H NMR spectrum of (bottom) protected compound **Sq-2-Lys(boc)-Naph** in and (top) **Sq-2-Lys-Naph (5.12)** in DMSO-d_6.

5.4: Anion binding studies

5.4.1: Fluorescence Spectroscopy Anion Interactions

With our newly synthesised fluorescent squaratide **5.12 (Sq-2-Lys-Naph)** in hand, fluorescence spectroscopy was carried out in order to gain insight into the fluorescence properties of **5.12 (Sq-2-Lys-Naph)** in the presence of various anions (F^-, Cl^-, Br^-, I^-, $H_2PO_4^-$, NO_3^-, $PHCOO^-$, and $CH_3CO_2^-$) and to assess its selectivity and binding ability (Figure 5.10). Upon excitation (λ_{ex} = 420 nm) **5.12 (Sq-2-Lys-Naph)** exhibited fluorescence at 540 nm in its unbound state, indicative of the emissive nature of the naphthalimide chromophore. The addition of various anions caused varying degrees of quenching in fluorescence intensity. Notably, **5.12 (Sq-2-Lys-Naph)** exhibited a pronounced fluorescence quenching effect upon interaction with fluoride (F^-) leading to a significant "turn-off" response, while other anions induce comparatively moderate to no changes in intensity. The significant fluorescence quenching observed in the presence of fluoride (F^-) provided crucial insights into the underlying quenching mechanism, suggesting that these anions induce deprotonation within the receptor's hydrogen-bonding framework, leading to diminished fluorescence intensity. The interaction with highly basic anions such as fluoride results in deprotonation that perturbs the electronic environment of the appended naphthalimide and facilitates photoinduced electron

transfer (PET) from the bound anion/receptor complex to the excited fluorophore, thereby enhancing non-radiative decay pathways and ultimately leading to fluorescence quenching of the naphthalimide core. The particularly strong quenching observed for fluoride is attributed to its high electronegativity and small ionic radius, which enable it to form stable hydrogen-bonded complexes and efficiently abstract protons from the squaramide NH groups. In contrast, anions such as bromide (Br^-), chloride (Cl^-), iodide (I^-), nitrate (NO_3^-), Benzoate ($PHCOO^-$) and Acetate (AcO^-) exhibit relatively minor effects on fluorescence intensity, suggesting weaker binding interactions with the receptor. The moderate quenching observed for dihydrogen phosphate ($H_2PO_4^-$) implies a partially stabilizing interaction, likely involving hydrogen bonding but without complete fluorescence suppression.

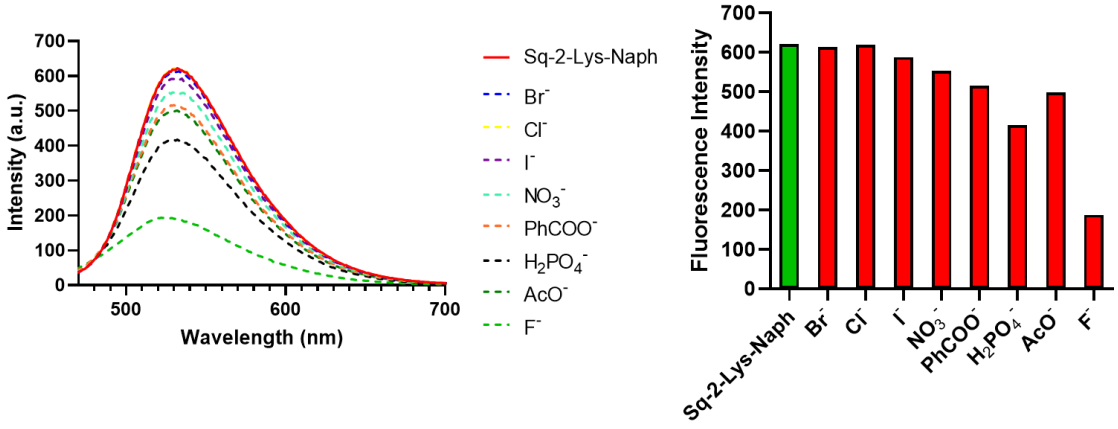

Figure 5.10: Fluorescent spectra of **5.12 (Sq-2-Lys-Naph)** (30 µM λ_{ex} = 420 nm) in the presence of 40 equiv of various anions in a DMSO solution.

5.4.2: Fluorescence Spectroscopy Anion Titration

The sensing properties of **5.12 (Sq-2-Lys-Naph)** for F^- were further studied through fluorescence titration experiments (Figure 5.11(a)). With the gradual addition of F^- the fluorescence intensity of **5.12 (Sq-2-Lys-Naph)** gradually decreased, indicating a close interaction between the receptor and anion. These titration results were interpreted using the open access BindFit software program to provide the apparent stability constants (K_a), by which the binding mode was best suited to a 1 : 1 binding model with an association constant of 622 ± 10 M^{-1}. This conclusion was further corroborated by a Job's plot analysis (Figure 5.11(b)), which displayed a maximum at a 0.5 molar fraction, consistent with a 1:1 binding stoichiometry.

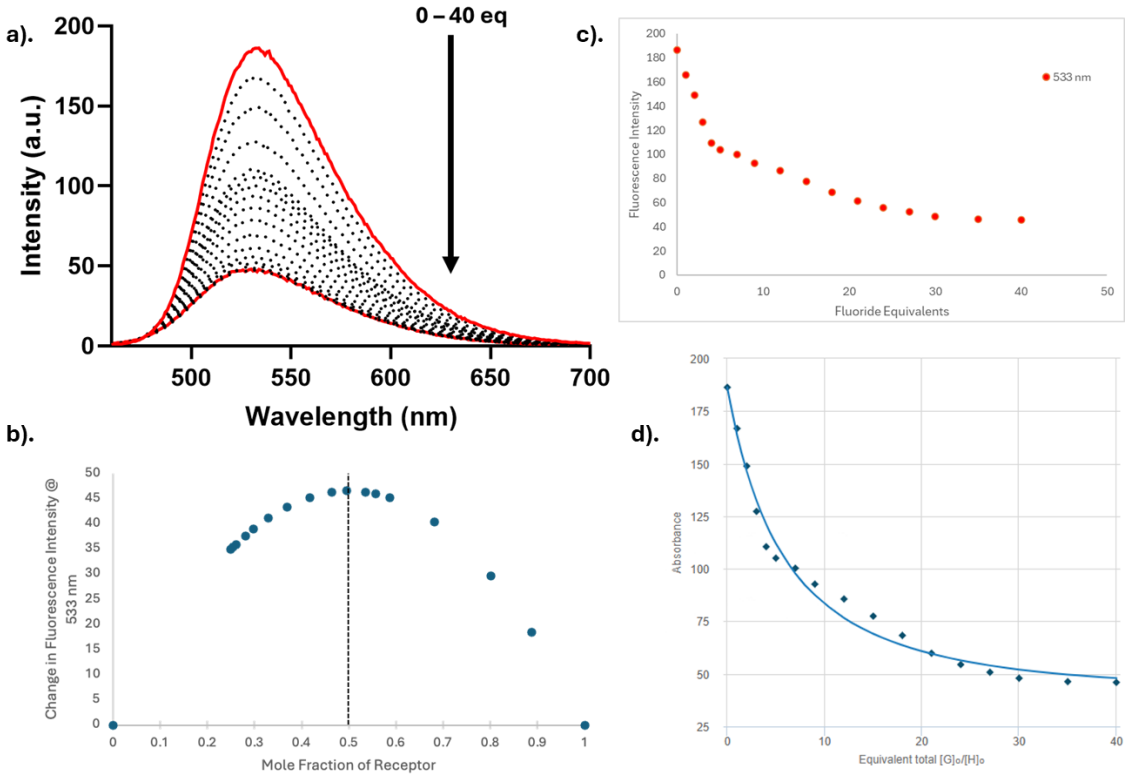

Figure 5.11: (a) Fluorescent spectra of **5.12 (Sq-2-Lys-Naph)** (10 µM λ_{ex} = 420 nm) upon titration with F^- (0 – 40 equiv) in a DMSO solution. **(b)** Jobs plot analysis of the fluorescent titration data of **5.12** and F^- **(c)** Absorbance changes observed upon the addition of F^- (0 – 40 equiv). **(d)** Fitted data of the chemical shift change of **5.12** against molar equivalents of TBAF.

5.4.3: UV-Vis Anion Titration

The UV-Vis absorption spectra (Figure 5.12) reveal a distinct two-phase interaction between the receptor and fluoride anions. Initially, the addition of fluoride leads to an increase in absorbance at ~300 nm, suggesting enhanced electronic interactions, likely due to strong hydrogen bonding between the squaramide NH groups and fluoride. However, at higher fluoride concentrations, the absorbance at ~300 nm decreases, while a broad absorption band emerges at ~400 nm. This spectral shift suggests that fluoride, beyond a critical concentration, induces deprotonation of the squaramide NH groups, disrupting the hydrogen-bonding network and altering the receptor's electronic environment. The emergence of a red-shifted absorption feature is characteristic of increased charge delocalization following deprotonation, likely leading to a change in **5.12 (Sq-2-Lys-Naph)** conjugation or electronic state.

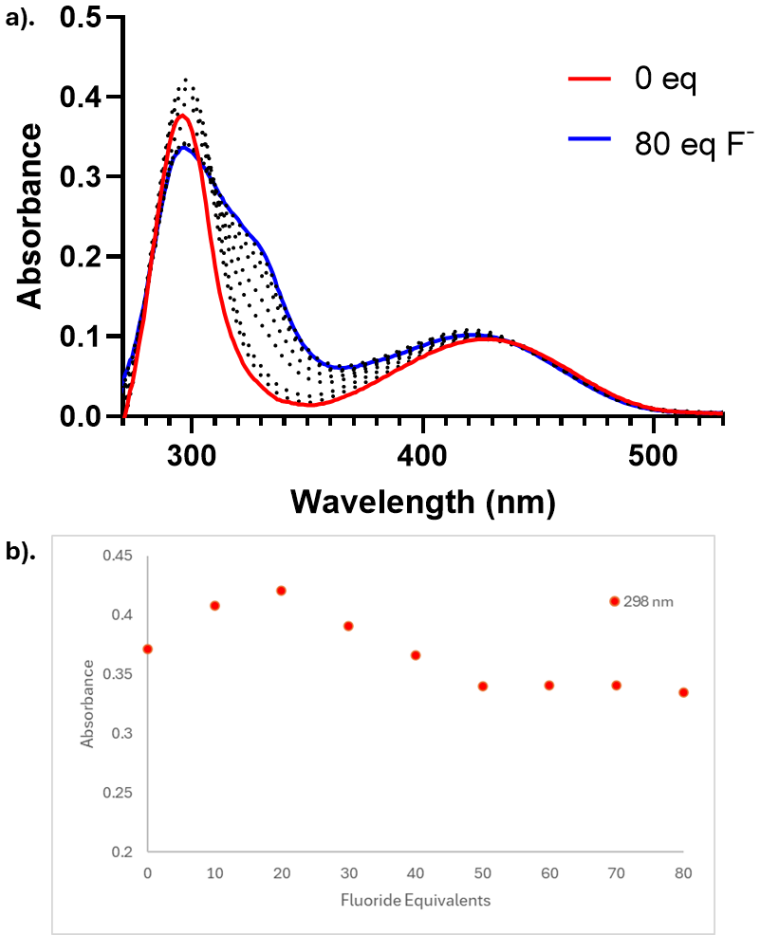

Figure 5.12: (a) UV-Vis spectra of **5.12 (Sq-2-Lys-Naph)** (30 µM) in the presence of 0 – 80 equiv. of F^- in a DMSO solution. **(b)** Absorbance changes observed at 298 nm.

5.4.4: Fluorescence Selectivity Studies

To further probe the selectivity of **5.12 (Sq-2-Lys-Naph)**, competitive binding experiments were carried out in which fluoride was first added to the receptor solution, followed by incremental addition of a second anion (Figure 5.13). The receptor alone exhibits strong fluorescence (green bar), indicative of an intact electronic structure that facilitates radiative emission. Upon the introduction of fluoride, a pronounced decrease in fluorescence intensity is observed across all anion-receptor complexes (red bars). The presence of competing halides, nitrate, benzoate, or dihydrogen phosphate did not lead to significant perturbation of the fluorescence intensity, with the quenched state remaining dominant. This finding confirms the strong preference of the receptor for fluoride, which outcompetes these other anions under the experimental conditions employed. Interestingly, a notable deviation from this behaviour was observed upon the

addition of acetate. In contrast to the other anions tested, acetate induced a partial recovery of fluorescence intensity, restoring emission to nearly 70–75% of its original value. This effect can be rationalised by considering the relative binding interactions at play: while fluoride is a stronger hydrogen bond acceptor, acetate possesses both size complementarity and a capacity to stabilise squaramide binding through multiple interaction sites. It is plausible that acetate displaces fluoride from the binding pocket or establishes an alternative equilibrium in which competition between the two anions perturbs the receptor's electronic environment differently, leading to reduced quenching of the fluorophore. Such behaviour highlights the subtle interplay between anion basicity, size, and binding mode in dictating the optical output of the system. The observed fluorescence recovery suggests that **5.12 (Sq-2-Lys-Naph)** may have potential as a dual-responsive receptor, capable not only of recognising fluoride selectively but also of differentiating acetate in competitive environments through a distinct "off–on" response.

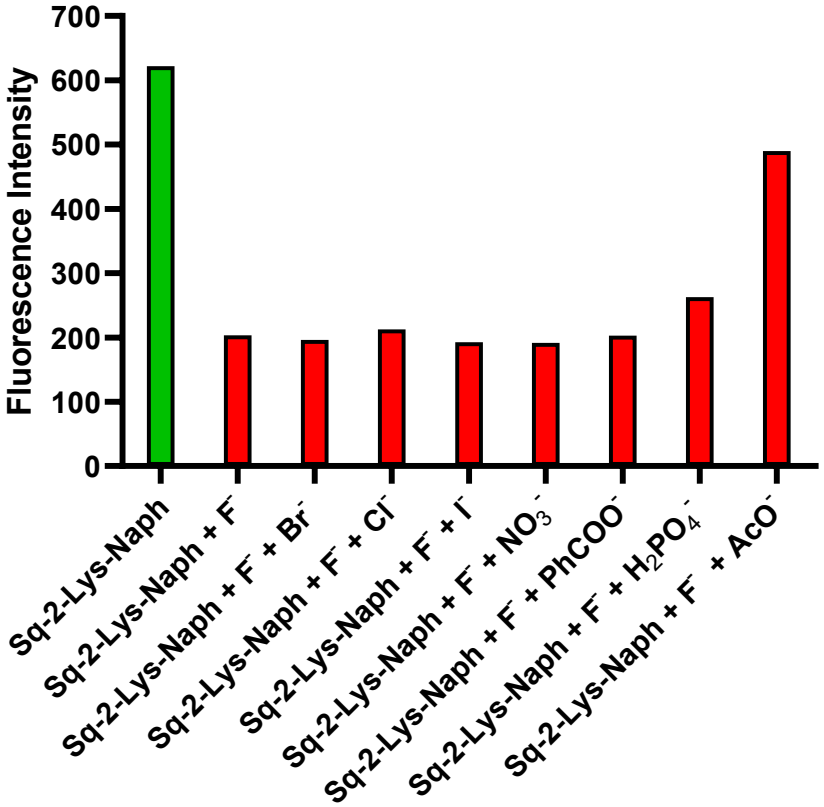

Figure 5.13: Fluorescence response at 540 nm of **5.12 (Sq-2-Lys-Naph)** (30 µM) containing 70 equiv. of F^- and various anions (70 equiv.) in a DMSO solution (excitation at 270 nm).

5.4.5: Fluorescence recovery study

To further elucidate the dynamic and potentially reversible interaction between fluoride and the squaramide receptor within the **5.12 (Sq-2-Lys-Naph)** construct, a competitive fluorescence titration experiment was undertaken (Figure 5.14). In this study, **5.12 (Sq-2-Lys-Naph)** was first treated with 80 equivalents of fluoride, leading to the expected and significant quenching of fluorescence, as previously established. Subsequently, incremental equivalents of acetate anion (ranging from 0 to 80 equivalents) were introduced into this pre-quenched system, and the resulting emission spectra were recorded. The spectral data reveal a compelling trend: upon sequential addition of acetate to the fluoride-bound sensor complex, a progressive recovery of fluorescence intensity was observed. The emission, initially suppressed by fluoride binding, gradually increased in response to acetate, ultimately approaching near baseline intensity of the unbound sensor. This strongly suggests a competitive displacement mechanism, wherein acetate effectively competes with fluoride for the squaramide binding site. Mechanistically, this recovery can be rationalized by considering the relative affinities of the two anions for the squaramide moiety. While fluoride, due to its high charge density and strong hydrogen bonding capabilities, forms a tight complex with the squaramide NH units, the introduction of a competing anion such as acetate which also possesses moderate hydrogen bonding ability, and a comparable basicity can perturb this equilibrium. The increasing concentration of acetate likely facilitates the displacement of bound fluoride, thereby releasing the squaramide receptor and restoring the native photophysical environment of the naphthalimide fluorophore. As the hydrogen bonding interactions with fluoride are disrupted, the photoinduced electron transfer (PET) process is suppressed, resulting in fluorescence reactivation. This competitive binding experiment not only confirms the reversibility of the fluoride–squaramide interaction but also provides compelling evidence for the non-covalent and equilibrium-driven nature of anion recognition in this system. Importantly, it demonstrates the utility of the sensor not merely as a static “turn-off” system but rather as a dynamic and responsive platform that can monitor real-time fluctuations in a competitive anionic composition. Such behaviour is particularly valuable in environmental or biological contexts where transient changes in fluoride concentration must be detected with high fidelity.

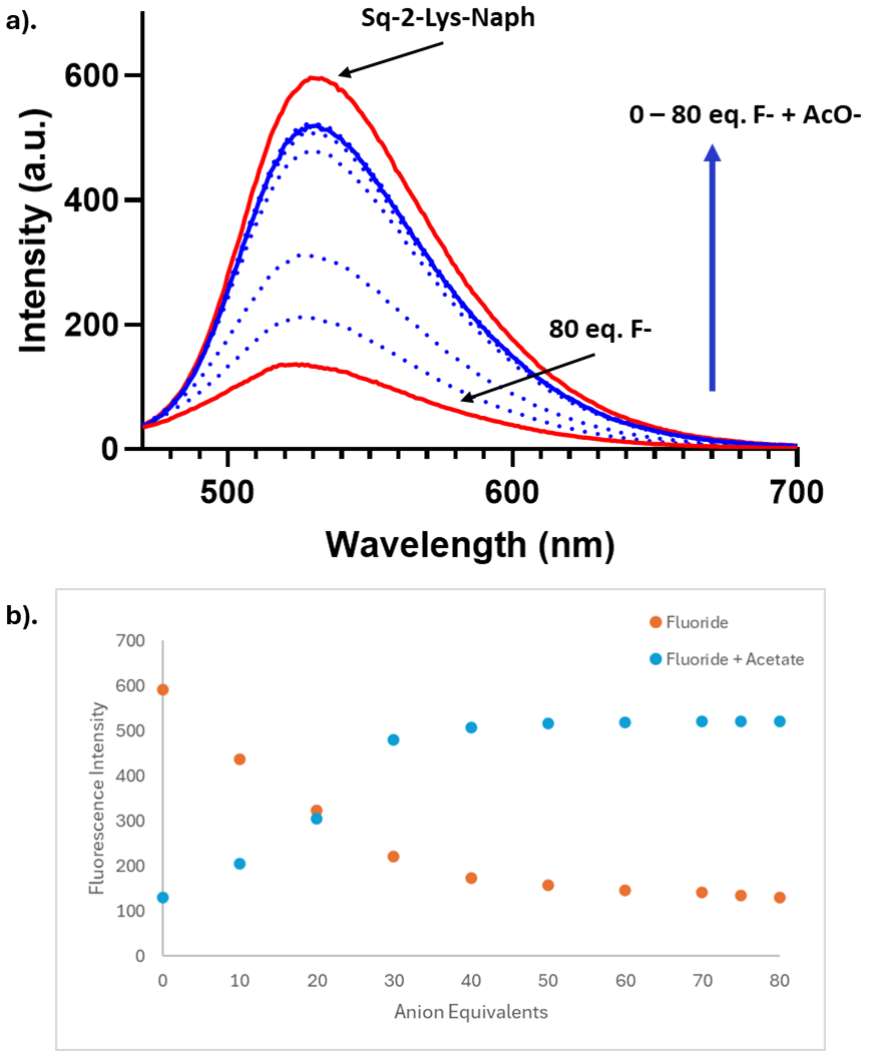

Figure 5.14: (a) Fluorescent spectra of **5.12 (Sq-2-Lys-Naph)** (30 µM λ_{ex} = 420 nm) upon titration with F^- (0 – 80 equiv.) followed by addition of AcO^- (0 – 80 equiv.) in a DMSO solution. **(b)** Absorbance changes observed upon the fluorescence titration of **5.12** with F^- and AcO^-.

5.4.6: Probing the Role of Protonation and Deprotonation in Fluorescence Modulation. To further interrogate the nature of fluorescence modulation of **5.12 (Sq-2-Lys-Naph)**, we evaluated its photophysical response to two chemically distinct species: tetrabutylammonium hydroxide (TBAOH) and hydrochloric acid (HCl) (Figure 5.15). This study was designed to determine whether general acid–base chemistry, independent of anion structure or size, could influence the emission behaviour of the system. The addition of TBAOH resulted in a moderate decrease in fluorescence intensity relative to

the free receptor accompanied by a distinct hypochromic (blue) shift in the emission maximum from approximately 540 nm to 515 nm, indicating a change in the local electronic environment around the naphthalimide fluorophore. Given the strong basicity of OH^-, its interaction with the squaramide units likely involves Brønsted deprotonation, which perturbs the local hydrogen-bonding environment and may facilitate photoinduced electron transfer (PET) processes that reduce emission. In contrast, the addition of HCl had no discernible effect on the fluorescence of **5.12 (Sq-2-Lys-Naph).** This indicates that protonation of the squaramide, or the presence of a strong acid, does not affect the photophysical properties of the system. Such behaviour rules out any general pH- or ionic strength-related quenching and demonstrates that neither the fluorophore nor the binding motif is responsive to acidic conditions under these experimental parameters. Crucially, this serves as a negative control that supports the earlier hypothesis: fluoride-induced fluorescence quenching is not a non-specific acid–base interaction but arises from a specific combination of strong hydrogen bonding and subsequent deprotonation, resulting in PET-driven emission loss.

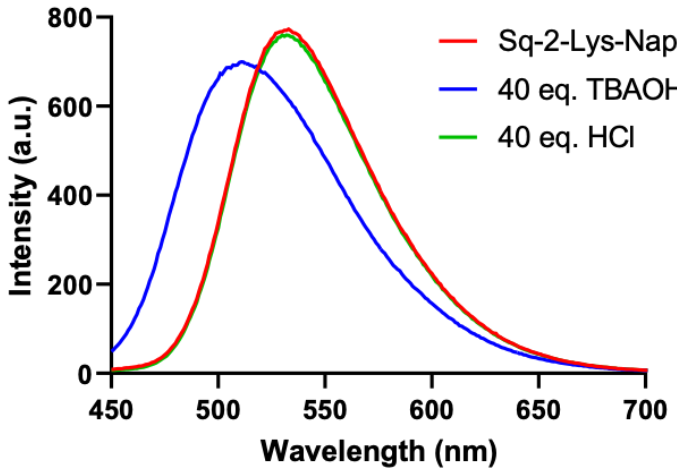

Figure 5.15: Fluorescent spectra of **5.12 (Sq-2-Lys-Naph)** (30 µM λ_{ex} = 420 nm) upon titration with TBAOH (40 equiv.) and HCl (40 equiv.) in a DMSO solution.

To better understand the relative contributions of basicity and structural recognition in the fluorescence quenching mechanism of **5.12 (Sq-2-Lys-Naph)**, a direct comparison was conducted between the effects of TBAF (fluoride) and TBAOH (hydroxide), each added at 40 equivalents (Figure 5.16). The resulting emission profiles provide clear evidence of differential quenching behaviour, reinforcing the specificity of the sensor toward fluoride. The dramatic difference between fluoride and hydroxide underscores

the fact that quenching is not merely a function of basicity, as hydroxide is in fact the stronger base. Instead, this behaviour demonstrates that anion geometry, size, and hydrogen bonding ability play a critical role in enabling productive interaction with the squaramide motif. Fluoride's small ionic radius and high charge density allow it to nestle into the hydrogen bonding pocket, while hydroxide—though strongly basic—lacks the same steric and electronic complementarity. Thus, this comparative study confirms that fluoride uniquely activates the sensor through a synergistic mechanism involving both anion binding and deprotonation, which together facilitate PET and fluorescence quenching. The lesser response to hydroxide further validates the selectivity and fine-tuned responsiveness of the sensor design, ensuring minimal interference from non-specific bases in real-world applications.

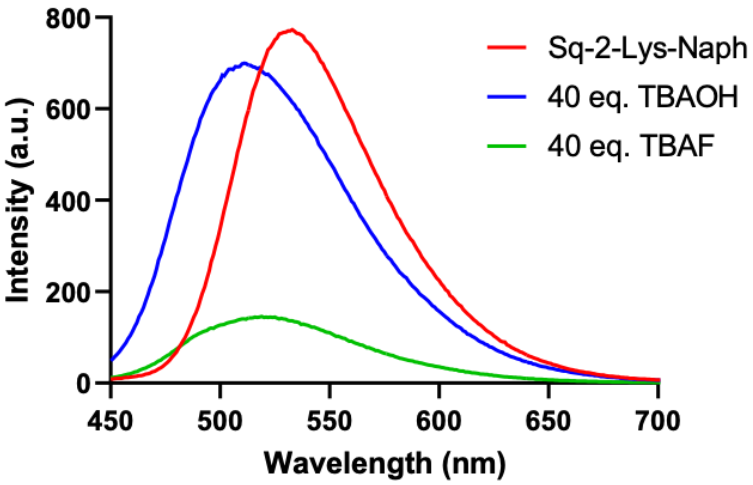

Figure 5.16: Fluorescent spectra of **5.12 (Sq-2-Lys-Naph)** (30 µM λ_{ex} = 420 nm) upon titration with TBAOH (40 equiv.) and TBAF (40 equiv.) in a DMSO solution.

5.4.6: ^{1}H NMR Anion Titration

To gain molecular-level insights into the anion binding mechanism between **5.12 (Sq-2-Lys-Naph)** and Fluoride, ^{1}H NMR titration was conducted in DMSO-d_6 (Figure 5.17) by incrementally adding 0–10 equivalents of tetrabutylammonium fluoride (TBAF). The aim of this study was to assess the hydrogen-bonding behaviour and protonation state of the receptor, and to determine how fluoride-induced structural changes may underpin the previously observed fluorescence quenching. Upon the gradual addition of fluoride, at

low concentrations, the NH proton resonances undergo a progressive downfield shift and peak broadening, indicative of an increasing hydrogen-bonding interaction between the receptor and fluoride anions. This deshielding effect, as a result of electron density around the NH protons decreasing due to anion binding suggests that fluoride initially engages in strong hydrogen bonding with the receptor's NH donor groups, thereby stabilizing an anion-receptor complex. As the fluoride concentration increases, the NH resonances become increasingly attenuated and eventually vanish, strongly suggesting that fluoride not only participates in hydrogen bonding but also induces deprotonation of the receptor. This transition is consistent with a well-established property of fluoride: its high basicity and ability to act as a proton acceptor, leading to deprotonation of the squaramide and amide NH groups as well as the lysine side chain. Furthermore, throughout the titration, the aromatic signals—particularly those associated with the naphthalimide moiety (marked in red, green, and blue)—exhibit only minor chemical shift perturbations, indicating that the fluorophore itself is not directly interacting with the fluoride. Instead, the fluorescence quenching observed in the emission studies likely originates from electronic effects induced by squaramide deprotonation, rather than fluorophore binding per se. This supports a photoinduced electron transfer (PET) mechanism, where deprotonation of the squaramide alters the electronic landscape in a manner that facilitates non-radiative relaxation of the excited state. Concomitant with NH deprotonation, a new, broad signal appears around 16 ppm, which is characteristic of the $[HF_2]^-$ bifluoride ion. The presence of this signal confirms the formation of a hydrogen-bonded fluoride–proton complex, arising from abstraction of a proton from the receptor followed by its capture by an additional equivalent of fluoride. The appearance and intensity of this bifluoride signal serves as direct evidence that the quenching of fluorescence observed in spectroscopic studies is tightly coupled to proton transfer processes, and not merely weak hydrogen bonding. This NMR titration therefore provides strong structural evidence that the sensor operates via a proton-coupled anion recognition mechanism, wherein the deprotonation of the squaramide plays a pivotal role in modulating fluorescence. The detection of $[HF_2]^-$ offers unambiguous confirmation of fluoride's basicity in this system, and highlights the tight coupling between structural, electronic, and photophysical changes upon anion binding. These findings support the broader conclusion that fluoride selectivity arises not only from

hydrogen-bonding complementarity, but also from its unique ability to induce proton transfer and disrupt the PET equilibrium within the receptor scaffold.

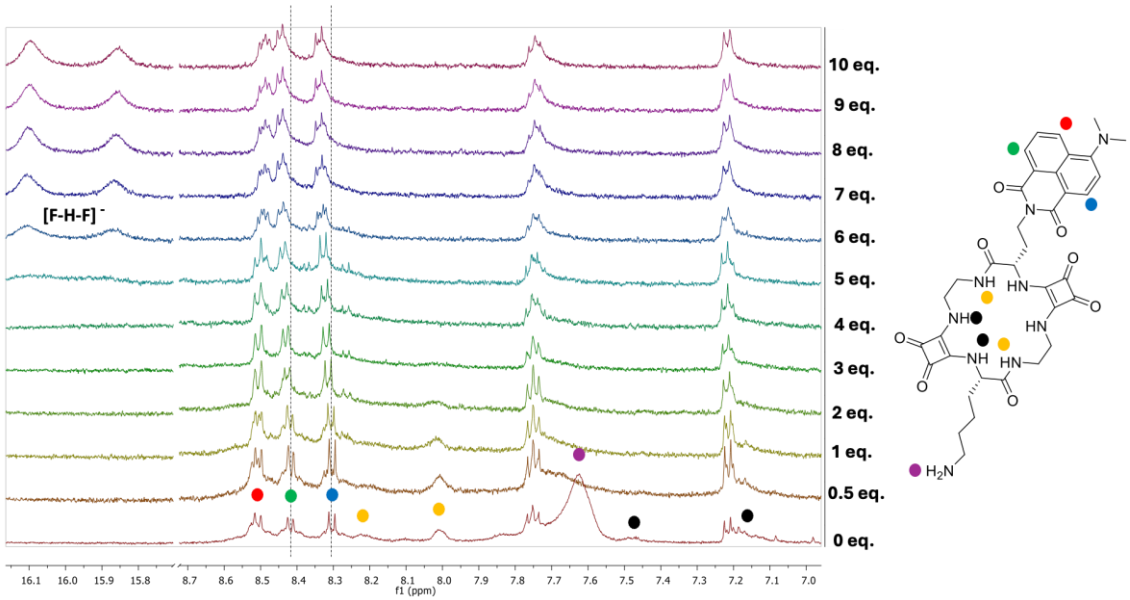

Figure 5.17: Partial ^{1}H NMR titration spectra of **5.12 (Sq-2-Lys-Naph)** (2.5 mM) in DMSO-d_6 with increasing concentrations of TBAF.

To probe the reversibility of the fluoride-induced deprotonation event and reinforce the mechanistic understanding derived from fluorescence studies, a competitive ^{1}H NMR experiment was conducted using **5.12 (Sq-2-Lys-Naph)** in the presence of fluoride and acetate anions (Figure 5.18). The receptor was first exposed to 5 equivalents of TBAF, followed by the addition of 10 equivalents of TBAOAc, and the resulting spectra were compared to those of the free **5.12 (Sq-2-Lys-Naph)** and to samples treated with fluoride or acetate alone. Upon fluoride addition (5 eq., green trace), the characteristic squaramide NH signals vanish, accompanied by the appearance of a broad singlet at ~16 ppm, attributed to the $[HF_2]^-$ bifluoride species. This signal is a well-established diagnostic marker of proton abstraction by fluoride, indicating that the NH protons in the squaratide backbone are deprotonated in the presence of excess fluoride. These results are fully consistent with a PET-induced fluorescence quenching mechanism previously observed, confirming that deprotonation at the squaratide core is central to the sensory response. Strikingly, after the addition of 10 eq. acetate to the fluoride-bound system (blue trace), the bifluoride peak at 16 ppm disappears, and two broad NH resonances re-emerge in the 8.6–8.9 ppm region (highlighted in the red box). The spectral pattern closely resembles that of the acetate-only sample (purple trace),

strongly suggesting that acetate is capable of reprotonating the squaramide NH's and reversing the fluoride-induced deactivation of **5.12 (Sq-2-Lys-Naph)**. This competitive reversal may be attributed to the proton-scavenging capacity of acetate, which can act as both a base and a weak acid in equilibrium. In this system, acetate likely serves as a proton shuttle, re-acidifying the deprotonated receptor through capture of the bifluoride proton or via direct hydrogen-bonding interactions that perturb the ion-pair stability. This suggests that the receptor–fluoride complex is not irreversibly deprotonated, but instead maintains a degree of reversibility, contingent on the identity and basicity of subsequent anions introduced. This result corroborates the proton-coupled sensing mechanism proposed earlier, and importantly, demonstrates a tuneable and reversible binding event at the molecular level.

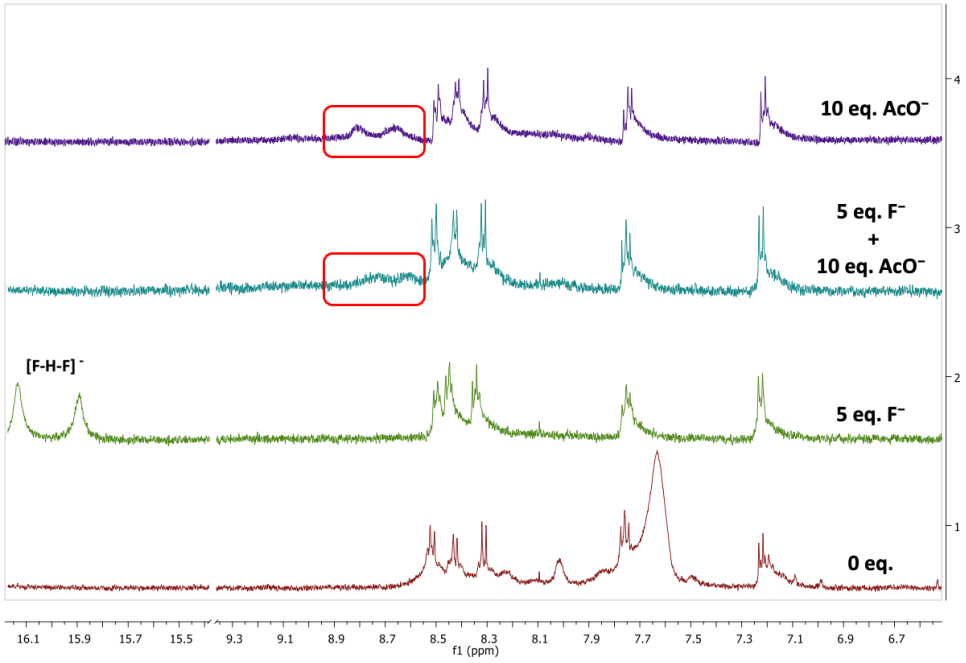

Figure 5.18: Partial ^{1}H NMR titration spectra of **5.12 (Sq-2-Lys-Naph)** (2.5 mM) in DMSO-d_6 with (red) 0 equiv. of anion, (green) 5 equiv. of F^-, and (blue) 5 equiv. of F^- and 10 equiv. of AcO^-, and (purple) 5 equiv. of AcO.

To substantiate the reversibility of fluoride-induced deprotonation and to independently examine the binding behaviour of acetate, a standalone ^{1}H NMR titration of **5.12 (Sq-2-Lys-Naph)** with 0–10 equivalents of TBAOAc was conducted (Figure 5.19). This titration aimed to confirm that the reprotonation observed in the competitive binding experiment (Figure 5.18) was indeed due to direct interaction between acetate and the

squaramide NH sites, and not merely the result of fluoride displacement or re-equilibration. The titration resulted in a complex set of data. The naphthalimide region of the spectrum introduces some complications, as its overlapping aromatic signals partially obscure the hydrogen bonding NH's during the titration, where the downfield-shifting NHs begin to coalesce with the aromatic envelope. In addition to this, we observe peak broadening and partial deprotonation, particularly on the lysine side chain NH_3^+ group as a result of acetate's basicity. This behaviour is consistent with prior observations in Chapter 2, where titration of (**2.17) Sq-2-Lys** with acetate led to similar base-induced deprotonation events taking place. Despite this, we still observe a progressive downfield shift the NH resonances indicative of hydrogen bonding whereby at 10 eq. of AcO^-, the NHs have shifted sufficiently downfield and emerge clearly in the 8.6 – 8.9 ppm range (red box), which match precisely with those observed in the competitive F^- + AcO^- spectrum (Figure 5.18) strongly supporting the hypothesis that acetate interacts with the receptor through hydrogen bonding. Taken together, these results demonstrate conclusive evidence that acetate is capable of reversing the fluoride-induced deprotonation, not just spectroscopically (as seen in fluorescence recovery), but also structurally at the atomic level, through hydrogen bonding and proton donation/exchange. The standalone acetate titration confirms the specificity and reproducibility of this recovery mechanism and provides additional evidence that multiple NH sites in the receptor are sensitive to base-mediated modulation. Collectively, these observations confirm that the binding of fluoride to the receptor is not irreversible, but rather competitively addressable by acetate, and that the new NH signals observed after F^- + AcO^- treatment arise from specific hydrogen bonding interactions rather than nonspecific reprotonation. This dynamic and reversible behaviour underpins the functional versatility of **5.12 (Sq-2-Lys-Naph)** and supports its utility in switchable and recyclable anion sensing applications.

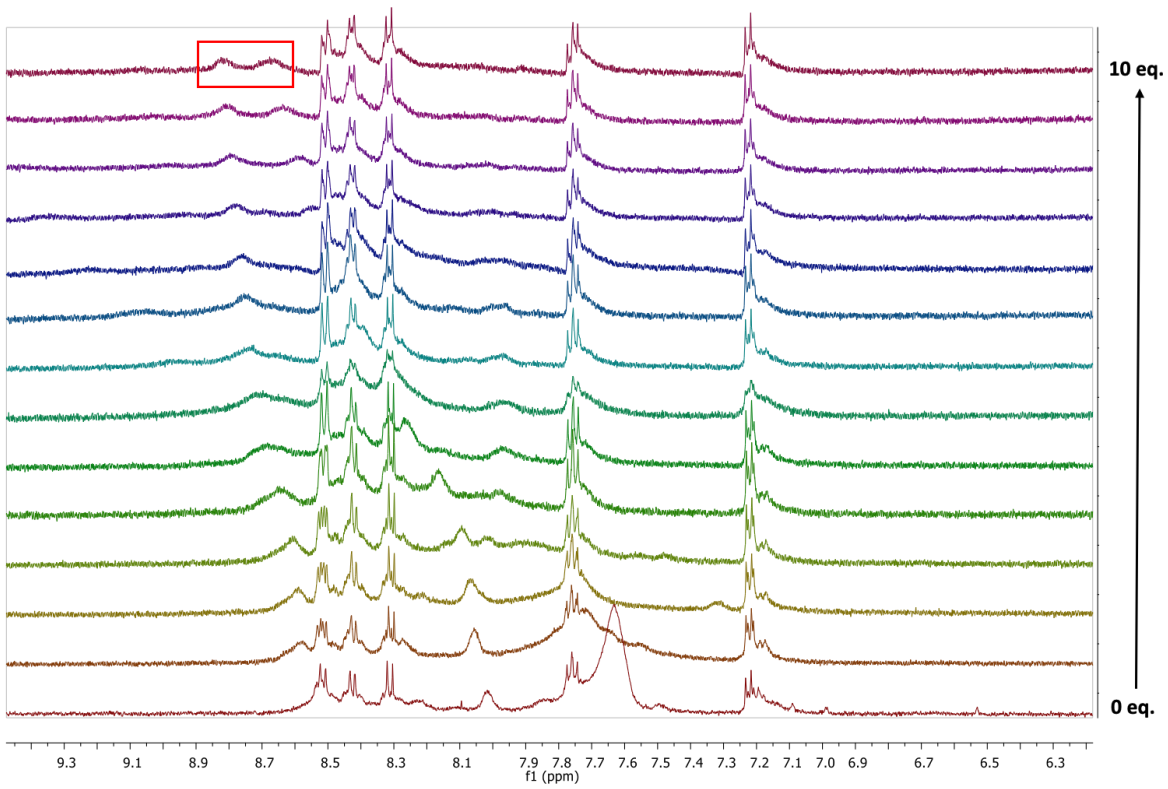

Figure 5.19: Partial ^{1}H NMR titration spectra of **5.12 (Sq-2-Lys-Naph)** (2.5 mM) in DMSO-d_6 with increasing concentrations of TBAAcO.

Given the complexity of the acetate titration spectra, quantitative binding information was nonetheless extractable by selectively tracking the downfield shifts of the NH resonances across the titration series. The data was analysed using the Bindfit software, which provided the best fit to a 2:1 host : guest binding model (Figure 5.20). The analysis yielded association constants of K_{11} = 327 M^{-1} and K_{12} = 15 M^{-1}, clearly showing that the receptor strongly favours the first binding event, while the second binding step is significantly weaker, likely influenced by electrostatic repulsion and partial deprotonation of the receptor under basic conditions. The binding profile accords with the structural observations from the TBAAcO^{-} titration, where hydrogen bonding interactions could still be resolved despite spectral overlap and broadening and complements the competitive binding experiments by quantitatively demonstrating that acetate engages **5.12 (Sq-2-Lys-Naph)** in a stepwise and cooperative manner. Together, the combined qualitative and quantitative data provide a comprehensive picture of acetate binding, reinforcing **5.12 (Sq-2-Lys-Naph)** ability to reverse fluoride-induced deprotonation through direct hydrogen bonding interactions.

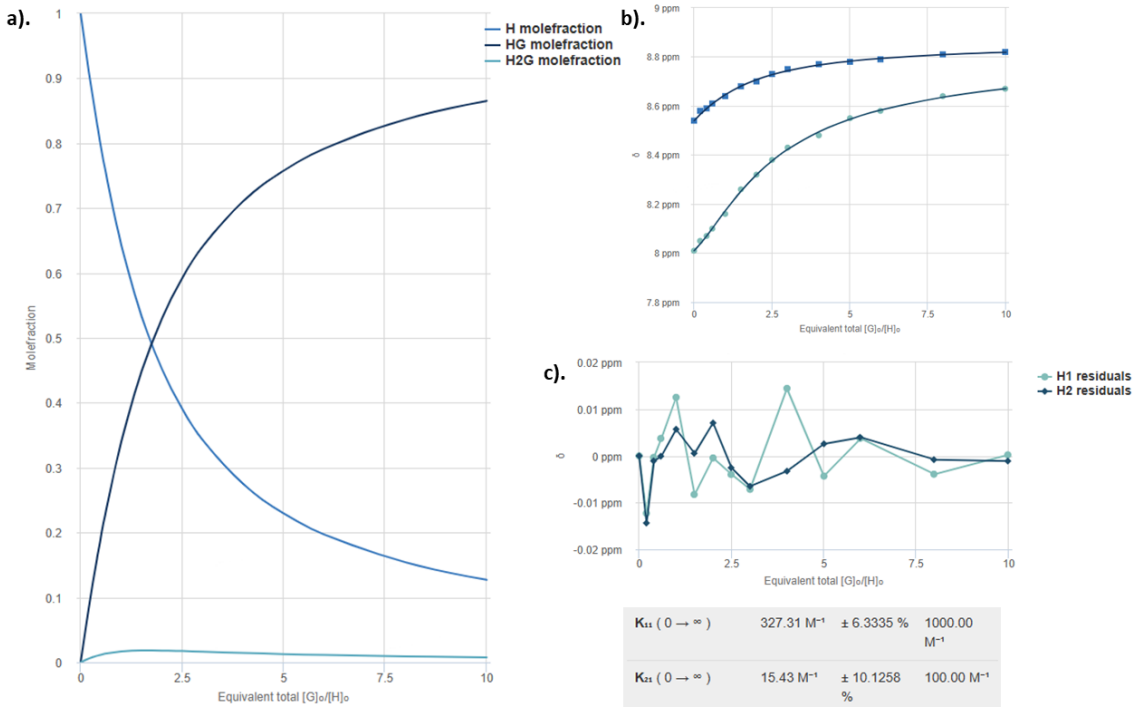

Figure 5.20: (a) Mole fraction plot of Host vs Host:guest fraction with increasing guest concentration for **5.12**. **(b)** Fitting binding isotherms of compound **5.12** with TBAAcO in DMSO-d_6 at 298 K, showing the changes in chemical shifts for the NH protons fitted to the 2:1 binding model (K_{11} = 327 M^{-1}), (K_{21} = 15 M^{-1}). **(c)** Residuals plot of **5.12**.

It is also important to consider the potential influence of trace protic impurities during the acetate binding experiments. TBAAcO is hygroscopic, and its preparation and handling under ambient conditions may result in the introduction of small amounts of water into the DMSO solution. In addition, equilibrium between acetate and trace moisture can lead to the in-situ formation of acetic acid. The presence of even minor quantities of acetic acid would be sufficient to reprotonate the highly acidic squaramide NH groups, thereby contributing to the recovery of fluorescence and the reappearance of NH resonances observed in both fluorescence and ^{1}H NMR experiments. However, while trace protic impurities may contribute to reprotonation, the observed fluorescence recovery cannot be explained solely by nonspecific protonation, as acetate is clearly involved in direct and competitive interactions with the receptor. Both fluorescence and ^{1}H NMR competition experiments demonstrate that acetate actively perturbs the fluoride-bound equilibrium. Furthermore, the standalone ^{1}H NMR titration of **Sq-2-Lys-Naph** with acetate shows progressive downfield shifting of the squaramide

NH signals, indicative of specific hydrogen-bonding interactions rather than nonspecific protonation alone. Quantitative binding analysis using Bindfit further demonstrates that acetate engages the receptor in a structured and preferential manner. Thus, although trace water or acetic acid may enhance reprotonation effects, the spectroscopic data confirm that acetate plays an active role in modulating the protonation state and binding equilibria of the squaratide, while also providing clear evidence for competitive fluoride displacement and preferential acetate binding.

5.5: Conclusion

This chapter has presented the rational design, synthesis, and comprehensive spectroscopic evaluation of a structurally novel fluorescent macrocyclic receptor, **5.12 (Sq-2-Lys-Naph)**, specifically engineered for the selective recognition and sensing of fluoride anions. Inspired by the hydrogen-bonding capabilities of squaramide moieties and the photophysical responsiveness of naphthalimide-derived amino acids, the receptor represents a successful integration of molecular recognition and fluorescence transduction within the framework. The synthetic strategy began with the construction of a naphthalimide-functionalized amino acid, which served not only as a fluorophore but also as a structurally compatible building block for macrocyclization. The final architecture, **5.12 (Sq-2-Lys-Naph)**, thus featured a conjugated, emissive scaffold with directional hydrogen-bond donors ideally suited for anion binding.

A suite of spectroscopic techniques—fluorescence emission, UV-Vis absorption, and ^{1}H NMR spectroscopy—was used to probe the receptor's interaction with a range of anions, with particular emphasis on fluoride. Fluorescence titration studies revealed that **5.12 (Sq-2-Lys-Naph)** undergoes a significant "turn-off" fluorescence response upon exposure to fluoride ions, whereas other tested anions (Cl^-, Br^-, I^-, NO_3^-, $PhCOO^-$, $H_2PO_4^-$, and AcO^-) produced only minor or limited effects on emission intensity. This strong selectivity toward fluoride is indicative of a highly specific interaction mechanism, most plausibly involving geometry-driven hydrogen bonding and subsequent deprotonation of the squaramide NH units, leading to photoinduced electron transfer (PET)-mediated quenching. The limited quenching observed with hydroxide ions (TBAOH) further supports the hypothesis that the receptor is sensitive not merely to basicity, but to structurally precise and directional hydrogen bond donors such as fluoride. Additional control experiments confirmed the robustness of this system. The addition of HCl, even in excess, produced no measurable change in fluorescence, highlighting the sensor's chemical stability under acidic conditions and ruling out general acid–base or ionic strength effects. In contrast, the fluorescence recovery observed upon sequential addition of acetate after fluoride exposure both spectroscopically and through NMR provided compelling evidence for the reversible nature of **5.12 (Sq-2-Lys-Naph)** deprotonation and the potential for anion exchange or regeneration of the active receptor state. Mechanistic insights gained from ^{1}H NMR titration experiments further

corroborated these findings. The gradual disappearance of squaramide NH resonances and appearance of a diagnostic $[HF_2]^-$ peak upon titration with fluoride confirms a proton transfer mechanism, rather than purely non-covalent association. Upon the addition of acetate to the fluoride-treated receptor, reprotonation of the squaramide NH was observed, along with disappearance of the bifluoride signal, directly confirming competitive displacement and structural recovery. To confirm that acetate alone was responsible for this reactivation, an independent titration of **5.12 (Sq-2-Lys-Naph)** with TBAAcO (0–10 eq.) was conducted. This experiment revealed a progressive downfield shift of the NH protons, converging at the same chemical shift as those observed in the competitive F^-/AcO^- NMR experiments. This not only confirms that acetate can restore the receptor's protonated state, but also underscores that the interaction is non-destructive, hydrogen-bond mediated, and chemically addressable. This dynamic interplay underscores a proton-coupled fluorescence quenching mechanism that is both specific and chemically addressable, lending valuable functional versatility to this receptor design. Together, these findings establish **5.12 (Sq-2-Lys-Naph)** as a chemically robust and selectively responsive anion sensor with high affinity for fluoride, offering a reliable photophysical readout and structural reversibility exhibiting a high degree of functional integration, coupling binding events with electronic reconfiguration in a manner that translates into clear, quantifiable fluorescence responses. From a broader perspective, this research advances the field of fluorescent peptidomimetic receptors, which have historically been underexplored for anion sensing. The successful demonstration of tuneable, environment-responsive fluorescence within a peptide-inspired macrocycle offers a promising platform for the development of next-generation anion sensors with potential applications in biological diagnostics, environmental monitoring, and molecular device engineering.

Chapter 6
Thesis Summary

6: Thesis summary

Designed artificial receptors that mimic natural systems in their ability to selectively recognise, sense, and transport a target ion provide connectivity and strengthen supramolecular assemblies for diverse applications from sustainable electronics to molecular medicine. The overarching aim of this thesis was to introduce the conception and development of a novel class of cyclic peptidomimetics that integrate the structural and functional features of peptides with the robust hydrogen-bonding properties of squaramides. These compounds, termed *squaratides*, represent a significant advance in supramolecular chemistry as they embody a hybrid molecular architecture that combines conformational control, chemical diversity, and tunable recognition properties within a single scaffold. The deliberate fusion of squaramide motifs into a peptide-like macrocyclic framework has created a new platform that transcends the limitations of each individual component, yielding systems that can operate at the interface of molecular recognition, membrane transport, and biological activity.

Chapter 2 details a robust synthetic strategy for the assembly and cyclisation of a series of macrocyclic squaratides with varied side-chain functionalities, with a particular emphasis on evaluating their anion recognition and discrimination properties. While the binding data yielded valuable insights into the host–guest interactions of these systems, the accurate determination of association constants (K_a) proved challenging. This difficulty stemmed from the inherent complexity of the squaratide architectures, which often undergo conformational rearrangements in solution and engage in multiple, overlapping binding interactions, leading to non-trivial stoichiometries. Compound **2.14 (Sq-2-Ala)**, employed as the reference system, displayed no evidence of self-aggregation in speciation studies and exhibited a straightforward 1:1 binding stoichiometry with both chloride (K_a = 692 M^{-1}) and acetate (K_a = 227 M^{-1}). Such behaviour can be attributed to its structural simplicity, arising from the absence of bulky or charged side chains, which minimises steric hindrance and electrostatic contributions. In contrast, compound **2.15 (Sq-2-Phe)** demonstrated pronounced self-association, most plausibly driven by intermolecular hydrogen bonding between squaramide motifs coupled with π–π stacking interactions of the phenylalanine residues. This aggregation behaviour significantly influenced its binding profile: while 1:1 binding was observed with chloride

(K_a = 520 M^{-1}), acetate binding proceeded through a more complex 2:1 mode (K_{11} = 8.3 × 10^3 M^{-1}, K_{21} = 3 × 10^3 M^{-1}). The introduction of acetate appears to disrupt these higher-order assemblies, liberating monomeric or partially dissociated oligomeric species that give rise to the observed stoichiometric complexity. Overall, these findings establish squaratides as highly effective anion receptors, showing notable selectivity for acetate in most cases, while also achieving unexpectedly strong chloride binding. Furthermore, the results underscore the profound influence of amino acid side-chain identity on both the supramolecular organisation of the receptors and their resultant host–guest properties.

In Chapter 3, the focus shifted from the solution-phase synthesis of squaratides described earlier in Chapter 2, to the development of a solid-phase synthetic pathway, which provided a more efficient and versatile approach for constructing this class of peptidomimetics. This methodology enabled the preparation of larger and more diverse squaratide scaffolds, including both linear and cyclic architectures, with precise control over chain length, ring size, and side-chain functionality. More importantly, the switch to solid phase synthesis proved highly effective for generating cyclic squaratides, thereby overcoming many of the synthetic limitations encountered in solution-phase strategies. This methodological advance provided not only synthetic efficiency but also tunable structural diversity, paving the way for exploring new functional properties of these receptors. The antimicrobial evaluation of these compounds revealed several key findings. First, cyclic squaratides were consistently active against Staphylococcus aureus, whereas linear and Boc-protected analogues were inactive. This result clearly established the importance of macrocyclic preorganisation and free cationic side-chain accessibility as prerequisites for biological function. Second, a clear ring-size dependence was observed: of the series studied, **Sq-3-Lys** emerged as the most potent compound, producing robust inhibition zones and displaying the lowest MIC values across both aqueous and organic media. This optimal activity likely arises from a balance between structural rigidity and charge distribution, as smaller or larger macrocycles proved less effective. Finally, proteomic and systems-level analyses revealed that **Sq-3-Lys** exerts a multifaceted mode of action. Treatment of S. aureus triggered upregulation of cell wall and metabolic stress pathways while simultaneously downregulating transcriptional and translational machinery, leading to a collapse of bacterial

homeostasis. This combination of membrane disruption and intracellular suppression mirrors the broad-spectrum activity of natural antimicrobial peptides, yet squaratides achieve this with the added advantages of protease stability and synthetic tunability.

In Chapter 4, the scope of squaratide chemistry was extended from anion recognition to anion transport, providing a key demonstration of how structural functionalisation can endow these macrocycles with new supramolecular properties. Starting from the parent scaffolds **Sq-2-Ala-Lys** and **Sq-2-Lys**, we pursued a rational design strategy in which the lysine side chain was derivatised with a 3,5-bis(trifluoromethyl)phenyl squarate unit giving rise to compounds **Sq-2-Ala-Lys(SqBisCF$_3$)** and **Sq-2-Lys(SqBisCF$_3$)**. This modification was intended to amplify hydrogen-bonding capability through an electronically activated aryl squaramide, while also increasing lipophilicity and bilayer partitioning. In parallel, incorporation of a fluorinated amino acid (**Sq-2-F$_5$Phe**) was explored to assess the influence of backbone fluorination on binding and transport behaviour. ^{1}H NMR titration experiments revealed that aryl-squaramide functionalisation profoundly strengthened chloride recognition. **Sq-2-Lys-(SqBisCF$_3$)** displayed strong and stepwise 1:2 binding, dominated by a high-affinity aryl squaramide interaction (K_{11} = 4035 M^{-1}), with a weaker secondary binding event assigned to macrocyclic NHs. In contrast, **Sq-2-Ala-Lys-(SqBisCF$_3$)** favoured a simpler 1:1 binding model (K_a = 217 M^{-1}), consistent with the absence of a second lysine-derived side chain to support cooperative binding. Lucigenin Cl^-/NO_3^- antiport assays translated these binding trends into functional transport outcomes. The parent squaratides and the fluorinated phenylalanine analogue displayed no detectable activity, despite initial expectations that fluorination might enhance bilayer partitioning. By contrast, both aryl-squaramide-functionalised receptors exhibited measurable transport, with **Sq-2-Lys(SqBisCF$_3$)** proving the most effective carrier (EC_{50} = 4 mol%), while **Sq-2-Ala-Lys(SqBisCF$_3$)** demonstrated weaker, cooperative transport (EC_{50} = 8 mol%). These results confirm that the electronically activated aryl squaramide is indispensable for enabling transport, by coupling strong, directional chloride binding with sufficient lipophilicity to mediate transmembrane exchange. The results highlight the delicate interplay between binding-site electronics, macrocyclic preorganisation, and lipophilicity in governing transport efficiency. Crucially, this chapter shows that squaratides can be transformed from passive solution receptors into active membrane

transporters through rational side-chain modification, significantly expanding their scope and positioning them as a new class of versatile supramolecular systems.

Finally, in Chapter 5, we set out to further push the boundaries of the already discussed versatility of squaratides. Through utilising our solid phase synthesis approach, we synthetised a fluorescent squaratide by incorporating a napthalamide based amino acid into the squaratide backbone, providing both structural contribution and an intrinsic optical signalling function. The combination of these features aimed to produce a system capable of selective anion recognition with real-time fluorescence-based detection. Fluorescence spectroscopy revealed that **Sq-2-Lys-Naph** undergoes a marked and reproducible "turn-off" emission response upon exposure to fluoride, with a maximum quenching of over 70% at 520 nm. This quenching effect was highly selective, as comparative studies with other anions—including halides (Cl^-, Br^-, I^-), oxoanions (NO_3^-, $H_2PO_4^-$), and carboxylates (AcO^-, $PhCOO^-$)—showed negligible interference. To investigate reversibility, competitive titration experiments were performed. After pre-equilibration with fluoride, the stepwise addition of acetate led to a progressive recovery of fluorescence, reaching approximately 80% of the original signal. This observation indicated that acetate is capable of displacing fluoride from the receptor, thereby interrupting the quenching mechanism and restoring the fluorophore's emissive state. Notably, no other tested anion was able to reverse the fluoride-induced quenching, demonstrating the receptor's utility not only as a binding host but also as a responsive sensor with potential applications in real-time monitoring of anionic species. The underlying molecular mechanism of recognition and sensing was interrogated using ^1H NMR spectroscopy. Titration with fluoride induced the gradual disappearance of squaramide NH resonances in the downfield region, concomitant with the appearance of a distinct peak at ~16 ppm, assigned to the $[HF_2]^-$ species. This transformation unambiguously confirms that fluoride does not merely hydrogen bond with the squaramide, but rather deprotonates it, forming a stabilized bifluoride complex. This chemical deprotonation offers a credible explanation for the optical "turn-off" behaviour, as the electronic environment of the naphthalimide fluorophore is significantly perturbed, likely through a photoinduced electron transfer (PET) pathway activated by NH removal. In a critical control experiment, addition of acetate to the fluoride-saturated receptor resulted in the disappearance of the $[HF_2]^-$ peak and

reappearance of the squaramide NH resonances, signifying reprotonation of the sensor, offering compelling structural evidence of reversible fluoride binding, mediated by competitive ion displacement. This chapter thus establishes a new class of chemically intelligent sensors that are modular, optically readable, and reversible, setting the foundation for the development of next-generation supramolecular sensors and diagnostic tools for future applications in environmental fluoride detection, bio responsive probes, and adaptive supramolecular materials.

6.1: Future Work

For chapter 2, Future work will aim to increase structural rigidity by replacing the ethylenediamine unit with more constrained diamines, such as cyclic or aromatic linkers. Introducing such rigidity would help to enforce a more defined geometry, reduce competing binding modes, and potentially enhance both affinity and selectivity. At the same time, a more rigid framework would simplify NMR titrations, enabling more reliable determination of binding constants and clearer insight into the binding mechanism. Ultimately, these modifications could yield squaratide receptors with improved performance and broader applicability in anion recognition and sensing.

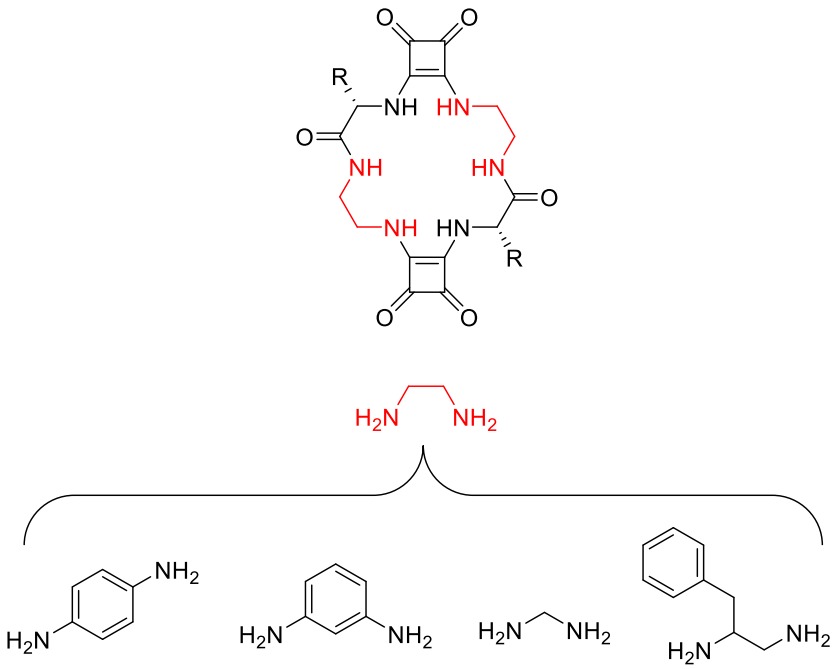

Figure 6.1: Proposed structures of future squaratide based anion receptors, replacing ethylenediamine with more rigid diamines.

In Chapter 3, future work will focus on the development of next-generation antimicrobial squaratides, building on the structure–activity relationships established in this study. While lysine-based macrocycles demonstrated clear activity against Staphylococcus aureus, the synthetic versatility of the solid-phase approach now provides the opportunity to explore new design principles that may further enhance potency, selectivity, and spectrum of activity. by expanding the scaffold beyond lysine-only systems. Incorporating arginine residues could enhance electrostatic binding through guanidinium interactions, while tryptophan residues may strengthen membrane insertion via hydrophobic and π–π interactions, both features characteristic of natural antimicrobial peptides. Further diversification, such as lipidated derivatives to increase membrane affinity or bicyclic architectures to improve structural rigidity, offers additional avenues for optimisation. These strategies, coupled with broader antimicrobial testing and selectivity studies, will guide the rational design of squaratides with improved potency, spectrum, and safety, positioning them as promising candidates for next-generation antimicrobial therapeutics.

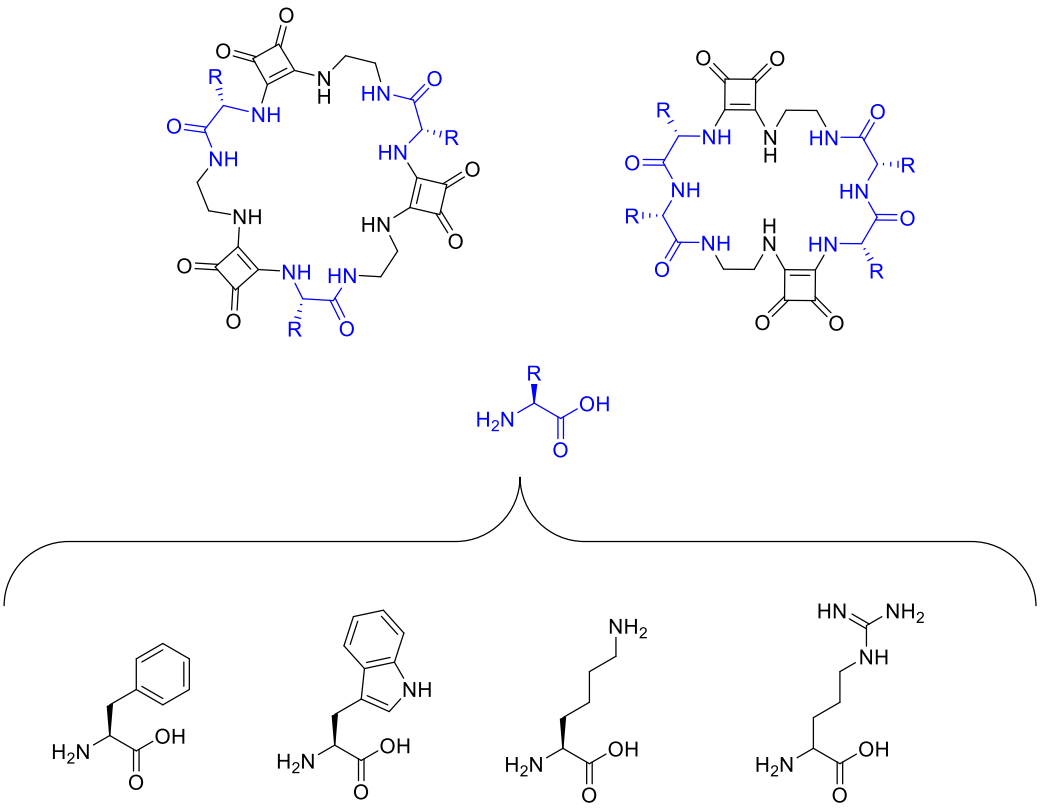

Figure 6.2: Proposed structures of future squaratide based antimicrobial peptide mimetics with varying amino acids.

Chapter 4 established the successful transformation of squaratides into functional anion transporters. Future work will focus on refining the design of squaratide-based transporters and exploring their functional scope. One promising direction is the systematic variation of aryl substituents on the squaramide unit to tune both binding strength and lipophilicity, with groups such as nitro, cyano, or perfluoroaryl potentially offering further enhancement, and developing multivalent receptors with improved cooperativity and faster transport kinetics, provided that macrocyclic symmetry is maintained to avoid the binding complexity seen in asymmetric derivatives. Beyond structural modification, future efforts could include testing in cell-based assays to evaluate cytotoxicity, selectivity, and therapeutic potential. Such investigations would not only validate the supramolecular principles demonstrated here but could also lay the groundwork for applying squaratides in areas such as channel replacement therapy or targeted ion modulation in disease contexts.

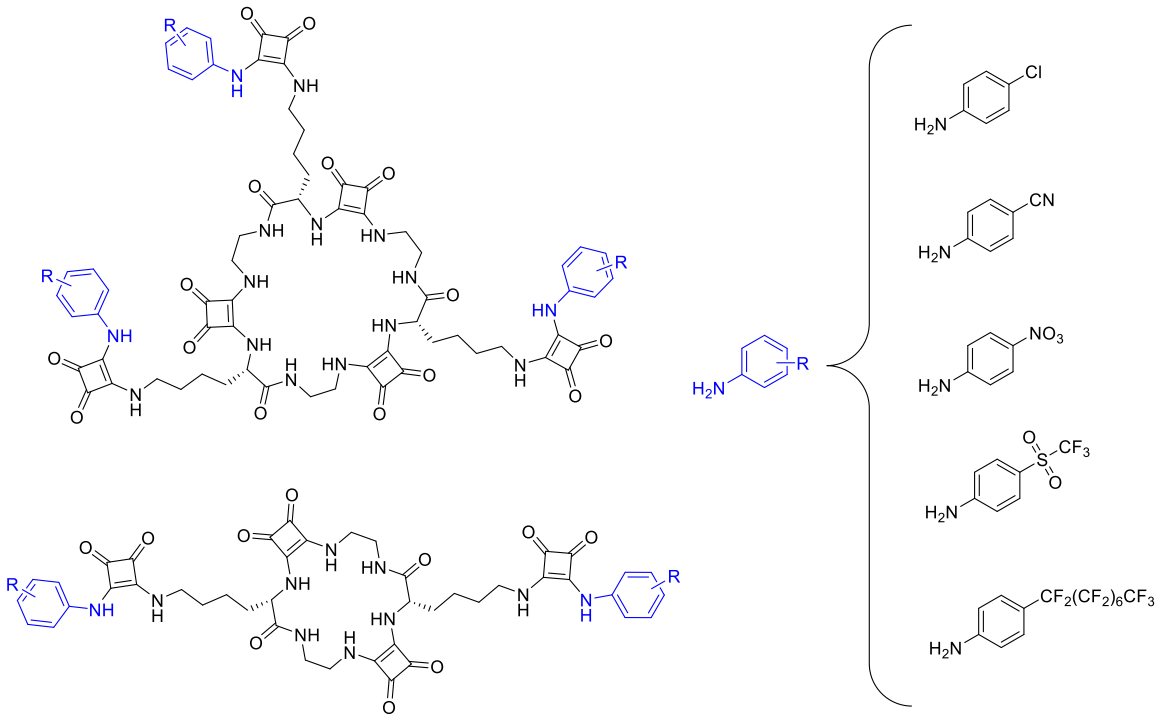

Figure 6.3: Proposed structures of future squaratide based anion transporters with various electron withdrawing aryl substituents.

In Chapter 5, future work will focus on expanding the scope and utility of **Sq-2-Lys-Naph** as a selective and reversible fluorescent sensor for fluoride, by exploring structural modifications aimed at enhancing performance and broadening application potential. A primary direction for future exploration involves the incorporation of alternative fluorescent amino acid residues into the squaratide backbone. This could significantly diversify the sensor's optical output, allowing tuning of excitation/emission wavelengths, improved quantum yields, and enhanced compatibility with multiplexed or biological systems. Such substitutions would also enable the development of ratiometric or dual-emission sensors, providing built-in calibration and improved quantitative reliability, with the potential of evolving into a broad class of adaptive, selective, and multifunctional sensors tailored for both fundamental study and real-world applications including environmental, biological, and industrial processes.

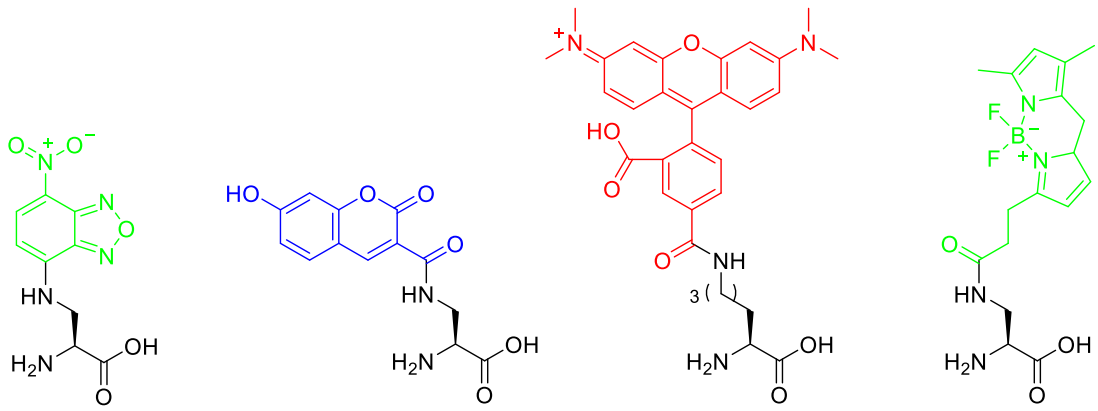

Figure 6.4: Chemical structures of unnatural fluorescent amino acids.

6.2: List of Publications

Mohammed, F. A.; Xiao, T.; Wang, L.; Elmes, R. B. P. Macrocyclic Receptors for Anion Recognition. *Chemical Communications* **2024**.

Tong, H.; **Mohammed, F. A**.; Elmes, R. B. P. Amino Acid – Squaramide Conjugates as Anion Binding Receptors. *Results in Chemistry* **2024**, *11*, 101777.

Brennan, L. E.; Luo, X.; **Mohammed, F. A.**; Kavanagh, K.; Robert. Uncovering the Potent Antimicrobial Activity of Squaramide Based Anionophores – Chloride Transport and Membrane Disruption. *Chemical Science* **2025**.

Inventor – Patent Application (Lipids and Lipid Nanoparticles) – Filed with the United States Patent and Trademark Office (USPTO), [August 2025]

Chapter 7
Experimental Procedures

7: Experimental Procedures

7.1: General Procedures and Instrumentation

All reagents were of commercial quality. Solvents were dried and purified by standard methods – DCM was distilled over CaH_2 and MeCN was dried over 3 Å molecular sieves. Anhydrous DMF was purchased from Sigma Aldrich. Analytical TLC was performed on aluminium sheets coated with a 0.2 mm layer of silica gel 60 F254. Silica gel 60 (230-400 mesh) was used for flash chromatography. Compounds were lyophilised on a Labconco Freezone 1 Dry system. LC-MS was performed on an Agilent Technologies 1200 series setup, utilising an Agilent Eclipse XDB-C18 (5µm, 4.6 x 150mm) column at 40°C. A flow rate of 0.2 mL min^{-1} and gradient of 0.1% of formic acid in CH_3CN (solvent A) in 0.1% of formic acid in H_2O (solvent B) was used as mobile phase. Electrospray in positive & negative mode(s) was used for ionisation. NMR spectra were recorded using a Bruker Ascend 500 spectrometer, operated at 500 MHz for ^1H NMR analysis and 126 MHz for ^{13}C analysis, both at 293 K. The residual solvent peak was used as an internal standard for DMSO-d_6 and TMS for $CDCl_3$. Chemical shifts (δ) were reported in ppm. NMR spectra were processed, and stack plots produced using MestReNova 6.0.2 software. The NMR spectra assignments were based on ^1H, ^{13}C, COSY, HSQC, and HMBC spectra. Multiplicity is given as s = singlet, bs = broad singlet, d = doublet, brd = broad doublet, dd = doublet of doublets, ddd= doublet of doublet of doublets, t = triplet, q = quartet, m = multiplet as appropriate, and *J* values are given in Hz. Infrared (IR) spectra were obtained *via* ATR as a solid on a zinc selenide crystal in the region of 4000 – 400 cm^{-1} using a Perkin Elmer Spectrum 100 FT-IR spectrophotometer. High resolution mass spectra (HRMS) were recorded – courtesy of Bath University – on an Agilent 6200 series TOF/6500 series Q-TOF instrument with an ESI source. Microwave (MW) experiments were carried out in sealed vessels in a CEM Discovery MW, with transversal IR sensor for reaction temperature monitoring. UV-visible spectroscopy measurements were made at 25 ºC on a Lambda 365 Perkin Elmer UV-vis spectrophotometer. Fluorescence emission spectra were performed at 25 ºC and 37 ºC on an Agilent Spectrofluorometer equipped with a 450 W xenon lamp for excitation. Starna and Hellma quartz cuvettes of 1 cm path length and several volumes were employed.

7.2: Synthetic methods – Chapter 2

Chapter 2 – general method A:

To a stirring solution of **2.11** (1 eq., 1.4 mmol, 0.4 g) in EtOH (24 mL), TEA (6 eq., 8.4 mmol, 1.18 mL) the relevant L – amino acid (2 eq., 2.8 mmol, 0.251 g) was added. The resulting mixture was stirred under reflux for 24 h. The reaction mixture was concentrated in vacuo, suspended in DCM (20 mL) and filtered. the solvent was removed in vacuo to afford crude product, which was purified via column chromatography (SiO_2), and triturated in diethyl ether to yield the title compound.

Chapter 2 – general method B:

The corresponding AA-Sq-EDA(Boc) monomers **(2.12(AA))** underwent boc deprotection using a 50:50 TFA: DCM solution, allowing the mixture to stir for 1 hour before being removed in vacuo, redissolved in MeOH and precipitated out of diethyl ether. The deprotected monomers (1 eq., 0.8 mmol, 0.274 g) was dissolved in DMF (9 mL) and NMM (6 eq., 4.82 mmol, 0.53 mL) was added and the resulting solution was stirred for 10min. To this solution PyBOP (3 eq., 2.41 mmol, 1.25 g) was added and allowed to stir for 48 hrs. The DMF was removed in vacuo and the crude mixture was triturated in Ethyl Acetate. The mixture was added to a falcon tube and centrifuged under 4000 RPM for 10 min (2 x Ethyl Acetate and 1x Diethyl Ether). The supernatant was dispelled, and the precipitate was dissolved in 50:50 MeCN/H_2O and lyophilized to afford the cyclic squaratides (**2.14 – 2.18** (Sq-2-AA)).

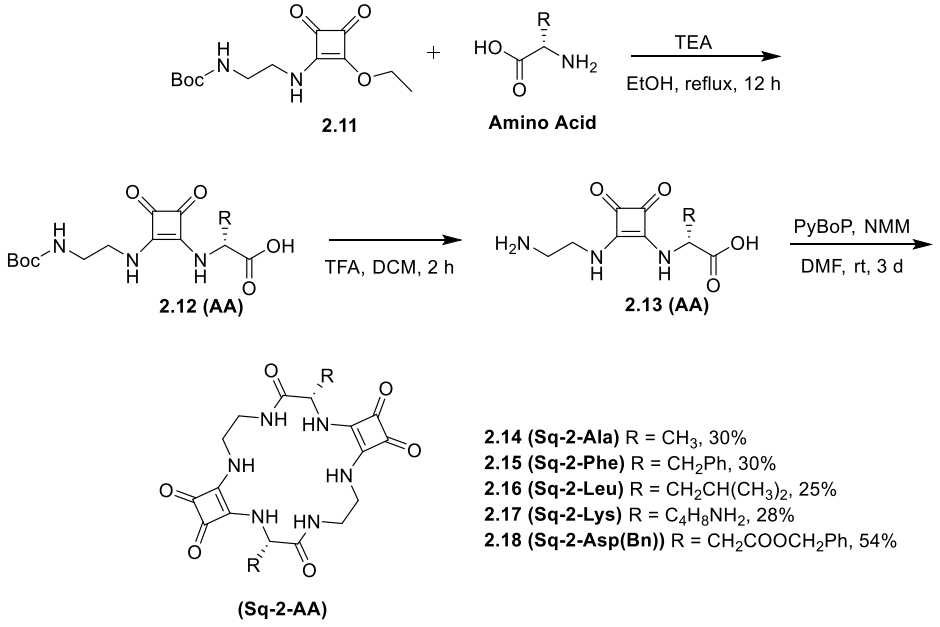

Scheme A1: General Synthetic Strategy towards 1st Generation Cyclic Squaratides.

3,4-diethoxyl-cyclobut-3-ene-1,2-dione (DeSq)

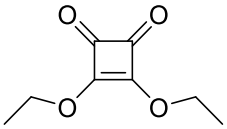

To a suspension of squaric acid (1 eq., 87.7 mmol, 10 g) in EtOH (125 mL) was added triethyl orthoformate (5 eq., 438 mmol, 66.2 mL) and the resulting solution was heated at reflux for 3 days. The solvent was removed in vacuo and the orange/yellow oily residue was purified by flash column chromatography eluting with DCM to yield a clear yellow oil in a 90% yield. **^{1}H NMR** (500 MHz, DMSO-d_6) δ 4.65 (q, *J* = 7.1 Hz, 4H), 1.37 (t, *J* = 7.1 Hz, 6H). **^{13}C NMR** (126 MHz, DMSO-d_6) δ 189.1, 183.7, 70.2, 54.9, 39.5, 15.3. All spectral data is in good agreement with literature.[328]

Tert-butyl (2-((2-ethoxy-3,4-dioxocyclobut-1-en-1- yl)amino)ethyl)carbamate (2.11)

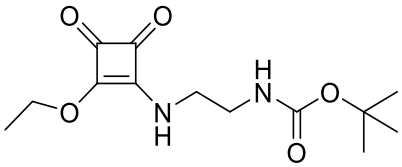

To a stirring solution of 3,4-diethoxyl-cyclobut-3-ene-1,2-dione (1.5 eq. 14 mmol, 2.39 g) in EtOH (50 mL), a solution of *N*-Boc-ethylenediamine (1 eq. 9.4 mmol, 1.5 g) in EtOH (70 mL) was added dropwise and the resulting solution was stirred under RT overnight. The solvent was removed in vacuo to yield a yellow mixture, which was then purified by column chromatography (SiO_2), using a 0 - 5% EtOH:DCM gradient as eluent to afford the product as a yellow solid (2.2 g, 82 %). **HRMS** (ESI+): m/z Calc. for $C_{13}H_{20}N_2O_5$ ($[M+H]^+$): 285.1376, found 285.1446 (1.42 ppm). **^{1}H NMR** (500 MHz, DMSO-d_6) δ 8.74 – 8.53 (t, 1H), 6.89 (d, *J* = 5.7 Hz, 1H), 4.63 (q, *J* = 6.5 Hz, 2H), 3.49 – 3.43 (m, 1H), 3.30 (d, *J* = 7.8 Hz, 1H), 3.08 (q, J = 6.1 Hz, 2H),(1.35 (s, 12H). **^{13}C NMR** (125 MHz, DMSO-d_6) δ 189.7, 182.7, 176.9, 173.2, 156.1, 78.3, 69.2, 44.6, 44.2, 40.8, 28.7, 16.2. **IR (ATR)**: ν_{max} (cm^{-1}) = 3232, 2970, 1698, 1686, 1598, 1538, 1335, 1286, 1248, 1163, 1095, 1051, 980, 855, 610.

(2-((2-((tert-butoxycarbonyl)amino)ethyl)amino)-3,4-dioxocyclobut-1-en-1-yl)-L-alanine

(2.12 (Ala))

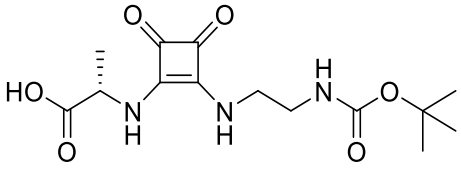

Compound **2.12 (Ala)** was synthesised as per **General method A** and was purified by flash chromatography in 0 - 30 % EtOH: DCM as eluent to afford the title compound as a white powder in a 64 % yield. **^{1}H NMR** (500 MHz, DMSO-d_6) δ 13.08 (s, 1H), 7.74 (s, 1H), 7.54 (s, 1H), 6.93 (t, *J* = 5.1 Hz, 1H), 4.63 (s, 1H), 3.52 (s, 2H), 3.09 (q, *J* = 5.9 Hz, 2H), 1.41 (d, *J* = 7.2 Hz, 3H), 1.36 (s, 9H). **^{13}C NMR** (126 MHz, DMSO-d_6) δ 183.2, 182.8, 174.1, 168.6, 167.4, 156.2, 78.3, 51.7, 43.6, 41.6, 28.7, 20.4. **IR (ATR):** v_{max} (cm^{-1}) = 3170, 2980, 1646, 1551, 1473, 1446, 1366, 1280, 1245, 1161, 651.

(2-((2-((tert-butoxycarbonyl)amino)ethyl)amino)-3,4-dioxocyclobut-1-en-1- yl)-L-phenylalanine

(2.12 (Phe))

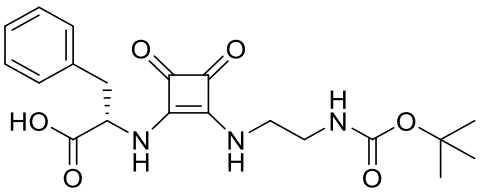

Compound **2.12 (Phe)** was synthesised as per **General method A** and was purified by flash chromatography in 0 - 30 % EtOH: DCM as eluent to afford the title compound as a Beige powder in a 45 % yield. **HRMS** (ESI+): m/z Calc. for $C_{20}H_{25}N_3O_6$ ($[M+H]^+$): 404.1755, found 404.1828 (2.86 ppm) **^{1}H NMR** (500 MHz, DMSO-d_6) δ 13.20 (s, 1H), 7.66 (s, 1H), 7.57 (s, 1H), 7.29 (t, *J* = 7.2 Hz, 2H), 7.22 (t, *J* = 7.2 Hz, 1H), 7.18 (d, *J* = 7.2 Hz, 2H), 6.92 (s, 1H), 4.92 (s, 1H), 3.50 (s, 2H), 3.16 (d, *J* = 9.6 Hz, 1H), 3.07 (q, *J* = 4.1 Hz, 2H), 3.02 (dd, *J* = 9.6 Hz, 1H), 1.36 (s, 9H). **^{13}C NMR** (126 MHz, DMSO-d_6) δ 183.3, 182.7, 172.7, 168.6, 167.3, 156.2, 136.7, 129.8, 128.8, 127.2, 78.3, 57.2, 43.5, 41.6, 39.7, 28.7. **IR (ATR)**: v_{max} (cm^{-1}) = 3300, 2980, 1741, 1651, 1570, 1520, 1449, 1364, 1277, 1164, 698, 605.

(2-((2-((tert-butoxycarbonyl)amino)ethyl)amino)-3,4-dioxocyclobut-1-en-1- yl)-L-leucine

(2.12 (Leu)):

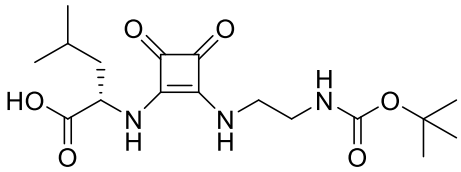

Compound **2.12 (Leu)** was synthesised as per **General method A** and was purified by flash chromatography in 0 - 30 % EtOH: DCM as eluent to afford the title compound as a white powder in a 76 % yield. **HRMS** (ESI+): m/z Calc. for $C_{17}H_{27}N_3O_6$ ($[M+H]^+$): 370.1911, found 370.1983 (3.13 ppm) **^{1}H NMR** (500 MHz, DMSO-d_6) δ 13.05 (s, 1H), 7.67 (s, 1H), 7.45 (s, 1H), 6.94 (s, 1H), 4.67 (s, 1H), 3.53 (s, 2H), 3.12 – 3.07 (q, 2H), 1.64 (d, *J* = 4.5 Hz, 1H), 1.64 – 1.57 (m, 2H), 1.36 (s, 9H), 0.90 (dd, *J* = 6.3 Hz, 6H). **^{13}C NMR** (126 MHz, DMSO-d_6) δ 183.2, 182.2, 174.0, 168.2, 158.4, 54.6, 43.9, 42.4, 41.6, 28.7, 24.7, 23.3. **IR (ATR)**: ν_{max} (cm^{-1}) = 3280, 2980, 1648, 1544, 1457, 1365, 1250, 1162.

N6 -((benzyloxy)carbonyl)-N2 -(2-((2-((tertbutoxycarbonyl)amino)ethyl)amino)-3,4-dioxocyclobut-1-en-1-yl)-L-lysine

(2.12 (Lys(Cbz))

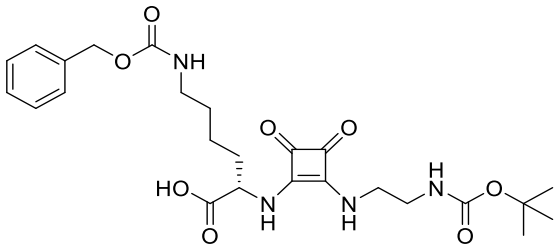

Compound **2.12 (Lys(Cbz))** was synthesised as per **General method A** and was purified by flash chromatography in 0 - 30 % EtOH: DCM as eluent to afford the title compound as a yellow powder in a 78 % yield. **HRMS** (ESI+): m/z Calc. for $C_{25}H_{34}N_4O_8$ ($[M+H]^+$): 519.2389, found 519.2461 (2.44 ppm) **^{1}H NMR** (500 MHz, DMSO-d_6) δ 12.94 (s, 1H), 7.72 (s, 1H), 7.53 (s, 1H), 7.36 (s, 2H), 7.34 (s, 1H), 7.33 (s, 2H), 7.24 (s, 1H), 6.92 (s, 1H), 4.99 (s, 2H), 4.63 (s, 1H), 3.52 (q, 2H), 3.10 (q, 2H), 2.97 (m, 2H), 1.75 (dm , 2H), 1.42 (m, 2H), 1.36 (s, 9H), 1.34 (m, 2H). **^{13}C NMR** (126 MHz, DMSO-d_6) δ 182.9, 182.4, 173.2, 168.2, 167.2, 156.2, 155.9, 137.4, 128.5, 127.8, 127.4, 78.0, 65.3, 55.6, 43.3, 41.2, 40.2, 33.2, 29.1, 28.3, 15.3. **IR (ATR):** ν_{max} (cm^{-1}) = 3290, 2930, 1670, 1582, 1522, 1456, 1364, 1246, 1142, 735, 696, 606.

(S)-4-(benzyloxy)-2-((2-((2-((tert-butoxycarbonyl)amino)ethyl)amino)-3,4-dioxocyclobut-1-en-1-yl)amino)-4-oxobutanoic acid

(2.12 (Asp(Bn))

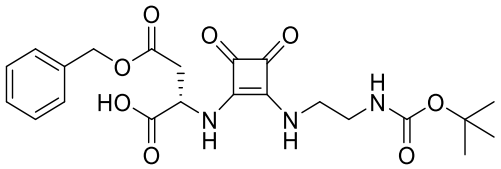

Compound **2.12 (Asp(Bn))** was synthesised as per **General method A** and was purified by flash chromatography in 0 - 30 % EtOH: DCM as eluent to afford the title compound as a yellow powder in an 80 % yield. **HRMS** (ESI+): m/z Calc. for $C_{22}H_{27}N_3O_8$ ($[M+H]^+$): 462.1809, found 462.1882 (2.37 ppm) **^{1}H NMR** (500 MHz, DMSO-d_6) δ 8.87 (s, 1H), 8.05 (s, 1H), 7.33 (d, *J* = 7.2 Hz, 2H), 7.32 (m, 2H), 7.31 – 7.27 (m, 1H), 7.25 (s, 1H), 5.02 (s, 2H), 4.59 (s, 1H), 3.52 (m, 2H), 2.93 (q, *J* = 7.1 Hz, 3H), 2.83 (dd, *J* = 6.6 Hz, 2H), 1.35 (s, 9H). **^{13}C NMR** (126 MHz, DMSO-d_6) δ 183.1, 182.7, 172.9, 170.8, 168.5, 167.8, 156.2, 136.7, 128.8, 128.3, 128.2, 78.1, 65.8, 55.0, 43.6, 41.4, 40.0, 28.7. **IR (ATR):** ν_{max} (cm^{-1}) = 3255, 2980, 1668, 1584, 1521, 1389, 1248, 1163, 736, 696.

(3S,14S)-3,14-dimethyl-2,5,8,13,16,19-hexaazatricyclo[18.2.0.09,12]docosa1(20),9(12)-diene-4,10,11,15,21,22-hexaone

(2.14 (Sq-2-Ala))

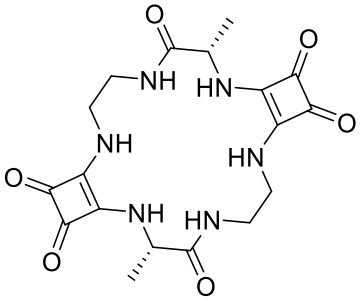

Compound **2.14** was synthesised as per **General method B** to afford the title compound as a beige powder in a 34 % yield. **HRMS** (ESI+): m/z Calc. for $C_{18}H_{22}N_6O_6$ ($[M+H]^+$): 419.1608, found 419.1681 (1.68 ppm). **^{1}H NMR** (500 MHz, DMSO-d_6) δ 8.06 (s, 2H), 7.54 (s, 2H), 7.17 (s, 2H), 4.54 (s, 2H), 3.78 (d, 3H), 2.88 (s, 2H), 1.24 (dd, *J* = 5.4 Hz, 6H). **^{13}C NMR** (126 MHz, DMSO-d_6) δ 183.0, 182.1, 172.4, 168.8, 168.3, 52.4, 44.0, 39.0, 20.6. **IR (ATR):** ν_{max} (cm^{-1}) = 3260, 2960, 1648, 1540, 1437, 1349, 647.

(3S,14S)-3,14-dibenzyl-2,5,8,13,16,19-hexaazatricyclo[18.2.0.09,12]docosa1(20),9(12)-diene-4,10,11,15,21,22-hexaone

(2.15 (Sq-2-Phe))

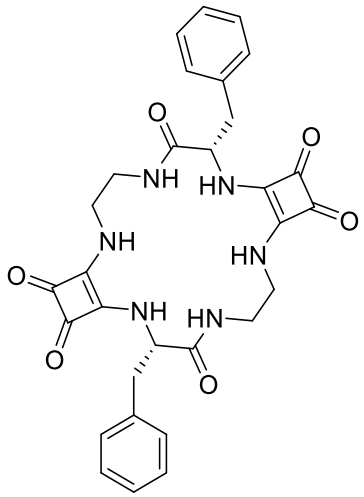

Compound **2.15** was synthesised as per **General method B** to afford the title compound as a beige powder in a 46 % yield. **HRMS** (ESI+): m/z Calc. for $C_{30}H_{30}N_6O_6$ ($[M+H]^+$): 571.2235, found 571.2309 (1.38 ppm). **^{1}H NMR** (500 MHz, DMSO-d_6) δ 8.10 (s, 2H), 7.53 (d, J = 7.1 Hz, 1H), 7.23 (t, *J* = 7.2 Hz, 10H), 7.05 (s, 1H), 4.72 (s, 2H), 3.76 (d, *J* = 7.3 Hz, 2H), 2.97 (s, 2H), 2.83 (s, 2H), 2.74 (s, 1H). **^{13}C NMR** (126 MHz, DMSO-d_6) δ 182.0, 181.2, 171.9, 168.5, 167.7, 137.5, 129.7, 128.6, 126.9, 58.0, 44.1, 38.9, 38.9. **IR (ATR)**: ν_{max} (cm^{-1}) = 3320, 3120, 2960, 1685, 1648, 1538, 1465, 1348, 745, 695.

(3S,14S)-3,14-diisobutyl-2,5,8,13,16,19- hexaazatricyclo[18.2.0.09,12]docosa-1(20),9(12)-diene-4,10,11,15,21,22- hexaone

(2.16 (Sq-2-Leu))

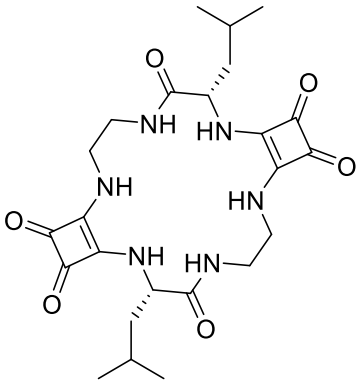

Compound **2.16** was synthesised as per **General method B** to afford the title compound as a beige powder in a 26 % yield. **HRMS** (ESI+): m/z Calc. for $C_{24}H_{34}N_6O_6$ ($[M+H]^+$): 503.2548, found 503.2621 (1.61 ppm). **^{1}H NMR** (500 MHz, DMSO-d_6) δ 8.13 (d, *J* = 7.5 Hz, 1H), 7.46 (d, *J* = 7.2 Hz, 1H), 7.08 (d, *J* = 7.0 Hz, 1H), 4.52 (q, *J* = 7.9 Hz, 2H), 3.87 (q, *J* = 10.4 Hz, 1H), 3.75 (q, J = 9.1 Hz, 1H), 2.82 (d, *J* = 13.1 Hz, 1H), 1.60 – 1.47 (m, 3H), 1.42 (s, 3H), 0.86 (dd, J = 6.1 Hz, 12H). **^{13}C NMR** (126 MHz, DMSO-d_6) δ δ 55.4, 44.2, 42.5, 24.6, 23.5, 22.1. **IR (ATR)**: ν_{max} (cm^{-1}) = 3340, 3170, 2960, 1790, 1683, 1645, 1539, 1463, 1349, 1275.

(3S,14S)-3,14-bis(4-aminobutyl)-2,5,8,13,16,19-hexaazatricyclo[18.2.0.0^{9,12}]docosa-1(20),9(12)-diene-4,10,11,15,21,22-hexaone

(2.17 (Sq-2-Lys))

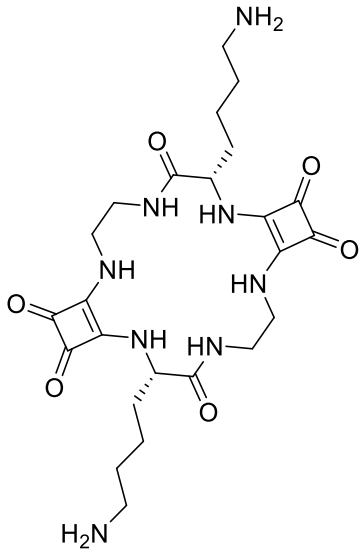

Compound **2.18** was synthesised as per **General method B** to afford the title compound as a beige powder in a 34 % yield. The resulting benzyl protected groups were deprotected in a HBr 33 % wt AcOH solution (3 mL) which was stirred for 20 min before being filtered and triturated in diethyl ether. The mixture was added to a falcon tube and centrifuged under 4000 RPM for 5 min (3x Diethyl Ether). The supernatant was dispelled, and the precipitate was dissolved in 50:50 MeCN/H_2O and lyophilized to yield the title compound as a beige powder in a 89 % yield. min) t_R = 26 min. **HRMS** (ESI+) m/z: Calc. for $C_{24}H_{36}N_8O_6$ ([M+H]$^+$): 533.2756, Found: 533.2828 (-0.33 ppm). **^{1}H NMR** (500 MHz, DMSO-d_6) δ 8.08 (s, 2H), 7.71 (s, 6H), 7.61 (s, 2H), 7.28 (s, 2H), 4.46 (s, 2H), 3.82 (d, *J* = 40.5 Hz, 4H), 2.89 (s, 2H), 2.75 (s, 5H), 1.66 (s, 2H), 1.53 (s, 7H), 1.29 (s, 5H). **^{13}C NMR** (126 MHz, DMSO-d_6) δ 182.9, 181.8, 171.8, 168.2, 166.7, 165.5, 158.7, 158.5, 148.9, 56.5, 49.5, 44.0, 40.8, 40.4, 40.4, 40.3, 40.2, 40.1, 39.9, 39.8, 39.1, 33.4, 27.1, 27.1, 22.4. **IR (ATR):** ν_{max}(cm^{-1}) = 2948, 1803, 1669, 1600, 1542, 1463, 1433, 1346, 1284, 1198, 1129, 836, 799, 720, 597, 517.

Dibenzyl 2,2'-((3S,14S)-4,10,11,15,21,22-hexaoxo-2,5,8,13,16,19-hexaazatricyclo [18.2.0.09,12]docosa-1(20),9(12)-diene-3,14-diyl)diacetate

(2.18 (Sq-2-Asp(Bn))

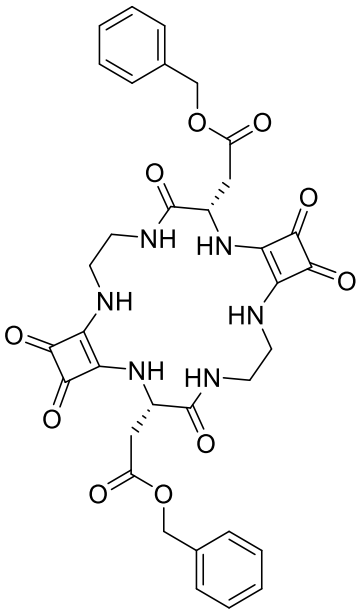

Compound **2.18** was synthesised as per **General method B** to afford the title compound as a beige powder in a 34 % yield. **HRMS** (ESI+): m/z Calc. for $C_{34}H_{34}N_6O_6$ ($[M+H]^+$): 687.2338 , found 687.2411 (0.22 ppm). **^{1}H NMR** (500 MHz, DMSO-d_6) δ 7.83 (s, 2H), 7.57 (s, 2H), 7.34 (m, 11H), 7.10 (s, 1H), 5.07 (d, 4H), 4.91 (m, 2H), 3.58 (m, 4H), 3.23 (m, 2H), 2.99 (m, 2H), 2.78 (dd, *J* = 8.2 Hz, 2H). **^{13}C NMR** (126 MHz, DMSO-d_6) δ 183.4, 181.0, 172.0, 170.6, 170.2, 167.4, 167.1, 136.4, 128.8, 128.5, 128.3, 66.3, 53.8, 43.0, 40.6, 37.7. **IR (ATR)**: ν_{max} (cm^{-1}) = 3325, 3135, 2828, 1726, 1684, 1647, 1548, 1455, 1431, 1354, 1305, 1270, 1166, 753, 699.

7.3: General Procedures for Solid Phase Peptide Synthesis (SPPS)

(A): Loading of First Amino Acid Residue

2-chlorotrityl chloride resin (*FluoroChem*) was weighed out into a 20 mL fritted-syringe. The resin was suspended in DCM (10 mL) and allowed to swell for ~1 hour. After this time, a solution of Fmoc amino-acid and DIPEA in DCM was added to the resin. The resin was let to shake for 2 hours. The resin was capped by treatment of *3x* DCM/MeOH/DIPEA (17:2:1) for ~ 5 mins then washed *3x* DCM, *3x* DMF, *3x* DCM, before being dried *in vacuo.*

Dry Fmoc amino-acid resin (approx. 5 µmol with respect to Fmoc) was weighed into two separate 10 mL volumetric flasks. 2 mL of 10% piperidine sol. (in DMF) was added and gently agitated for 30 minutes. The solution(s) were diluted to 10 mL with MeCN. 2 mL of each of solution was transferred to two individual 25 mL volumetric flasks and diluted to the mark again with MeCN (solution 1 and solution 2, i.e. Duplicate). A reference solution was prepared in a similar manner as above, but without the addition of resin. Each cuvette was filled by taking 2.5 mL of each sample (Sol. 1, Sol. 2 & Ref.), before being placed into the spectrophotometer. The absorbance of each sample was recorded at 304 nm, and an estimate of first residue attachment was obtained from the following equation:

$$Fmoc\ Loading: mmol\ g^{-1} = \left(Abs_{sample(average)} - Abs_{Ref}\right) x \left(\frac{16.4}{mg\ of\ resin_{(average)}}\right)$$

(B): Sequential Amino Acid Coupling

The Fmoc amino-acid resin was swelled in DCM for ~30 before being subjected to Fmoc-deprotection. The resin was treated with *3x* 20% Piperidine sol. (DMF) for ~5 minutes followed by subsequent washing with *3x* DMF, *3x* DCM and *3x* DMF. A solution of Fmoc-AA, PyBOP and NMM in DMF was added to the resin and allowed to shake for 90 minutes. The new AA-resin was then washed with *3x* DCM, *3x* DMF and *3x* DCM, before being dried *in vacuo*.

(C): Addition of Diethyl Squarate to the resin

The Fmoc amino-acid resin was swelled in DCM for ~30 before being subjected to Fmoc-deprotection. The resin was treated with *3x* 20% Piperidine sol. (DMF) for ~5 minutes followed by subsequent washing with *3x* DMF, *3x* DCM and *3x* DMF. The peptide resin was treated with a solution of DeSq (408 µl, 2.76 mmol, 8 eq.) and TEA (240 µl, 1.72 mmol, 5 eq.) in DMF (10 mL) for 5 hrs. LC-MS indicated complete consumption of starting material. The new resin was washed with *3x* DCM, *3x* DMF and *3x* DCM

(D): Addition of ethylenediamine to the resin

The peptide resin was treated with a solution of EDA (576 µl, 8.62 mmol, 25 eq.) in DMF (8 mL) for 2 hrs. LC-MS indicated complete consumption of starting material. The new resin was washed with *3x* DCM, *3x* DMF and *3x* DCM.

(E): Cleavage of amino acid sequence from resin

A spatula tip amount of dry Fmoc-AA resin was placed into a glass vial and treated with a 30% HFIP/DCM solution (1 mL) for 90 minutes (with gentle agitation). After this time, the *cleavage solution* and resin were filtered through a glass pasteur pipette fitted with cotton wool. The HFIP/DCM was removed from the filtrate via evaporation with a stream of compressed nitrogen gas. The residue that remained was redissolved in MeCN / H_2O (50:50) prior to LC-MS analysis.

(F): Global Resin cleavage

The peptide resin was treated with a 30% HFIP/DCM solution (3 mL) for 90 minutes (with gentle agitation). the cleavage solution was emptied to a small glass vial and evaporated with compressed air. The residue that remained was dissolved in MeCN / H_2O (50:50) and lyophilized to afford the desired protected linear squaratide.

(G): Cyclisation of linear protected squaratides

The protected linear Squaratide (0.33 mmol) was dissolved in a minimal amount of DMF. NMM (2.0 mmol) was added, and the solution was stirred for 10 mins. The solvent volume was increased to give a final concentration of 3.5 mM. To this solution PyBOP (1.0 mmol) was added and the solution was allowed to stir for 48 hrs. Reaction progress

was monitored via LC-MS. At the end of this time, the DMF was removed in vacuo and the crude mixture was triturated in ethyl acetate. The mixture was added to a falcon tube and centrifuged at 4000 RPM for 10 min (2 x ethyl acetate and 1x diethyl ether). The supernatant was dispelled, and the precipitate was dissolved in 50:50 MeCN/H_2O and lyophilized to afford the cyclic protected squaratide.

(H): Boc deprotection of squaratides

Protected cyclic peptide was dissolved in 50:50 TFA/DCM (4 mL) and allowed to stir at r.t.p for 3 hours. LC-MS indicated the complete consumption of starting material. Thus, the TFA/DCM was evaporated. The resulting oil was re-dissolved in a minimum amount of MeOH, before being added dropwise to cold diethyl ether. The precipitate was filtered, then re-dissolved in a 50:50 solution containing MeCN/H_2O and lyophilized to afford the final deprotected product

7.4: Synthetic methods – Chapter 3

Sq-K(boc)-2-Cl-Trt (A)

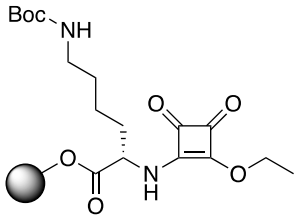

First residue loading (Fmoc-Lys(Boc)-OH) was performed as outlined in general procedures **A** and **C**. LC-MS indicated complete consumption of starting material, the resin was washed with *3x* DCM, *3x* DMF and *3x* DCM. **LC-MS** (0-100%) gradient of A in B, 55 min) t_R = 28 mins

EDA-Sq-K(boc)-2-Cl-Trt (B)

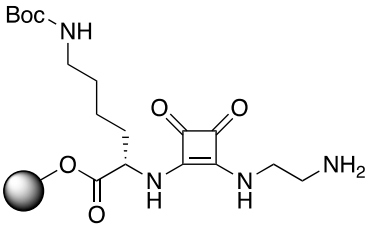

EDA-Sq-K(boc)-2-Cl-Trt was synthesised as outlined General procedures **D**. LC-MS indicated complete consumption of starting material the resin was washed with *3x* DCM, *3x* DMF and *3x* DCM. **LC-MS** (0-100%) gradient of A in B, 55 min) t_R = 24 mins

EDA-Sq-K(boc)-EDA-Sq-K(boc)-OH

ASq-2-Lys(Boc)

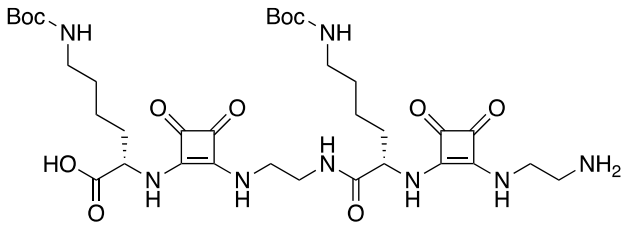

(Asq-2-Lys(Boc)) was synthesised as outlined in general procedures (**B,C,D**) followed by resin removal via 30% HFIP/DCM (General Procedure **F**) to afford the linear Squaratide (Asq-2-Lys(Boc)) as an off-white solid – without further purification. **LC-MS** (0-100%) gradient of A in B, 55 min) t_R = 27 min. **HRMS** (ESI+) m/z: Calc. for $C_{34}H_{54}N_8O_{11}$ ($[M+H]^+$): 751.3904, Found: 751.3978 (-1.09 ppm). **^{1}H NMR** (500 MHz, DMSO-d_6) δ 9.11 – 7.58 (m, 5H), 6.54 (d, *J* = 180.1 Hz, 2H), 5.16 (dt, *J* = 13.6, 6.8 Hz, 1H), 4.61 (d, *J* = 43.8 Hz, 1H), 4.33 (s, 1H), 4.04 (d, *J* = 6.3 Hz, 1H), 3.78 (s, 1H), 3.71 (s, 2H), 3.36 (s, 10H), 3.03 (dd, *J* = 11.8, 5.9 Hz, 2H), 2.91 – 2.81 (m, 4H), 1.66 (ddd, *J* = 21.0, 19.5, 7.1 Hz, 4H), 1.36 (s, 18H), 1.30 – 1.15 (m, 4H). **^{13}C NMR** (126 MHz, DMSO-d_6) δ 183.4, 183.3, 182.8, 182.7, 169.4, 168.9, 156, 77.8, 77.7, 68.2, 67.9, 67.7, 67.4, 41.7, 29.8, 29.6, 28.7, 28.5, 23.1, 22.9, 22.6.

EDA-Sq-K(boc)-EDA-Sq-K(boc)-EDA-Sq-K(boc)-OH

ASq-3-Lys(Boc)

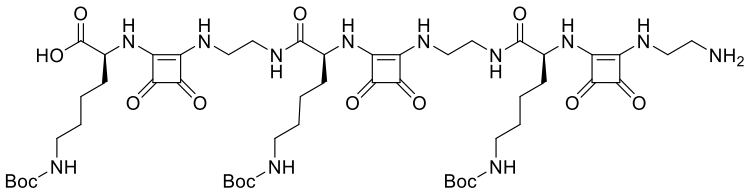

(Asq-3-Lys(Boc)) was synthesised as outlined in general procedures (**B,C,D**) followed by resin removal via 30% HFIP/DCM (General Procedure **F**) to afford the linear Squaratide (Asq-3-Lys(Boc)) as an off-white solid – without further purification. **LC-MS** (0-100%) gradient of A in B, 55 min) t_R = 28 min. **HRMS** (ESI+) m/z: Calc. for $C_{51}H_{80}N_{12}O_{16}$ ($[M+H]^+$): 1117.5776, Found: 1117.5855 (-3.47 ppm). **^{1}H NMR** (500 MHz, DMSO-d_6) δ 8.48 (s, 1H), 7.84 (dd, *J* = 133.6, 75.7 Hz, 8H), 6.78 – 6.64 (m, 3H), 6.36 (s, 1H), 5.17 (dt, *J* = 13.6, 6.8 Hz, 1H), 4.59 (s, 2H), 4.34 (d, *J* = 1.4 Hz, 1H), 4.02 (d, *J* = 3.5 Hz, 1H), 3.73 (d, *J* = 5.9 Hz, 2H), 3.60 (dd, *J* = 3.5, 1.2 Hz, 2H), 3.54 (dd, *J* = 13.0, 7.4 Hz, 2H), 3.10 – 2.99 (m, 3H), 2.87 (dd, *J* = 14.8, 8.9 Hz, 8H), 1.74 (dd, *J* = 16.1, 5.9 Hz, 4H), 1.67 – 1.52 (m, 4H), 1.36 (s, 27H), 1.28 – 1.18 (m, 6H). **^{13}C NMR** (126 MHz, DMSO-d_6) δ 183, 182.8, 182.6, 182.4, 156, 155.9, 77.8, 77.7, 67.7, 49.5, 41.5, 31.1, 29.8, 29.7, 28.7, 28.6, 22.9, 22.6, 22.5.

EDA-Sq-K(boc)-EDA-Sq-K(boc)-EDA-Sq-K(boc)-EDA-Sq-K(boc)-OH

ASq-4-Lys(Boc)

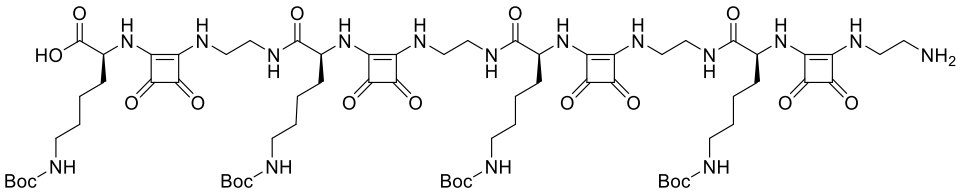

(Asq-4-Lys(Boc)) was synthesised as outlined in general procedures (**B,C,D**) followed by resin removal via 30% HFIP/DCM (General Procedure **F**) to afford the linear Squaratide (Asq-4-Lys(Boc)) as an off-white solid – without further purification. LC-MS (0-100%) gradient of A in B, 55 min) t_R = 28 min. **HRMS** (ESI+) m/z: Calc. for $C_{68}H_{106}N_{16}O_{21}$ ($[M+H]^+$): 1483.7667, Found: ($[M+2Na]^{+2}$): 764.3740 (-3.47 ppm). **^{1}H NMR** (500 MHz, DMSO-d_6) δ 8.53 (s, 1H), 8.39 – 7.52 (m, 10H), 6.90 (s, 1H), 6.81 – 6.61 (m, 4H), 6.52 (s, 1H), 6.37 (s, 1H), 5.17 (dt, *J* = 13.6, 6.8 Hz, 1H), 4.78 (s, 1H), 4.61 (s, 3H), 4.35 (s, 1H), 4.04 (d, *J* = 5.7 Hz, 1H), 3.90 (s, 1H), 3.72 (s, 3H), 3.56 (s, 9H), 3.18 (s, 4H), 3.07 – 3.01 (m, 3H), 2.90 – 2.81 (m, 8H), 2.68 (dd, *J* = 19.0, 5.2 Hz, 1H), 2.34 – 2.28 (m, 1H), 1.82 – 1.57 (m, 8H), 1.51 (d, *J* = 32.2 Hz, 8H), 1.36 (s, 36H), 1.20 (d, *J* = 31.2 Hz, 8H). **^{13}C NMR** (126 MHz, DMSO-d_6) δ 183.2, 183, 182.6, 182.4, 156, 148.8, 77.8, 67.7, 29.7, 28.7, 22.6, 22.5, 22.3.

EDA-Sq-K(boc)-EDA-Sq-K(boc)-EDA-Sq-K(boc)-EDA-Sq-K(boc)-EDA-Sq-K(boc)-OH

ASq-5-Lys(Boc)

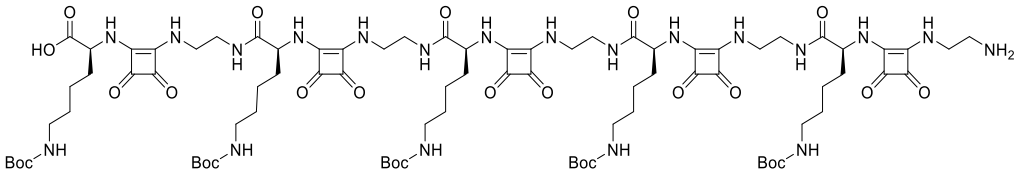

(Asq-5-Lys(Boc)) was synthesised as outlined in general procedures (**B,C,D**) followed by resin removal via 30% HFIP/DCM (General Procedure **G**) to afford the linear Squaratide (Asq-5-Lys(Boc)) as an off-white solid – without further purification. **LC-MS** (0-100%) gradient of A in B, 55 min) t_R = 29 min. **HRMS** (ES+) m/z: Calc. for $C_{85}H_{132}N_{20}O_{26}$ ($[M+H]^+$): 1849.9573, Found: ($[M+3Na]^{+3}$): 639.9516 (-2.65 ppm). **^{1}H NMR** (500 MHz, DMSO-d_6) δ 8.54 (s, 2H), 8.40 – 7.62 (m, 11H), 6.73 (d, *J* = 5.6 Hz, 4H), 6.37 (s, 1H), 5.17 (dt, *J* = 13.6, 6.8 Hz, 2H), 4.61 (s, 3H), 4.35 (d, *J* = 4.8 Hz, 1H), 4.03 (d, *J* = 4.1 Hz, 1H), 3.70 (s, 3H), 3.57 (dd, *J* = 24.6, 2.6 Hz, 6H), 3.36 (s, 18H), 3.29 (s, 7H), 3.02 (t, *J* = 5.9 Hz, 2H), 2.93 – 2.80 (m, 10H), 1.69 (d, *J* = 6.6 Hz, 4H), 1.60 (dd, *J* = 13.6, 8.4 Hz, 4H), 1.36 (s, 45H), 1.23 (s, 10H). **^{13}C NMR** (126 MHz, DMSO-d_6) δ 183.2, 183.0, 182.5, 181.7, 156, 148.9, 77.8, 76, 67.9, 67.7, 67.4, 49.5, 29.7, 28.7, 28.5, 22.4, 22.3.

Sq-2-Lys(Boc)

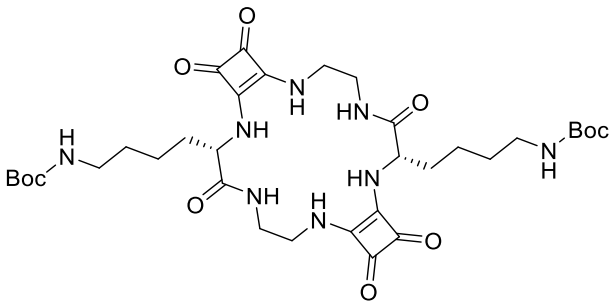

The Linear Squaratide was subjected to cyclisation which was carried out as described in the General procedures for SPPS (**G**) to afford the Cyclic protected product **(Sq-2-Lys(Boc))** as an off-white solid. (100 mg, 65 %). **LC-MS** (0-100%) gradient of A in B, 55 min) t_R = 28 min. **HRMS** (ESI+) m/z: Calc. for $C_{34}H_{52}N_8O_{10}$ ($[M+H]^+$): 733.3789, Found: 733.3862 (-2.32 ppm). **^{1}H NMR** (500 MHz, DMSO-d_6) δ 8.12 (d, *J* = 7.6 Hz, 1H), 7.76 (s, 1H), 7.67 (s, 1H), 7.50 (d, *J* = 9.1 Hz, 1H), 7.16 (d, *J* = 9.0 Hz, 1H), 6.76 (t, *J* = 5.4 Hz, 2H), 6.40 (s, 1H), 4.65 (d, *J* = 31.8 Hz, 1H), 4.52 – 4.39 (m, 1H), 3.87 (dd, *J* = 22.0, 10.2 Hz, 1H), 3.78 (dd, *J* = 22.3, 11.8 Hz, 1H), 3.65 – 3.46 (m, 1H), 3.29 (d, *J* = 9.4 Hz, 1H), 3.02 (dd, *J* = 8.5, 4.6 Hz, 1H), 2.85 (dd, *J* = 12.4, 6.4 Hz, 5H), 1.60 (d, *J* = 6.1 Hz, 2H), 1.47 (d, *J* = 11.2 Hz, 2H), 1.36 (s, 18H), 1.26 – 1.13 (m, 4H). **^{13}C NMR** (126 MHz, DMSO-d_6) δ 182.8, 181.7, 172, 168.1, 156.0, 77.7, 56.6, 44.1, 40.3, 40.2, 38.7, 33.8, 29.5, 28.7, 22.6.

(2.17) Sq-2-Lys

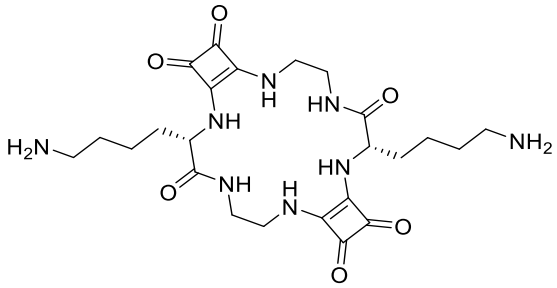

The protected cyclic squaratide Sq-2-Lys(Boc) was subjected to Boc deprotection via 50:50 TFA/DCM as outlined in general procedures for SPPS (**H**) to afford the final deprotected product **(Sq-2-Lys)** as an off-white solid (43 mg, 87 %). LC-MS (0-100%) gradient of A in B, 55 min) t_R = 9 min. **HRMS** (ESI) m/z: Calc. for $C_{24}H_{36}N_8O_6$ ($[M+H]^+$): 533.2756, Found: 533.2828 (-0,33 ppm). **^{1}H NMR** (500 MHz, DMSO-d_6) δ 8.08 (s, 2H), 7.71 (s, 6H), 7.61 (s, 2H), 7.28 (s, 2H), 4.46 (s, 2H), 3.82 (d, *J* = 40.5 Hz, 4H), 2.89 (s, 2H), 2.75 (s, 5H), 1.66 (s, 2H), 1.53 (s, 7H), 1.29 (s, 5H). **^{13}C NMR** (126 MHz, DMSO-d_6) δ 182.9, 181.8, 171.8, 168.2, 166.7, 165.5, 158.7, 158.5, 148.9, 56.5, 49.5, 44.0, 40.8, 40.4, 40.3, 40.2, 40.1, 39.9, 39.8, 39.1, 33.4, 27.1, 22.4. **IR (ATR):** v_{max}(cm^{-1}) = 2948, 1803, 1669, 1600, 1542, 1463, 1433, 1346, 1284, 1198, 1129, 836, 799, 720, 597, 517.

Sq-3-Lys(Boc)

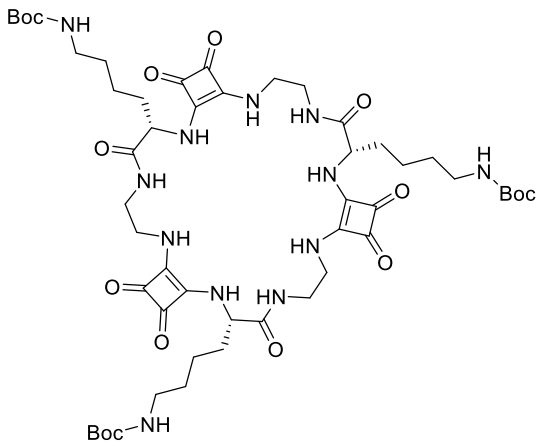

The Linear Squaratide was subjected to cyclisation which was carried out as described in the General procedures for SPPS (**G**) to afford the Cyclic protected product **(Sq-3-Lys(Boc))** as an off-white solid. (100 mg, 61 %). **LC-MS** (0-100%) gradient of A in B, 55 min) t_R = 28 min. **HRMS** (ESI+) m/z: Calc. for $C_{51}H_{78}N_{12}O_{15}$ ($[M+H]^+$): 1099.5676, Found: 1099.5750 (-3.06 ppm). **^{1}H NMR** (500 MHz, DMSO-d_6) δ 8.51 (s, 1H), 8.29 (s, 1H), 8.15 – 7.90 (m, 1H), 7.67 (dt, *J* = 49.9, 19.1 Hz, 4H), 7.45 – 7.16 (m, 1H), 6.74 (dd, *J* = 13.4, 8.0 Hz, 3H), 6.39 (s, 1H), 4.62 (s, 1H), 4.55 (s, 1H), 4.31 (s, 1H), 4.15 (s, 1H), 3.97 (s, 1H), 3.72 – 3.49 (m, 4H), 3.45 (d, *J* = 6.4 Hz, 1H), 3.29 (s, 3H), 3.02 (dd, *J* = 10.5, 6.6 Hz, 1H), 2.92 – 2.81 (m, 6H), 1.69 (ddd, *J* = 59.1, 28.9, 4.5 Hz, 6H), 1.37 (s, 27H), 1.23 (s, 6H). **^{13}C NMR** (126 MHz, DMSO-d_6) δ 183.0, 182.4, 156, 148.9, 82.6, 77.8, 63.9, 53.0, 49.5, 46.3, 29.7, 28.7, 26.4, 22.3.

(3.5) Sq-3-Lys

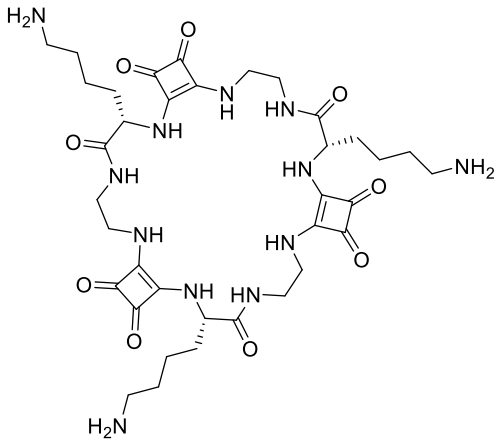

The protected cyclic squaratide Sq-3-Lys(Boc) was subjected to Boc deprotection via 50:50 TFA/DCM as outlined in general procedures for SPPS (**H**) to afford the final deprotected product **(Sq-3-Lys)** as an off-white solid (60 mg, 89 %). **LC-MS** (0-100%) gradient of A in B, 55 min) t_R = 9 min. **HRMS** (ESI+) m/z: Calc. for $C_{36}H_{54}N_{12}O_9$ ($[M+H]^+$): 799.4129, Found: 799.4201 (-1.02 ppm). **^{1}H NMR** (500 MHz, DMSO-d_6) δ 8.54 (s, 1H), 8.32 (s, 1H), 7.90 – 7.64 (m, 16H), 4.56 (d, *J* = 47.3 Hz, 2H), 3.62 (s, 3H), 3.54 (s, 2H), 3.27 (s, 3H), 2.77 (d, *J* = 4.8 Hz, 7H), 1.74 (dd, *J* = 12.4, 8.2 Hz, 3H), 1.62 (d, *J* = 7.2 Hz, 3H), 1.55 – 1.49 (m, 6H), 1.31 (d, *J* = 7.0 Hz, 6H). **^{13}C NMR** (126 MHz, DMSO-d_6) δ 158.9, 158.6, 148.7, 99.1, 49.5, 43.4, 40.5, 40.4, 40.3, 40.3, 40.2, 40.1, 39.9, 39.8, 39.1, 31.1, 27.1, 22.3. **IR (ATR):** ν_{max}(cm^{-1}) = 3239, 2941, 1799, 1666, 1588, 1524, 1467, 1431, 1349, 1290, 1197, 1177, 1127, 835, 799, 720, 631, 598, 516, 438.

Sq-4-Lys(Boc)

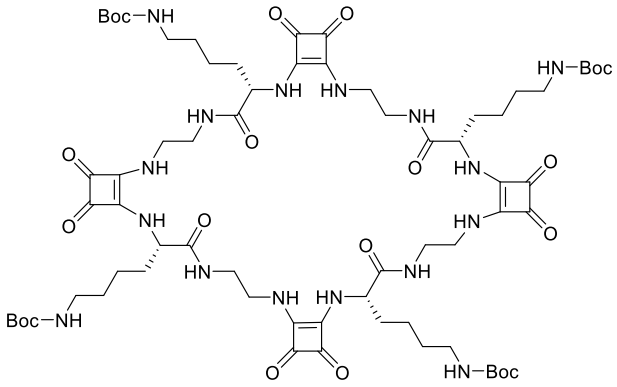

The Linear Squaratide was subjected to cyclisation which was carried out as described in the General procedures for SPPS (**G**) to afford the Cyclic protected product **(Sq-4-Lys(Boc))** as an off-white solid. (150 mg, 49 %). **LC-MS** (0-100%) gradient of A in B, 55 min) t_R = 32 min. **HRMS** (ESI+) m/z: Calc. for $C_{68}H_{104}N_{16}O_{20}$ ($[M+H]^+$): 1465.7596, Found: ($[M+2Na]^{+2}$): 755.3687 (-1.17 ppm). **^{1}H NMR** (500 MHz, DMSO-d_6) δ 8.50 (s, 3H), 8.09 (dd, *J* = 105.6, 48.3 Hz, 2H), 7.67 (dd, *J* = 33.1, 13.6 Hz, 7H), 6.81 – 6.64 (m, 4H), 6.37 (s, 1H), 4.60 (s, 3H), 4.14 (s, 1H), 3.95 (s, 1H), 3.73 – 3.57 (m, 4H), 3.53 (s, 4H), 3.27 (s, 5H), 3.01 (dd, *J* = 8.5, 4.7 Hz, 1H), 2.86 (d, *J* = 4.6 Hz, 8H), 1.75 – 1.52 (m, 8H), 1.35 (s, 45H), 1.21 (d, *J* = 6.2 Hz, 8H). **^{13}C NMR** (126 MHz, DMSO-d_6) δ 183.2, 182.8, 182.3, 156.0, 148.8, 77.8, 49.5, 29.7, 28.7, 22.4.

(3.6) Sq-4-Lys

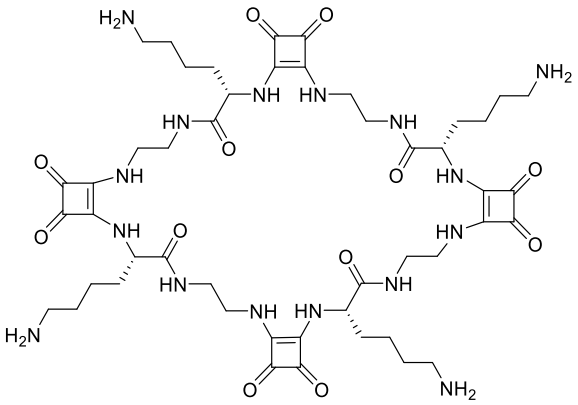

The protected cyclic squaratide Sq-4-Lys(Boc) was subjected to Boc deprotection via 50:50 TFA/DCM as outlined in general procedures for SPPS (**H**) to afford the final deprotected product **(Sq-4-Lys)** as an off-white solid (90 mg, 90 %). **LC-MS** (0-100%) gradient of A in B, 55 min) t_R = 19 min. **HRMS** (ESI+) m/z: Calc. for $C_{48}H_{72}N_{16}O_{12}$ ($[M+H]^+$): 1065.5493, Found: 1065.5580 (-2.12 ppm). **^{1}H NMR** (500 MHz, DMSO-d_6) δ 8.48 (s, 3H), 8.25 (s, 1H), 8.01 (d, *J* = 39.0 Hz, 1H), 7.77 (s, 18H), 4.60 (s, 3H), 4.18 (s, 1H), 3.60 (d, *J* = 45.9 Hz, 8H), 3.30 – 3.13 (m, 5H), 2.83 – 2.69 (m, 8H), 1.70 (d, *J* = 35.4 Hz, 4H), 1.59 (d, *J* = 13.1 Hz, 4H), 1.57 – 1.48 (m, *J* = 5.5 Hz, 8H), 1.30 (d, *J* = 6.1 Hz, 8H). **^{13}C NMR** (126 MHz, DMSO-d_6) δ 158.88, 158.63, 149.1, 116.2, 49.1, 40.4, 40.4, 40.3, 40.2, 40.1, 39.9, 39.8, 39.1, 27.2, 22.1. **IR (ATR):** ν_{max}(cm^{-1}) = 3247, 2940, 1800, 1665, 1588, 1527, 1466, 1430, 1347, 1290, 1197, 1177, 1127, 835, 798, 720, 596, 515, 434.

Sq-5-Lys(Boc)

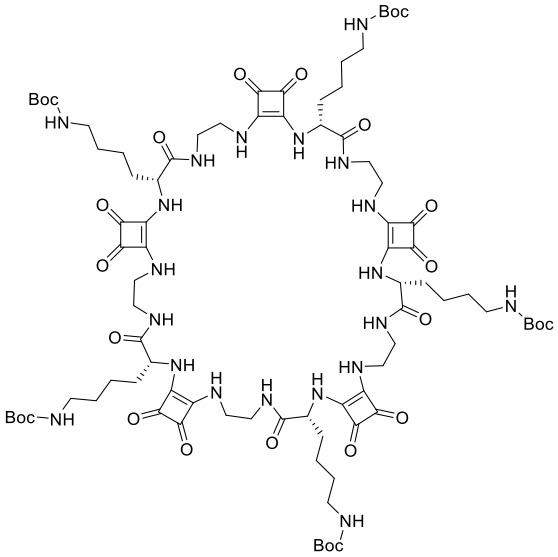

The Linear Squaratide was subjected to cyclisation which was carried out as described in the General procedures for SPPS (**G**) to afford the Cyclic protected product **(Sq-5-Lys(Boc))** as an off-white solid. (150 mg, 48 %). **LC-MS** (0-100%) gradient of A in B, 55 min) t_R = 33.3 min. **HRMS** (ESI+) m/z: Calc. for $C_{85}H_{130}N_{20}O_{25}$ ($[M+H]^+$):1830.9473, Found: ($[M+2Na]^{+2}$): 938.9643 (-2.35 ppm). **^{1}H NMR** (500 MHz, DMSO-d_6) δ 8.49 (s, 3H), 8.31 (s, 1H), 8.03 (dd, *J* = 51.4, 36.9 Hz, 1H), 7.69 (d, *J* = 35.1 Hz, 8H), 6.73 (s, 4H), 6.37 (s, 1H), 4.61 (s, 4H), 4.14 (s, 1H), 3.98 (d, *J* = 14.2 Hz, 1H), 3.62 (d, *J* = 9.0 Hz, 4H), 3.53 (d, *J* = 6.2 Hz, 4H), 3.28 (s, 6H), 3.02 (dd, *J* = 6.5, 2.7 Hz, 1H), 2.85 (t, *J* = 15.2 Hz, 10H), 1.78 – 1.63 (m, 5H), 1.63 – 1.49 (m, 5H), 1.36 (s, 45H), 1.22 (d, *J* = 6.8 Hz, 10H). **^{13}C NMR** (126 MHz, DMSO-d_6) δ 183, 182.6, 168.4, 167.2, 156, 148.8, 77.8, 63.9, 56.5, 53, 43.1, 40.9, 40.5, 40.4, 40.2, 35.1, 29.7, 28.7, 28.5, 22.4.

(3.7) Sq-5-Lys

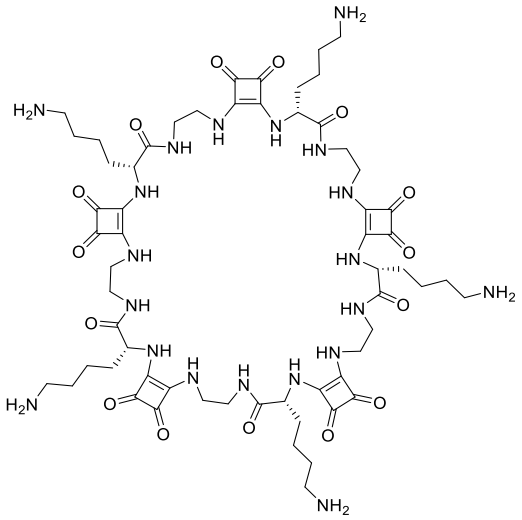

The protected cyclic squaratide Sq-5-Lys(Boc) was subjected to Boc deprotection via 50:50 TFA/DCM as outlined in general procedures for SPPS (**H**) to afford the final deprotected product **(Sq-5-Lys)** as an off-white solid (87 mg, 89 %). **LC-MS** (0-100%) gradient of A in B, 55 min) t_R = 17 min. **HRMS** (ESI+) m/z: Calc. for $C_{60}H_{90}N_{20}O_{15}$ ($[M+H]^+$): 1331.6870, Found: 1331.6957 (-1.81 ppm). **^{1}H NMR** (500 MHz, DMSO-d_6) δ 8.52 (d, *J* = 20.7 Hz, 4H), 8.32 (s, 1H), 8.23 (d, *J* = 15.0 Hz, 1H), 8.07 (s, 1H), 7.82 (dd, *J* = 32.0, 10.6 Hz, 23H), 4.59 (s, 4H), 4.16 (s, 1H), 3.76 – 3.46 (m, 9H), 3.34 – 3.19 (m, 9H), 2.76 (s, 10H), 1.73 (dd, *J* = 7.6, 5.9 Hz, 5H), 1.61 (d, *J* = 6.0 Hz, 5H), 1.52 (d, *J* = 5.2 Hz, 10H), 1.29 (s, 10H). **^{13}C NMR** (126 MHz, DMSO-d_6) δ 159.4, 158.8, 158.1, 148.7, 49.5, 42, 41.8, 41.6, 41.4, 41.3, 41.3, 41.2, 41.1, 40.9, 40.8, 40.7, 40.5, 40.4, 40.3, 40.2, 40.1, 39.9, 39.8, 39.1, 39, 38.8, 38.8, 38.7, 38.5, 38.3, 38.2, 31.1, 30.8, 27.2, 26.5. **IR (ATR):** ν_{max}(cm^{-1}) = 3253, 2942, 1800, 1665, 1587, 1526, 1467, 1431, 1348, 1291, 1197, 1177, 1128, 835, 798, 720, 596, 515, 433, 404.

7.5: Synthetic methods – Chapter 4

3-ethoxy-4-(3,5-bis(trifluoromethyl)phenyl)amino-cyclobut-3-ene-1,2-dione (SqBisCF$_3$)

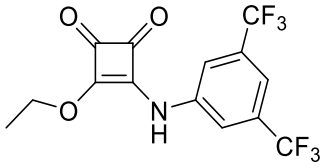

3,5-bis(trifluoromethyl)aniline (1.24 g, 5.4 mmol), was dissolved in 20 mL of ethanol and added to a suspension of diethyl squarate (DeSq) (0.97 g, 5.5 mmol) and zinc trifluoromethanesulfonate (0.25 g, 0.7 mmol) in ethanol. The suspension was stirred overnight at room temperature. The solvent was removed under vacuum, and the residue was subsequently suspended in NH_4Cl 1M. After filtering, the solid was washed several times with NH_4Cl and water. The crude products were recrystallized in ether to afford the final compound, **SqBisCF$_3$** as a pale yellow solid (1.56 g, 80%). **^{1}H NMR** (500 MHz, DMSO-d_6) δ 11.20 (s, 1H), 8.03 (s, 2H), 7.76 (s, 1H), 4.80 (q, *J* = 7.1 Hz, 2H), 1.41 (t, *J* = 7.1 Hz, 3H). **^{13}C NMR** (126 MHz, DMSO-d_6) δ 187.9, 184.9, 179.7, 169.6, 140.6, 132, 131.7, 131.4, 131.2, 126.8, 124.6, 122.4, 120.2, 119.8, 116.7, 70.5, 15.8. All spectral data shows good agreement with literature. [329]

Sq-K(boc)-2-Cl-Trt

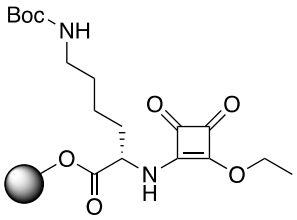

First residue loading (Fmoc-Lys(Boc)-OH) was performed as outlined in general procedures **A** and **C**. LC-MS indicated complete consumption of starting material, the resin was washed with *3x* DCM, *3x* DMF and *3x* DCM. **LC-MS** (0-100%) gradient of A in B, 55 min) t_R = 28 mins.

EDA-Sq-K(boc)-2-Cl-Trt

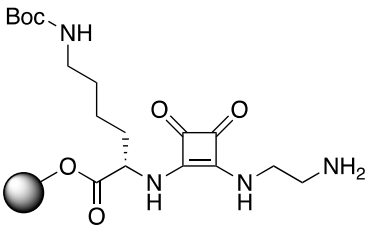

EDA-Sq-K(boc)-2-Cl-Trt was synthesised as outlined General procedures **D**. LC-MS indicated complete consumption of starting material, the resin was washed with *3x* DCM, *3x* DMF and *3x* DCM. **LC-MS** (0-100%) gradient of A in B, 55 min) t_R = 24 mins

EDA-Sq-A-EDA-Sq-K(boc)-2-OH

(ASq-2-Ala-Lys(Boc))

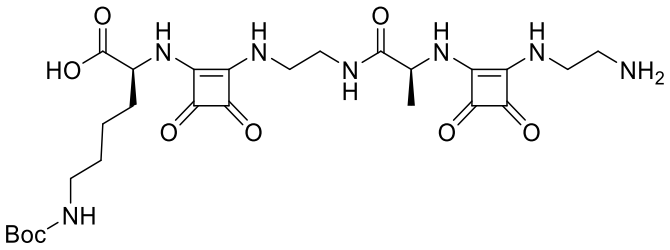

(Asq-2-Ala-Lys(Boc)) was synthesised as outlined in general procedures (**B,C,D**) followed by resin removal via 30% HFIP/DCM (General Procedure **F**) to afford the linear Squaratide (Asq-2-Ala-Lys(Boc)) as an off-white solid – without further purification. **LC-MS** (0-100%) gradient of A in B, 55 min) t_R = 23 min.

EDA-Sq-F-EDA-Sq-K(boc)-2-OH

(ASq-2-Phe-Lys(Boc))

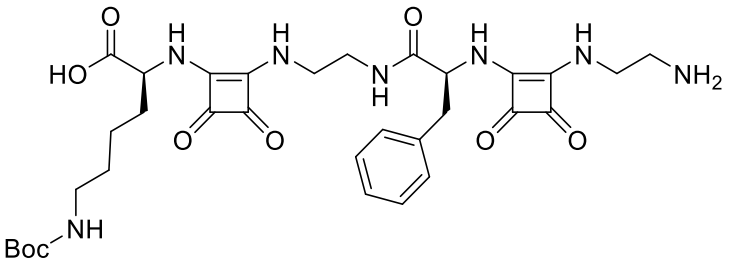

(ASq-2-Phe-Lys(Boc)) was synthesised as outlined in general procedures (**B,C,D**) followed by resin removal via 30% HFIP/DCM (General Procedure **F**) to afford the linear Squaratide (ASq-2-F_5Phe-Lys(Boc)) as an off-white solid – without further purification. **LC-MS** (0-100%) gradient of A in B, 55 min) t_R = 26 min. **HRMS** (ESI+) m/z: Calc. for $C_{32}H_{43}N_7O_9$ ($[M+H]^+$): 670.3125, Found: 670.3199 (0.41 ppm).

EDA-Sq-F_5Phe-EDA-Sq-K(boc)-2-OH

(ASq-2-F_5Phe-Lys(Boc))

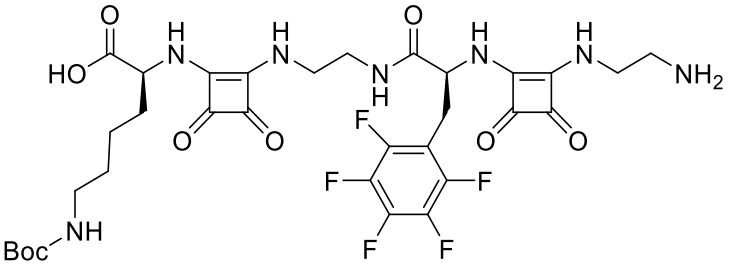

(ASq-2-F_5Phe-Lys(Boc)) was synthesised as outlined in general procedures (**B,C,D**) followed by resin removal via 30% HFIP/DCM (General Procedure **F**) to afford the linear Squaratide (ASq-2-F_5Phe-Lys(Boc)) as an off-white solid – without further purification. **LC-MS** (0-100%) gradient of A in B, 55 min) t_R = 27 min. **HRMS** (ESI+) m/z: Calc. for $C_{32}H_{38}F_5N_7O_9$ ($[M+H]^+$): 760.2657, Found: 760.2729 (0.79 ppm).

(4.16) Sq-2-Ala-Lys

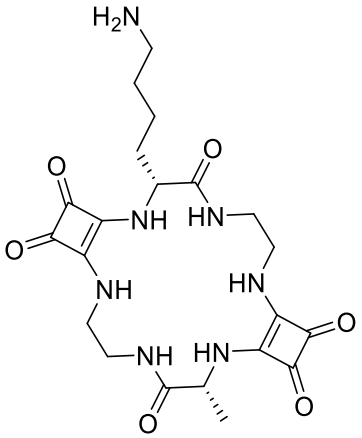

The Linear Squaratide was subjected to cyclisation which was carried out as described in the General procedures for SPPS (**G**) to afford the Cyclic protected product **Sq-2-Ala-Lys(Boc)** as an off-white solid. (100 mg, 67%). The protected cyclic squaratide was then subjected to Boc deprotection via 50:50 TFA/DCM as outlined in general procedures for SPPS (**H**) to afford the final deprotected product **(Sq-2-Ala-Lys)** as an off-white solid (74 mg, 90 %). **LC-MS** (0-100%) gradient of A in B, 55 min) t_R = 18 min. **HRMS** (ESI+) m/z: Calc. for $C_{21}H_{29}N_7O_6$ ($[M+H]^+$): 476.2179, Found: 476.2252 (0.03 ppm). **^{1}H NMR** (500 MHz, DMSO-d_6) δ 8.49 (d, *J* = 31.2 Hz, 1H), 8.05 (d, *J* = 8.3 Hz, 1H), 7.68 (dd, *J* = 74.6, 39.3 Hz, 6H), 7.23 (s, 1H), 4.59 (dd, *J* = 76.3, 38.8 Hz, 2H), 3.84 (dd, *J* = 30.3, 22.4 Hz, 2H), 3.58 (s, 2H), 3.25 (dd, *J* = 10.9, 6.1 Hz, 2H), 2.88 (s, 1H), 2.75 (d, *J* = 5.2 Hz, 2H), 1.65 (s, 1H), 1.58 – 1.46 (m, 3H), 1.36 – 1.23 (m, 5H). **^{13}C NMR** (126 MHz, DMSO-d_6) δ 183, 158.7, 158.2, 52.4, 44.4, 40.5, 40.4, 40.4, 40.3, 40.2, 40.1, 40, 39.9, 39.8, 39.1, 27.1, 22.4, 20.6, 19.8. **IR (ATR):** ν_{max}(cm^{-1}) = 3234, 2941, 1802, 1653, 1575, 1527, 1465, 1432, 1347, 1261, 1198, 1173, 1128, 947, 885, 834, 798, 720, 643, 596, 511, 438, 423.

(4.17) Sq-2-Ala-Lys(SqBisCF_3)

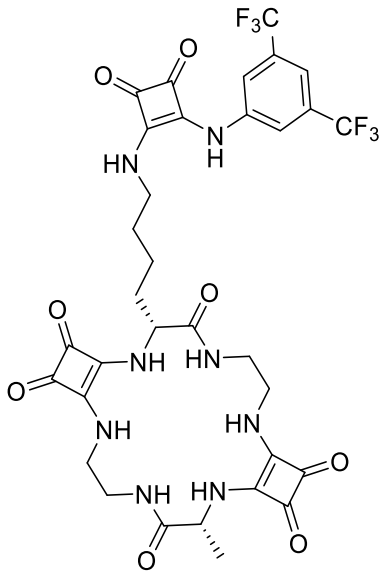

Sq-2-Ala-Lys (96 mg, 0.2 mmol, 1 eq) and Triethylamine (113 µL, 0.8 mmol, 4 eq) were dissolved in DMF. Whilst stirring, 3-ethoxy-4-(3,5-bis(trifluoromethyl)phenyl)amino-cyclobut-3-ene-1,2-dione (143 mg 0.4 mmol, 2 eq) was dissolved in a minimal amount of DMF and added dropwise to the reaction mixture. The reaction was stirred overnight at room temperature before being concentrated in *vacuo.* The resultant crude mixture was triturated with EtOAc. The precipitate was washed with EtOAc (2 x 4 mL) followed by a 50: 50 mixture of ACN/H_2O (2 x 4 mL) to afford the title compound as a beige solid (118 mg, 75 %). **LC-MS** (0-100%) gradient of A in B, 55 min) t_R = 28 min. **HRMS** (ESI+) m/z: Calc. for $C_{33}H_{32}F_6N_8O_8$ ($[M+H]^+$): 783.2240, Found: 783.2313 (-0.89 ppm). **^{1}H NMR** (500 MHz, DMSO-d_6) δ 10.07 (s, 1H), 8.40 (d, *J* = 35.1 Hz, 1H), 8.03 (s, 1H), 7.96 (d, *J* = 11.9 Hz, 2H), 7.64 (s, 2H), 7.59 (s, 1H), 7.54 (s, 1H), 7.42 (s, 1H), 7.07 (s, 1H), 4.68 – 4.35 (m, 2H), 3.72 (dd, *J* = 43.2, 11.7 Hz, 3H), 3.51 (s, 4H), 3.18 – 3.06 (m, 1H), 2.78 (d, *J* = 7.3 Hz, 1H), 1.59 – 1.41 (m, 4H), 1.23 (d, *J* = 6.2 Hz, 3H), 1.17 (d, *J* = 4.8 Hz, 2H). **^{13}C NMR** (126 MHz, DMSO-d_6) δ 185.1, 182.9, 181.1, 170.6, 162.9, 141.6, 131.8, 131.6, 124.6, 122.3, 118.4, 56.5, 52.3, 44.1, 40.5, , 40.4, 40.3, 40.2, 40.1, 40, 30.4, 21.6, 20.6. **IR (ATR):** ν_{max}(cm^{-1}) = 3171, 2944, 1798, 1650, 1544, 1465, 1379, 1307, 1278, 1186, 1121, 1032, 939, 885, 834, 724, 700, 681, 621, 498, 414.

(4.18) Sq-2-Lys(SqBisCF$_3$)

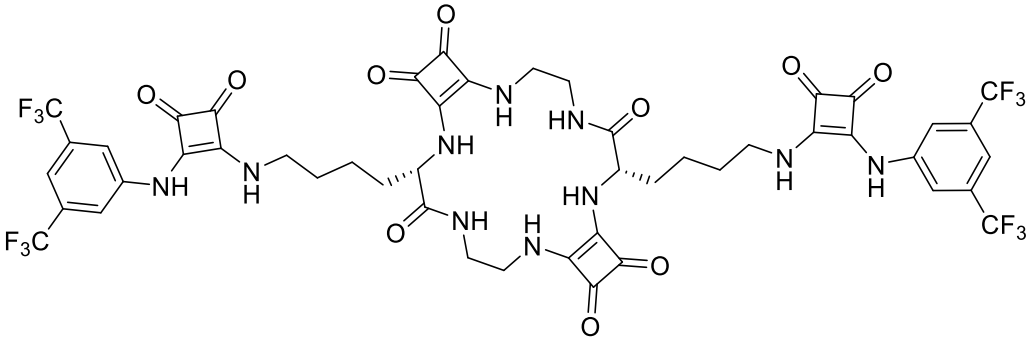

Sq-2--Lys (92 mg, 0.18 mmol, 1 eq) and Triethylamine (120 µL, 0.9 mmol, 5 eq) were dissolved in DMF. Whilst stirring, 3-ethoxy-4-(3,5-bis(trifluoromethyl)phenyl)amino-cyclobut-3-ene-1,2-dione (183 mg 0.54 mmol, 3 eq) was dissolved in a minimal amount of DMF and added dropwise to the reaction mixture. The reaction was stirred overnight at room temperature before being concentrated in *vacuo.* The resultant crude mixture was triturated with EtOAc. The precipitate was washed with EtOAc (2 x 4 mL) followed by a 50: 50 mixture of ACN/H_2O (2 x 4 mL) to afford the title compound as a beige solid (154 mg, 78 %). **LC-MS** (0-100%) gradient of A in B, 55 min) t_R = 27 min. **HRMS** (ESI+) m/z: Calc. for $C_{48}H_{42}F_{12}N_{10}O_{10}$ ($[M+H]^+$): 1147.2879, Found ($[M+Na]^+$): 1169.2770 (-1.33 ppm). **^{1}H NMR** (500 MHz, DMSO-d_6) δ 10.12 (s, 2H), 8.06 (d, *J* = 6.0 Hz, 2H), 7.97 (s, 3H), 7.94 – 7.85 (m, 2H), 7.69 (s, 2H), 7.58 (s, 2H), 7.40 (d, *J* = 8.9 Hz, 1H), 7.07 (d, *J* = 8.4 Hz, 1H), 4.56 (s, 1H), 4.41 (d, *J* = 4.8 Hz, 2H), 3.84 – 3.63 (m, 3H), 3.51 (d, *J* = 5.1 Hz, 4H), 3.08 – 2.99 (m, 2H), 2.74 (d, *J* = 10.0 Hz, 2H), 1.61 – 1.43 (m, 8H), 1.24 (d, *J* = 5.5 Hz, 4H), 1.11 (t, *J* = 7.3 Hz, 3H). **^{13}C NMR** (126 MHz, DMSO-d_6) δ 185.2, 180.7, 172, 170.2, 162.7, 141.6, 131.9, 124.7, 122.5, 118.4, 115.1, 56.3, 46.2, 44.1, 40.8, 40.5, 40.4, 40.3, 40.2, 40.1, 40, 39.9, 39.9, 39.4, 22.1, 9.1. **IR (ATR):** ν_{max}(cm^{-1}) = 3173, 2946, 1796, 1667, 1567, 1458, 1377, 1277, 1173, 1123, 1017, 940, 886, 828, 721, 700, 681, 620, 416.

(4.19) (Sq-2-Phe-Lys)

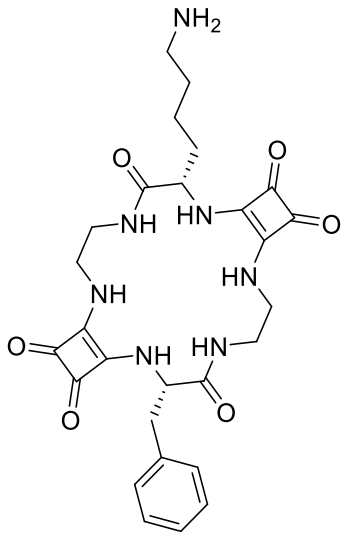

The Linear Squaratide was subjected to cyclisation which was carried out as described in the General procedures for SPPS (**G**) to afford the Cyclic protected product **(Sq-2-Phe-Lys(Boc))** as an off-white solid. (150 mg, 65 %). The protected cyclic squaratide Sq-5-Lys(Boc) was then subjected to Boc deprotection via 50:50 TFA/DCM as outlined in general procedures for SPPS (**H**) to afford the final deprotected product **(Sq-2-Phe-Lys)** as an off-white solid (110 mg, 88 %). **LC-MS** (0-100%) gradient of A in B, 55 min) t_R = 23 min. **HRMS** (ESI+) m/z: Calc. for $C_{27}H_{33}N_7O_6$ ($[M+H]^+$): 552.2495, Found: 552.2566 (0.49 ppm). **^{1}H NMR** (500 MHz, DMSO-d_6) δ 8.73 (s, 1H), 8.53 (s, 1H), 8.13 (dd, *J* = 22.3, 5.8 Hz, 1H), 7.80 (s, 3H), 7.71 (s, 3H), 7.29 – 7.08 (m, 5H), 4.67 (d, *J* = 6.3 Hz, 1H), 4.45 (d, *J* = 4.6 Hz, 1H), 3.88 (d, *J* = 9.5 Hz, 2H), 3.67 (d, *J* = 11.0 Hz, 2H), 3.55 (s, 1H), 3.27 (dd, *J* = 22.3, 9.8 Hz, 1H), 3.10 (s, 4H), 2.89 (s, 2H), 2.74 (s, 2H), 1.84 (t, *J* = 6.7 Hz, 1H), 1.71 (s, 1H), 1.60 – 1.49 (m, 2H), 1.30 (s, 2H). **^{13}C NMR** (126 MHz, DMSO-d_6) δ 183.1, 171.6, 170.7, 169.1, 167.8, 159.2, 158.7, 136.7, 129.8, 128.5, 126.9, 58, 56.2, 45.4, 45.2, 40.4, 40.3, 40.3, 40.2, 40.1, 39.1, 27.3, 24.1, 22. **IR (ATR):** ν_{max}(cm^{-1}) = 3154, 3059, 2933, 1795, 1693 1651, 1537, 1475, 1434, 1351, 1268, 1177, 1134, 1101, 1029, 1000, 884, 824, 798, 781, 720, 699, 626, 608, 543, 496, 443.

(4.20) (Sq-2-F_5Phe-Lys)

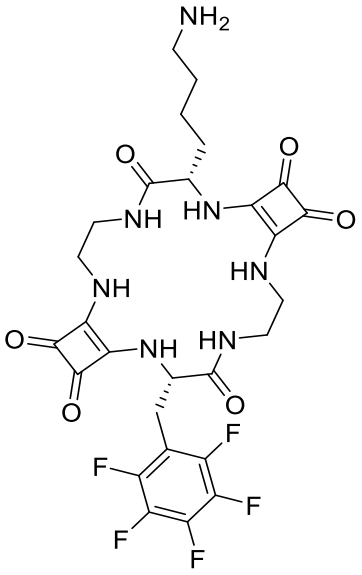

The Linear Squaratide was subjected to cyclisation which was carried out as described in the General procedures for SPPS (**G**) to afford the Cyclic protected product **(Sq-2-F_5Phe-Lys(Boc))** as an off-white solid. (75 mg, 62 %). The protected cyclic squaratide Sq-5-Lys(Boc) was then subjected to Boc deprotection via 50:50 TFA/DCM as outlined in general procedures for SPPS (**H**) to afford the final deprotected product **(Sq-2-F_5Phe-Lys)** as an off-white solid (59 mg, 92 %). **LC-MS** (0-100%) gradient of A in B, 55 min) t_R = 25 min. **HRMS** (ESI+) m/z: Calc. for $C_{27}H_{28}F_5N_7O_6$ ($[M+H]^+$): 642.2023, Found: 642.2097(0.28 ppm). **^{1}H NMR** (500 MHz, DMSO-d_6) δ 8.69 (s, 1H), 8.48 (d, *J* = 9.0 Hz, 1H), 8.25 (d, *J* = 8.9 Hz, 1H), 8.15 (dd, *J* = 26.5, 4.7 Hz, 1H), 8.04 (d, *J* = 9.0 Hz, 1H), 7.91 – 7.81 (m, 2H), 7.72 – 7.61 (m, 3H), 4.83 – 4.68 (m, 1H), 4.56 – 4.42 (m, 1H), 3.78 (s, 3H), 3.30 – 3.22 (m, 2H), 3.11 (s, 2H), 3.02 – 2.97 (m, 1H), 2.92 – 2.86 (m, 1H), 2.82 (s, 1H), 2.76 (s, 2H), 1.84 (t, *J* = 6.8 Hz, 2H), 1.57 – 1.50 (m, 2H), 1.32 (t, *J* = 13.9 Hz, 2H). **^{13}C NMR** (126 MHz, DMSO-d_6) δ 183.3, 183.1, 182.3, 181.9, 171.4, 169.7, 168.9, 167.8, 167.3, 158.7, 158.4, 56.6, 55.9, 45.3, 43.9, 43.6, 40.9, 39.1, 32.4, 27.1, 24.1, 22.3. **IR (ATR):** ν_{max}(cm^{-1}) = 3170, 2946, 1803, 1655, 1549, 1523, 1502, 1467, 1348, 1290, 1201, 1132, 1052, 1013, 981, 952, 863, 821, 721, 636, 601, 569, 503, 475, 433, 404.

7.6: Synthetic methods – Chapter 5

6-(dimethylamino)-1H,3H-benzo[de]isochromene-1,3-dione (5.7)

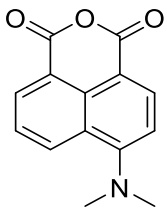

Dimethylamine (3.9 eq. 14 mmol, 1.148 g) and Copper sulfate pentahydrate (0.12 eq. 0.433 mmol, 0.108 g) were added to a solution of 4- Bromo-1,8-naphthalenedicarboxylic anhydride (**5.6**) (1 eq. 3.610 mmol, 1 g) in DMF (20 mL), then the mixture was stirred at 150 C for 10 h. The reaction solution was poured into distilled water (250 mL), and the yellow precipitate was filtered out and dried to obtain compound **5.7** as a yellow powder (0.783 g, 90% yield). All spectral data is in good agreement with that reported.[330]

(R)-2-((tert-butoxycarbonyl)amino)-4-(6-(dimethylamino)-1,3-dioxo-1H-benzo[de]isoquinolin-2(3H)-yl)butanoic acid (5.9)

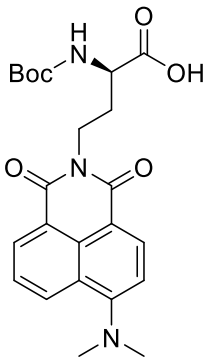

5.7 (1 eq. 1.243 mmol, 0.300 g) was kept under a nitrogen atmosphere in a three neck round bottom flask fitted with water condenser. Dioxane (25 mL) was added through a septum whereupon the mixture was heated at reflux and stirred vigorously. Boc-D-Dab-OH (**5.8**) (1 eq. 1.243 mmol, 0.271 g) was dissolved in an aqueous solution (5 mL) containing $NaHCO_3$ (4.5 eq. 5.59 mmol, 0.470 g) and added into the reaction mixture. The reaction mixture was heated at reflux for 2 h. The mixture was concentrated under reduced pressure and water (50 mL) was added. The water phase was washed with Et_2O (2 60 mL) and acidified with 2 N HCl till pH 3 in an ice-bath whereupon a yellow precipitate formed. The aqueous phase was extracted with DCM (3 x 80 mL) and the combined organic layers were dried over Na_2SO_4, filtered and concentrated under reduced pressure. The crude product was purified by column chromatography (40–50% ethyl acetate in hexane containing 0.1% AcOH) to afford **5.9** as a yellow solid (0.373 g, 68%). All spectral data is in good agreement with that reported.[323]

(R)-2-((((9H-fluoren-9-yl)methoxy)carbonyl)amino)-4-(6-(dimethylamino)-1,3-dioxo-1H-benzo[de]isoquinolin-2(3H)-yl)butanoic acid (5.11)

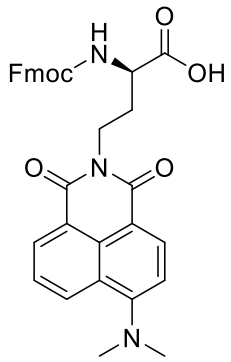

5.9 (1 eq. 0.792 mmol, 0.350 g) was dissolved in DCM (3 mL). Cold trifluoroacetic acid (3 mL) was added over 5 min and the reaction mixture was stirred for 2 h. The reaction mixture was concentrated to dryness under reduced pressure and excess TFA removed by coevaporation with chloroform (3 x 10 mL). The crude product was dried under vacuum then dissolved in water (4 mL) containing $NaHCO_3$ (5 eq. 3.81 mmol, 0.293 g). Dioxane (10 mL) was added, followed by Fmoc-OSu (1.1 eq. 0.871 mmol, 0.534 g). The reaction mixture was stirred at 0 C for 2 h. The reaction mixture was diluted with water (20 mL). The aqueous layer was washed with Et_2O (2 x 20 mL) and acidified with 6 N HCl to adjust the pH to 6. The product was extracted with DCM (3 x 25 mL) and the combined organic layers were dried over Na_2SO_4, filtered and concentrated under reduced pressure. The crude compound was purified by column chromatography (0.5–1% MeOH in DCM containing 0.1% AcOH) to afford **5.11** as a yellow solid (0.283 g, 69%). All spectral data is in good agreement with that reported.[323]

Sq-K(boc)-2-Cl-Trt

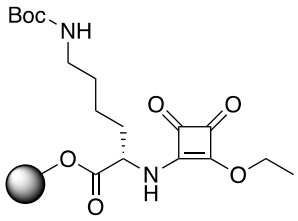

First residue loading (Fmoc-Lys(Boc)-OH) was performed as outlined in general procedures **A** and **C**. LC-MS indicated complete consumption of starting material the resin was washed with *3x* DCM, *3x* DMF and *3x* DCM. **LC-MS** (0-100%) gradient of A in B, 55 min) t_R = 28 mins

EDA-Sq-K(boc)-2-Cl-Trt

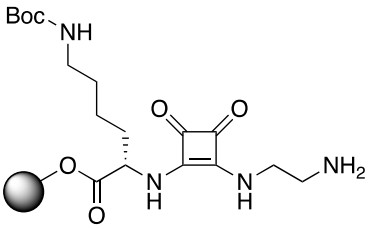

EDA-Sq-K(boc)-2-Cl-Trt was synthesised as outlined General procedures **D**. LC-MS indicated complete consumption of starting material, the resin was washed with *3x* DCM, *3x* DMF and *3x* DCM. **LC-MS** (0-100%) gradient of A in B, 55 min) t_R = 24 mins

EDA-Sq-Naph-EDA-Sq-K(boc)-2-OH

(ASq-2-Lys(Boc)-Naph)

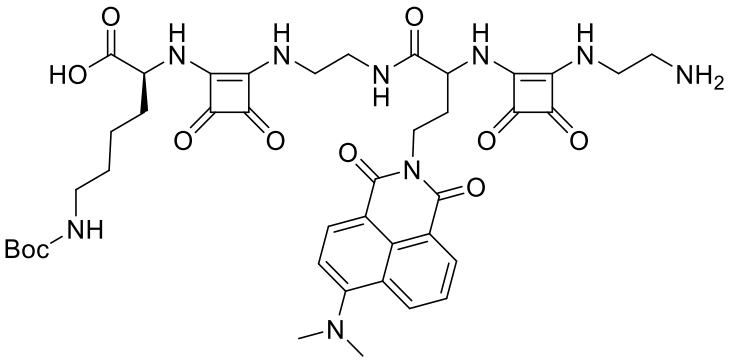

(ASq-2-Lys(Boc)-Naph) was synthesised as outlined in general procedures (**B,C,D**) followed by resin removal via 30% HFIP/DCM (General Procedure **G**) to afford the linear Squaratide (ASq-2-Lys(Boc)-Naph) as an off-white solid – without further purification. **LC-MS** (0-100%) gradient of A in B, 55 min) t_R = 27 min. **HRMS** (ESI+) m/z: Calc. for $C_{41}H_{51}N_9O_{11}$ ($[M+H]^+$): 846.3704, Found: 846.3776 (-0.51 ppm).

Sq-2-Lys(boc)-Naph

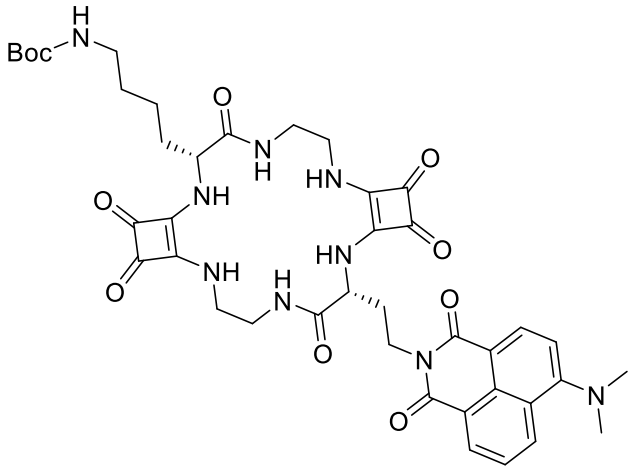

The Linear Squaratide was subjected to cyclisation which was carried out as described in the General procedures for SPPS (**F**) to afford the Cyclic protected product **Sq-2-Lys(boc)-Naph** as an off-white solid. (80 mg, 62 %). **LC-MS** (0-100%) gradient of A in B, 55 min) t_R = 41 min. **HRMS** (ESI+) m/z: Calc. for $C_{41}H_{49}N_9O_{10}$ ($[M+H]^+$): 828.3597, Found: 828.3668 (-0.65 ppm).

Sq-2-Lys-Naph

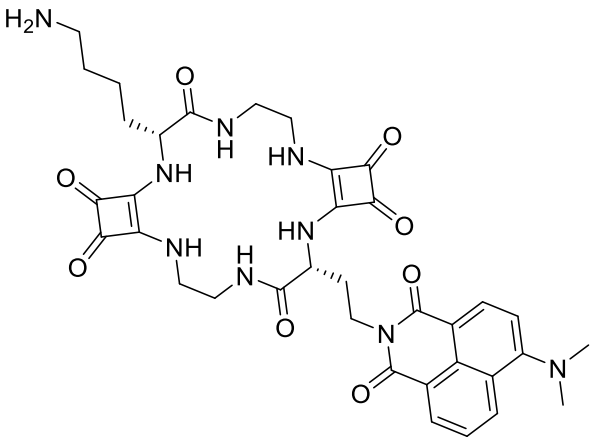

The protected cyclic squaratide Sq-2-Lys(boc)-Naph was subjected to Boc deprotection via 50:50 TFA/DCM as outlined in general procedures for SPPS (**G**) to afford the final deprotected product **(Sq-2-Lys-Naph)** as an off-white solid (40 mg, 89 %). **LC-MS** (0-100%) gradient of A in B, 55 min) t_R = 27 min. **HRMS** (ESI+) m/z: Calc. for $C_{41}H_{51}N_9O_{11}$ ($[M+H]^+$): 728.3080, Found: 728.3151 (0.27 ppm). **^{1}H NMR** (500 MHz, DMSO-d_6) δ 8.51 (d, *J* = 7.7 Hz, 2H), 8.42 (d, *J* = 6.8 Hz, 2H), 8.30 (d, *J* = 8.3 Hz, 2H), 8.18 (s, 1H), 8.03 (s, 1H), 7.74 (dd, *J* = 20.0, 12.4 Hz, 11H), 7.55 (s, 1H), 7.22 (d, *J* = 8.4 Hz, 2H), 5.04 – 3.65 (m, 11H), 3.54 (s, 4H), 3.21 (d, *J* = 5.6 Hz, 2H), 3.09 (d, *J* = 4.4 Hz, 10H), 2.76 (s, 4H), 2.55 (s, 3H), 2.14 – 1.83 (m, 4H), 1.81 (s, 2H), 1.74 (d, *J* = 3.4 Hz, 2H), 1.58 (s, 2H), 1.58 – 1.48 (m, 5H), 1.30 (d, *J* = 5.1 Hz, 4H). **^{13}C NMR** (126 MHz, DMSO-d_6) δ 183.1, 183, 182.9, 164.1, 163.4, 158.6, 158.3, 157, 132.1, 131.1, 130.6, 125.4, 122.5, 114.1, 113.8, 44.4, 43.5, 40.8, 27.1, 22.9. **IR (ATR):** ν_{max}(cm^{-1}) = 3255, 2945, 1799, 1670, 1584, 1530, 1456, 1432, 1387, 1352, 1292, 1247, 1200, 1178, 1131, 1082, 1018, 952, 834, 799, 781, 758, 720, 593, 501, 473, 458, 425, 408.

7.7: Interpreting LC-MS Data

This section provides a brief overview of how to interpret LC-MS data, using compound **2.17** as an example (see spectra below).

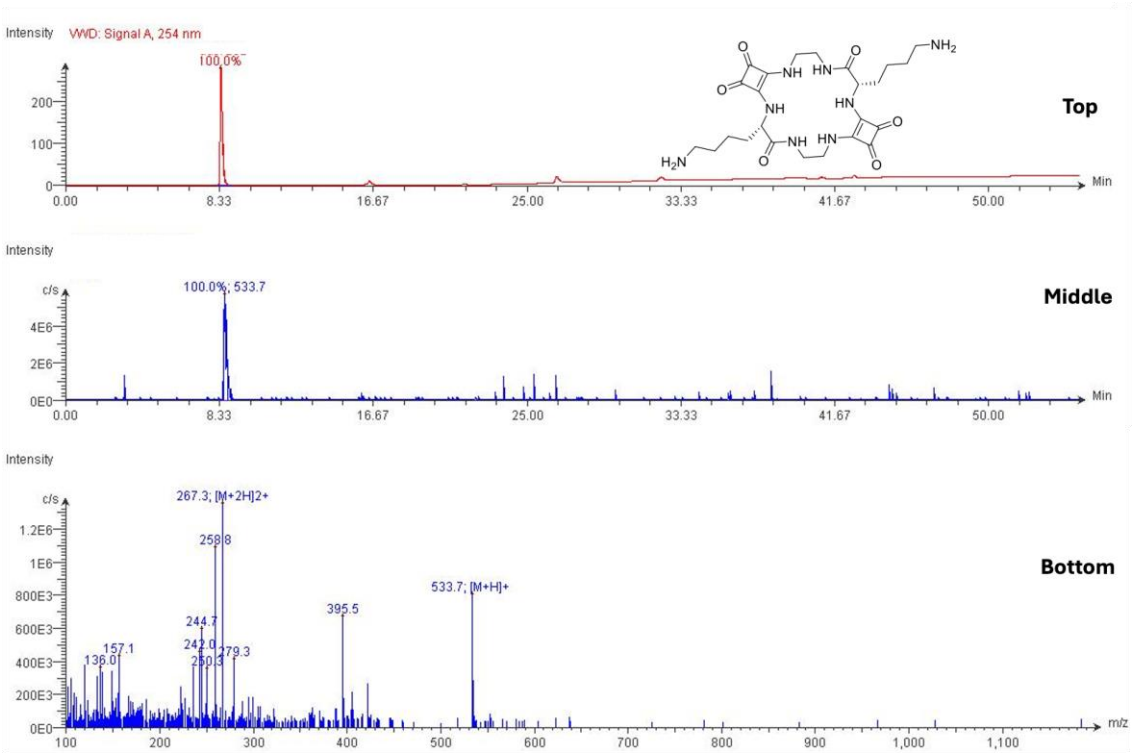

The **top** spectrum shows an HPLC chromatogram obtained with a deuterium lamp at 254 nm. Only a single UV peak is visible, which indicates the presence of one UV-active compound in the sample. This compound has a retention time (t_R) of 8.33 minutes.

The next spectrum (**middle**) is an Extracted Ion Chromatogram (XIC) recorded in positive mode (ESI+). It displays the signal intensity at a selected m/z value—in this case, the target ion $[M+H]^+$ with a mass of 533.7 $g \cdot mol^{-1}$—as a function of retention time. The fact that the $[M+H]^+$ signal coincides precisely with the UV peak strongly supports that the chromatographic peak corresponds to the expected compound.

The lower spectra (**bottom**) show the full mass spectra acquired under the UV peak at t_R = 8.33 min, in the ESI+ mode. These spectra reveal the full range of ions present beneath the UV signal, typically including the target mass and possible adducts. In this example, strong ionization was observed, with the expected ions detected at $[M+H]^+$ = 533.7 $g \cdot mol^{-1}$ (ESI+) and $[M+2H]^{+2}$ = 267.3 $g \cdot mol^{-1}$ (ESI+)

7.8: Loading of First Amino Acid Residue

2-chlorotrityl chloride resin (FluoroChem) was weighed out into a 20 mL fritted syringe. The resin was suspended in 10 mL of DCM and allowed to swell for ~1 hour. After this time, a solution of Fmoc amino-acid and DIPEA in DCM was added to the resin. The resin was agitated gently for 2 hours, then washed consecutively with 3x DCM/MeOH/DIPEA (17:2:1), 3x DCM, 3x DMF, 3x DCM, before being dried in vacuo.

Dry Fmoc amino-acid resin (approx. 5 µmol with respect to Fmoc) was weighed into two separate 10 mL volumetric flasks. 2 mL of 10% Piperidine sol. (in DMF) was added and agitated gently for 30 minutes. The solution(s) were diluted to 10 mL with MeCN. 2 mL of each solution was transferred to two individual 25 mL volumetric flasks and diluted to the mark again with MeCN (solution 1 and solution 2, i.e. Duplicate). A reference solution was prepared in a similar manner as above, but without the addition of resin. Each cuvette was filled by taking 2.5 mL of each sample (Sol. 1, Sol. 2 & Ref.), before being placed into the spectrophotometer. The absorbance of each sample was recorded at 304 nm, and an estimate of first residue attachment was obtained from the following equation:

$$Fmoc\ Loading: mmol\ g^{-1} = \left(Abs_{sample(average)} - Abs_{Ref}\right) x \left(\frac{16.4}{mg\ of\ resin_{(average)}}\right)$$

The value 16.4 is derived from the Beer–Lambert law ($A = \varepsilon cl$), using a path length of 1 cm and the molar extinction coefficient of the dibenzofulvene–piperidine adduct formed upon Fmoc cleavage ($\varepsilon \approx 7.62$ L mmol^{-1} cm^{-1} at 304 nm). The constant incorporates the cumulative dilution factors applied during sample preparation (2 mL cleaved solution diluted to 10 mL, followed by a 2 mL aliquot diluted to 25 mL), as well as unit conversions required to express the final loading in mmol g^{-1}. Combining these factors yields the numerical constant 16.4 used in the loading calculation.

7.9: Anion binding studies

All tetrabutylammonium halide salts (TBAX) and the receptors were lyophilised before use, and halide salts were stored under vacuum in a desiccator. Solutions of the TBA salts were made up in DMSO-d6, which was dried over 3Å molecular sieves before use, to a concentration of 300 mM. An aliquot of stock solution of receptor in DMSO-d_6 was diluted to 1 mL (2.5 mM). 600 µL of this solution was added to an NMR and the ^{1}H NMR spectrum was recorded. Subsequent additions of aliquots of TBAX solutions were added to the NMR tube and shaken vigorously to ensure homogenisation. This process was repeated up to 22 equivalents of halide was reached. The ^{1}H NMR spectra were analysed and processed, and stackplots were generated using MestReNova 6.0.2 software. A global fitting analysis assuming a 1:1 binding model (or in certain instances a 1:2 binding model when indicated by shifts within the obtained spectra – 3.27) was employed to provide the binding constant (K_a/M^{-1}), by fitting of the chemical shift changes of the NH signals as function of anion concentration using the open access BindFit software program.

7.10: *Staphylococcus aureus* culture conditions

Staphylococcus aureus culture was conducted in the Medical Mycology Lab at Maynooth University by Dr. Poonam Ratrey. *S. aureus* (ATCC33951) was cultured at 37 °C in Nutrient broth (Oxoid), in an orbital shaker at 200 rpm. Stocks were kept on nutrient agar, stored at 4 °C for up to 2 months, or as glycerol stocks (50/50 glycerol:culture), stored at -70 °C indefinitely

7.11: Disk diffusion and broth dilution assay

Antibacterial activity screening of the linear, boc-protected, and cyclic squaratides was done by the disk diffusion assay, which was conducted in the Medical Mycology Lab at Maynooth University by Dr. Poonam Ratrey. To screen the compounds, they were dissolved in sterile water or DMSO at the highest concentration of 10 mg/mL immediately before the assay. Overnight lag- phase cultures were diluted in freshly autoclaved media to get mid logarithmic phase bacteria in the optical density (600 nm) range 0.5 to 0.7. 20 µL of the bacterial suspensions were spread with a sterile spreader,

ensuring a lawn-like growth in the agar plates. Sterile filter disks, cut uniformly and autoclaved, were carefully placed onto the agar plate containing bacterial cells using sterile forceps and pressed gently to allow for adherence to the agar base. 10 µL of drugs were added on top of the sterile filter disks, keeping a positive control of 100 % ethanol and solvent only (water or DMSO) as the negative control. The agar plate is sealed with parafilm and incubated overnight in a static incubator at 37 °C. The following day, the agar plate with disks was observed for zones of inhibition (ZOI), signifying antibacterial activity of the compound. The inhibitory concentration values were quantitatively probed by the advanced method of broth microdilution. Briefly, freshly obtained mid-logarithmic cells were diluted further in the media to get 5 x 10^5 CFU/mL, and 90 µL aliquots of this bacterial suspension were challenged with 10 µL of drugs of varying concentration, beginning with the highest concentration of 1000 µg/mL, followed by two-fold serial dilution, in a 96-well plate. The positive control was untreated bacteria while broth media alone without cells served as a negative control for the broth dilution assay to determine the minimum inhibitory concentration (MIC). The 96-well plate with added drugs and cells was incubated overnight in static conditions at 37 °C, and post-incubation, optical density or absorbance was measured at 600 nm in a BioTek microplate reader, and using the following relation, the percentage of growth inhibition was calculated.

$$\% \text{ Inhibition} = \frac{\text{Positive control OD} - \text{sample OD}}{\text{positive control OD} - \text{negative control OD}} \times 100$$

7.12: Proteomics analysis

Proteomic analysis was conducted in the Medical Mycology Lab at Maynooth University by Dr. Poonam Ratrey. Bacterial cells were cultured freshly for 24 hours just before the experiment. 5 mL samples of the freshly cultured cells were diluted with an equal amount of sterile media in 50 mL Falcon tubes. We kept four biological replicates of the untreated control group and the trimer-treated group at a final concentration of 500 µg/mL, prepared in water. The cells were incubated for 6 hours in a shaking incubator at 37 °C. Post-treatment cells were pelleted down by centrifugation at 2500 rpm for 15 minutes. This was followed by discarding the supernatant and washing the cells by vortexing with 20 mL of sterile PBS. After washing, PBS was removed again by

centrifuging at 2500 rpm for 15 minutes. After washing, the cell pellets were resuspended 1 mL of lysis buffer (pH 8) prepared with 8 M urea, 2 M thiourea, 0.1 M Tris-HCl, and a mixture of five protease inhibitors, namely 10 µg/mL aprotinin, 1 mM/mL phenylmethylsulfonyl fluoride (PMSF), leupeptin, pepstatin A, and Tosyllysine Chloromethyl Ketone hydrochloride (TLCK). The cells were lysed by probe sonication for 10 seconds, three times, in 15 mL Falcon tubes, with the sonicator tip sterilized between samples. The supernatant was collected after pelleting down the cell debris by centrifugation at 14,500 x g for 10 minutes. The proteins obtained after cell lysis were precipitated in acetone with a sample to acetone ratio of 1:3, in the freezer at -20 °C overnight. The next day, acetone was discarded, and proteins were resuspended in 25 µL of resuspension buffer (lysis buffer without protease inhibitors). To aid resuspension, pellets were bath sonicated for 5 minutes, followed by 1 minute vortex. Protein quantifications were done with 2 µL aliquots of the resuspended samples using the Qubit™ quantification system (Invitrogen). Samples with similar and closer Qubit™ values, were selected for further proteome analysis (n=3, per sample group, i.e., treated and control). To 20 µL aliquots of the resuspended samples, 105 µL of ammonium bicarbonate (50 mM) and 1 µL 0.5 M dithiothreitol were added, and the samples were incubated at 56°C for 20 min. The samples were allowed to cool down to room temperature and were alkylated with 2.7 µL 0.5 M iodoacetamide and further incubated in dark for 15 minutes at room temperature. Protein digestion was done by adding 1 µL 1% (w/v) ProteaseMAX Surfactant Trypsin Enhancer (Promega) and 1 µL of Sequence Grade Trypsin (0.5 µg/µL) under incubation for 18 hours at 37°C. Digestion was quenched by adding 1 µL trifluoroacetic acid (100 % TFA) and incubating for 5 minutes at room temperature. The samples were centrifuged at 14,500 x g for 10 minutes. The resulting supernatants containing peptides were eluted through C-18 spin columns (Pierce). The purified peptides were dried in a vacuum concentrator (Savant SpeedVac DNA 130, Thermoscientific) at 38°C for 2 hours and resuspended in 2 % acetonitrile and 0.05 % TFA, sonicated for 5 minutes in bath sonication to aid resuspension. The samples were centrifuged at 14,500 x g for 10 minutes to pellet debris. 2 µL of the purified sample supernatants containing 750 ng of protein were used for mass spectrometry analysis.

7.13: Mass spectrometry (Proteomics)

Purified extracts, 2 µL, were injected into Vanquish HPLC coupled with FAIMS Pro Duo connected to Q Exactive Plus Hybrid Quadrupole-orbitrap mass spectrometer (Thermo Fisher Scientific), following previously outlines protocols[331]. Raw MS/MS data were processed using the Andromeda search engine in MaxQuant software v.2.0.3.0 using a *Staphylococcus aureus* NCT8325 reference proteome obtained from a UniProt-SWISS-PROT to identify proteins.

7.14: Data Analysis (Proteomics)

Protein quantification and label-free quantification (LFQ) normalisation were processed through MaxQuant software v.2.0.3.0 for the *S. aureus* NCT8325 proteome using previously reported protocols[331]. The resulting LFQ intensity values were processed using Perseus v.1.6.15.0 to obtain statistical and graphical analyses. To quantitatively measure protein abundance, the normalized LFQ intensity values were used. Proteins from the generated data matrix were filtered to remove contaminants. LFQ intensities were log2-transformed, and samples were grouped accordingly (control and treated). Proteins that were not detected in at least one group out of the three replicates were removed from further analysis. A data imputation step was included to replace missing values with values that imitate signals of low-abundance proteins chosen randomly from a distribution specified by a downshift of 1.8 times the mean standard deviation of all measured values and a width of 0.3 times this standard deviation. Using the normalized intensity values, principal component analysis (PCA) was performed in all the biological replicates (n = 3), which resolved them into the corresponding sample groups (control and treated). A pair-wise Student's t-tests were performed using a cut-off of $p < 0.05$ on the post-imputation dataset to visualize the difference. Log *p*-values were plotted with respect to log2 fold change on the x-axis to generate volcano plots for each pairwise comparison. Statistically significant and differentially abundant (SSDA) proteins (ANOVA, $p < 0.05$) with a relative fold change greater than ± 1.5 were considered for analysis. To obtain a protein heat map, SSDA proteins were z-score-normalized and then used for hierarchical clustering. For generating protein/protein interaction networks and pathway analysis, for treatment versus control sample groups, the Search Tool for the Retrieval of Interacting Genes/Proteins (STRING) v12.0 www.string-db.org/ was used to map SSDA

proteins using their corresponding gene names retrieved from UniProt gene lists for *S. aureus* NCTC 8325 to gain insights into their roles within the cell.

7.15: Lucigenin Cl^-/NO_3^- anion exchange assay

LUV preparation and Lucigenin assays were carried out following procedures outlined by Valkenier and co-workers.8 Large unilamellar liposomes (LUVs) were synthesized using 1- palmitoyl-2-oleoyl-sn-glycero-3-phosphocholine (POPC) (11.2 µmol, soln. in $CHCl_3$) and Cholesterol (4.8 µmol) mixed in a ratio of 7:3. This mixture was brought to dryness under gentle vacuum and subsequently, the mixture was rehydrated in an aqueous Lucigenin solution (1 mL, 0.8mM lucigenin in 225 mM $NaNO_3$) and stirred for 1 h to obtain heterogeneous vesicles. After that, the vesicles underwent 9 freeze-thaw cycles and were extruded through a 0.2 mm polycarbonate membrane 29 times to obtain monodisperse LUVs. A Sephadex G-100 size-exclusion column was employed to remove any unencapsulated lucigenin. The collected liposomes were diluted to 40 mL with 225 mM $NaNO_3$ to obtain a homogeneous 0.4 mM liposome solution. Lucigenin fluorescence quenching was monitored in a time dependent manner using an Agilent Spectrofluorimeter to access Clinflux (λex = 430 nm, λem = 505 nm). Cl^- transport behaviour was initiated at t=0 s by adding each compound as a solvate in DMSO followed by a 25 mM NaCl pulse (75µL, 1 M NaCl in 225 nm $NaNO_3$) to a 3 mL liposome solution. The data was collected for at least 600 s and then Triton X-100 (5% w/w in water) was added to lyse the liposomes, and normalize to 100% efflux. The recorded data was normalised and the fraction fluorescence intensity at 270 s of each tested concentration of transporters (mol%) was plotted against transporter concentration (mol%). The data obtained was fitted to the Hill equation to obtain the EC50 value at 270 s (the concentration to obtain the half maximum effect) by using Originlab 2024b or Graphpad Prism 10:

$$y = START + (END - START) * x^n / (k^n + x^n)$$

Where n is the Hill coefficient, *k* presents the EC_{50} value.

7.16: Fluorescence Titrations

Fluorescence titrations were carried out using an Agilent Spectrofluorometer equipped with a 450 W xenon lamp for excitation. A stock solution of the receptor was prepared in DMSO before being diluted to a final volume of 2.5 mL in a fluorescence cuvette to result in a final concentration of 10 μM. All tetrabutylammonium halide salts (TBAX) were made up in a stock solution in DMSO and Subsequent additions of aliquots of TBAX solutions were added to the fluorescent cuvette and shaken ensure homogenisation. The excitation wavelength was selected, and emission slit widths were adjusted before running the fluorescence experiments.

Bibliography

Bibliography

(1) Desiraju, G. R. Chemistry beyond the molecule. *Nature* **2001**, *412* (6845), 397–400. DOI: 10.1038/35086640.
(2) Lehn, J.-M. Supramolecular Chemistry—Scope and Perspectives Molecules, Supermolecules, and Molecular Devices (Nobel Lecture). *Angewandte Chemie International Edition in English* **1988**, *27* (1), 89–112. DOI: https://doi.org/10.1002/anie.198800891.
(3) Cram, D. J. The Design of Molecular Hosts, Guests, and Their Complexes (Nobel Lecture). *Angewandte Chemie International Edition in English* **1988**, *27* (8), 1009–1020. DOI: https://doi.org/10.1002/anie.198810093.
(4) Pedersen, C. J. The Discovery of Crown Ethers (Noble Lecture). *Angewandte Chemie International Edition in English* **1988**, *27* (8), 1021–1027. DOI: https://doi.org/10.1002/anie.198810211.
(5) Park, C. H.; Simmons, H. E. Macrobicyclic amines. III. Encapsulation of halide ions by in,in-1,(k + 2)-diazabicyclo[k.l.m.]alkane ammonium ions. *Journal of the American Chemical Society* **1968**, *90* (9), 2431–2432. DOI: 10.1021/ja01011a047.
(6) Kolesnichenko, I. V.; Anslyn, E. V. Practical applications of supramolecular chemistry. *Chemical Society Reviews* **2017**, *46* (9), 2385–2390, 10.1039/C7CS00078B. DOI: 10.1039/C7CS00078B.
(7) Kumar, D.; Sharma, D.; Singh, G.; Singh, M.; Rathore, M. Lipoidal Soft Hybrid Biocarriers of Supramolecular Construction for Drug Delivery. *ISRN pharmaceutics* **2012**, *2012*, 474830. DOI: 10.5402/2012/474830.
(8) Gellman, S. H. Introduction: Molecular Recognition. *Chemical Reviews* **1997**, *97* (5), 1231–1232. DOI: 10.1021/cr970328j.
(9) Seitz, W. R.; Grenier, C. J.; Csoros, J. R.; Yang, R.; Ren, T. Molecular Recognition: Perspective and a New Approach. *Sensors* **2021**, *21* (8), 2757.
(10) Crowley, P. B. Origins of the Host–Guest Terminology. *Crystal Growth & Design* **2023**, *23* (12), 8469–8473. DOI: 10.1021/acs.cgd.3c00985.
(11) Sayed, M.; Pal, H. An overview from simple host–guest systems to progressively complex supramolecular assemblies. *Physical Chemistry Chemical Physics* **2021**, *23* (46), 26085–26107, 10.1039/D1CP03556H. DOI: 10.1039/D1CP03556H.
(12) Tu, Y.; Peng, F.; Adawy, A.; Men, Y.; Abdelmohsen, L. K. E. A.; Wilson, D. A. Mimicking the Cell: Bio-Inspired Functions of Supramolecular Assemblies. *Chemical Reviews* **2016**, *116* (4), 2023–2078. DOI: 10.1021/acs.chemrev.5b00344.
(13) Stupp, S. I.; Palmer, L. C. Supramolecular Chemistry and Self-Assembly in Organic Materials Design. *Chemistry of Materials* **2014**, *26* (1), 507–518. DOI: 10.1021/cm403028b.
(14) Chow, C.-F.; Jose, D. A.; Selvakumar, P. M. Editorial: Supramolecular Chemistry at the Interface of Environmental and Food Science. *Frontiers in Chemistry* **2021**, *9*, Editorial. DOI: 10.3389/fchem.2021.680372.
(15) Teresa Albelda, M.; Frías, J. C.; García-España, E.; Schneider, H.-J. Supramolecular complexation for environmental control. *Chemical Society Reviews* **2012**, *41* (10), 3859–3877, 10.1039/C2CS35008D. DOI: 10.1039/C2CS35008D.
(16) Zhang, G.; Lin, W.; Huang, F.; Sessler, J.; Khashab, N. M. Industrial Separation Challenges: How Does Supramolecular Chemistry Help? *Journal of the American Chemical Society* **2023**, *145* (35), 19143–19163. DOI: 10.1021/jacs.3c06175.

(17) Gale, P. A. Anion coordination and anion-directed assembly: highlights from 1997 and 1998. *Coordination Chemistry Reviews* **2000**, *199* (1), 181–233. DOI: https://doi.org/10.1016/S0010-8545(99)00149-6.
(18) Bondy, C. R.; Loeb, S. J. Amide based receptors for anions. *Coordination Chemistry Reviews* **2003**, *240* (1), 77–99. DOI: https://doi.org/10.1016/S0010-8545(02)00304-1.
(19) Beer, P. D.; Gale, P. A. Anion Recognition and Sensing: The State of the Art and Future Perspectives. *Angewandte Chemie International Edition* **2001**, *40* (3), 486–516. DOI: https://doi.org/10.1002/1521-3773(20010202)40:3<486::AID-ANIE486>3.0.CO;2-P.
(20) Behrend, R.; Meyer, E.; Rusche, F. I. Ueber Condensationsproducte aus Glycoluril und Formaldehyd. *Justus Liebigs Annalen der Chemie* **1905**, *339* (1), 1–37. DOI: https://doi.org/10.1002/jlac.19053390102.
(21) Dutzler, R.; Campbell, E. B.; Cadene, M.; Chait, B. T.; MacKinnon, R. X-ray structure of a ClC chloride channel at 3.0 Å reveals the molecular basis of anion selectivity. *Nature* **2002**, *415* (6869), 287–294. DOI: 10.1038/415287a.
(22) Macknight, A. D. C. The role of anions in cellular volume regulation. *Pflügers Archiv* **1985**, *405* (1), S12–S16. DOI: 10.1007/BF00581773.
(23) The Disorders Induced by Iodine Deficiency. *Thyroid®* **1994**, *4* (1), 107–128. DOI: 10.1089/thy.1994.4.107.
(24) Hatch-McChesney, A.; Lieberman, H. R. Iodine and Iodine Deficiency: A Comprehensive Review of a Re-Emerging Issue. *Nutrients* **2022**, *14* (17). DOI: 10.3390/nu14173474 From NLM.
(25) Berend, K.; van Hulsteijn, L. H.; Gans, R. O. Chloride: the queen of electrolytes? *Eur J Intern Med* **2012**, *23* (3), 203–211. DOI: 10.1016/j.ejim.2011.11.013 From NLM.
(26) Deane, N.; Ziff, M.; Smith, H. W. The distribution of total body chloride in man. *J Clin Invest* **1952**, *31* (2), 200–203. DOI: 10.1172/jci102592 From NLM.
(27) Welsh, M. J.; Smith, A. E. Molecular mechanisms of CFTR chloride channel dysfunction in cystic fibrosis. *Cell* **1993**, *73* (7), 1251–1254. DOI: 10.1016/0092-8674(93)90353-r From NLM.
(28) Rein, J. L.; Coca, S. G. "I don't get no respect": the role of chloride in acute kidney injury. *Am J Physiol Renal Physiol* **2019**, *316* (3), F587–f605. DOI: 10.1152/ajprenal.00130.2018 From NLM.
(29) Pfortmueller, C. A.; Uehlinger, D.; von Haehling, S.; Schefold, J. C. Serum chloride levels in critical illness-the hidden story. *Intensive Care Med Exp* **2018**, *6* (1), 10. DOI: 10.1186/s40635-018-0174-5 From NLM.
(30) Markovich, D. Physiological roles and regulation of mammalian sulfate transporters. *Physiol Rev* **2001**, *81* (4), 1499–1533. DOI: 10.1152/physrev.2001.81.4.1499 From NLM.
(31) Pfau, A.; López-Cayuqueo, K. I.; Scherer, N.; Wuttke, M.; Wernstedt, A.; González Fassrainer, D.; Smith, D. E. C.; van de Kamp, J. M.; Ziegeler, K.; Eckardt, K.-U.; et al. SLC26A1 is a major determinant of sulfate homeostasis in humans. *The Journal of Clinical Investigation* **2023**, *133* (3). DOI: 10.1172/JCI161849.
(32) Perez, S.; Makshakova, O.; Angulo, J.; Bedini, E.; Bisio, A.; de Paz, J. L.; Fadda, E.; Guerrini, M.; Hricovini, M.; Hricovini, M.; et al. Glycosaminoglycans: What Remains To Be Deciphered? *JACS Au* **2023**, *3* (3), 628–656. DOI: 10.1021/jacsau.2c00569.
(33) Wildi, L. M.; Raynauld, J.-P.; Martel-Pelletier, J.; Beaulieu, A.; Bessette, L.; Morin, F.; Abram, F.; Dorais, M.; Pelletier, J.-P. Chondroitin sulphate reduces both cartilage

volume loss and bone marrow lesions in knee osteoarthritis patients starting as early as 6 months after initiation of therapy: a randomised, double-blind, placebo-controlled pilot study using MRI. *Annals of the Rheumatic Diseases* **2011**, *70* (6), 982–989. DOI: 10.1136/ard.2010.140848.
(34) Alnouti, Y. Bile Acid sulfation: a pathway of bile acid elimination and detoxification. *Toxicol Sci* **2009**, *108* (2), 225–246. DOI: 10.1093/toxsci/kfn268 From NLM.
(35) Huegel, J.; Sgariglia, F.; Enomoto-Iwamoto, M.; Koyama, E.; Dormans, J. P.; Pacifici, M. Heparan sulfate in skeletal development, growth, and pathology: the case of hereditary multiple exostoses. *Dev Dyn* **2013**, *242* (9), 1021–1032. DOI: 10.1002/dvdy.24010 From NLM.
(36) Dou, L.; Jourde-Chiche, N.; Faure, V.; Cerini, C.; Berland, Y.; Dignat-George, F.; Brunet, P. The uremic solute indoxyl sulfate induces oxidative stress in endothelial cells. *J Thromb Haemost* **2007**, *5* (6), 1302–1308. DOI: 10.1111/j.1538-7836.2007.02540.x From NLM.
(37) Karniski, L. P. Mutations in the diastrophic dysplasia sulfate transporter (DTDST) gene: correlation between sulfate transport activity and chondrodysplasia phenotype. *Hum Mol Genet* **2001**, *10* (14), 1485–1490. DOI: 10.1093/hmg/10.14.1485 From NLM.
(38) Lin, Q.; Deng, Y. Is Sulfate Radical a ROS? *Environmental Science & Technology* **2021**, *55* (22), 15010–15012. DOI: 10.1021/acs.est.1c06651.
(39) Fontecilla-Camps, J. C. The Complex Roles of Adenosine Triphosphate in Bioenergetics. *ChemBioChem* **2022**, *23* (10), e202200064. DOI: https://doi.org/10.1002/cbic.202200064.
(40) Stincone, A.; Prigione, A.; Cramer, T.; Wamelink, M. M. C.; Campbell, K.; Cheung, E.; Olin-Sandoval, V.; Grüning, N.-M.; Krüger, A.; Tauqeer Alam, M.; et al. The return of metabolism: biochemistry and physiology of the pentose phosphate pathway. *Biological Reviews* **2015**, *90* (3), 927–963. DOI: https://doi.org/10.1111/brv.12140.
(41) Komaba, H.; Fukagawa, M. Phosphate—a poison for humans? *Kidney International* **2016**, *90* (4), 753–763. DOI: https://doi.org/10.1016/j.kint.2016.03.039.
(42) Boyer, P. D. Energy, Life, and ATP (Nobel Lecture). *Angewandte Chemie International Edition* **1998**, *37* (17), 2296–2307. DOI: https://doi.org/10.1002/(SICI)1521-3773(19980918)37:17<2296::AID-ANIE2296>3.0.CO;2-W.
(43) Nath, S. Beyond binding change: the molecular mechanism of ATP hydrolysis by F1-ATPase and its biochemical consequences. *Frontiers in Chemistry* **2023**, *11*, Original Research. DOI: 10.3389/fchem.2023.1058500.
(44) Chu, X. Y.; Xu, Y. Y.; Tong, X. Y.; Wang, G.; Zhang, H. Y. The Legend of ATP: From Origin of Life to Precision Medicine. *Metabolites* **2022**, *12* (5). DOI: 10.3390/metabo12050461 From NLM.
(45) Takeda, E.; Yamamoto, H.; Nashiki, K.; Sato, T.; Arai, H.; Taketani, Y. Inorganic phosphate homeostasis and the role of dietary phosphorus. *J Cell Mol Med* **2004**, *8* (2), 191–200. DOI: 10.1111/j.1582-4934.2004.tb00274.x From NLM.
(46) Butusov, M.; Jernelöv, A. The Role of Phosphorus in the Origin of Life and in Evolution. In *Phosphorus: An Element that could have been called Lucifer*, Butusov, M., Jernelöv, A. Eds.; Springer New York, 2013; pp 1–12.

(47) Ganz, D.; Harijan, D.; Wagenknecht, H. A. Labelling of DNA and RNA in the cellular environment by means of bioorthogonal cycloaddition chemistry. *RSC Chem Biol* **2020**, *1* (3), 86–97. DOI: 10.1039/d0cb00047g From NLM.
(48) Shannon, R. D. Revised effective ionic radii and systematic studies of interatomic distances in halides and chalcogenides. *Acta Crystallographica Section A* **1976**, *32* (5), 751–767. DOI: https://doi.org/10.1107/S0567739476001551.
(49) Kumawat, L. K.; Wynne, C.; Cappello, E.; Fisher, P.; Brennan, L. E.; Strofaldi, A.; McManus, J. J.; Hawes, C. S.; Jolliffe, K. A.; Gunnlaugsson, T.; et al. Squaramide-Based Self-Associating Amphiphiles for Anion Recognition. *Chempluschem* **2021**, *86* (8), 1058–1068. DOI: 10.1002/cplu.202100275 From NLM.
(50) Busschaert, N.; Elmes, R. B. P.; Czech, D. D.; Wu, X.; Kirby, I. L.; Peck, E. M.; Hendzel, K. D.; Shaw, S. K.; Chan, B.; Smith, B. D.; et al. Thiosquaramides: pH switchable anion transporters. *Chemical Science* **2014**, *5* (9), 3617–3626, 10.1039/C4SC01629G. DOI: 10.1039/C4SC01629G.
(51) Sengupta, A.; Liu, Y.; Flood, A. H.; Raghavachari, K. Anion-Binding Macrocycles Operate Beyond the Electrostatic Regime: Interaction Distances Matter. *Chemistry – A European Journal* **2018**, *24* (54), 14409–14417. DOI: https://doi.org/10.1002/chem.201802657.
(52) Hofmeister, F. Zur Lehre von der Wirkung der Salze. *Archiv für experimentelle Pathologie und Pharmakologie* **1888**, *24* (4), 247–260. DOI: 10.1007/BF01918191.
(53) Jungwirth, P. Hofmeister Series of Ions: A Simple Theory of a Not So Simple Reality. *The Journal of Physical Chemistry Letters* **2013**, *4* (24), 4258–4259. DOI: 10.1021/jz402369u.
(54) Evans, N. H.; Beer, P. D. Advances in Anion Supramolecular Chemistry: From Recognition to Chemical Applications. *Angewandte Chemie International Edition* **2014**, *53* (44), 11716–11754. DOI: https://doi.org/10.1002/anie.201309937.
(55) Riordan, J. F. Arginyl residues and anion binding sites in proteins. *Molecular and Cellular Biochemistry* **1979**, *26* (2), 71–92. DOI: 10.1007/BF00232886.
(56) Chavali, S. S.; Cavender, C. E.; Mathews, D. H.; Wedekind, J. E. Arginine Forks Are a Widespread Motif to Recognize Phosphate Backbones and Guanine Nucleobases in the RNA Major Groove. *J Am Chem Soc* **2020**, *142* (47), 19835–19839. DOI: 10.1021/jacs.0c09689 From NLM.
(57) Tong, H.; Ali Mohammed, F.; Elmes, R. B. P. Amino acid – Squaramide conjugates as anion binding receptors. *Results in Chemistry* **2024**, *11*, 101777. DOI: https://doi.org/10.1016/j.rechem.2024.101777.
(58) Harris, W. R.; Nesset-Tollefson, D.; Stenback, J. Z.; Mohamed-Hani, N. Site selectivity in the binding of inorganic anions to serum transferrin. *Journal of Inorganic Biochemistry* **1990**, *38* (3), 175–183. DOI: https://doi.org/10.1016/0162-0134(90)84011-D.
(59) Baker, E. N.; Anderson, B. F.; Baker, H. M.; Haridas, M.; Norris, G. E.; Rumball, S. V.; Smith, C. A. Metal and anion binding sites in lactoferrin and related proteins. *Pure and Applied Chemistry* **1990**, *62* (6), 1067–1070. DOI: doi:10.1351/pac199062061067 (accessed 2024-12-01).
(60) Baker, E. N.; Lindley, P. F. New perspectives on the structure and function of transferrins. *J Inorg Biochem* **1992**, *47* (3-4), 147–160. DOI: 10.1016/0162-0134(92)84061-q From NLM.
(61) Langridge, R.; Shinagawa, H.; Pardee, A. B. Sulfate-Binding Protein from Salmonella typhimurium: Physical Properties. *Science* **1970**, *169* (3940), 59–61. DOI: doi:10.1126/science.169.3940.59.

(62) Pflugrath, J. W.; Quiocho, F. A. The 2 A resolution structure of the sulfate-binding protein involved in active transport in Salmonella typhimurium. *J Mol Biol* **1988**, *200* (1), 163–180. DOI: 10.1016/0022-2836(88)90341-5 From NLM.
(63) Luecke, H.; Quiocho, F. A. High specificity of a phosphate transport protein determined by hydrogen bonds. *Nature* **1990**, *347* (6291), 402–406. DOI: 10.1038/347402a0 From NLM.
(64) Kubik, S. Amino acid containing anion receptors. *Chemical Society Reviews* **2009**, *38* (2), 585–605, 10.1039/B810531F. DOI: 10.1039/B810531F.
(65) Molina, P.; Zapata, F.; Caballero, A. Anion Recognition Strategies Based on Combined Noncovalent Interactions. *Chemical Reviews* **2017**, *117* (15), 9907–9972. DOI: 10.1021/acs.chemrev.6b00814.
(66) Macreadie, L. K.; Gilchrist, A. M.; McNaughton, D. A.; Ryder, W. G.; Fares, M.; Gale, P. A. Progress in anion receptor chemistry. *Chem* **2022**, *8* (1), 46–118. DOI: https://doi.org/10.1016/j.chempr.2021.10.029.
(67) Langton, M. J.; Serpell, C. J.; Beer, P. D. Anion Recognition in Water: Recent Advances from a Supramolecular and Macromolecular Perspective. *Angewandte Chemie International Edition* **2016**, *55* (6), 1974–1987. DOI: https://doi.org/10.1002/anie.201506589.
(68) Butler, S. J.; Jolliffe, K. A. Anion Receptors for the Discrimination of ATP and ADP in Biological Media. *ChemPlusChem* **2021**, *86* (1), 59–70. DOI: https://doi.org/10.1002/cplu.202000567.
(69) Gale, Philip A.; Howe, Ethan N. W.; Wu, X. Anion Receptor Chemistry. *Chem* **2016**, *1* (3), 351–422. DOI: https://doi.org/10.1016/j.chempr.2016.08.004.
(70) Allison, S. J.; Bryk, J.; Clemett, C. J.; Faulkner, R. A.; Ginger, M.; Griffiths, H. B. S.; Harmer, J.; Jane Owen-Lynch, P.; Pinder, E.; Wurdak, H.; et al. Self-assembly of an anion receptor with metal-dependent kinase inhibition and potent in vitro anti-cancer properties. *Nature Communications* **2021**, *12* (1), 3898. DOI: 10.1038/s41467-021-23983-3.
(71) Ha, S.; Lee, J.; Kim, K.-s.; Choi, E. J.; Nhem, P.; Song, C. Anion-Responsive Thiourea-Based Gel Actuator. *Chemistry of Materials* **2019**, *31* (15), 5735–5741. DOI: 10.1021/acs.chemmater.9b01715.
(72) Graf, E.; Lehn, J. M. Anion cryptates: highly stable and selective macrotricyclic anion inclusion complexes. *Journal of the American Chemical Society* **1976**, *98* (20), 6403–6405. DOI: 10.1021/ja00436a066.
(73) Lehn, J. M.; Sonveaux, E.; Willard, A. K. Molecular recognition. Anion cryptates of a macrobicyclic receptor molecule for linear triatomic species. *Journal of the American Chemical Society* **1978**, *100* (15), 4914–4916. DOI: 10.1021/ja00483a059.
(74) Dietrich, B.; Guilhem, J.; Lehn, J.-M.; Pascard, C.; Sonveaux, E. Molecular Recognition in Anion Coordination Chemistry. Structure, Binding Constants and Receptor-Substrate Complementarity of a Series of Anion Cryptates of a Macrobicyclic Receptor Molecule. *Helvetica Chimica Acta* **1984**, *67* (1), 91–104. DOI: https://doi.org/10.1002/hlca.19840670112.
(75) Schmidtchen, F. P. Macrotricyclic Quaternary Ammonium Salts: Enzyme-Analogous Activity. *Angewandte Chemie International Edition in English* **1981**, *20* (5), 466–468. DOI: https://doi.org/10.1002/anie.198104662.
(76) Schmidtchen, F. P. Inclusion of Anions in Macrotricyclic Quaternary Ammonium Salts. *Angewandte Chemie International Edition in English* **1977**, *16* (10), 720–721. DOI: https://doi.org/10.1002/anie.197707201.

(77) Worm, K.; Schmidtchen, F. P. Molecular Recognition of Anions by Zwitterionic Host Molecules in Water. *Angewandte Chemie International Edition in English* **1995**, *34* (1), 65–66. DOI: https://doi.org/10.1002/anie.199500651.
(78) Berger, M.; Schmidtchen, F. P. Zwitterionic Guanidinium Compounds Serve as Electroneutral Anion Hosts. *Journal of the American Chemical Society* **1999**, *121* (43), 9986–9993. DOI: 10.1021/ja992028k.
(79) Thordarson, P. Determining association constants from titration experiments in supramolecular chemistry. *Chemical Society Reviews* **2011**, *40* (3), 1305–1323, 10.1039/C0CS00062K. DOI: 10.1039/C0CS00062K.
(80) Rodriguez-Docampo, Z.; Eugenieva-Ilieva, E.; Reyheller, C.; Belenguer, A.; Kubik, S.; Otto, S. Dynamic combinatorial development of a neutral synthetic receptor that binds sulfate with nanomolar affinity in aqueous solution. *Chemical Communications* **2011**, *47*, 9798–9800. DOI: 10.1039/c1cc13451e.
(81) Riel, A. M. S.; Decato, D. A.; Sun, J.; Massena, C. J.; Jessop, M. J.; Berryman, O. B. The intramolecular hydrogen bonded–halogen bond: a new strategy for preorganization and enhanced binding. *Chemical Science* **2018**, *9* (26), 5828–5836, 10.1039/C8SC01973H. DOI: 10.1039/C8SC01973H.
(82) Cram, D. J.; Cram, J. M. Host-Guest Chemistry. *Science* **1974**, *183* (4127), 803–809. DOI: doi:10.1126/science.183.4127.803.
(83) Kaabel, S.; Adamson, J.; Topić, F.; Kiesilä, A.; Kalenius, E.; Öeren, M.; Reimund, M.; Prigorchenko, E.; Lõokene, A.; Reich, H. J.; et al. Chiral hemicucurbit[8]uril as an anion receptor: selectivity to size, shape and charge distribution. *Chemical Science* **2017**, *8* (3), 2184–2190, 10.1039/C6SC05058A. DOI: 10.1039/C6SC05058A.
(84) Li, Z.-Y.; Su, H.-K.; Tong, H.-X.; Yin, Y.; Xiao, T.; Sun, X.-Q.; Jiang, J.; Wang, L. Calix[4]arene containing thiourea and coumarin functionality as highly selective fluorescent and colorimetric chemosensor for fluoride ion. *Spectrochimica Acta Part A: Molecular and Biomolecular Spectroscopy* **2018**, *200*, 307–312. DOI: https://doi.org/10.1016/j.saa.2018.04.040.
(85) Yudin, A. K. Macrocycles: lessons from the distant past, recent developments, and future directions. *Chemical Science* **2015**, *6* (1), 30–49, 10.1039/C4SC03089C. DOI: 10.1039/C4SC03089C.
(86) Wu, X.; Gilchrist, A. M.; Gale, P. A. Prospects and Challenges in Anion Recognition and Transport. *Chem* **2020**, *6* (6), 1296–1309. DOI: https://doi.org/10.1016/j.chempr.2020.05.001.
(87) Chen, L.; Berry, S. N.; Wu, X.; Howe, E. N. W.; Gale, P. A. Advances in Anion Receptor Chemistry. *Chem* **2020**, *6* (1), 61–141. DOI: https://doi.org/10.1016/j.chempr.2019.12.002.
(88) Peng, R.; Xu, Y.; Cao, Q. Recent advances in click-derived macrocycles for ions recognition. *Chinese Chemical Letters* **2018**, *29* (10), 1465–1474. DOI: https://doi.org/10.1016/j.cclet.2018.09.001.
(89) Ghale, G.; Nau, W. M. Dynamically Analyte-Responsive Macrocyclic Host–Fluorophore Systems. *Accounts of Chemical Research* **2014**, *47* (7), 2150–2159. DOI: 10.1021/ar500116d.
(90) Li, A.; Zhai, H.; Li, J.; He, Q. Practical Applications of Supramolecular Extraction with Macrocycles. *Chemistry Letters* **2020**, *49* (10), 1125–1135. DOI: 10.1246/cl.200409 (accessed 5/30/2024).
(91) Zhang, Q.; Zhou, Y.; Ahmed, M.; Khashab, N. M.; Han, W.; Wang, H.; Page, Z. A.; Sessler, J. L. Anion extractants constructed by macrocycle-based anion recognition.

Journal of Materials Chemistry A **2022**, *10* (29), 15297–15308, 10.1039/D2TA03791B. DOI: 10.1039/D2TA03791B.
(92) Pan, Y.-C.; Tian, J.-H.; Guo, D.-S. Molecular Recognition with Macrocyclic Receptors for Application in Precision Medicine. *Accounts of Chemical Research* **2023**, *56* (24), 3626–3639. DOI: 10.1021/acs.accounts.3c00585.
(93) Pinalli, R.; Pedrini, A.; Dalcanale, E. Biochemical sensing with macrocyclic receptors. *Chemical Society Reviews* **2018**, *47* (18), 7006–7026, 10.1039/C8CS00271A. DOI: 10.1039/C8CS00271A.
(94) Padnya, P. L.; Wu, X.; Erxleben, A.; Braga, S. S. Editorial: Design of Macrocyclic Compounds for Biomedical Applications. *Frontiers in Chemistry* **2021**, *9*, Editorial. DOI: 10.3389/fchem.2021.730111.
(95) Barbette, F.; Rascalou, F.; Chollet, H.; Babouhot, J. L.; Denat, F.; Guilard, R. Extraction of uranyl ions from aqueous solutions using silica-gel-bound macrocycles for alpha contaminated waste water treatment. *Analytica Chimica Acta* **2004**, *502* (2), 179–187. DOI: https://doi.org/10.1016/j.aca.2003.09.065.
(96) Cao, D.; Kou, Y.; Liang, J.; Chen, Z.; Wang, L.; Meier, H. A Facile and Efficient Preparation of Pillararenes and a Pillarquinone. *Angewandte Chemie International Edition* **2009**, *48* (51), 9721–9723. DOI: https://doi.org/10.1002/anie.200904765.
(97) Cheng, S.-Q.; Lin, Q.; Li, S.-L.; Guo, Y.-X.; Han, X.-L.; Sun, Y.; Liu, Y. Recent advancements in supramolecular macrocycles for two-dimensional membranes for separations. *Green Chemistry* **2023**, *25* (18), 7026–7040, 10.1039/D3GC01996A. DOI: 10.1039/D3GC01996A.
(98) Zhang, Z.-Y.; Li, C. Biphen[n]arenes: Modular Synthesis, Customizable Cavity Sizes, and Diverse Skeletons. *Accounts of Chemical Research* **2022**, *55* (6), 916–929. DOI: 10.1021/acs.accounts.2c00043.
(99) Pancholi, J.; Beer, P. D. Halogen bonding motifs for anion recognition. *Coordination Chemistry Reviews* **2020**, *416*, 213281. DOI: https://doi.org/10.1016/j.ccr.2020.213281.
(100) Qiao, B.; Anderson, J. R.; Pink, M.; Flood, A. H. Size-matched recognition of large anions by cyanostar macrocycles is saved when solvent-bias is avoided. *Chemical Communications* **2016**, *52* (56), 8683–8686, 10.1039/C6CC03463B. DOI: 10.1039/C6CC03463B.
(101) Sohn, D. H.; Kim, N.; Jang, S.; Kang, J. A fluoride selective water-soluble anion receptor based on a 1,2-phenylenediacetic acid and calcium ion dimer. *New Journal of Chemistry* **2019**, *43* (34), 13690–13695, 10.1039/C9NJ01436E. DOI: 10.1039/C9NJ01436E.
(102) Gamez, P.; Mooibroek, T. J.; Teat, S. J.; Reedijk, J. Anion Binding Involving π-Acidic Heteroaromatic Rings. *Accounts of Chemical Research* **2007**, *40* (6), 435–444. DOI: 10.1021/ar7000099.
(103) Carnegie, R. S.; Gibb, C. L. D.; Gibb, B. C. Anion Complexation and The Hofmeister Effect. *Angewandte Chemie International Edition* **2014**, *53* (43), 11498–11500. DOI: https://doi.org/10.1002/anie.201405796.
(104) Zhang, T.; Zhou, L.-P.; Guo, X.-Q.; Cai, L.-X.; Sun, Q.-F. Adaptive self-assembly and induced-fit transformations of anion-binding metal-organic macrocycles. *Nature Communications* **2017**, *8* (1), 15898. DOI: 10.1038/ncomms15898.
(105) Abdurakhmanova, E. R.; Cmoch, P.; Szumna, A. Three modes of interactions between anions and phenolic macrocycles: a comparative study. *Organic & Biomolecular Chemistry* **2022**, *20* (25), 5095–5103, 10.1039/D2OB00880G. DOI: 10.1039/D2OB00880G.

(106) Liu, Z.; Zhou, Y.; Yuan, L. Hydrogen-bonded aromatic amide macrocycles: synthesis, properties and functions. *Organic & Biomolecular Chemistry* **2022**, *20* (46), 9023–9051, 10.1039/D2OB01263D. DOI: 10.1039/D2OB01263D.
(107) Choi, K.; Hamilton, A. D. Macrocyclic anion receptors based on directed hydrogen bonding interactions. *Coordination Chemistry Reviews* **2003**, *240* (1), 101–110. DOI: https://doi.org/10.1016/S0010-8545(02)00305-3.
(108) Desiraju, G. R. Hydrogen Bridges in Crystal Engineering: Interactions without Borders. *Accounts of Chemical Research* **2002**, *35* (7), 565–573. DOI: 10.1021/ar010054t.
(109) Smith, P. J.; Reddington, M. V.; Wilcox, C. S. Ion pair binding by a urea in chloroform solution. *Tetrahedron Letters* **1992**, *33* (41), 6085–6088. DOI: https://doi.org/10.1016/S0040-4039(00)60012-6.
(110) Shang, X.; Yang, Z.; Fu, J.; Zhao, P.; Xu, X. The Synthesis and Anion Recognition Property of Symmetrical Chemosensors Involving Thiourea Groups: Theory and Experiments. *Sensors* **2015**, *15* (11), 28166–28176.
(111) Amendola, V.; Bergamaschi, G.; Boiocchi, M.; Fabbrizzi, L.; Milani, M. The Squaramide versus Urea Contest for Anion Recognition. *Chemistry – A European Journal* **2010**, *16* (14), 4368–4380. DOI: https://doi.org/10.1002/chem.200903190.
(112) Marchetti, L. A.; Kumawat, L. K.; Mao, N.; Stephens, J. C.; Elmes, R. B. P. The Versatility of Squaramides: From Supramolecular Chemistry to Chemical Biology. *Chem* **2019**, *5* (6), 1398–1485. DOI: https://doi.org/10.1016/j.chempr.2019.02.027.
(113) Butler, S. M.; Hountondji, M.; Berry, S. N.; Tan, J.; Macia, L.; Jolliffe, K. A. A macrocyclic fluorescent probe for the detection of citrate. *Organic & Biomolecular Chemistry* **2023**, *21* (42), 8548–8553, 10.1039/D3OB01442H. DOI: 10.1039/D3OB01442H.
(114) Luo, N.; Li, J.; Sun, T.; Wan, S.; Li, P.; Wu, N.; Yan, Y.; Bao, X. Carbazole sulfonamide-based macrocyclic receptors capable of selective complexation of fluoride ion. *RSC Advances* **2021**, *11* (17), 10203–10211, 10.1039/D1RA01285A. DOI: 10.1039/D1RA01285A.
(115) Butler, S. M.; Jolliffe, K. A. Molecular recognition and sensing of dicarboxylates and dicarboxylic acids. *Organic & Biomolecular Chemistry* **2020**, *18* (41), 8236–8254, 10.1039/D0OB01761B. DOI: 10.1039/D0OB01761B.
(116) Sikora, K.; Jaśkiewicz, M.; Neubauer, D.; Migoń, D.; Kamysz, W. The Role of Counter-Ions in Peptides—An Overview. *Pharmaceuticals* **2020**, *13* (12), 442.
(117) Chakrabarti, P. Anion Binding Sites in Protein Structures. *Journal of Molecular Biology* **1993**, *234* (2), 463–482. DOI: https://doi.org/10.1006/jmbi.1993.1599.
(118) Elmes, R. B. P.; Jolliffe, K. A. Anion recognition by cyclic peptides. *Chemical Communications* **2015**, *51* (24), 4951–4968, 10.1039/C4CC10095F. DOI: 10.1039/C4CC10095F.
(119) Butler, S. J.; Jolliffe, K. A. Synthesis of a family of cyclic peptide-based anion receptors. *Organic & Biomolecular Chemistry* **2011**, *9* (9), 3471–3483, 10.1039/C0OB01072C. DOI: 10.1039/C0OB01072C.
(120) Davey, S. G. Running rings around chloride. *Nature Reviews Chemistry* **2020**, *4* (5), 228–228. DOI: 10.1038/s41570-020-0185-0.
(121) Kubik, S. Anion Recognition in Aqueous Media by Cyclopeptides and Other Synthetic Receptors. *Accounts of Chemical Research* **2017**, *50* (11), 2870–2878. DOI: 10.1021/acs.accounts.7b00458.

(122) Larnaudie, S. C.; Brendel, J. C.; Jolliffe, K. A.; Perrier, S. Cyclic peptide–polymer conjugates: Grafting-to vs grafting-from. *Journal of Polymer Science Part A: Polymer Chemistry* **2016**, *54* (7), 1003–1011. DOI: https://doi.org/10.1002/pola.27937.
(123) Chapman, R.; Danial, M.; Koh, M. L.; Jolliffe, K. A.; Perrier, S. Design and properties of functional nanotubes from the self-assembly of cyclic peptide templates. *Chemical Society Reviews* **2012**, *41* (18), 6023–6041, 10.1039/C2CS35172B. DOI: 10.1039/C2CS35172B.
(124) Sergeant, G. E.; Jolliffe, K. A. Anion recognition using a simple cyclic peptide. *Supramolecular Chemistry* **2020**, *32* (3), 233–237. DOI: 10.1080/10610278.2020.1732377.
(125) Sommer, F.; Marcus, Y.; Kubik, S. Effects of Solvent Properties on the Anion Binding of Neutral Water-Soluble Bis(cyclopeptides) in Water and Aqueous Solvent Mixtures. *ACS Omega* **2017**, *2* (7), 3669–3680. DOI: 10.1021/acsomega.7b00867.
(126) Schaly, A.; Belda, R.; García-España, E.; Kubik, S. Selective Recognition of Sulfate Anions by a Cyclopeptide-Derived Receptor in Aqueous Phosphate Buffer. *Organic Letters* **2013**, *15* (24), 6238–6241. DOI: 10.1021/ol4030919.
(127) Kubik, S.; Goddard, R. Fine Tuning of the Cation Affinity of Artificial Receptors Based on Cyclic Peptides by Intramolecular Conformational Control. *European Journal of Organic Chemistry* **2001**, *2001* (2), 311–322. DOI: https://doi.org/10.1002/1099-0690(200101)2001:2<311::AID-EJOC311>3.0.CO;2-M.
(128) Fiehn, T.; Goddard, R.; Seidel, R. W.; Kubik, S. A Cyclopeptide-Derived Molecular Cage for Sulfate Ions That Closes with a Click. *Chemistry – A European Journal* **2010**, *16* (24), 7241–7255. DOI: https://doi.org/10.1002/chem.201000308.
(129) Mesquita, L. M.; Anhäuser, J.; Bellaire, D.; Becker, S.; Lützen, A.; Kubik, S. Palladium(II)-Mediated Assembly of a M2L2 Macrocycle and M3L6 Cage from a Cyclopeptide-Derived Ligand. *Organic Letters* **2019**, *21* (16), 6442–6446. DOI: 10.1021/acs.orglett.9b02338.
(130) Petters, I.; Modrušan, M.; Vidović, N.; Crnolatac, I.; Cindro, N.; Piantanida, I.; Speranza, G.; Horvat, G.; Tomišić, V. Anion-Sensing Properties of Cyclopentaphenylalanine. *Molecules* **2022**, *27* (12), 3918.
(131) Picci, G.; Carreira-Barral, I.; Alonso-Carrillo, D.; Busonera, C.; Milia, J.; Quesada, R.; Caltagirone, C. The role of indolyl substituents in squaramide-based anionophores. *Organic & Biomolecular Chemistry* **2022**, *20* (40), 7981–7986, 10.1039/D2OB01444K. DOI: 10.1039/D2OB01444K.
(132) Picci, G.; Aragoni, M. C.; Arca, M.; Caltagirone, C.; Formica, M.; Fusi, V.; Giorgi, L.; Ingargiola, F.; Lippolis, V.; Macedi, E.; et al. Fluorescent sensing of non-steroidal anti-inflammatory drugs naproxen and ketoprofen by dansylated squaramide-based receptors. *Organic & Biomolecular Chemistry* **2023**, *21* (14), 2968–2975, 10.1039/D3OB00324H. DOI: 10.1039/D3OB00324H.
(133) Picci, G.; Farotto, S.; Milia, J.; Caltagirone, C.; Lippolis, V.; Aragoni, M. C.; Di Natale, C.; Paolesse, R.; Lvova, L. Potentiometric Sensing of Nonsteroidal Painkillers by Acyclic Squaramide Ionophores. *ACS Sensors* **2023**, *8* (8), 3225–3239. DOI: 10.1021/acssensors.3c00981.
(134) Bao, X.; Wu, X.; Berry, S. N.; Howe, E. N. W.; Chang, Y.-T.; Gale, P. A. Fluorescent squaramides as anion receptors and transmembrane anion transporters. *Chemical Communications* **2018**, *54* (11), 1363–1366, 10.1039/C7CC08706C. DOI: 10.1039/C7CC08706C.

(135) Marques, I.; Costa, P. M. R.; Q. Miranda, M.; Busschaert, N.; Howe, E. N. W.; Clarke, H. J.; Haynes, C. J. E.; Kirby, I. L.; Rodilla, A. M.; Pérez-Tomás, R.; et al. Full elucidation of the transmembrane anion transport mechanism of squaramides using in silico investigations. *Physical Chemistry Chemical Physics* **2018**, *20* (32), 20796–20811, 10.1039/C8CP02576B. DOI: 10.1039/C8CP02576B.
(136) Zhang, S.; Wang, Y.; Xie, W.; Howe, E. N. W.; Busschaert, N.; Sauvat, A.; Leduc, M.; Gomes-da-Silva, L. C.; Chen, G.; Martins, I.; et al. Squaramide-based synthetic chloride transporters activate TFEB but block autophagic flux. *Cell Death & Disease* **2019**, *10* (3), 242. DOI: 10.1038/s41419-019-1474-8.
(137) Qin, L.; Hartley, A.; Turner, P.; Elmes, R. B. P.; Jolliffe, K. A. Macrocyclic squaramides: anion receptors with high sulfate binding affinity and selectivity in aqueous media. *Chemical Science* **2016**, *7* (7), 4563–4572, 10.1039/C6SC01011C. DOI: 10.1039/C6SC01011C.
(138) Qin, L.; Wright, J. R.; Lane, J. D. E.; Berry, S. N.; Elmes, R. B. P.; Jolliffe, K. A. Receptors for sulfate that function across a wide pH range in mixed aqueous–DMSO media. *Chemical Communications* **2019**, *55* (82), 12312–12315, 10.1039/C9CC06812K. DOI: 10.1039/C9CC06812K.
(139) Qin, L.; Vervuurt, S. J. N.; Elmes, R. B. P.; Berry, S. N.; Proschogo, N.; Jolliffe, K. A. Extraction and transport of sulfate using macrocyclic squaramide receptors. *Chemical Science* **2020**, *11* (1), 201–207, 10.1039/C9SC04786G. DOI: 10.1039/C9SC04786G.
(140) Zaleskaya, M.; Karbarz, M.; Wilczek, M.; Dobrzycki, Ł.; Romański, J. Cooperative Transport and Selective Extraction of Sulfates by a Squaramide-Based Ion Pair Receptor: A Case of Adaptable Selectivity. *Inorganic Chemistry* **2020**, *59* (18), 13749–13759. DOI: 10.1021/acs.inorgchem.0c02114.
(141) Zaleskaya-Hernik, M.; Megiel, E.; Romański, J. Utilizing a polymer containing squaramide-based ion pair receptors for salt extraction. *Journal of Molecular Liquids* **2022**, *361*, 119600. DOI: https://doi.org/10.1016/j.molliq.2022.119600.
(142) Zaleskaya-Hernik, M.; Dobrzycki, Ł.; Romański, J. Interaction of Ions in Organic and Aqueous Media with an Ion-Pair Sensor Equipped with a BODIPY Reporter: An ON1-OFF-ON2-ON3 Fluorescent Assay. *International Journal of Molecular Sciences* **2023**, *24* (10), 8536.
(143) Zaleskaya, M.; Jagleniec, D.; Romański, J. Macrocyclic squaramides as ion pair receptors and fluorescent sensors selective towards sulfates. *Dalton Transactions* **2021**, *50* (11), 3904–3915, 10.1039/D0DT04273K. DOI: 10.1039/D0DT04273K.
(144) Saha, I.; Lee, J. T.; Lee, C.-H. Recent Advancements in Calix[4]pyrrole-Based Anion-Receptor Chemistry. *European Journal of Organic Chemistry* **2015**, *2015* (18), 3859–3885. DOI: https://doi.org/10.1002/ejoc.201403701.
(145) Gale, P. A.; Sessler, J. L.; Král, V.; Lynch, V. Calix[4]pyrroles: Old Yet New Anion-Binding Agents. *Journal of the American Chemical Society* **1996**, *118* (21), 5140–5141. DOI: 10.1021/ja960307r.
(146) Villarón, D.; Brugman, G. E. A.; Siegler, M. A.; Wezenberg, S. J. Photoswitching of halide-binding affinity and selectivity in dithienylethene-strapped calix[4]pyrrole. *Chemical Communications* **2023**, *59* (56), 8688–8691, 10.1039/D3CC02264A. DOI: 10.1039/D3CC02264A.
(147) Xiong, S.; Chen, F.; Zhao, T.; Li, A.; Xu, G.; Sessler, J. L.; He, Q. Selective Inclusion of Fluoride within the Cavity of a Two-Wall Bis-calix[4]pyrrole. *Organic Letters* **2020**, *22* (11), 4451–4455. DOI: 10.1021/acs.orglett.0c01440.

(148) Zhu, S. S.; Staats, H.; Brandhorst, K.; Grunenberg, J.; Gruppi, F.; Dalcanale, E.; Lützen, A.; Rissanen, K.; Schalley, C. A. Anion Binding to Resorcinarene-Based Cavitands: The Importance of C□H···Anion Interactions. *Angewandte Chemie International Edition* **2008**, *47* (4), 788–792. DOI: https://doi.org/10.1002/anie.200703451.
(149) Ilioudis, C. A.; Tocher, D. A.; Steed, J. W. A Highly Efficient, Preorganized Macrobicyclic Receptor for Halides Based on CH··· and NH···Anion Interactions. *Journal of the American Chemical Society* **2004**, *126* (39), 12395–12402. DOI: 10.1021/ja047070g.
(150) Li, Y.; Flood, A. H. Pure C□H Hydrogen Bonding to Chloride Ions: A Preorganized and Rigid Macrocyclic Receptor. *Angewandte Chemie International Edition* **2008**, *47* (14), 2649–2652. DOI: https://doi.org/10.1002/anie.200704717.
(151) Lee, S.; Chen, C.-H.; Flood, A. H. A pentagonal cyanostar macrocycle with cyanostilbene CH donors binds anions and forms dialkylphosphate [3]rotaxanes. *Nature Chemistry* **2013**, *5* (8), 704–710. DOI: 10.1038/nchem.1668.
(152) Zeynaloo, E.; Zahran, E. M.; Fatila, E. M.; Flood, A. H.; Bachas, L. G. Anion-Selective Electrodes Based On a CH-Hydrogen Bonding Bis-macrocyclic Ionophore with a Clamshell Architecture. *Analytical Chemistry* **2021**, *93* (13), 5412–5419. DOI: 10.1021/acs.analchem.0c04801.
(153) Sheetz, E. G.; Zhang, Z.; Marogil, A.; Che, M.; Pink, M.; Carta, V.; Raghavachari, K.; Flood, A. H. High-fidelity Recognition of Organotrifluoroborate Anions (R−BF3−) as Designer Guest Molecules. *Chemistry – A European Journal* **2022**, *28* (60), e202201584. DOI: https://doi.org/10.1002/chem.202201584.
(154) Liu, C.-Z.; Koppireddi, S.; Wang, H.; Zhang, D.-W.; Li, Z.-T. Halogen bonding-driven formation of supramolecular macrocycles and double helix. *Chinese Chemical Letters* **2019**, *30* (5), 953–956. DOI: https://doi.org/10.1016/j.cclet.2019.02.010.
(155) Brown, A.; Beer, P. D. Halogen bonding anion recognition. *Chemical Communications* **2016**, *52* (56), 8645–8658, 10.1039/C6CC03638D. DOI: 10.1039/C6CC03638D.
(156) White, N. G.; Caballero, A.; Beer, P. D. Observation of strong halogen bonds in the solid state structures of bis-haloimidazolium macrocycles. *CrystEngComm* **2014**, *16* (18), 3722–3729, 10.1039/C3CE41944D. DOI: 10.1039/C3CE41944D.
(157) Tse, Y. C.; Docker, A.; Zhang, Z.; Beer, P. D. Lithium halide ion-pair recognition with halogen bonding and chalcogen bonding heteroditopic macrocycles. *Chemical Communications* **2021**, *57* (40), 4950–4953, 10.1039/D1CC01287H. DOI: 10.1039/D1CC01287H.
(158) Bunchuay, T.; Boonpalit, K.; Docker, A.; Ruengsuk, A.; Tantirungrotechai, J.; Sukwattanasinitt, M.; Surawatanawong, P.; Beer, P. D. Charge neutral halogen bonding tetradentate-iodotriazole macrocycles capable of anion recognition and sensing in highly competitive aqueous media. *Chemical Communications* **2021**, *57* (90), 11976–11979, 10.1039/D1CC05037K. DOI: 10.1039/D1CC05037K.
(159) Zhao, T.; Lynch, V. M.; Sessler, J. L. Tetradentate halogen bonding macrocyclic anion receptor inspired by the “Texas-sized” molecular box. *Organic & Biomolecular Chemistry* **2022**, *20* (5), 980–983, 10.1039/D1OB02381K. DOI: 10.1039/D1OB02381K.
(160) Gong, H.-Y.; Rambo, B. M.; Karnas, E.; Lynch, V. M.; Sessler, J. L. A ‘Texas-sized’ molecular box that forms an anion-induced supramolecular necklace. *Nature Chemistry* **2010**, *2* (5), 406–409. DOI: 10.1038/nchem.597.

(161) Tuo, D.-H.; Ao, Y.-F.; Wang, Q.-Q.; Wang, D.-X. Naphthalene-Pillared Benzene Triimide Cage: An Efficient Receptor for Polyhedral Anions and a General Tool for Probing Theoretically-Existing Anion-π Binding Motifs. *CCS Chemistry* **2022**, *4* (8), 2806–2815. DOI: doi:10.31635/ccschem.021.202101366.
(162) Li, W.; Qin, P.; Zhao, X.-X.; Qu, W.-J.; Lin, Q.; Yao, H.; Wei, T.-B.; Zhang, Y.-M.; Liu, Y.; Shi, B. Fluorinated leaning pillar[6]arene: synthesis, structure and selective iodide anion binding by anion–π interactions. *Organic & Biomolecular Chemistry* **2022**, *20* (46), 9122–9126, 10.1039/D2OB01579J. DOI: 10.1039/D2OB01579J.
(163) Huang, F.; Anslyn, E. V. Introduction: Supramolecular Chemistry. *Chemical Reviews* **2015**, *115* (15), 6999–7000. DOI: 10.1021/acs.chemrev.5b00352.
(164) Haino, T. Molecular-recognition-directed formation of supramolecular polymers. *Polymer Journal* **2013**, *45* (4), 363–383. DOI: 10.1038/pj.2012.144.
(165) Busschaert, N.; Caltagirone, C.; Van Rossom, W.; Gale, P. A. Applications of Supramolecular Anion Recognition. *Chemical Reviews* **2015**, *115* (15), 8038–8155. DOI: 10.1021/acs.chemrev.5b00099.
(166) Garcia Jimenez, D.; Poongavanam, V.; Kihlberg, J. Macrocycles in Drug Discovery—Learning from the Past for the Future. *Journal of Medicinal Chemistry* **2023**, *66* (8), 5377−5396. DOI: 10.1021/acs.jmedchem.3c00134.
(167) Chen, Y.; Guerin, S.; Yuan, H.; O'Donnell, J.; Xue, B.; Cazade, P.-A.; Haq, E. U.; Shimon, L. J. W.; Rencus-Lazar, S.; Tofail, S. A. M.; et al. Guest Molecule-Mediated Energy Harvesting in a Conformationally Sensitive Peptide–Metal Organic Framework. *Journal of the American Chemical Society* **2022**, *144* (8), 3468–3476. DOI: 10.1021/jacs.1c11750.
(168) Gale, P. A.; Caltagirone, C. Anion sensing by small molecules and molecular ensembles. *Chemical Society Reviews* **2015**, *44* (13), 4212–4227, 10.1039/C4CS00179F. DOI: 10.1039/C4CS00179F.
(169) Zhou, H.-X.; Pang, X. Electrostatic Interactions in Protein Structure, Folding, Binding, and Condensation. *Chemical Reviews* **2018**, *118* (4), 1691–1741. DOI: 10.1021/acs.chemrev.7b00305.
(170) Sergeant, G.; Jolliffe, K. Anion recognition using a simple cyclic peptide. *Supramolecular Chemistry* **2020**, *32*, 1–5. DOI: 10.1080/10610278.2020.1732377.
(171) Zhou, D.; Chen, Y.; He, J.; Zhang, Q.; Jiang, Z.; Yang, G. Applications and prospects of synthetic receptors for therapeutic protein delivery. *European Journal of Pharmaceutics and Biopharmaceutics* **2025**, *214*, 114789. DOI: https://doi.org/10.1016/j.ejpb.2025.114789.
(172) Wang, Q.-Q. Anion Recognition-Directed Supramolecular Catalysis with Functional Macrocycles and Molecular Cages. *Accounts of Chemical Research* **2024**, *57* (21), 3227–3240. DOI: 10.1021/acs.accounts.4c00583.
(173) Ren, B.; Sun, Y.; Xin, P. Recent Advances in Artificial Anion Channels and Their Selectivity. *ChemPlusChem* **2024**, *89* (12), e202400466. DOI: https://doi.org/10.1002/cplu.202400466.
(174) Mungalpara, D.; Stegmüller, S.; Kubik, S. A neutral halogen bonding macrocyclic anion receptor based on a pseudocyclopeptide with three 5-iodo-1,2,3-triazole subunits. *Chemical Communications* **2017**, *53* (37), 5095–5098, 10.1039/C7CC02424J. DOI: 10.1039/C7CC02424J.
(175) Somogyi, L.; Haberhauer, G.; Rebek, J. Improved synthesis of functionalized molecular platforms related to marine cyclopeptides. *Tetrahedron* **2001**, *57* (9), 1699–1708. DOI: https://doi.org/10.1016/S0040-4020(00)01173-X.

(176) Haberhauer, G.; Rominger, F. Syntheses and Structures of Imidazole Analogues of Lissoclinum Cyclopeptides. *European Journal of Organic Chemistry* **2003**, *2003* (16), 3209–3218. DOI: https://doi.org/10.1002/ejoc.200300207.
(177) Haberhauer, G.; Oeser, T.; Rominger, F. Molecular Scaffold for the Construction of Three-Armed and Cage-Like Receptors. *Chemistry – A European Journal* **2005**, *11* (22), 6718–6726. DOI: https://doi.org/10.1002/chem.200500224.
(178) Haberhauer, G.; Pintér, Á.; Oeser, T.; Rominger, F. Synthesis and Structural Investigation of C4- and C2-Symmetric Molecular Scaffolds Based on Imidazole Peptides. *European Journal of Organic Chemistry* **2007**, *2007* (11), 1779–1792. DOI: https://doi.org/10.1002/ejoc.200600942.
(179) Schnopp, M.; Ernst, S.; Haberhauer, G. Anion Recognition by Neutral Macrocyclic Azole Amides. *European Journal of Organic Chemistry* **2009**, *2009* (2), 213–222. DOI: https://doi.org/10.1002/ejoc.200800811.
(180) Dobscha, J. R.; Castillo, H. D.; Li, Y.; Fadler, R. E.; Taylor, R. D.; Brown, A. A.; Trainor, C. Q.; Tait, S. L.; Flood, A. H. Sequence-Defined Macrocycles for Understanding and Controlling the Build-up of Hierarchical Order in Self-Assembled 2D Arrays. *Journal of the American Chemical Society* **2019**, *141* (44), 17588–17600. DOI: 10.1021/jacs.9b06410.
(181) Meisel, J. W.; Hu, C. T.; Hamilton, A. D. Heterofunctionalized Cavitands by Macrocyclization of Sequence-Defined Foldamers. *Organic Letters* **2019**, *21* (19), 7763–7767. DOI: 10.1021/acs.orglett.9b02708.
(182) Rodríguez-Vázquez, N.; Amorín, M.; Alfonso, I.; Granja, J. R. Anion Recognition and Induced Self-Assembly of an α,γ-Cyclic Peptide To Form Spherical Clusters. *Angewandte Chemie International Edition* **2016**, *55* (14), 4504–4508. DOI: https://doi.org/10.1002/anie.201511857.
(183) Fuertes, A.; Amorín, M.; Granja, J. R. Versatile symport transporters based on cyclic peptide dimers. *Chemical Communications* **2020**, *56* (1), 46–49, 10.1039/C9CC06644F. DOI: 10.1039/C9CC06644F.
(184) Kubik, S. Synthetic Receptors Based on Abiotic Cyclo(pseudo)peptides. *Molecules* **2022**, *27* (9). DOI: 10.3390/molecules27092821 From NLM.
(185) Burade, S. S.; Pawar, S. V.; Saha, T.; Kumbhar, N.; Kotmale, A. S.; Ahmad, M.; Talukdar, P.; Dhavale, D. D. Sugar-derived oxazolone pseudotetrapeptide as γ-turn inducer and anion-selective transporter. *Beilstein Journal of Organic Chemistry* **2019**, *15*, 2419–2427. DOI: 10.3762/bjoc.15.234.
(186) Diemer, V.; Fischer, L.; Kauffmann, B.; Guichard, G. Anion Recognition by Aliphatic Helical Oligoureas. *Chemistry – A European Journal* **2016**, *22* (44), 15684–15692. DOI: https://doi.org/10.1002/chem.201602481.
(187) Elmes, R. B. P.; K. Y. Yuen, K.; Jolliffe, K. A. Sulfate-Selective Recognition by Using Neutral Dipeptide Anion Receptors in Aqueous Solution. *Chemistry – A European Journal* **2014**, *20* (24), 7373–7380. DOI: https://doi.org/10.1002/chem.201400292.
(188) Amendola, V.; Fabbrizzi, L.; Mosca, L.; Schmidtchen, F.-P. Urea-, Squaramide-, and Sulfonamide-Based Anion Receptors: A Thermodynamic Study. *Chemistry – A European Journal* **2011**, *17* (21), 5972–5981. DOI: https://doi.org/10.1002/chem.201003411.
(189) Edwards, S. J.; Valkenier, H.; Busschaert, N.; Gale, P. A.; Davis, A. P. High-Affinity Anion Binding by Steroidal Squaramide Receptors. *Angewandte Chemie International Edition* **2015**, *54* (15), 4592–4596. DOI: https://doi.org/10.1002/anie.201411805.

(190) Saez Talens, V.; Englebienne, P.; Trinh, T. T.; Noteborn, W. E. M.; Voets, I. K.; Kieltyka, R. E. Aromatic Gain in a Supramolecular Polymer. *Angewandte Chemie International Edition* **2015**, *54* (36), 10502–10506. DOI: https://doi.org/10.1002/anie.201503905.
(191) Elmes, R. B. P.; Jolliffe, K. A. Amino acid-based squaramides for anion recognition. *Supramolecular Chemistry* **2015**, *27* (5-6), 321–328. DOI: 10.1080/10610278.2014.976221.
(192) Levy, A. A.; Rains, H. C.; Smiles, S. CCCCLII.—The rearrangement of hydroxy-sulphones. Part I. *Journal of the Chemical Society (Resumed)* **1931**, (0), 3264–3269, 10.1039/JR9310003264. DOI: 10.1039/JR9310003264.
(193) Truce, W. E.; Kreider, E. M.; Brand, W. W. The Smiles and Related Rearrangements of Aromatic Systems. In *Organic Reactions*, pp 99–215.
(194) Liu, H.; Tomooka, C. S.; Moore, H. W. An Efficient General Synthesis of Squarate Esters. *Synthetic Communications* **1997**, *27* (12), 2177–2180. DOI: 10.1080/00397919708006826.
(195) Chung, B. K. W.; White, C. J.; Scully, C. C. G.; Yudin, A. K. The reactivity and conformational control of cyclic tetrapeptides derived from aziridine-containing amino acids. *Chemical Science* **2016**, *7* (11), 6662–6668, 10.1039/C6SC01687A. DOI: 10.1039/C6SC01687A.
(196) De Riccardis, F. The Challenge of Conformational Isomerism in Cyclic Peptoids. *European Journal of Organic Chemistry* **2020**, *2020* (20), 2981–2994. DOI: https://doi.org/10.1002/ejoc.201901838.
(197) Grimme, S.; Antony, J.; Ehrlich, S.; Krieg, H. A consistent and accurate ab initio parametrization of density functional dispersion correction (DFT-D) for the 94 elements H-Pu. *The Journal of Chemical Physics* **2010**, *132* (15). DOI: 10.1063/1.3382344 (accessed 11/8/2023).
(198) Mennucci, B.; Tomasi, J. Continuum solvation models: A new approach to the problem of solute's charge distribution and cavity boundaries. *The Journal of Chemical Physics* **1997**, *106* (12), 5151–5158. DOI: 10.1063/1.473558 (accessed 11/8/2023).
(199) *Gaussian 16 Rev. C.01*; Wallingford, CT, 2016.
(200) Elmes, R. B. P.; Turner, P.; Jolliffe, K. A. Colorimetric and Luminescent Sensors for Chloride: Hydrogen Bonding vs Deprotonation. *Organic Letters* **2013**, *15* (22), 5638–5641. DOI: 10.1021/ol402500q.
(201) Brynn Hibbert, D.; Thordarson, P. The death of the Job plot, transparency, open science and online tools, uncertainty estimation methods and other developments in supramolecular chemistry data analysis. *Chemical Communications* **2016**, *52* (87), 12792–12805, 10.1039/C6CC03888C. DOI: 10.1039/C6CC03888C.
(202) Prestinaci, F.; Pezzotti, P.; Pantosti, A. Antimicrobial resistance: a global multifaceted phenomenon. *Pathog Glob Health* **2015**, *109* (7), 309–318. DOI: 10.1179/2047773215y.0000000030 From NLM.
(203) Salam, M. A.; Al-Amin, M. Y.; Salam, M. T.; Pawar, J. S.; Akhter, N.; Rabaan, A. A.; Alqumber, M. A. A. Antimicrobial Resistance: A Growing Serious Threat for Global Public Health. *Healthcare (Basel)* **2023**, *11* (13). DOI: 10.3390/healthcare11131946 From NLM.
(204) Almutairy, B. Extensively and multidrug-resistant bacterial strains: case studies of antibiotics resistance. *Frontiers in Microbiology* **2024**, *Volume 15 - 2024*, Review. DOI: 10.3389/fmicb.2024.1381511.

(205) Oliveira, M.; Antunes, W.; Mota, S.; Madureira-Carvalho, Á.; Dinis-Oliveira, R. J.; Dias da Silva, D. An Overview of the Recent Advances in Antimicrobial Resistance. *Microorganisms* **2024**, *12* (9), 1920.
(206) Bobate, S.; Mahalle, S.; Dafale, N. A.; Bajaj, A. Emergence of environmental antibiotic resistance: Mechanism, monitoring and management. *Environmental Advances* **2023**, *13*, 100409. DOI: https://doi.org/10.1016/j.envadv.2023.100409.
(207) EclinicalMedicine. Antimicrobial resistance: a top ten global public health threat. *EClinicalMedicine* **2021**, *41*, 101221. DOI: 10.1016/j.eclinm.2021.101221 From NLM.
(208) Walsh, T. R.; Gales, A. C.; Laxminarayan, R.; Dodd, P. C. Antimicrobial Resistance: Addressing a Global Threat to Humanity. *PLOS Medicine* **2023**, *20* (7), e1004264. DOI: 10.1371/journal.pmed.1004264.
(209) Chinemerem Nwobodo, D.; Ugwu, M. C.; Oliseloke Anie, C.; Al-Ouqaili, M. T. S.; Chinedu Ikem, J.; Victor Chigozie, U.; Saki, M. Antibiotic resistance: The challenges and some emerging strategies for tackling a global menace. *J Clin Lab Anal* **2022**, *36* (9), e24655. DOI: 10.1002/jcla.24655 From NLM.
(210) Ahmed, S. K.; Hussein, S.; Qurbani, K.; Ibrahim, R. H.; Fareeq, A.; Mahmood, K. A.; Mohamed, M. G. Antimicrobial resistance: Impacts, challenges, and future prospects. *Journal of Medicine, Surgery, and Public Health* **2024**, *2*, 100081. DOI: https://doi.org/10.1016/j.glmedi.2024.100081.
(211) Muteeb, G.; Rehman, M. T.; Shahwan, M.; Aatif, M. Origin of Antibiotics and Antibiotic Resistance, and Their Impacts on Drug Development: A Narrative Review. *Pharmaceuticals (Basel)* **2023**, *16* (11). DOI: 10.3390/ph16111615 From NLM.
(212) Singha, B.; Singh, V.; Soni, V. Alternative therapeutics to control antimicrobial resistance: a general perspective. *Frontiers in Drug Discovery* **2024**, *Volume 4 - 2024*, Review. DOI: 10.3389/fddsv.2024.1385460.
(213) Huan, Y.; Kong, Q.; Mou, H.; Yi, H. Antimicrobial Peptides: Classification, Design, Application and Research Progress in Multiple Fields. *Frontiers in Microbiology* **2020**, *Volume 11 - 2020*, Review. DOI: 10.3389/fmicb.2020.582779.
(214) Jones, E. M.; Smart, A.; Bloomberg, G.; Burgess, L.; Millar, M. R. Lactoferricin, a new antimicrobial peptide. *J Appl Bacteriol* **1994**, *77* (2), 208–214. DOI: 10.1111/j.1365-2672.1994.tb03065.x From NLM.
(215) Anumudu, C.; Hart, A.; Miri, T.; Onyeaka, H. Recent Advances in the Application of the Antimicrobial Peptide Nisin in the Inactivation of Spore-Forming Bacteria in Foods. *Molecules* **2021**, *26* (18). DOI: 10.3390/molecules26185552 From NLM.
(216) Brady, D.; Grapputo, A.; Romoli, O.; Sandrelli, F. Insect Cecropins, Antimicrobial Peptides with Potential Therapeutic Applications. *Int J Mol Sci* **2019**, *20* (23). DOI: 10.3390/ijms20235862 From NLM.
(217) Hoskin, D. W.; Ramamoorthy, A. Studies on anticancer activities of antimicrobial peptides. *Biochimica et Biophysica Acta (BBA) - Biomembranes* **2008**, *1778* (2), 357–375. DOI: https://doi.org/10.1016/j.bbamem.2007.11.008.
(218) Zhang, Q. Y.; Yan, Z. B.; Meng, Y. M.; Hong, X. Y.; Shao, G.; Ma, J. J.; Cheng, X. R.; Liu, J.; Kang, J.; Fu, C. Y. Antimicrobial peptides: mechanism of action, activity and clinical potential. *Mil Med Res* **2021**, *8* (1), 48. DOI: 10.1186/s40779-021-00343-2 From NLM.
(219) Zhang, L.-j.; Gallo, R. L. Antimicrobial peptides. *Current Biology* **2016**, *26* (1), R14–R19. DOI: https://doi.org/10.1016/j.cub.2015.11.017.

(220) Zhang, Q. Antimicrobial peptides: from discovery to developmental applications. *Appl Environ Microbiol* **2025**, *91* (4), e0211524. DOI: 10.1128/aem.02115-24 From NLM.
(221) K R, G.; Balenahalli Narasingappa, R.; Vishnu Vyas, G. Unveiling mechanisms of antimicrobial peptide: Actions beyond the membranes disruption. *Heliyon* **2024**, *10* (19), e38079. DOI: https://doi.org/10.1016/j.heliyon.2024.e38079.
(222) Mba, I. E.; Nweze, E. I. Antimicrobial Peptides Therapy: An Emerging Alternative for Treating Drug-Resistant Bacteria. *Yale J Biol Med* **2022**, *95* (4), 445–463. From NLM.
(223) Aunpad, R.; Thitirungreangchai, T. Advancing antimicrobial peptides: Overcoming challenges in the era of bacterial resistance. *Biochimie* **2025**. DOI: https://doi.org/10.1016/j.biochi.2025.07.019.
(224) Erdem Büyükkiraz, M.; Kesmen, Z. Antimicrobial peptides (AMPs): A promising class of antimicrobial compounds. *Journal of Applied Microbiology* **2022**, *132* (3), 1573–1596. DOI: https://doi.org/10.1111/jam.15314.
(225) Zheng, S.; Tu, Y.; Li, B.; Qu, G.; Li, A.; Peng, X.; Li, S.; Shao, C. Antimicrobial peptide biological activity, delivery systems and clinical translation status and challenges. *Journal of Translational Medicine* **2025**, *23* (1), 292. DOI: 10.1186/s12967-025-06321-9.
(226) Gong, Y.; Wang, H.; Sun, J. AMP-Mimetic Antimicrobial Polymer-Involved Synergic Therapy with Various Coagents for Improved Efficiency. *Biomacromolecules* **2024**, *25* (8), 4619–4638. DOI: 10.1021/acs.biomac.3c01458.
(227) Teng, P.; Shao, H.; Huang, B.; Xie, J.; Cui, S.; Wang, K.; Cai, J. Small Molecular Mimetics of Antimicrobial Peptides as a Promising Therapy To Combat Bacterial Resistance. *J Med Chem* **2023**, *66* (4), 2211–2234. DOI: 10.1021/acs.jmedchem.2c00757 From NLM.
(228) Rotem, S.; Mor, A. Antimicrobial peptide mimics for improved therapeutic properties. *Biochimica et Biophysica Acta (BBA) - Biomembranes* **2009**, *1788* (8), 1582–1592. DOI: https://doi.org/10.1016/j.bbamem.2008.10.020.
(229) Gan, B. H.; Gaynord, J.; Rowe, S. M.; Deingruber, T.; Spring, D. R. The multifaceted nature of antimicrobial peptides: current synthetic chemistry approaches and future directions. *Chem Soc Rev* **2021**, *50* (13), 7820–7880. DOI: 10.1039/d0cs00729c From NLM.
(230) Mwangi, J.; Kamau, P. M.; Thuku, R. C.; Lai, R. Design methods for antimicrobial peptides with improved performance. *Zool Res* **2023**, *44* (6), 1095–1114. DOI: 10.24272/j.issn.2095-8137.2023.246 From NLM.
(231) Méndez-Samperio, P. Peptidomimetics as a new generation of antimicrobial agents: current progress. *Infect Drug Resist* **2014**, *7*, 229–237. DOI: 10.2147/idr.S49229 From NLM.
(232) Su, M.; Su, Y. Recent Advances in Amphipathic Peptidomimetics as Antimicrobial Agents to Combat Drug Resistance. *Molecules* **2024**, *29* (11), 2492.
(233) Lai, Z.; Yuan, X.; Chen, H.; Zhu, Y.; Dong, N.; Shan, A. Strategies employed in the design of antimicrobial peptides with enhanced proteolytic stability. *Biotechnology Advances* **2022**, *59*, 107962. DOI: https://doi.org/10.1016/j.biotechadv.2022.107962.
(234) Clapperton, A. M.; Babi, J.; Tran, H. A Field Guide to Optimizing Peptoid Synthesis. *ACS Polymers Au* **2022**, *2* (6), 417–429. DOI: 10.1021/acspolymersau.2c00036.

(235) Xie, J.; Hu, W.; Feng, X.; Liu, Z.; Zhou, M.; Liu, R. Synthesis and antimicrobial applications of α-peptoid polymers. *Chemical Science* **2025**, *16* (28), 12679–12701, 10.1039/D5SC03968A. DOI: 10.1039/D5SC03968A.
(236) Webster, A. M.; Cobb, S. L. Recent Advances in the Synthesis of Peptoid Macrocycles. *Chemistry – A European Journal* **2018**, *24* (30), 7560–7573. DOI: https://doi.org/10.1002/chem.201705340.
(237) Zhu, J.; Chen, S.; Liu, Z.; Guo, J.; Cao, S.; Long, S. Recent advances in anticancer peptoids. *Bioorganic Chemistry* **2023**, *139*, 106686. DOI: https://doi.org/10.1016/j.bioorg.2023.106686.
(238) Mojsoska, B.; Zuckermann, R. N.; Jenssen, H. Structure-Activity Relationship Study of Novel Peptoids That Mimic the Structure of Antimicrobial Peptides. *Antimicrobial Agents and Chemotherapy* **2015**, *59* (7), 4112–4120. DOI: doi:10.1128/aac.00237-15.
(239) Tew, G. N.; Scott, R. W.; Klein, M. L.; DeGrado, W. F. De Novo Design of Antimicrobial Polymers, Foldamers, and Small Molecules: From Discovery to Practical Applications. *Accounts of Chemical Research* **2010**, *43* (1), 30–39. DOI: 10.1021/ar900036b.
(240) Choi, S.; Isaacs, A.; Clements, D.; Liu, D.; Kim, H.; Scott, R. W.; Winkler, J. D.; DeGrado, W. F. De novo design and in vivo activity of conformationally restrained antimicrobial arylamide foldamers. *Proceedings of the National Academy of Sciences* **2009**, *106* (17), 6968–6973. DOI: doi:10.1073/pnas.0811818106.
(241) Liu, Z.; Abramyan, A. M.; Pophristic, V. Helical arylamide foldamers: structure prediction by molecular dynamics simulations. *New Journal of Chemistry* **2015**, *39* (5), 3229–3240, 10.1039/C4NJ01925C. DOI: 10.1039/C4NJ01925C.
(242) Mensa, B.; Kim, Y. H.; Choi, S.; Scott, R.; Caputo, G. A.; DeGrado, W. F. Antibacterial mechanism of action of arylamide foldamers. *Antimicrob Agents Chemother* **2011**, *55* (11), 5043–5053. DOI: 10.1128/aac.05009-11 From NLM.
(243) Mitra, S.; Chen, M.-T.; Stedman, F.; Hernandez, J.; Kumble, G.; Kang, X.; Zhang, C.; Tang, G.; Reed, I.; Daugherty, I. Q.; et al. Cyclization of Two Antimicrobial Peptides Improves Their Activity. *ACS Omega* **2025**, *10* (9), 9728–9740. DOI: 10.1021/acsomega.4c11466.
(244) Falanga, A.; Nigro, E.; De Biasi, M. G.; Daniele, A.; Morelli, G.; Galdiero, S.; Scudiero, O. Cyclic Peptides as Novel Therapeutic Microbicides: Engineering of Human Defensin Mimetics. *Molecules* **2017**, *22* (7). DOI: 10.3390/molecules22071217 From NLM.
(245) Chan, L. Y.; Zhang, V. M.; Huang, Y.-h.; Waters, N. C.; Bansal, P. S.; Craik, D. J.; Daly, N. L. Cyclization of the Antimicrobial Peptide Gomesin with Native Chemical Ligation: Influences on Stability and Bioactivity. *ChemBioChem* **2013**, *14* (5), 617–624. DOI: https://doi.org/10.1002/cbic.201300034.
(246) Bellotto, O.; Semeraro, S.; Bandiera, A.; Tramer, F.; Pavan, N.; Marchesan, S. Polymer Conjugates of Antimicrobial Peptides (AMPs) with d-Amino Acids (d-aa): State of the Art and Future Opportunities. *Pharmaceutics* **2022**, *14* (2). DOI: 10.3390/pharmaceutics14020446 From NLM.
(247) Yang, R.; Ma, X.; Peng, F.; Wen, J.; Allahou, L. W.; Williams, G. R.; Knowles, J. C.; Poma, A. Advances in antimicrobial peptides: From mechanistic insights to chemical modifications. *Biotechnology Advances* **2025**, *81*, 108570. DOI: https://doi.org/10.1016/j.biotechadv.2025.108570.
(248) Xu, S.; Tan, P.; Tang, Q.; Wang, T.; Ding, Y.; Fu, H.; Zhang, Y.; Zhou, C.; Song, M.; Tang, Q.; et al. Enhancing the stability of antimicrobial peptides: From design

strategies to applications. *Chemical Engineering Journal* **2023**, *475*, 145923. DOI: https://doi.org/10.1016/j.cej.2023.145923.
(249) Drayton, M.; Deisinger, J. P.; Ludwig, K. C.; Raheem, N.; Müller, A.; Schneider, T.; Straus, S. K. Host Defense Peptides: Dual Antimicrobial and Immunomodulatory Action. *Int J Mol Sci* **2021**, *22* (20). DOI: 10.3390/ijms222011172 From NLM.
(250) Koprivnjak, T.; Peschel, A. Bacterial resistance mechanisms against host defense peptides. *Cell Mol Life Sci* **2011**, *68* (13), 2243–2254. DOI: 10.1007/s00018-011-0716-4 From NLM.
(251) Acconcia, C.; Paladino, A.; Valle, M. d.; Farina, B.; Del Gatto, A.; Gaetano, S. D.; Capasso, D.; Gentile, M. T.; Malgieri, G.; Isernia, C.; et al. High-Resolution Conformational Analysis of RGDechi-Derived Peptides Based on a Combination of NMR Spectroscopy and MD Simulations. *International Journal of Molecular Sciences* **2022**, *23* (19), 11039.
(252) Damjanovic, J.; Miao, J.; Huang, H.; Lin, Y.-S. Elucidating Solution Structures of Cyclic Peptides Using Molecular Dynamics Simulations. *Chemical Reviews* **2021**, *121* (4), 2292–2324. DOI: 10.1021/acs.chemrev.0c01087.
(253) Ratrey, P.; Das Mahapatra, A.; Pandit, S.; Hadianawala, M.; Majhi, S.; Mishra, A.; Datta, B. Emergent antibacterial activity of N-(thiazol-2-yl)benzenesulfonamides in conjunction with cell-penetrating octaarginine. *RSC Advances* **2021**, *11* (46), 28581–28592, 10.1039/D1RA03882F. DOI: 10.1039/D1RA03882F.
(254) Ahn, M.; Jacob, B.; Gunasekaran, P.; Murugan, R. N.; Ryu, E. K.; Lee, G.-h.; Hyun, J.-K.; Cheong, C.; Kim, N.-H.; Shin, S. Y.; et al. Poly-lysine peptidomimetics having potent antimicrobial activity without hemolytic activity. *Amino Acids* **2014**, *46* (9), 2259–2269. DOI: 10.1007/s00726-014-1778-z.
(255) Mookherjee, N.; Anderson, M. A.; Haagsman, H. P.; Davidson, D. J. Antimicrobial host defence peptides: functions and clinical potential. *Nature Reviews Drug Discovery* **2020**, *19* (5), 311–332. DOI: 10.1038/s41573-019-0058-8.
(256) Stauber, T.; Jentsch, T. J. Chloride in Vesicular Trafficking and Function. *Annual Review of Physiology* **2013**, *75* (Volume 75, 2013), 453–477. DOI: https://doi.org/10.1146/annurev-physiol-030212-183702.
(257) Jentsch, T. J.; Pusch, M. CLC Chloride Channels and Transporters: Structure, Function, Physiology, and Disease. *Physiol Rev* **2018**, *98* (3), 1493–1590. DOI: 10.1152/physrev.00047.2017 From NLM.
(258) Hoffmann, E. K.; Lambert, I. H.; Pedersen, S. F. Physiology of cell volume regulation in vertebrates. *Physiol Rev* **2009**, *89* (1), 193–277. DOI: 10.1152/physrev.00037.2007 From NLM.
(259) Gamba, G. Molecular physiology and pathophysiology of electroneutral cation-chloride cotransporters. *Physiol Rev* **2005**, *85* (2), 423–493. DOI: 10.1152/physrev.00011.2004 From NLM.
(260) Duran, C.; Thompson, C. H.; Xiao, Q.; Hartzell, H. C. Chloride channels: often enigmatic, rarely predictable. *Annu Rev Physiol* **2010**, *72*, 95–121. DOI: 10.1146/annurev-physiol-021909-135811 From NLM.
(261) Jentsch, T. J.; Stein, V.; Weinreich, F.; Zdebik, A. A. Molecular structure and physiological function of chloride channels. *Physiol Rev* **2002**, *82* (2), 503–568. DOI: 10.1152/physrev.00029.2001 From NLM.
(262) Cutting, G. R. Cystic fibrosis genetics: from molecular understanding to clinical application. *Nature Reviews Genetics* **2015**, *16* (1), 45–56. DOI: 10.1038/nrg3849.

(263) Hwang, T. C.; Kirk, K. L. The CFTR ion channel: gating, regulation, and anion permeation. *Cold Spring Harb Perspect Med* **2013**, *3* (1), a009498. DOI: 10.1101/cshperspect.a009498 From NLM.
(264) Riordan, J. R.; Rommens, J. M.; Kerem, B.; Alon, N.; Rozmahel, R.; Grzelczak, Z.; Zielenski, J.; Lok, S.; Plavsic, N.; Chou, J. L.; et al. Identification of the cystic fibrosis gene: cloning and characterization of complementary DNA. *Science* **1989**, *245* (4922), 1066–1073. DOI: 10.1126/science.2475911 From NLM.
(265) Gale, P. A.; Davis, J. T.; Quesada, R. Anion transport and supramolecular medicinal chemistry. *Chemical Society Reviews* **2017**, *46* (9), 2497–2519, 10.1039/C7CS00159B. DOI: 10.1039/C7CS00159B.
(266) Davis, J. T.; Okunola, O.; Quesada, R. Recent advances in the transmembrane transport of anions. *Chemical Society Reviews* **2010**, *39* (10), 3843–3862, 10.1039/B926164H. DOI: 10.1039/B926164H.
(267) Wu, X.; Howe, E. N. W.; Gale, P. A. Supramolecular Transmembrane Anion Transport: New Assays and Insights. *Acc Chem Res* **2018**, *51* (8), 1870–1879. DOI: 10.1021/acs.accounts.8b00264 From NLM.
(268) Hernando, E.; Capurro, V.; Cossu, C.; Fiore, M.; García-Valverde, M.; Soto-Cerrato, V.; Pérez-Tomás, R.; Moran, O.; Zegarra-Moran, O.; Quesada, R. Small molecule anionophores promote transmembrane anion permeation matching CFTR activity. *Scientific Reports* **2018**, *8* (1), 2608. DOI: 10.1038/s41598-018-20708-3.
(269) Davis, A. P.; Sheppard, D. N.; Smith, B. D. Development of synthetic membrane transporters for anions. *Chemical Society Reviews* **2007**, *36* (2), 348–357, 10.1039/B512651G. DOI: 10.1039/B512651G.
(270) Yang, J.; Yu, G.; Sessler, J. L.; Shin, I.; Gale, P. A.; Huang, F. Artificial transmembrane ion transporters as potential therapeutics. *Chem* **2021**, *7* (12), 3256–3291. DOI: https://doi.org/10.1016/j.chempr.2021.10.028.
(271) Li, H.; Valkenier, H.; Judd, L. W.; Brotherhood, P. R.; Hussain, S.; Cooper, J. A.; Jurček, O.; Sparkes, H. A.; Sheppard, D. N.; Davis, A. P. Efficient, non-toxic anion transport by synthetic carriers in cells and epithelia. *Nat Chem* **2016**, *8* (1), 24–32. DOI: 10.1038/nchem.2384 From NLM.
(272) Picci, G.; Marchesan, S.; Caltagirone, C. Ion Channels and Transporters as Therapeutic Agents: From Biomolecules to Supramolecular Medicinal Chemistry. *Biomedicines* **2022**, *10* (4). DOI: 10.3390/biomedicines10040885 From NLM.
(273) Sessler, J. L.; Eller, L. R.; Cho, W.-S.; Nicolaou, S.; Aguilar, A.; Lee, J. T.; Lynch, V. M.; Magda, D. J. Synthesis, Anion-Binding Properties, and In Vitro Anticancer Activity of Prodigiosin Analogues. *Angewandte Chemie International Edition* **2005**, *44* (37), 5989–5992. DOI: https://doi.org/10.1002/anie.200501740.
(274) Ko, S. K.; Kim, S. K.; Share, A.; Lynch, V. M.; Park, J.; Namkung, W.; Van Rossom, W.; Busschaert, N.; Gale, P. A.; Sessler, J. L.; et al. Synthetic ion transporters can induce apoptosis by facilitating chloride anion transport into cells. *Nat Chem* **2014**, *6* (10), 885–892. DOI: 10.1038/nchem.2021 From NLM.
(275) Ko, S.-K.; Kim, S. K.; Share, A.; Lynch, V. M.; Park, J.; Namkung, W.; Van Rossom, W.; Busschaert, N.; Gale, P. A.; Sessler, J. L.; et al. Synthetic ion transporters can induce apoptosis by facilitating chloride anion transport into cells. *Nature Chemistry* **2014**, *6* (10), 885–892. DOI: 10.1038/nchem.2021.
(276) Vargas Jentzsch, A.; Emery, D.; Mareda, J.; Metrangolo, P.; Resnati, G.; Matile, S. Ditopic Ion Transport Systems: Anion–π Interactions and Halogen Bonds at Work.

Angewandte Chemie International Edition **2011**, *50* (49), 11675–11678. DOI: https://doi.org/10.1002/anie.201104966.
(277) Shi, S.; Tian, J.; Luo, Y. Recent advances in fluorinated products biosynthesis. *Bioresource Technology Reports* **2022**, *20*, 101288. DOI: https://doi.org/10.1016/j.biteb.2022.101288.
(278) Busschaert, N.; Wenzel, M.; Light, M. E.; Iglesias-Hernández, P.; Pérez-Tomás, R.; Gale, P. A. Structure–Activity Relationships in Tripodal Transmembrane Anion Transporters: The Effect of Fluorination. *Journal of the American Chemical Society* **2011**, *133* (35), 14136–14148. DOI: 10.1021/ja205884y.
(279) Howe, E. N. W.; Busschaert, N.; Wu, X.; Berry, S. N.; Ho, J.; Light, M. E.; Czech, D. D.; Klein, H. A.; Kitchen, J. A.; Gale, P. A. pH-Regulated Nonelectrogenic Anion Transport by Phenylthiosemicarbazones. *Journal of the American Chemical Society* **2016**, *138* (26), 8301–8308. DOI: 10.1021/jacs.6b04656.
(280) Karagiannidis, L. E.; Haynes, C. J. E.; Holder, K. J.; Kirby, I. L.; Moore, S. J.; Wells, N. J.; Gale, P. A. Highly effective yet simple transmembrane anion transporters based upon ortho-phenylenediamine bis-ureas. *Chemical Communications* **2014**, *50* (81), 12050–12053, 10.1039/C4CC05519E. DOI: 10.1039/C4CC05519E.
(281) Valkenier, H.; Akrawi, O.; Jurček, P.; Sleziaková, K.; Lízal, T.; Bartik, K.; Šindelář, V. Fluorinated Bambusurils as Highly Effective and Selective Transmembrane Cl−/HCO3− Antiporters. *Chem* **2019**, *5* (2), 429–444. DOI: https://doi.org/10.1016/j.chempr.2018.11.008.
(282) Amendola, V.; Esteban-Gómez, D.; Fabbrizzi, L.; Licchelli, M. What Anions Do to N−H-Containing Receptors. *Accounts of Chemical Research* **2006**, *39* (5), 343–353. DOI: 10.1021/ar050195l.
(283) Busschaert, N.; Kirby, I. L.; Young, S.; Coles, S. J.; Horton, P. N.; Light, M. E.; Gale, P. A. Squaramides as potent transmembrane anion transporters. *Angew Chem Int Ed Engl* **2012**, *51* (18), 4426–4430. DOI: 10.1002/anie.201200729 From NLM.
(284) McNaughton, D. A.; Ryder, W. G.; Gilchrist, A. M.; Wang, P.; Fares, M.; Wu, X.; Gale, P. A. New insights and discoveries in anion receptor chemistry. *Chem* **2023**, *9* (11), 3045–3112. DOI: https://doi.org/10.1016/j.chempr.2023.07.006.
(285) Busschaert, N.; Kirby, I. L.; Young, S.; Coles, S. J.; Horton, P. N.; Light, M. E.; Gale, P. A. Squaramides as Potent Transmembrane Anion Transporters. *Angewandte Chemie International Edition* **2012**, *51* (18), 4426–4430. DOI: https://doi.org/10.1002/anie.201200729.
(286) Brennan, L. E.; Luo, X.; Mohammed, F. A.; Kavanagh, K.; Elmes, R. B. P. Uncovering the potent antimicrobial activity of squaramide based anionophores – chloride transport and membrane disruption. *Chemical Science* **2025**, *16* (9), 4075–4084, 10.1039/D4SC01693A. DOI: 10.1039/D4SC01693A.
(287) Brennan, L. E.; Kumawat, L. K.; Piatek, M. E.; Kinross, A. J.; McNaughton, D. A.; Marchetti, L.; Geraghty, C.; Wynne, C.; Tong, H.; Kavanagh, O. N.; et al. Potent antimicrobial effect induced by disruption of chloride homeostasis. *Chem* **2023**, *9* (11), 3138–3158. DOI: https://doi.org/10.1016/j.chempr.2023.07.014.
(288) Ian Storer, R.; Aciro, C.; Jones, L. H. Squaramides: physical properties, synthesis and applications. *Chemical Society Reviews* **2011**, *40* (5), 2330–2346, 10.1039/C0CS00200C. DOI: 10.1039/C0CS00200C.
(289) Agnew-Francis, K. A.; Williams, C. M. Squaramides as Bioisosteres in Contemporary Drug Design. *Chemical Reviews* **2020**, *120* (20), 11616–11650. DOI: 10.1021/acs.chemrev.0c00416.

(290) Picci, G.; Montis, R.; Lippolis, V.; Caltagirone, C. Squaramide-based receptors in anion supramolecular chemistry: insights into anion binding, sensing, transport and extraction. *Chemical Society Reviews* **2024**, *53* (8), 3952–3975, 10.1039/D3CS01165H. DOI: 10.1039/D3CS01165H.
(291) Rosenau, C. P.; Jelier, B. J.; Gossert, A. D.; Togni, A. Exposing the Origins of Irreproducibility in Fluorine NMR Spectroscopy. *Angewandte Chemie International Edition* **2018**, *57* (30), 9528–9533. DOI: https://doi.org/10.1002/anie.201802620.
(292) Chvojka, M.; Singh, A.; Cataldo, A.; Torres-Huerta, A.; Konopka, M.; Šindelář, V.; Valkenier, H. The Lucigenin Assay: Measuring Anion Transport in Lipid Vesicles. *Analysis & Sensing* **2024**, *4* (2), e202300044. DOI: https://doi.org/10.1002/anse.202300044.
(293) Purser, S.; Moore, P. R.; Swallow, S.; Gouverneur, V. Fluorine in medicinal chemistry. *Chemical Society Reviews* **2008**, *37* (2), 320–330, 10.1039/B610213C. DOI: 10.1039/B610213C.
(294) Jowett, L. A.; Howe, E. N. W.; Wu, X.; Busschaert, N.; Gale, P. A. New Insights into the Anion Transport Selectivity and Mechanism of Tren-based Tris-(thio)ureas. *Chemistry – A European Journal* **2018**, *24* (41), 10475–10487. DOI: https://doi.org/10.1002/chem.201801463.
(295) Gazzano, E.; Bergandi, L.; Riganti, C.; Aldieri, E.; Doublier, S.; Costamagna, C.; Bosia, A.; Ghigo, D. Fluoride Effects: The Two Faces of Janus. *Current Medicinal Chemistry* **2010**, *17* (22), 2431–2441. DOI: http://dx.doi.org/10.2174/092986710791698503.
(296) Sharma, D.; Singh, A.; Verma, K.; Paliwal, S.; Sharma, S.; Dwivedi, J. Fluoride: A review of pre-clinical and clinical studies. *Environmental Toxicology and Pharmacology* **2017**, *56*, 297–313. DOI: https://doi.org/10.1016/j.etap.2017.10.008.
(297) Clarkson, J. J.; McLoughlin, J. Role of fluoride in oral health promotion. *International Dental Journal* **2000**, *50* (3), 119–128. DOI: https://doi.org/10.1111/j.1875-595X.2000.tb00552.x.
(298) Zuo, H.; Chen, L.; Kong, M.; Qiu, L.; Lü, P.; Wu, P.; Yang, Y.; Chen, K. Toxic effects of fluoride on organisms. *Life Sciences* **2018**, *198*, 18–24. DOI: https://doi.org/10.1016/j.lfs.2018.02.001.
(299) Kabir, H.; Gupta, A. K.; Tripathy, S. Fluoride and human health: Systematic appraisal of sources, exposures, metabolism, and toxicity. *Critical Reviews in Environmental Science and Technology* **2020**, *50* (11), 1116–1193. DOI: 10.1080/10643389.2019.1647028.
(300) Han, J.; Kiss, L.; Mei, H.; Remete, A. M.; Ponikvar-Svet, M.; Sedgwick, D. M.; Roman, R.; Fustero, S.; Moriwaki, H.; Soloshonok, V. A. Chemical Aspects of Human and Environmental Overload with Fluorine. *Chemical Reviews* **2021**, *121* (8), 4678–4742. DOI: 10.1021/acs.chemrev.0c01263.
(301) Shah, P.; Westwell, A. D. The role of fluorine in medicinal chemistry. *Journal of Enzyme Inhibition and Medicinal Chemistry* **2007**, *22* (5), 527–540. DOI: 10.1080/14756360701425014.
(302) Hinterholzinger, F. M.; Rühle, B.; Wuttke, S.; Karaghiosoff, K.; Bein, T. Highly sensitive and selective fluoride detection in water through fluorophore release from a metal-organic framework. *Scientific Reports* **2013**, *3* (1), 2562. DOI: 10.1038/srep02562.
(303) Miretzky, P.; Cirelli, A. F. Fluoride removal from water by chitosan derivatives and composites: A review. *Journal of Fluorine Chemistry* **2011**, *132* (4), 231–240. DOI: https://doi.org/10.1016/j.jfluchem.2011.02.001.

(304) Zhan, C.-G.; Dixon, D. A. Hydration of the Fluoride Anion: Structures and Absolute Hydration Free Energy from First-Principles Electronic Structure Calculations. *The Journal of Physical Chemistry A* **2004**, *108* (11), 2020–2029. DOI: 10.1021/jp0311512.
(305) Jiao, Y.; Zhu, B.; Chen, J.; Duan, X. Fluorescent sensing of fluoride in cellular system. *Theranostics* **2015**, *5* (2), 173–187. DOI: 10.7150/thno.9860 From NLM.
(306) Xiong, S.; Nanda Kishore, M. V.; Zhou, W.; He, Q. Recent advances in selective recognition of fluoride with macrocyclic receptors. *Coordination Chemistry Reviews* **2022**, *461*, 214480. DOI: https://doi.org/10.1016/j.ccr.2022.214480.
(307) Bianchi, A. *Anion Coordination Chemistry*; 2012.
(308) Gale, P. A. Anion receptor chemistry. *Chemical Communications* **2011**, *47* (1), 82–86, 10.1039/C0CC00656D. DOI: 10.1039/C0CC00656D.
(309) Mohammed, F. A.; Xiao, T.; Wang, L.; Elmes, R. B. P. Macrocyclic receptors for anion recognition. *Chemical Communications* **2024**, *60* (83), 11812–11836, 10.1039/D4CC04521A. DOI: 10.1039/D4CC04521A.
(310) Pan, Y. C.; Tian, J. H.; Guo, D. S. Molecular Recognition with Macrocyclic Receptors for Application in Precision Medicine. *Acc Chem Res* **2023**, *56* (24), 3626–3639. DOI: 10.1021/acs.accounts.3c00585 From NLM.
(311) Wong, J. K.; Todd, M. H.; Rutledge, P. J. Recent Advances in Macrocyclic Fluorescent Probes for Ion Sensing. *Molecules* **2017**, *22* (2). DOI: 10.3390/molecules22020200 From NLM.
(312) Han, X.-N.; Han, Y.; Chen, C.-F. Fluorescent Macrocyclic Arenes: Synthesis and Applications. *Angewandte Chemie International Edition* **2025**, *64* (12), e202424276. DOI: https://doi.org/10.1002/anie.202424276.
(313) Royer, C. A. Fluorescence Spectroscopy. In *Protein Stability and Folding: Theory and Practice*, Shirley, B. A. Ed.; Humana Press, 1995; pp 65–89.
(314) Gunnlaugsson, T.; Davis, A. P.; O'Brien, J. E.; Glynn, M. Fluorescent Sensing of Pyrophosphate and Bis-carboxylates with Charge Neutral PET Chemosensors. *Organic Letters* **2002**, *4* (15), 2449–2452. DOI: 10.1021/ol026004l.
(315) Goshisht, M. K.; Tripathi, N. Fluorescence-based sensors as an emerging tool for anion detection: mechanism, sensory materials and applications. *Journal of Materials Chemistry C* **2021**, *9* (31), 9820–9850, 10.1039/D1TC01990B. DOI: 10.1039/D1TC01990B.
(316) Kubik, S. Anion recognition in water. *Chemical Society Reviews* **2010**, *39* (10), 3648–3663, 10.1039/B926166B. DOI: 10.1039/B926166B.
(317) Huang, X.-h.; Lu, Y.; He, Y.-b.; Chen, Z.-h. A Metal–Macrocycle Complex as a Fluorescent Sensor for Biological Phosphate Ions in Aqueous Solution. *European Journal of Organic Chemistry* **2010**, *2010* (10), 1921–1927. DOI: https://doi.org/10.1002/ejoc.200901328.
(318) Zhou, H.; Zhao, Y.; Gao, G.; Li, S.; Lan, J.; You, J. Highly Selective Fluorescent Recognition of Sulfate in Water by Two Rigid Tetrakisimidazolium Macrocycles with Peripheral Chains. *Journal of the American Chemical Society* **2013**, *135* (40), 14908–14911. DOI: 10.1021/ja406638b.
(319) Liu, Y.; Zhao, Z.; Huo, R.; Liu, Q. Two macrocycle-based sensors for anions sensing. *Scientific Reports* **2019**, *9* (1), 502. DOI: 10.1038/s41598-018-36916-w.
(320) Cho, J.; Kim, S. Fluorescent calix[4]triazole for selective fluoride anion sensing. *RSC Advances* **2025**, *15* (6), 4342–4347, 10.1039/D5RA00014A. DOI: 10.1039/D5RA00014A.

(321) Nemati, M.; Hosseinzadeh, R.; Zadmard, R.; Mohadjerani, M. Highly selective colorimetric and fluorescent chemosensor for fluoride based on fluorenone armed calix[4]arene. *Sensors and Actuators B: Chemical* **2017**, *241*, 690–697. DOI: https://doi.org/10.1016/j.snb.2016.10.140.
(322) Oshchepkov, A. S.; Shumilova, T. A.; Namashivaya, S. R.; Fedorova, O. A.; Dorovatovskii, P. V.; Khrustalev, V. N.; Kataev, E. A. Hybrid Macrocycles for Selective Binding and Sensing of Fluoride in Aqueous Solution. *The Journal of Organic Chemistry* **2018**, *83* (4), 2145–2153. DOI: 10.1021/acs.joc.7b03077.
(323) Maity, J.; Honcharenko, D.; Strömberg, R. Synthesis of fluorescent d-amino acids with 4-acetamidobiphenyl and 4-N,N-dimethylamino-1,8-naphthalimido containing side chains. *Tetrahedron Letters* **2015**, *56* (33), 4780–4783. DOI: https://doi.org/10.1016/j.tetlet.2015.06.059.
(324) Jain, A. N.; Brueckner, A. C.; Jorge, C.; Cleves, A. E.; Khandelwal, P.; Cortes, J. C.; Mueller, L. Complex peptide macrocycle optimization: combining NMR restraints with conformational analysis to guide structure-based and ligand-based design. *J Comput Aided Mol Des* **2023**, *37* (11), 519–535. DOI: 10.1007/s10822-023-00524-2 From NLM.
(325) Bonnet, P.; Agrafiotis, D. K.; Zhu, F.; Martin, E. Conformational Analysis of Macrocycles: Finding What Common Search Methods Miss. *Journal of Chemical Information and Modeling* **2009**, *49* (10), 2242–2259. DOI: 10.1021/ci900238a.
(326) Kessler, H. Conformation and Biological Activity of Cyclic Peptides. *Angewandte Chemie International Edition in English* **1982**, *21* (7), 512–523. DOI: https://doi.org/10.1002/anie.198205121.
(327) Martínez-Crespo, L.; Whitehead, G. F. S.; Vitórica-Yrezábal, I. J.; Webb, S. J. Cooperative intra- and intermolecular hydrogen bonding in scaffolded squaramide arrays. *Chemical Science* **2024**, *15* (41), 17120–17127, 10.1039/D4SC04337E. DOI: 10.1039/D4SC04337E.
(328) Marchetti, L. A.; Krämer, T.; Elmes, R. B. P. Amidosquaramides – a new anion binding motif with pH sensitive anion transport properties. *Organic & Biomolecular Chemistry* **2022**, *20* (35), 7056–7066, 10.1039/D2OB01176J. DOI: 10.1039/D2OB01176J.
(329) Bujosa, S.; Castellanos, E.; Frontera, A.; Rotger, C.; Costa, A.; Soberats, B. Self-assembly of amphiphilic aryl-squaramides in water driven by dipolar π–π interactions. *Organic & Biomolecular Chemistry* **2020**, *18* (5), 888–894, 10.1039/C9OB02085C. DOI: 10.1039/C9OB02085C.
(330) Liang, D.; Yu, C.; Qin, X.; Yang, X.; Dong, X.; Hu, M.; Du, L.; Li, M. Discovery of small-molecule fluorescent probes for C-Met. *European Journal of Medicinal Chemistry* **2022**, *230*, 114114. DOI: https://doi.org/10.1016/j.ejmech.2022.114114.
(331) Curtis, A.; Harrison, F.; Kavanagh, K. Proteomic characterization of Aspergillus fumigatus - host interactions using the ex-vivo pig lung (EVPL) model. *Virulence* **2025**, *16* (1), 2530675. DOI: 10.1080/21505594.2025.2530675 From NLM.

Appendix

Appendix

Chapter 2 – Supplementary Characterisation Data

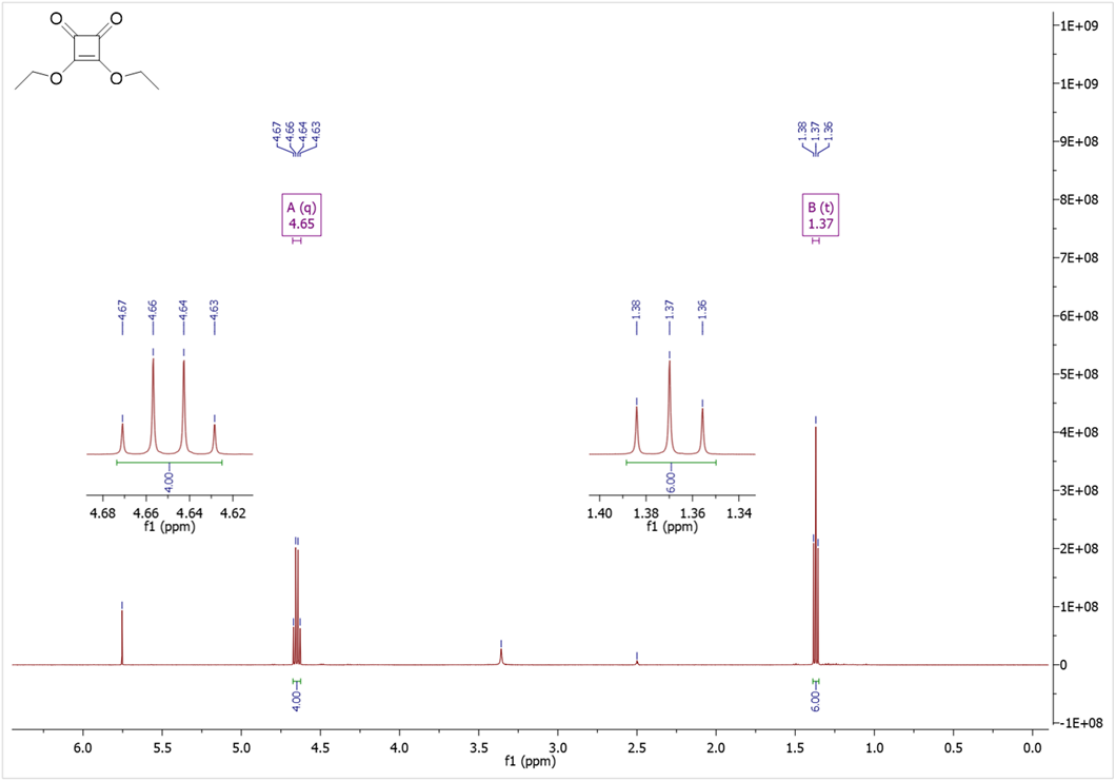

Figure A2.1: ^{1}H NMR spectrum of **DeSq** in DMSO-d_6.

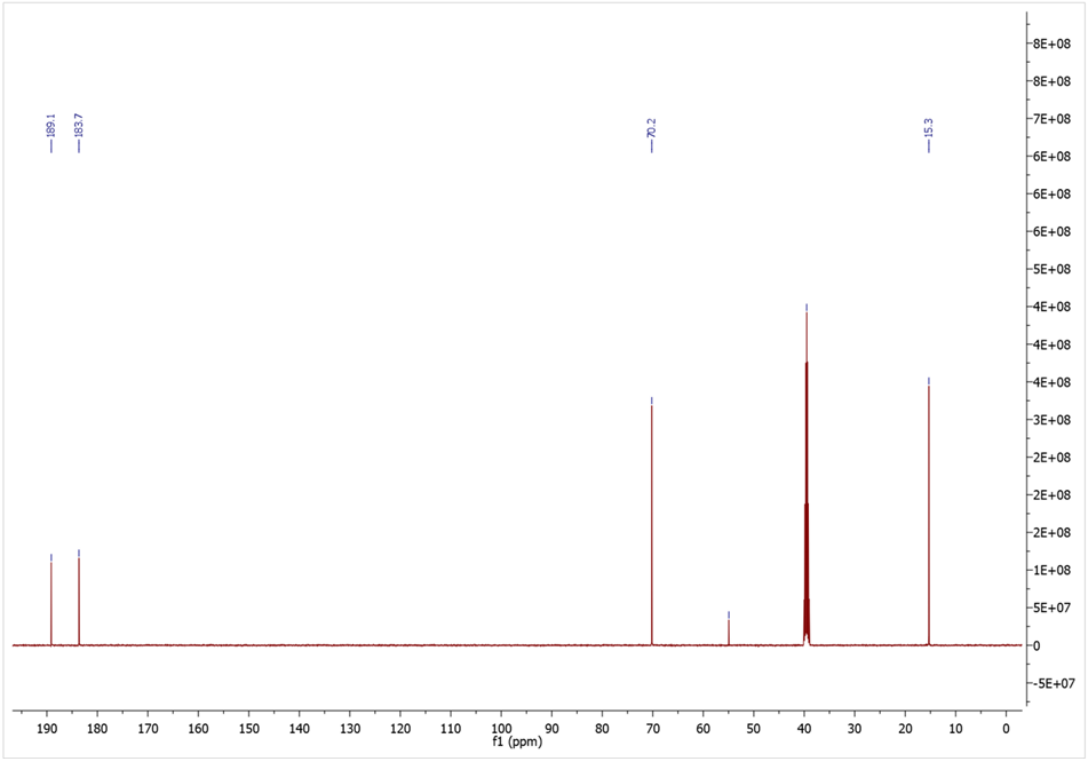

Figure A2.2: ^{13}C NMR spectrum of **DeSq** in DMSO-d_6.

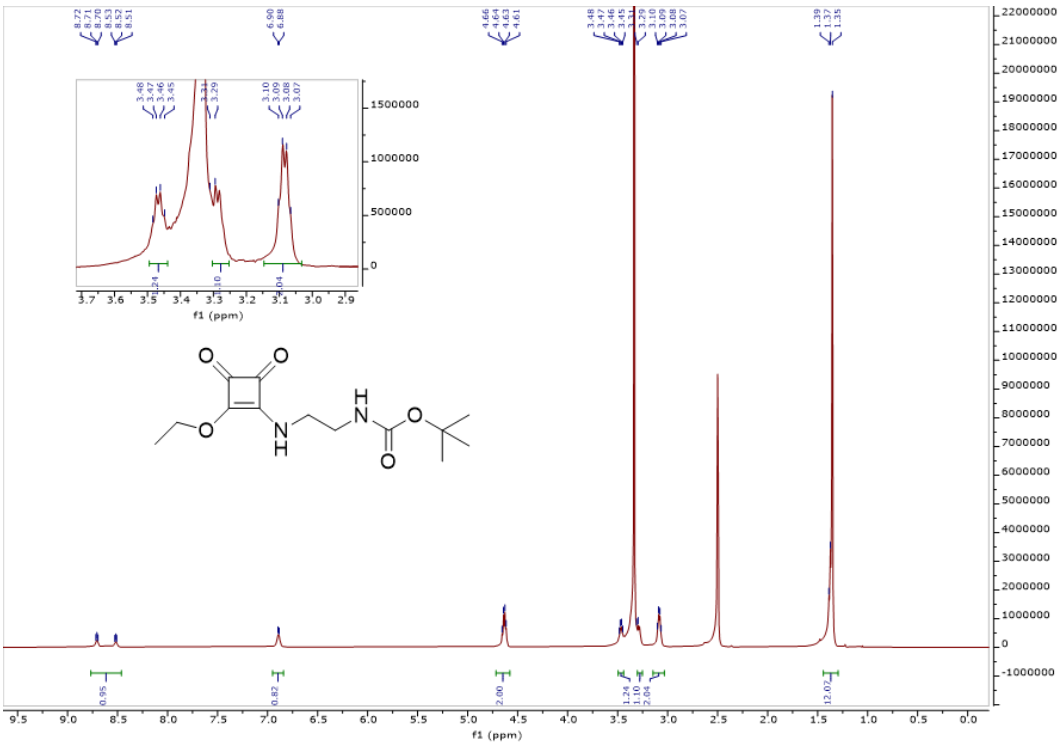

Figure A2.3: ^{1}H NMR spectrum of **2.11** in DMSO-d_6.

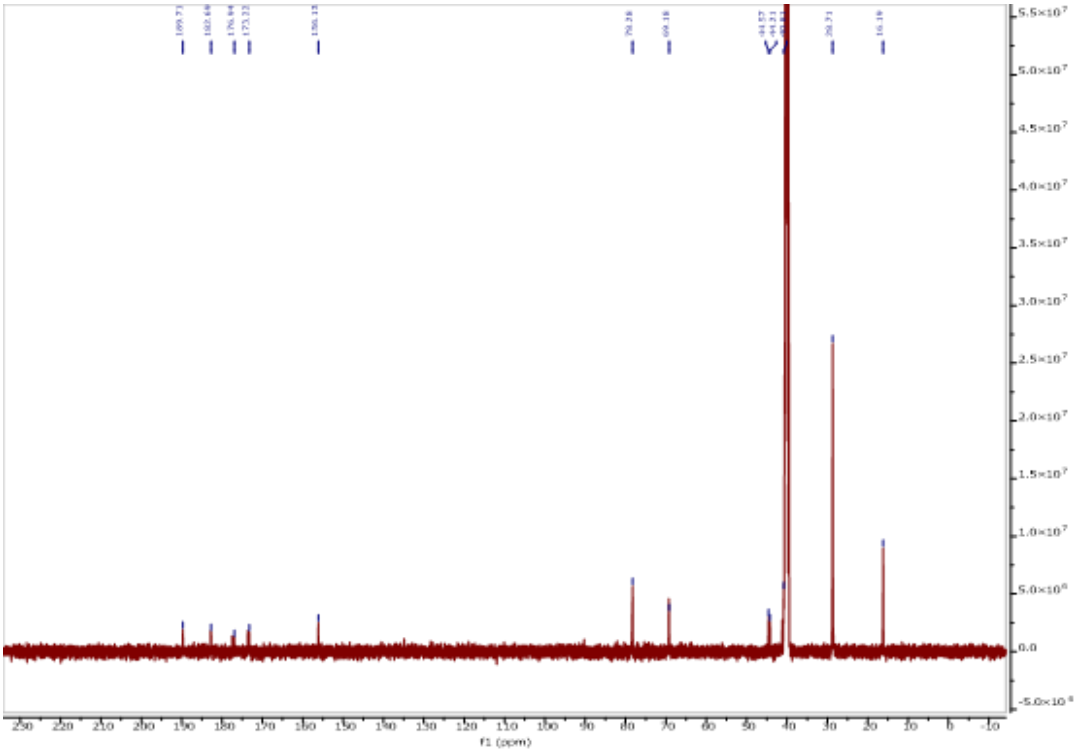

Figure A2.4: ^{13}C NMR spectrum of **2.11** in DMSO-d_6.

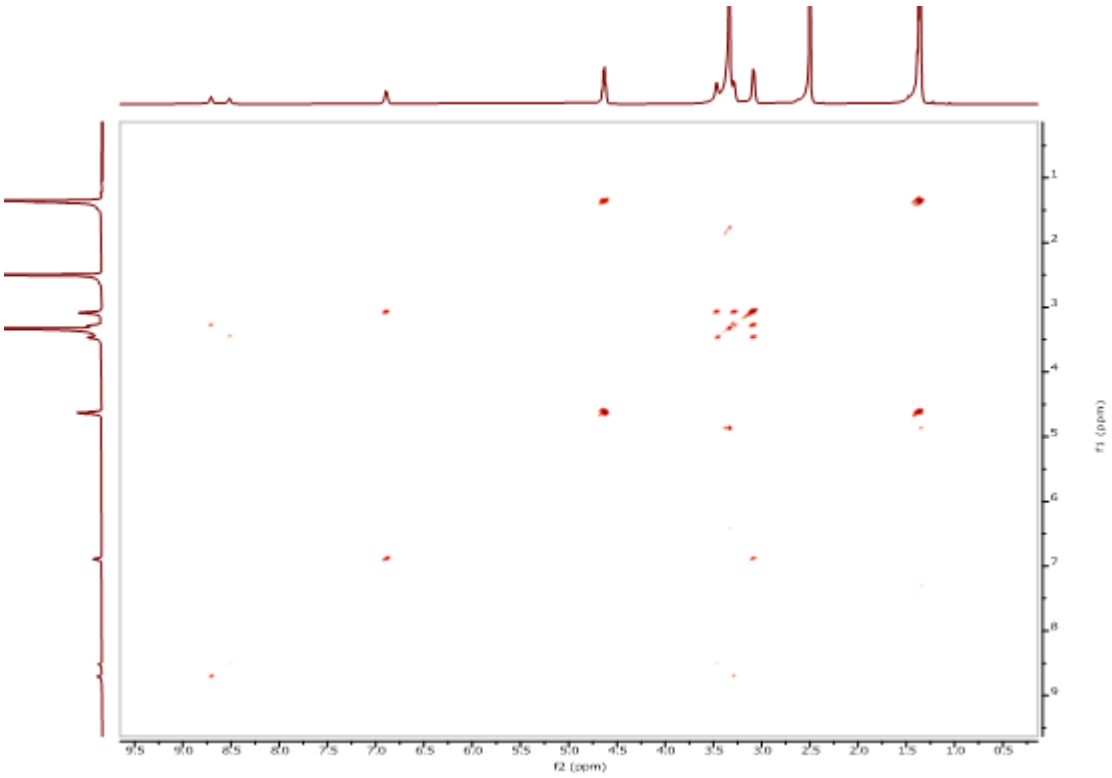

Figure A2.5: COSY spectrum of **2.11** in DMSO-d_6.

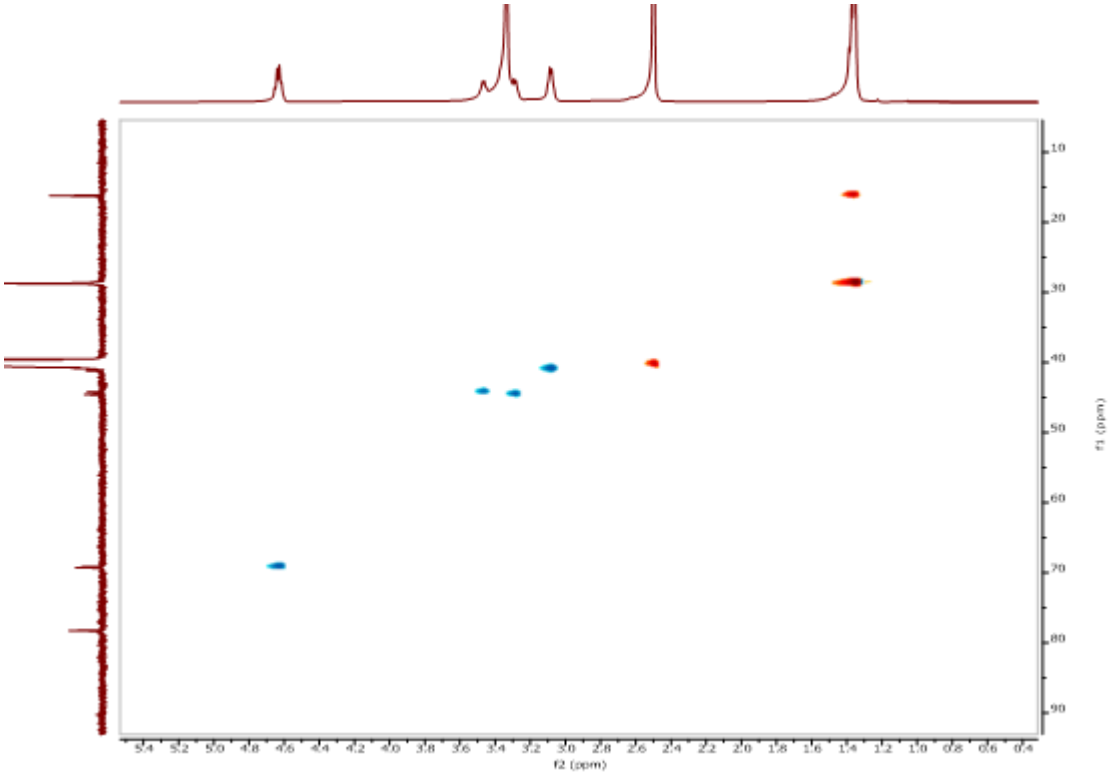

Figure A2.6: HSQC spectrum of **2.11** in DMSO-d_6**.**

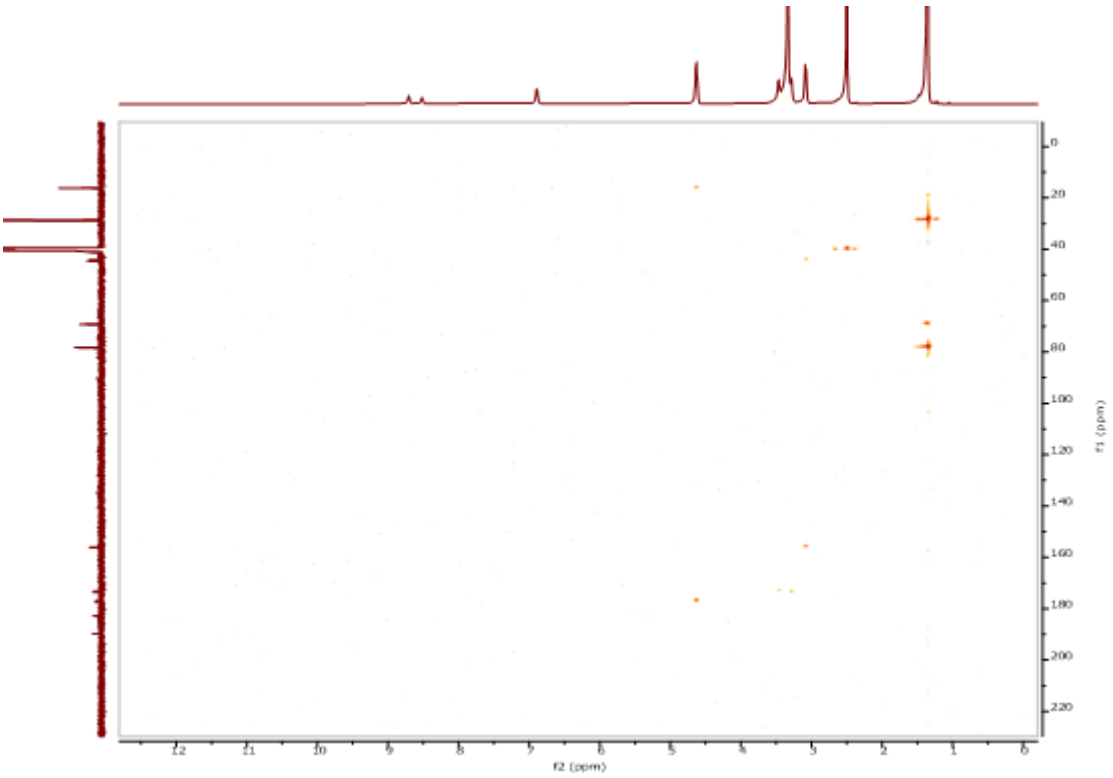

Figure A2.7: HMBC spectrum of **2.11** in DMSO-d_6.

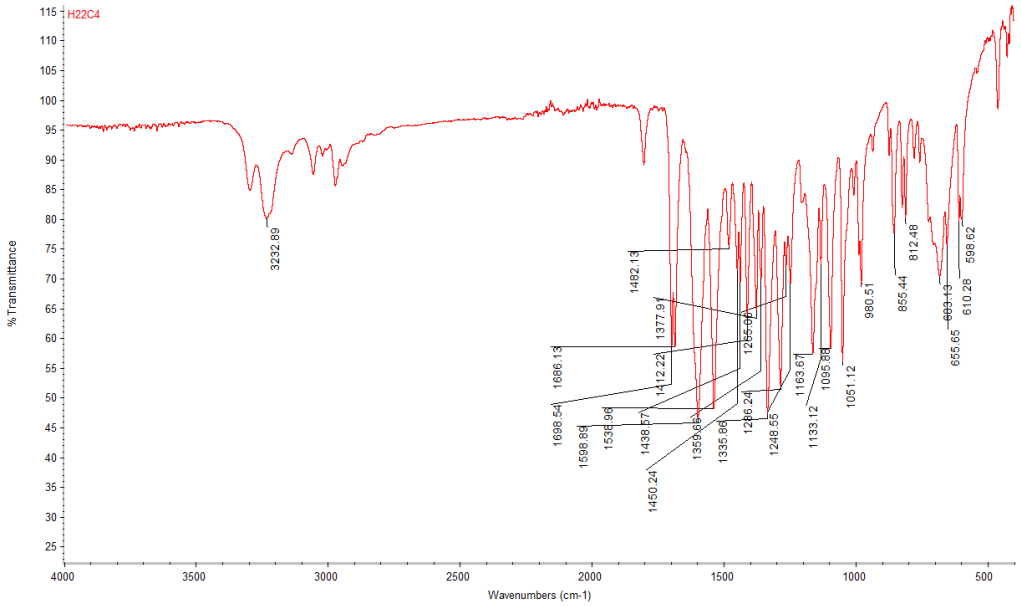

Figure A2.8: IR spectrum of **2.11**.

Compound Table

Compound Label	RT (min)	Observed mass (m/z)	Neutral observed mass (Da)	Theoretical mass (Da)	Mass error (ppm)	Isotope match score (%)
Cpd 1: C13 H20 N2 O5	0.70	285.1446	284.1376	284.1372	1.42	99.85

Figure: Extracted ion chromatogram (EIC) of compound.

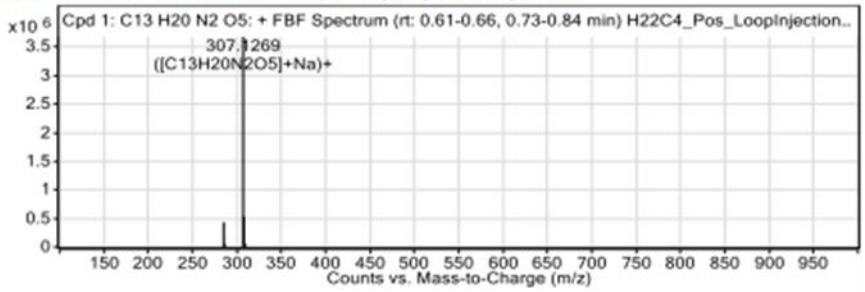

Figure: Full range view of Compound spectra and potential adducts.

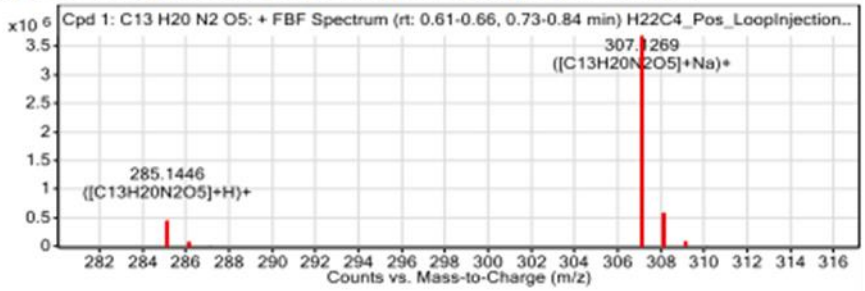

Figure: Zoomed Compound spectra view
(red boxes indicating expected theoretical isotope spacing and abundance)

Compound isotope peak List

m/z	z	Abund	Formula	Ion
285.1446	1	434247.8	C13H20N2O5	(M+H)+
286.1477	1	63944.5	C13H20N2O5	(M+H)+
287.1497	1	8403.3	C13H20N2O5	(M+H)+
307.1269	1	3678654.0	C13H20N2O5	(M+Na)+
308.1300	1	535498.0	C13H20N2O5	(M+Na)+
309.1318	1	65255.1	C13H20N2O5	(M+Na)+
310.1341	1	5866.4	C13H20N2O5	(M+Na)+

Figure A2.9: HRMS data of **2.11**.

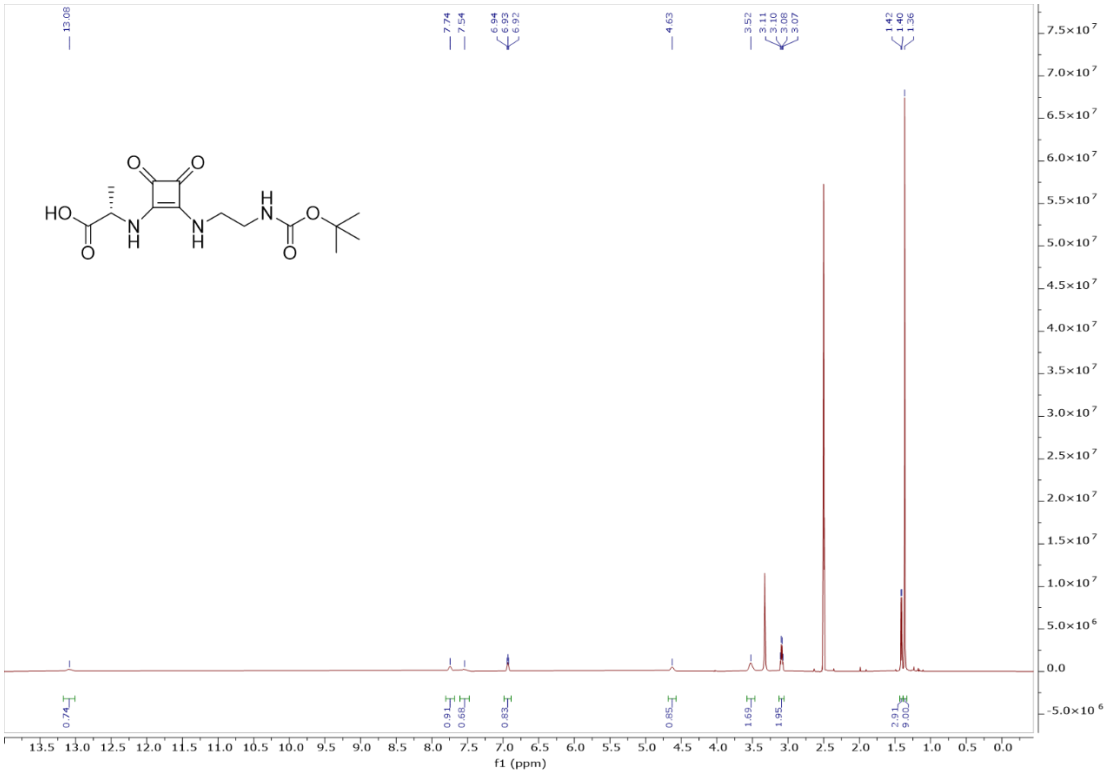

Figure A2.10: ^{1}H NMR spectrum of **2.12(Ala)** in DMSO-d_6.

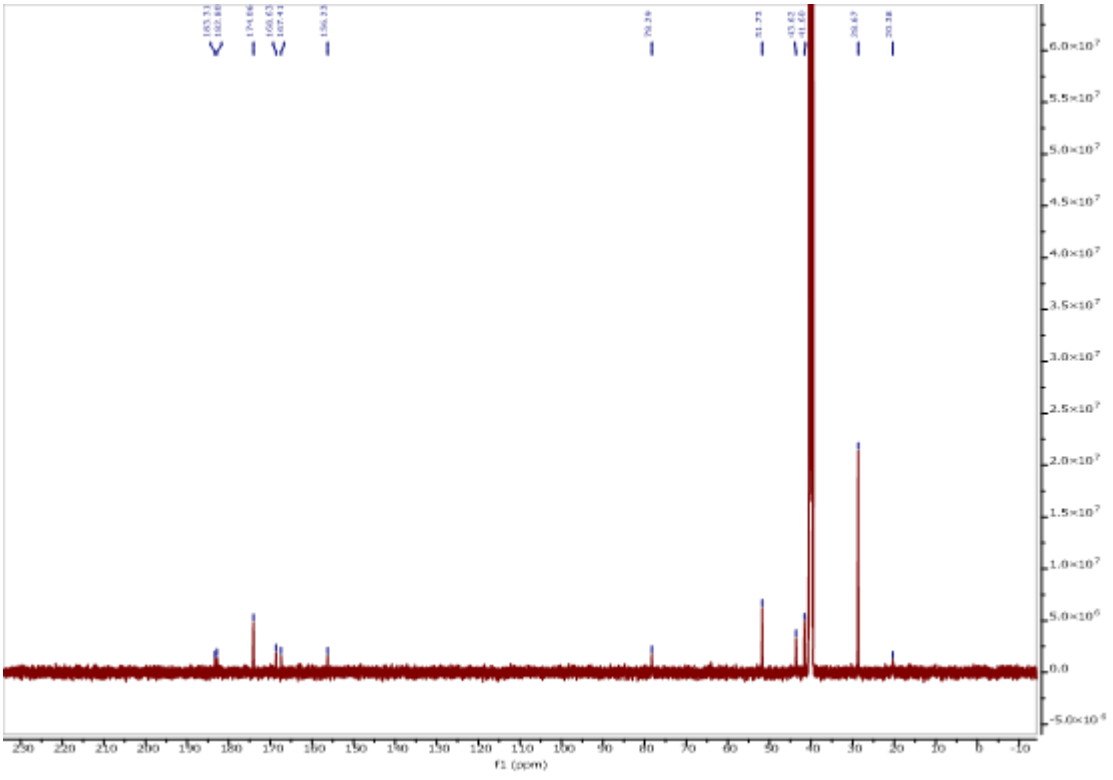

Figure A2.11: ^{13}C NMR spectrum of **2.12(Ala)** in DMSO-d_6.

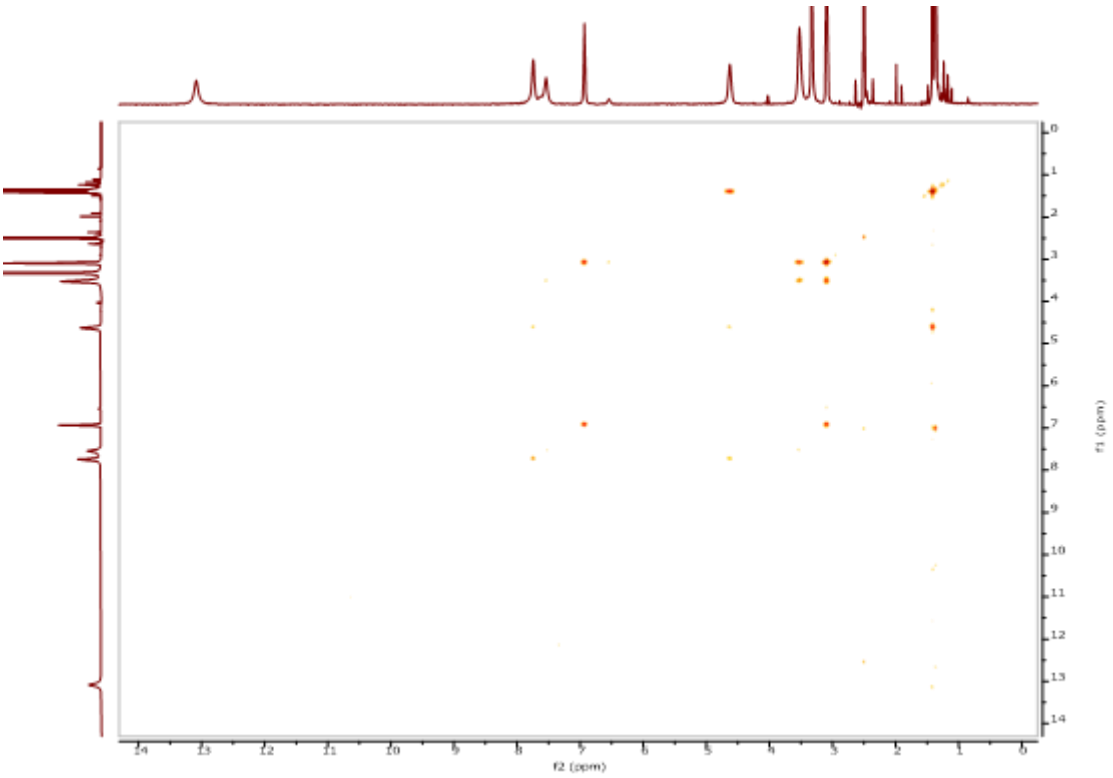

Figure A2.12: COSY spectrum of **2.12(Ala)** in DMSO-d_6.

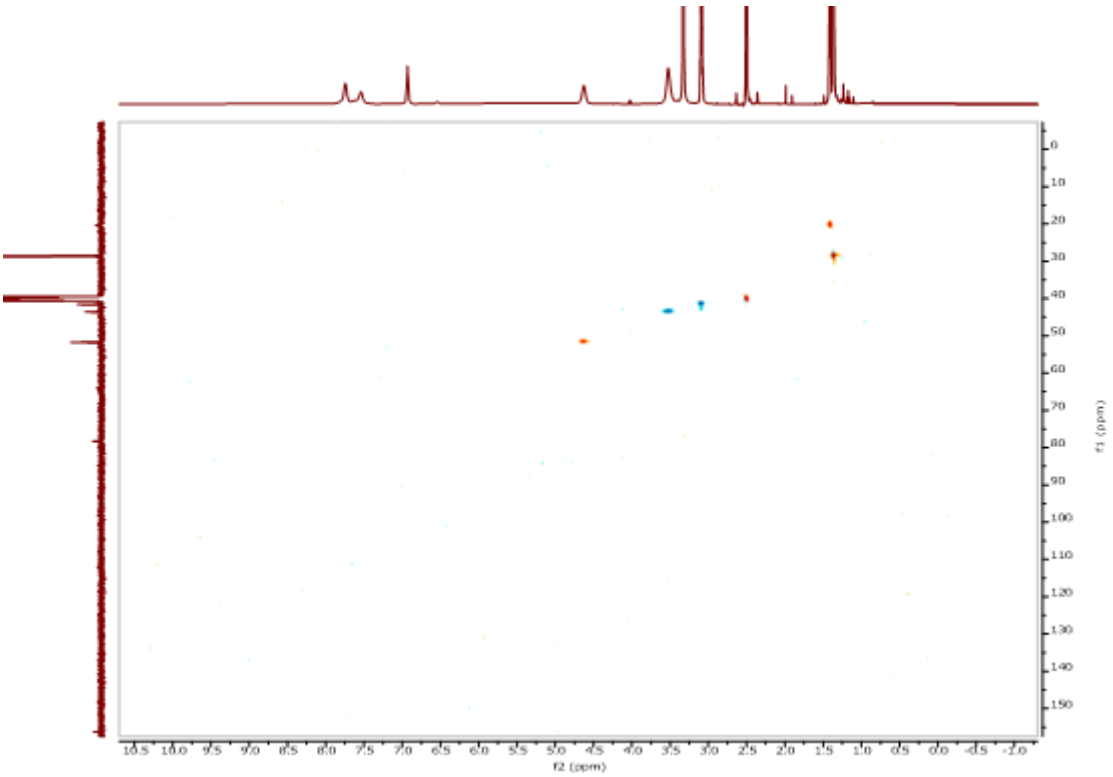

Figure A2.13: HSQC spectrum of **2.12(Ala)** in DMSO-d_6.

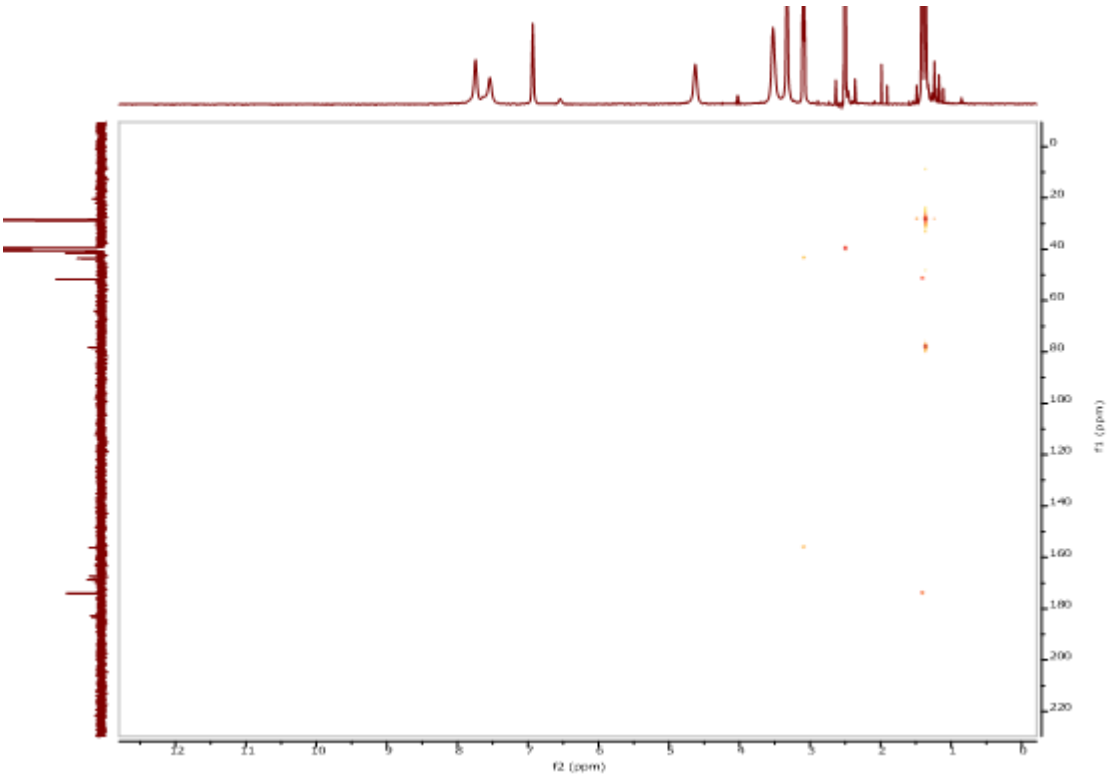

Figure A2.14: HMBC spectrum of **2.12(Ala)** in DMSO-d_6.

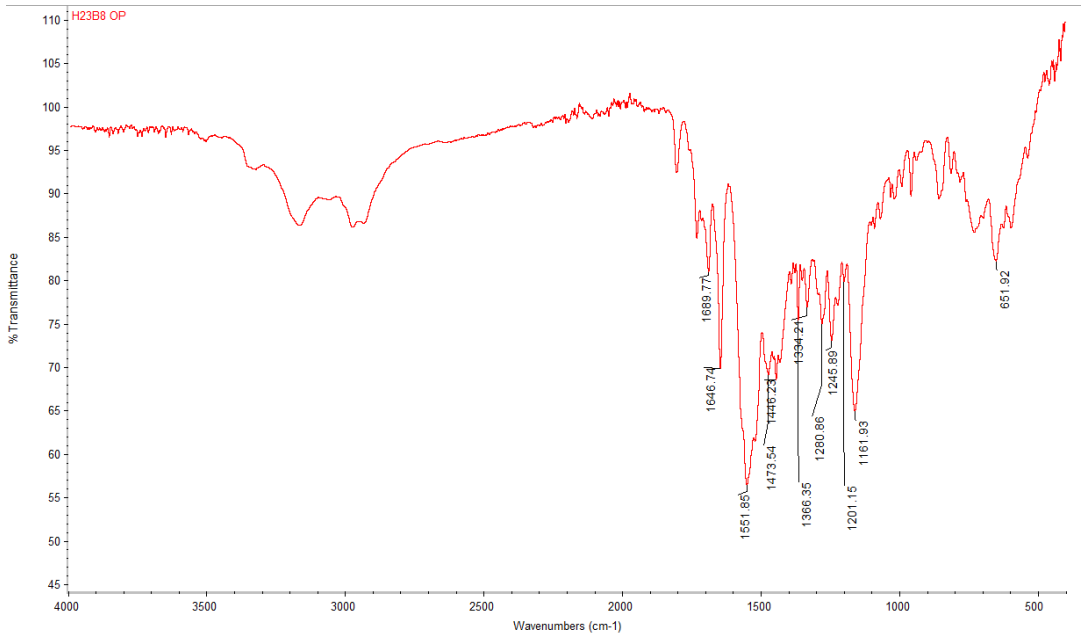

Figure A2.15: IR spectrum of **2.12(Ala)**.

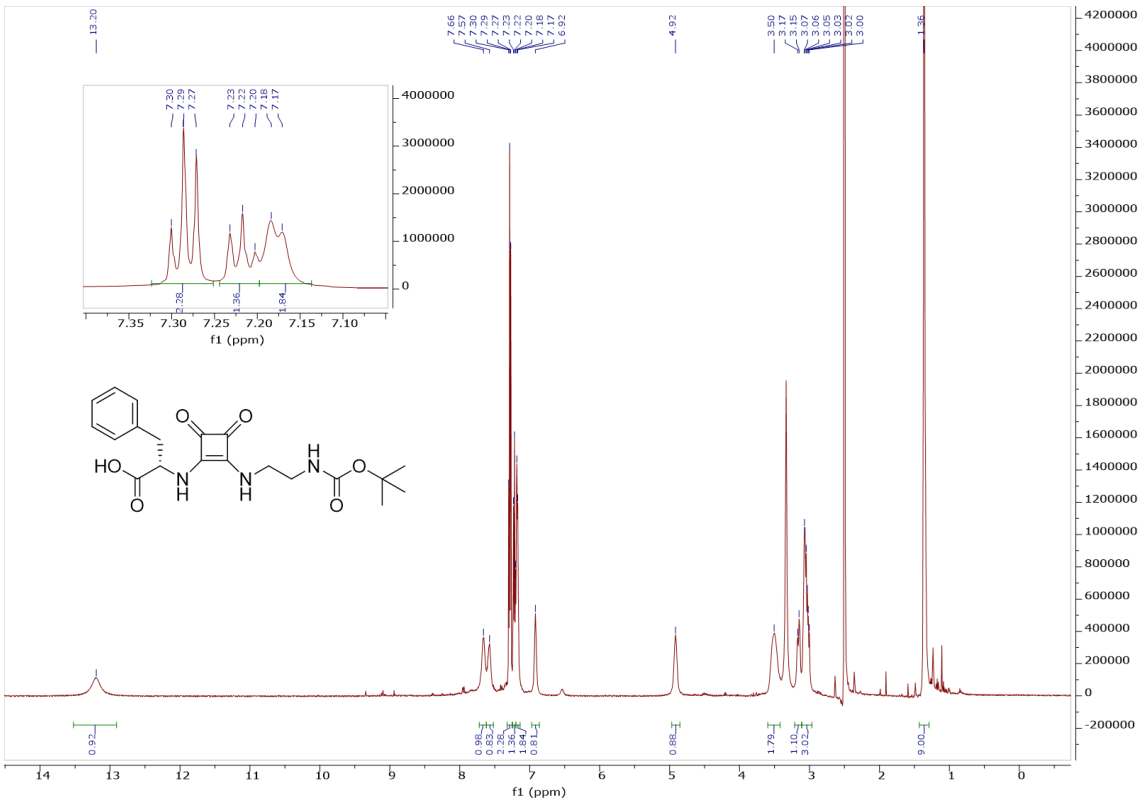

Figure A2.16: ^{1}H NMR spectrum of **2.12(Phe)** in DMSO-d_6.

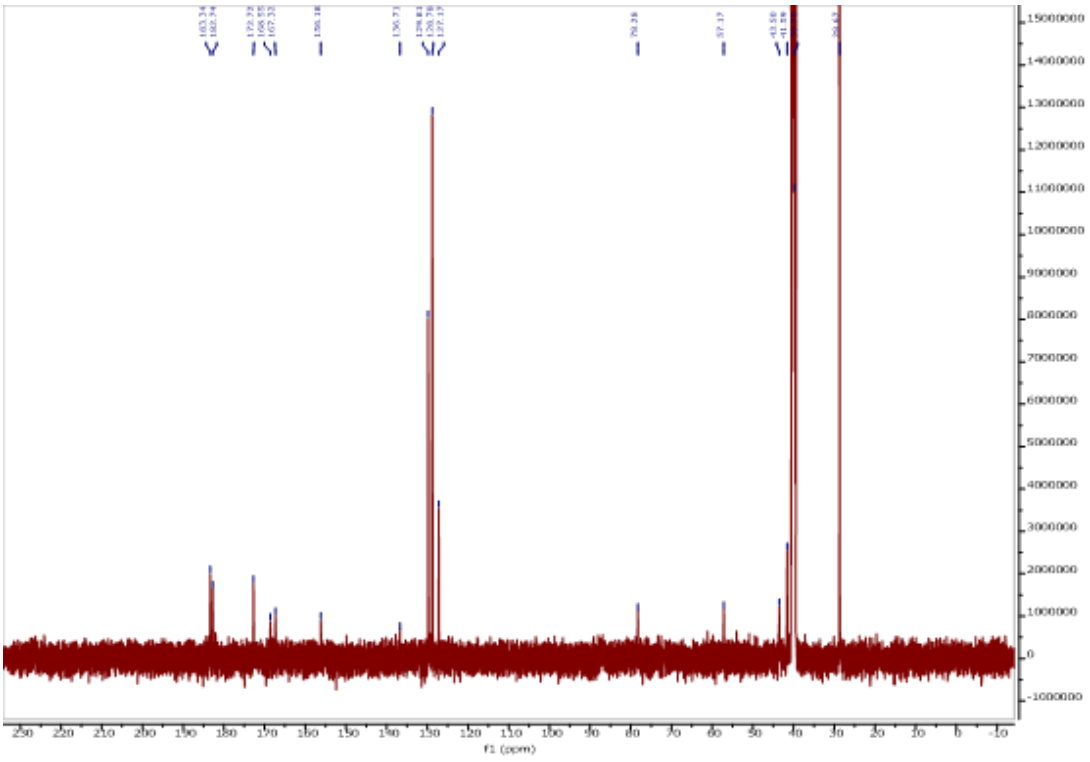

Figure A2.17: ^{13}C NMR spectrum of **2.12(Phe)** in DMSO-d_6.

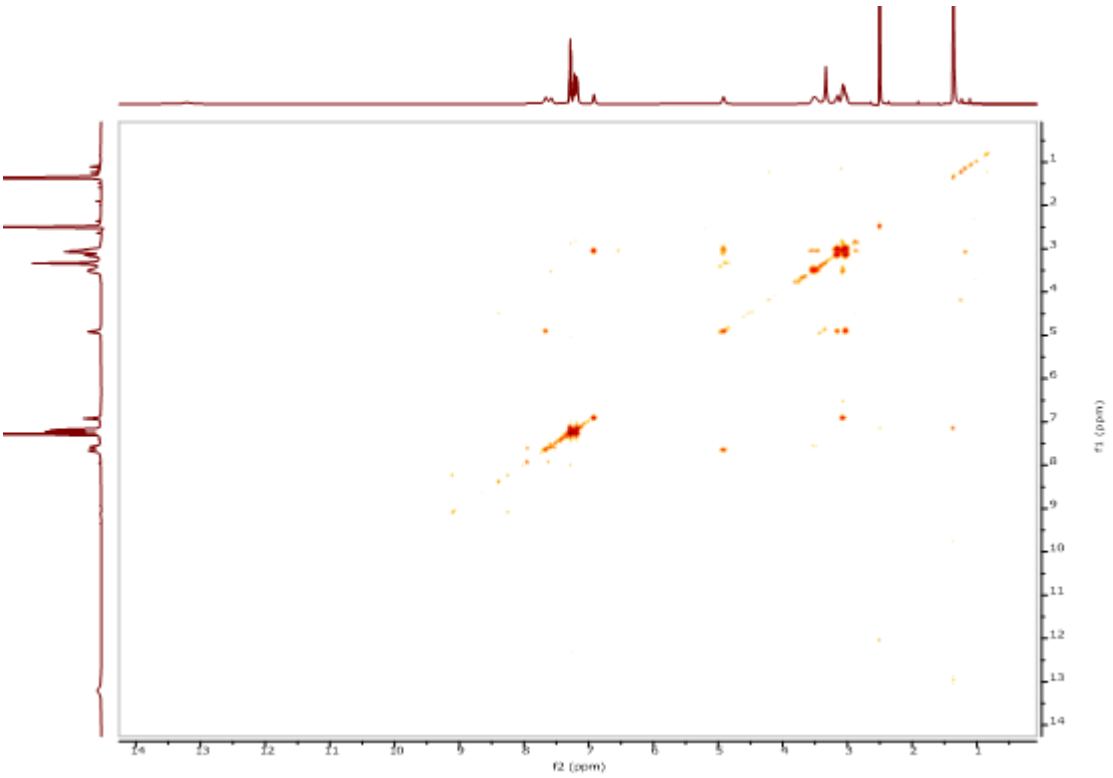

Figure A2.18: COSY spectrum of **2.12(Phe)** in DMSO-d_6.

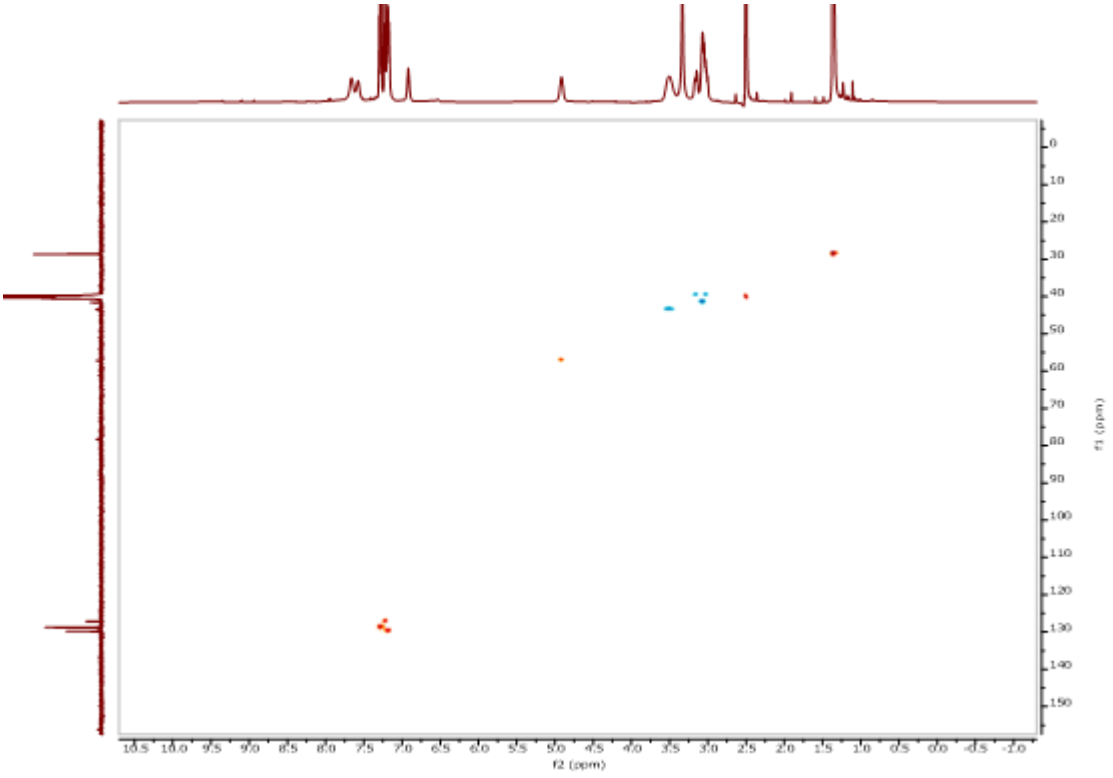

Figure A2.19: HSQC spectrum of **2.12(Phe)** in DMSO-d_6.

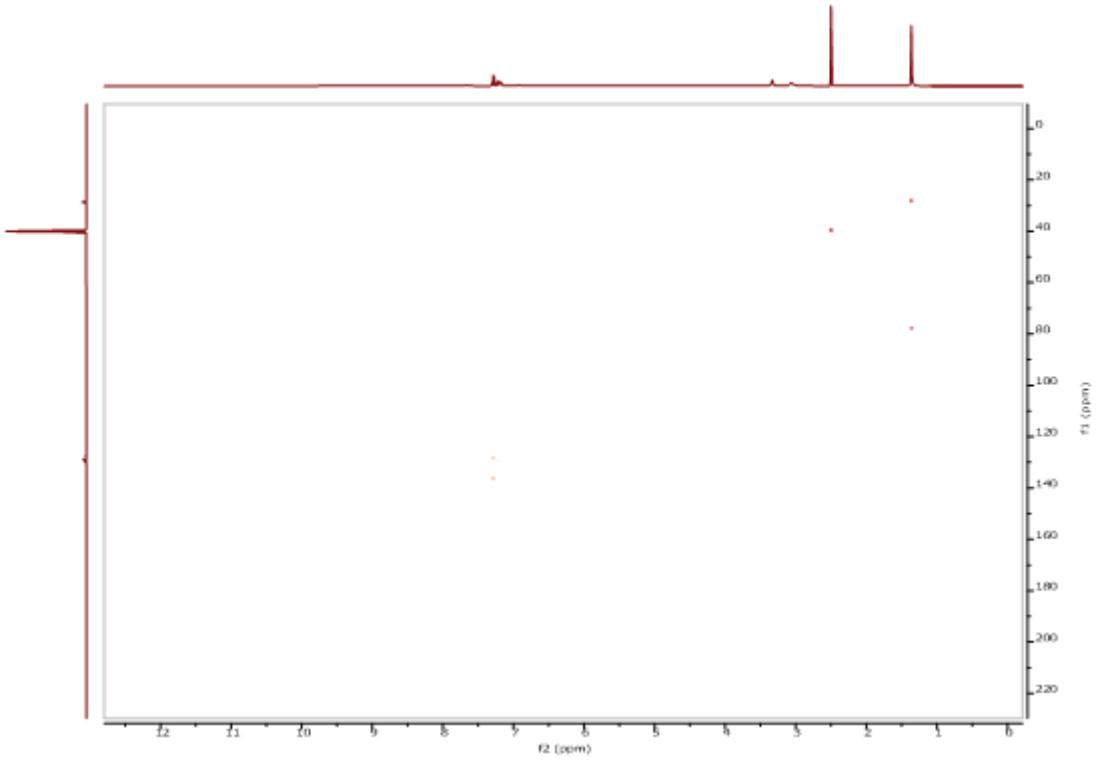

Figure A2.20: HMBC spectrum of **2.12(Phe)** in DMSO-d_6.

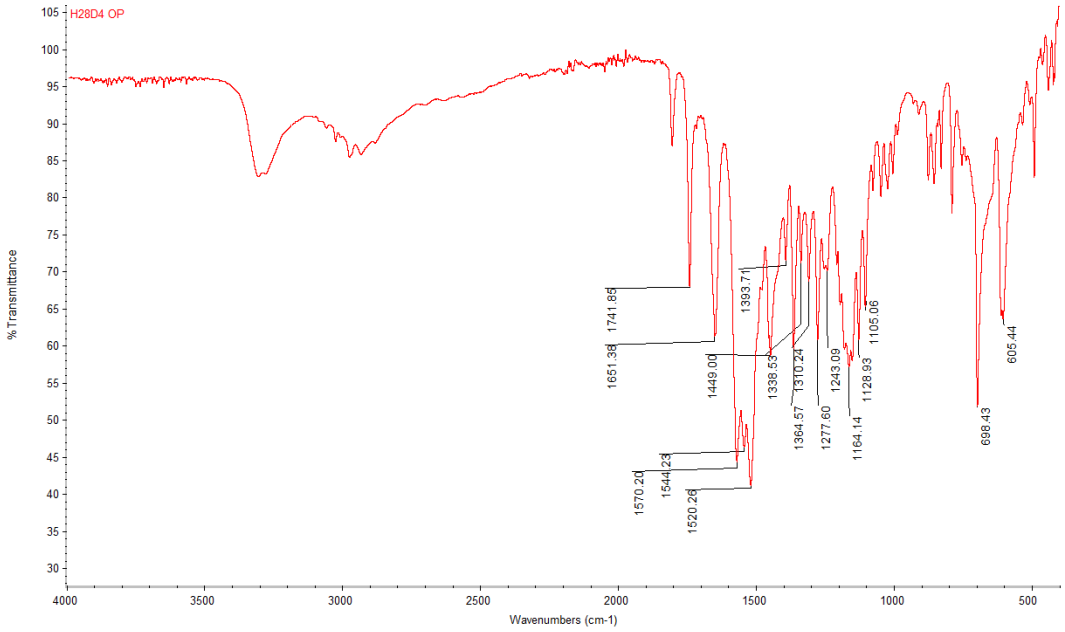

Figure A2.21: IR spectrum of **2.12(Phe)**.

Compound Table

Compound Label	RT (min)	Observed mass (m/z)	Neutral observed mass (Da)	Theoretical mass (Da)	Mass error (ppm)	Isotope match score (%)
Cpd 1: C20 H25 N3 O6	0.74	426.1647	403.1755	403.1743	2.86	99.54

Figure: Extracted ion chromatogram (EIC) of compound.

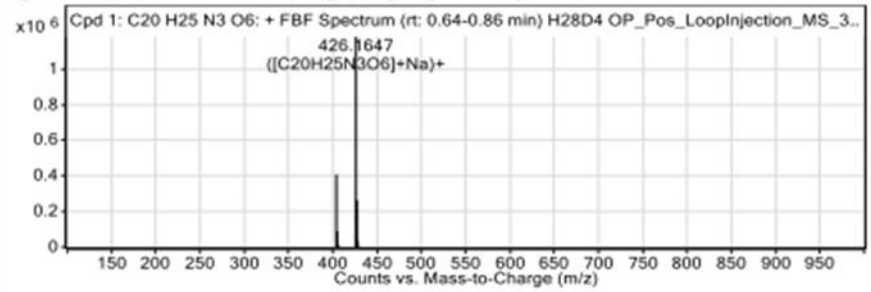

Figure: Full range view of Compound spectra and potential adducts.

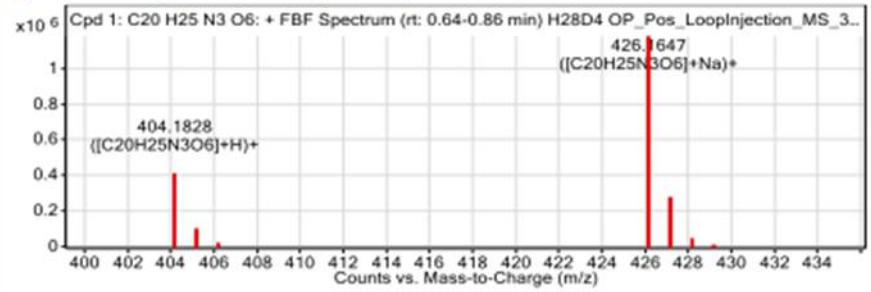

Figure: Zoomed Compound spectra view
(red boxes indicating expected theoretical isotope spacing and abundance)

Compound isotope peak List

m/z	z	Abund	Formula	Ion
404.1828	1	408251.9	C20H25N3O6	(M+H)+
405.1855	1	88539.2	C20H25N3O6	(M+H)+
406.1882	1	13455.7	C20H25N3O6	(M+H)+
426.1647	1	1181203.0	C20H25N3O6	(M+Na)+
427.1679	1	263832.3	C20H25N3O6	(M+Na)+
428.1697	1	37134.2	C20H25N3O6	(M+Na)+
429.1724	1	4641.3	C20H25N3O6	(M+Na)+

Figure A2.22: HRMS data of **2.12(Phe)**.

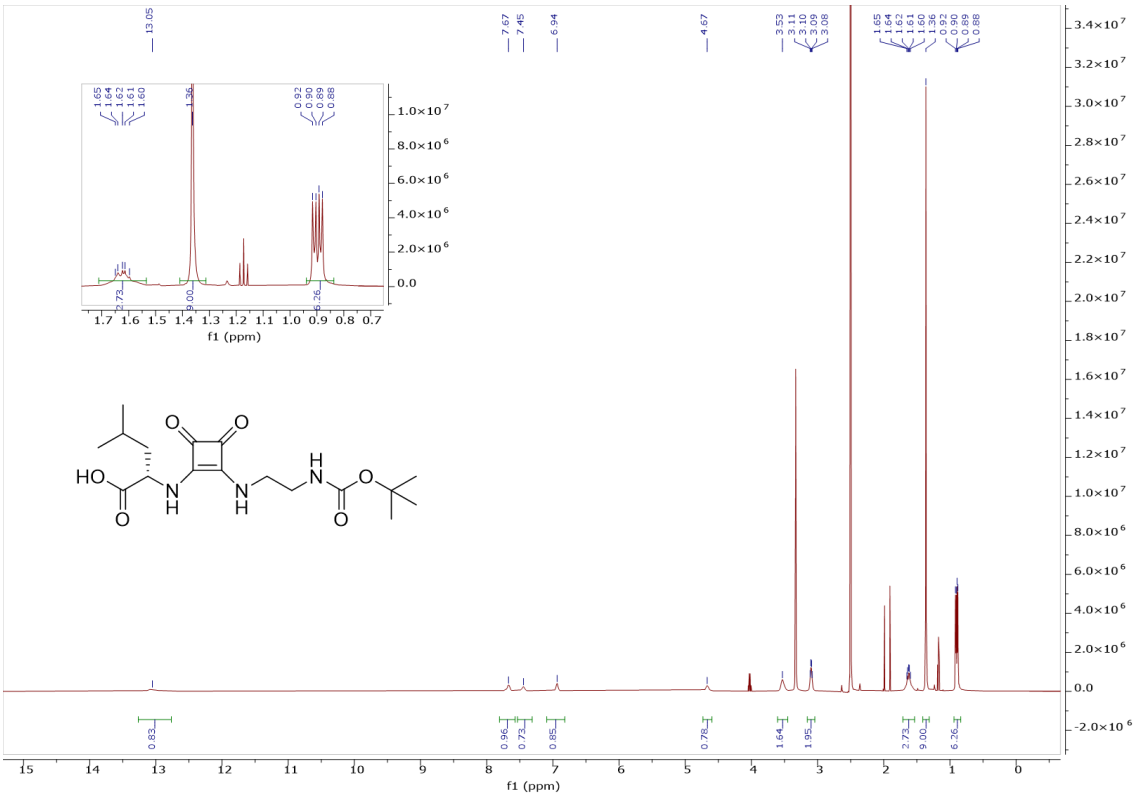

Figure A2.23: ^{1}H NMR spectrum of **2.12(Leu)** in DMSO-d_6.

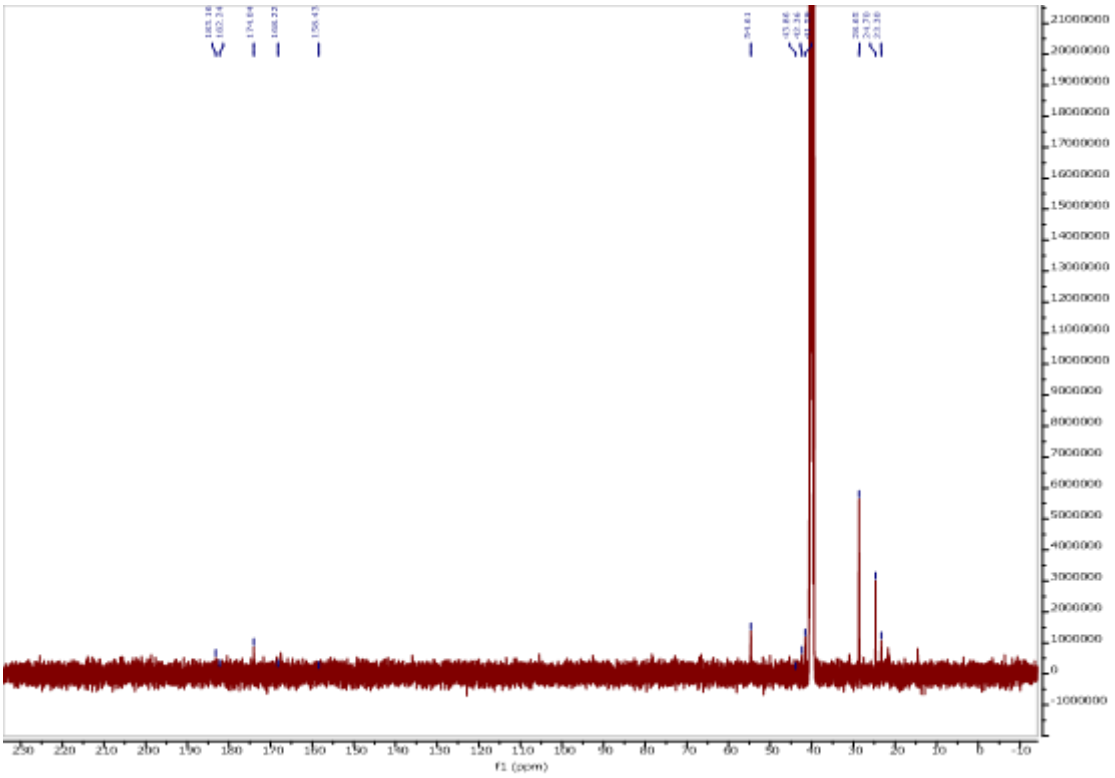

Figure A2.24: ^{13}C NMR spectrum of **2.12(Leu)** in DMSO-d_6.

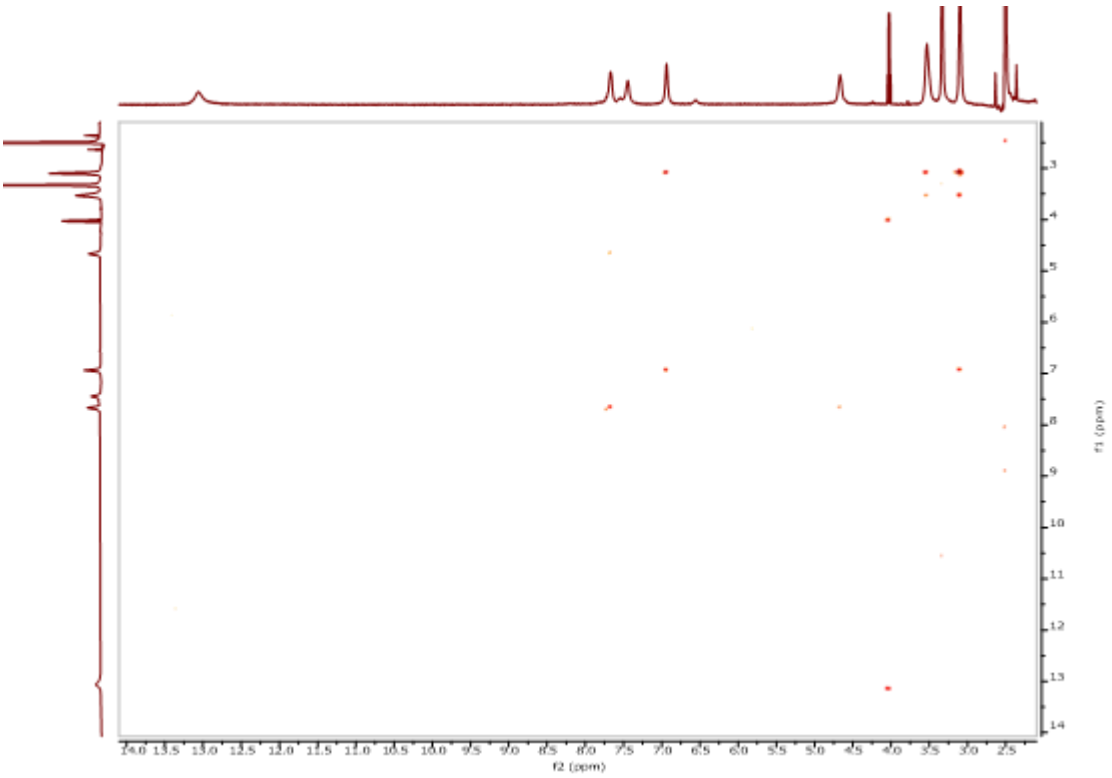

Figure A2.25: COSY spectrum of **2.12(Leu)** in DMSO-d_6.

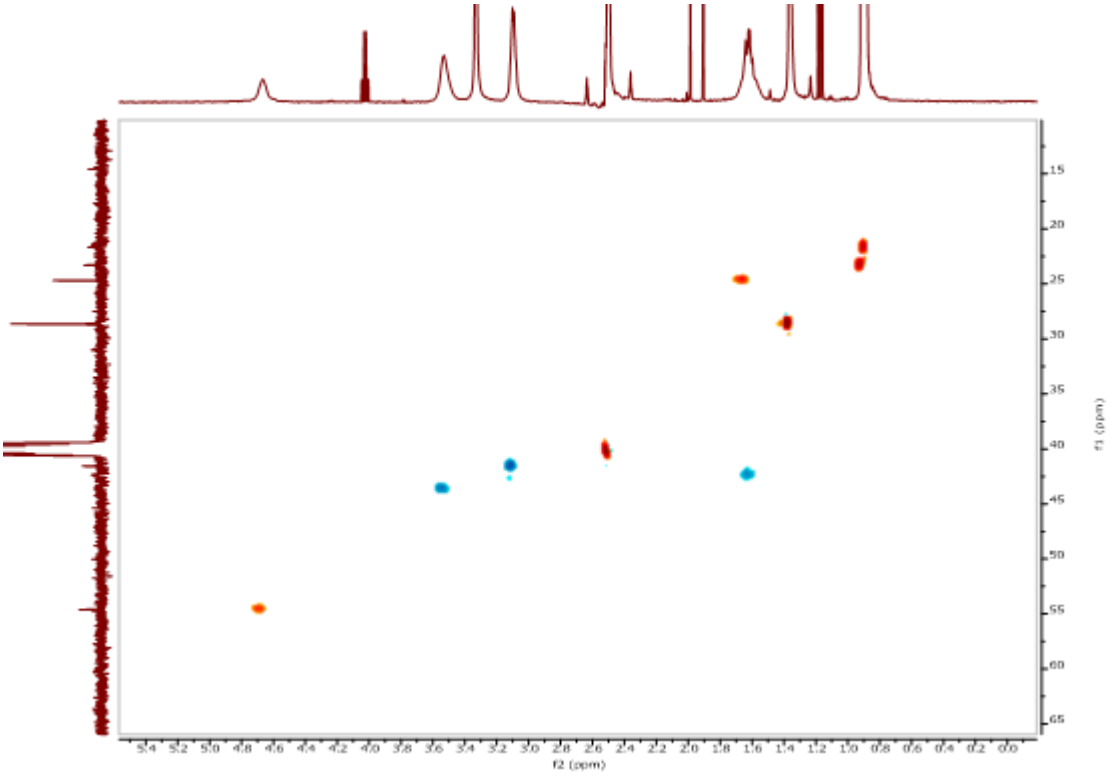

Figure A2.26: HSQC spectrum of **2.12(Leu)** in DMSO-d_6.

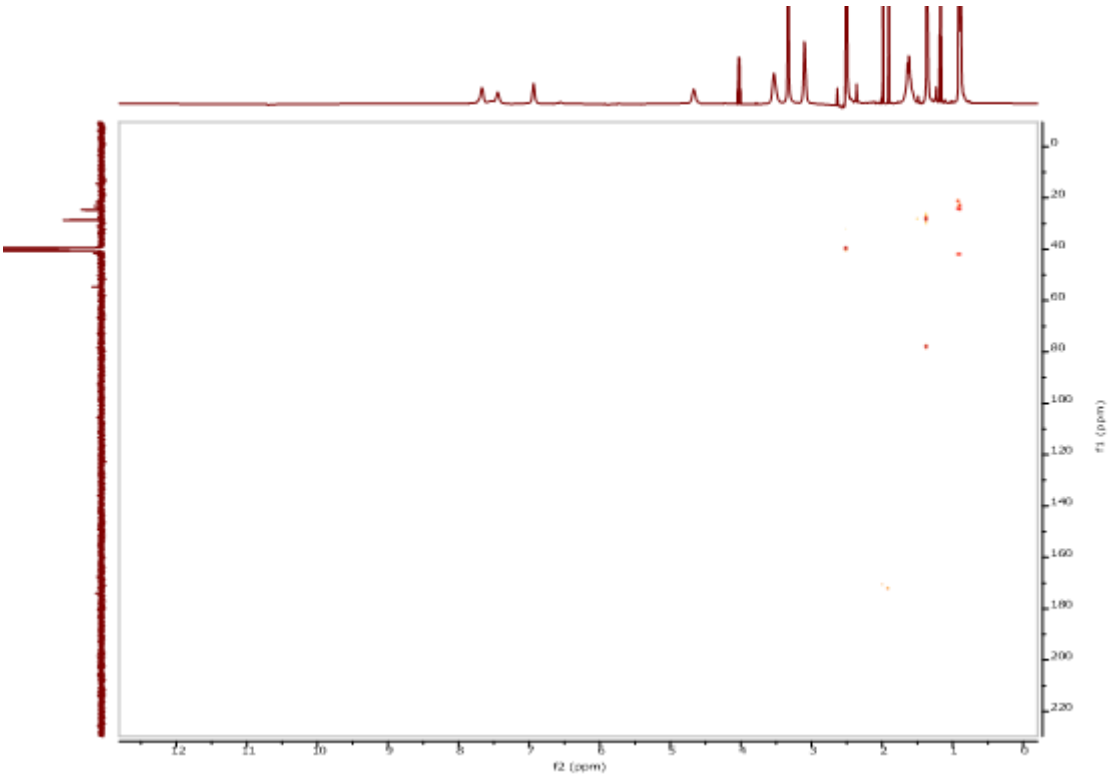

Figure A2.27: HMBC spectrum of **2.12(Leu)** in DMSO-d_6.

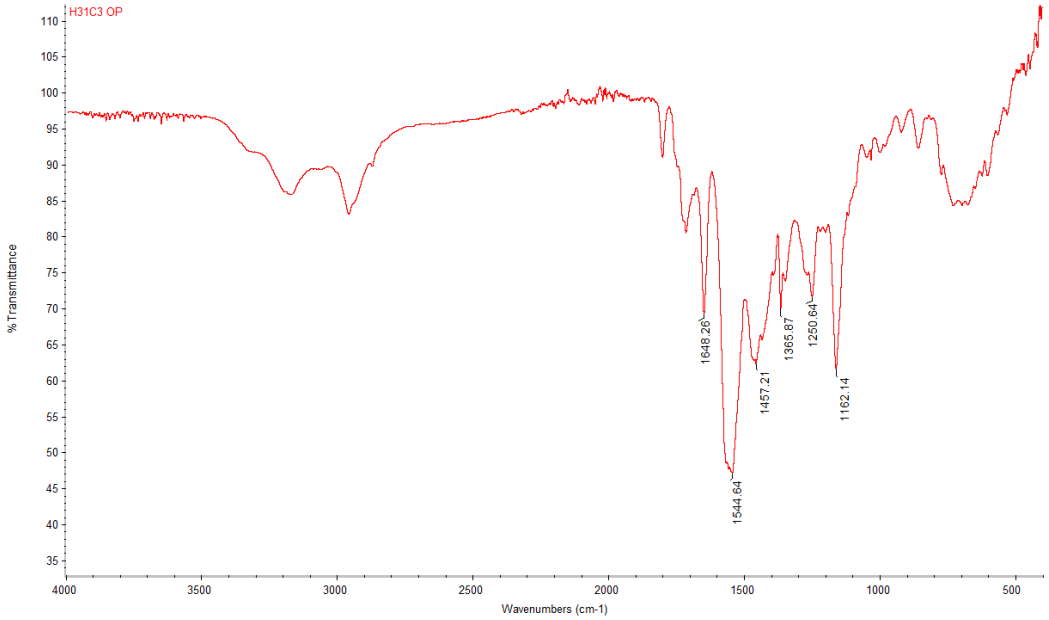

Figure A2.28: IR spectrum of **2.12(Leu)**.

Compound Table

Compound Label	RT (min)	Observed mass (m/z)	Neutral observed mass (Da)	Theoretical mass (Da)	Mass error (ppm)	Isotope match score (%)
Cpd 1: C17 H27 N3 O6	0.74	370.1983	369.1911	369.1900	3.13	97.08

Figure: Extracted ion chromatogram (EIC) of compound.

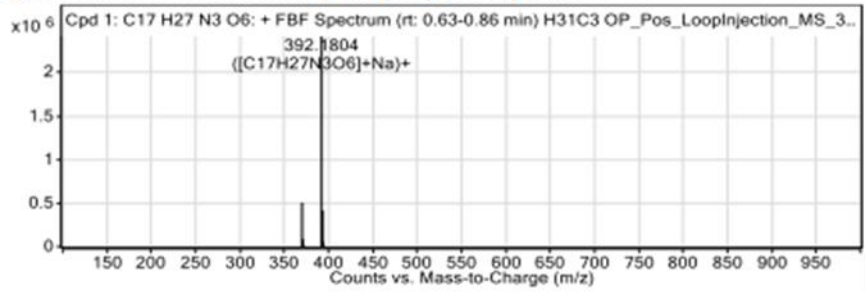

Figure: Full range view of Compound spectra and potential adducts.

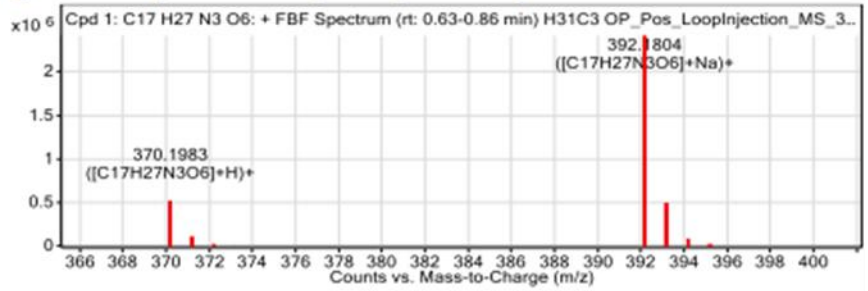

Figure: Zoomed Compound spectra view
(red boxes indicating expected theoretical isotope spacing and abundance)

Compound isotope peak List

m/z	z	Abund	Formula	Ion
370.1983	1	506355.9	C17H27N3O6	(M+H)+
371.2012	1	88085.4	C17H27N3O6	(M+H)+
372.2041	1	13308.9	C17H27N3O6	(M+H)+
373.2097	1	1829.4	C17H27N3O6	(M+H)+
392.1804	1	2415472.3	C17H27N3O6	(M+Na)+
393.1836	1	416800.6	C17H27N3O6	(M+Na)+
394.1852	1	56654.9	C17H27N3O6	(M+Na)+
395.1878	1	6374.4	C17H27N3O6	(M+Na)+

Figure A2.29: HRMS data of **2.12(Leu)**.

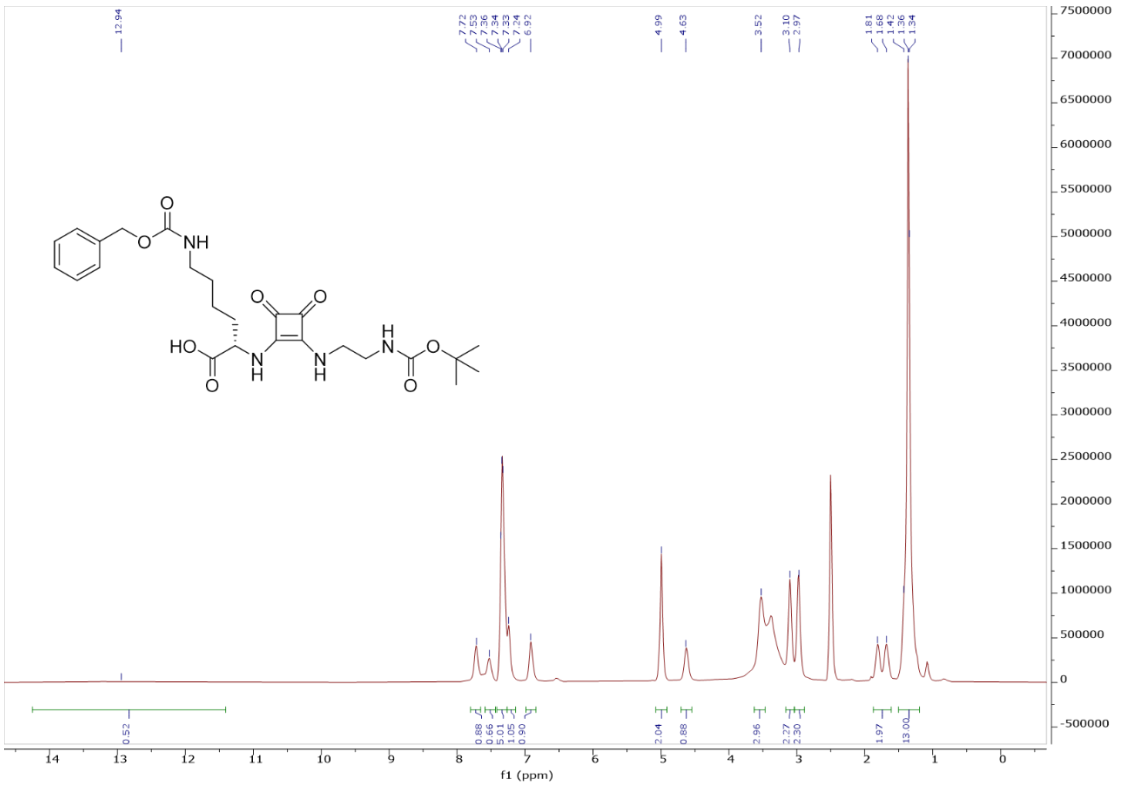

Figure A2.30: ^{1}H NMR spectrum of **2.12(Lys(Cbz))** in DMSO-d_6.

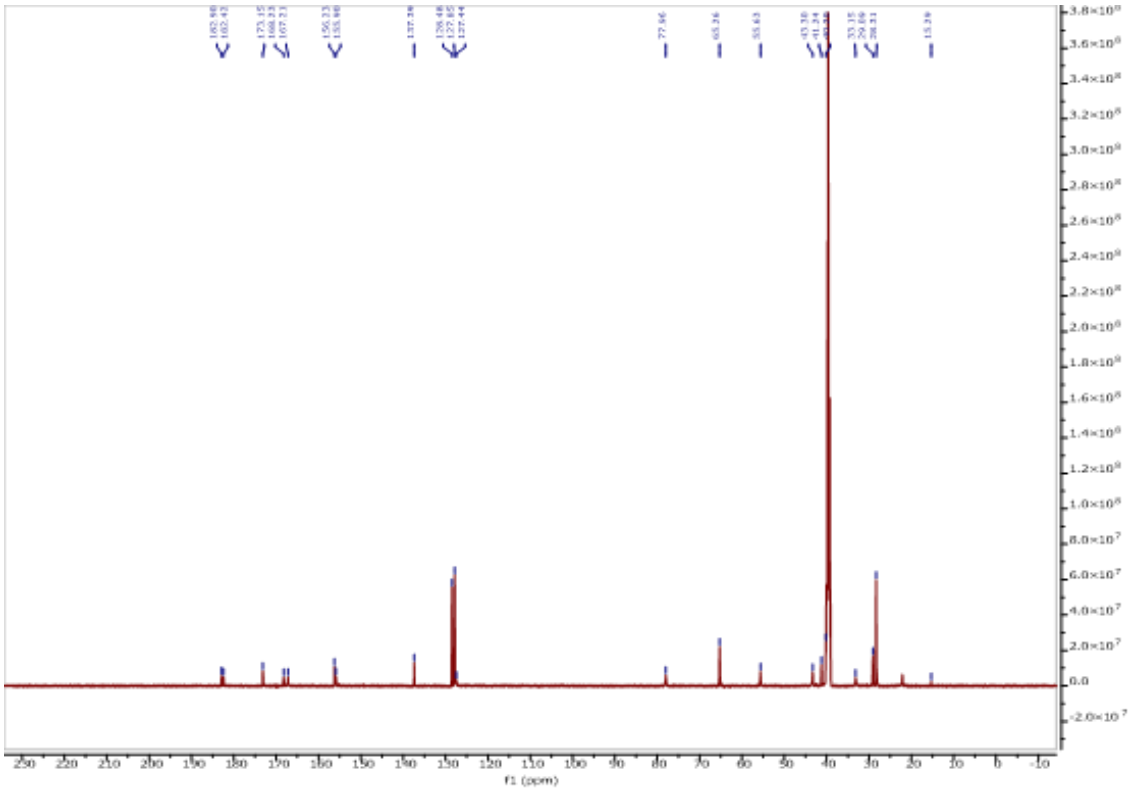

Figure A2.31: ^{13}C NMR spectrum of **2.12(Lys(Cbz))** in DMSO-d_6.

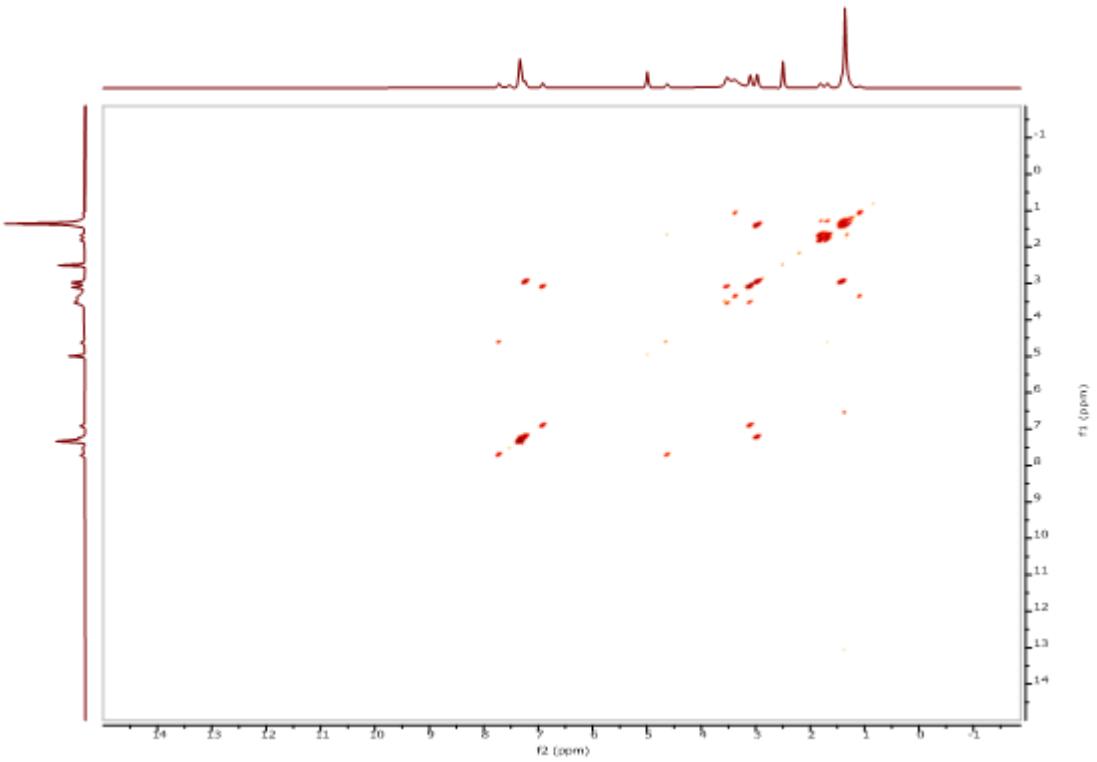

Figure A2.32: COSY spectrum of **2.12(Lys(Cbz))** in DMSO-d_6.

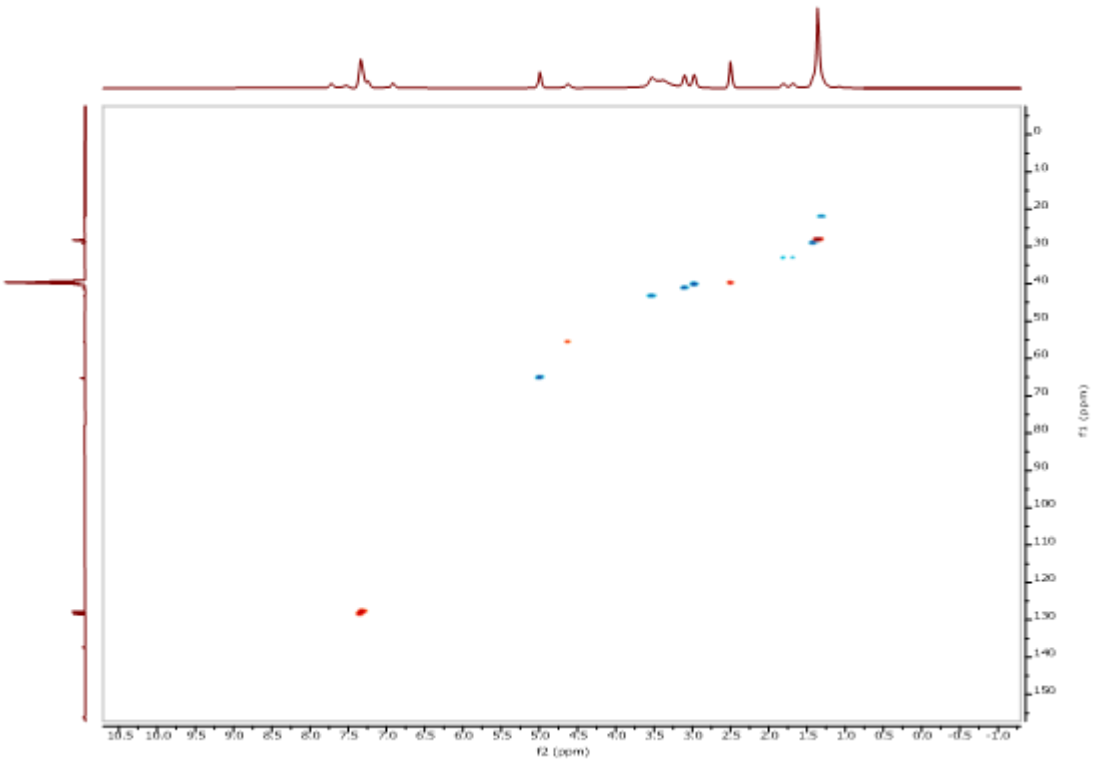

Figure A2.33: HSQC spectrum of **2.12(Lys(Cbz))** in DMSO-d_6.

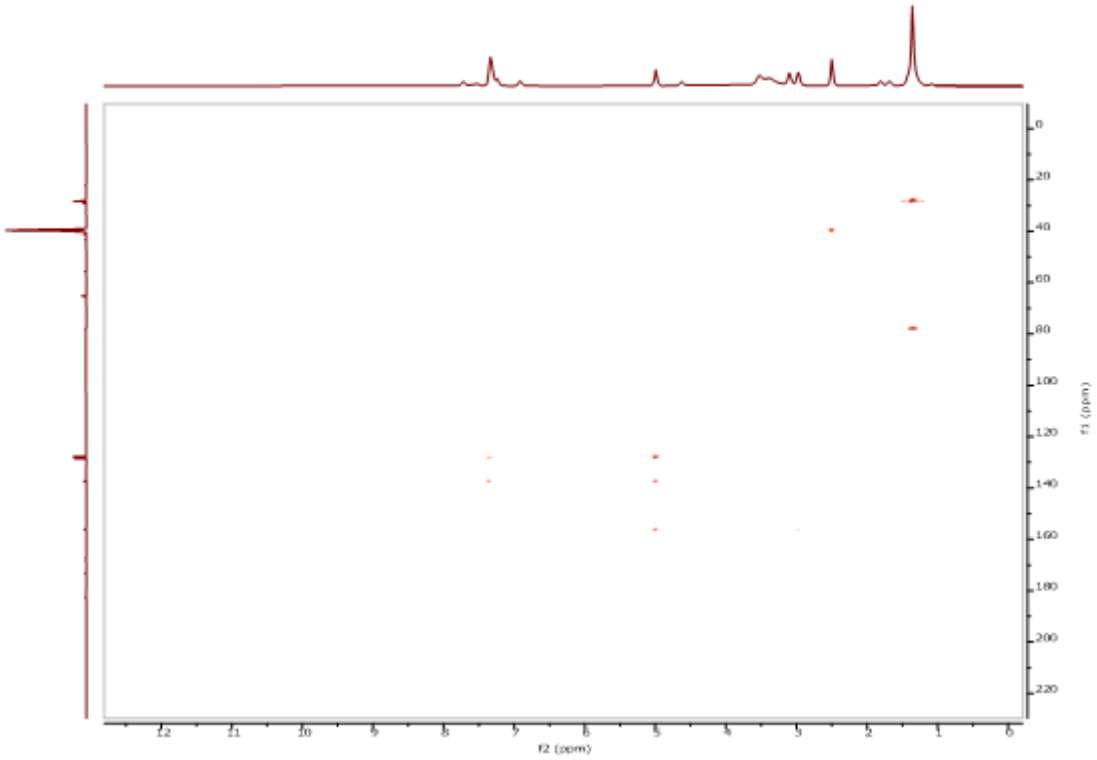

Figure A2.34: HMBC spectrum **2.12(Lys(Cbz))** in DMSO-d_6.

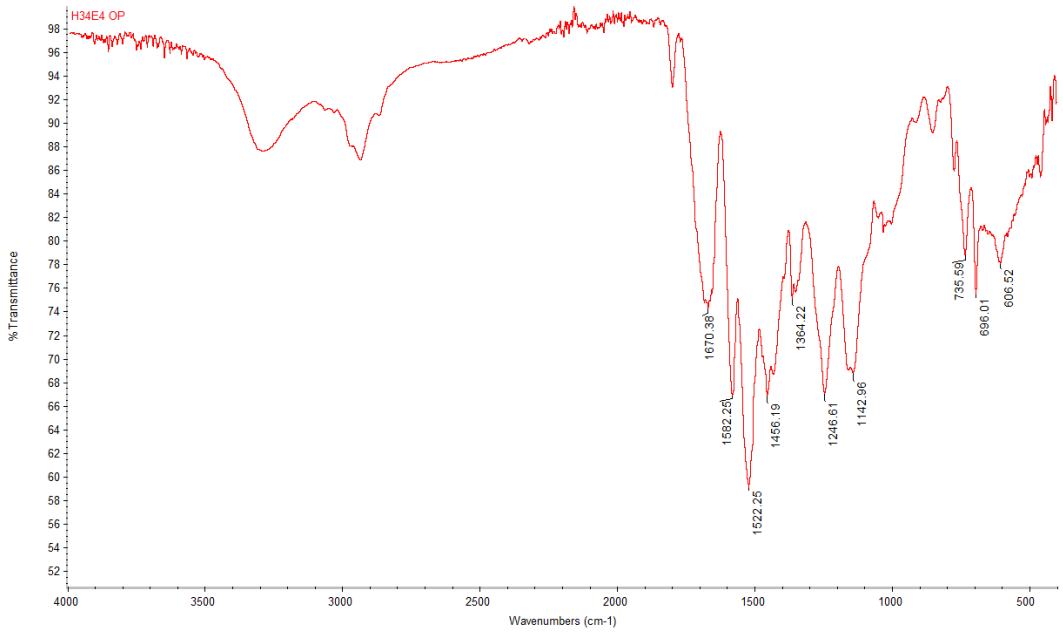

Figure A2.35: IR spectrum of **2.12(Lys(Cbz))**.

Compound Table

Compound Label	RT (min)	Observed mass (m/z)	Neutral observed mass (Da)	Theoretical mass (Da)	Mass error (ppm)	Isotope match score (%)
Cpd 1: C25 H34 N4 O8	0.72	541.2282	518.2389	518.2377	2.44	96.50

Figure: Extracted ion chromatogram (EIC) of compound.

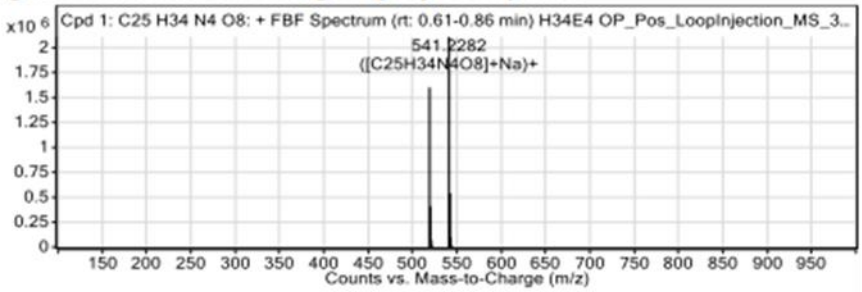

Figure: Full range view of Compound spectra and potential adducts.

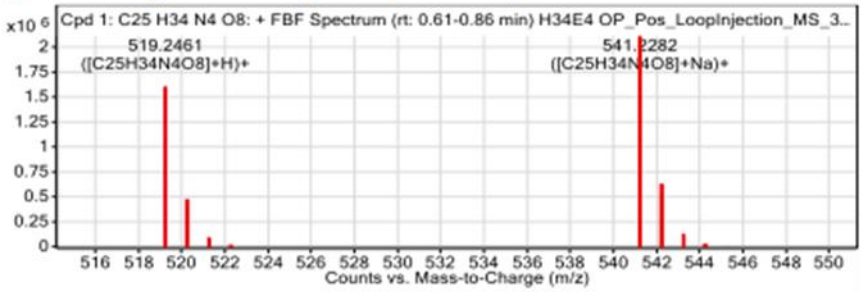

Figure: Zoomed Compound spectra view
(red boxes indicating expected theoretical isotope spacing and abundance)

Compound isotope peak List

m/z	z	Abund	Formula	Ion
519.2461	1	1602232.6	C25H34N4O8	(M+H)+
520.2495	1	409955.0	C25H34N4O8	(M+H)+
521.2513	1	70866.1	C25H34N4O8	(M+H)+
522.2539	1	10462.1	C25H34N4O8	(M+H)+
541.2282	1	2111013.3	C25H34N4O8	(M+Na)+
542.2314	1	541873.3	C25H34N4O8	(M+Na)+
543.2335	1	99468.6	C25H34N4O8	(M+Na)+
544.2357	1	13380.4	C25H34N4O8	(M+Na)+
545.2352	1	1984.5	C25H34N4O8	(M+Na)+

Figure A2.36: HRMS data of **2.12(Lys(Cbz))**.

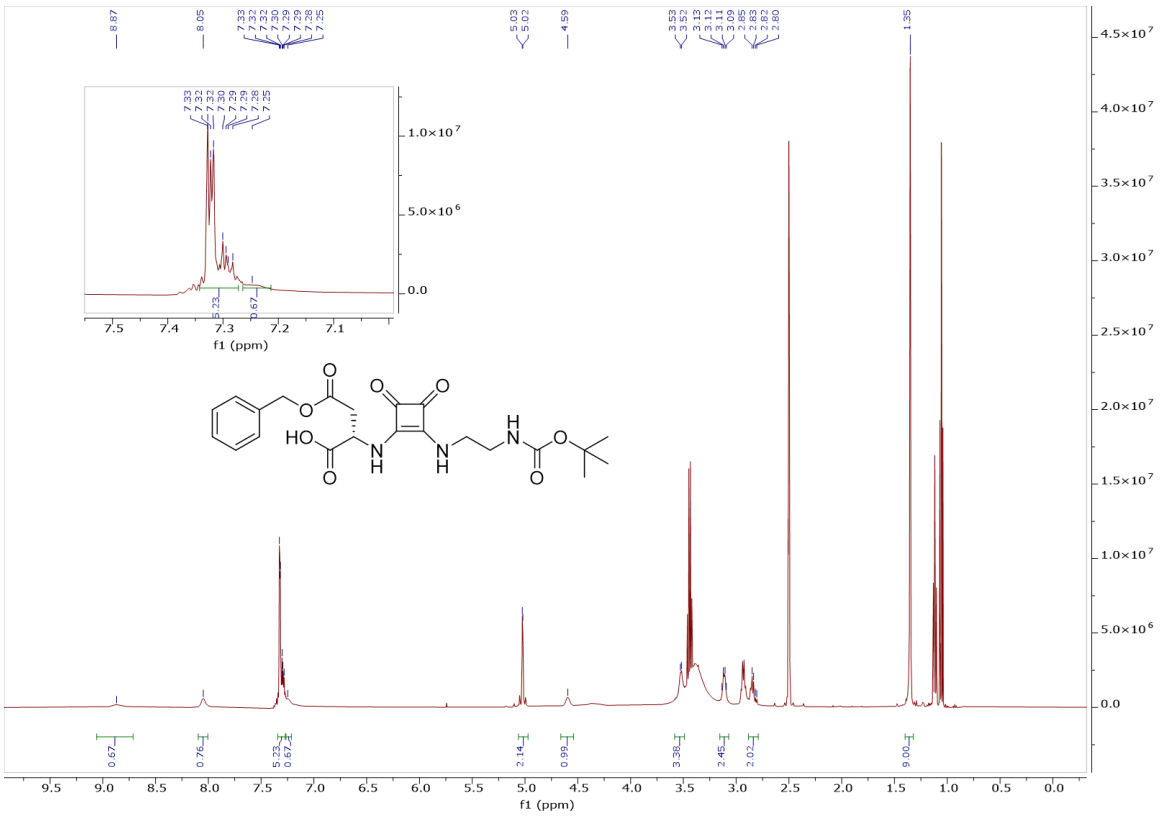

Figure A2.36: ^{1}H NMR spectrum of **2.12(Asp(Bn))** in DMSO-d_6.

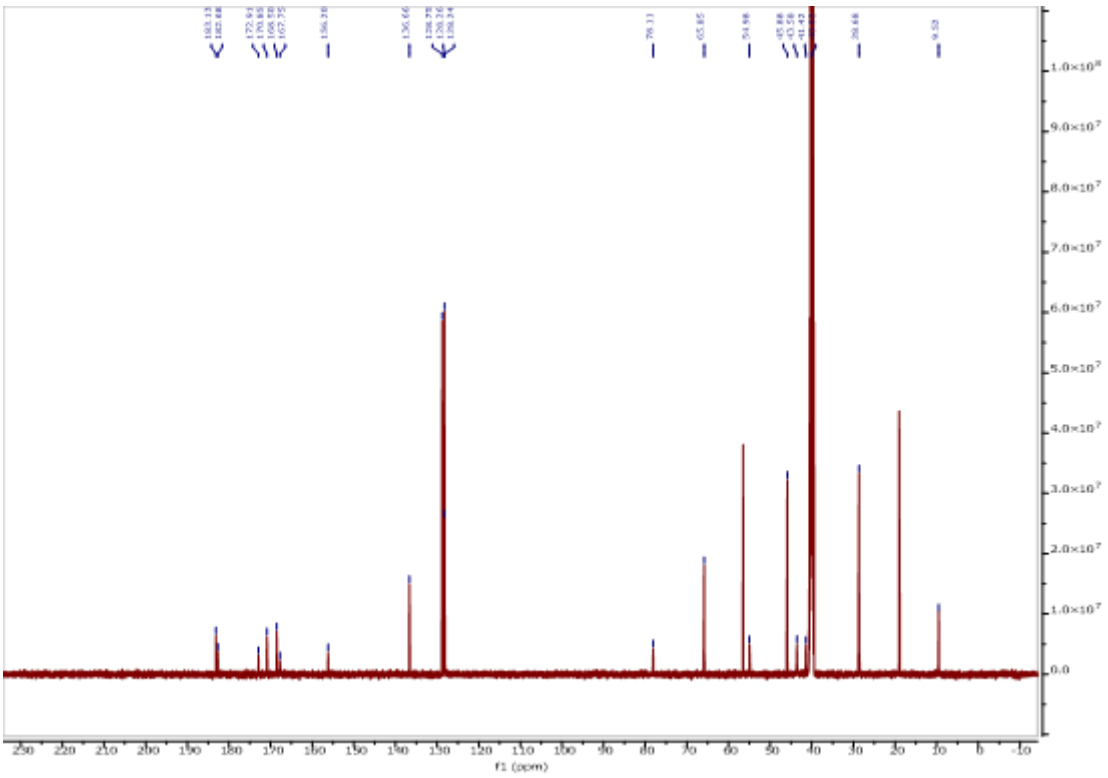

Figure A2.37: ^{13}C NMR spectrum of **2.12(Asp(Bn))** in DMSO-d_6.

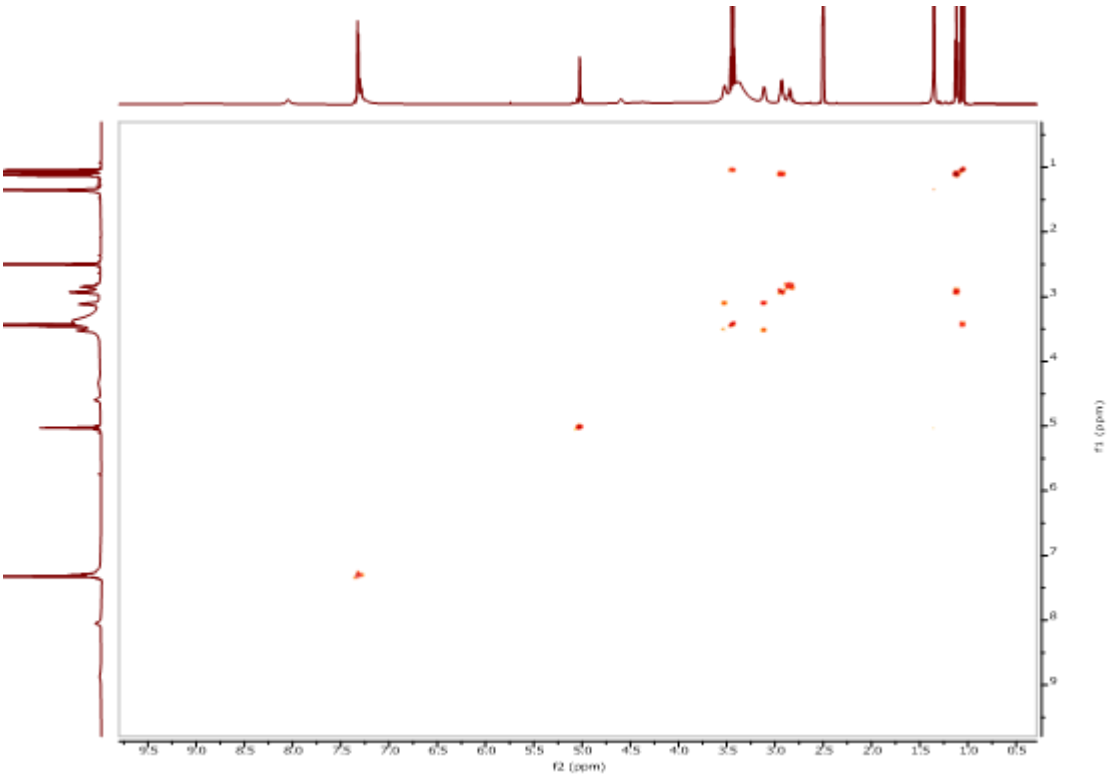

Figure A2.38: COSY spectrum of **2.12(Asp(Bn))** in DMSO-d_6.

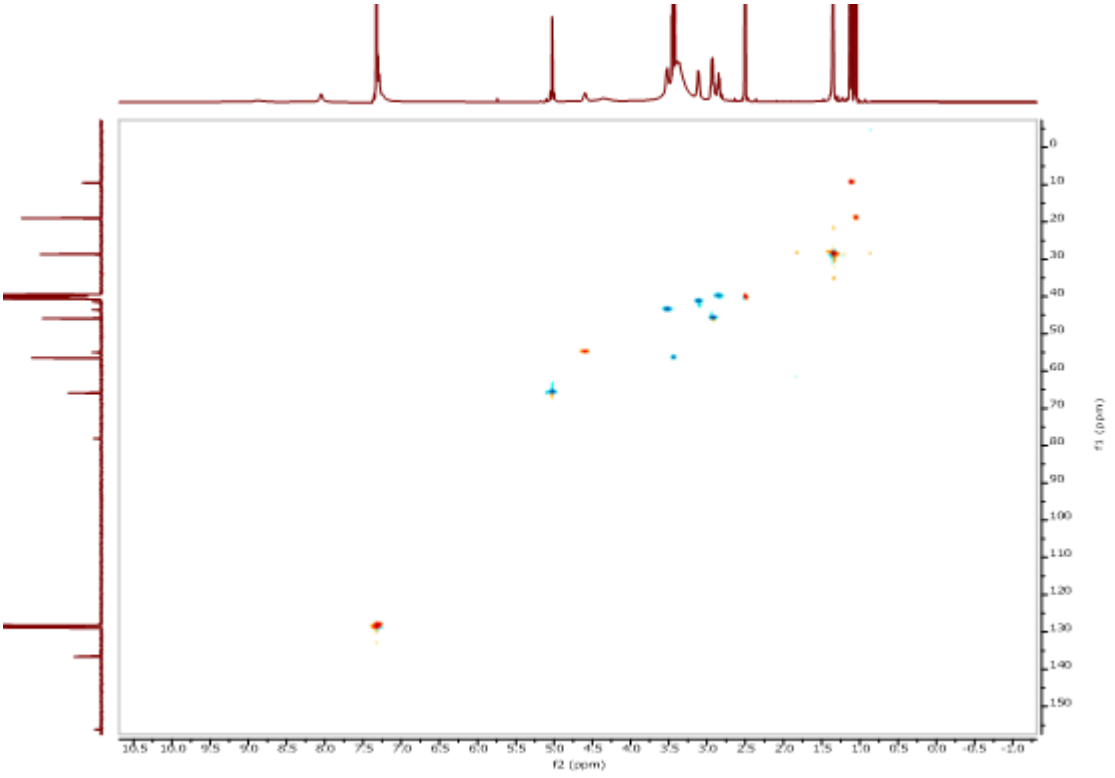

Figure A2.39: HSQC spectrum of **2.12(Asp(Bn))** in DMSO-d_6.

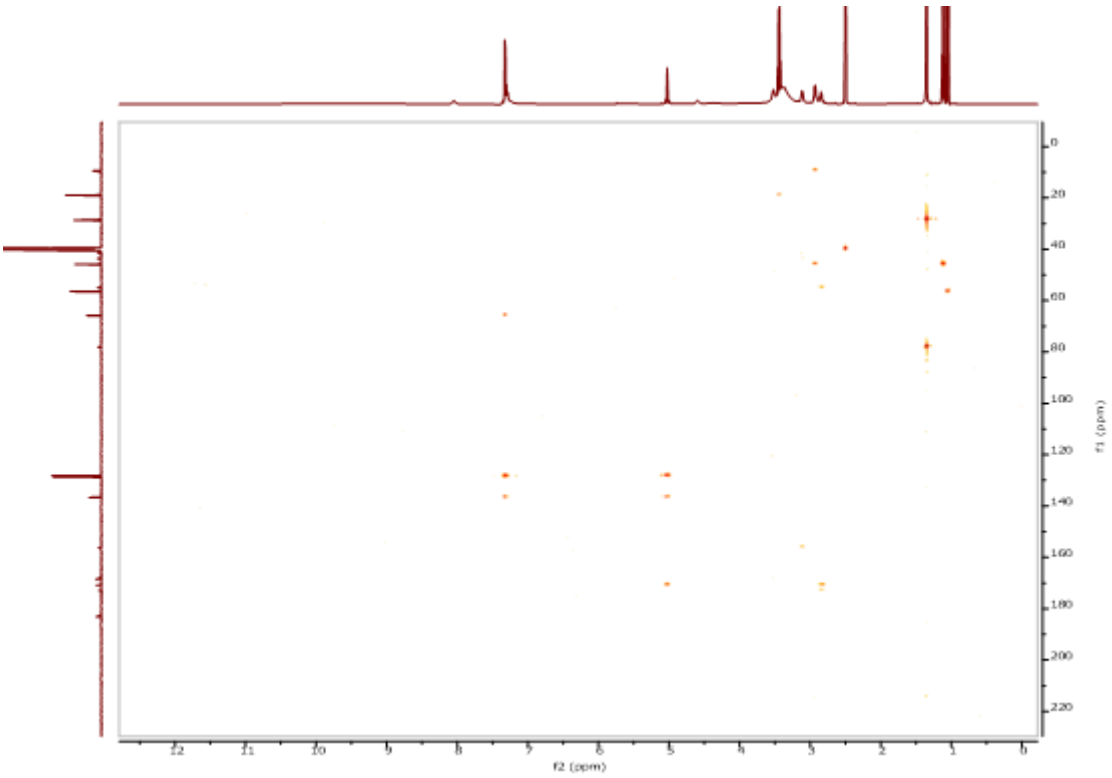

Figure A2.40: HMBC spectrum of **2.12(Asp(Bn))** in DMSO-d_6.

Compound Table

Compound Label	RT (min)	Observed mass (m/z)	Neutral observed mass (Da)	Theoretical mass (Da)	Mass error (ppm)	Isotope match score (%)
Cpd 1: C22 H27 N3 O8	0.71	462.1882	461.1809	461.1798	2.37	98.67

Figure: Extracted ion chromatogram (EIC) of compound.

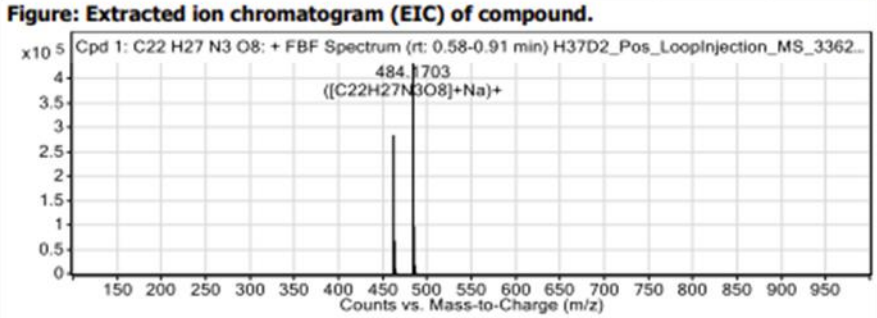

Figure: Full range view of Compound spectra and potential adducts.

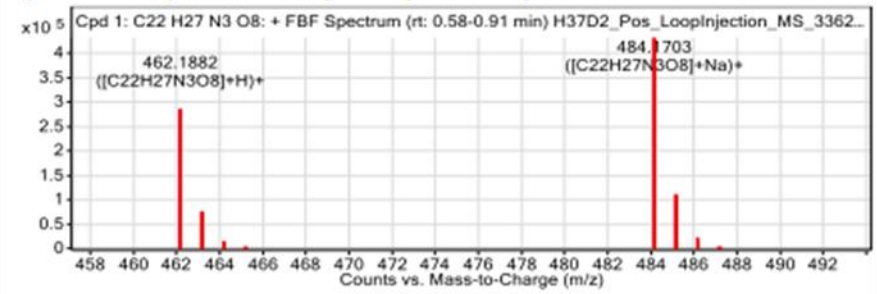

Figure: Zoomed Compound spectra view
(red boxes indicating expected theoretical isotope spacing and abundance)

Compound isotope peak List

m/z	z	Abund	Formula	Ion
462.1882	1	283909.5	C22H27N3O8	(M+H)+
463.1910	1	67625.4	C22H27N3O8	(M+H)+
464.1935	1	11674.0	C22H27N3O8	(M+H)+
465.1974	1	1929.7	C22H27N3O8	(M+H)+
484.1703	1	431395.2	C22H27N3O8	(M+Na)+
485.1727	1	97269.2	C22H27N3O8	(M+Na)+
486.1745	1	17508.3	C22H27N3O8	(M+Na)+
487.1750	1	2899.4	C22H27N3O8	(M+Na)+

Figure A2.41: HRMS data of **2.12(Asp(Bn))**.

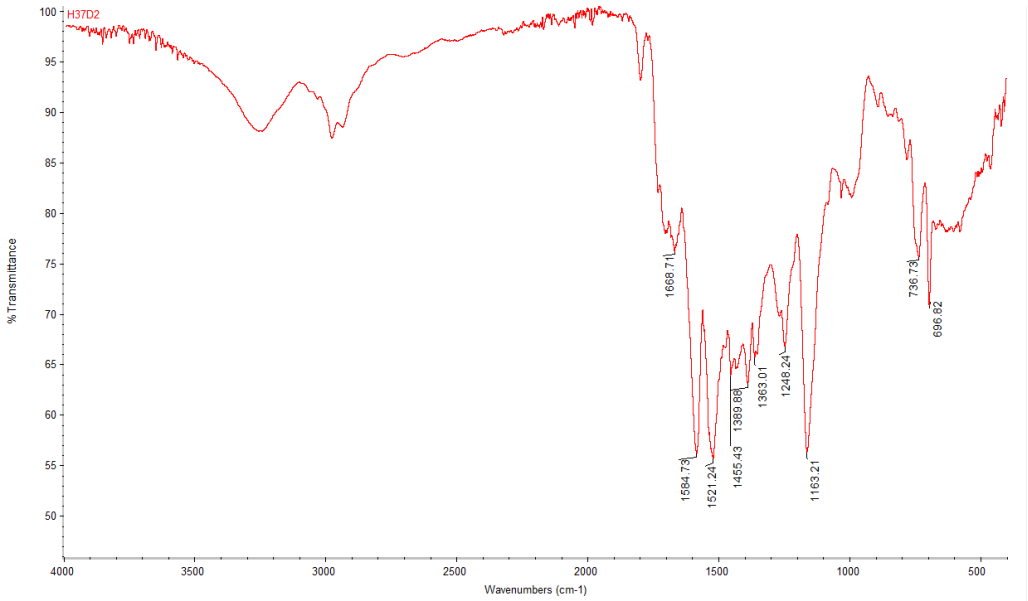

Figure A2.42: IR spectrum of **2.12(Asp(Bn))**.

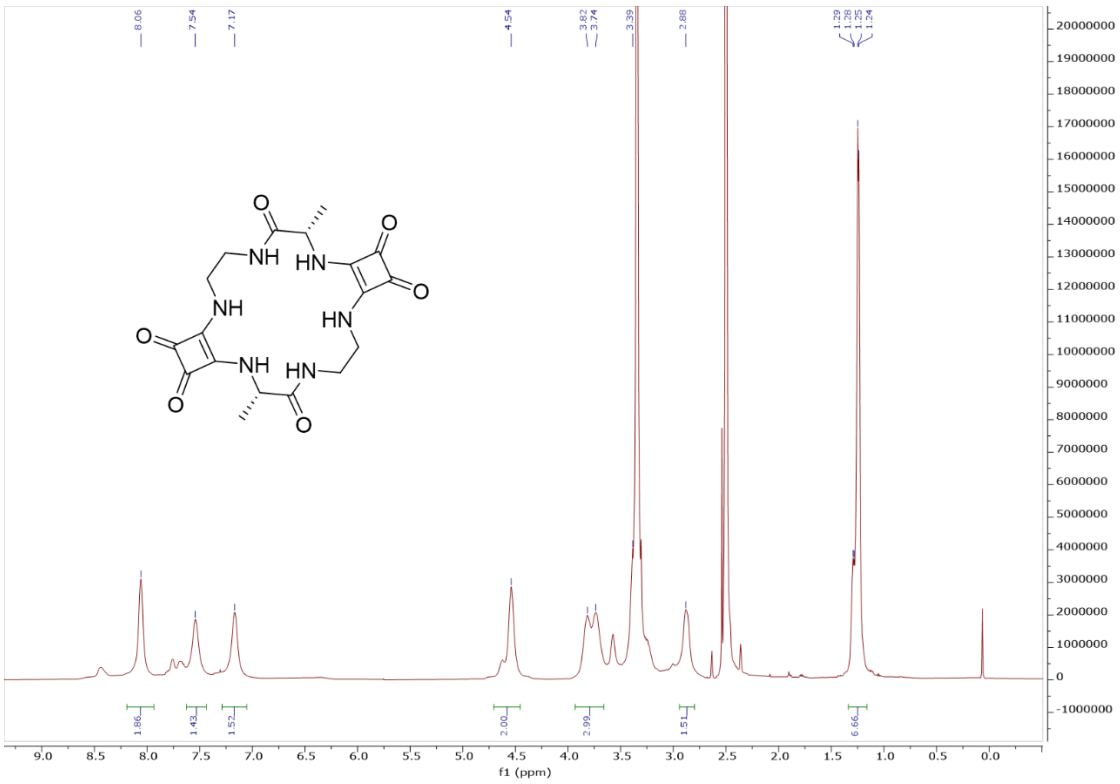

Figure A2.43: ^{1}H NMR spectrum of **2.14 (Sq-2-Ala)** in DMSO-d_6.

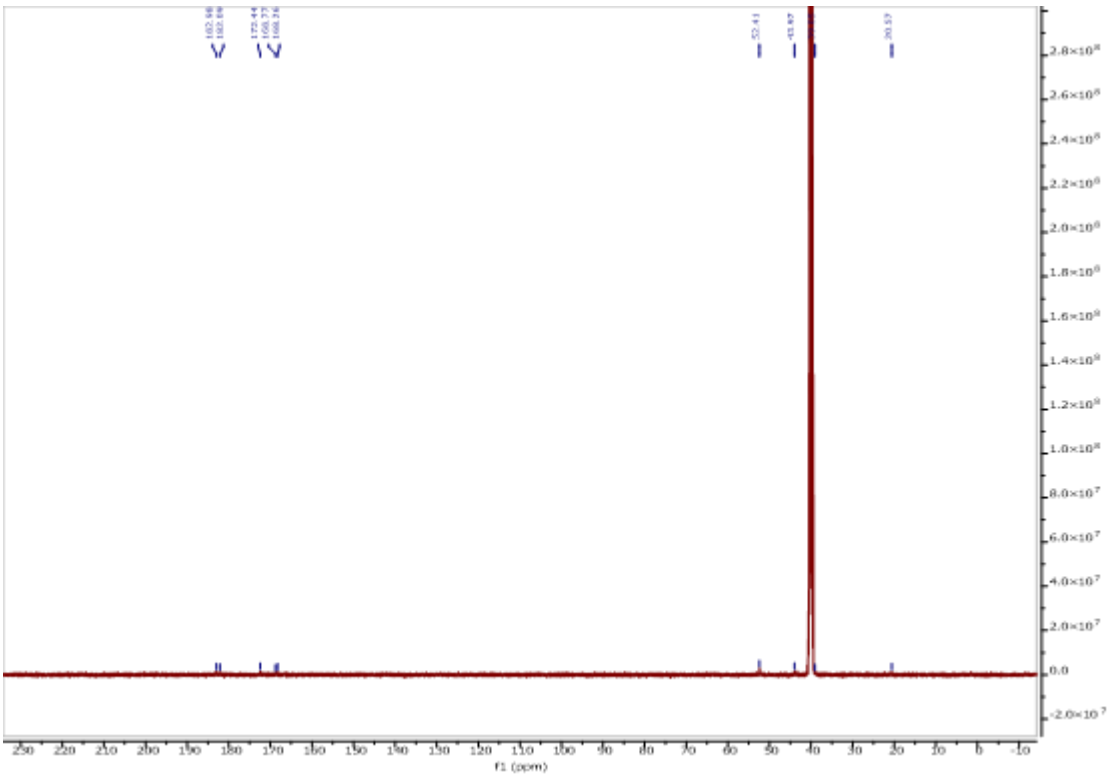

Figure A2.44: ^{13}C NMR spectrum of **2.14 (Sq-2-Ala)** in DMSO-d_6.

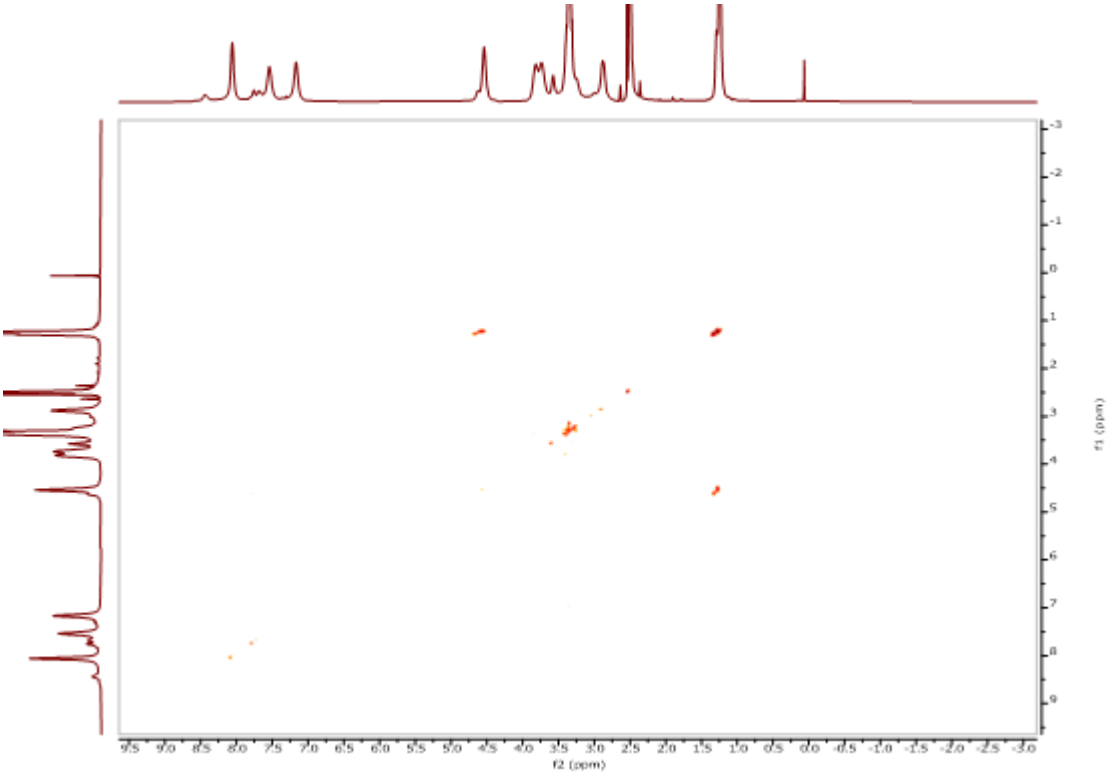

Figure A2.45: COSY spectrum of **2.14 (Sq-2-Ala)** in DMSO-d_6.

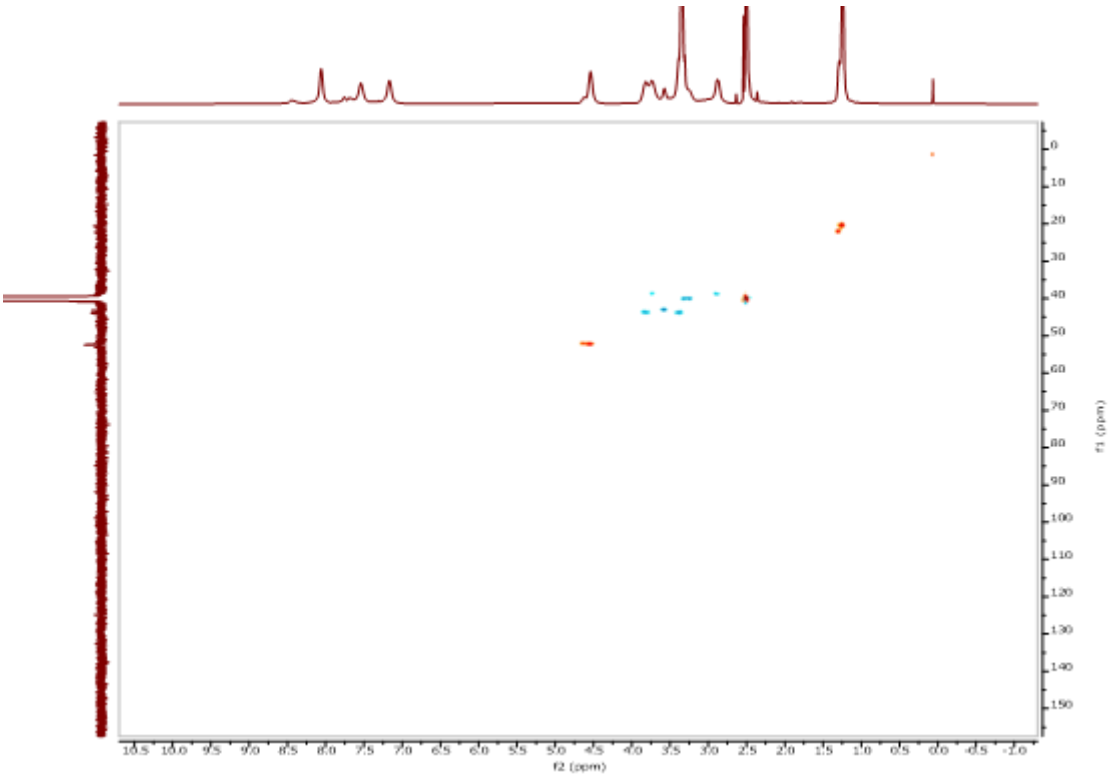

Figure A2.46: HSQC spectrum of **2.14 (Sq-2-Ala)** in DMSO-d_6.

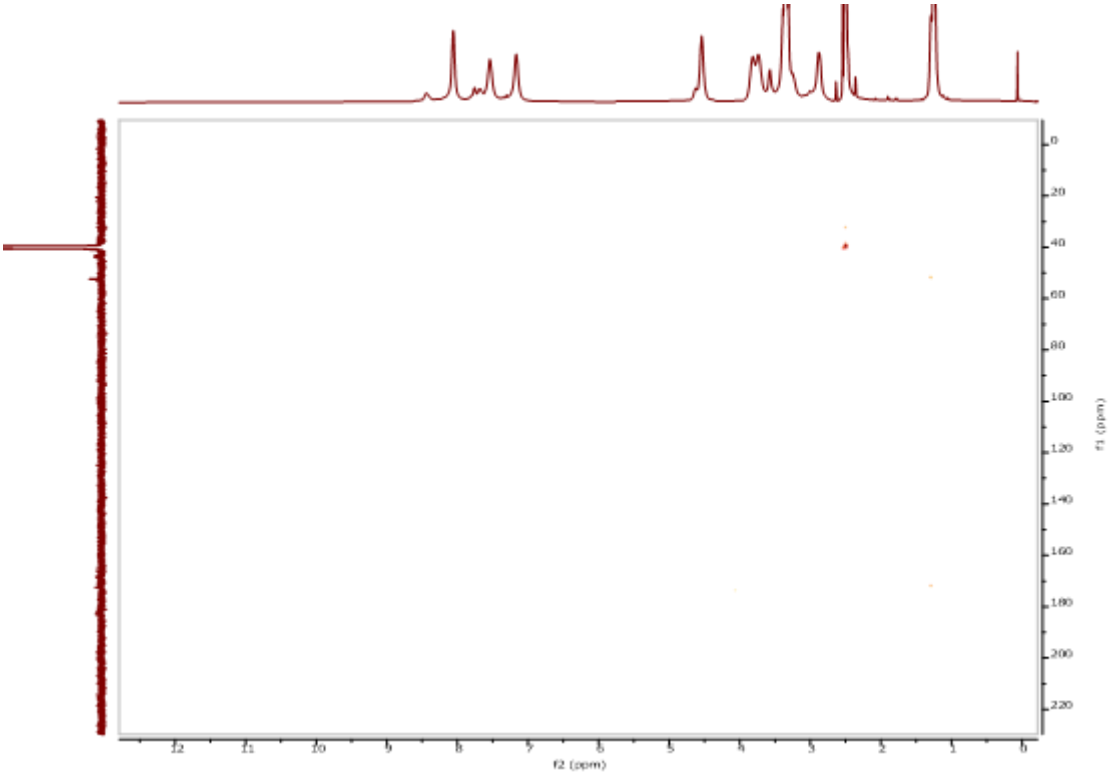

Figure A2.47: HMBC spectrum of **2.14 (Sq-2-Ala)** in DMSO-d_6.

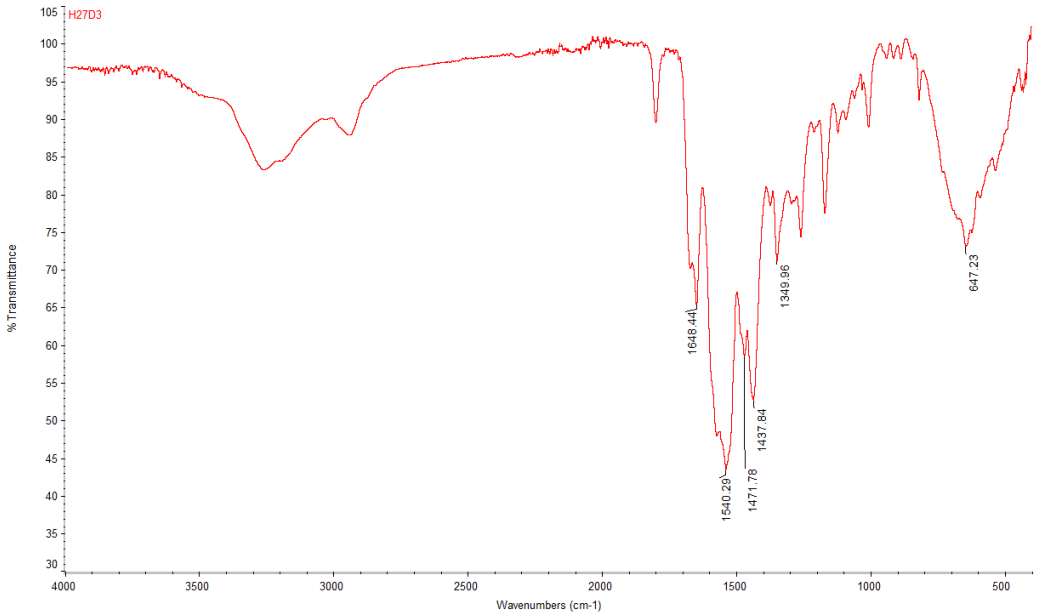

Figure A2.48: IR spectrum of **2.14 (Sq-2-Ala)**.

Compound Table

Compound Label	RT (min)	Observed mass (m/z)	Neutral observed mass (Da)	Theoretical mass (Da)	Mass error (ppm)	Isotope match score (%)
Cpd 1: C18 H22 N6 O6	0.69	441.1500	418.1608	418.1601	1.68	97.96

Figure: Extracted ion chromatogram (EIC) of compound.

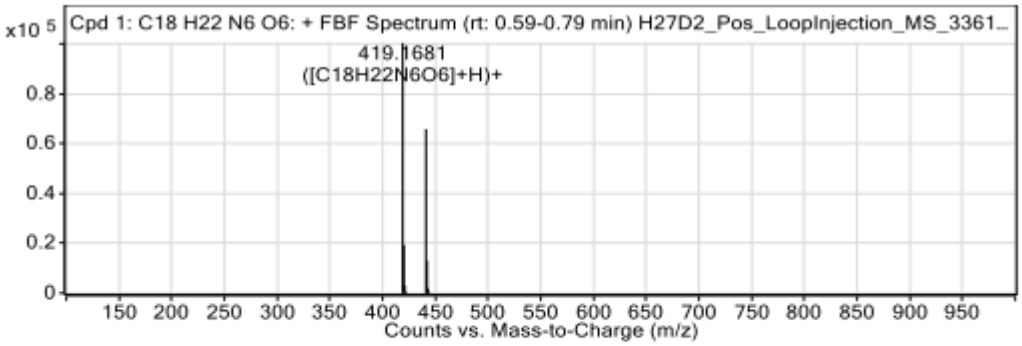

Figure: Full range view of Compound spectra and potential adducts.

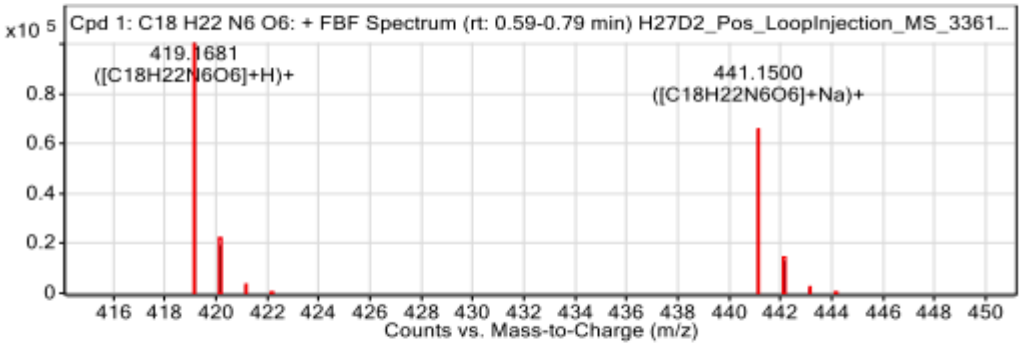

Figure: Zoomed Compound spectra view
(red boxes indicating expected theoretical isotope spacing and abundance)

Compound isotope peak List

m/z	z	Abund	Formula	Ion
419.1681	1	100720.4	C18H22N6O6	(M+H)+
420.1706	1	19354.7	C18H22N6O6	(M+H)+
421.1730	1	3027.0	C18H22N6O6	(M+H)+
422.1768	1	449.2	C18H22N6O6	(M+H)+
441.1500	1	65932.4	C18H22N6O6	(M+Na)+
442.1529	1	13102.1	C18H22N6O6	(M+Na)+
443.1548	1	1856.9	C18H22N6O6	(M+Na)+
444.1550	1	334.9	C18H22N6O6	(M+Na)+

Figure A2.49: HRMS data of **2.14 (Sq-2-Ala)**

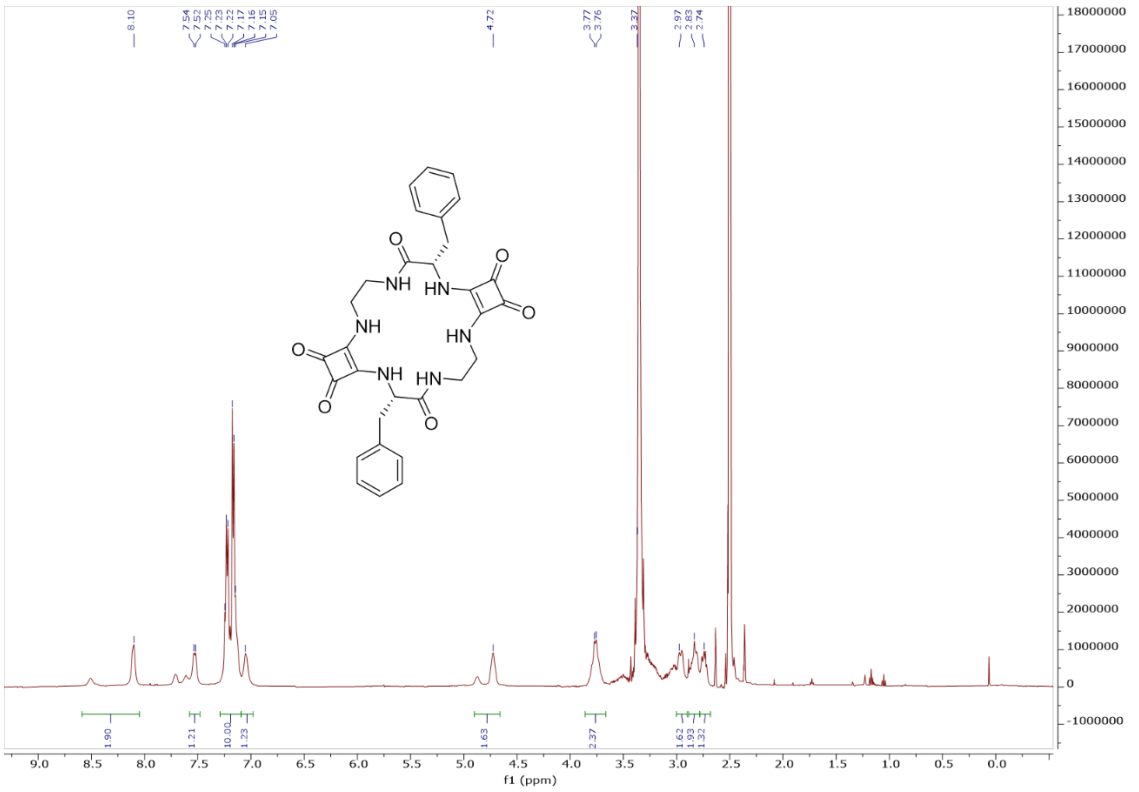

Figure A2.50: ^{1}H NMR spectrum of **2.15 (Sq-2-Phe)** in DMSO-d_6.

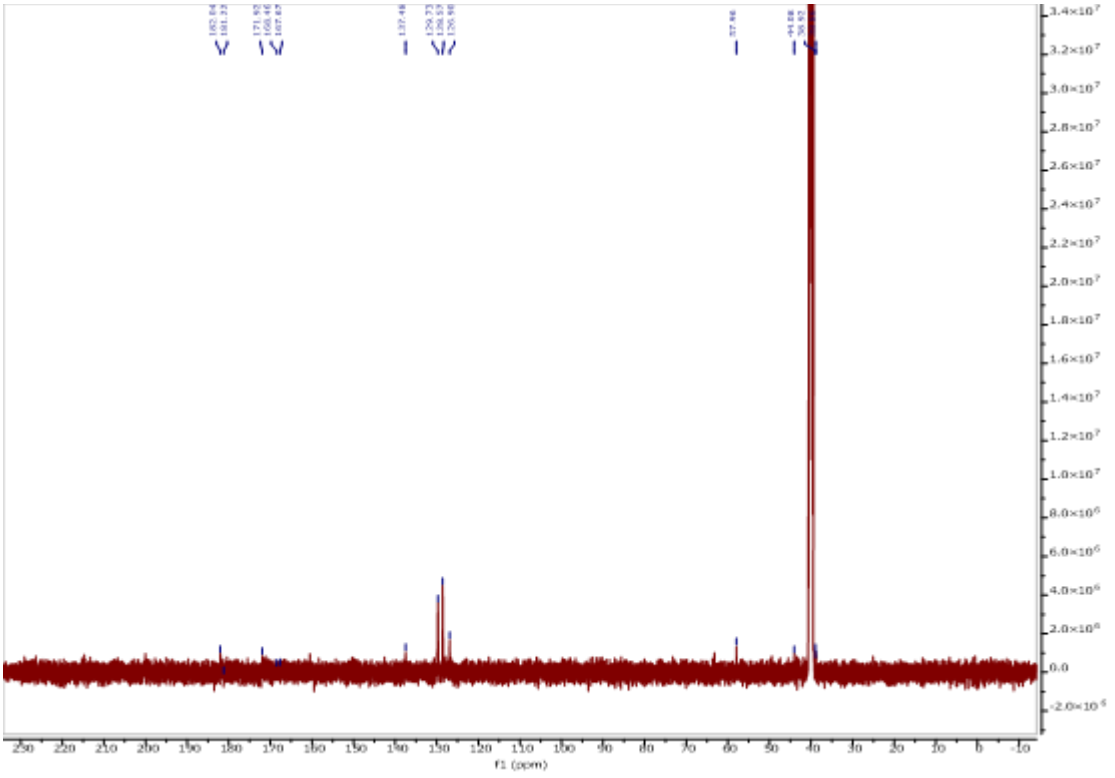

Figure A2.51: ^{13}C NMR spectrum of **2.15 (Sq-2-Phe)** in DMSO-d_6.

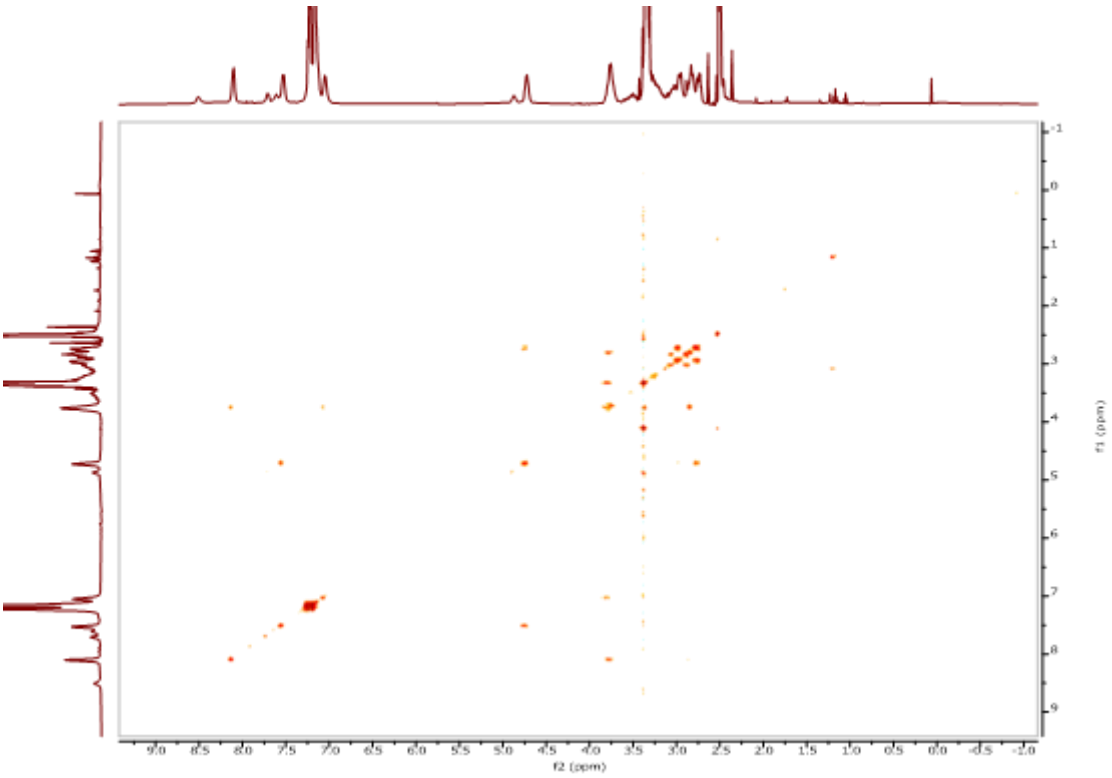

Figure A2.52: COSY spectrum of **2.15 (Sq-2-Phe)** in DMSO-d_6.

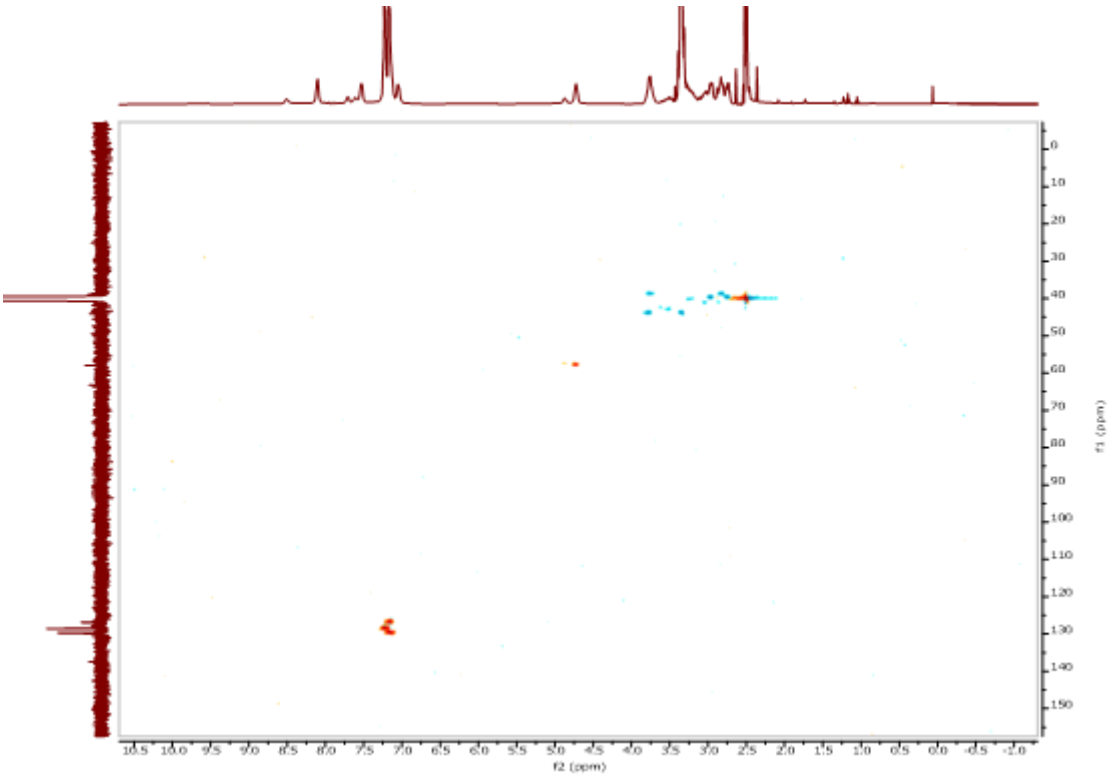

Figure A2.53: HSQC spectrum of **2.15 (Sq-2-Phe)** in DMSO-d_6.

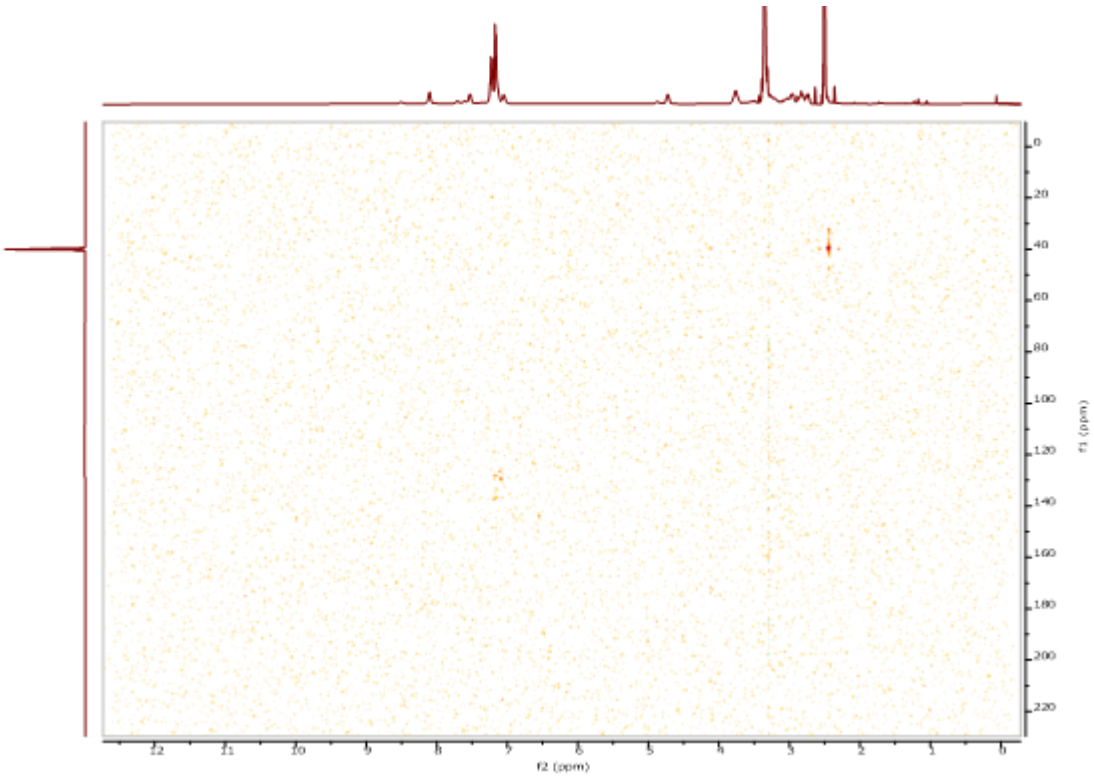

Figure A48: HMBC spectrum of **2.15 (Sq-2-Phe)** in DMSO-d_6.

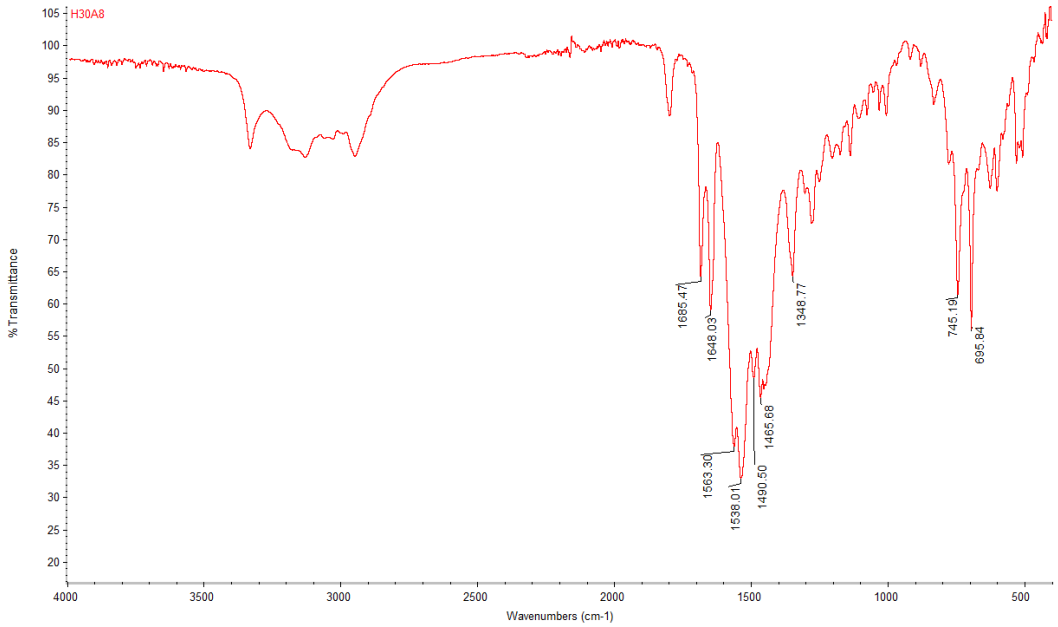

Figure A2.54: IR spectrum of **2.15 (Sq-2-Phe)**

Compound Table

Compound Label	RT (min)	Observed mass (m/z)	Neutral observed mass (Da)	Theoretical mass (Da)	Mass error (ppm)	Isotope match score (%)
Cpd 1: C30 H30 N6 O6	0.71	571.2309	570.2235	570.2227	1.38	98.59

Figure: Extracted ion chromatogram (EIC) of compound.

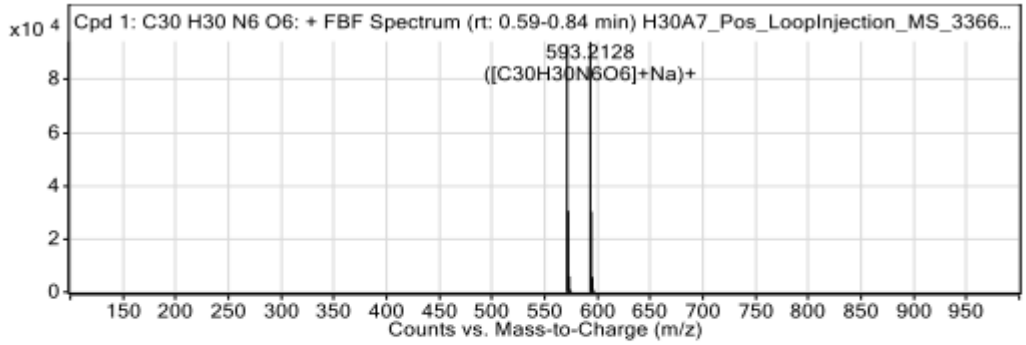

Figure: Full range view of Compound spectra and potential adducts.

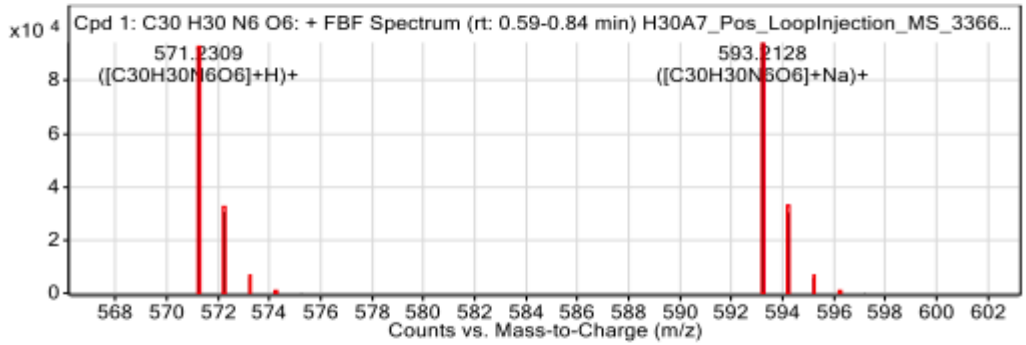

Figure: Zoomed Compound spectra view
(red boxes indicating expected theoretical isotope spacing and abundance)

Compound isotope peak List

m/z	z	Abund	Formula	Ion
571.2309	1	93039.2	C30H30N6O6	(M+H)+
572.2337	1	30574.3	C30H30N6O6	(M+H)+
573.2362	1	5949.9	C30H30N6O6	(M+H)+
574.2380	1	944.1	C30H30N6O6	(M+H)+
575.2424	1	154.9	C30H30N6O6	(M+H)+
593.2128	1	94281.0	C30H30N6O6	(M+Na)+
594.2154	1	30331.3	C30H30N6O6	(M+Na)+
595.2179	1	5687.7	C30H30N6O6	(M+Na)+
596.2209	1	880.1	C30H30N6O6	(M+Na)+
597.1953	1	149.3	C30H30N6O6	(M+Na)+

Figure A2.55: HRMS data of **2.15 (Sq-2-Phe)**

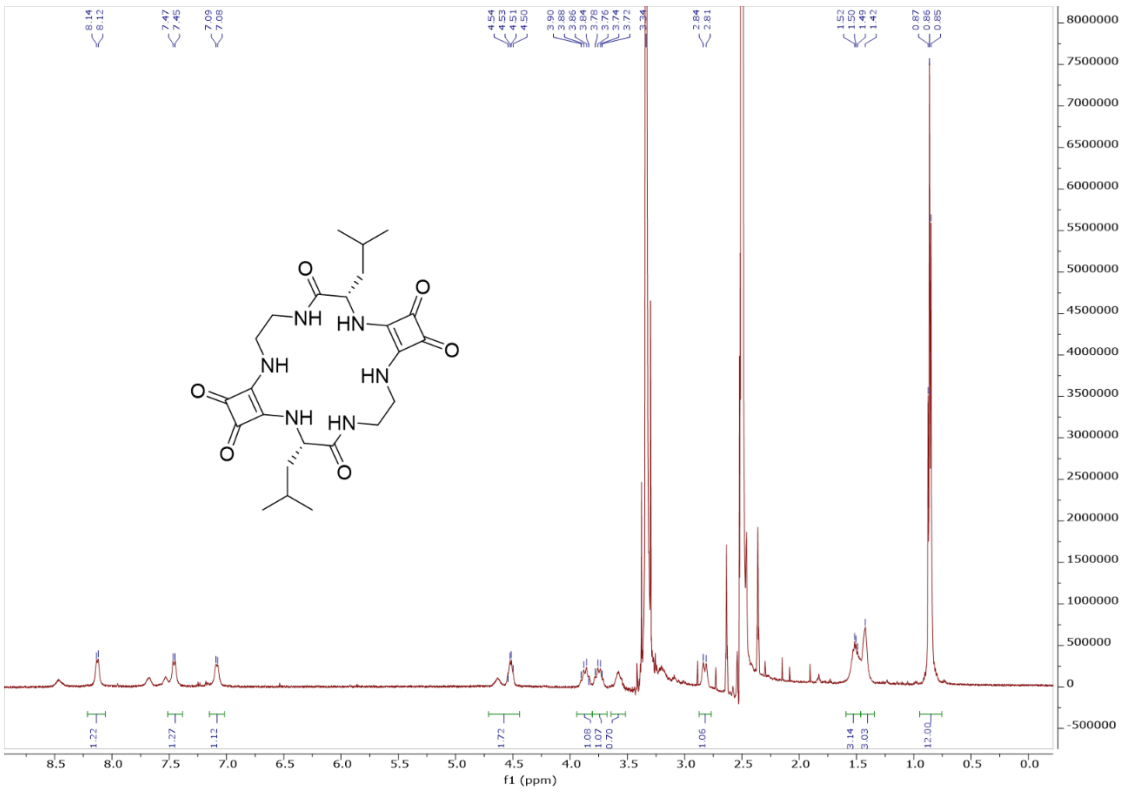

Figure A2.56: ^{1}H NMR spectrum of **2.16 (Sq-2-Leu)** in DMSO-d_6.

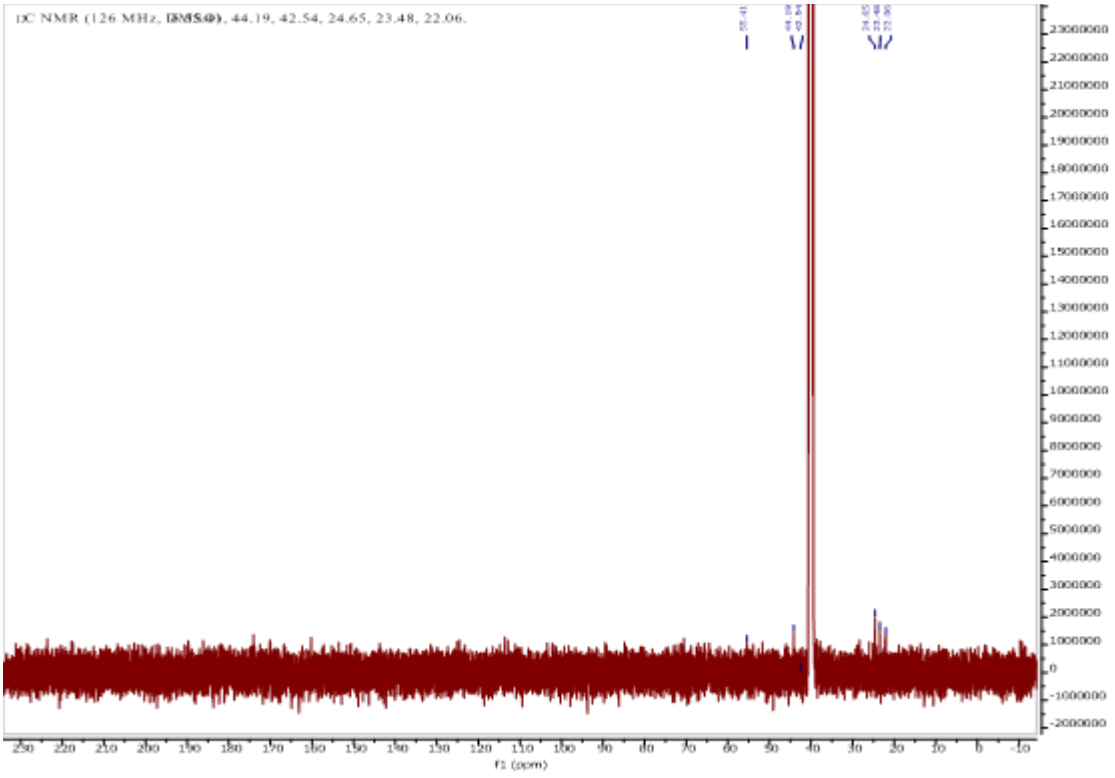

Figure A2.57: ^{13}C NMR spectrum of **2.16 (Sq-2-Leu)** in DMSO-d_6.

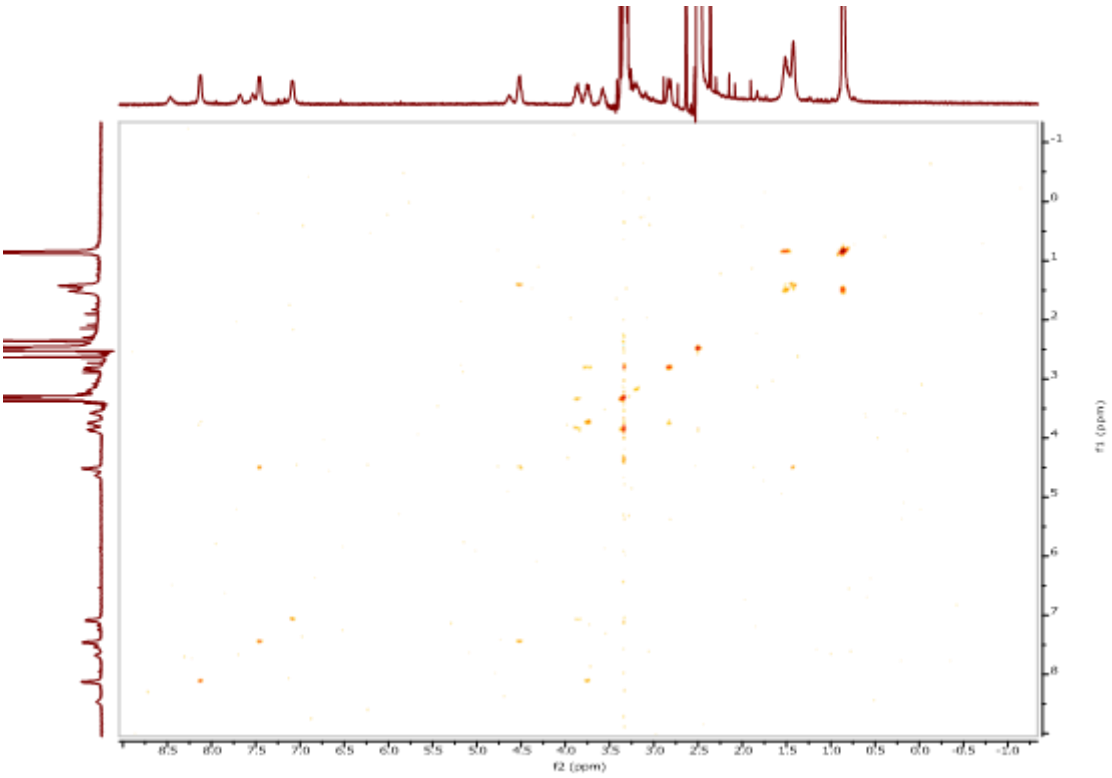

Figure A2.58: COSY spectrum of **2.16 (Sq-2-Leu)** in DMSO-d_6.

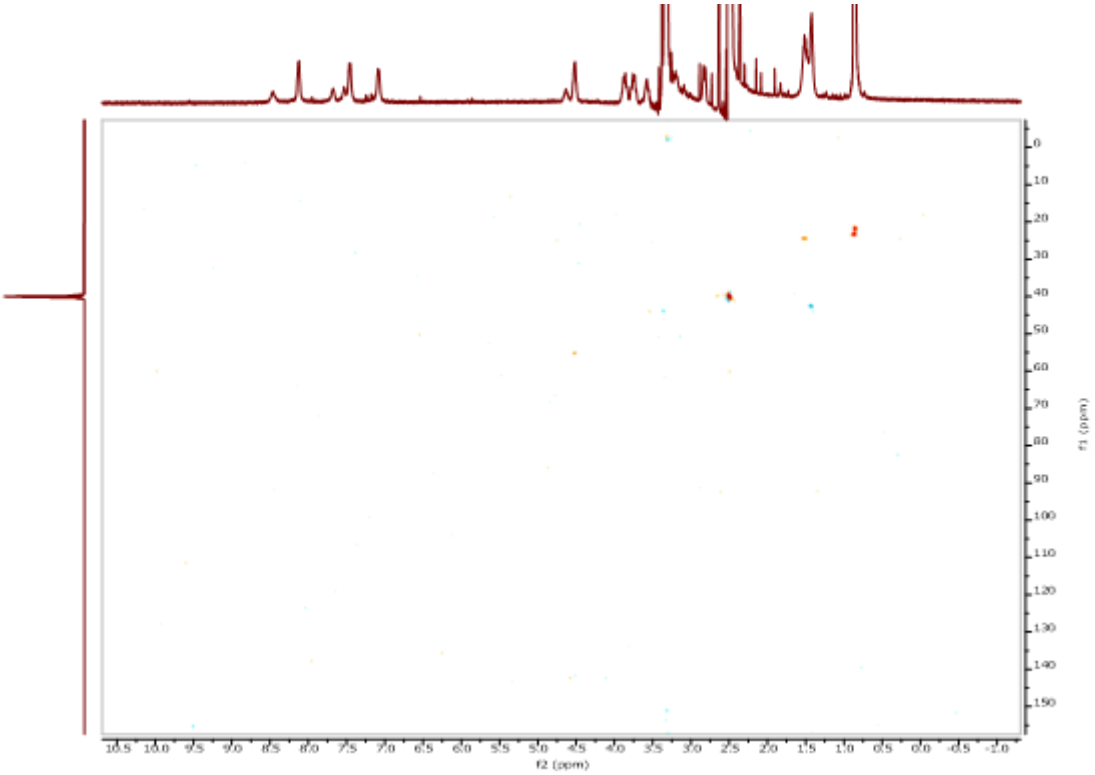

Figure A2.59: HSQC spectrum of **2.16 (Sq-2-Leu)** in DMSO-d_6.

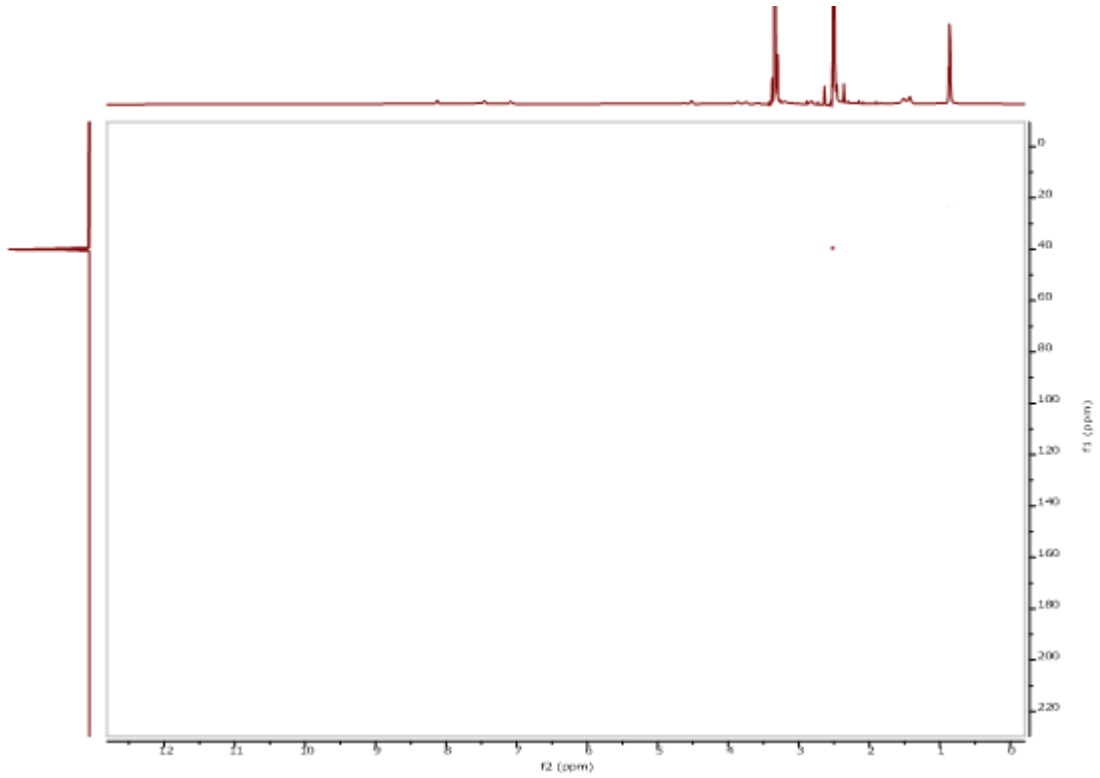

Figure A2.60: HMBC spectrum of **2.16 (Sq-2-Leu)** in DMSO-d_6.

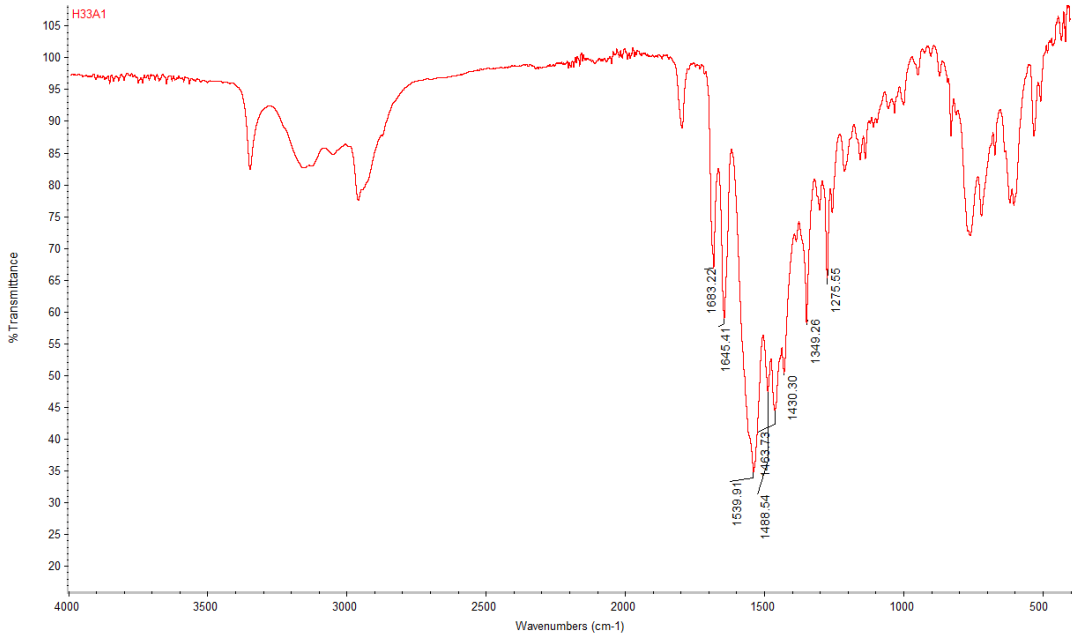

Figure A2.61: IR spectrum of **2.16 (Sq-2-Leu)**

Compound Table

Compound Label	RT (min)	Observed mass (m/z)	Neutral observed mass (Da)	Theoretical mass (Da)	Mass error (ppm)	Isotope match score (%)
Cpd 1: C24 H34 N6 O6	0.69	503.2621	502.2548	502.2540	1.61	98.86

Figure: Extracted ion chromatogram (EIC) of compound.

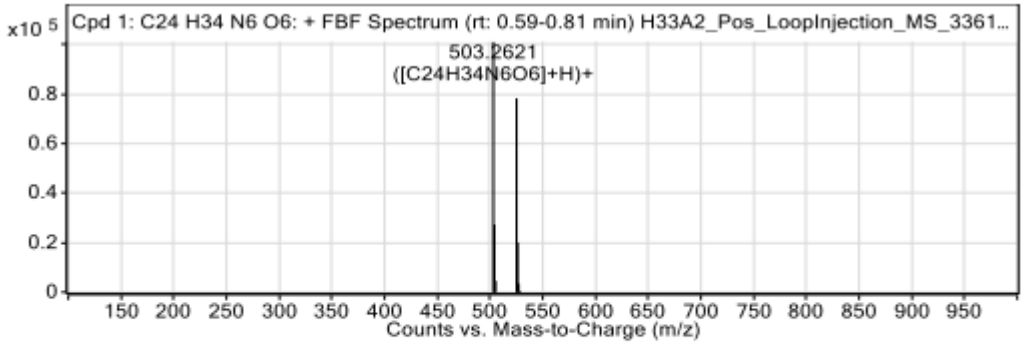

Figure: Full range view of Compound spectra and potential adducts.

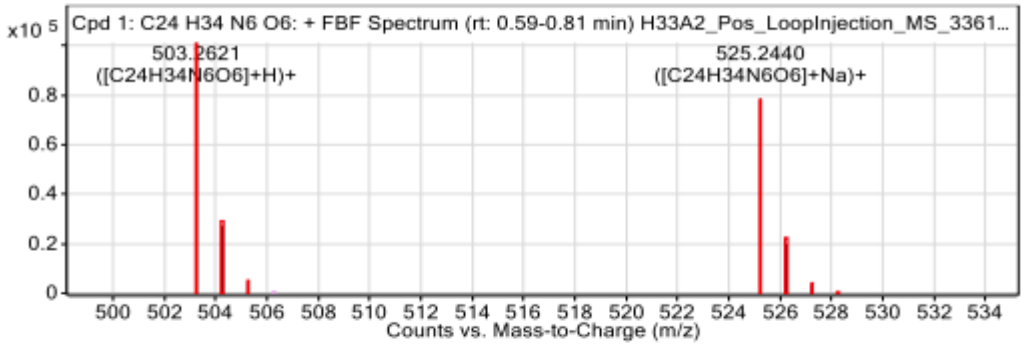

Figure: Zoomed Compound spectra view
(red boxes indicating expected theoretical isotope spacing and abundance)

Compound isotope peak List

m/z	z	Abund	Formula	Ion
503.2621	1	101174.8	C24H34N6O6	(M+H)+
504.2649	1	27291.0	C24H34N6O6	(M+H)+
505.2682	1	4574.2	C24H34N6O6	(M+H)+
525.2440	1	78263.4	C24H34N6O6	(M+Na)+
526.2465	1	19998.0	C24H34N6O6	(M+Na)+
527.2492	1	3481.3	C24H34N6O6	(M+Na)+
528.2534	1	525.3	C24H34N6O6	(M+Na)+

Figure A2.62: HRMS data of **2.16 (Sq-2-Leu)**

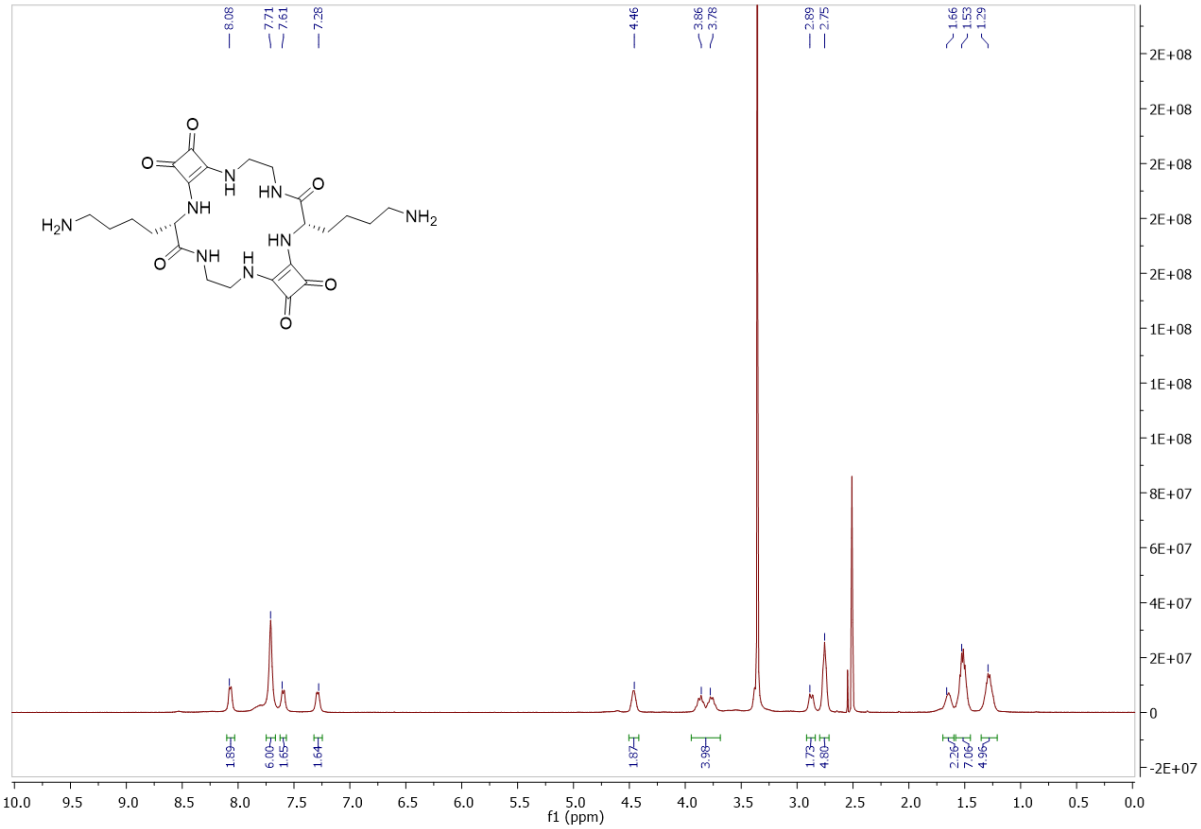

Figure A2.63: ^{1}H NMR spectrum of **2.17 (Sq-2-Lys)** in DMSO-d_6.

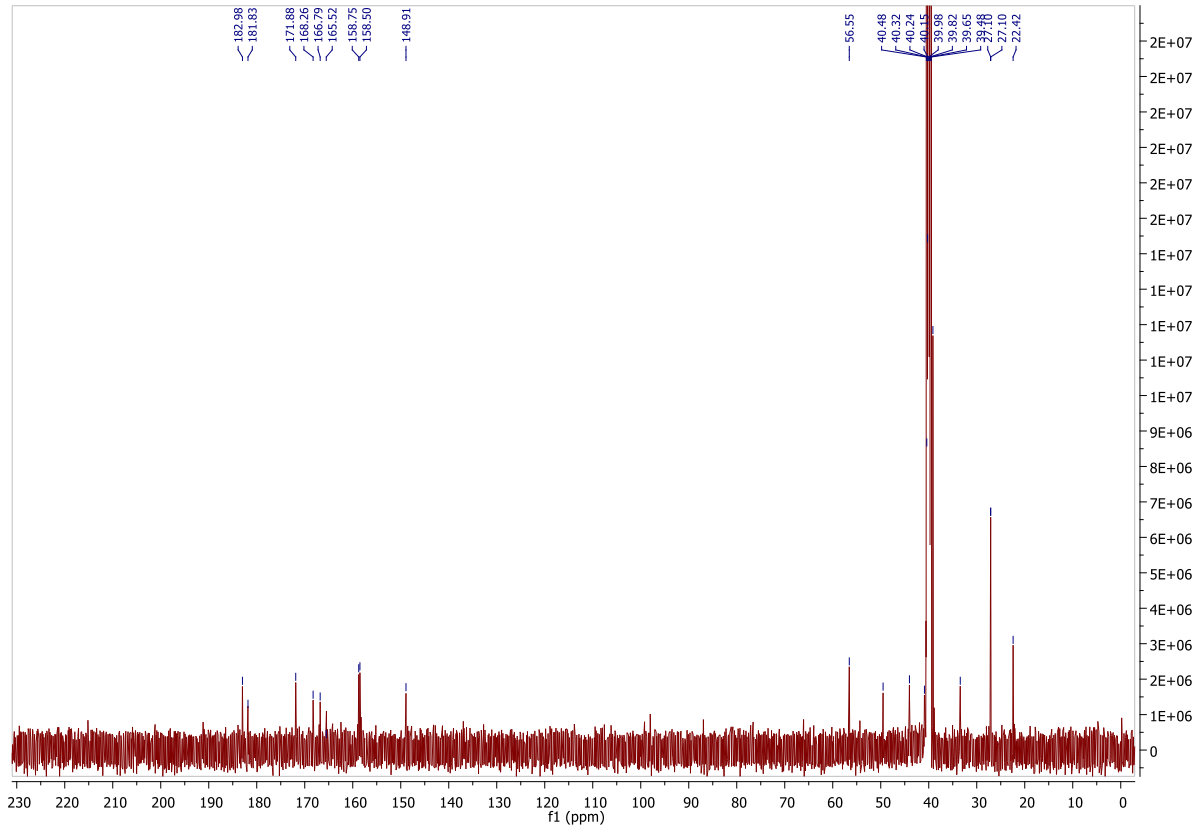

Figure A2.64: ^{13}C NMR spectrum of **2.17 (Sq-2-Lys)** in DMSO-d_6.

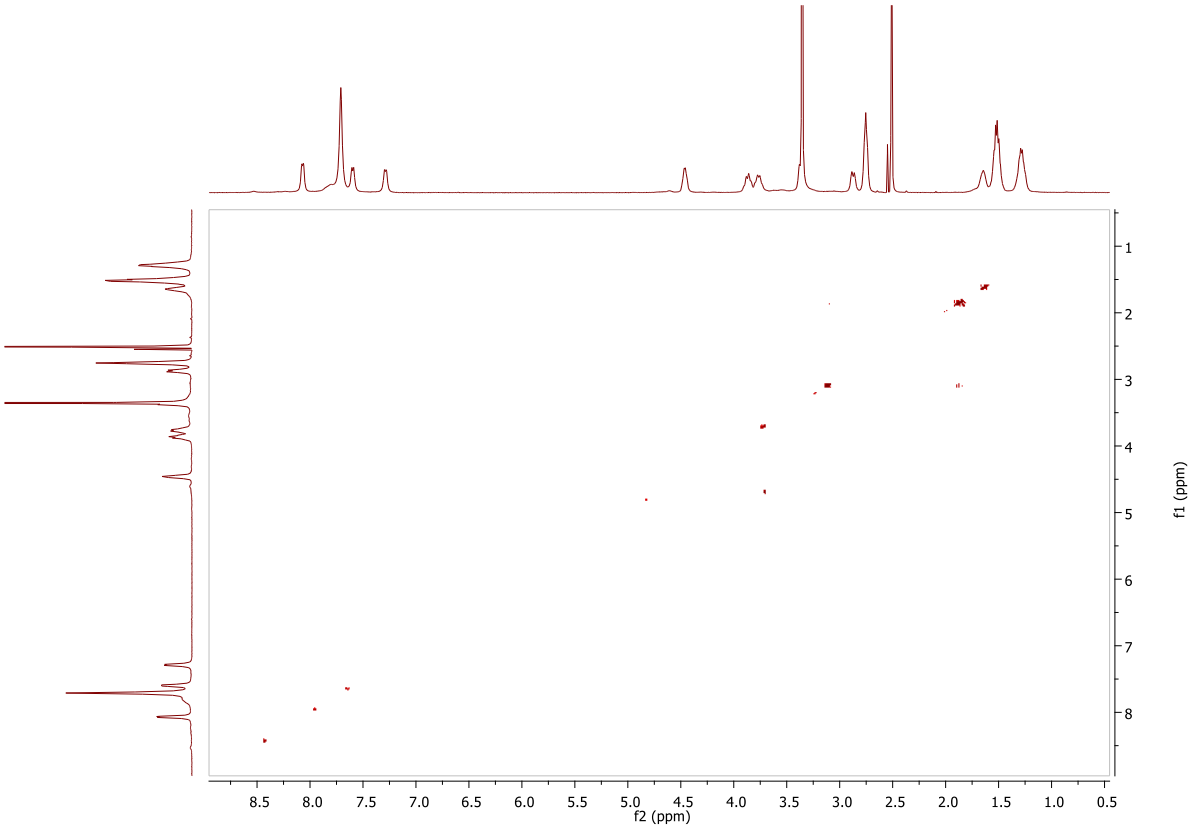

Figure A2.65: COSY spectrum of **2.17 (Sq-2-Lys)** in DMSO-d_6.

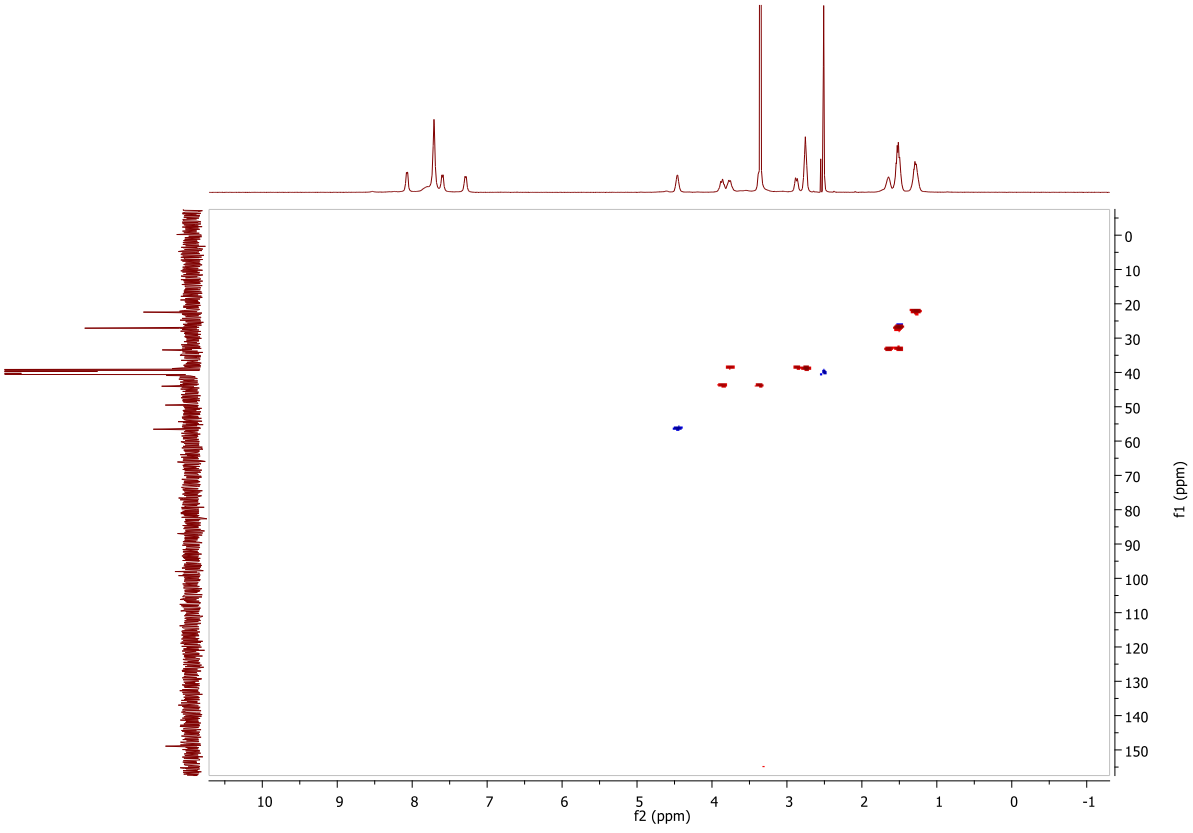

Figure A2.66: HSQC spectrum of **2.17 (Sq-2-Lys)** in DMSO-d_6.

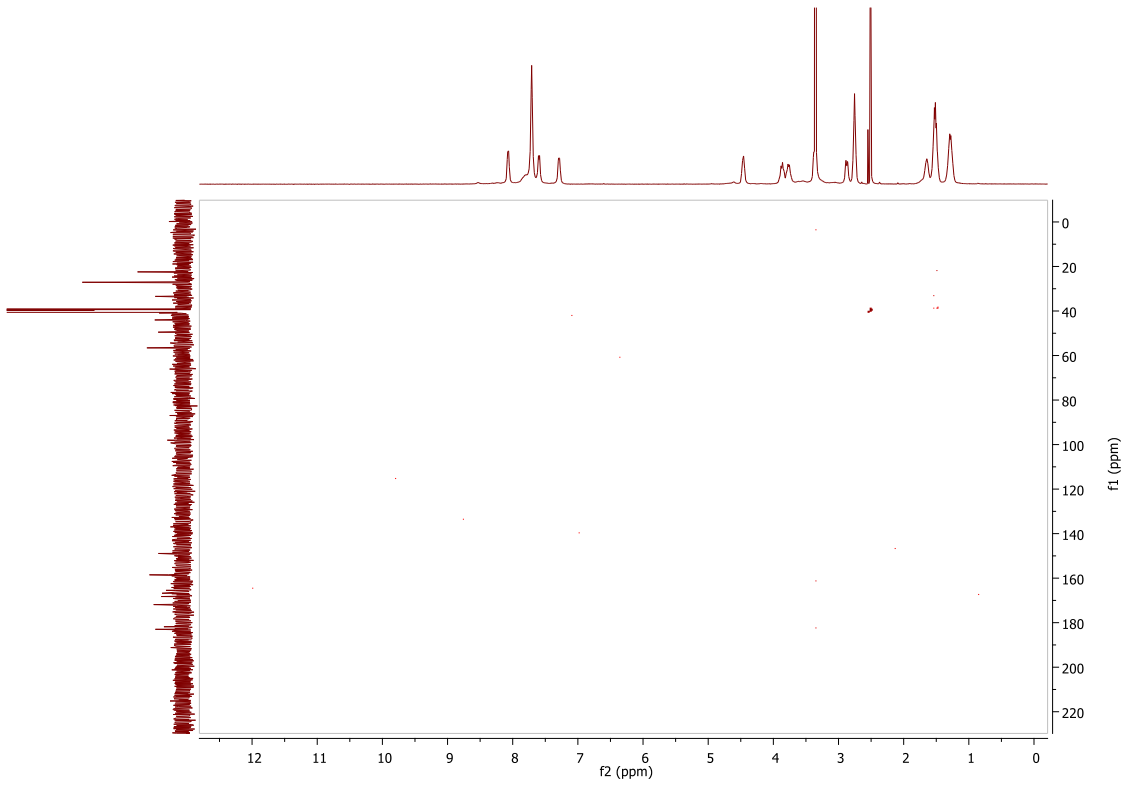

Figure A2.67: HMBC spectrum of **2.17 (Sq-2-Lys)** in DMSO-d_6.

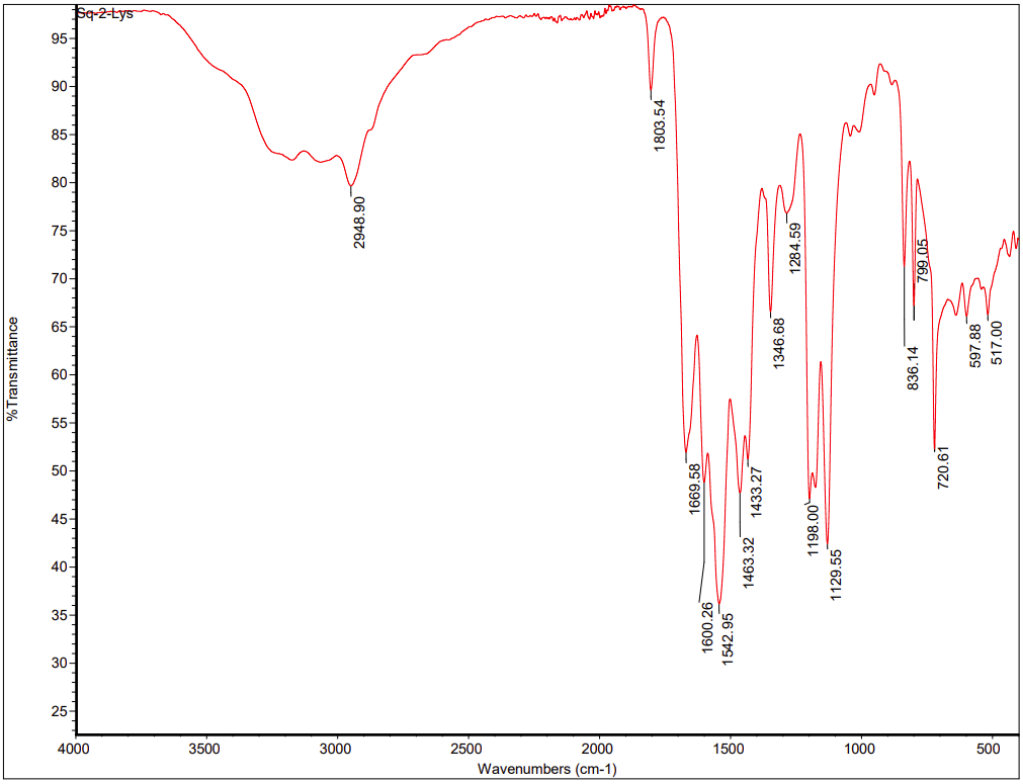

Figure A2.68: IR spectrum of **2.17 (Sq-2-Lys)**

Compound Table

Compound Label	RT (min)	Observed mass (m/z)	Neutral observed mass (Da)	Theoretical mass (Da)	Mass error (ppm)	Isotope match score (%)
Cpd 1: C24 H36 N8 O6	0.75	533.2828	532.2756	532.2758	-0.33	98.94

Mass errors of between -5.00 and 5.00 ppm with isotope match scores above 60% are considered confirmation of molecular formulae

Figure: Extracted ion chromatogram (EIC) of compound.

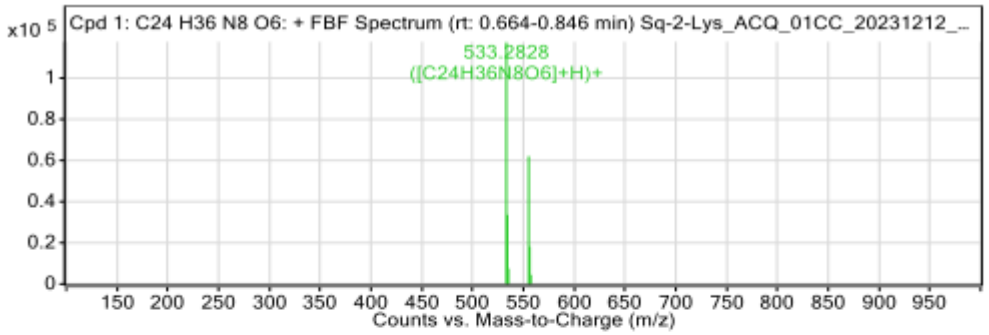

Figure: Full range view of Compound spectra and potential adducts.

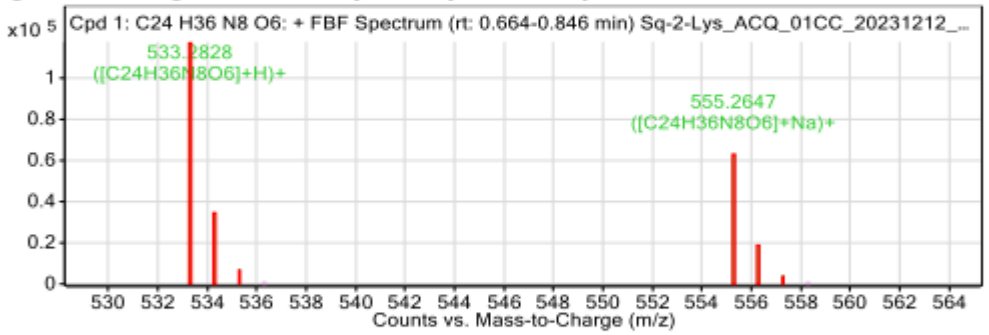

Figure: Zoomed Compound spectra view
(red boxes indicating expected theoretical isotope spacing and abundance)

Compound isotope peak List

m/z	z	Abund	Formula	Ion
533.2828	1	117360.2	C24H36N8O6	(M+H)+
534.2856	1	33513.8	C24H36N8O6	(M+H)+
535.2884	1	7453.1	C24H36N8O6	(M+H)+
555.2647	1	61934.6	C24H36N8O6	(M+Na)+
556.2677	1	18164.1	C24H36N8O6	(M+Na)+
557.2744	1	4436.2	C24H36N8O6	(M+Na)+

Figure A2.69: HRMS data of **2.17 (Sq-2-Lys)**

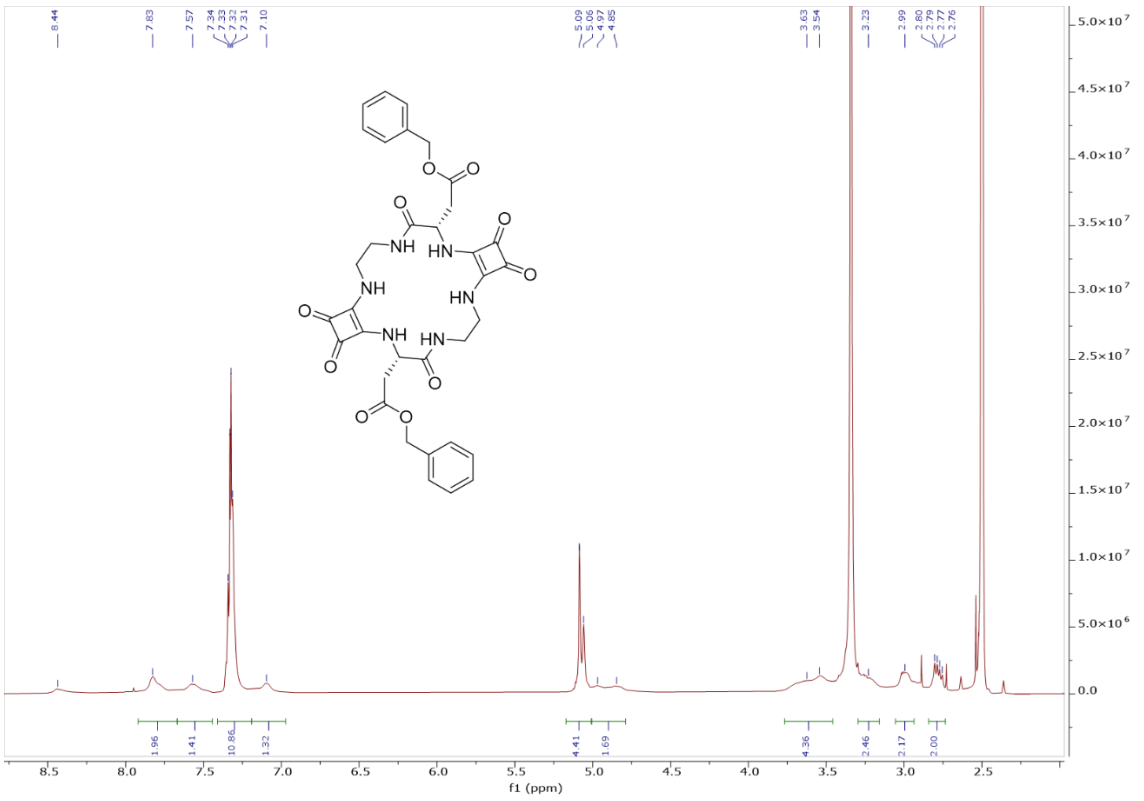

Figure A2.70: ^{1}H NMR spectrum of **2.18 (Sq-2-Asp(Bn))** in DMSO-d_6.

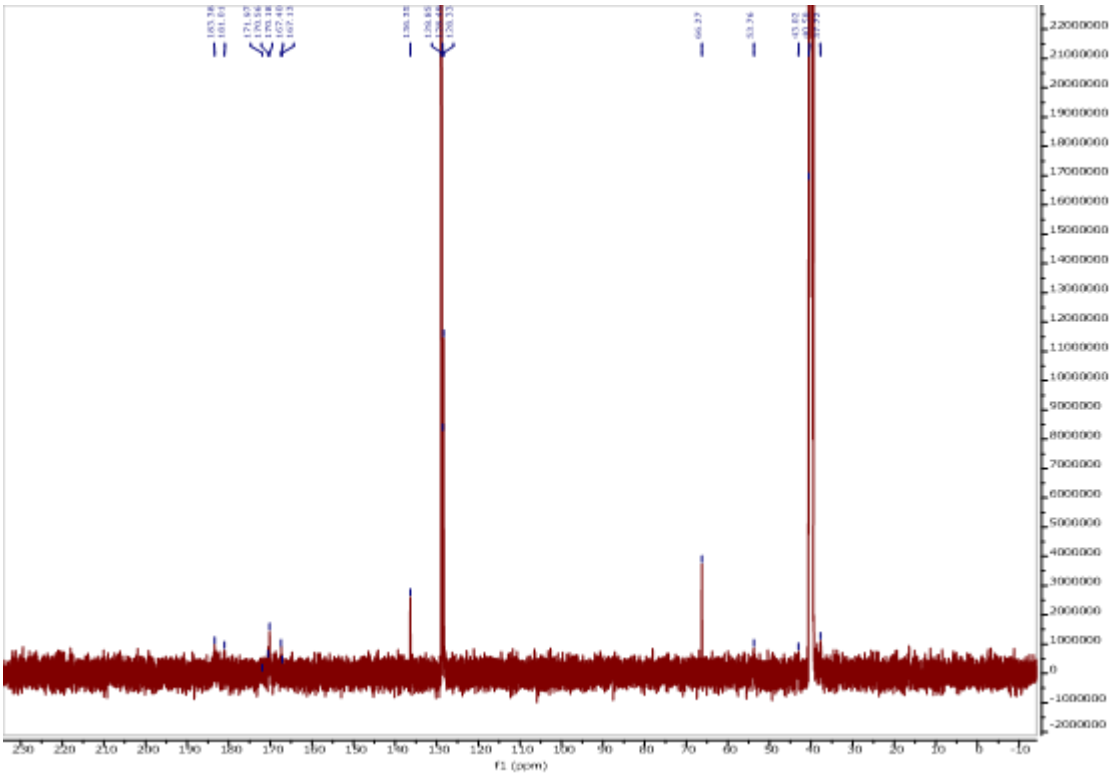

Figure A2.71: ^{13}C NMR spectrum of **2.18 (Sq-2-Asp(Bn))** in DMSO-d_6.

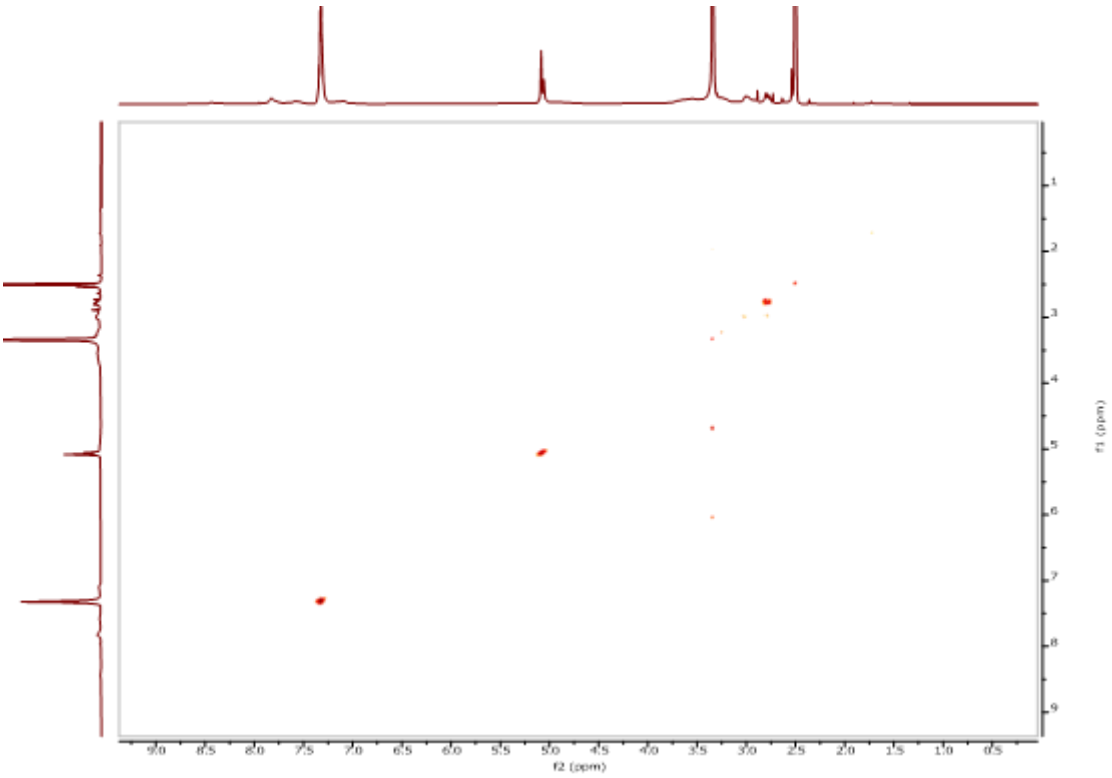

Figure A2.72: COSY spectrum of **2.18 (Sq-2-Asp(Bn))** in DMSO-d_6.

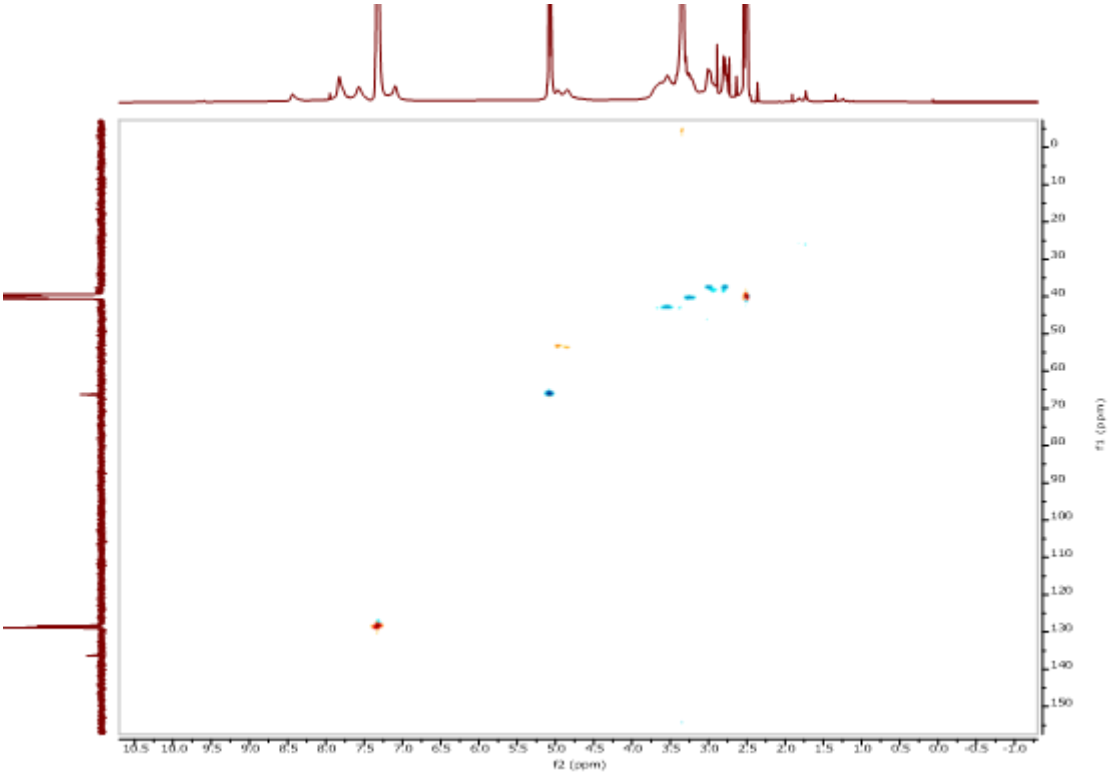

Figure A2.73: HSQC spectrum of **2.18 (Sq-2-Asp(Bn))** in DMSO-d_6.

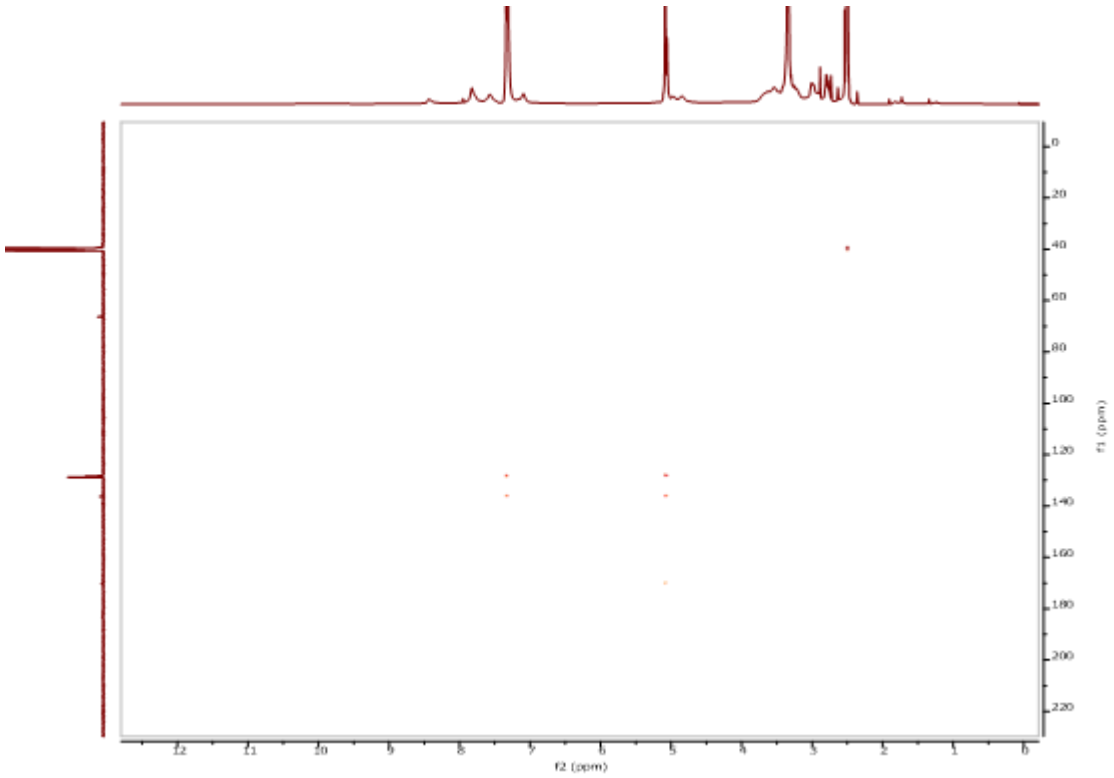

Figure A2.74: HMBC spectrum of **2.18 (Sq-2-Asp(Bn))** in DMSO-d_6.

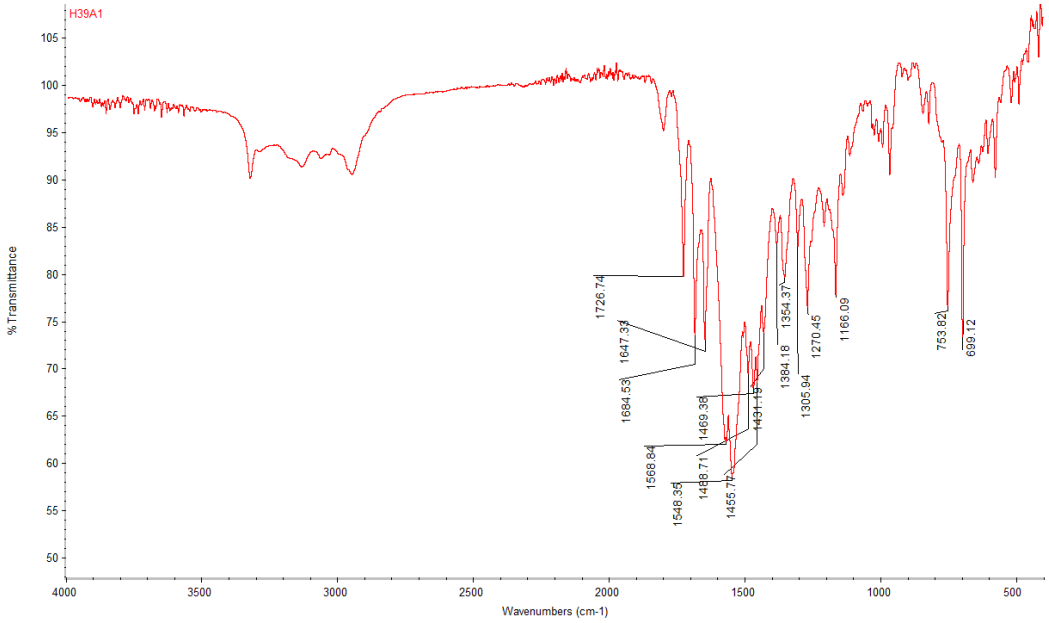

Figure A2.75: IR spectrum of **2.18 (Sq-2-Asp(Bn))**

Compound Table

Compound Label	RT (min)	Observed mass (m/z)	Neutral observed mass (Da)	Theoretical mass (Da)	Mass error (ppm)	Isotope match score (%)
Cpd 1: C34 H34 N6 O10	0.73	709.2229	686.2338	686.2336	0.22	99.81

Figure: Extracted ion chromatogram (EIC) of compound.

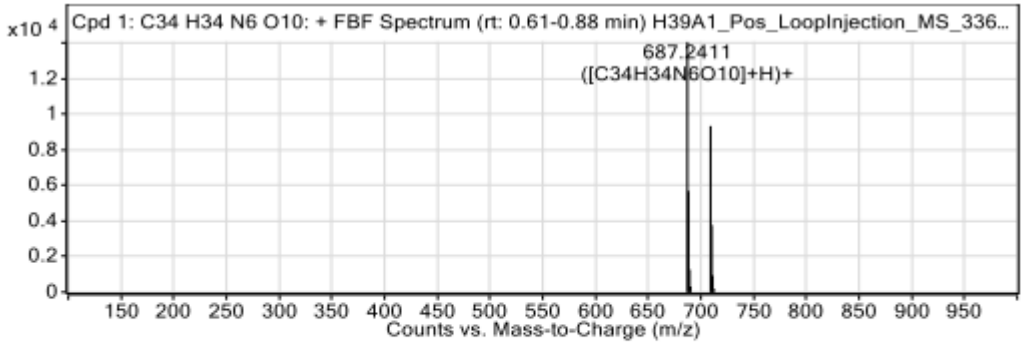

Figure: Full range view of Compound spectra and potential adducts.

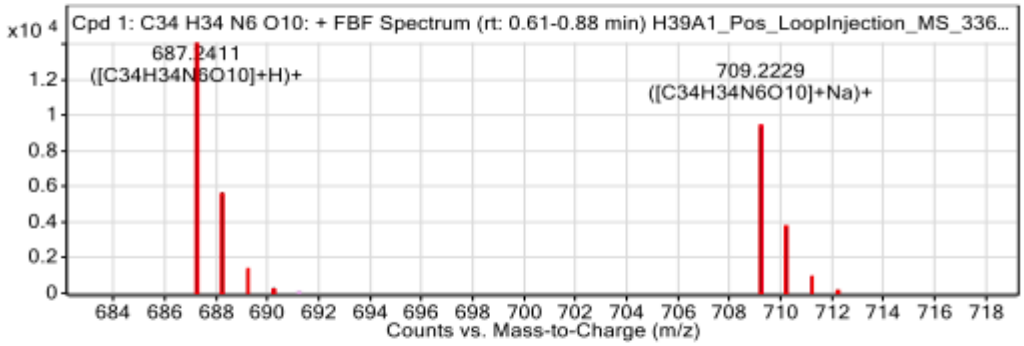

Figure: Zoomed Compound spectra view
(red boxes indicating expected theoretical isotope spacing and abundance)

Compound isotope peak List

m/z	z	Abund	Formula	Ion
687.2411	1	14083.9	C34H34N6O10	(M+H)+
688.2443	1	5686.3	C34H34N6O10	(M+H)+
689.2466	1	1272.8	C34H34N6O10	(M+H)+
690.2499	1	317.7	C34H34N6O10	(M+H)+
709.2229	1	9337.3	C34H34N6O10	(M+Na)+
710.2259	1	3771.1	C34H34N6O10	(M+Na)+
711.2284	1	937.2	C34H34N6O10	(M+Na)+
712.2314	1	198.5	C34H34N6O10	(M+Na)+

Figure A2.76: HRMS data of **2.18 (Sq-2-Asp(Bn))**

Chapter 2 – ^{1}H NMR Anion Binding Data

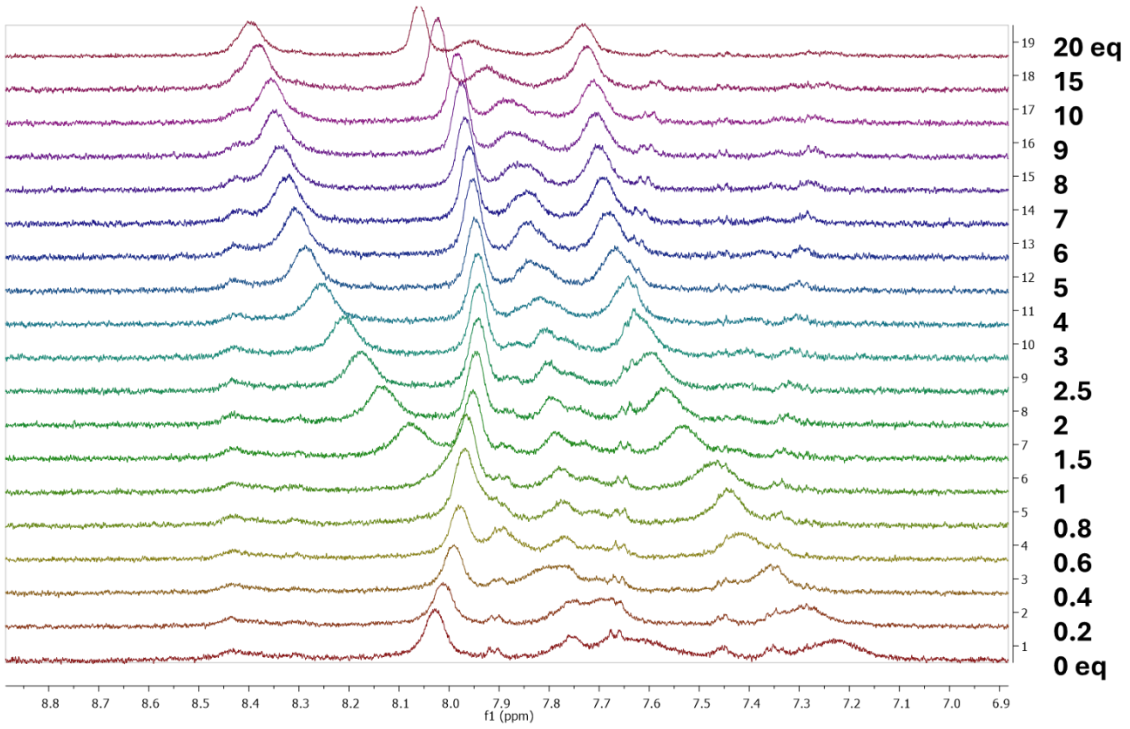

Figure A2.77: ^{1}H NMR titration of compound **2.14 (Sq-2-Ala)** with TBACl in DMSO-d_6

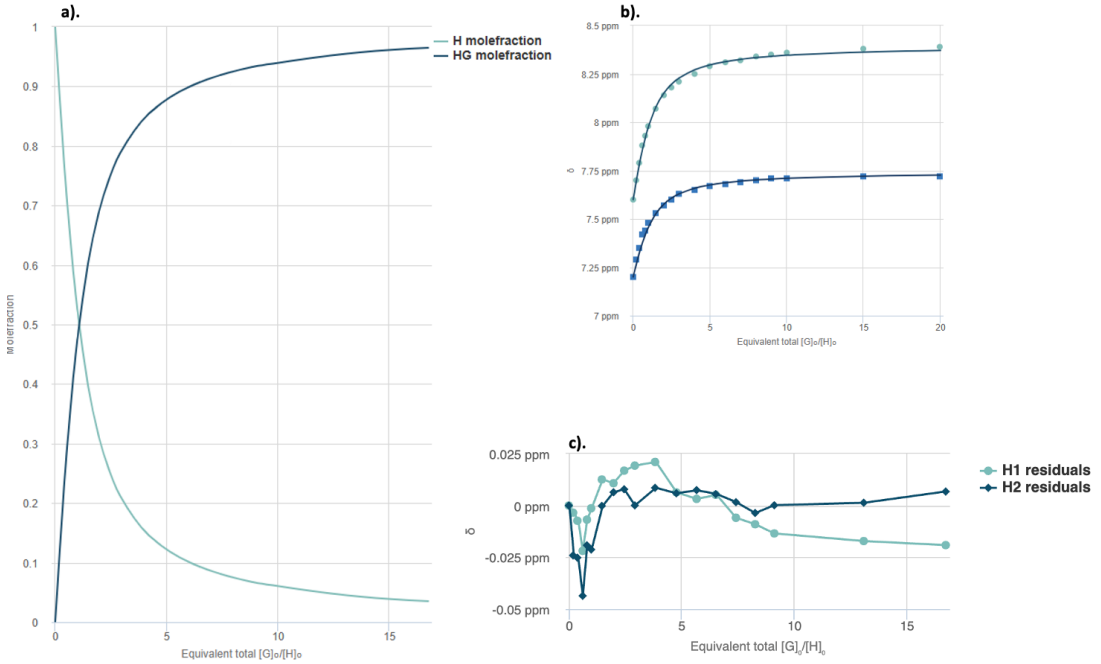

Figure A2.78: a). Mole fraction plot of Host vs Host:guest fraction with increasing guest concentration for **2.14. b).** Fitting binding isotherms of compound **2.14 (Sq-2-Ala)** with TBACl in DMSO-d_6 at 298 K, showing the changes in chemical shifts for the squaramide NH protons fitted to the 1:1 binding model (K_a = 692 M^{-1}). **c).** Residuals plot of **2.14**.

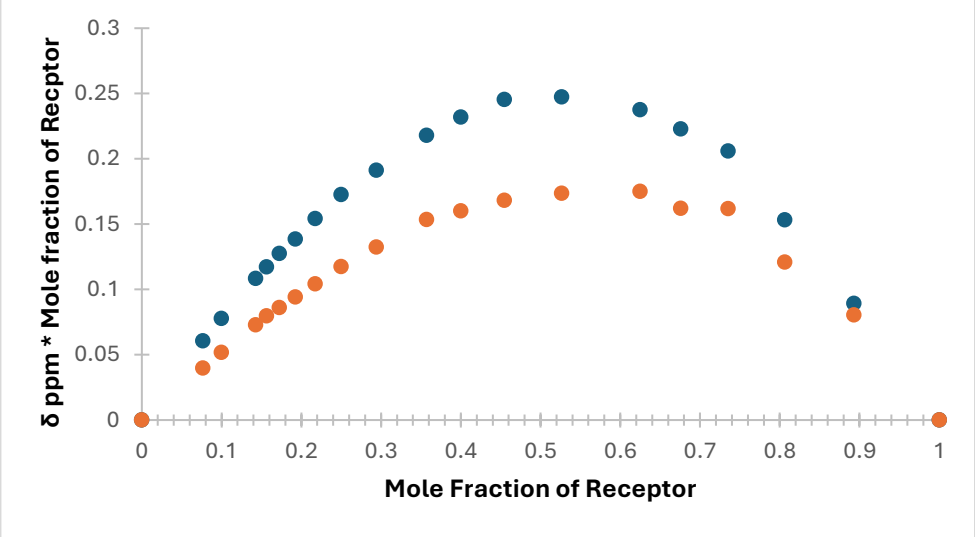

Figure A2.79: Jobs plot of **2.14 (Sq-2-Ala)** with TBACl in DMSO-d_6

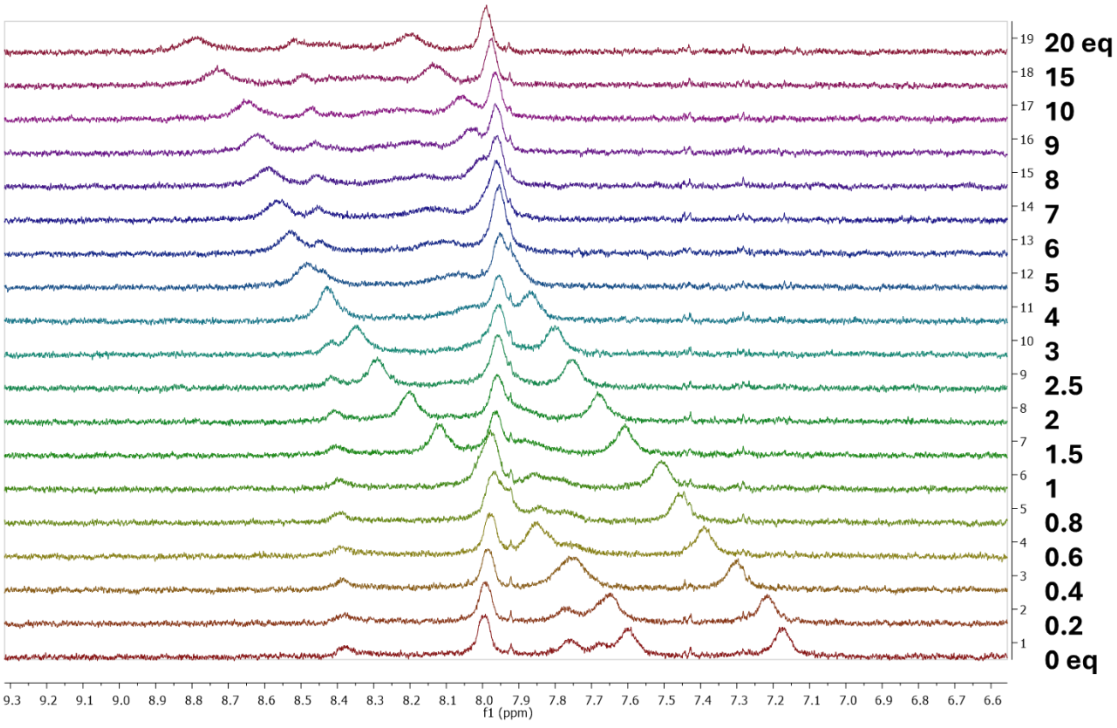

Figure A2.80: ^{1}H NMR titration of compound **2.14 (Sq-2-Ala)** with TBAAcO in DMSO-d_6

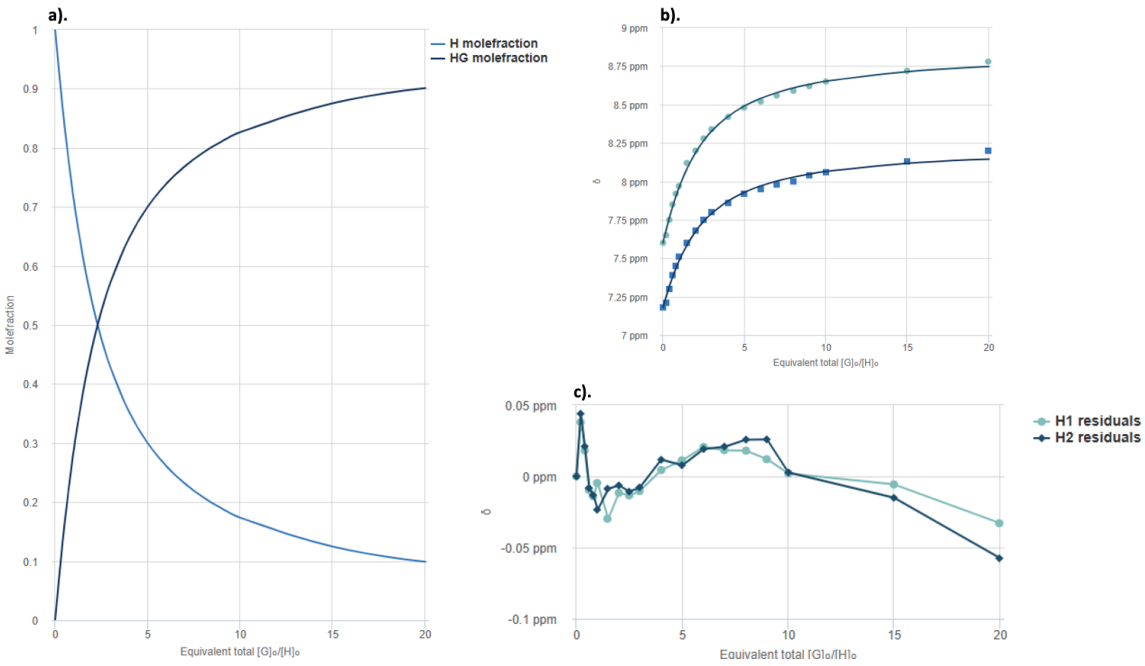

Figure A2.81: a). Mole fraction plot of Host vs Host:guest fraction with increasing guest concentration for **2.14. b).** Fitting binding isotherms of compound **2.14 (Sq-2-Ala)** with TBAAcO in DMSO-d_6 at 298 K, showing the changes in chemical shifts for the squaramide NH protons fitted to the 1:1 binding model (K_a = 227 M^{-1}). **c).** Residuals plot of **2.14**.

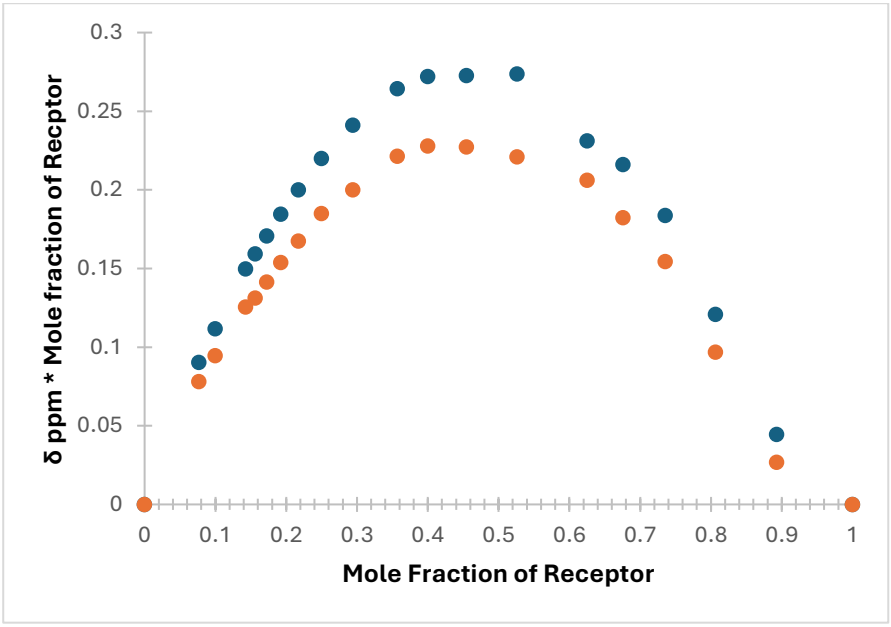

Figure A2.82: Jobs plot of **2.14 (Sq-2-Ala)** with TBAAcO in DMSO-d_6

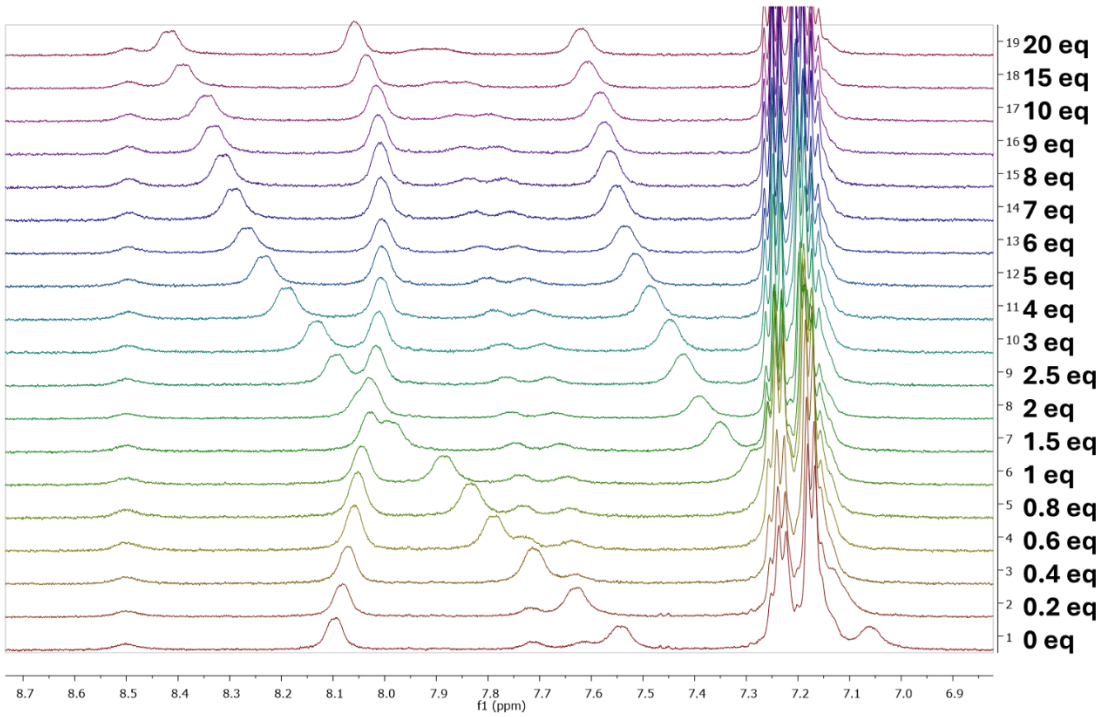

Figure A2.83: ^{1}H NMR titration of compound **2.15 (Sq-2-Phe)** with TBACl in DMSO-d_6

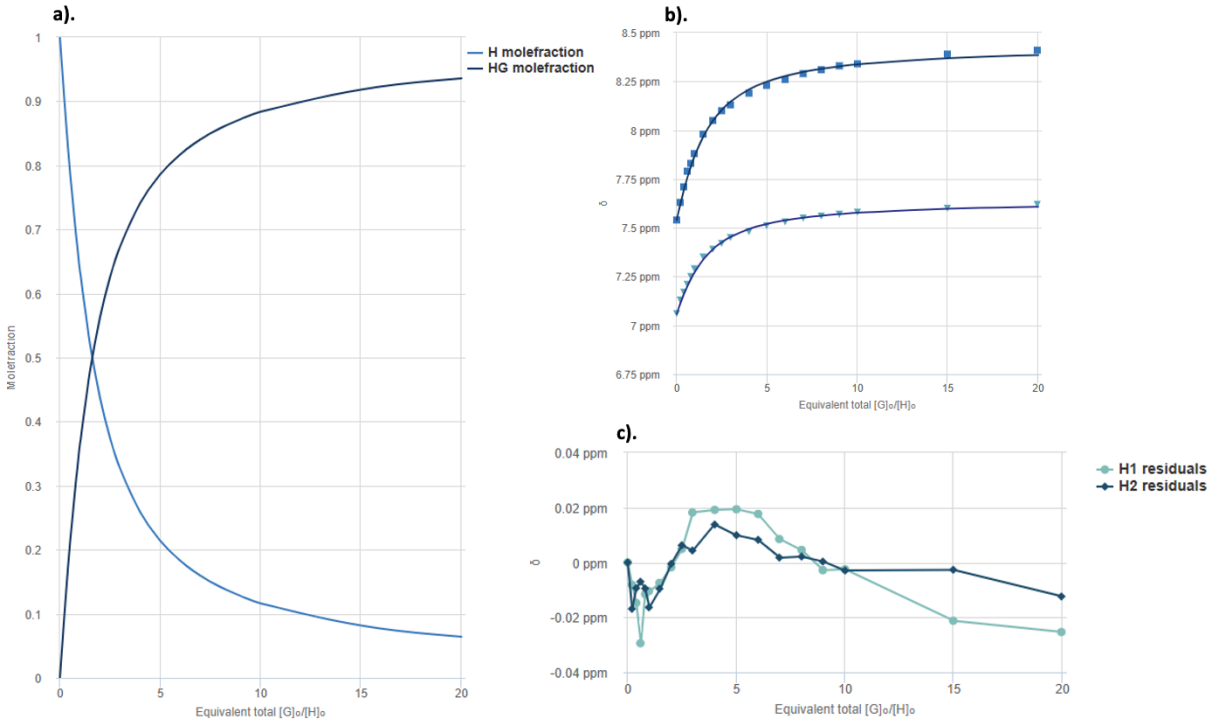

Figure A2.84: a). Mole fraction plot of Host vs Host:guest fraction with increasing guest concentration for **2.15 b).** Fitting binding isotherms of compound **2.15 (Sq-2-Phe)** with TBACl in DMSO-d_6 at 298 K, showing the changes in chemical shifts for the squaramide NH protons fitted to the 1:1 binding model (K_a = 366 M^{-1}). **c).** Residuals plot of **2.15**.

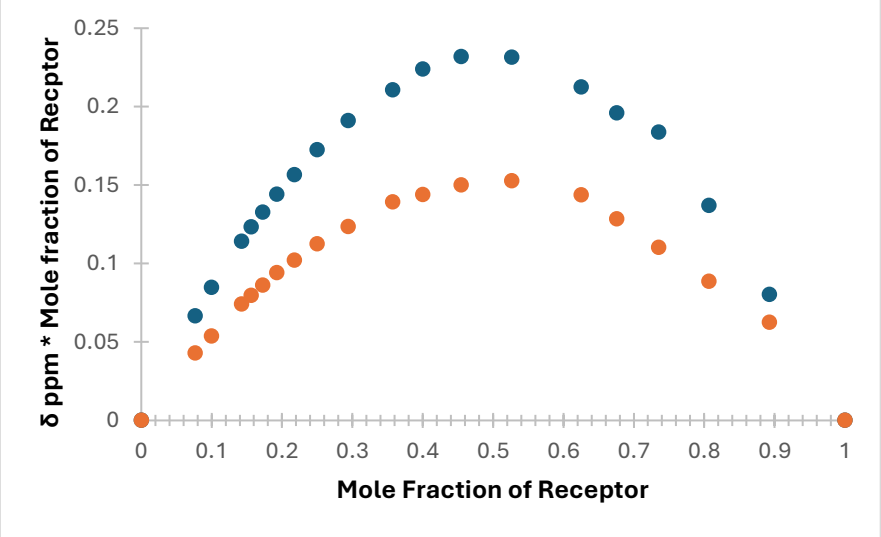

Figure A2.85: Jobs plot of **2.15 (Sq-2-Phe)** with TBACl in DMSO-d_6

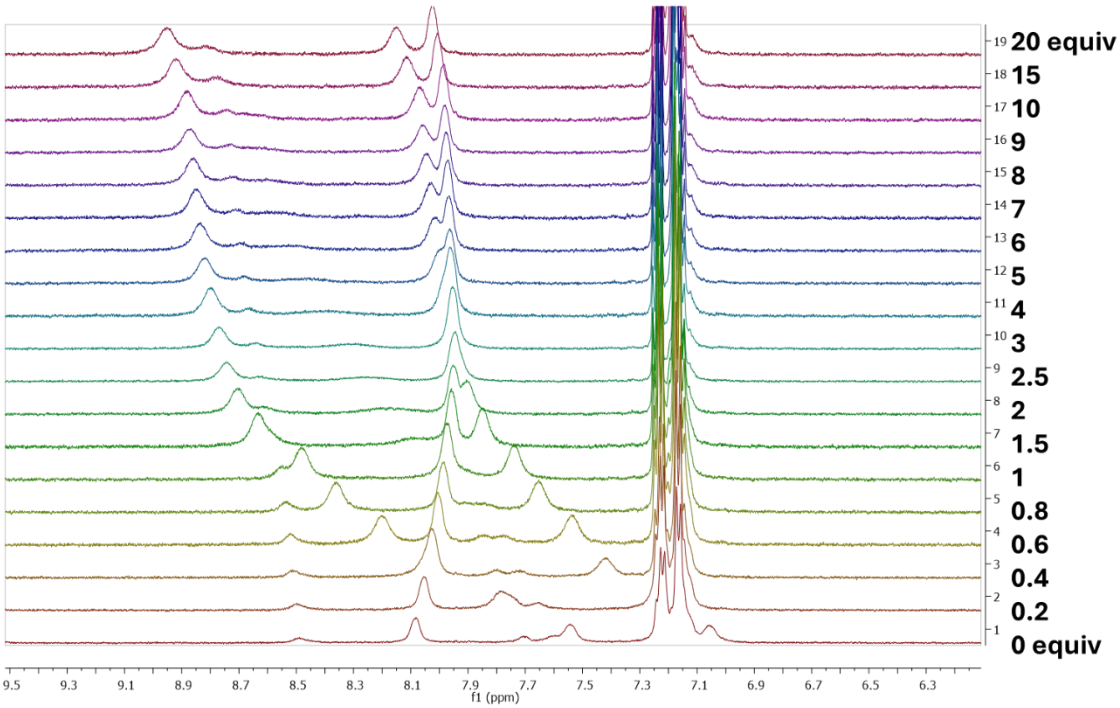

Figure A2.86: ^{1}H NMR titration of compound **2.15 (Sq-2-Phe)** with TBAAcO in DMSO-d_6

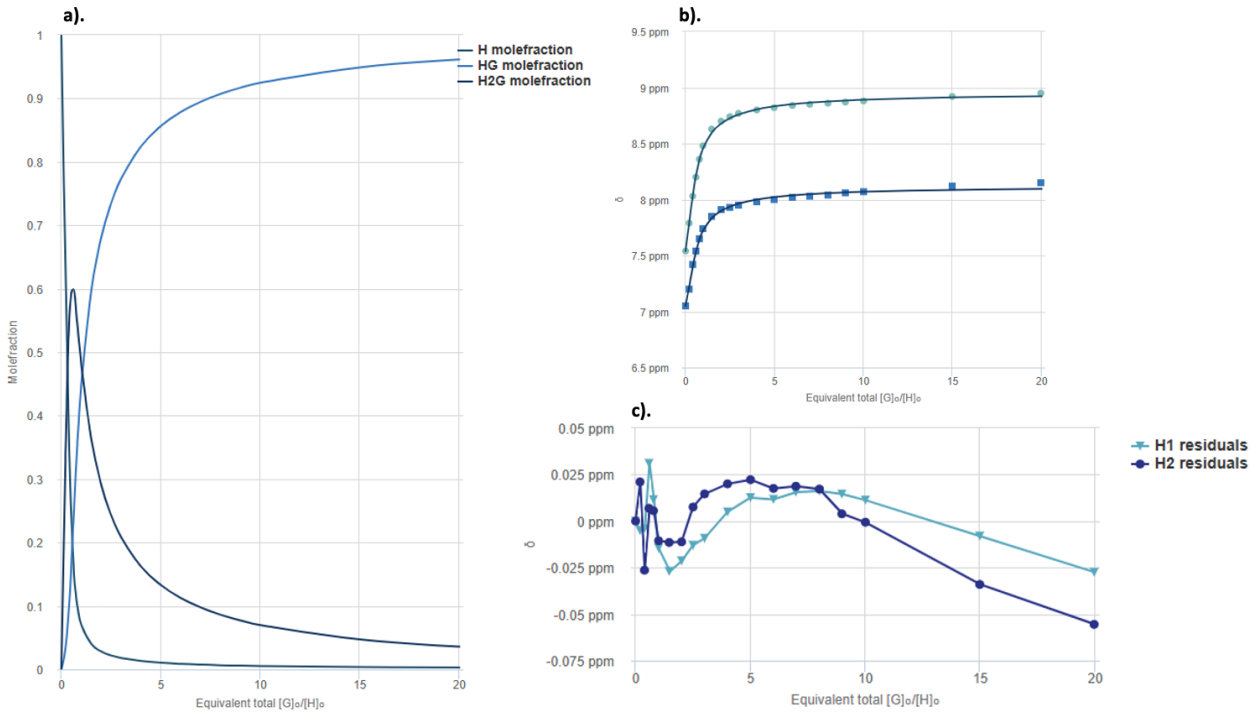

Figure A2.87: a). Mole fraction plot of Host vs Host:guest fraction with increasing guest concentration for **2.15. b).** Fitting binding isotherms of compound **2.15 (Sq-2-Phe)** with TBAAcO in DMSO-d_6 at 298 K, showing the changes in chemical shifts for the squaramide NH protons fitted to the 2:1 binding model (K_{21} = 3 x 10^3 M^{-1}). **c).** Residuals plot of **2.15**.

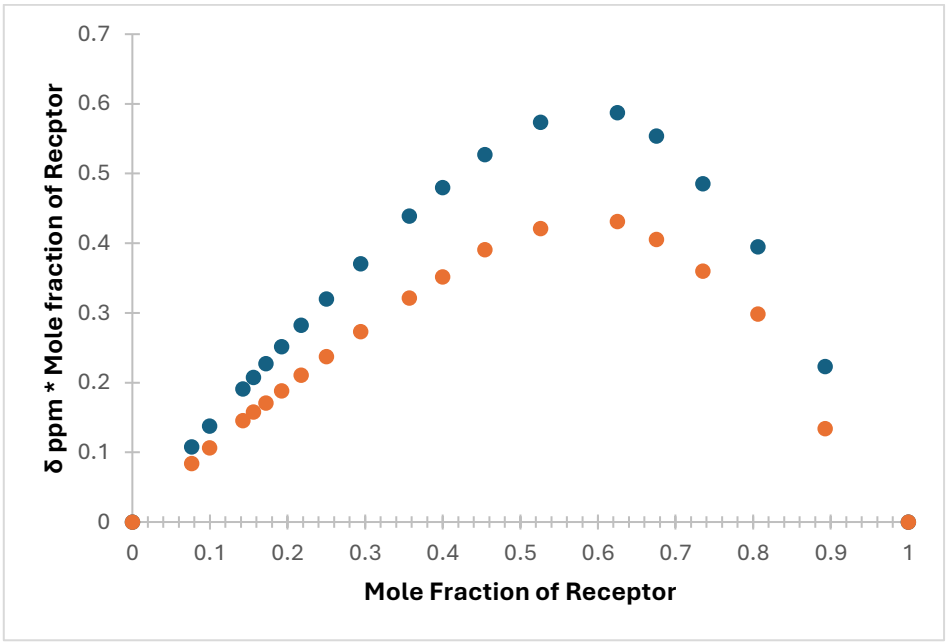

Figure A2.88: Jobs plot of **2.15 (Sq-2-Phe)** with TBAAcO in DMSO-d_6

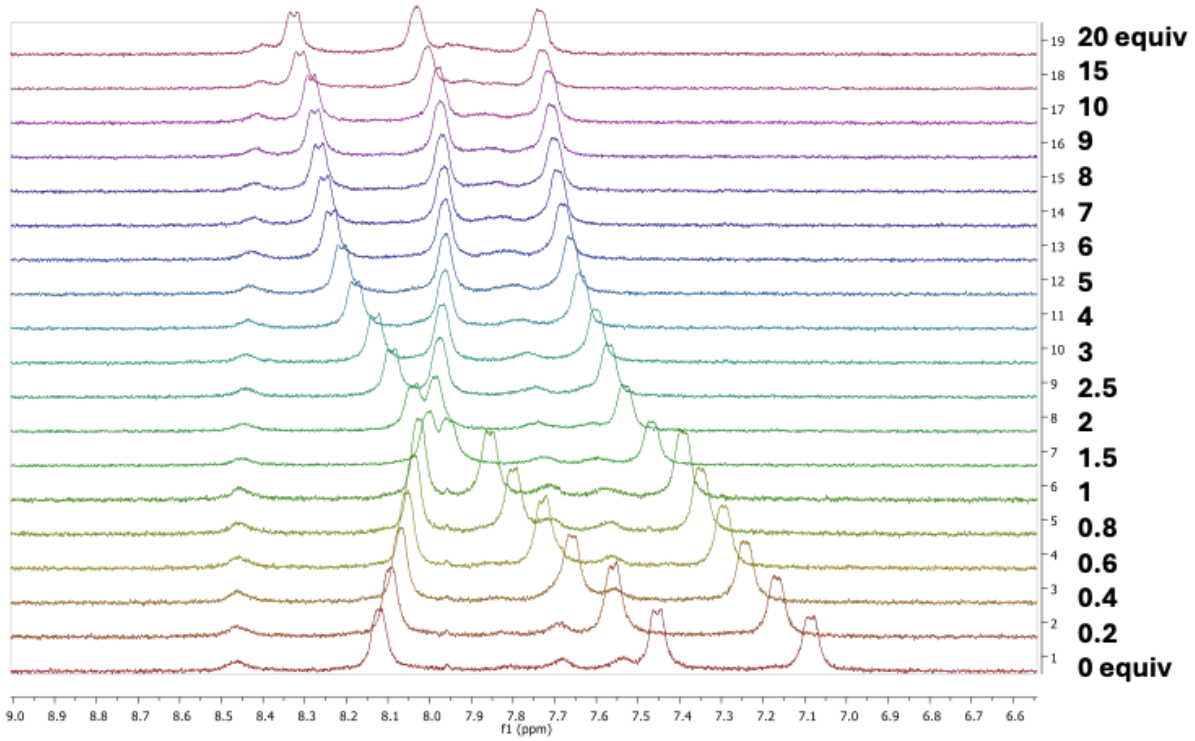

Figure A2.89: ^{1}H NMR titration of compound **2.16 (Sq-2-Leu)** with TBACl in DMSO-d_6

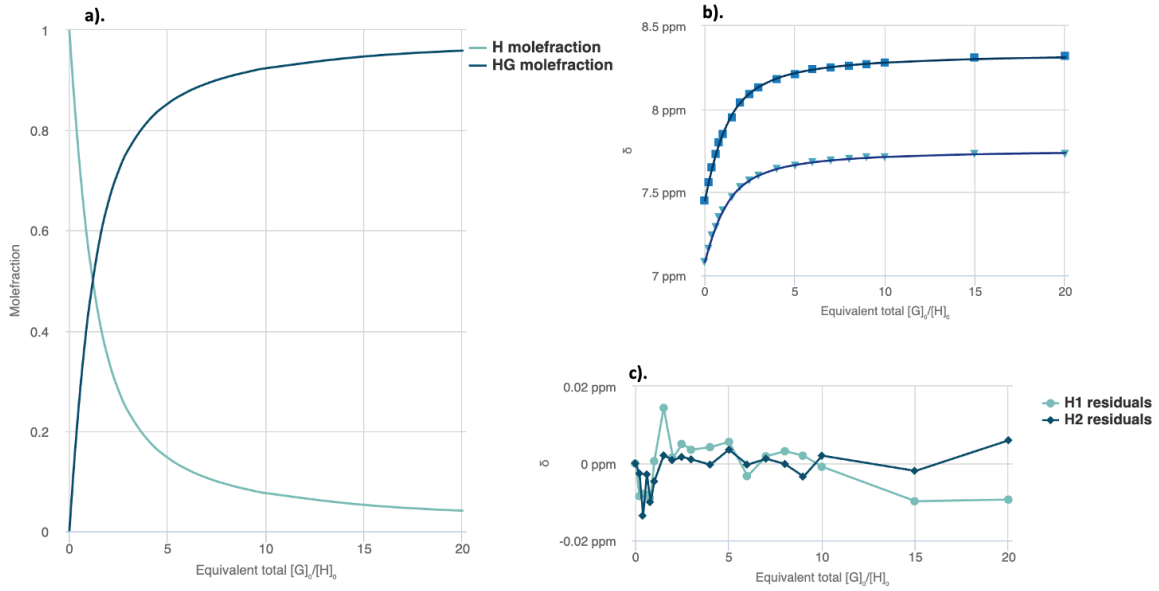

Figure A2.90: a). Mole fraction plot of Host vs Host:guest fraction with increasing guest concentration for **2.16. b).** Fitting binding isotherms of compound **2.16 (Sq-2-Leu)** with TBACl in DMSO-d_6 at 298 K, showing the changes in chemical shifts for the squaramide NH protons fitted to the 1:1 binding model (K_a = 588 M^{-1}). **c).** Residuals plot of **2.16**.

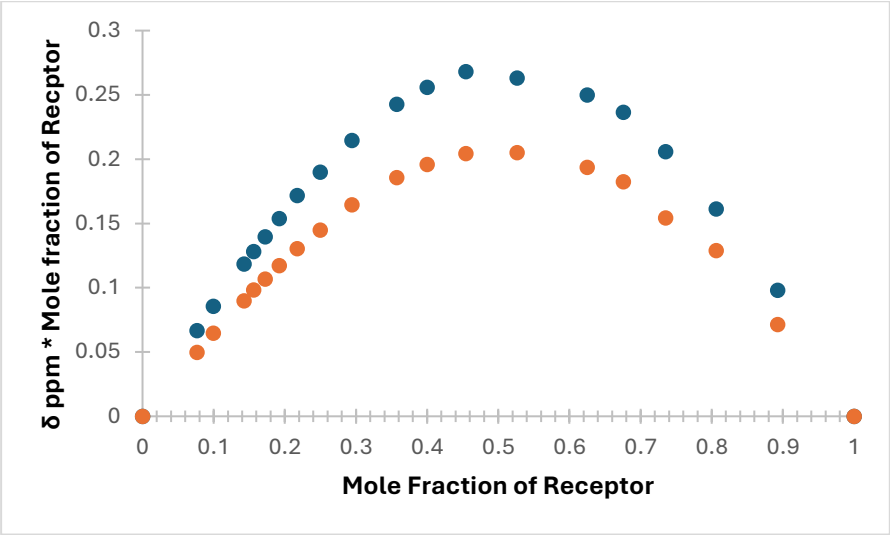

Figure A2.91: Jobs plot of **2.16 (Sq-2-Leu)** with TBACl in DMSO-d_6

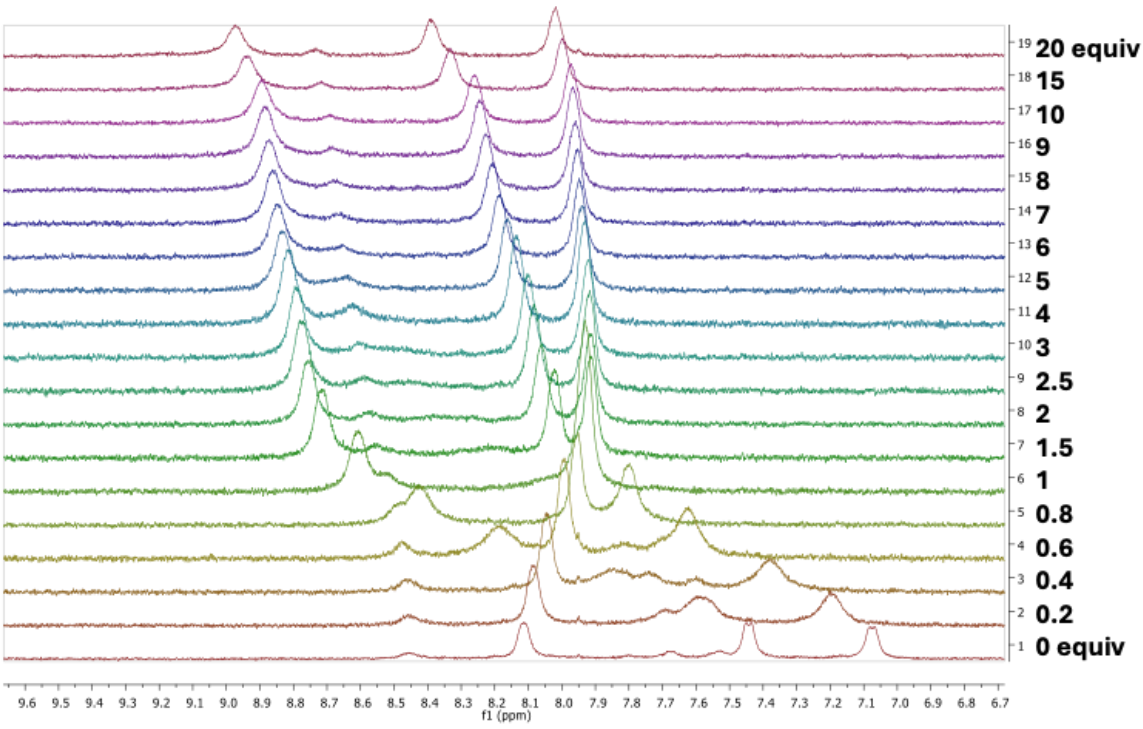

Figure A2.92: ^{1}H NMR titration of compound **2.16 (Sq-2-Leu)** with TBAAcO in DMSO-d_6

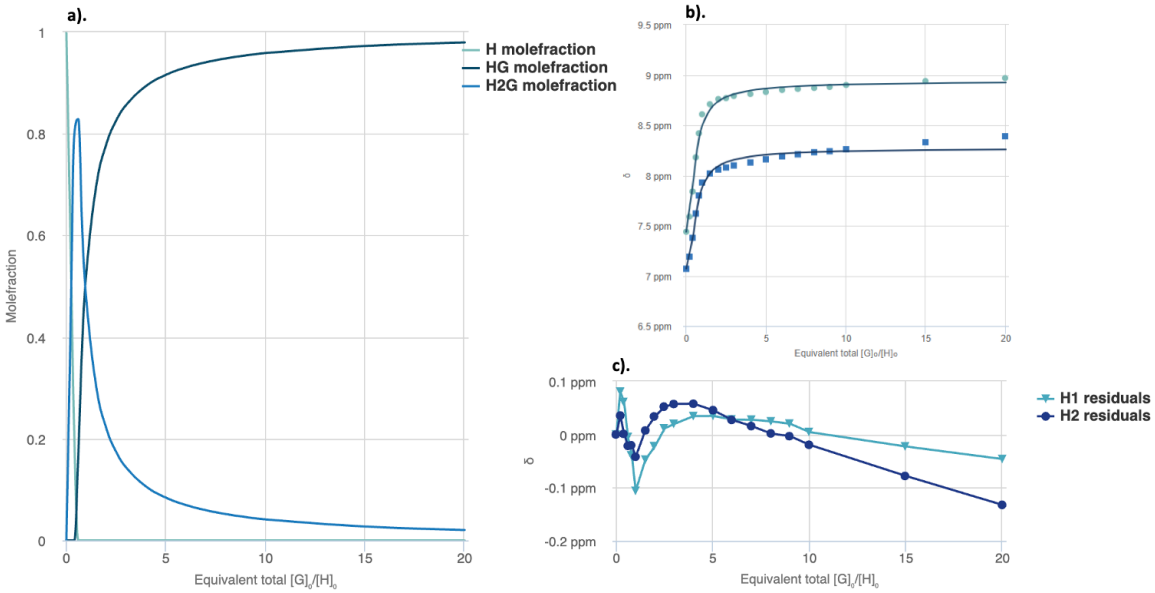

Figure A2.93: a). Mole fraction plot of Host vs Host:guest fraction with increasing guest concentration for **2.16. b).** Fitting binding isotherms of compound **2.16 (Sq-2-Leu)** with TBAAcO in DMSO-d_6 at 298 K, showing the changes in chemical shifts for the squaramide NH protons fitted to the 2:1 binding model (K_{21} = 10^4 M^{-1}). **c).** Residuals plot of **2.16**.

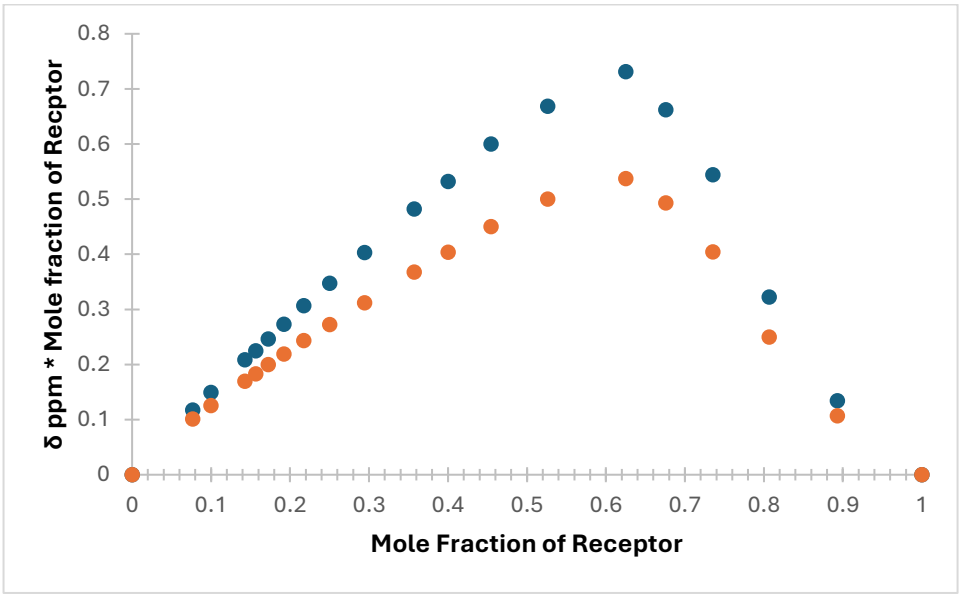

Figure A2.94: Jobs plot of **2.16 (Sq-2-Leu)** with TBAAcO in DMSO-d_6

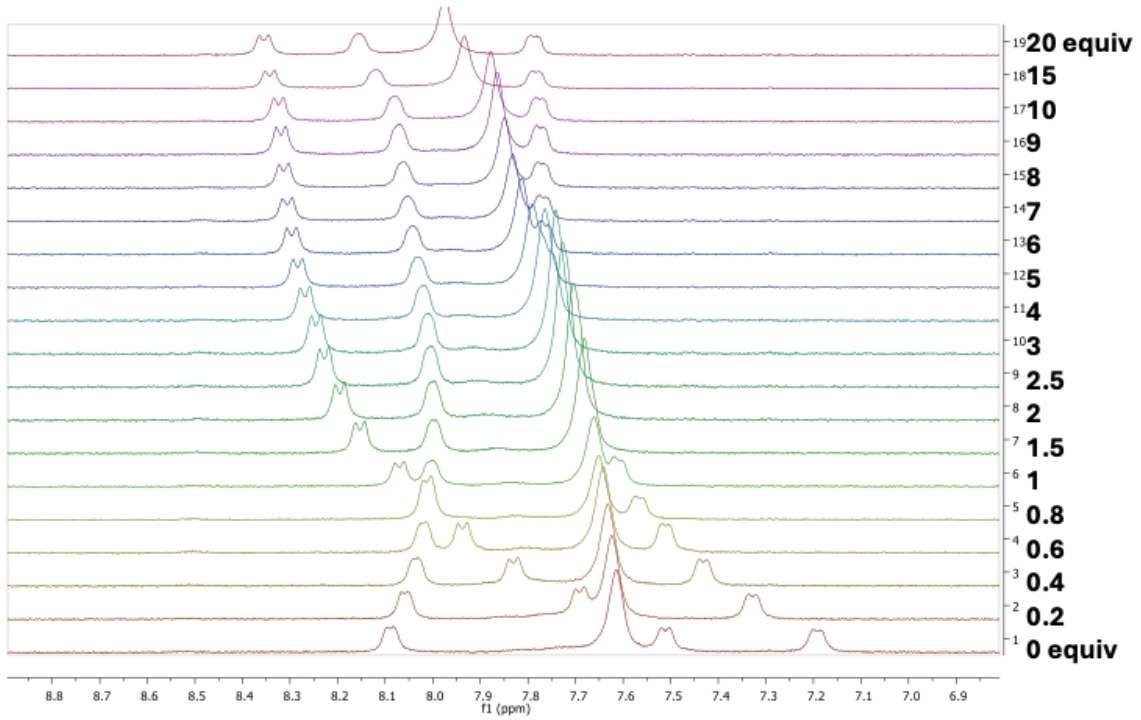

Figure A2.95: ^{1}H NMR titration of compound **2.17 (Sq-2-Lys)** with TBACl in DMSO-d_6

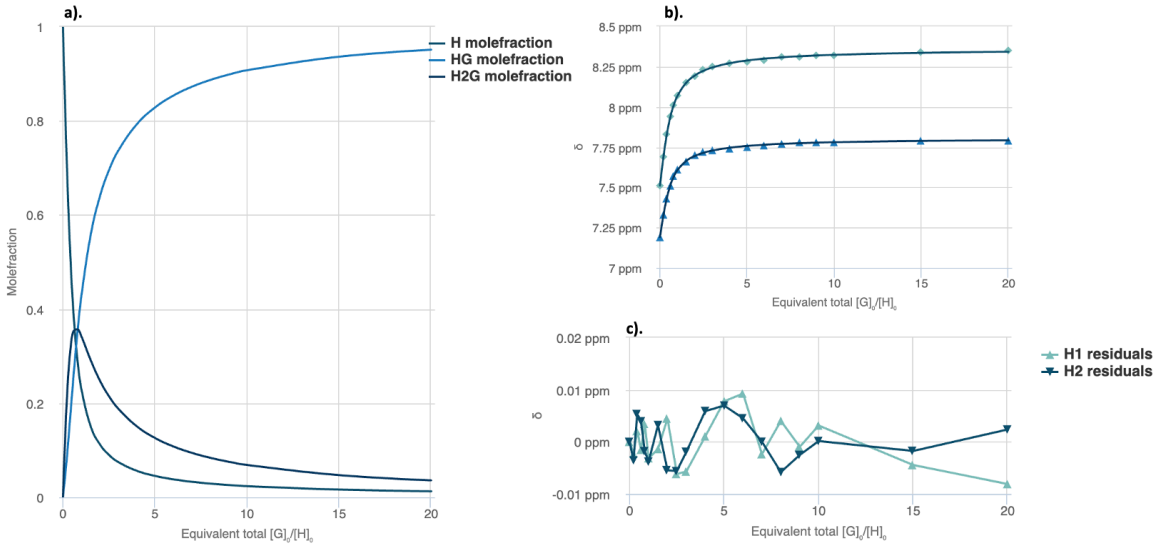

Figure A2.96: a). Mole fraction plot of Host vs Host:guest fraction with increasing guest concentration for **2.17. b).** Fitting binding isotherms of compound **2.17 (Sq-2-Lys)** with TBACl in DMSO-d_6 at 298 K, showing the changes in chemical shifts for the squaramide NH protons fitted to the 2:1 binding model (K_{21} = 703 M^{-1}). **c).** Residuals plot of **2.17**.

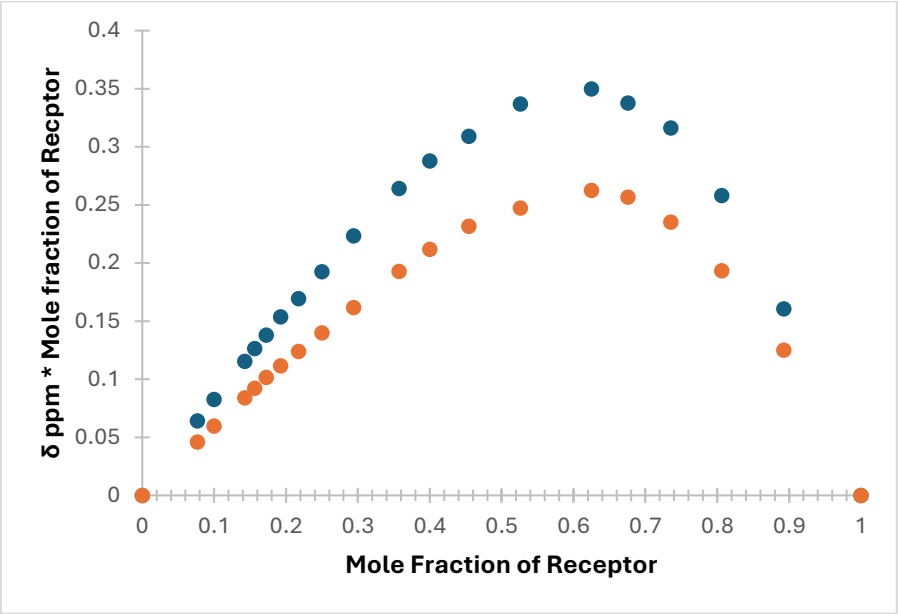

Figure A2.97: Jobs plot of **2.17 (Sq-2-Lys)** with TBACl in DMSO-d_6

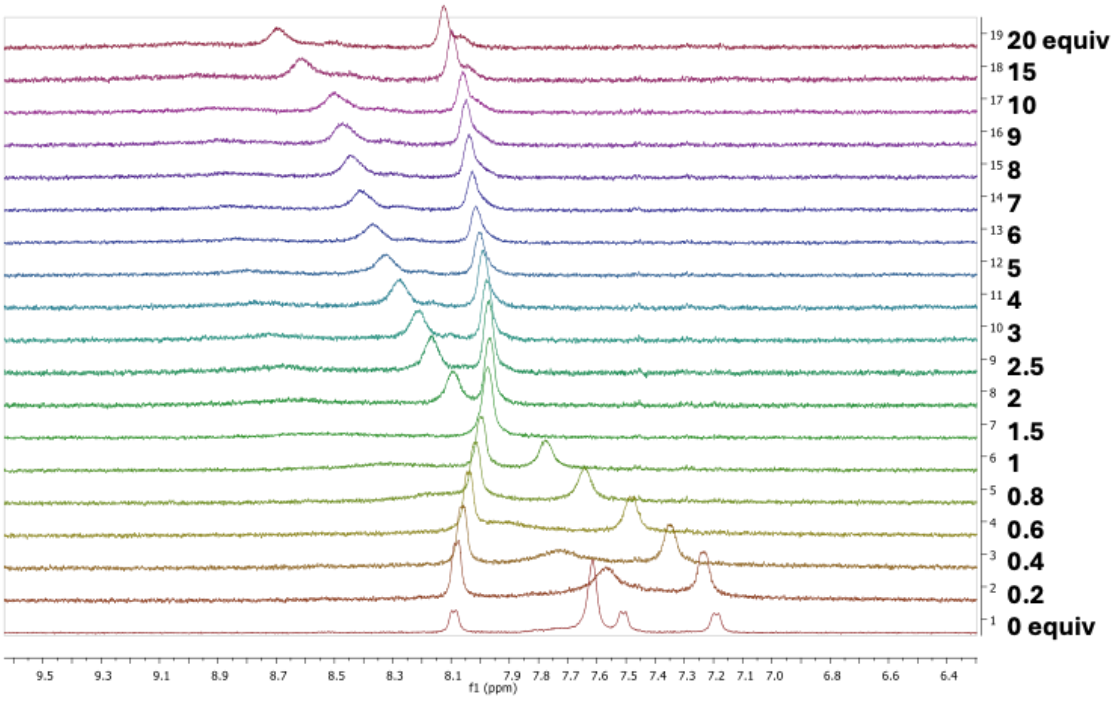

Figure A2.98: ^{1}H NMR titration of compound **2.17 (Sq-2-Lys)** with TBAAcO in DMSO-d_6

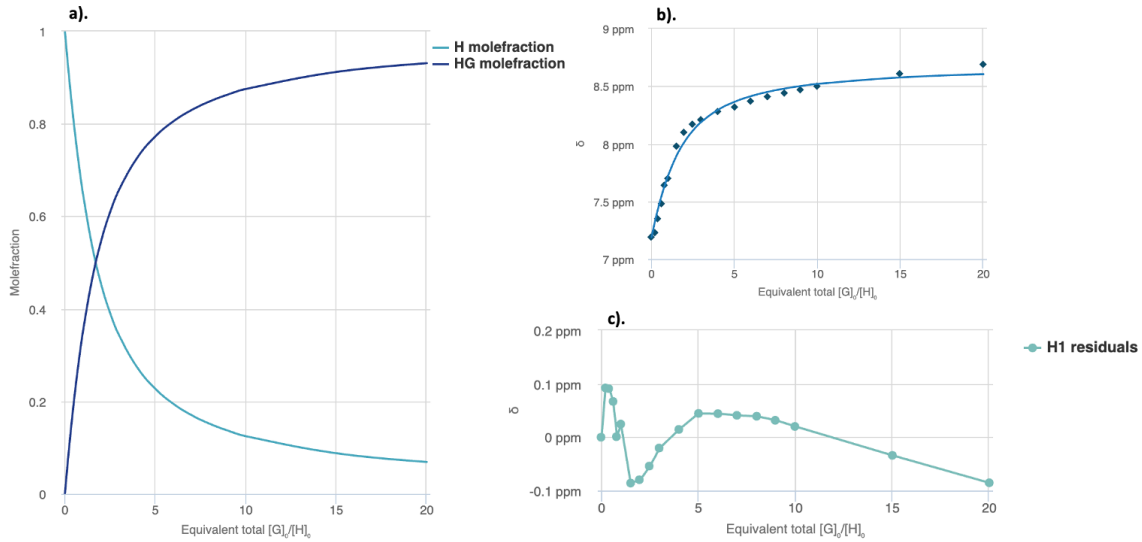

Figure A2.99: a). Mole fraction plot of Host vs Host:guest fraction with increasing guest concentration for **2.17. b).** Fitting binding isotherms of compound **2.17 (Sq-2-Lys)** with TBAAcO in DMSO-d_6 at 298 K, showing the changes in chemical shifts for the squaramide NH protons fitted to the 1:1 binding model (K_a = 333 M^{-1}). **c).** Residuals plot of **2.17**.

Figure A2.100: Jobs plot of **2.17 (Sq-2-Lys)** with TBAAcO in DMSO-d_6

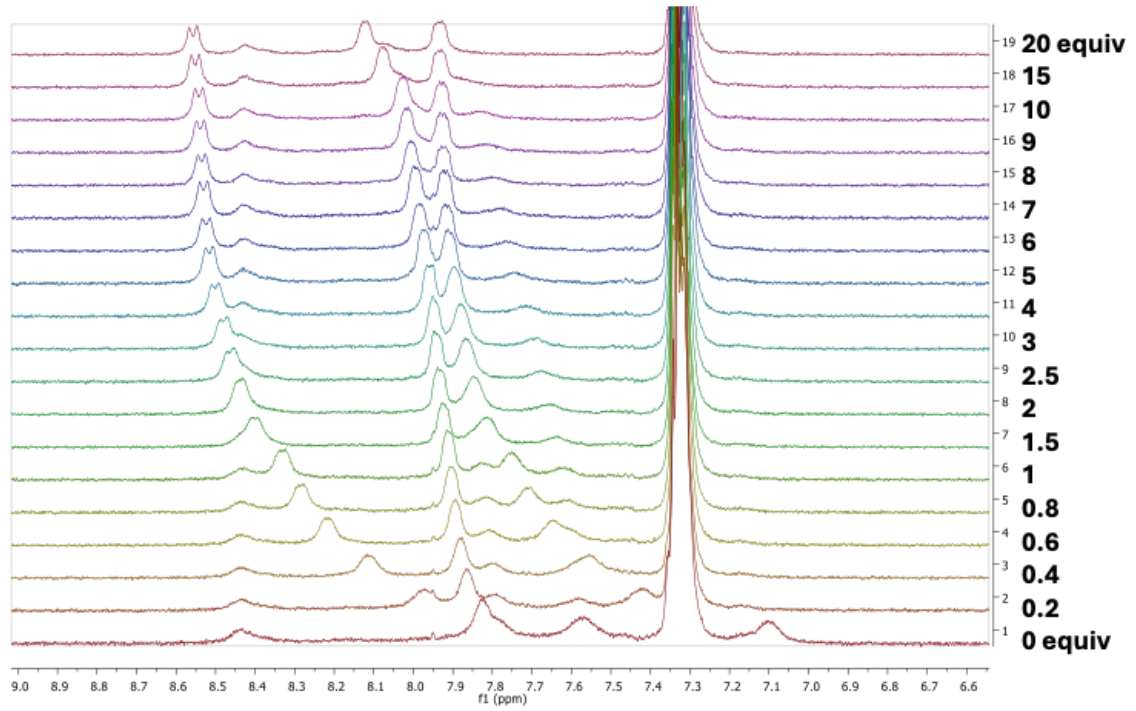

Figure A2.101: ^{1}H NMR titration of compound **2.18 (Sq-2-Asp(Bn))** with TBACl in DMSO-d_6

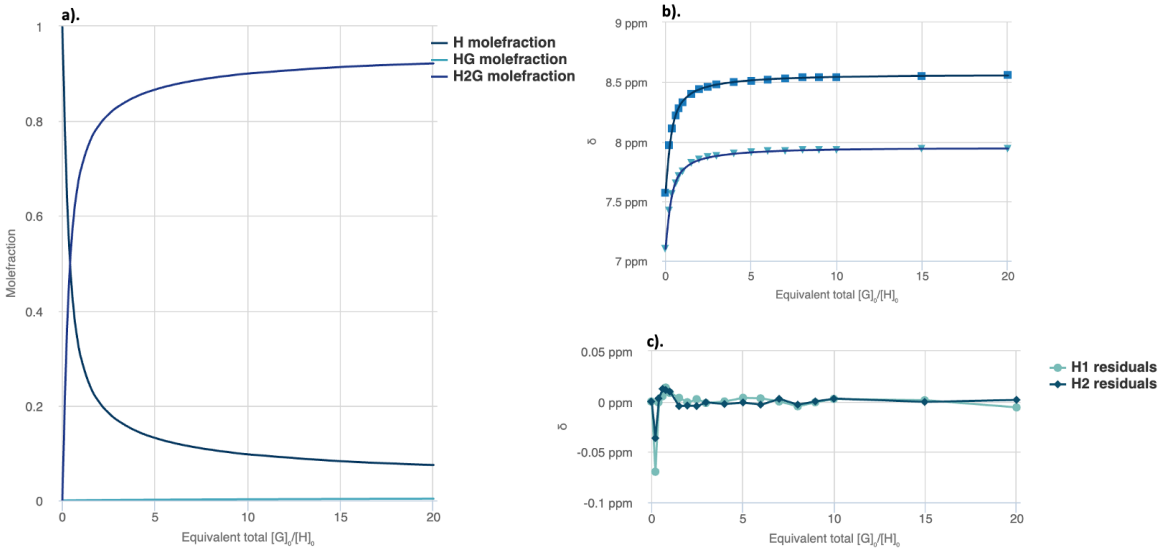

Figure A2.102: a). Mole fraction plot of Host vs Host:guest fraction with increasing guest concentration for **2.18. b).** Fitting binding isotherms of compound **2.18 (Sq-2-Asp(Bn))** with TBACl in DMSO-d_6 at 298 K, showing the changes in chemical shifts for the squaramide NH protons fitted to the 2:1 binding model (K_{21} = 10^4 M^{-1}). **c).** Residuals plot of **2.18**.

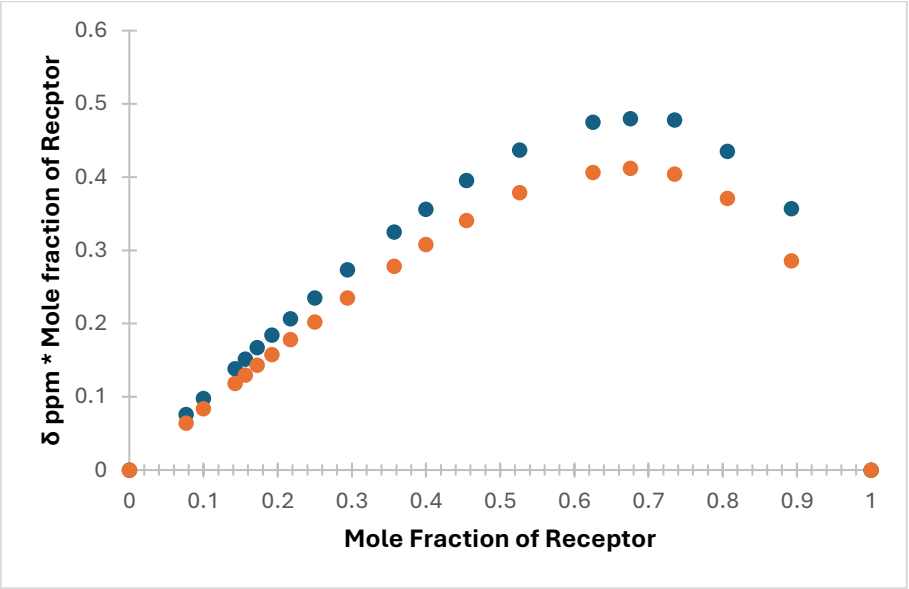

Figure A2.103: Jobs plot of **2.18 (Sq-2-Asp(Bn))** with TBACl in DMSO-d_6

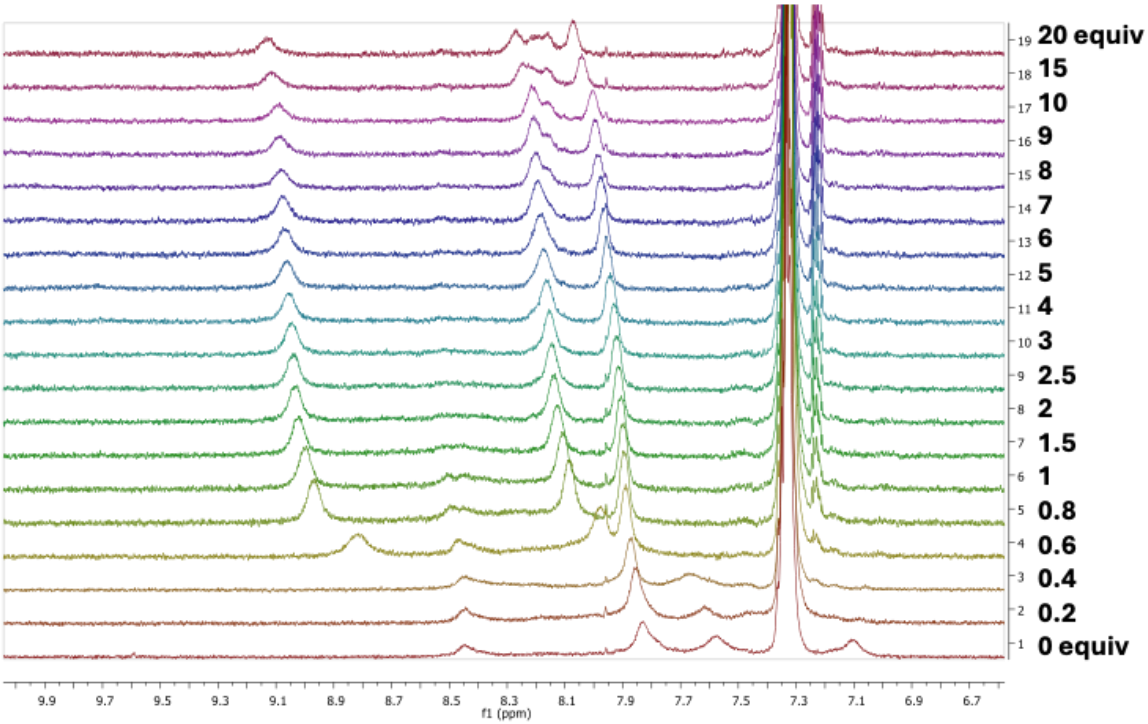

Figure A2.104: ^{1}H NMR titration of compound **2.18 (Sq-2-Asp(Bn))** with TBAAcO in DMSO-d_6

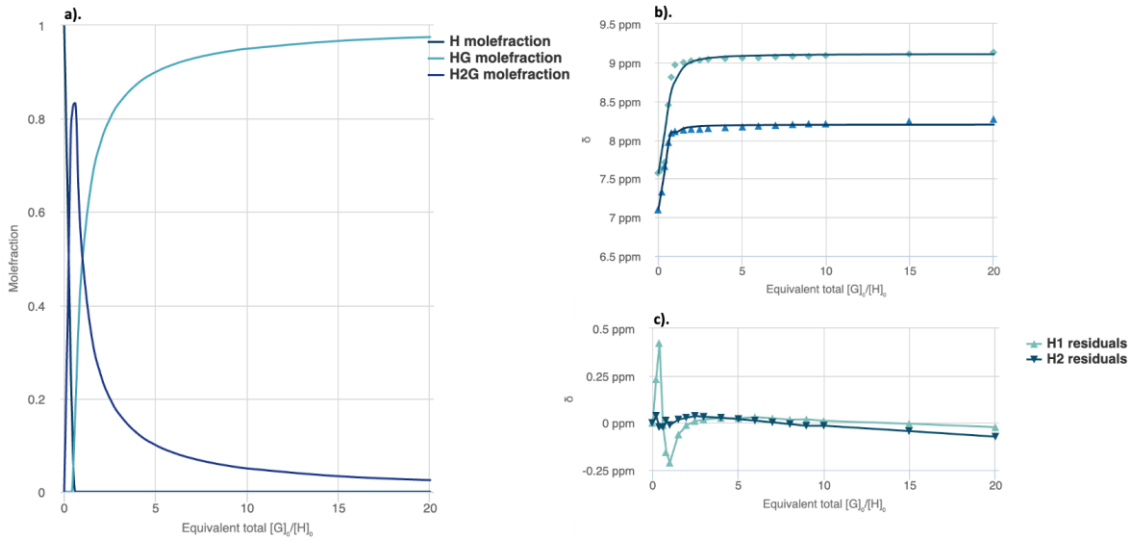

Figure A2.105: a). Mole fraction plot of Host vs Host:guest fraction with increasing guest concentration for **2.18. b).** Fitting binding isotherms of compound **2.18 (Sq-2-Asp(Bn))** with TBAAcO in DMSO-d_6 at 298 K, showing the changes in chemical shifts for the squaramide NH protons fitted to the 2:1 binding model (K_{21} = 10^4 M^{-1}). **c).** Residuals plot of **2.18**.

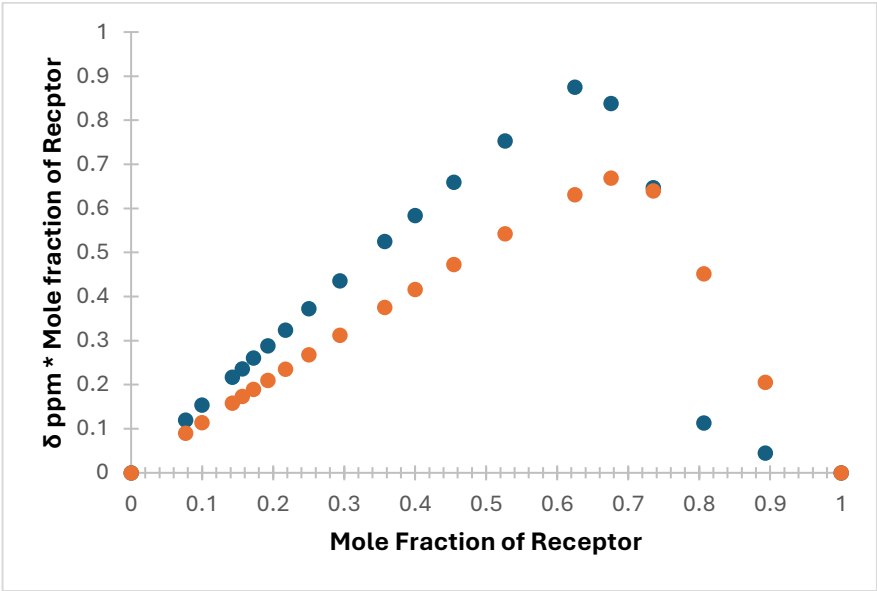

Figure A2.106: Jobs plot of **2.18 (Sq-2-Asp(Bn))** with TBAAcO in DMSO-d_6

Chapter 2 – X-Ray Crystallography Data

Table A2.1: Crystal data and structure refinement for **2.14 (Sq-2-Ala)**.

Identification code	Sq-2-Ala
Empirical formula	$C_{22}H_{34}N_6O_8S_2$
Formula weight	574.67
Temperature/K	150.0
Crystal system	monoclinic
Space group	$P2_1$
a/Å	8.8611(3)
b/Å	10.5198(4)
c/Å	15.0198(5)
α/°	90
β/°	103.0770(10)
γ/°	90
Volume/Å^3	1363.79(8)
Z	2
ρ_{calc}g/cm^3	1.399
μ/mm^1	0.252
F(000)	608.0
Crystal size/mm^3	0.36 × 0.29 × 0.16
Radiation	MoKα (λ = 0.71073)
2Θ range for data collection/°	6.106 to 61.062
Index ranges	-12 ≤ h ≤ 12, -15 ≤ k ≤ 15, -21 ≤ l ≤ 21
Reflections collected	38125
Independent reflections	8257 [R_{int} = 0.0228, R_{sigma} = 0.0182]
Data/restraints/parameters	8257/1/349
Goodness-of-fit on F^2	1.047
Final R indexes [I>=2σ (I)]	R_1 = 0.0246, wR_2 = 0.0658
Final R indexes [all data]	R_1 = 0.0255, wR_2 = 0.0664
Largest diff. peak/hole / e Å^{-3}	0.29/-0.29
Flack parameter	0.002(9)
CCDC No.	2287336

Table A2.2: Hydrogen bonding parameters for **2.14 (Sq-2-Ala)**.

D	H	A	d(D-H)/Å	d(H-A)/Å	d(D-A)/Å	D-H-A/°
N1	H1	O7	0.88	1.87	2.7330(16)	165.3
N2	H2	O7	0.88	2.25	3.0364(17)	148.7
N3	H3	O8[1]	0.88	2.17	3.0172(18)	160.7
N4	H4	O2[2]	0.88	2.08	2.9180(15)	157.9
N5	H5	O2[2]	0.88	2.04	2.8818(16)	159.3
N6	H6	O8[3]	0.88	1.95	2.7737(16)	155.9

[1]1-*x*,1/2+*y*,-*z*; [2]-1+*x*,+*y*,+*z*; [3]1-*x*,-1/2+*y*,-*z*

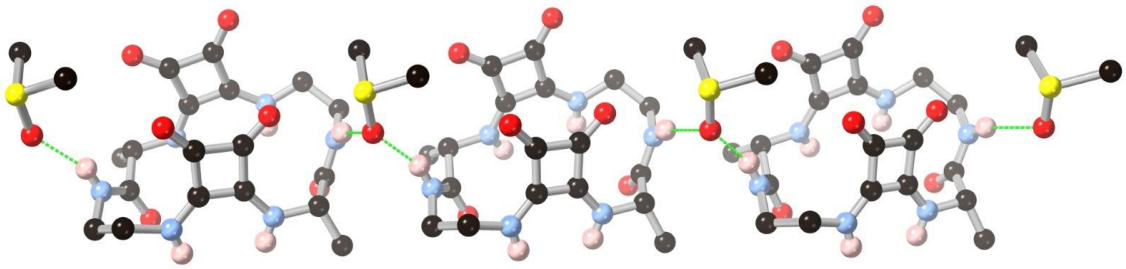

Figure A2.107: The hydrogen bonding mode of the amide groups within **2.14 (Sq-2-Ala)** macrocycle forming a complementary 1-dimensional chain through the DMSO solvate, perpendicular to that formed by the squaramide···squaramide contacts. Selected hydrogen atoms and DMSO molecules are omitted for clarity.

Chapter 3 – Supplementary Characterisation Data

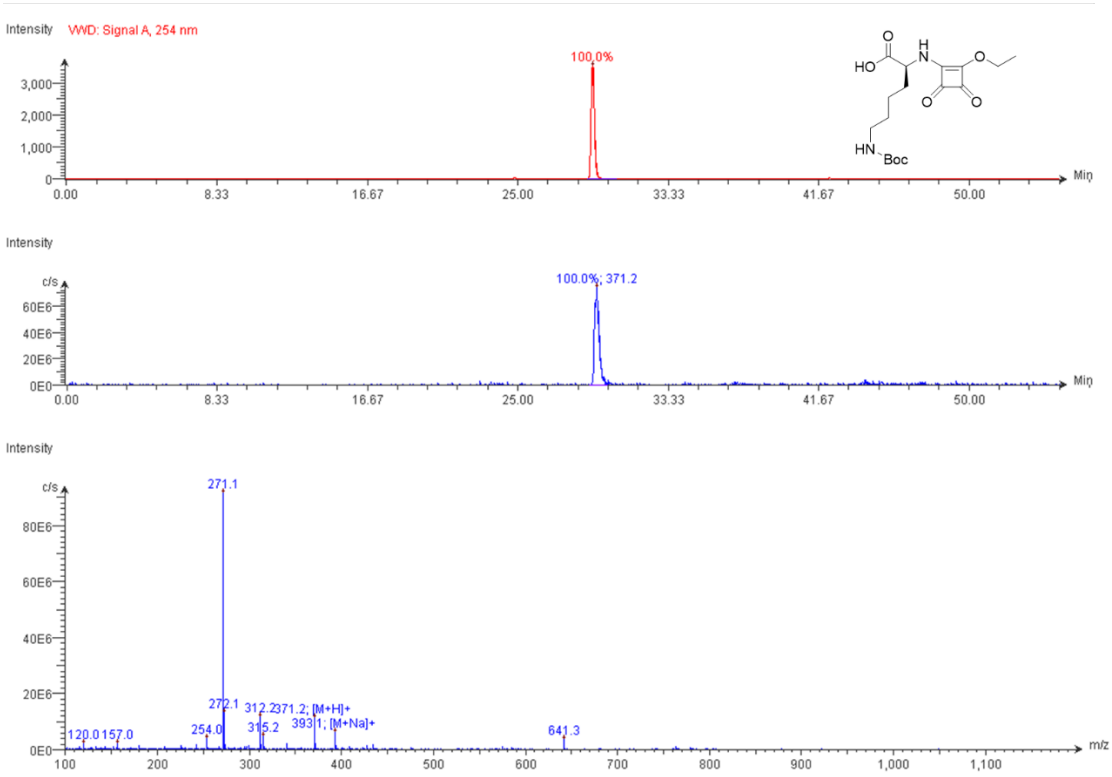

Figure A3.1: LC-MS data for **A.**

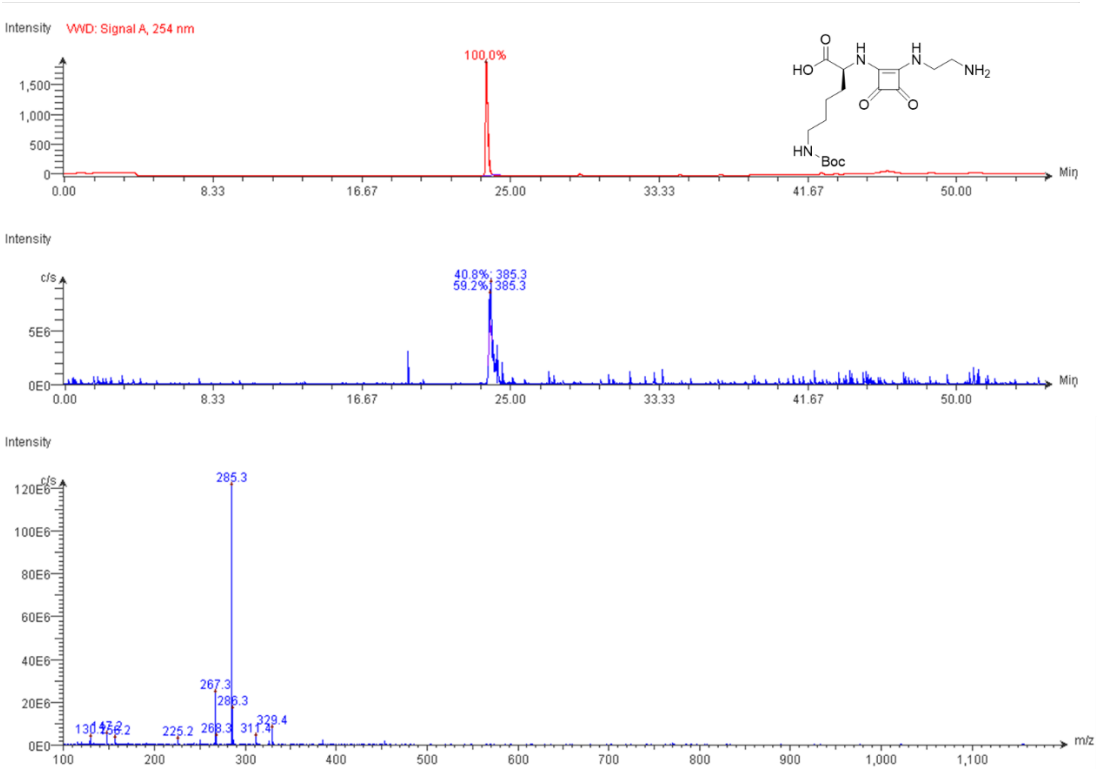

Figure A3.2: LC-MS data for **B.**

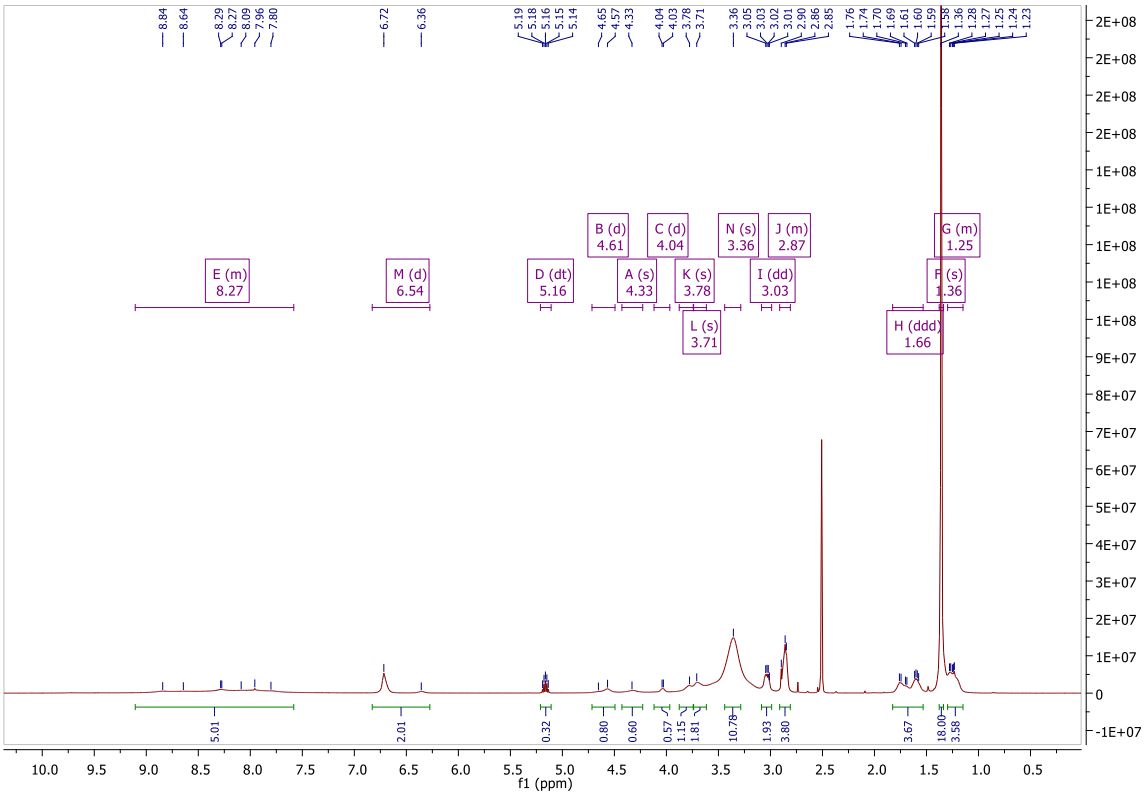

Figure A3.3: ^{1}H NMR spectrum of **ASq-2-Lys(Boc)** in DMSO-d_6.

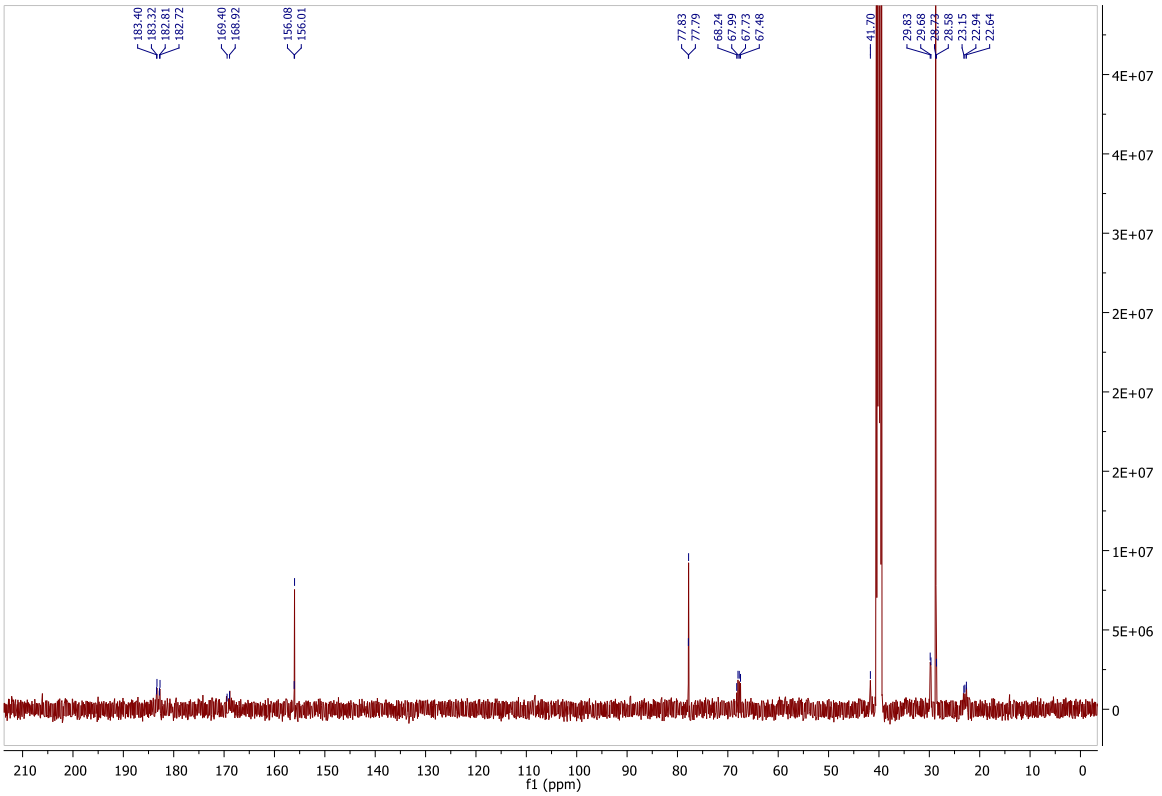

Figure A3.4: ^{13}C NMR spectrum of **ASq-2-Lys(Boc)** in DMSO-d_6.

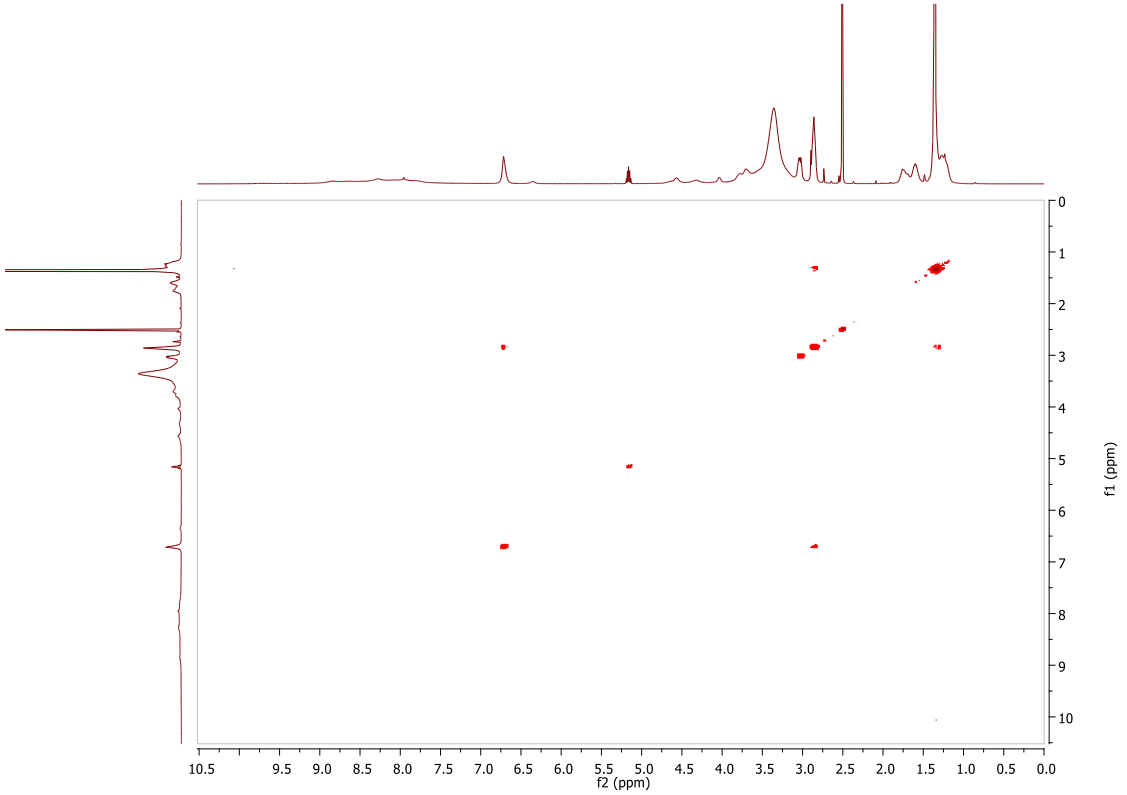

Figure A3.5: COSY spectrum of **ASq-2-Lys(Boc)** in DMSO-d_6.

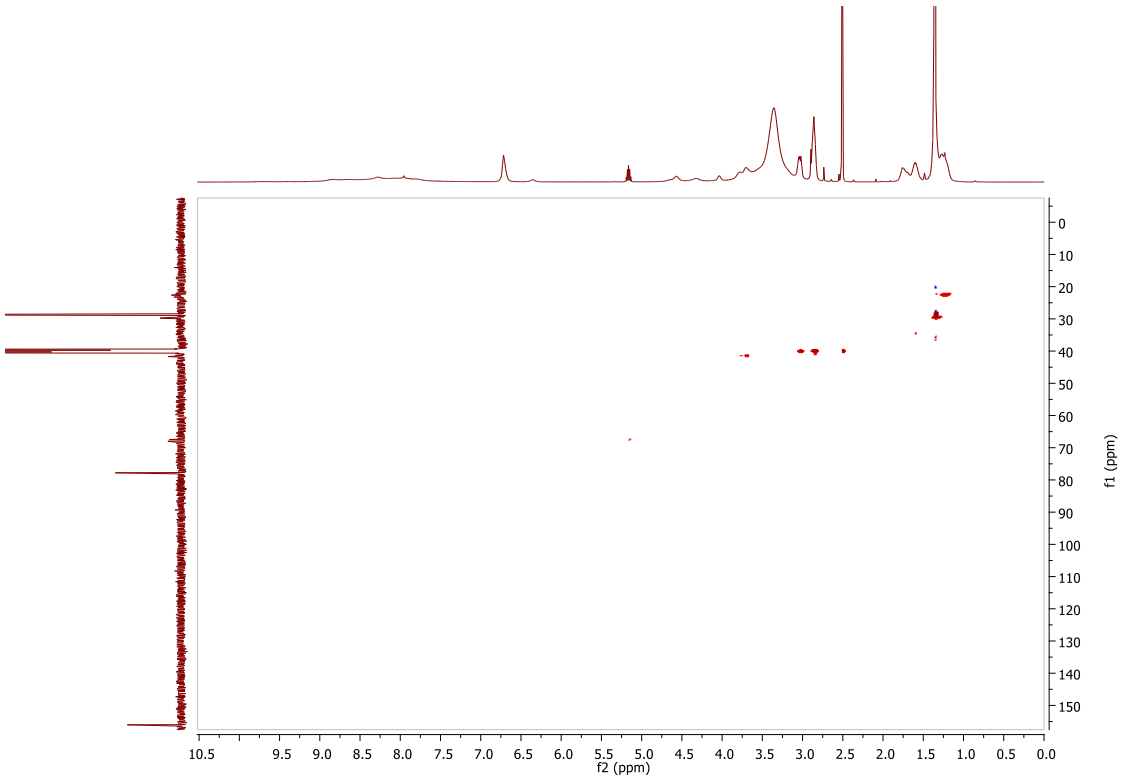

Figure A3.6: HSQC spectrum of **ASq-2-Lys(Boc)** in DMSO-d_6.

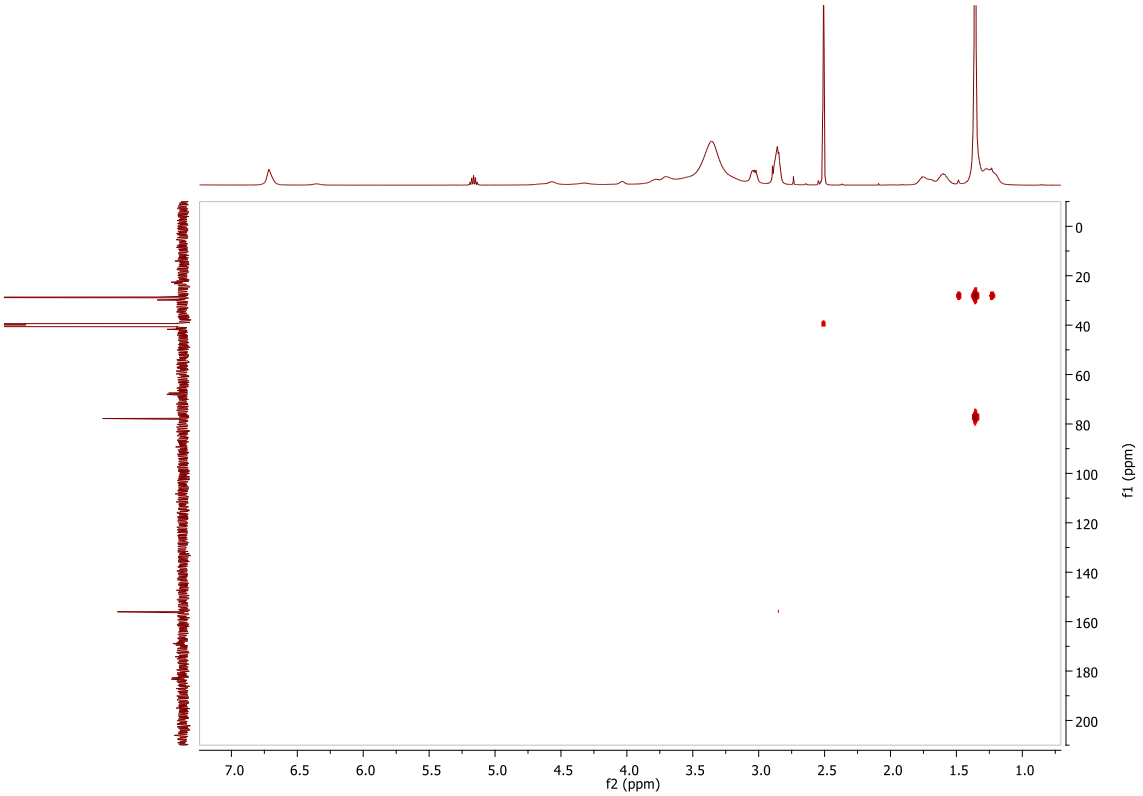

Figure A3.7: HMBC spectrum of **ASq-2-Lys(Boc)** in DMSO-d_6.

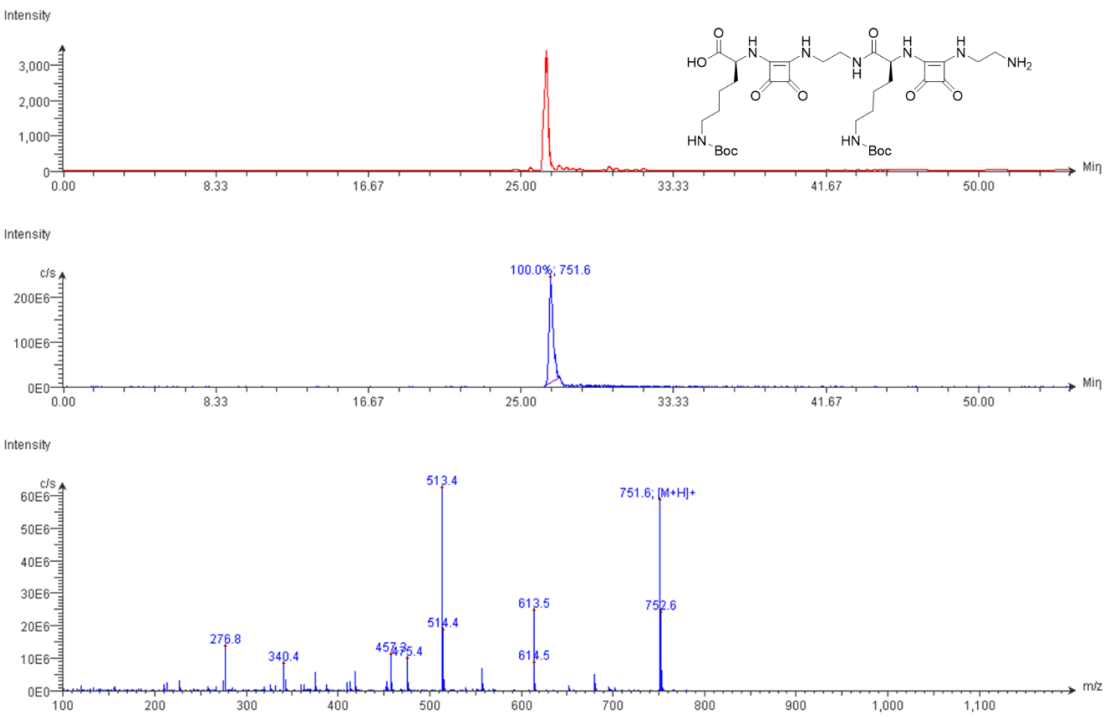

Figure A3.8: LC-MS data for **ASq-2-Lys(Boc)**.

Compound Table

Compound Label	RT (min)	Observed mass (m/z)	Neutral observed mass (Da)	Theoretical mass (Da)	Mass error (ppm)	Isotope match score (%)
Cpd 1: C34 H54 N8 O11	0.69	751.3978	750.3904	750.3912	-1.09	99.54

Figure: Extracted ion chromatogram (EIC) of compound.

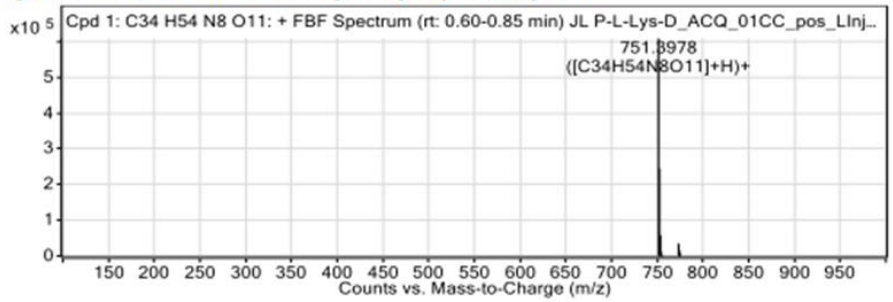

Figure: Full range view of Compound spectra and potential adducts.

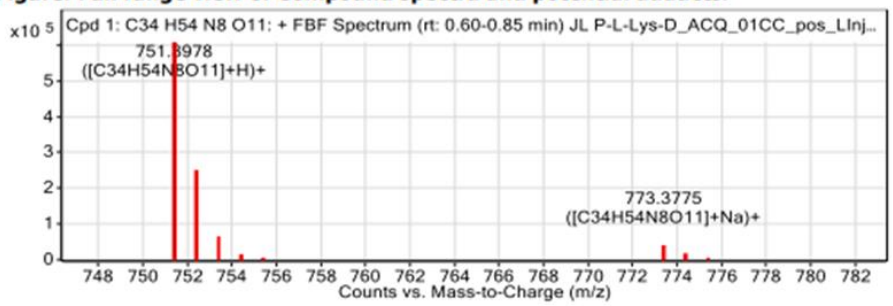

Figure: Zoomed Compound spectra view
(red boxes indicating expected theoretical isotope spacing and abundance)

Compound isotope peak List

m/z	z	Abund	Formula	Ion
751.3978	1	608699.9	C34H54N8O11	(M+H)+
752.4011	1	244918.6	C34H54N8O11	(M+H)+
753.4036	1	58151.5	C34H54N8O11	(M+H)+
754.4036	1	12342.0	C34H54N8O11	(M+H)+
755.3881	1	2721.8	C34H54N8O11	(M+H)+
773.3775	1	34896.5	C34H54N8O11	(M+Na)+
774.3796	1	15475.6	C34H54N8O11	(M+Na)+
775.3783	1	4589.3	C34H54N8O11	(M+Na)+

Figure A3.9: HRMS data for **ASq-2-Lys(Boc)**.

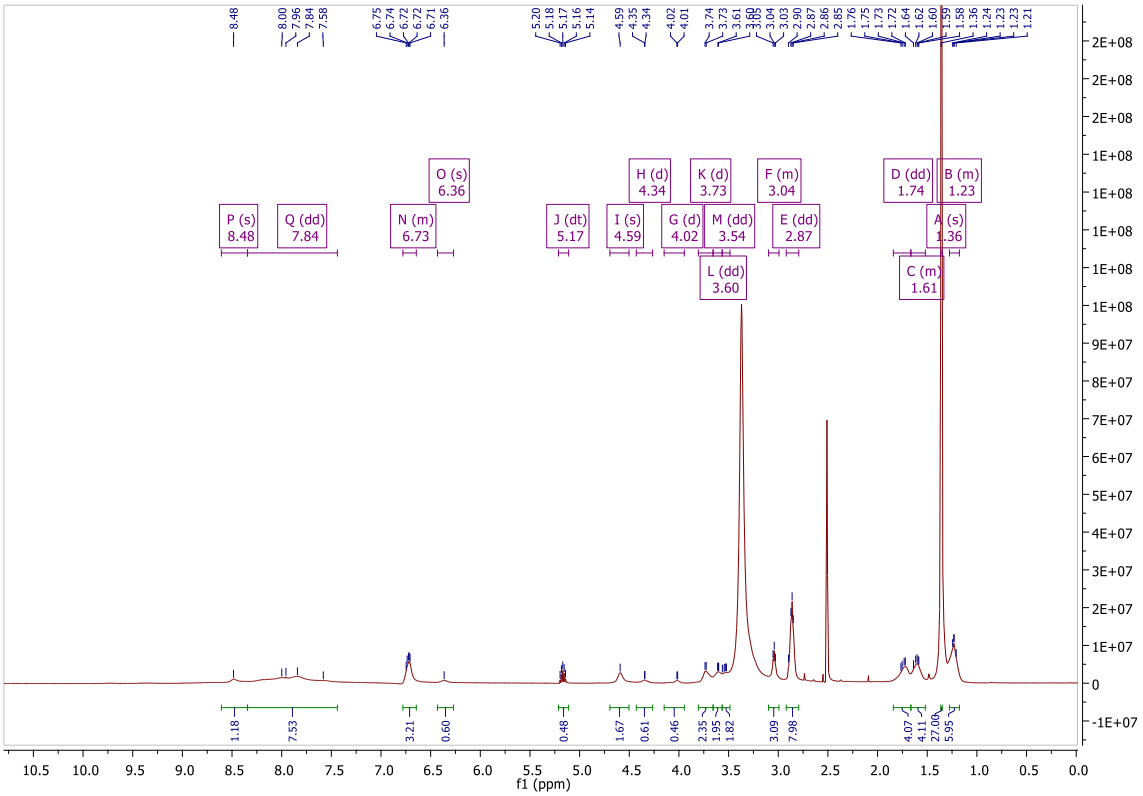

Figure A3.10: ^{1}H NMR spectrum of **ASq-3-Lys(Boc)** in DMSO-d_6.

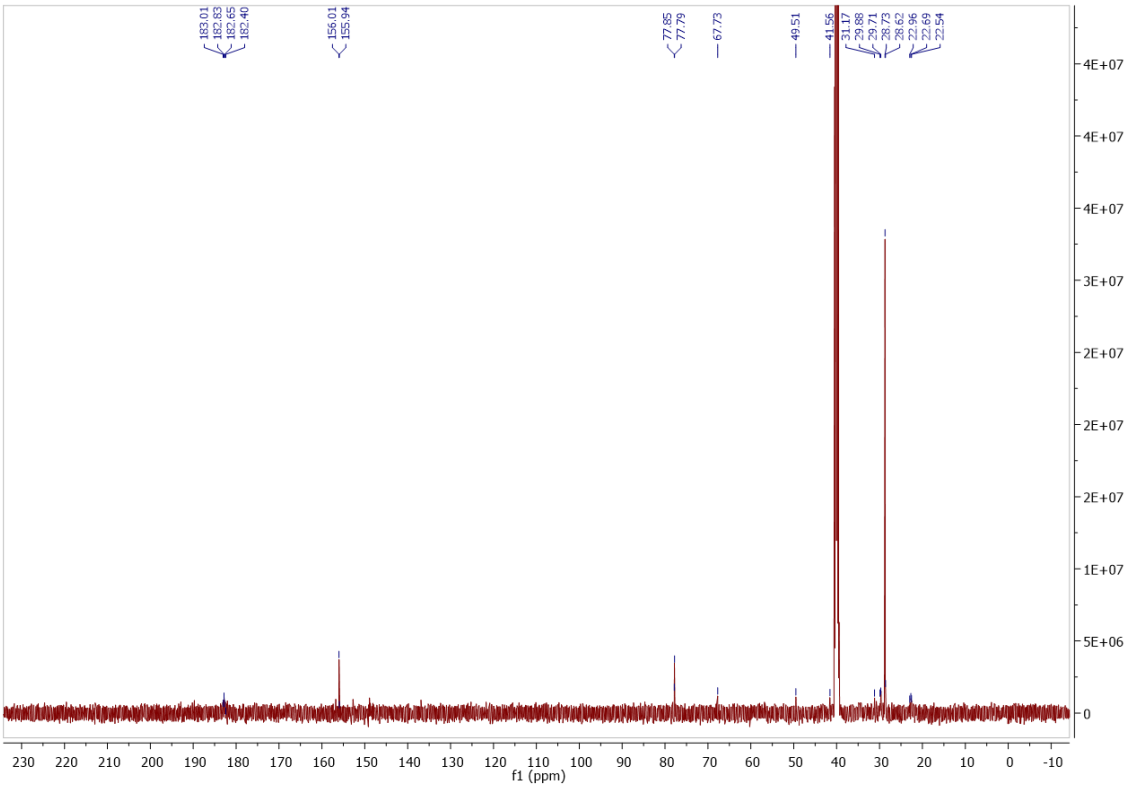

Figure A3.11: ^{13}C NMR spectrum of **ASq-3-Lys(Boc)** in DMSO-d_6.

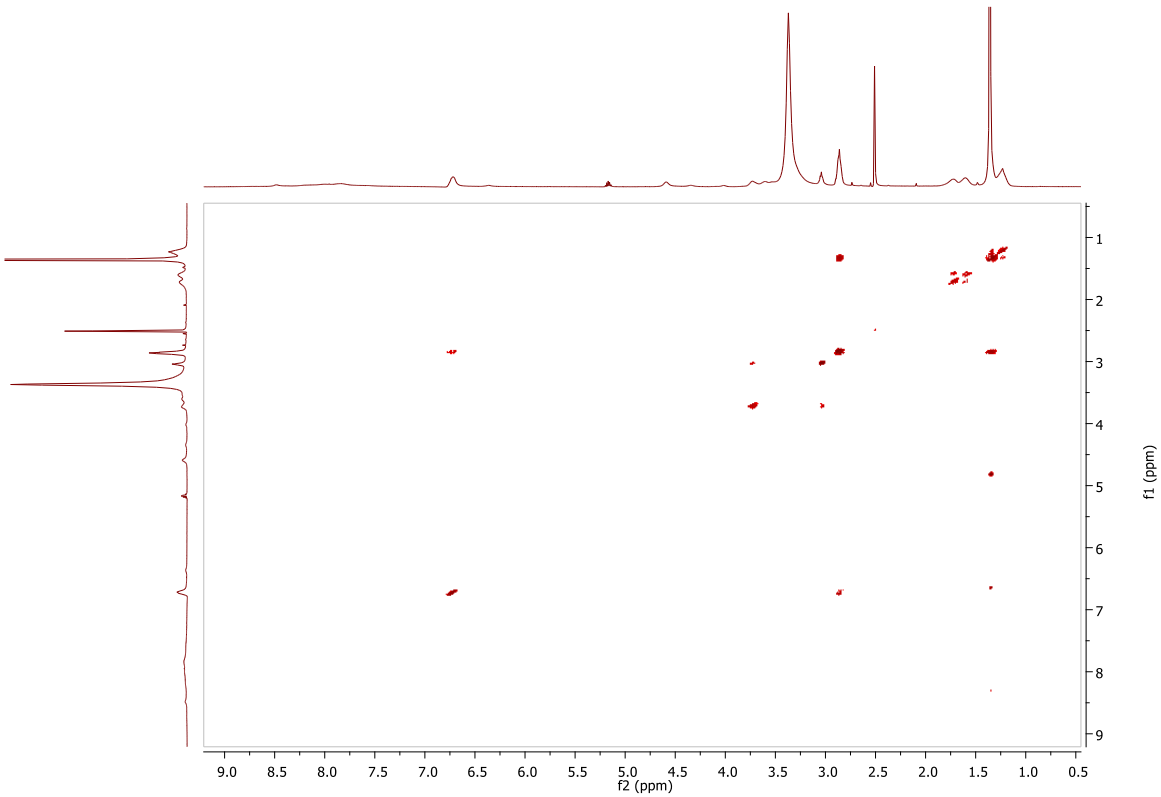

Figure A3.12: COSY spectrum of **ASq-3-Lys(Boc)** in DMSO-d_6.

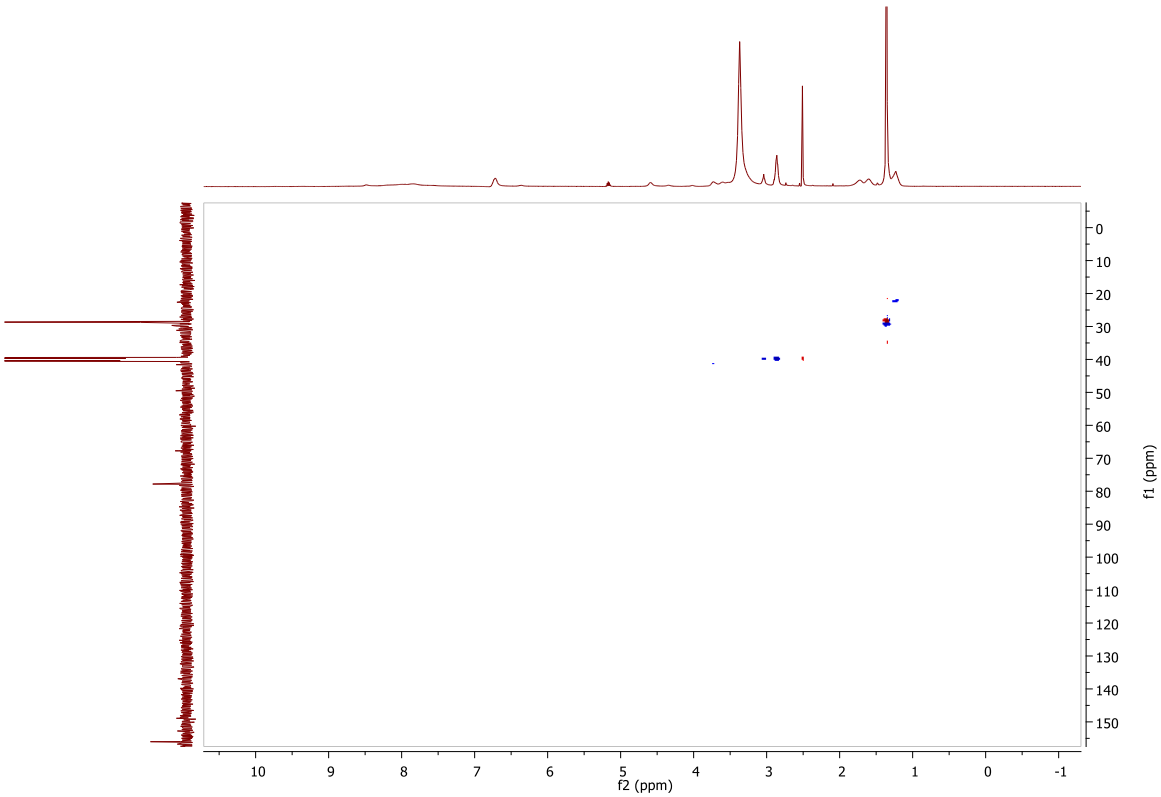

Figure A3.13: HSQC spectrum of **ASq-3-Lys(Boc)** in DMSO-d_6.

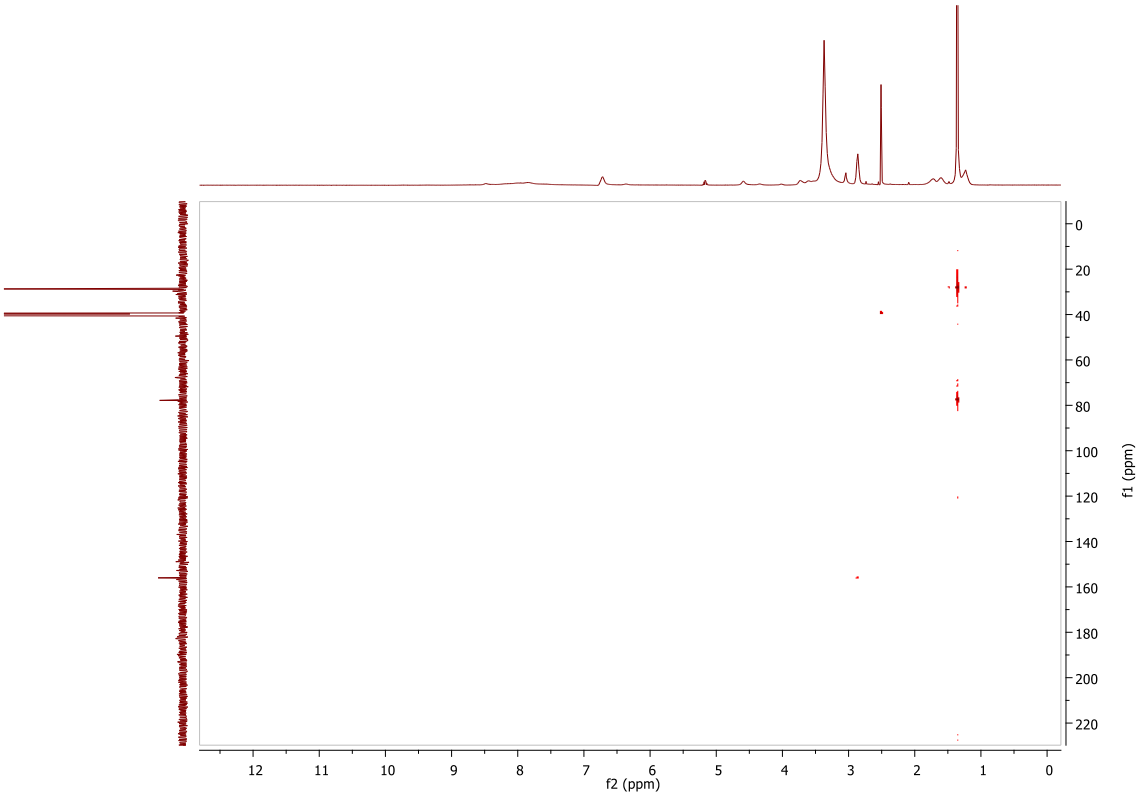

Figure 3.14: HMBC spectrum of **ASq-3-Lys(Boc)** in DMSO-d_6.

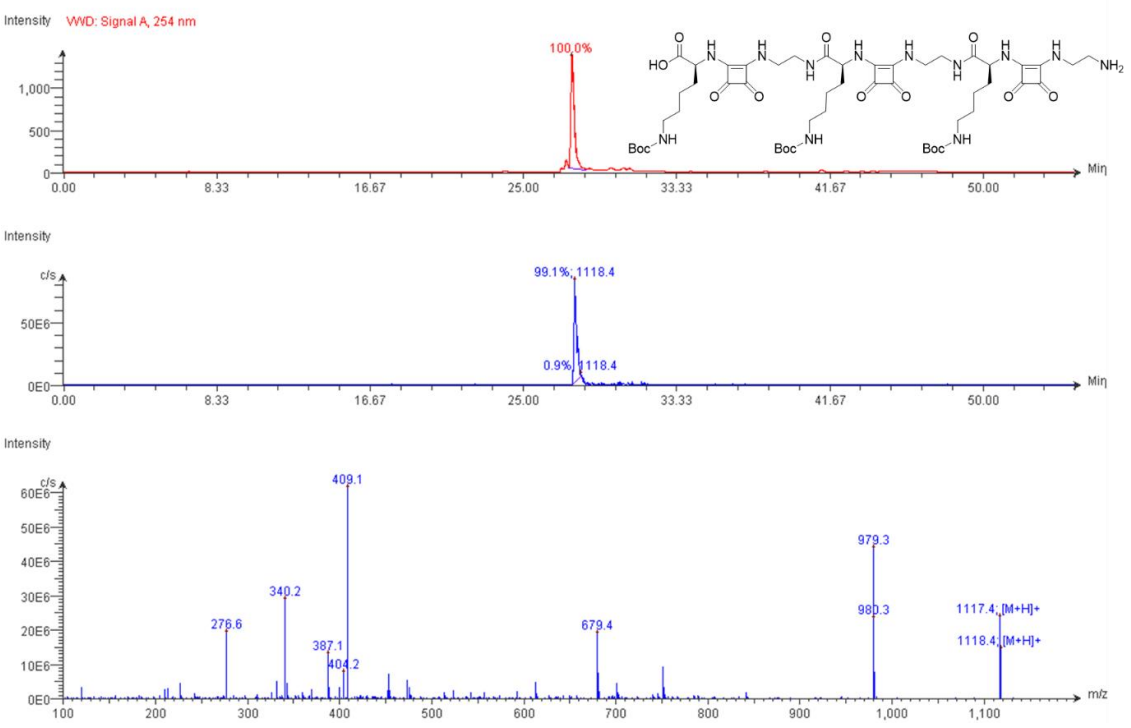

Figure A3.15: LC-MS data for **ASq-3-Lys(Boc)**.

Compound Table

Compound Label	RT (min)	Observed mass (m/z)	Neutral observed mass (Da)	Theoretical mass (Da)	Mass error (ppm)	Isotope match score (%)
Cpd 1: C51 H80 N12 O16	0.70	1117.5855	1116.5776	1116.5815	-3.47	98.09

Figure: Full range view of Compound spectra and potential adducts.

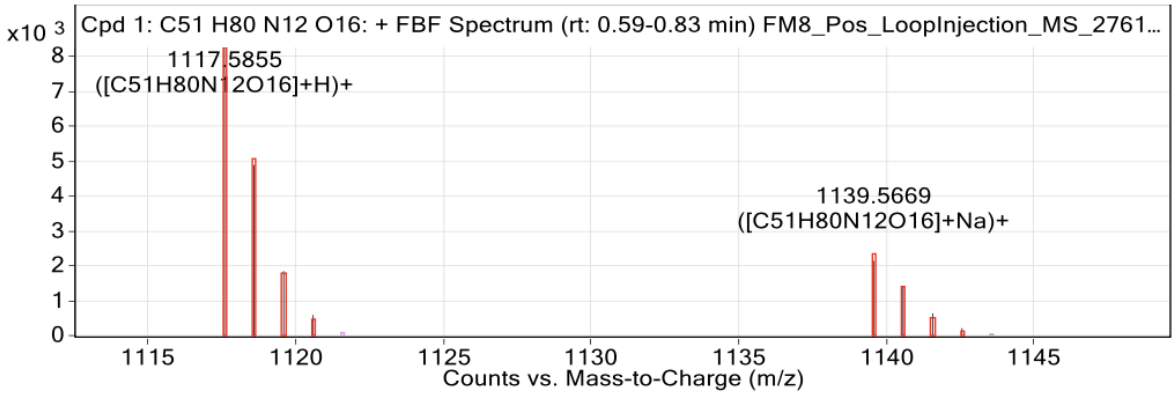

Figure: Zoomed Compound spectra view
(red boxes indicating expected theoretical isotope spacing and abundance)

Compound isotope peak List

m/z	z	Abund	Formula	Ion
1117.5855	1	8269.1	C51H80N12O16	(M+H)+
1118.5880	1	4891.8	C51H80N12O16	(M+H)+
1119.5907	1	1844.2	C51H80N12O16	(M+H)+
1120.5915	1	591.1	C51H80N12O16	(M+H)+
1139.5669	1	2147.4	C51H80N12O16	(M+Na)+
1140.5687	1	1391.4	C51H80N12O16	(M+Na)+
1141.5700	1	637.8	C51H80N12O16	(M+Na)+
1142.5647	1	211.2	C51H80N12O16	(M+Na)+

Figure A3.16: HRMS data for **ASq-3-Lys(Boc)**.

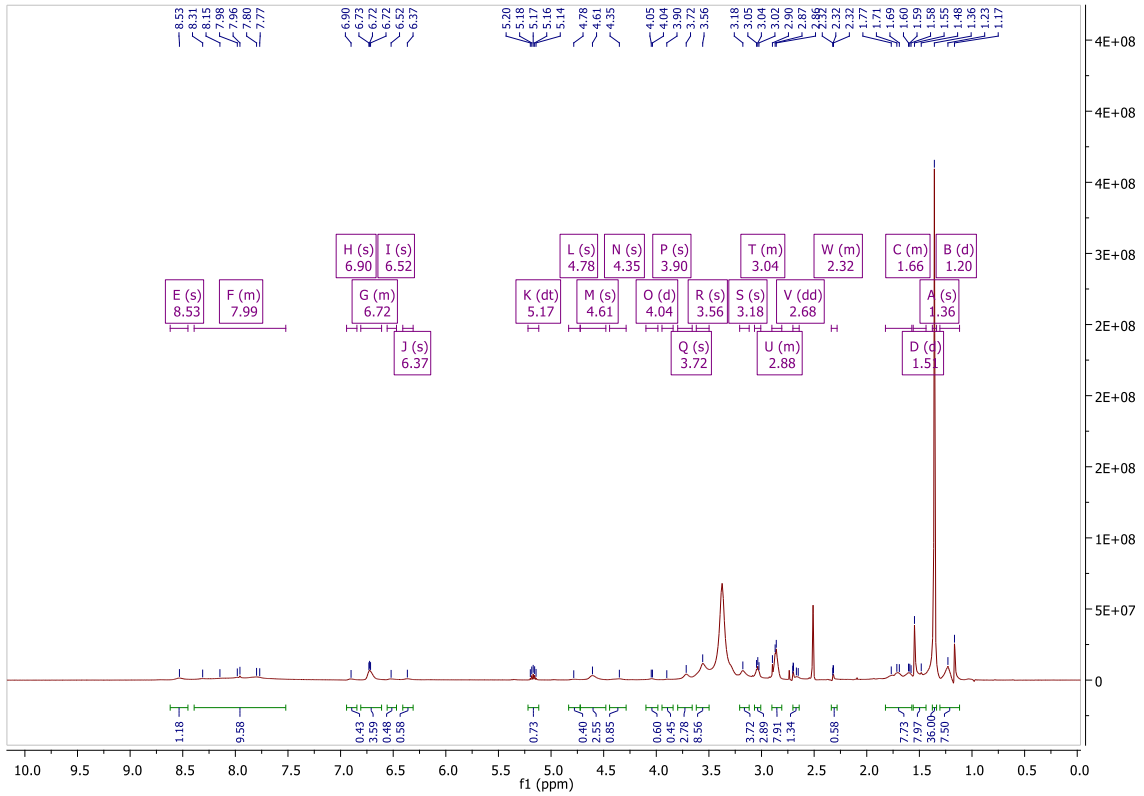

Figure A3.17: ^{1}H NMR spectrum of **ASq-4-Lys(Boc)** in DMSO-d_6.

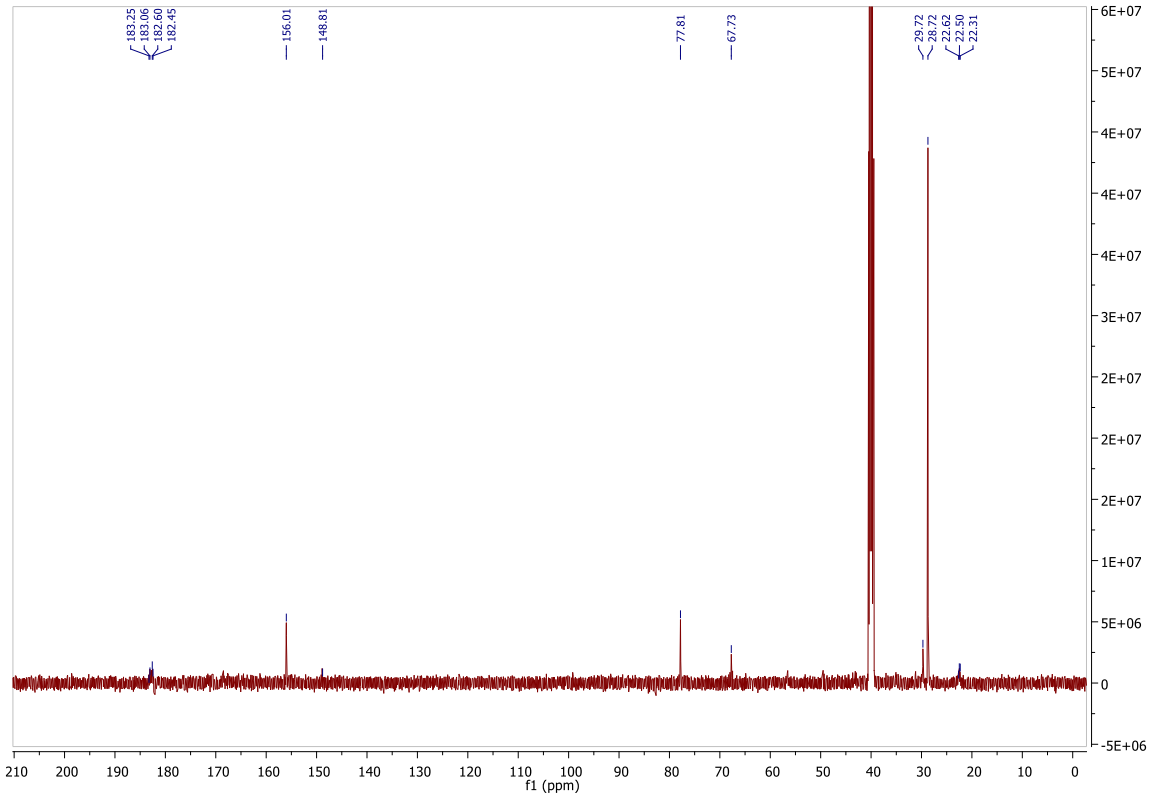

Figure A3.18: ^{13}C NMR spectrum of **ASq-4-Lys(Boc)** in DMSO-d_6.

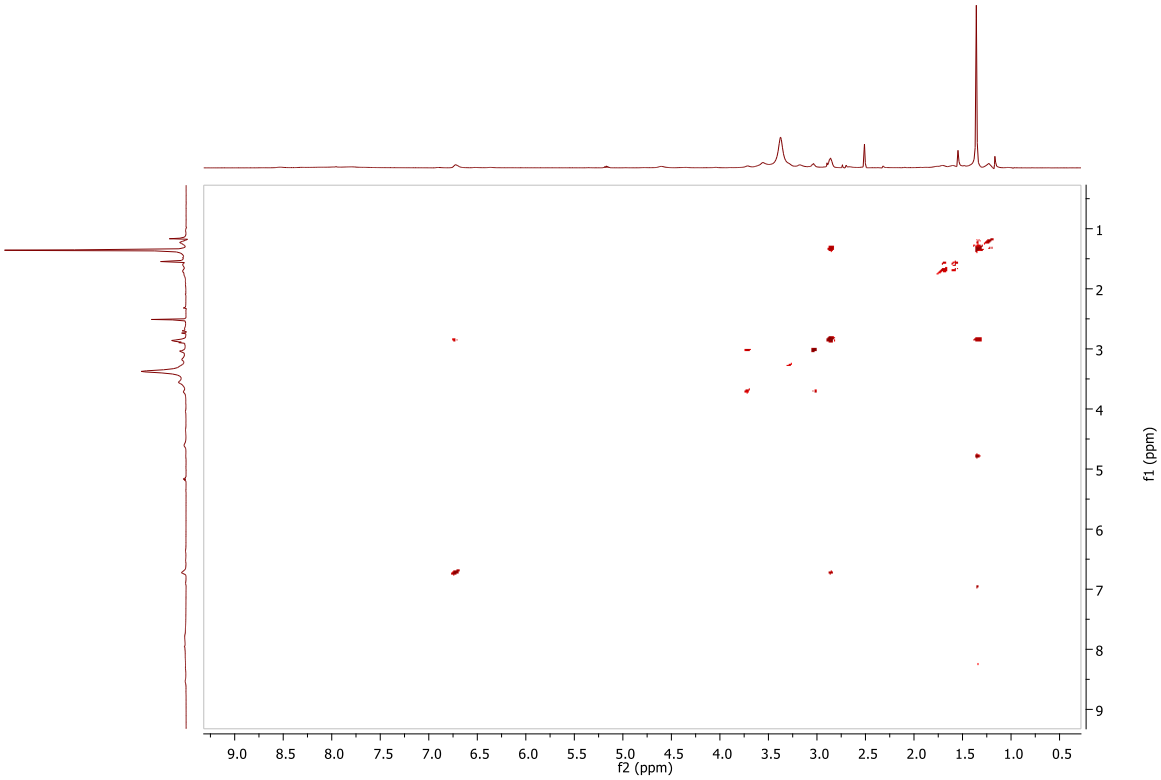

Figure A3.19: COSY spectrum of **ASq-4-Lys(Boc)** in DMSO-d_6.

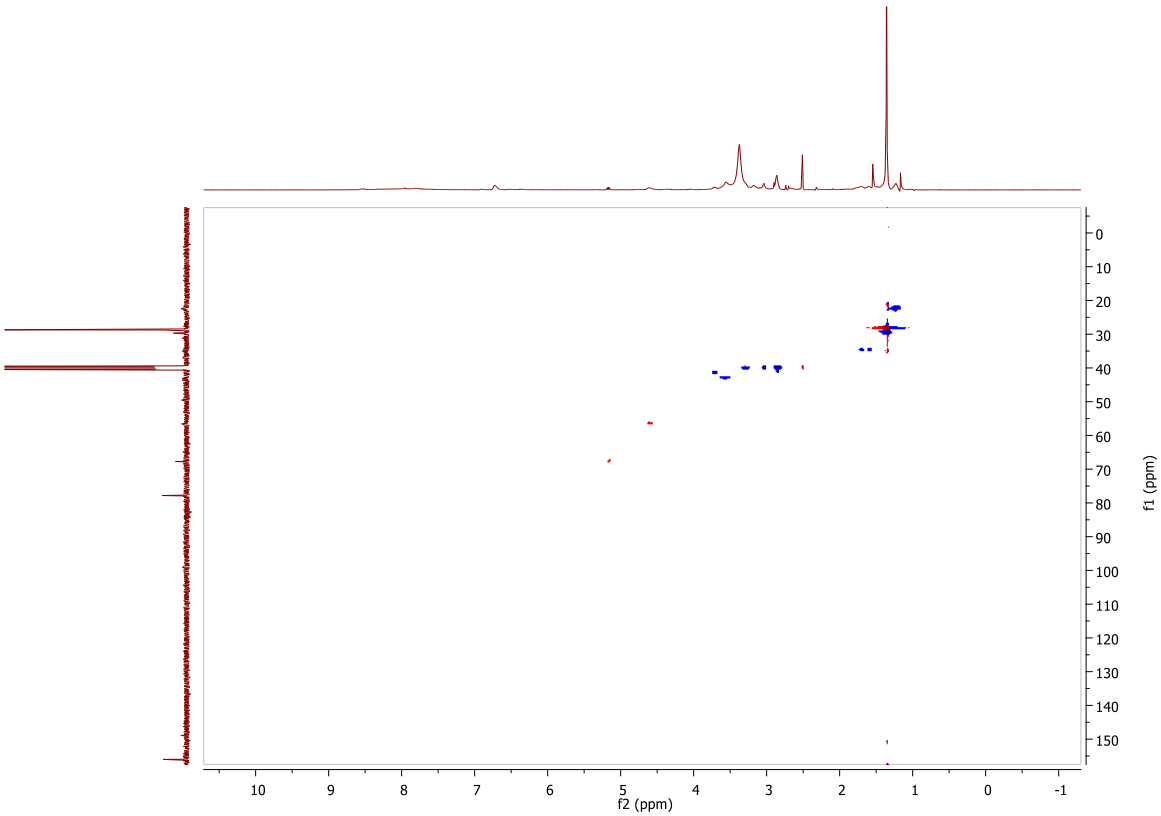

Figure A3.20: HSQC spectrum of **ASq-4-Lys(Boc)** in DMSO-d_6.

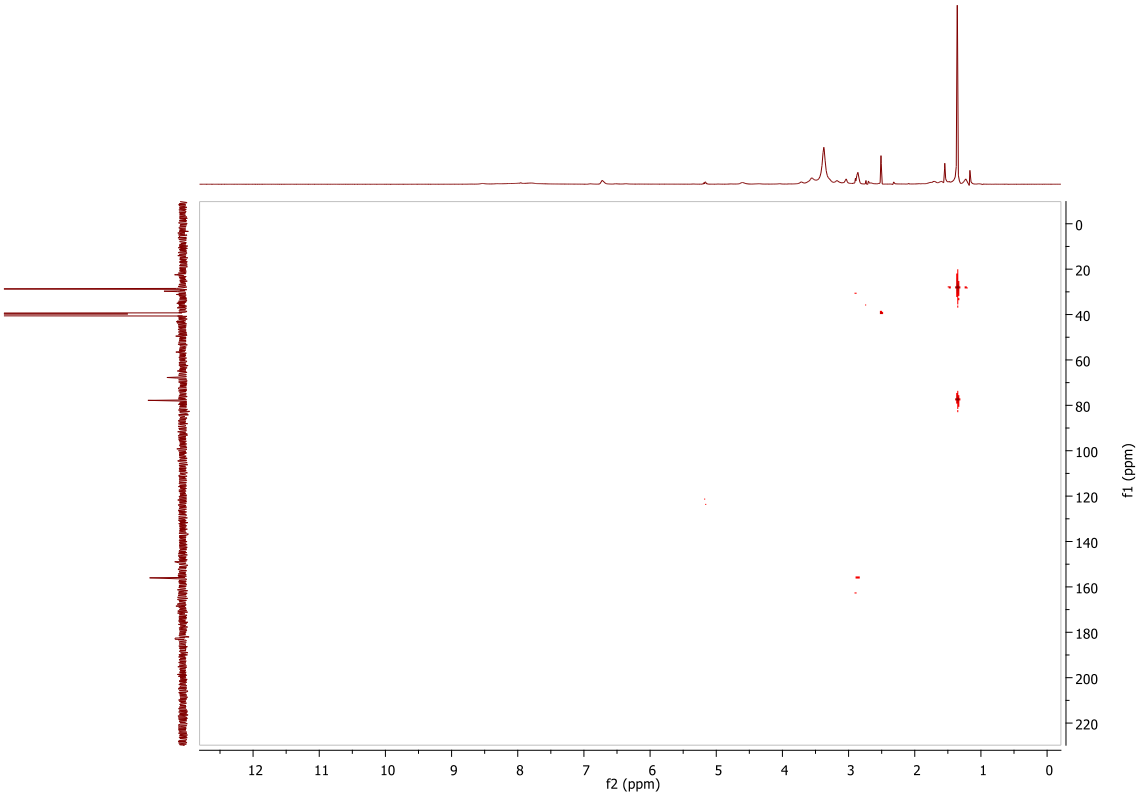

Figure A3.21: HMBC spectrum of **ASq-4-Lys(Boc)** in DMSO-d_6.

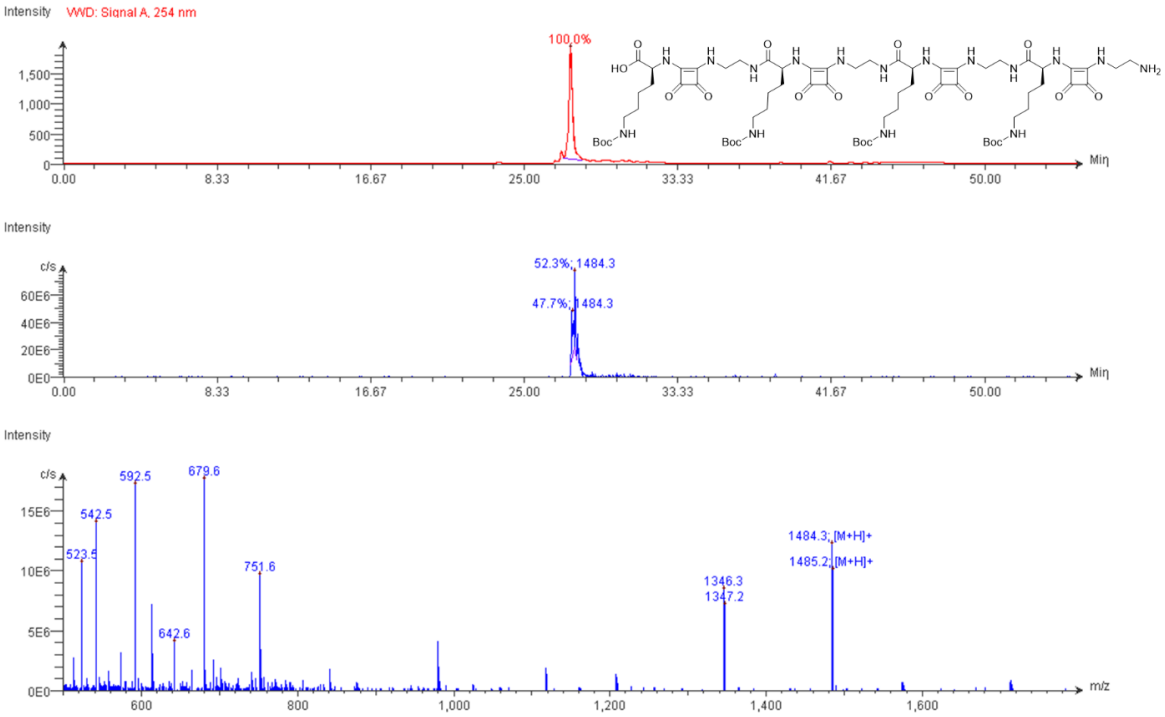

Figure A3.22: LC-MS data for **ASq-4-Lys(Boc)**.

Compound Table

Compound Label	RT (min)	Observed mass (m/z)	Neutral observed mass (Da)	Theoretical mass (Da)	Mass error (ppm)	Isotope match score (%)
Cpd 1: C68 H106 N16 O21	0.71	742.3919	1482.7667	1482.7718	-3.47	93.88

Figure: Extracted ion chromatogram (EIC) of compound.

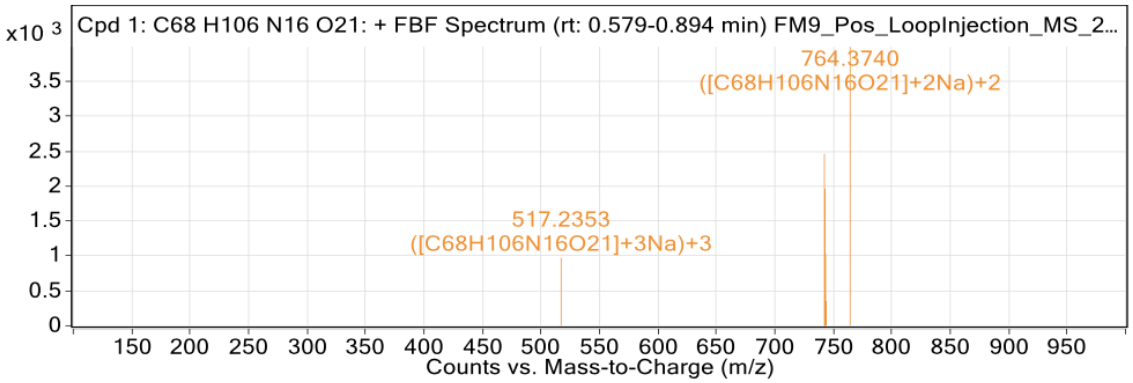

Figure: Full range view of Compound spectra and potential adducts.

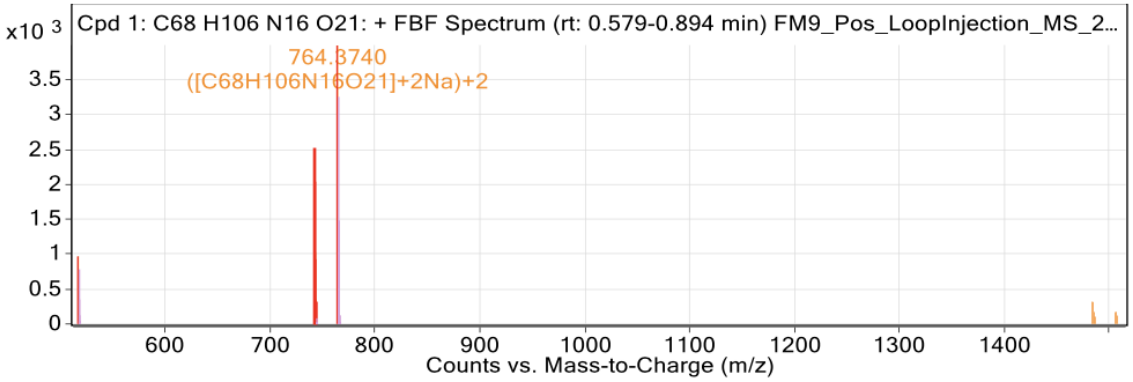

Figure: Zoomed Compound spectra view
(red boxes indicating expected theoretical isotope spacing and abundance)

Compound isotope peak List

m/z	z	Abund	Formula	Ion
517.2353	3	971.7	C68H106N16O21	(M+3Na)+3
742.3919	2	2464.1	C68H106N16O21	(M+2H)+2
742.8936	2	1963.7	C68H106N16O21	(M+2H)+2
743.3942	2	1029.0	C68H106N16O21	(M+2H)+2
743.8965	2	350.5	C68H106N16O21	(M+2H)+2
764.3740	2	3997.2	C68H106N16O21	(M+2Na)+2
1483.7738	1	319.5	C68H106N16O21	(M+H)+
1484.7757	1	315.3	C68H106N16O21	(M+H)+
1505.7590	1	170.6	C68H106N16O21	(M+Na)+
1506.7644	1	174.3	C68H106N16O21	(M+Na)+

Figure A3.23: HRMS data for **ASq-4-Lys(Boc)**.

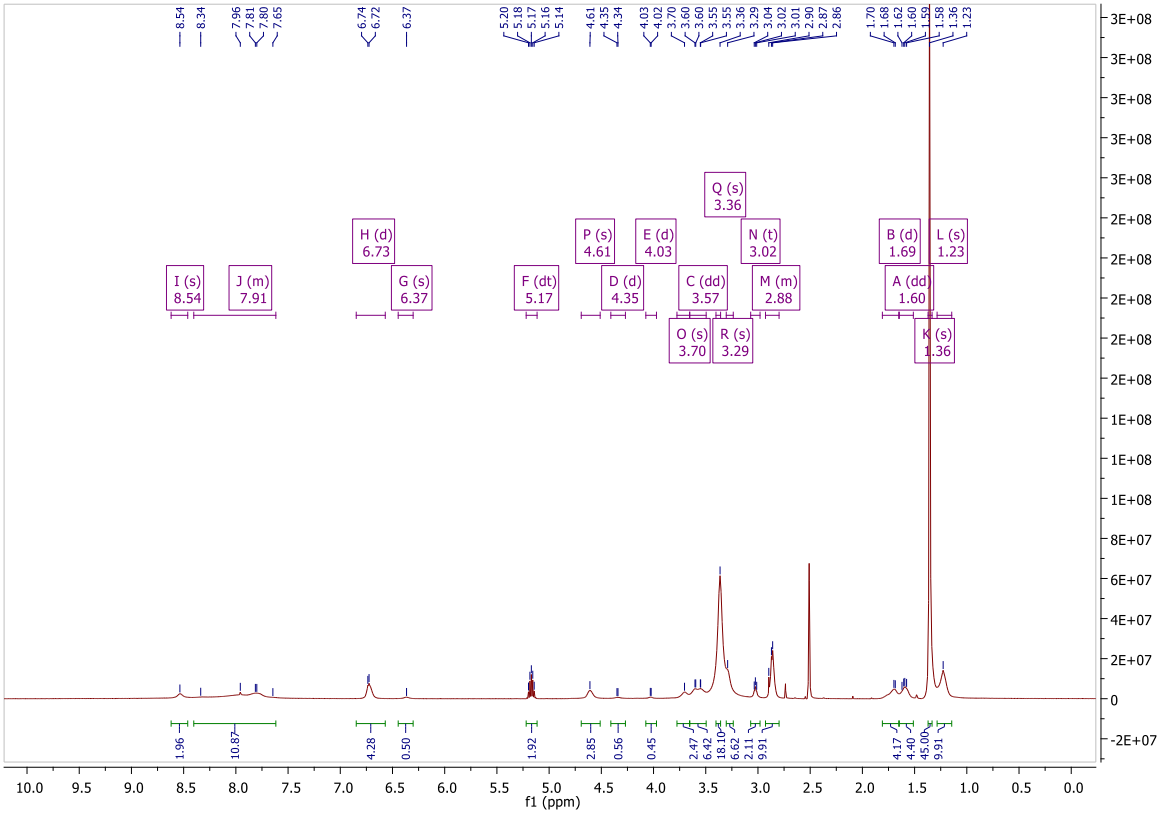

Figure A3.24: ^{1}H NMR spectrum of **ASq-5-Lys(Boc)** in DMSO-d_6.

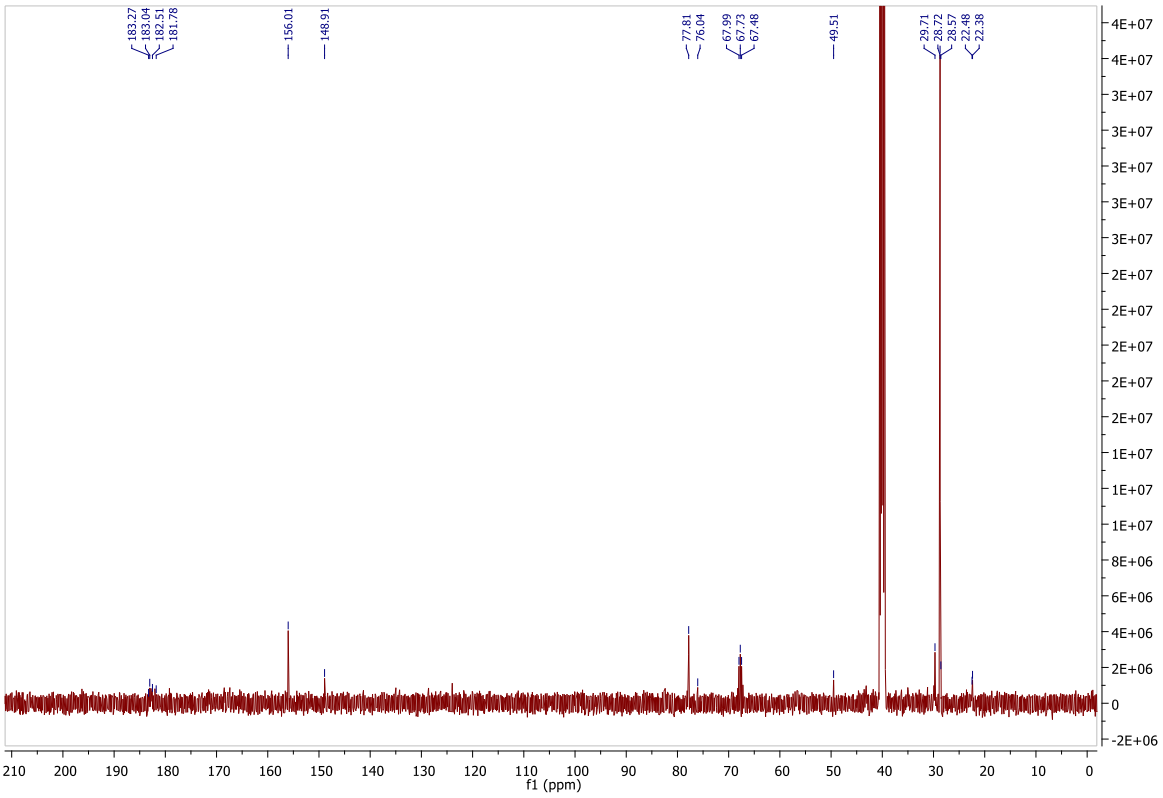

Figure A3.25: ^{13}C NMR spectrum of **ASq-5-Lys(Boc)** in DMSO-d_6.

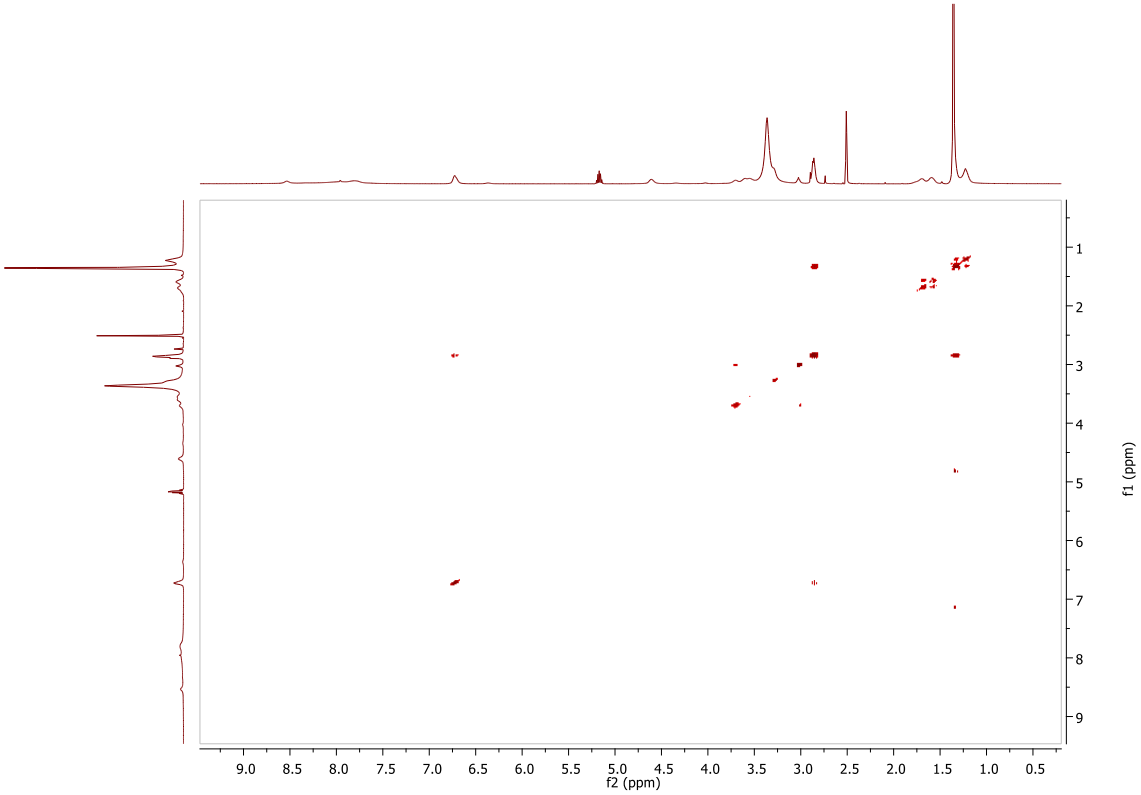

Figure A3.26: COSY spectrum of **ASq-5-Lys(Boc)** in DMSO-d_6.

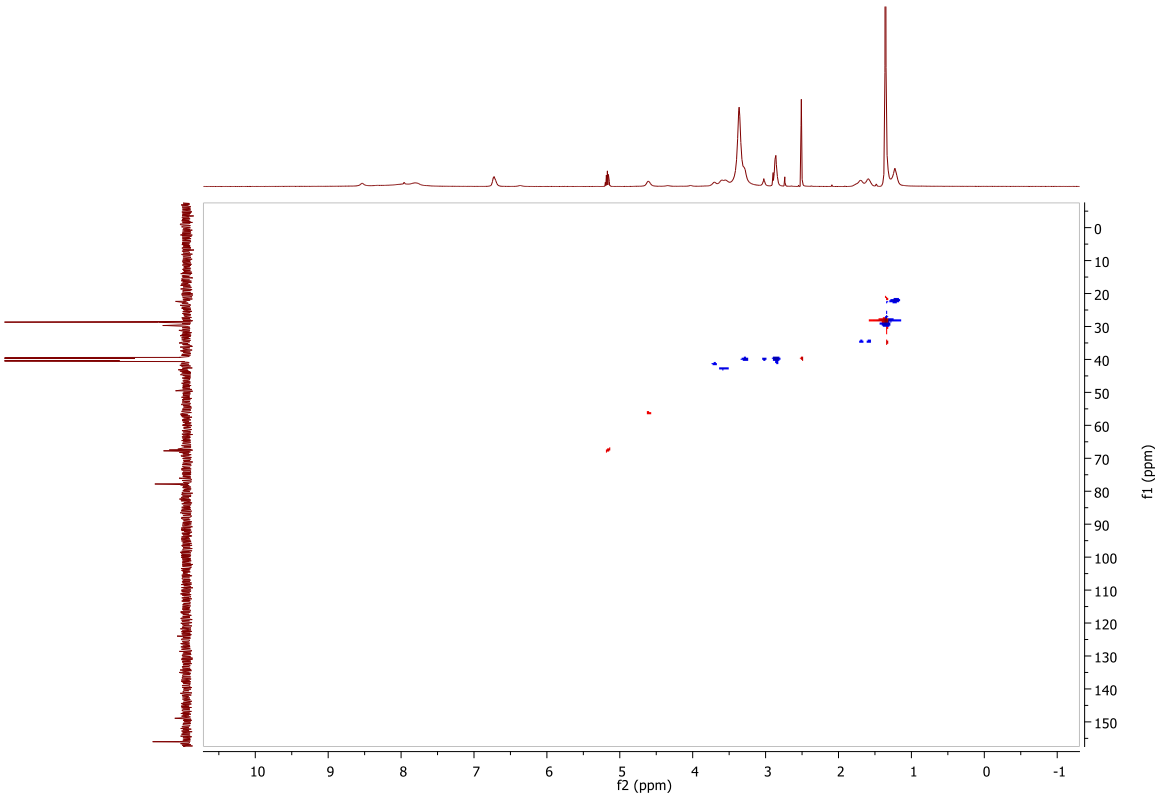

Figure A3.27: HSQC spectrum of **ASq-5-Lys(Boc)** in DMSO-d_6.

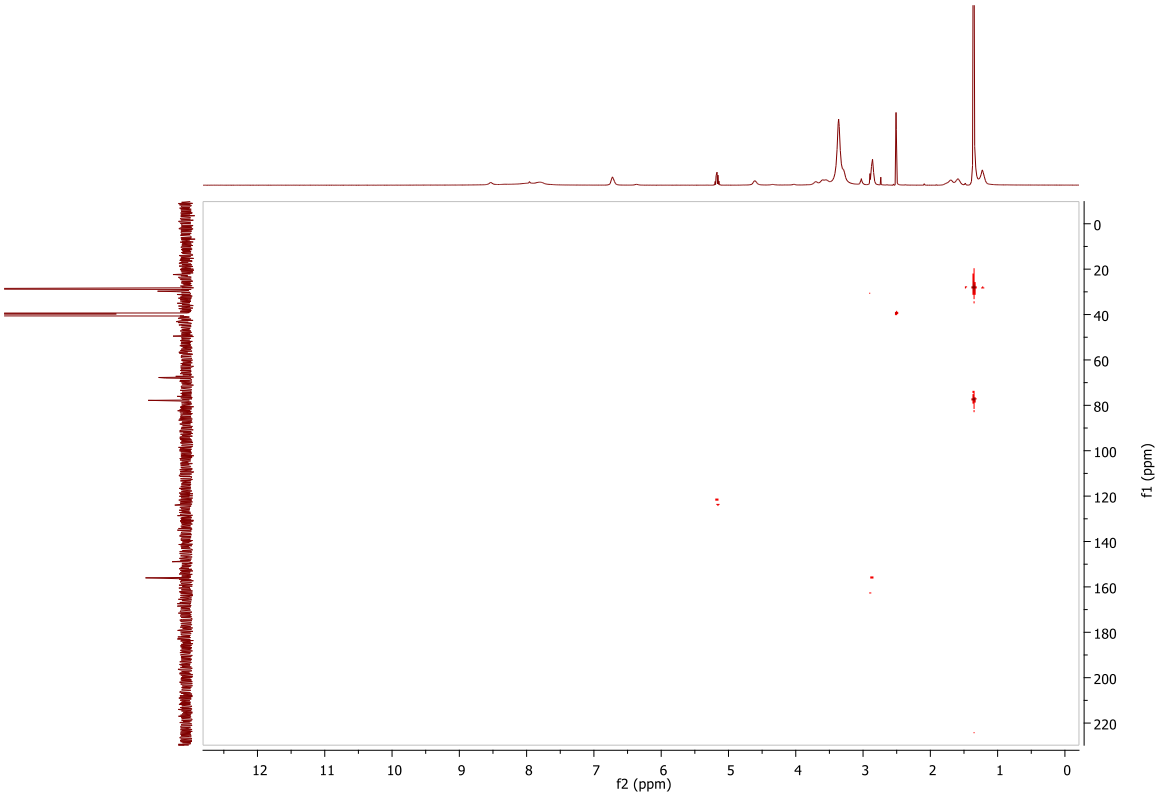

Figure A3.28: HMBC spectrum of **ASq-5-Lys(Boc)** in DMSO-d_6.

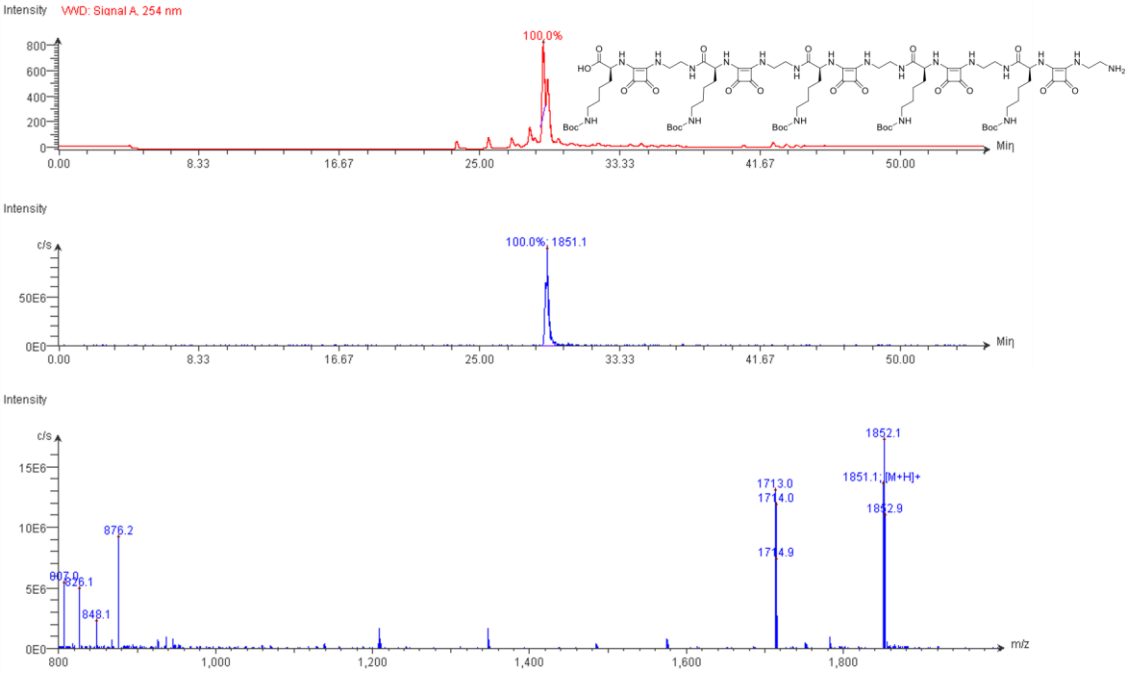

Figure A3.29: LC-MS data for **ASq-5-Lys(Boc)**.

Compound Table

Compound Label	RT (min)	Observed mass (m/z)	Neutral observed mass (Da)	Theoretical mass (Da)	Mass error (ppm)	Isotope match score (%)
Cpd 1: C85 H132 N20 O26	0.71	925.9878	1848.9573	1848.9622	-2.65	98.54

Figure: Extracted ion chromatogram (EIC) of compound.

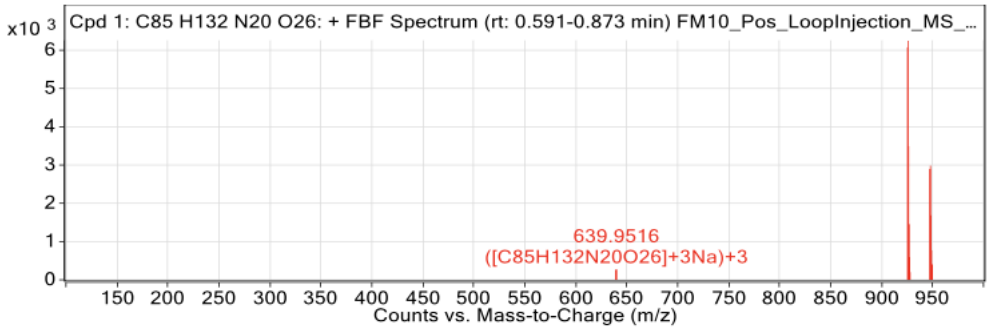

Figure: Full range view of Compound spectra and potential adducts.

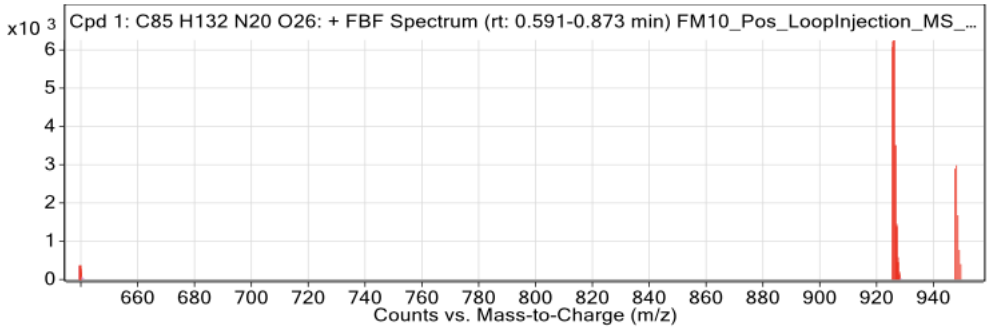

Figure: Zoomed Compound spectra view
(red boxes indicating expected theoretical isotope spacing and abundance)

Compound isotope peak List

m/z	z	Abund	Formula	Ion
639.6311	3	263.1	C85H132N20O26	(M+3Na)+3
925.4861	2	6075.6	C85H132N20O26	(M+2H)+2
925.9878	2	6257.5	C85H132N20O26	(M+2H)+2
926.4892	2	3494.1	C85H132N20O26	(M+2H)+2
926.9904	2	1453.9	C85H132N20O26	(M+2H)+2
927.4918	2	579.7	C85H132N20O26	(M+2H)+2
947.4683	2	2896.3	C85H132N20O26	(M+2Na)+2
947.9705	2	2983.6	C85H132N20O26	(M+2Na)+2
948.4711	2	1679.3	C85H132N20O26	(M+2Na)+2
948.9731	2	771.2	C85H132N20O26	(M+2Na)+2

Figure A3.30: HRMS data for **ASq-5-Lys(Boc)**.

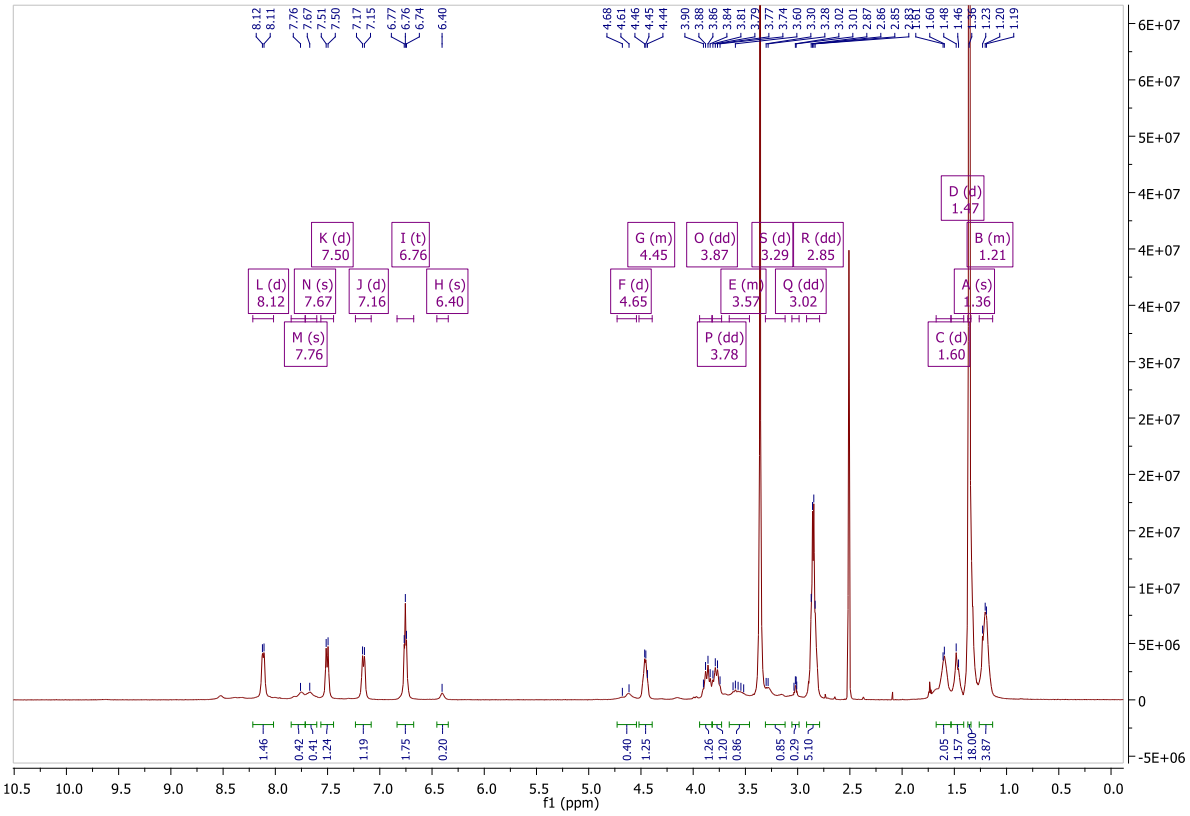

Figure A3.31: ^{1}H NMR spectrum of **Sq-2-Lys(Boc)** in DMSO-d_6.

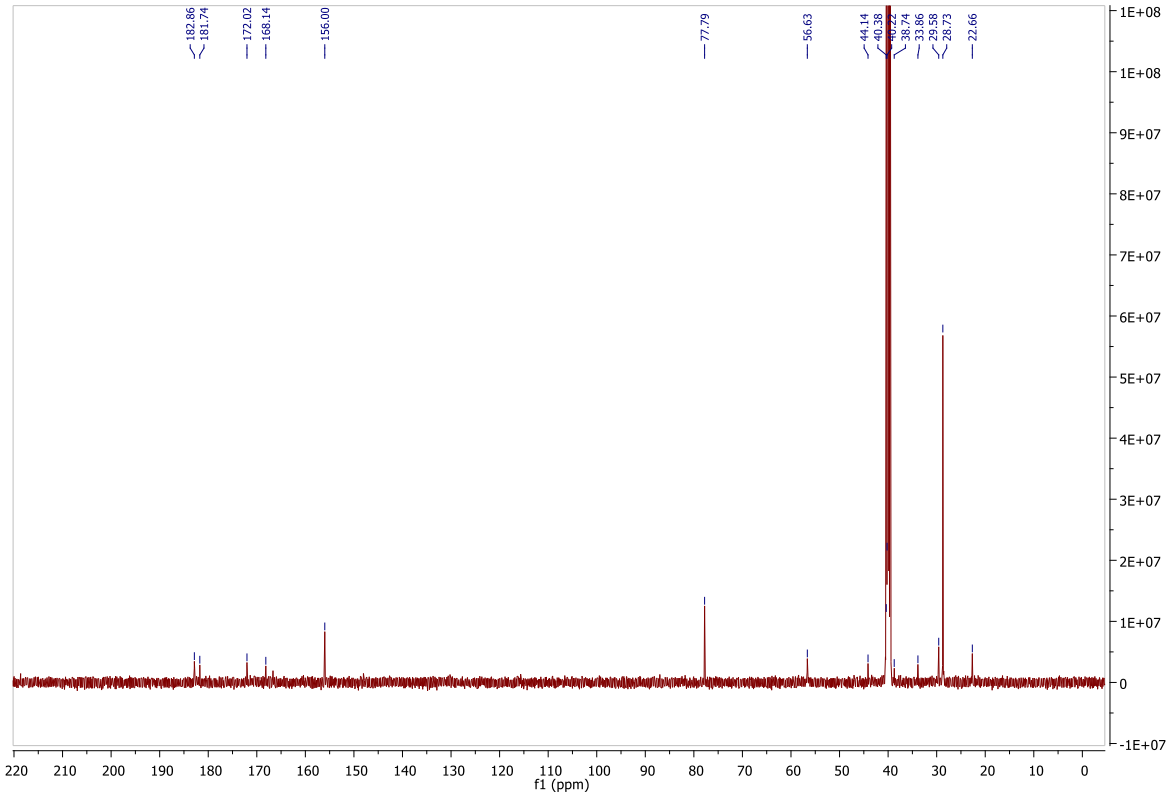

Figure A3.32: ^{13}C NMR spectrum of **Sq-2-Lys(Boc)** in DMSO-d_6.

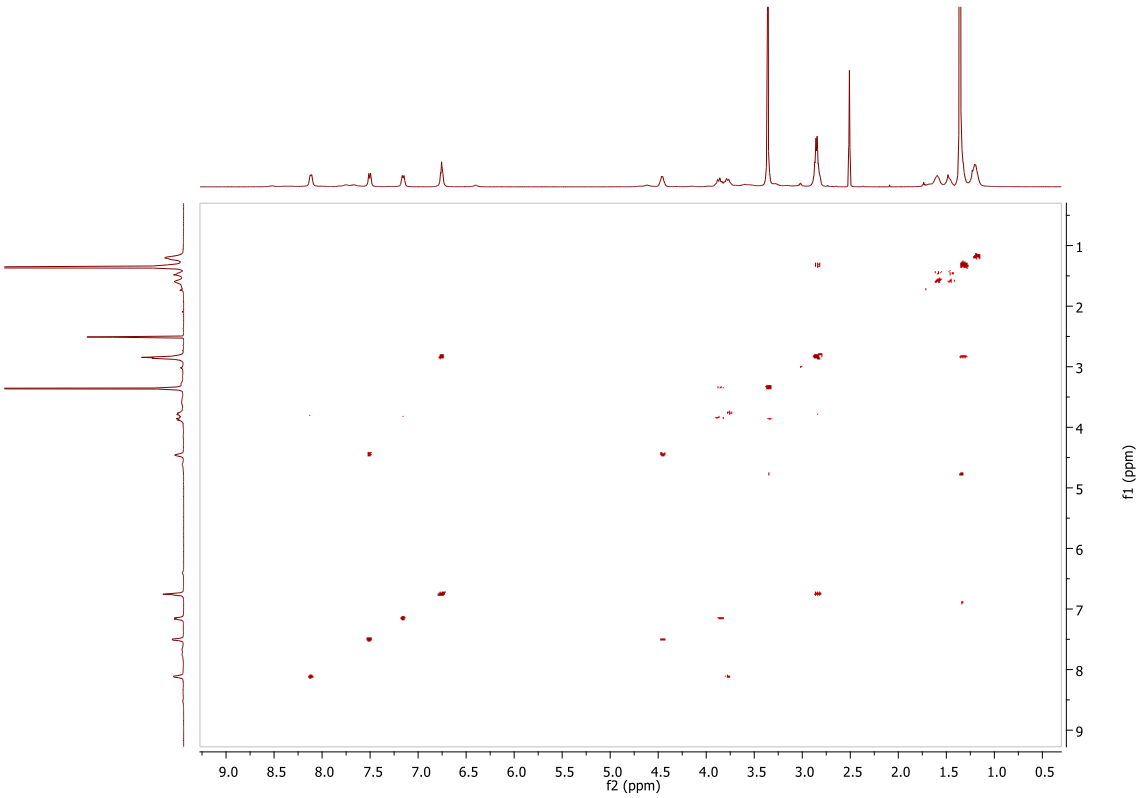

Figure A3.33: COSY spectrum of **Sq-2-Lys(Boc)** in DMSO-d_6.

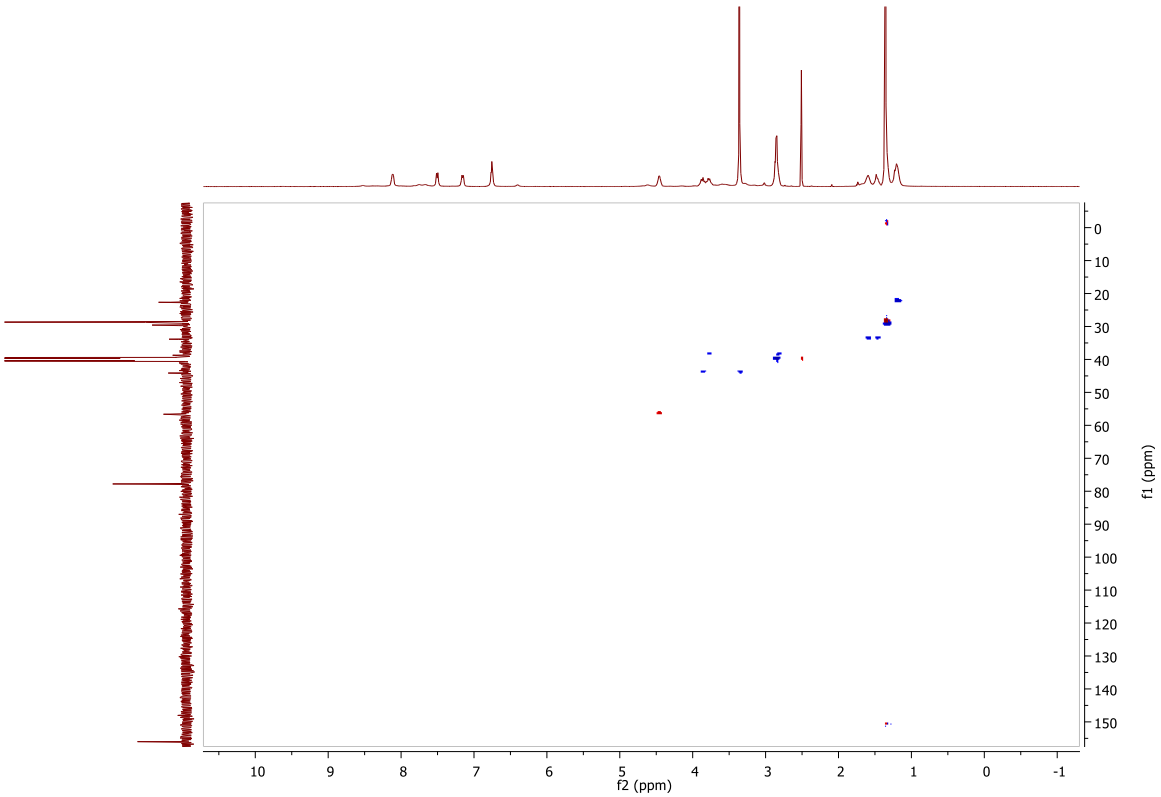

Figure A3.34: HSQC spectrum of **Sq-2-Lys(Boc)** in DMSO-d_6.

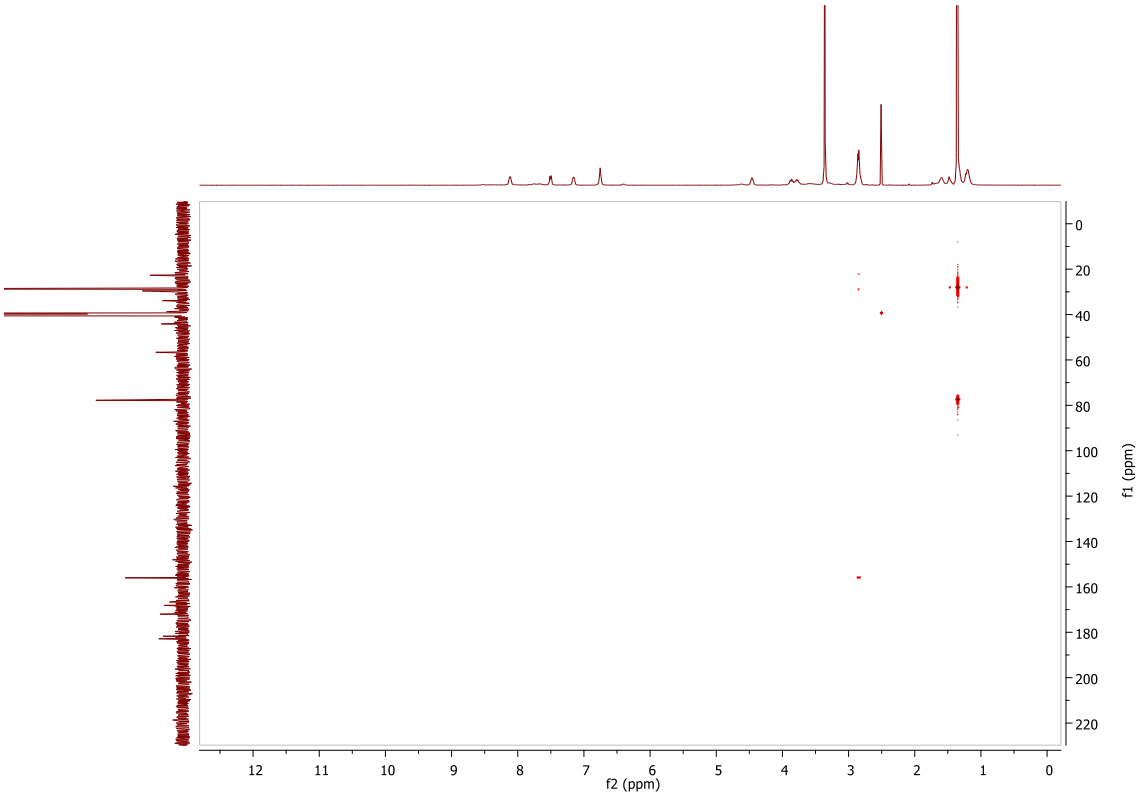

Figure A3.35: HMBC spectrum of **Sq-2-Lys(Boc)** in DMSO-d_6.

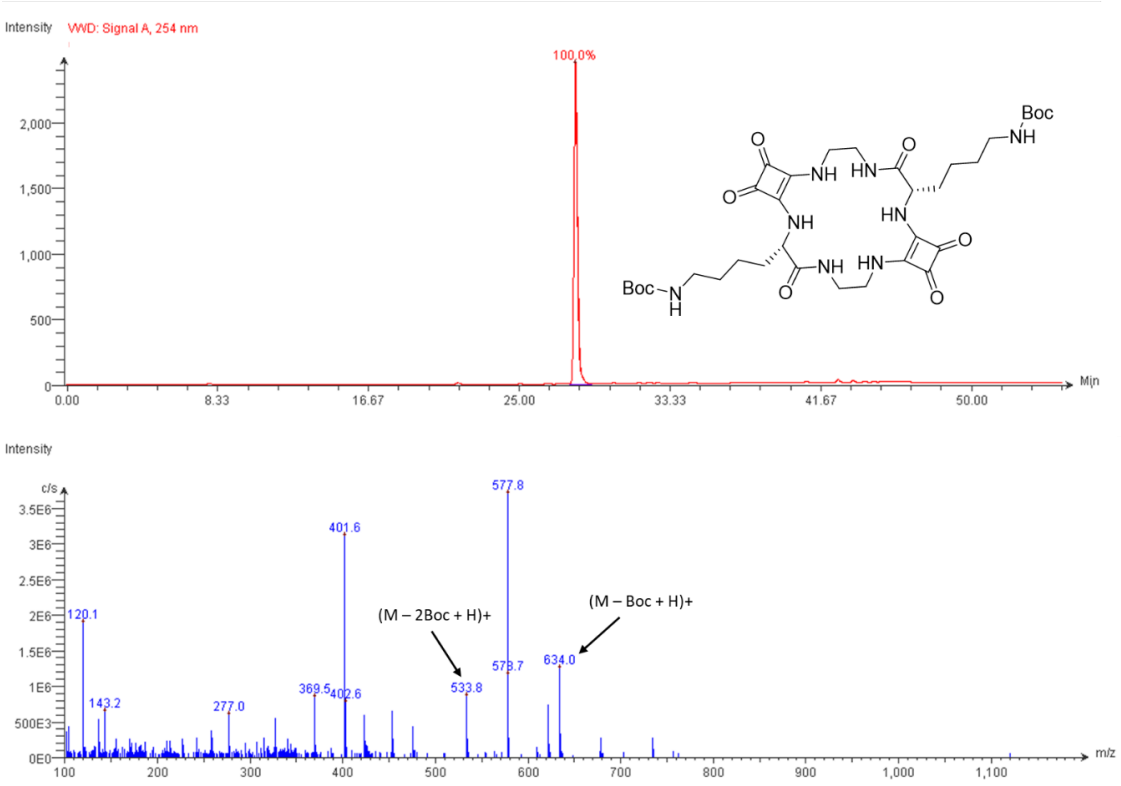

Figure A3.36: LC-MS data for **Sq-2-Lys(Boc)**.

Compound Table

Compound Label	RT (min)	Observed mass (m/z)	Neutral observed mass (Da)	Theoretical mass (Da)	Mass error (ppm)	Isotope match score (%)
Cpd 1: C34 H52 N8 O10	0.73	755.3677	732.3789	732.3806	-2.32	98.33

Mass errors of between -5.00 and 5.00 ppm with isotope match scores above 60% are considered confirmation of molecular formulae

Figure: Extracted ion chromatogram (EIC) of compound.

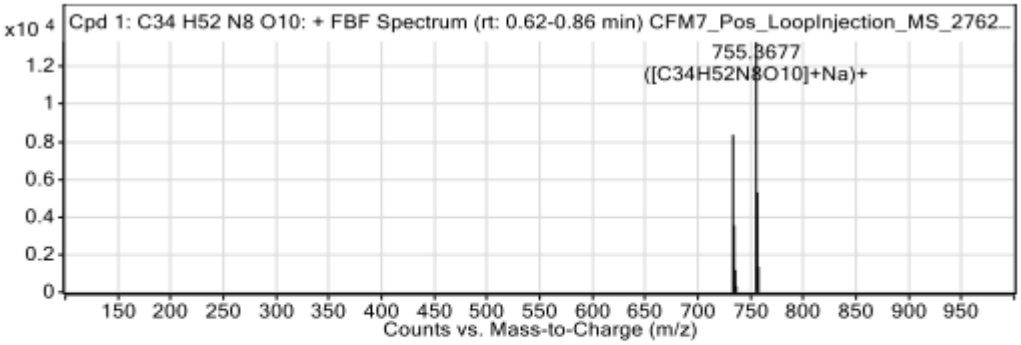

Figure: Full range view of Compound spectra and potential adducts.

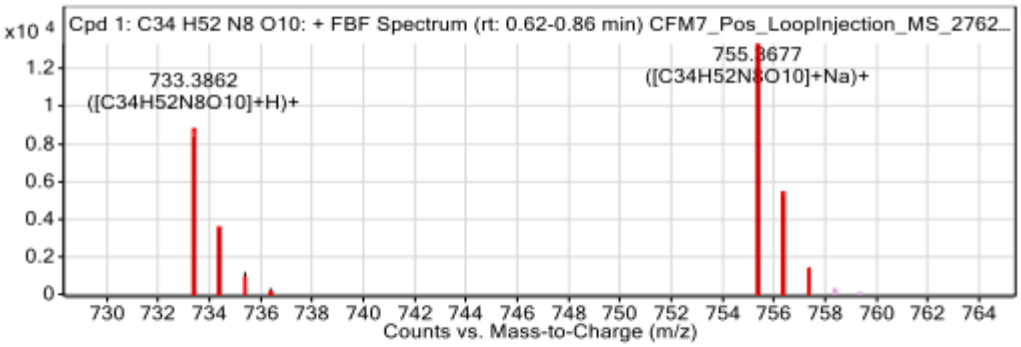

Figure: Zoomed Compound spectra view
(red boxes indicating expected theoretical isotope spacing and abundance)

Compound isotope peak List

m/z	z	Abund	Formula	Ion
733.3862	1	8370.1	C34H52N8O10	(M+H)+
734.3905	1	3555.3	C34H52N8O10	(M+H)+
735.3939	1	1180.8	C34H52N8O10	(M+H)+
736.3946	1	326.8	C34H52N8O10	(M+H)+
755.3677	1	13330.6	C34H52N8O10	(M+Na)+
756.3708	1	5303.1	C34H52N8O10	(M+Na)+
757.3740	1	1353.7	C34H52N8O10	(M+Na)+

Figure A3.37: HRMS data for **Sq-2-Lys(Boc)**.

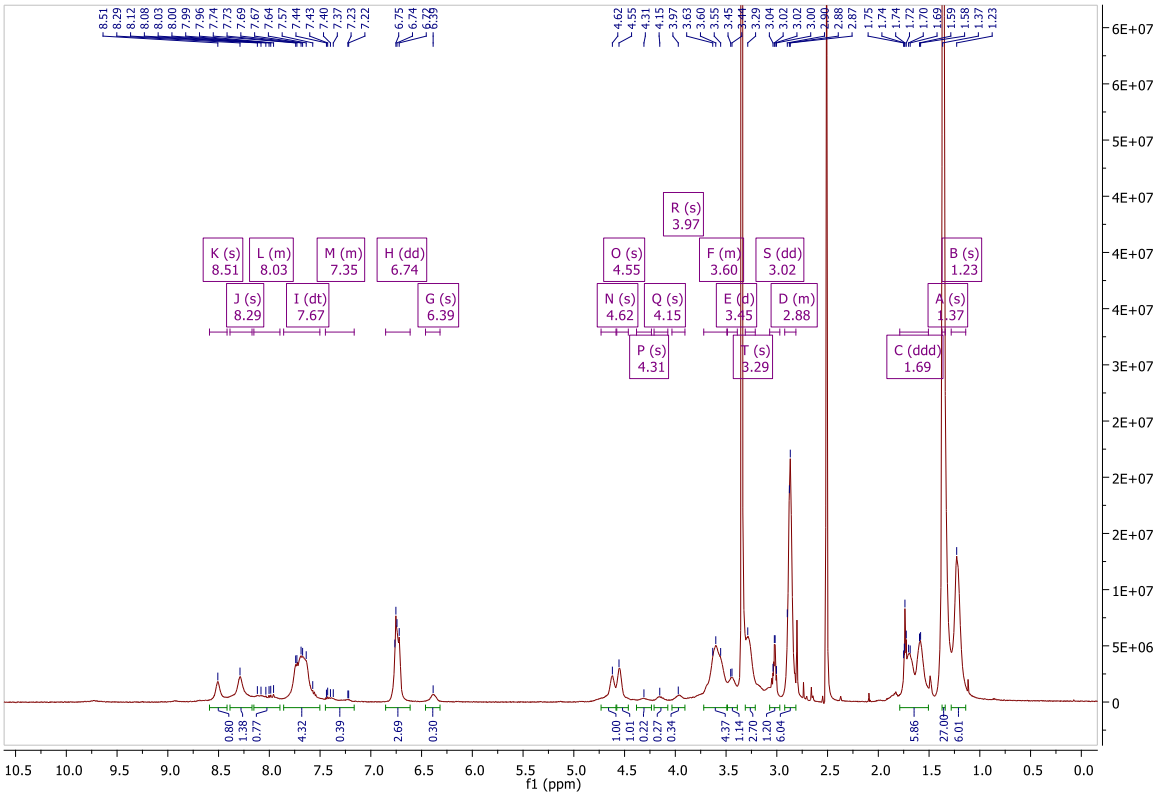

Figure A3.38: ^{1}H NMR spectrum of **Sq-3-Lys(Boc)** in DMSO-d_6.

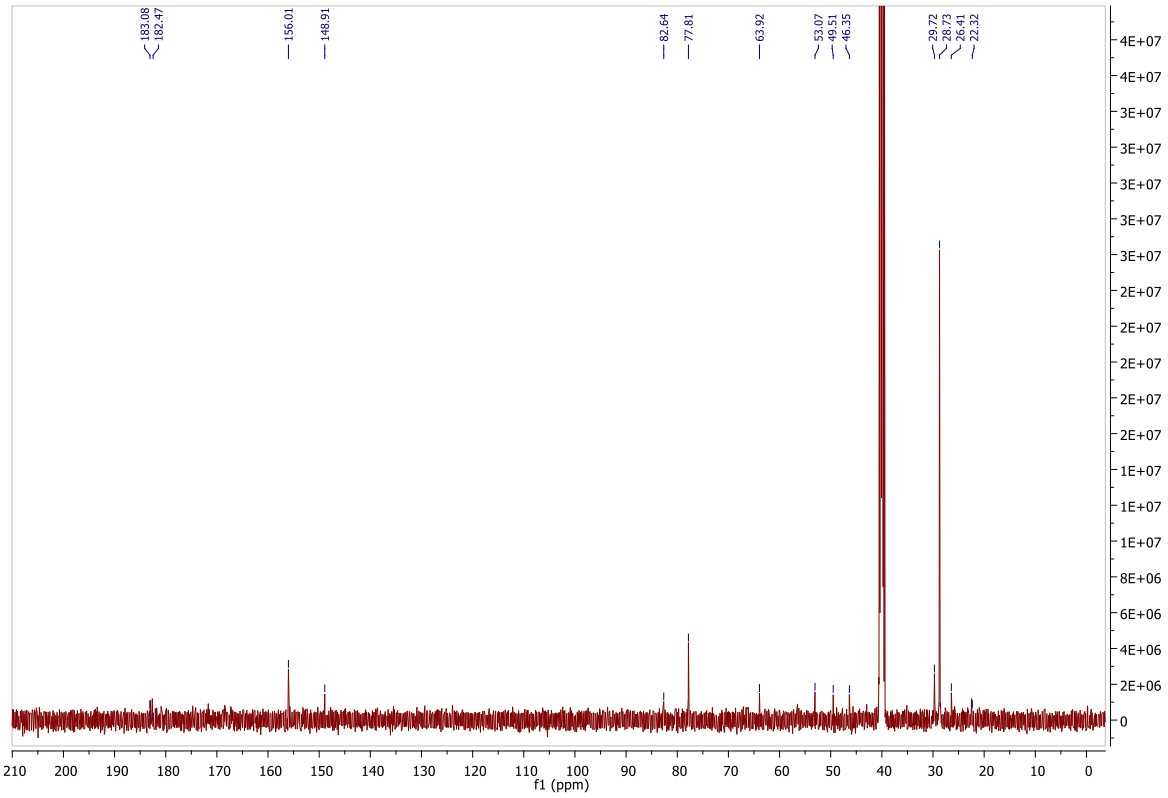

Figure A3.39: ^{13}C NMR spectrum of **Sq-3-Lys(Boc)** in DMSO-d_6.

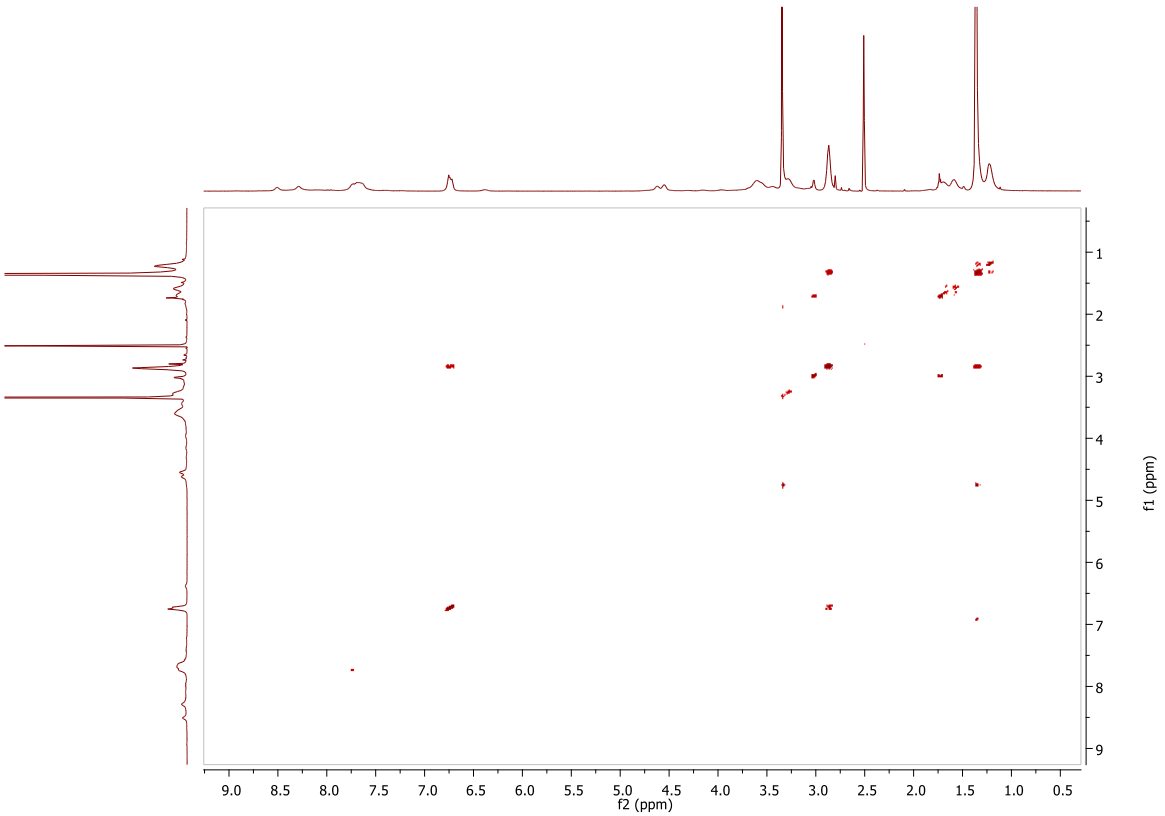

Figure A3.40: COSY spectrum of **Sq-3-Lys(Boc)** in DMSO-d_6.

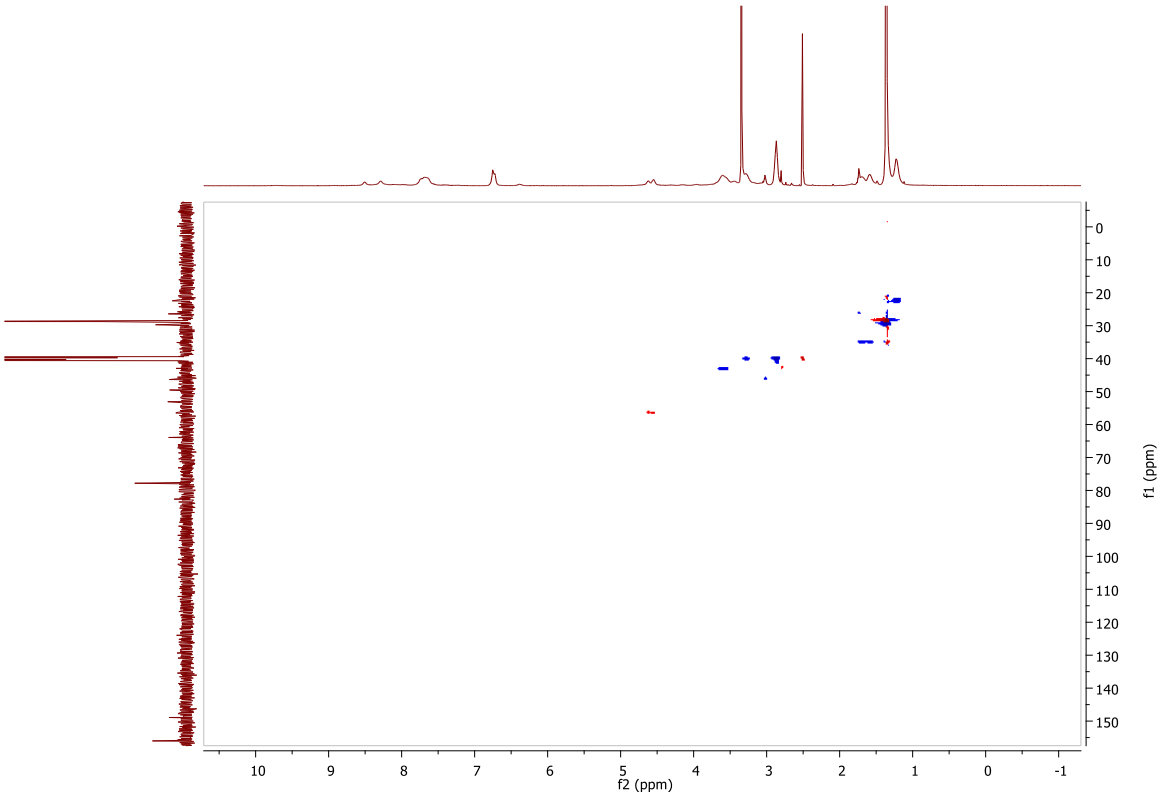

Figure A3.41: HSQC spectrum of **Sq-3-Lys(Boc)** in DMSO-d_6.

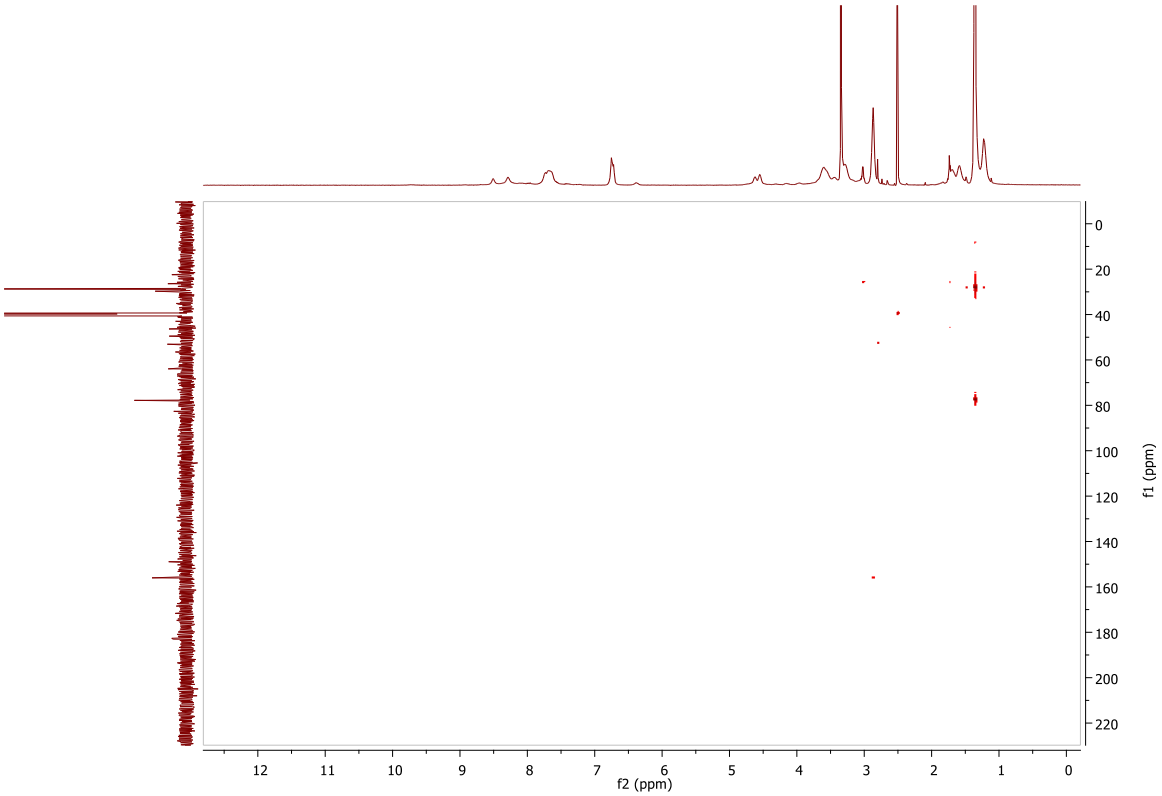

Figure A3.42: HMBC spectrum of **Sq-3-Lys(Boc)** in DMSO-d_6.

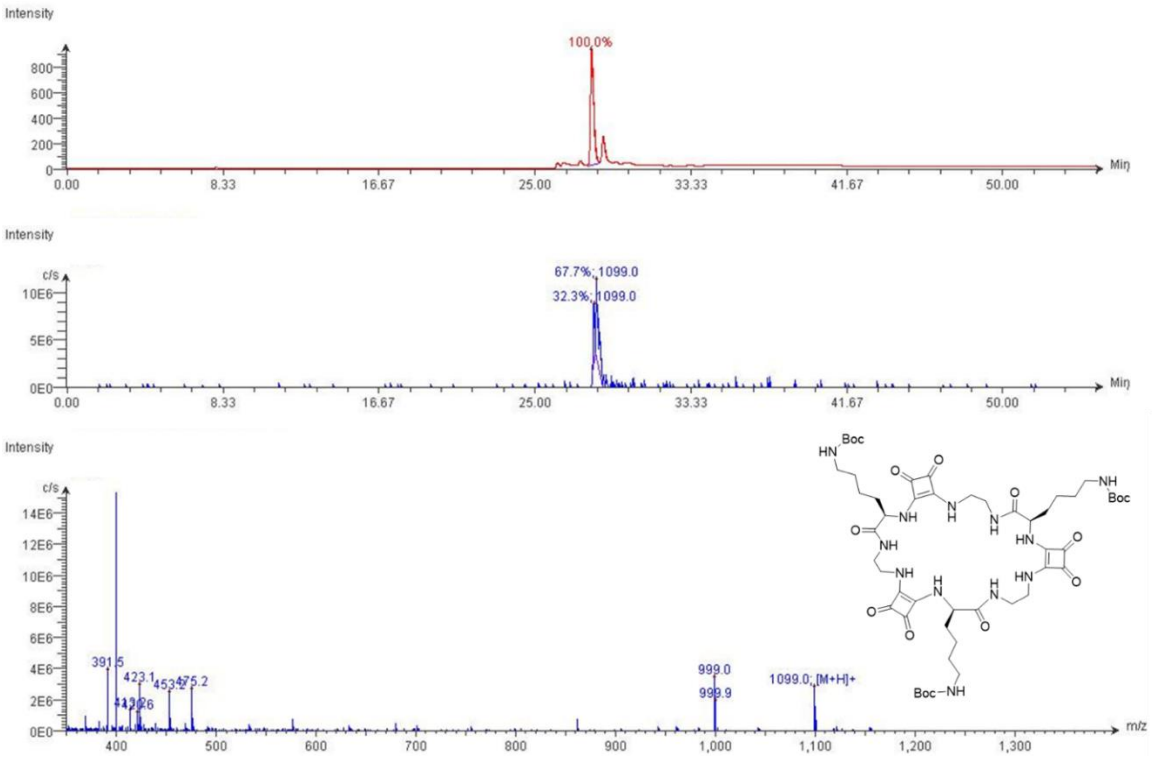

Figure A3.43: LC-MS data for **Sq-3-Lys(Boc)**.

Compound Table

Compound Label	RT (min)	Observed mass (m/z)	Neutral observed mass (Da)	Theoretical mass (Da)	Mass error (ppm)	Isotope match score (%)
Cpd 1: C51 H78 N12 O15	0.69	1121.5565	1098.5676	1098.5710	-3.06	98.41

Mass errors of between -5.00 and 5.00 ppm with isotope match scores above 60% are considered confirmation of molecular formulae

Figure: Full range view of Compound spectra and potential adducts.

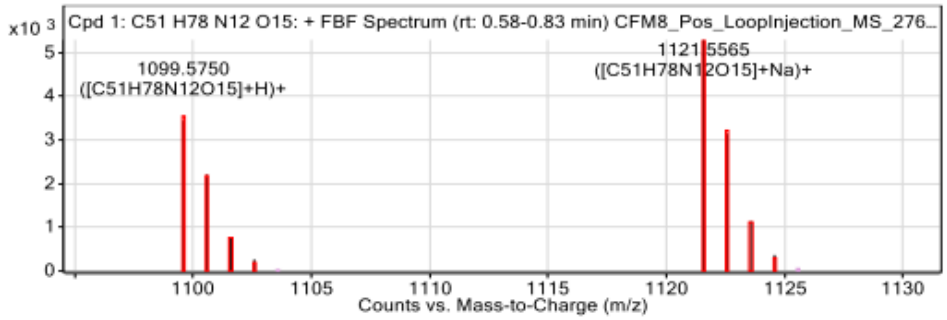

Figure: Zoomed Compound spectra view
(red boxes indicating expected theoretical isotope spacing and abundance)

Compound isotope peak List

m/z	z	Abund	Formula	Ion
1099.5750	1	3441.5	C51H78N12O15	(M+H)+
1100.5777	1	2206.1	C51H78N12O15	(M+H)+
1101.5805	1	775.9	C51H78N12O15	(M+H)+
1102.5825	1	264.9	C51H78N12O15	(M+H)+
1121.5565	1	5296.2	C51H78N12O15	(M+Na)+
1122.5599	1	3144.3	C51H78N12O15	(M+Na)+
1123.5630	1	1138.4	C51H78N12O15	(M+Na)+
1124.5669	1	368.3	C51H78N12O15	(M+Na)+

Figure A3.44: HRMS data for **Sq-3-Lys(Boc)**.

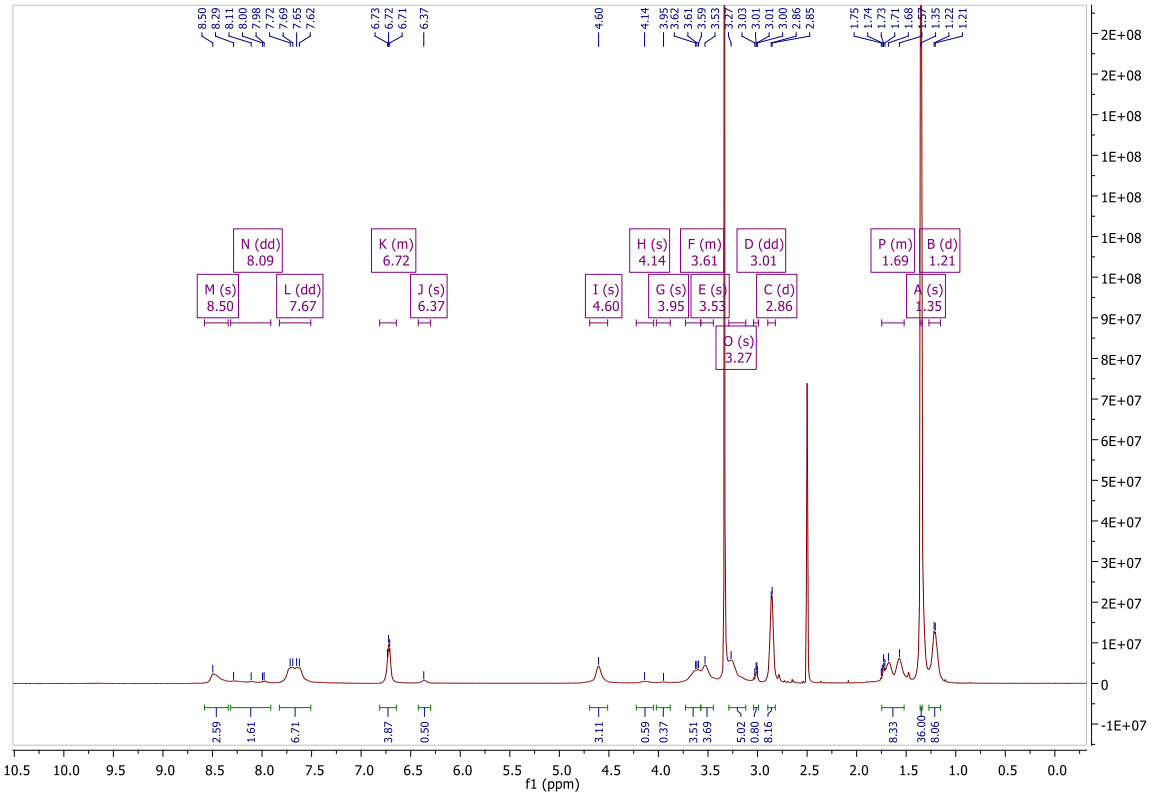

Figure A3.45: ^{1}H NMR spectrum of **Sq-4-Lys(Boc)** in DMSO-d_6.

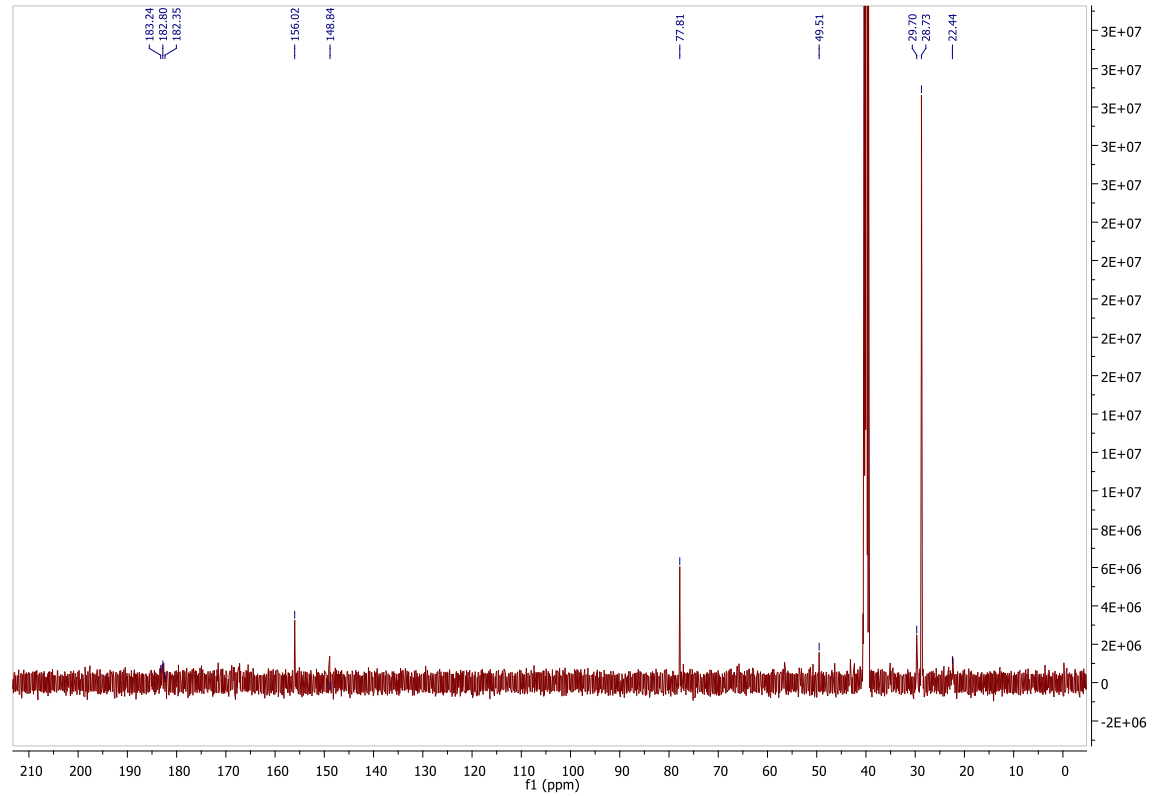

Figure A3.46: ^{13}C NMR spectrum of **Sq-4-Lys(Boc)** in DMSO-d_6.

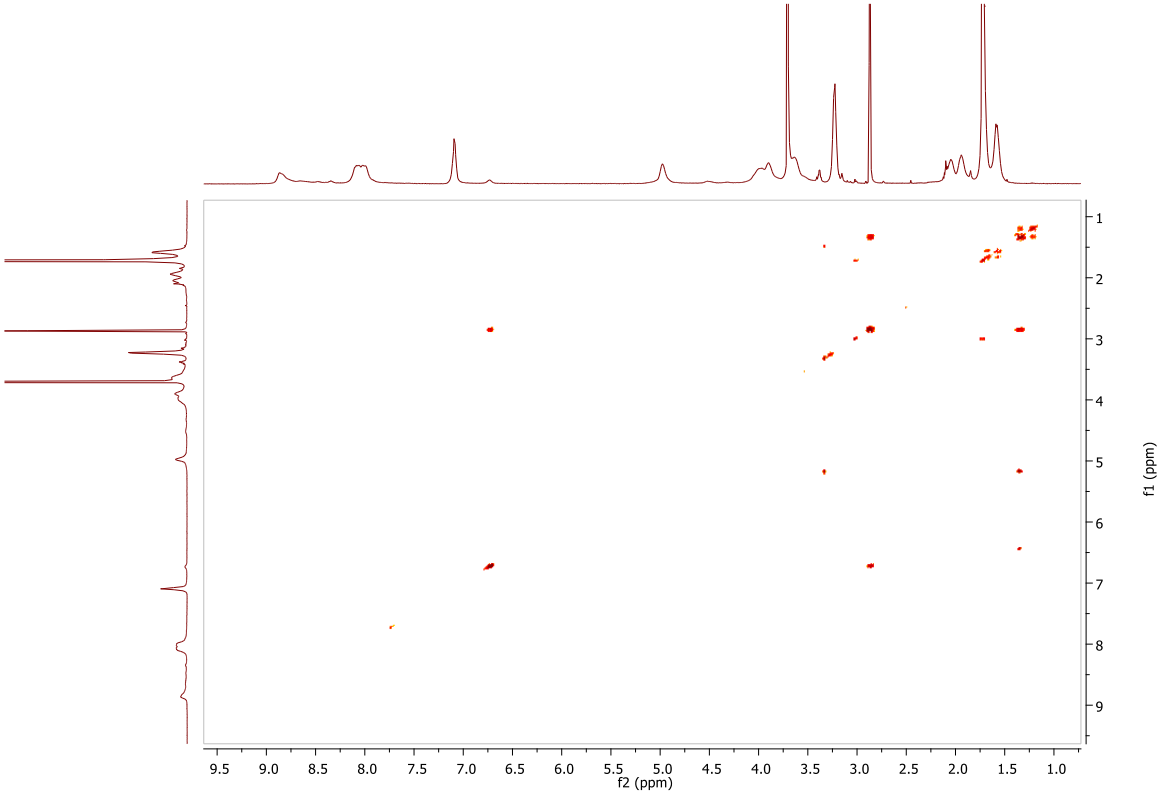

Figure A3.47: COSY spectrum of **Sq-4-Lys(Boc)** in DMSO-d_6.

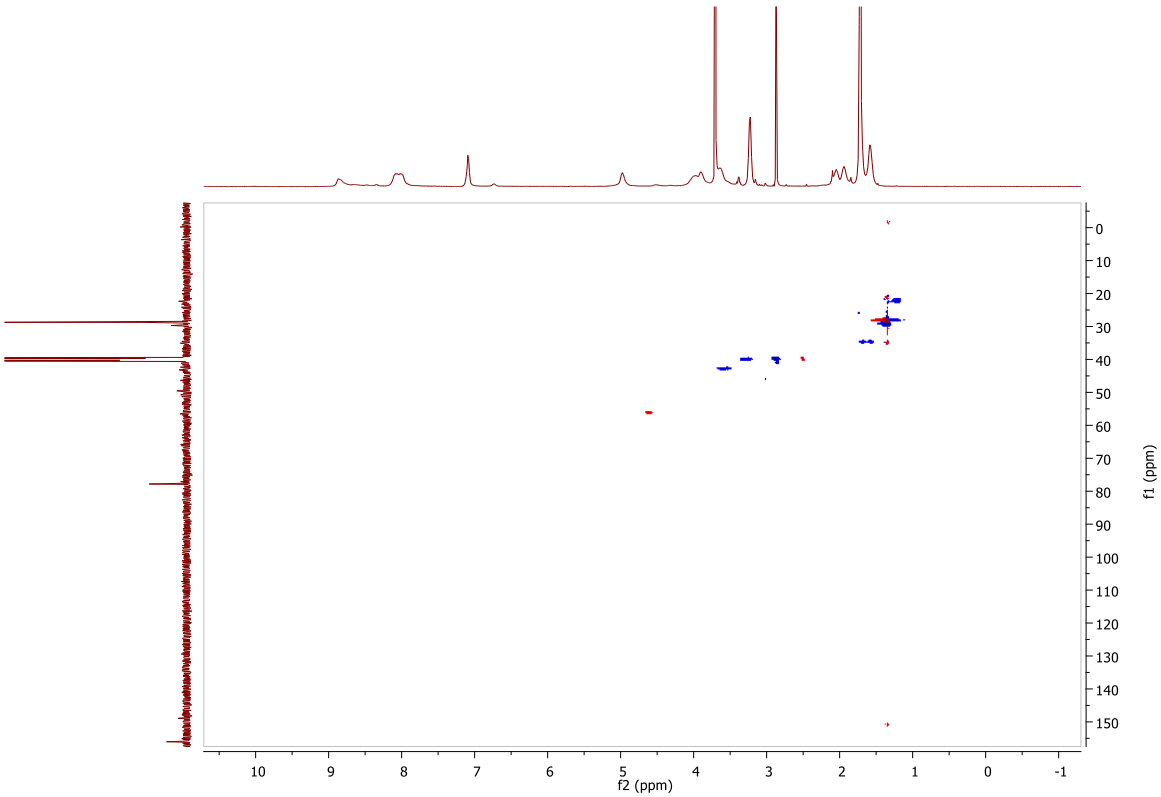

Figure A3.48: HSQC spectrum of **Sq-4-Lys(Boc)** in DMSO-d_6.

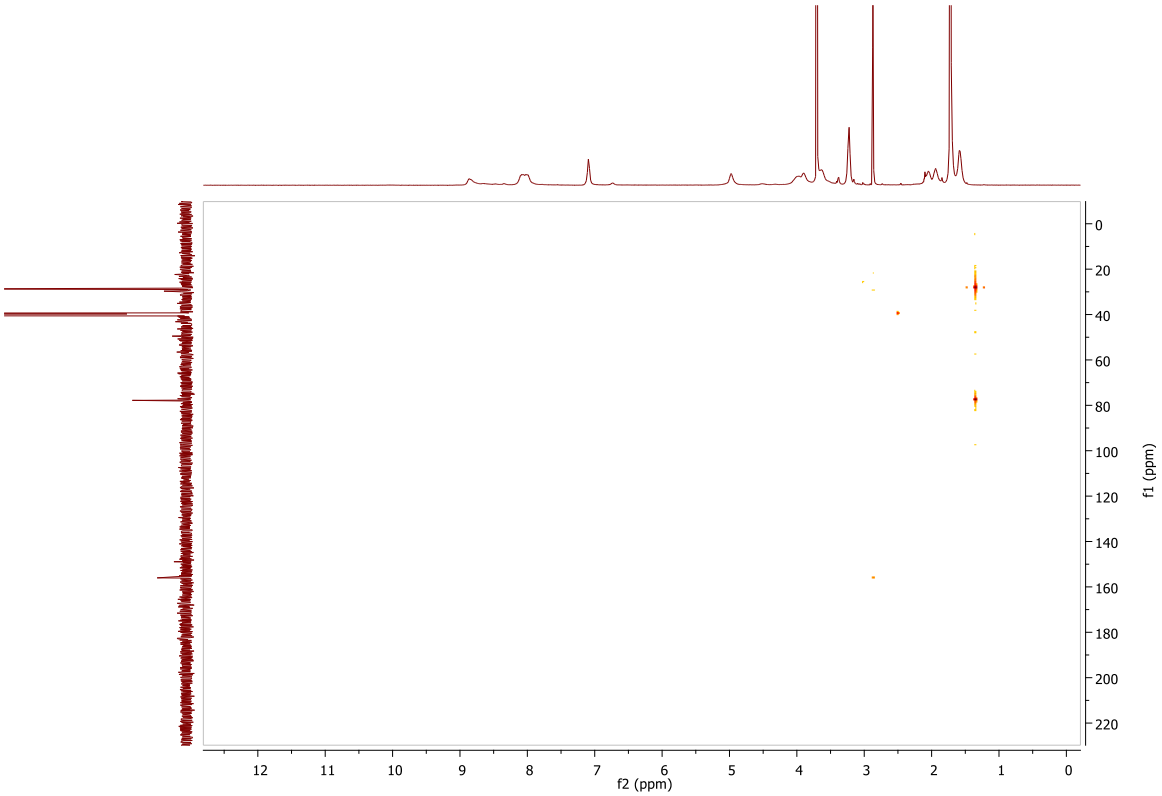

Figure A3.49: HMBC spectrum of **Sq-4-Lys(Boc)** in DMSO-d_6.

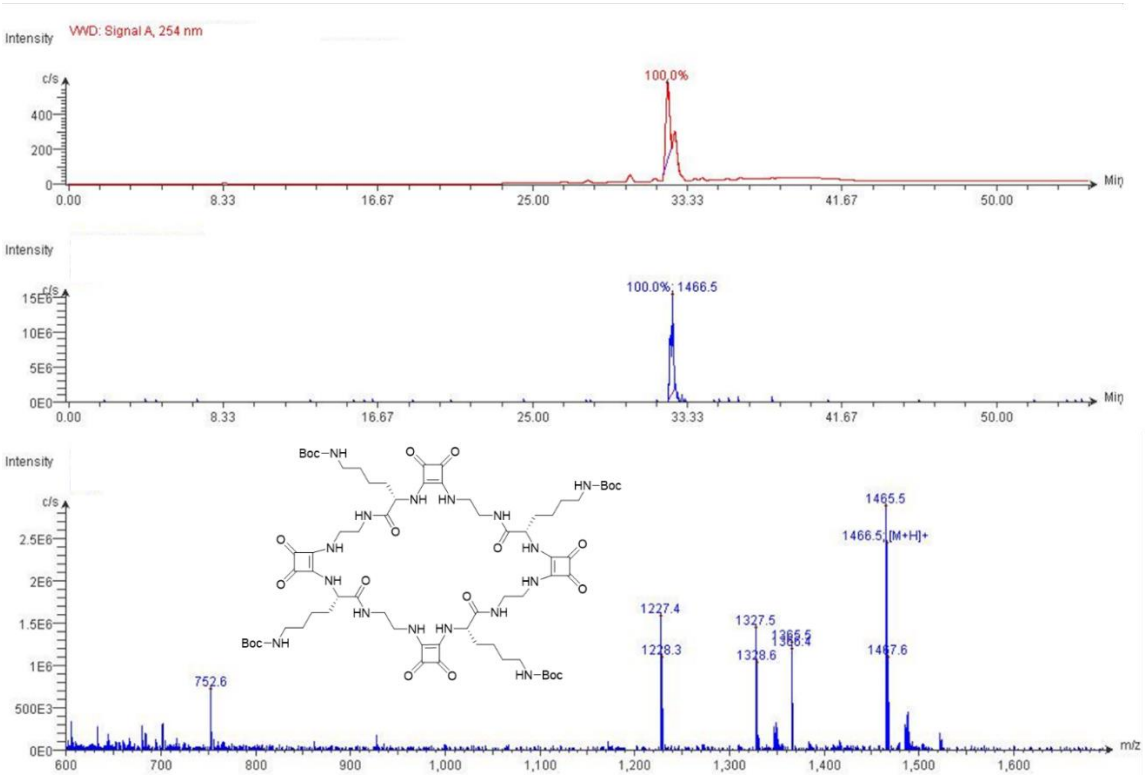

Figure A3.50: LC-MS data for **Sq-4-Lys(Boc)**.

Compound Table

Compound Label	RT (min)	Observed mass (m/z)	Neutral observed mass (Da)	Theoretical mass (Da)	Mass error (ppm)	Isotope match score (%)
Cpd 1: C68 H104 N16 O20	0.74	755.3687	1464.7596	1464.7613	-1.17	94.98

Mass errors of between -5.00 and 5.00 ppm with isotope match scores above 60% are considered confirmation of molecular formulae

Figure: Extracted ion chromatogram (EIC) of compound.

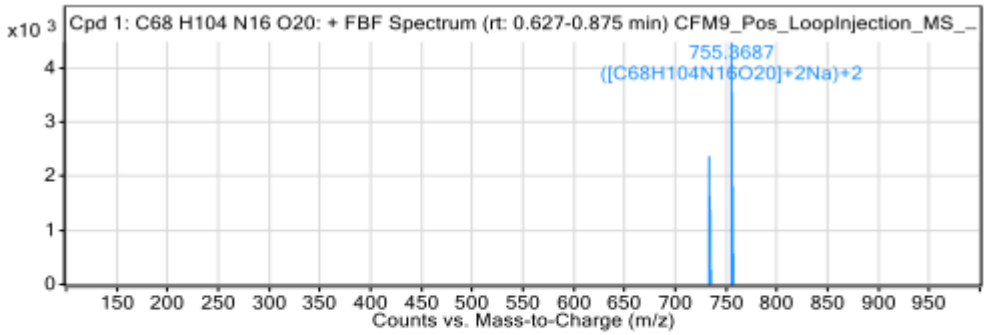

Figure: Full range view of Compound spectra and potential adducts.

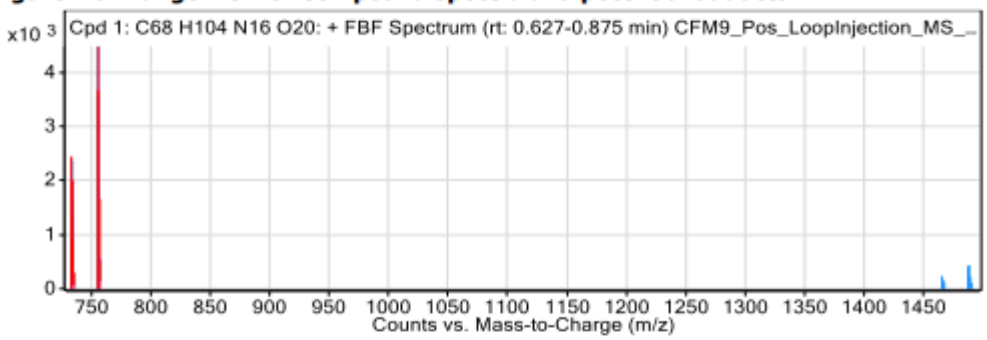

Figure: Zoomed Compound spectra view
(red boxes indicating expected theoretical isotope spacing and abundance)

Compound isotope peak List

m/z	z	Abund	Formula	Ion
733.3863	2	2372.3	C68H104N16O20	(M+2H)+2
733.8885	2	1634.4	C68H104N16O20	(M+2H)+2
734.3942	2	1376.8	C68H104N16O20	(M+2H)+2
755.3687	2	4482.0	C68H104N16O20	(M+2Na)+2
755.8700	2	3551.5	C68H104N16O20	(M+2Na)+2
756.3728	2	1811.0	C68H104N16O20	(M+2Na)+2
756.8719	2	567.3	C68H104N16O20	(M+2Na)+2
1465.7645	1	235.9	C68H104N16O20	(M+H)+
1487.7461	1	415.5	C68H104N16O20	(M+Na)+
1488.7489	1	437.5	C68H104N16O20	(M+Na)+

Figure A3.51: HRMS data for **Sq-4-Lys(Boc)**.

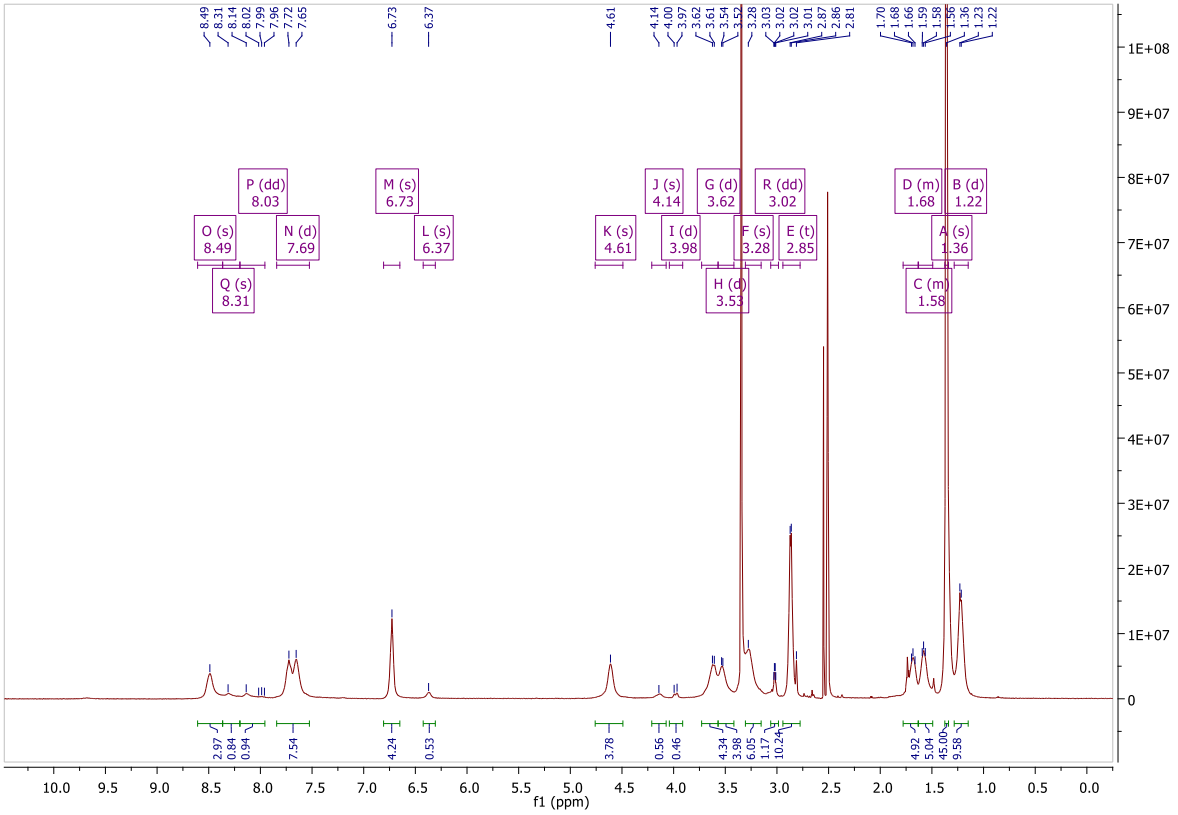

Figure A3.52: ^{1}H NMR spectrum of **Sq-5-Lys(Boc)** in DMSO-d_6.

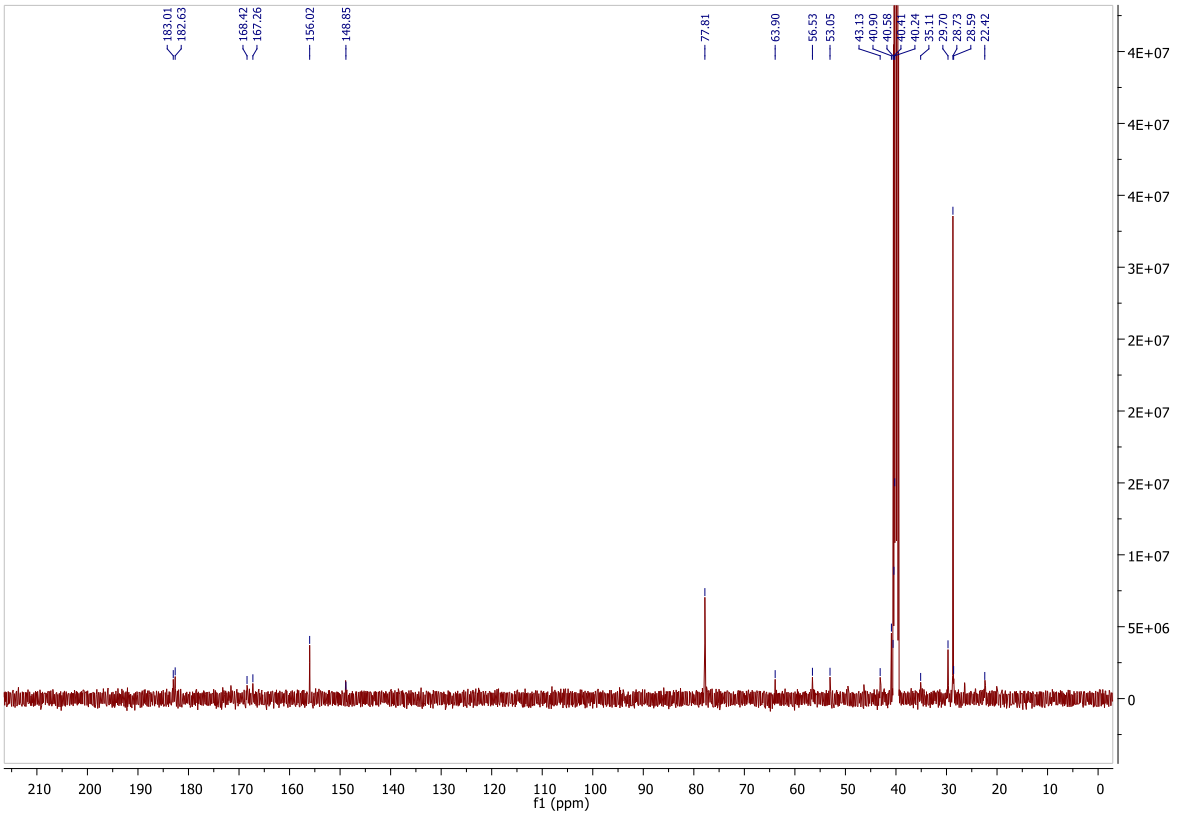

Figure A3.53: ^{13}C NMR spectrum of **Sq-5-Lys(Boc)** in DMSO-d_6.

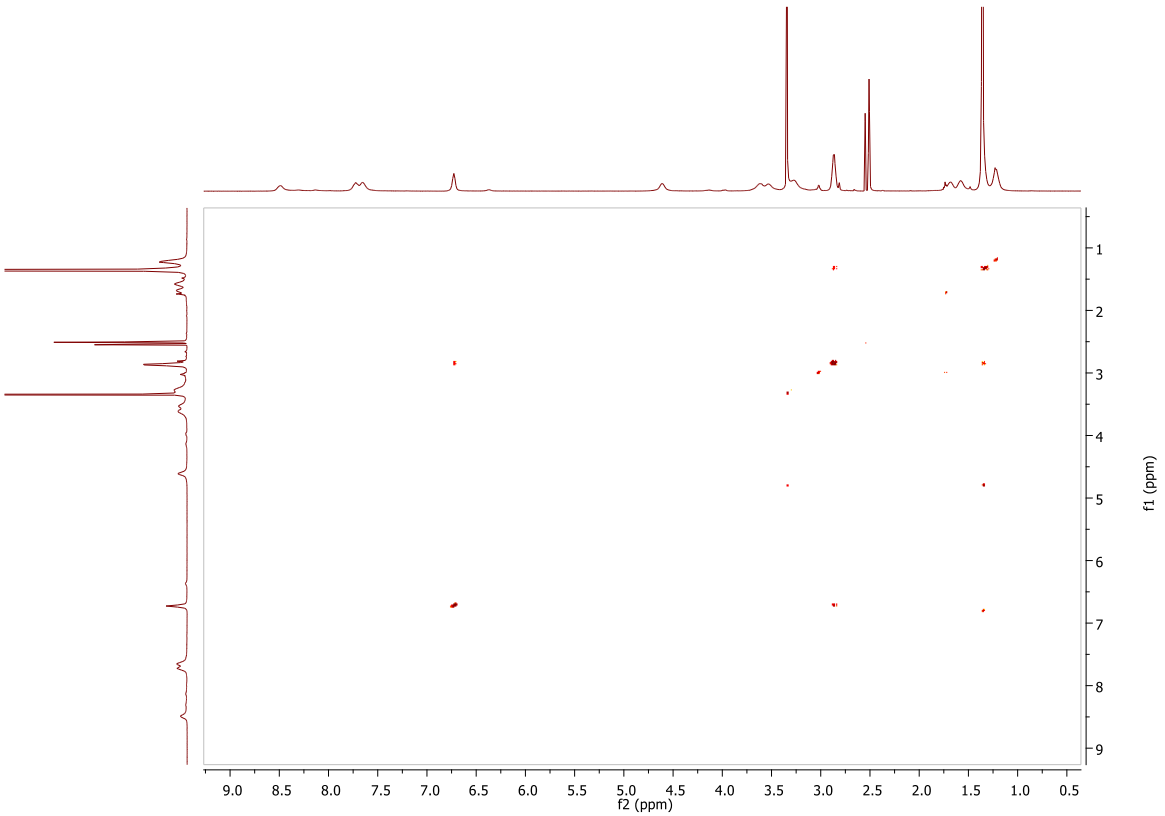

Figure A3.54: COSY spectrum of **Sq-5-Lys(Boc)** in DMSO-d_6.

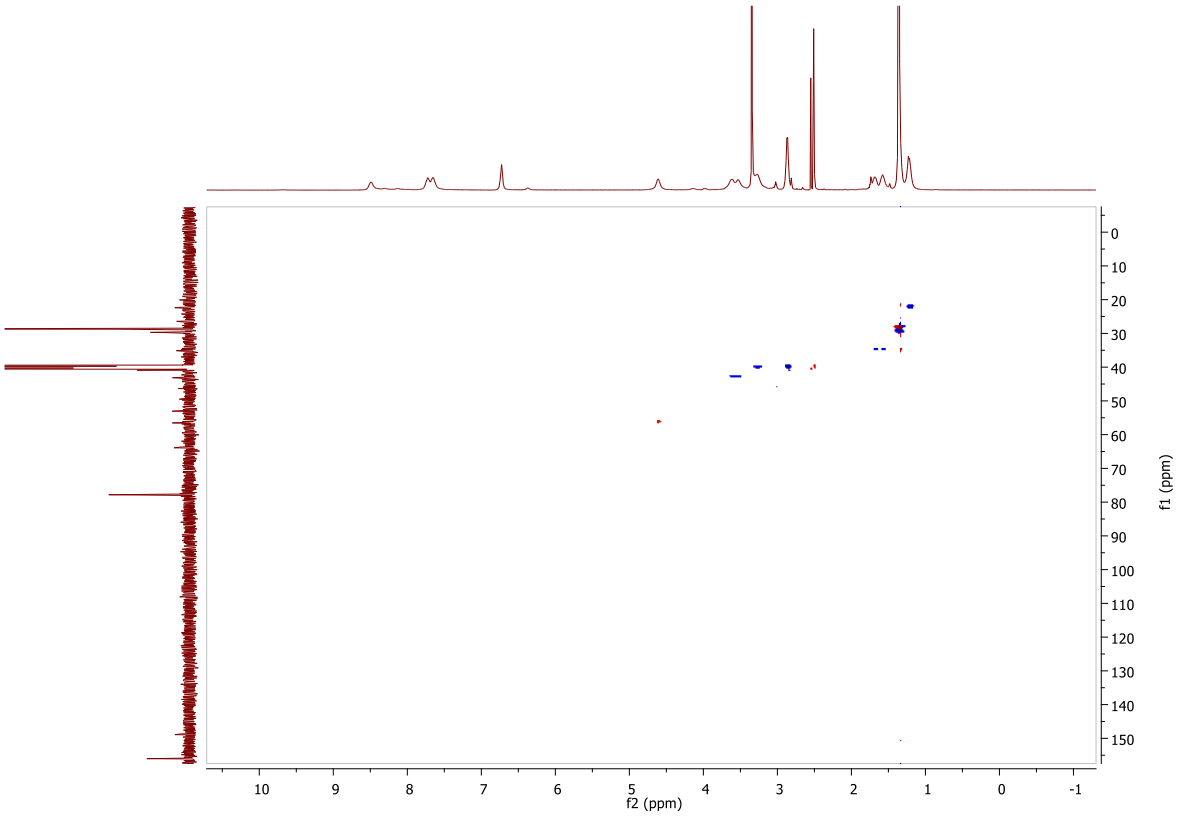

Figure A3.55: HSQC spectrum of **Sq-5-Lys(Boc)** in DMSO-d_6.

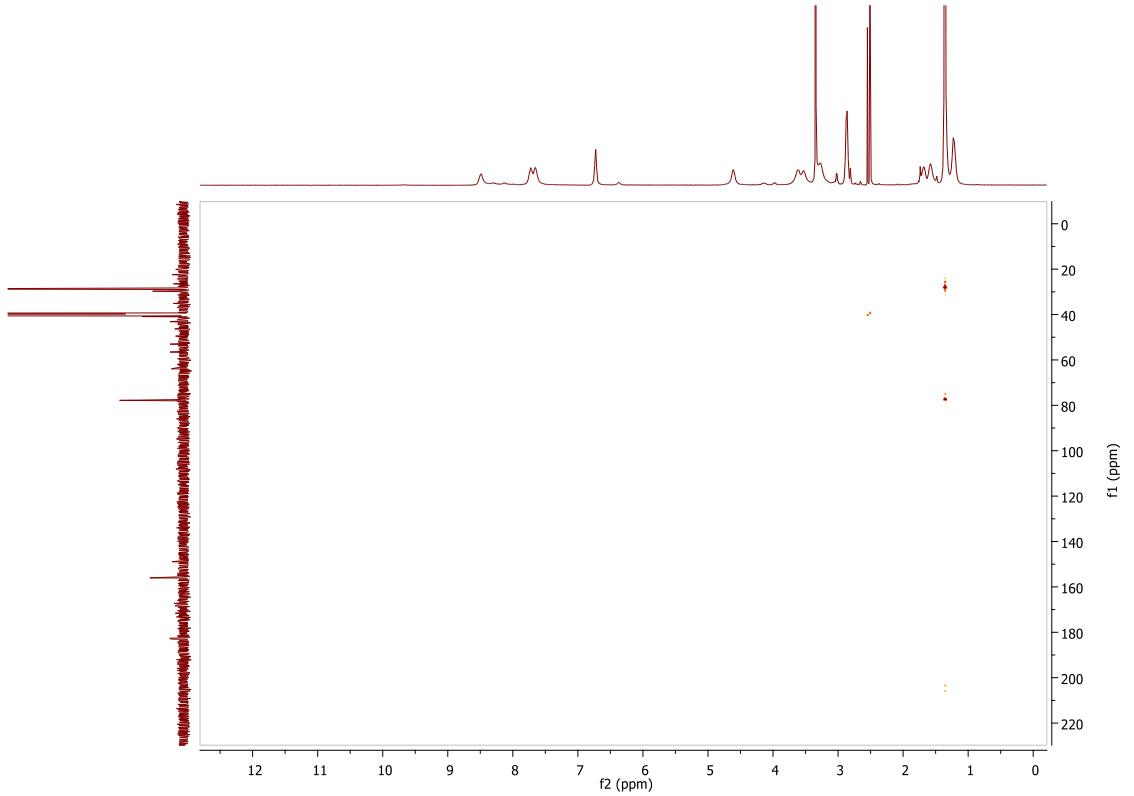

Figure A3.56: HMBC spectrum of **Sq-5-Lys(Boc)** in DMSO-d_6.

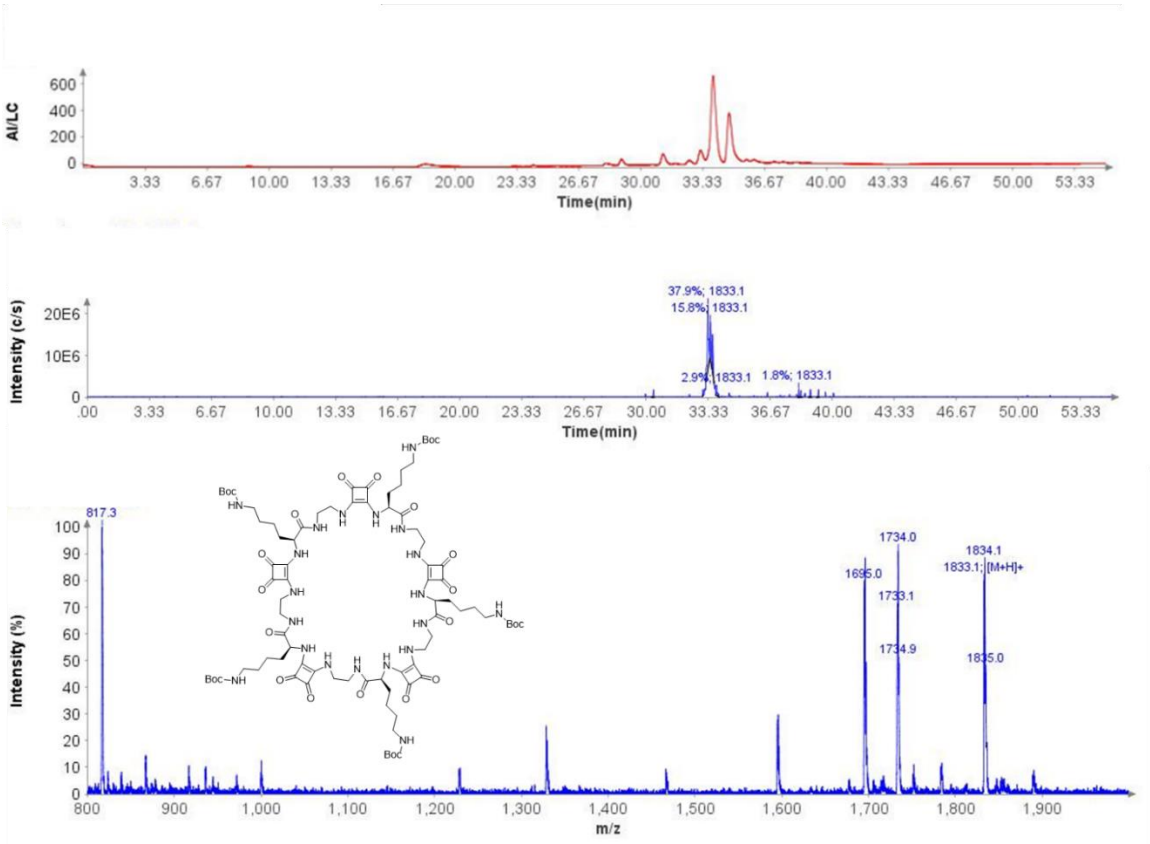

Figure A3.57: LC-MS data for **Sq-5-Lys(Boc)**.

Compound Table

Compound Label	RT (min)	Observed mass (m/z)	Neutral observed mass (Da)	Theoretical mass (Da)	Mass error (ppm)	Isotope match score (%)
Cpd 1: C85 H130 N20 O25	0.70	916.4820	1830.9473	1830.9516	-2.35	91.12

Mass errors of between -5.00 and 5.00 ppm with isotope match scores above 60% are considered confirmation of molecular formulae

Figure: Full range view of Compound spectra and potential adducts.

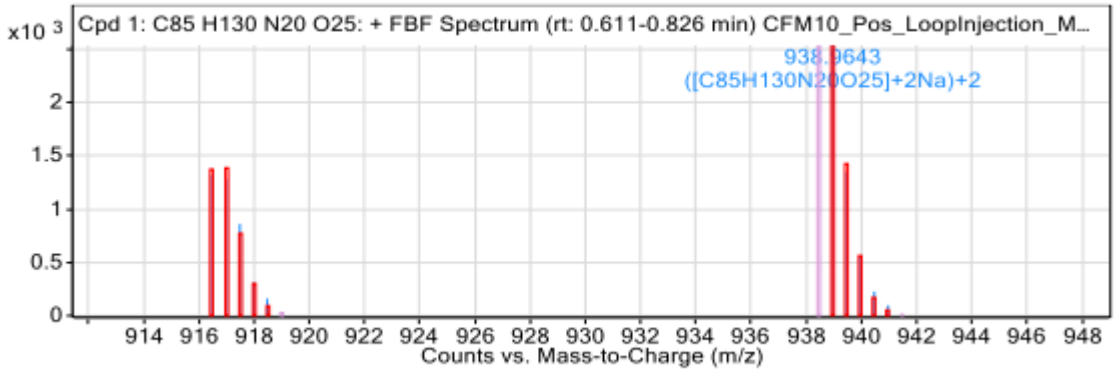

Figure: Zoomed Compound spectra view
(red boxes indicating expected theoretical isotope spacing and abundance)

Compound isotope peak List

m/z	z	Abund	Formula	Ion
916.4820	2	1320.3	C85H130N20O25	(M+2H)+2
916.9825	2	1283.7	C85H130N20O25	(M+2H)+2
917.4850	2	861.2	C85H130N20O25	(M+2H)+2
917.9873	2	311.2	C85H130N20O25	(M+2H)+2
918.4757	2	160.1	C85H130N20O25	(M+2H)+2
938.9643	2	2539.9	C85H130N20O25	(M+2Na)+2
939.4654	2	1345.8	C85H130N20O25	(M+2Na)+2
939.9661	2	560.4	C85H130N20O25	(M+2Na)+2
940.4673	2	227.3	C85H130N20O25	(M+2Na)+2
940.9681	2	98.0	C85H130N20O25	(M+2Na)+2

Figure A3.58: HRMS data for **Sq-5-Lys(Boc)**.

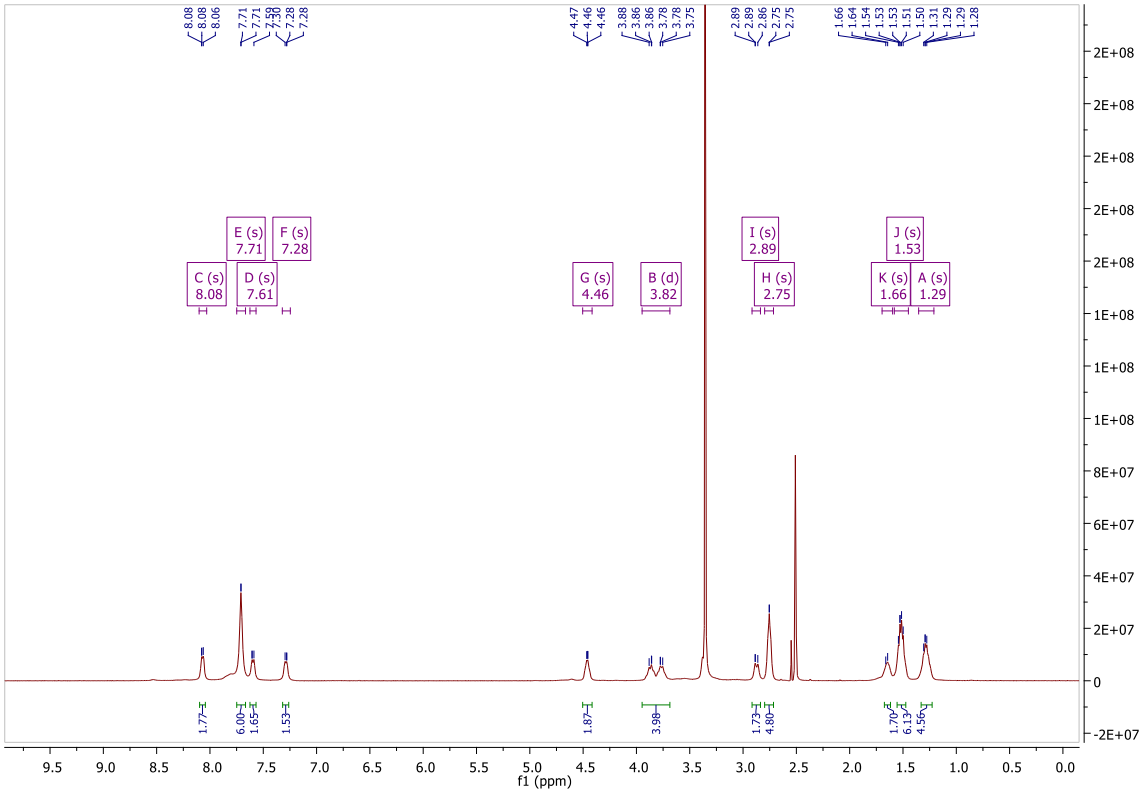

Figure A3.59: ^{1}H NMR spectrum of **2.17 (Sq-2-Lys)** in DMSO-d_6.

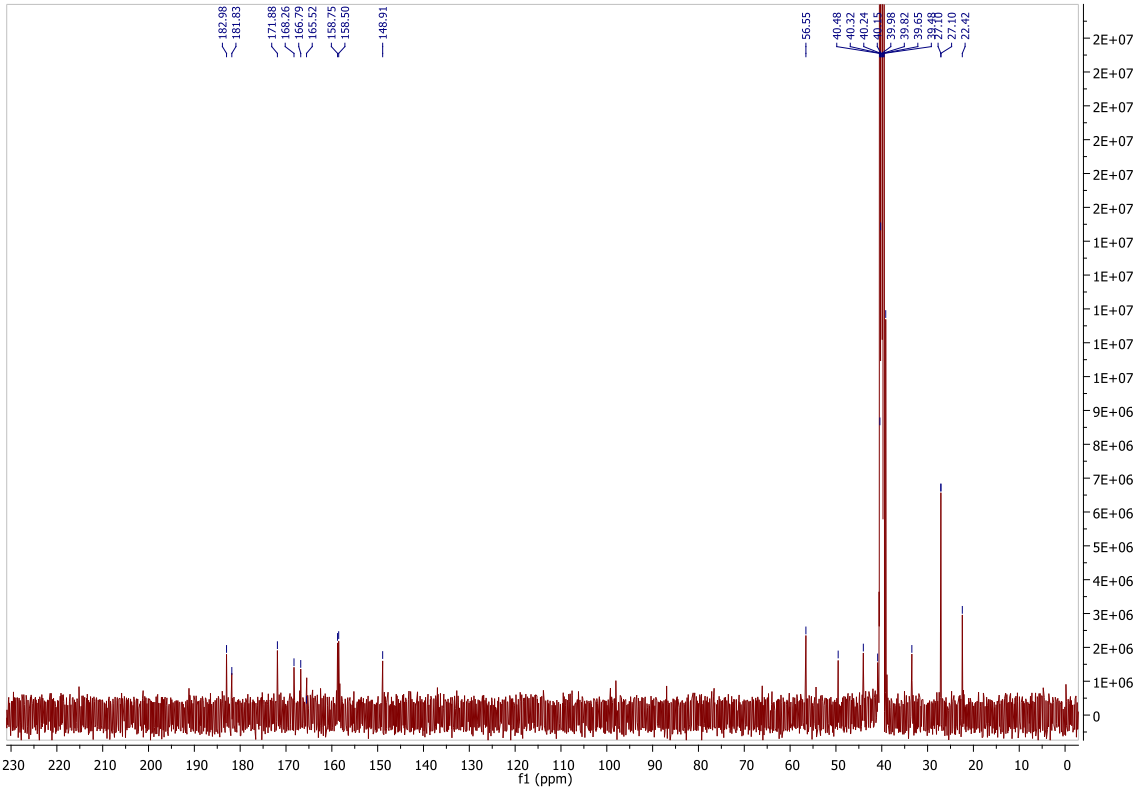

Figure A3.60: ^{13}C NMR spectrum of **2.17 (Sq-2-Lys)** in DMSO-d_6.

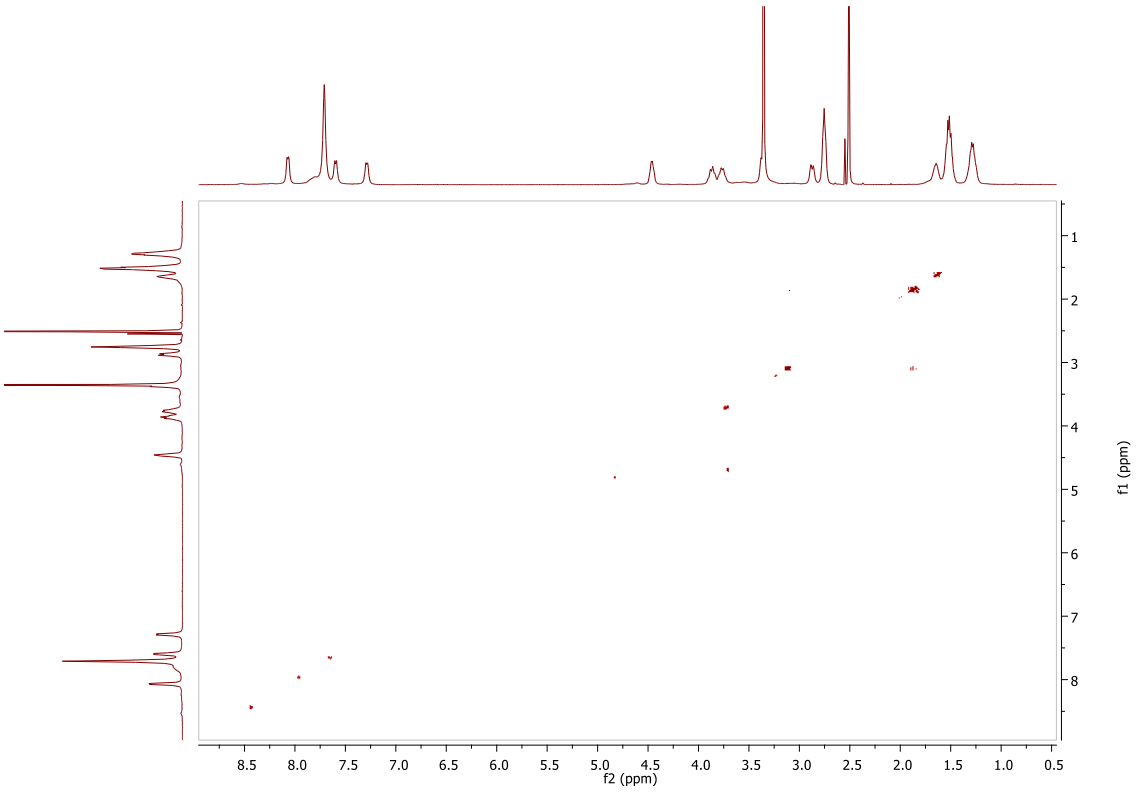

Figure A3.61: COSY spectrum of **2.17 (Sq-2-Lys)** in DMSO-d_6.

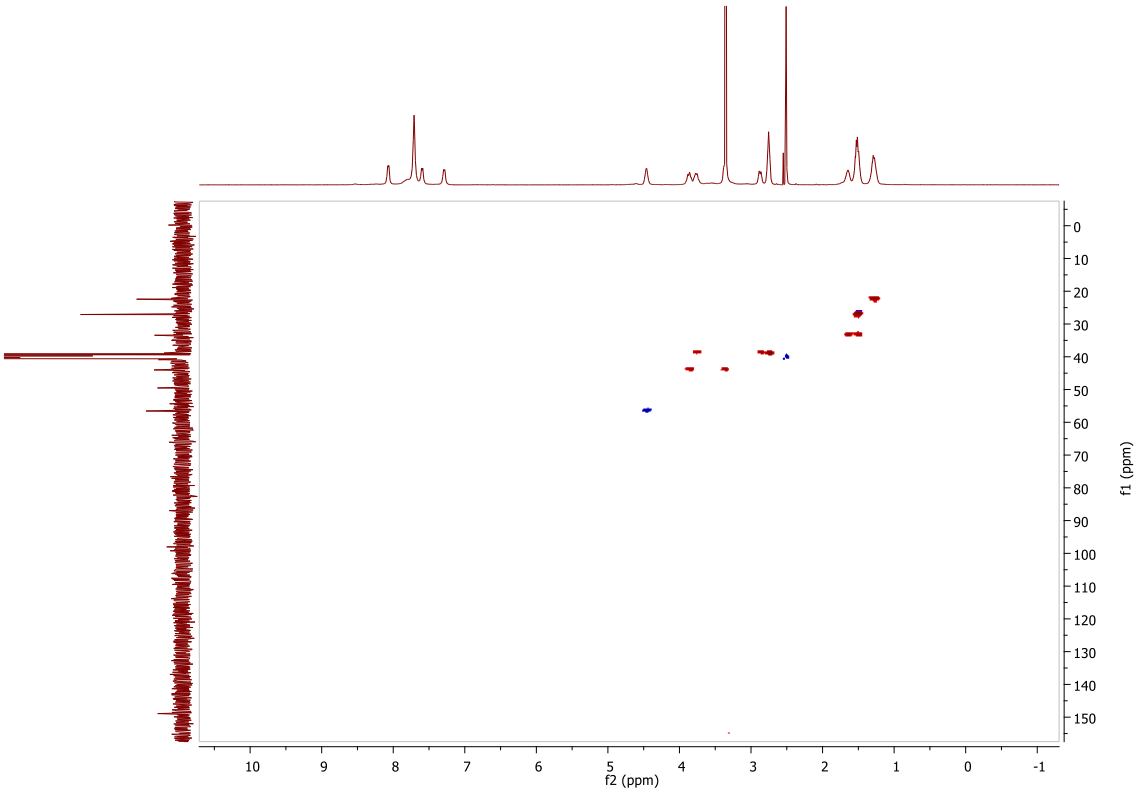

Figure A3.62: HSQC spectrum of **2.17 (Sq-2-Lys)** in DMSO-d_6.

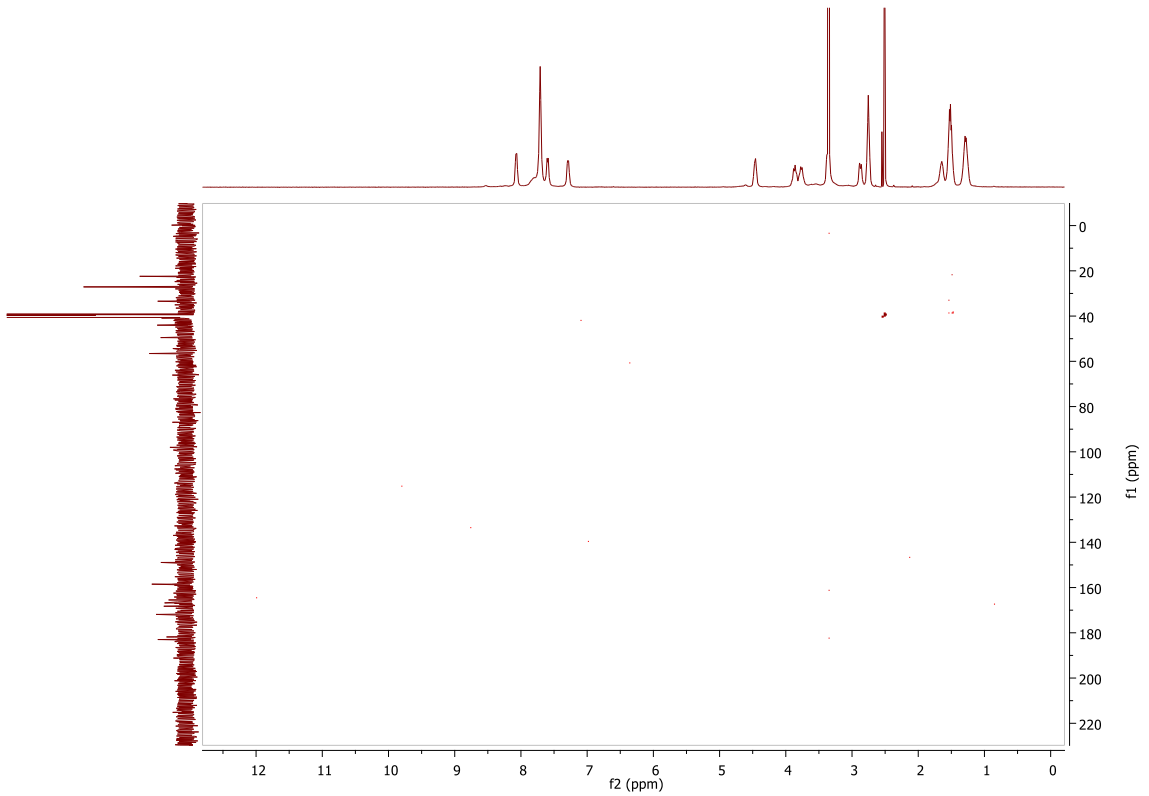

Figure A3.63: HMBC spectrum of **2.17 (Sq-2-Lys)** in DMSO-d_6.

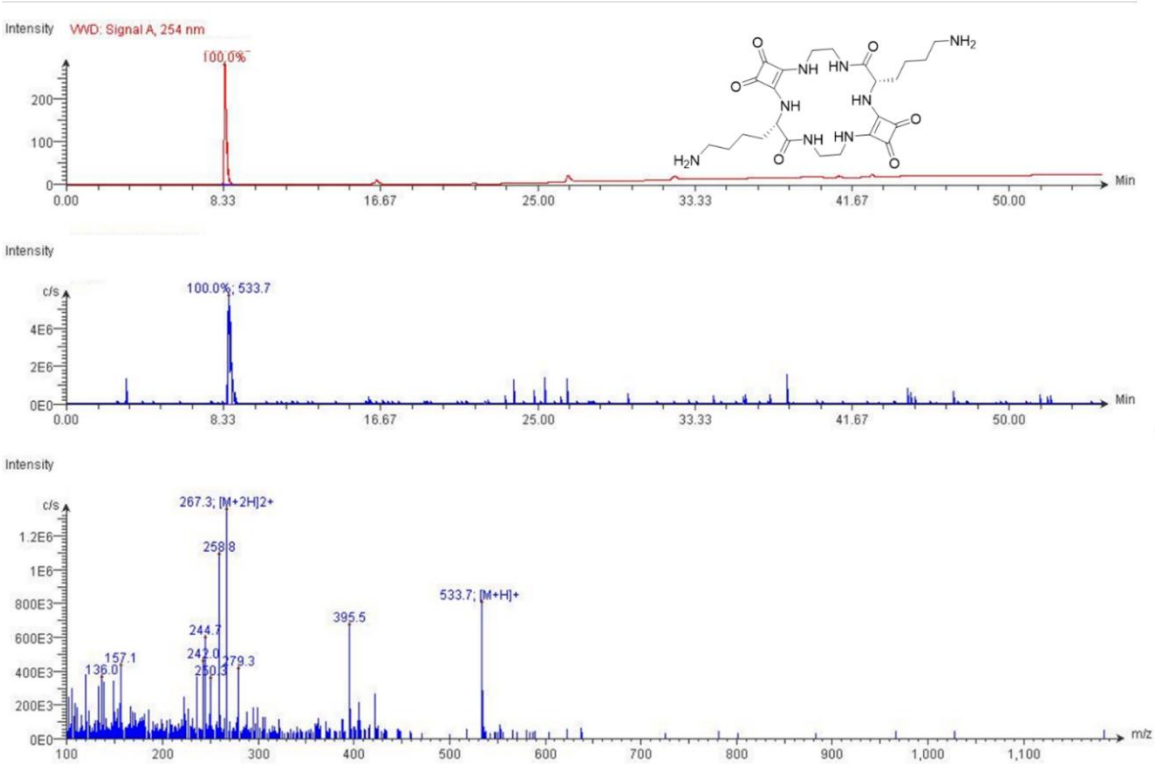

Figure A3.64: LC-MS data for **2.17 (Sq-2-Lys)**.

Compound Table

Compound Label	RT (min)	Observed mass (m/z)	Neutral observed mass (Da)	Theoretical mass (Da)	Mass error (ppm)	Isotope match score (%)
Cpd 1: C24 H36 N8 O6	0.75	533.2828	532.2756	532.2758	-0.33	98.94

Mass errors of between -5.00 and 5.00 ppm with isotope match scores above 60% are considered confirmation of molecular formulae

Figure: Extracted ion chromatogram (EIC) of compound.

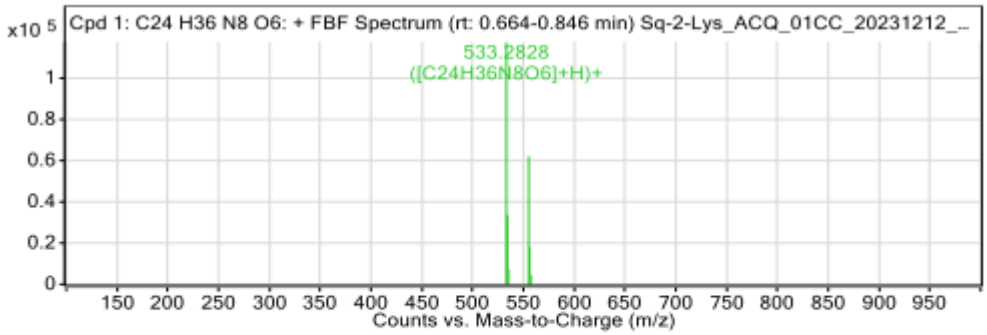

Figure: Full range view of Compound spectra and potential adducts.

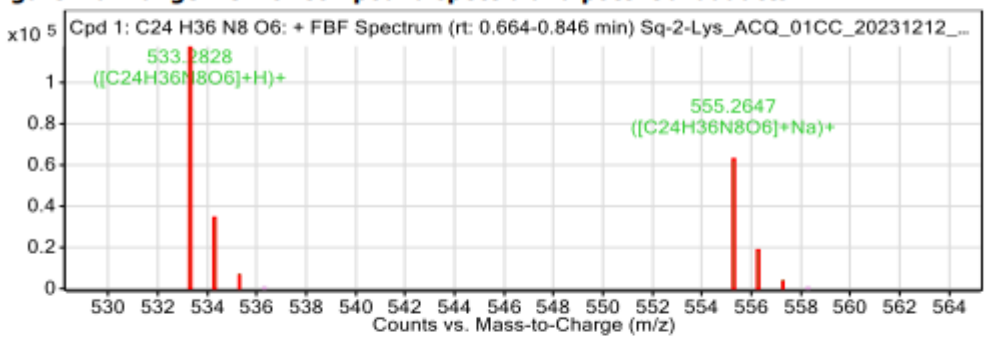

Figure: Zoomed Compound spectra view
(red boxes indicating expected theoretical isotope spacing and abundance)

Compound isotope peak List

m/z	z	Abund	Formula	Ion
533.2828	1	117360.2	C24H36N8O6	(M+H)+
534.2856	1	33513.8	C24H36N8O6	(M+H)+
535.2884	1	7453.1	C24H36N8O6	(M+H)+
555.2647	1	61934.6	C24H36N8O6	(M+Na)+
556.2677	1	18164.1	C24H36N8O6	(M+Na)+
557.2744	1	4436.2	C24H36N8O6	(M+Na)+

Figure A3.65: HRMS data for **2.17 (Sq-2-Lys)**.

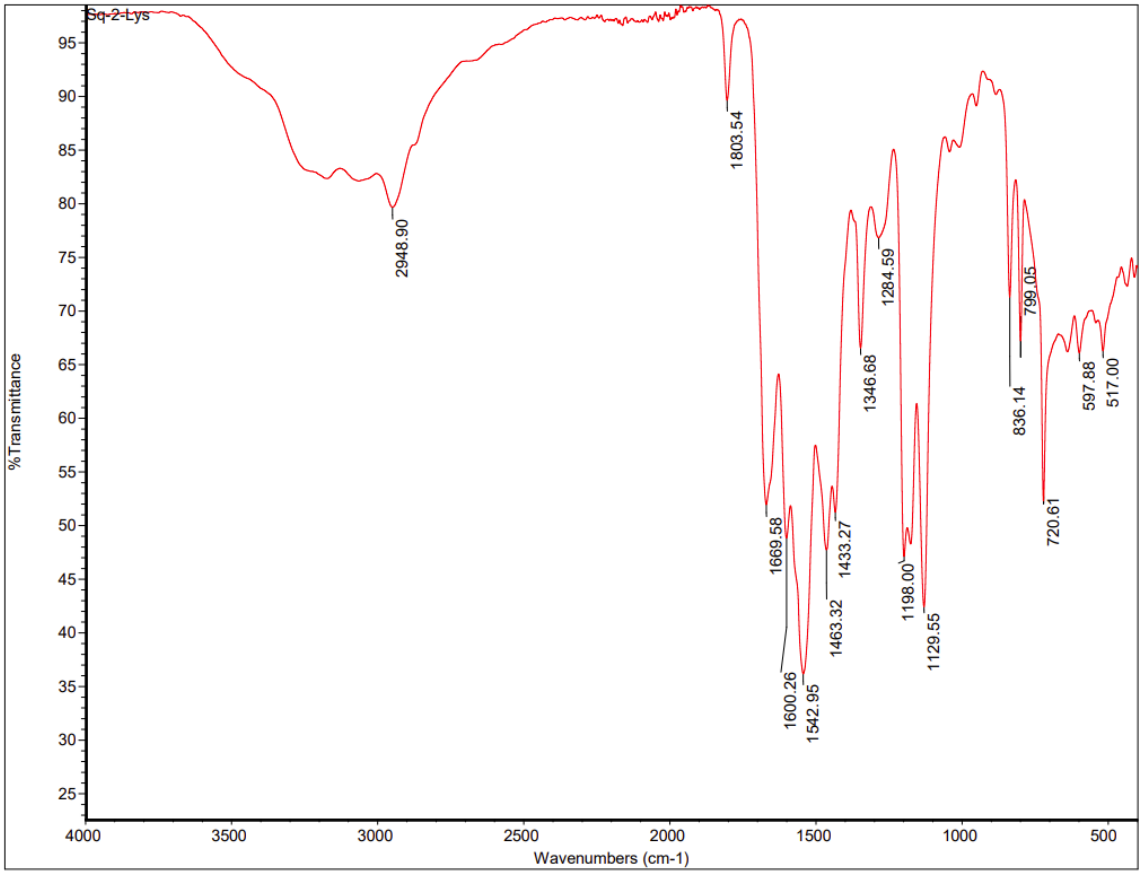

Figure A3.66: IR spectrum of **2.17 (Sq-2-Lys)**

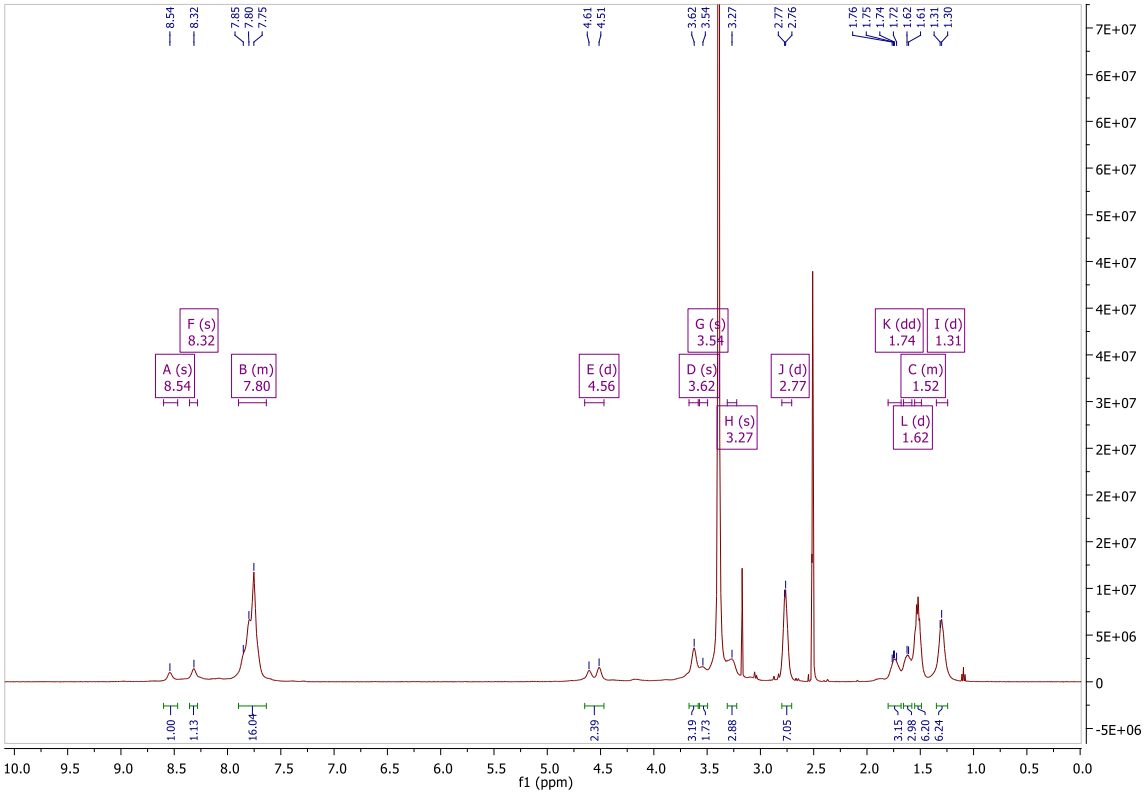

Figure A3.67: ^{1}H NMR spectrum of **3.5 (Sq-3-Lys)** in DMSO-d_6.

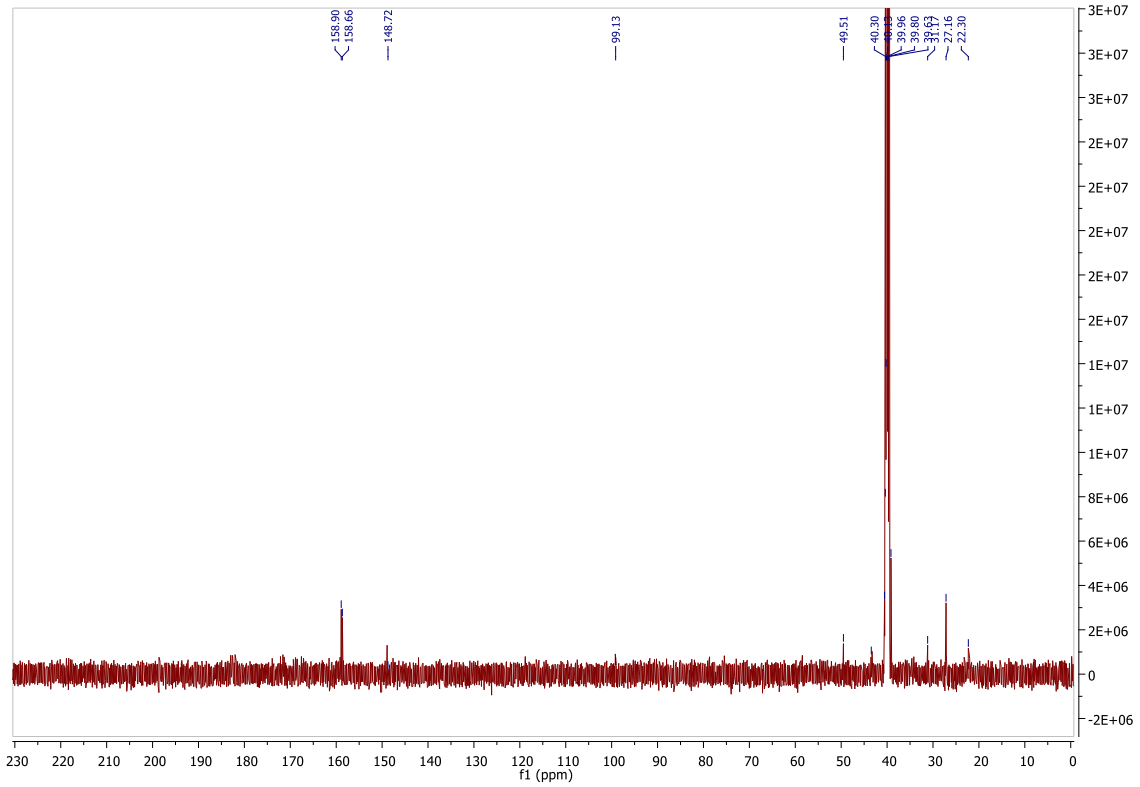

Figure A3.68: ^{13}C NMR spectrum of **3.5 (Sq-3-Lys)** in DMSO-d_6.

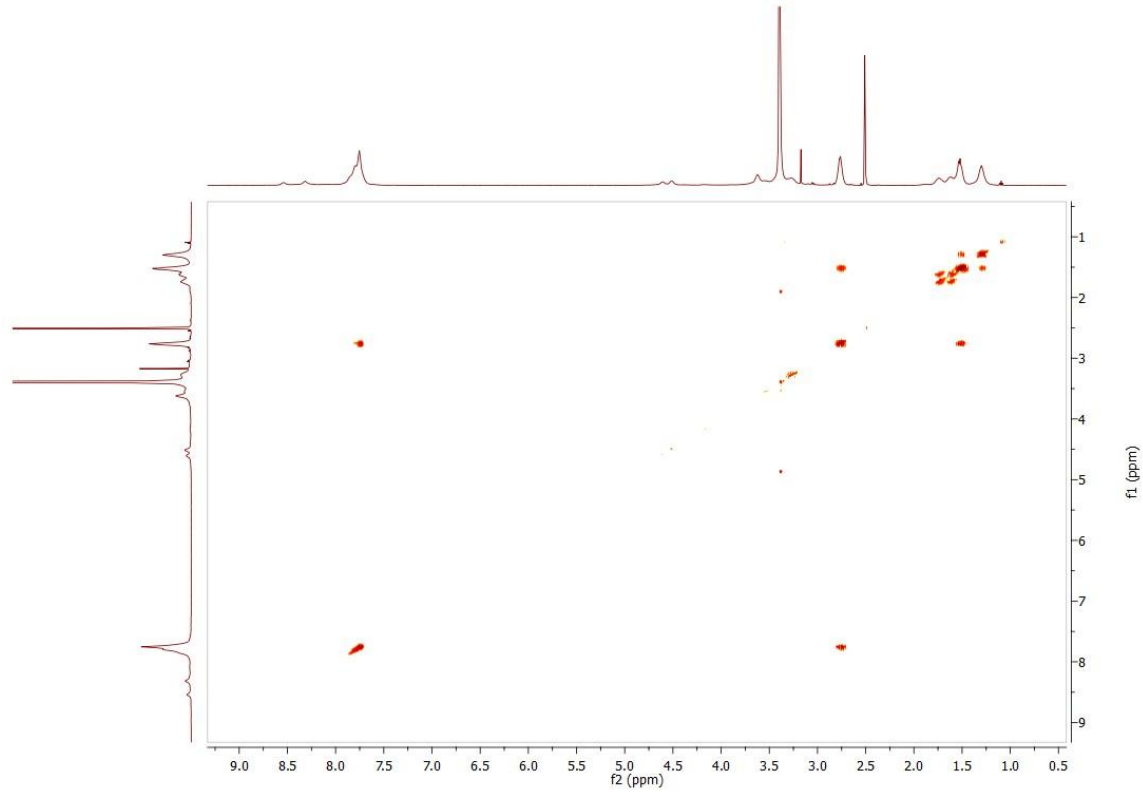

Figure A3.69: COSY spectrum of **3.5 (Sq-3-Lys)** in DMSO-d_6.

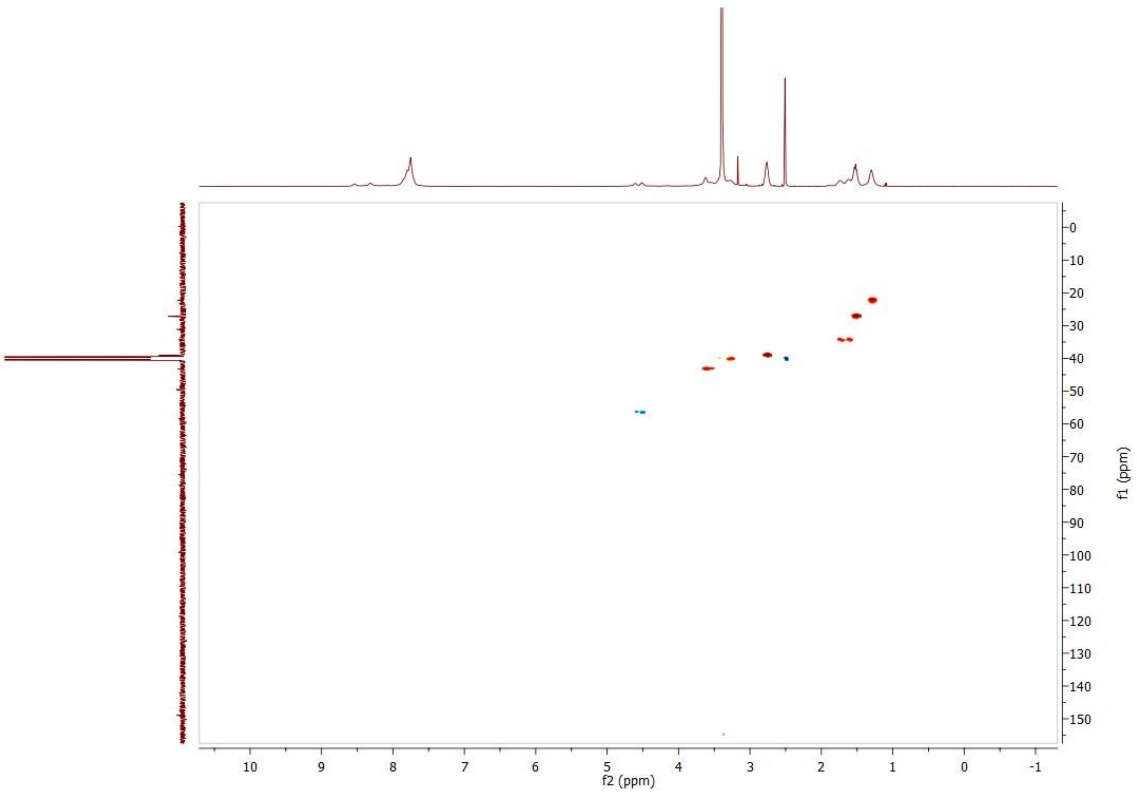

Figure A3.70: HSQC spectrum of **3.5 (Sq-3-Lys)** in DMSO-d_6.

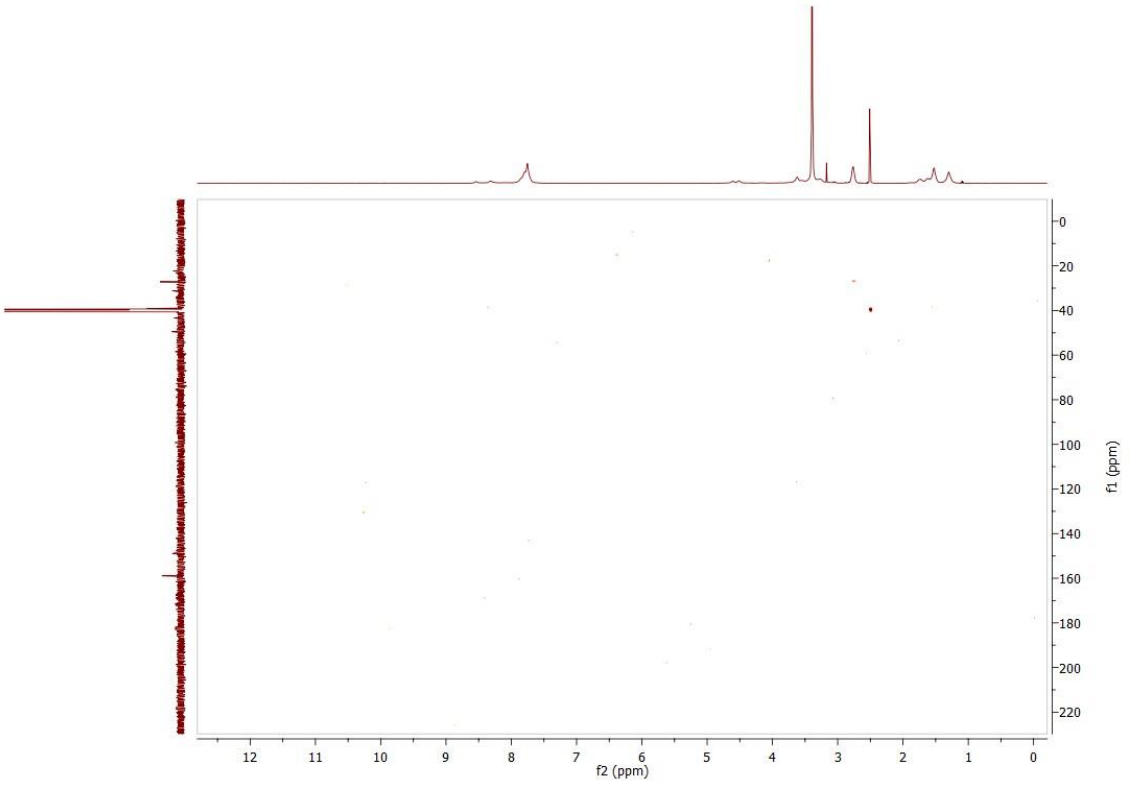

Figure A3.71: HMBC spectrum of **3.5 (Sq-3-Lys)** in DMSO-d_6.

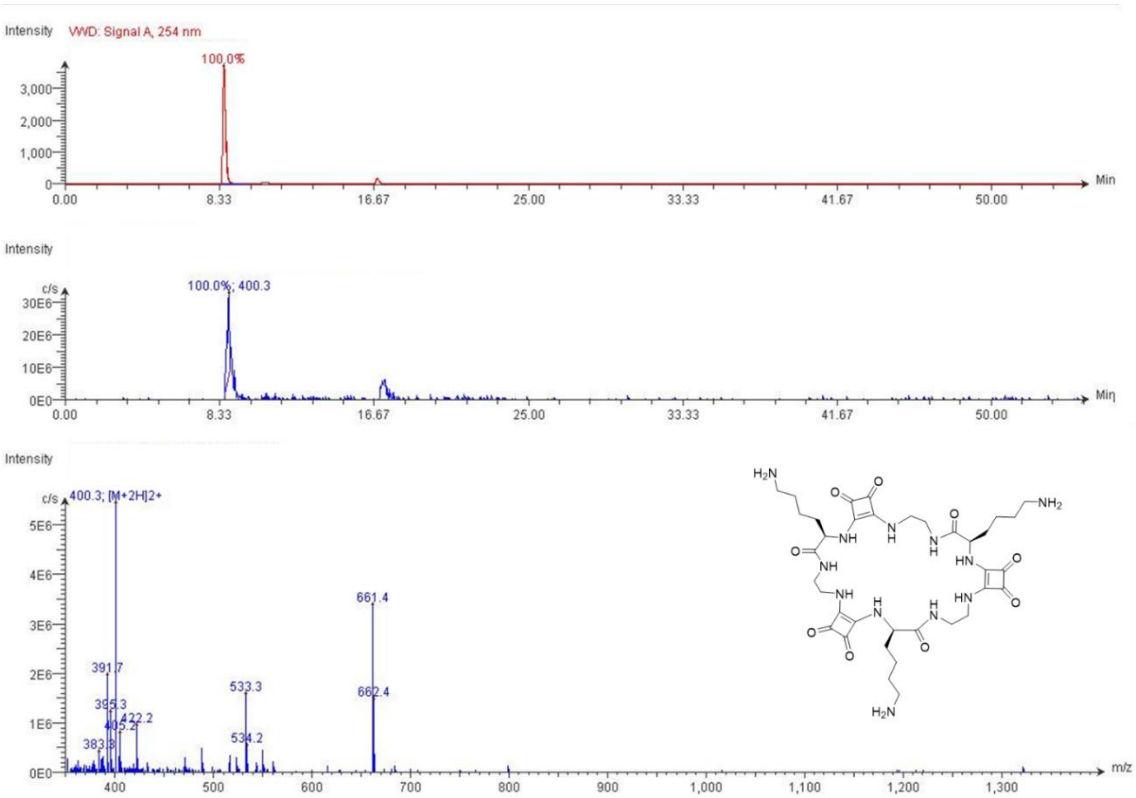

Figure A3.72: LC-MS data for **3.5 (Sq-3-Lys)**.

Compound Table

Compound Label	RT (min)	Observed mass (m/z)	Neutral observed mass (Da)	Theoretical mass (Da)	Mass error (ppm)	Isotope match score (%)
Cpd 1: C36 H54 N12 O9	0.74	799.4201	798.4129	798.4137	-1.02	99.00

Mass errors of between -5.00 and 5.00 ppm with isotope match scores above 60% are considered confirmation of molecular formulae

Figure: Extracted ion chromatogram (EIC) of compound.

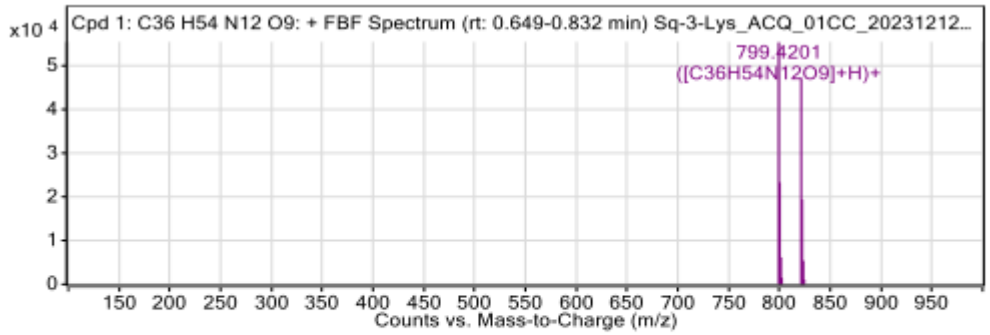

Figure: Full range view of Compound spectra and potential adducts.

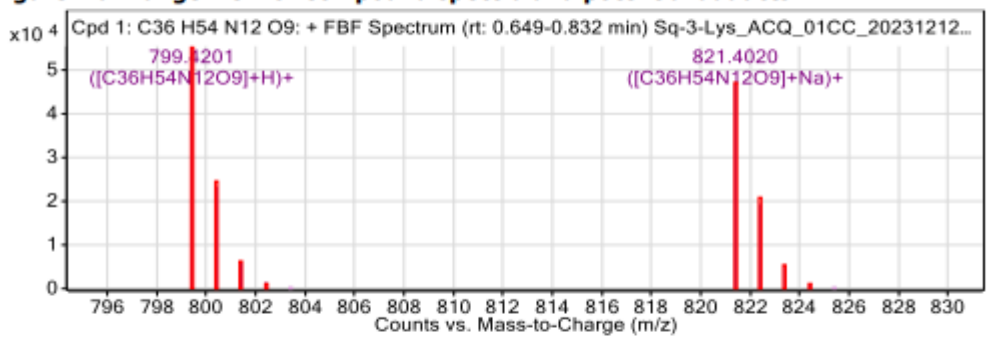

Figure: Zoomed Compound spectra view
(red boxes indicating expected theoretical isotope spacing and abundance)

Compound isotope peak List

m/z	z	Abund	Formula	Ion
799.4201	1	55446.5	C36H54N12O9	(M+H)+
800.4229	1	23318.6	C36H54N12O9	(M+H)+
801.4254	1	6169.5	C36H54N12O9	(M+H)+
802.4241	1	1443.3	C36H54N12O9	(M+H)+
821.4020	1	47213.6	C36H54N12O9	(M+Na)+
822.4052	1	19382.2	C36H54N12O9	(M+Na)+
823.4075	1	5401.5	C36H54N12O9	(M+Na)+
824.4139	1	1100.3	C36H54N12O9	(M+Na)+

Figure A3.73: HRMS data for **3.5 (Sq-3-Lys)**.

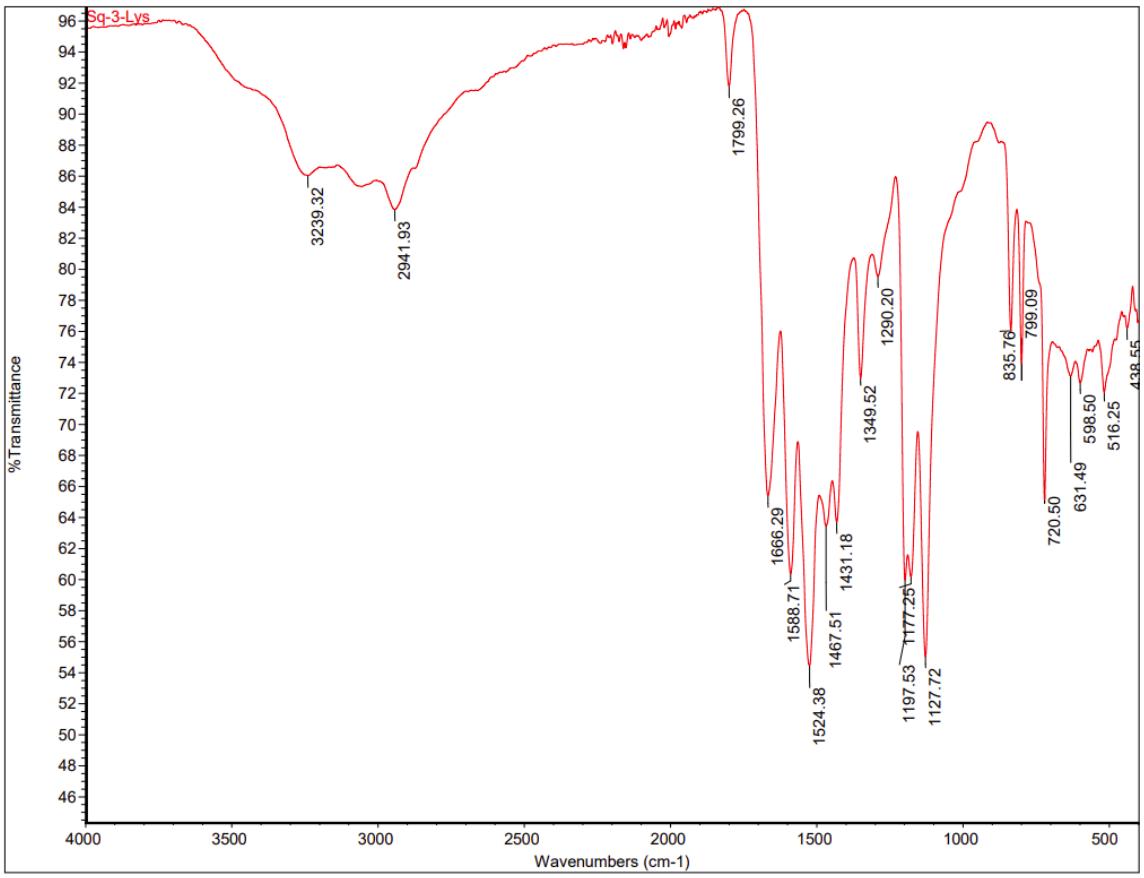

Figure A3.74: IR spectrum of **3.6 (Sq-4-Lys)**.

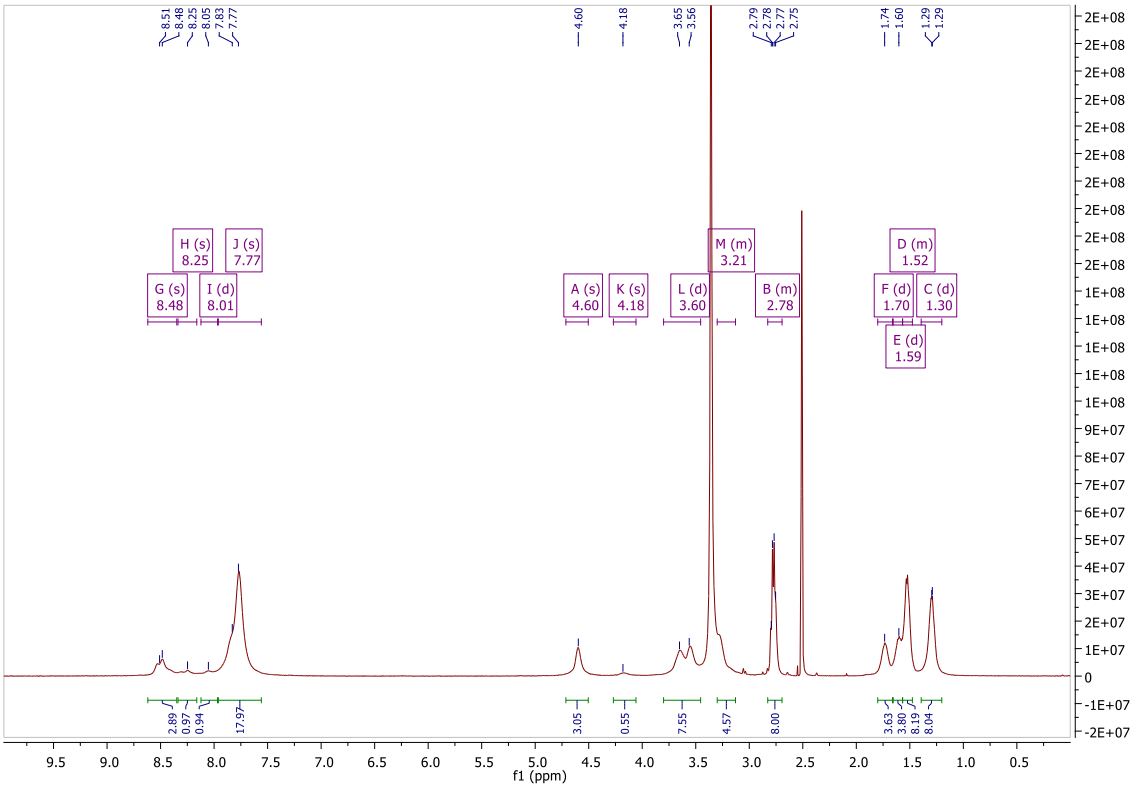

Figure A3.75: ^{1}H NMR spectrum of **3.6 (Sq-4-Lys)** in DMSO-d_6.

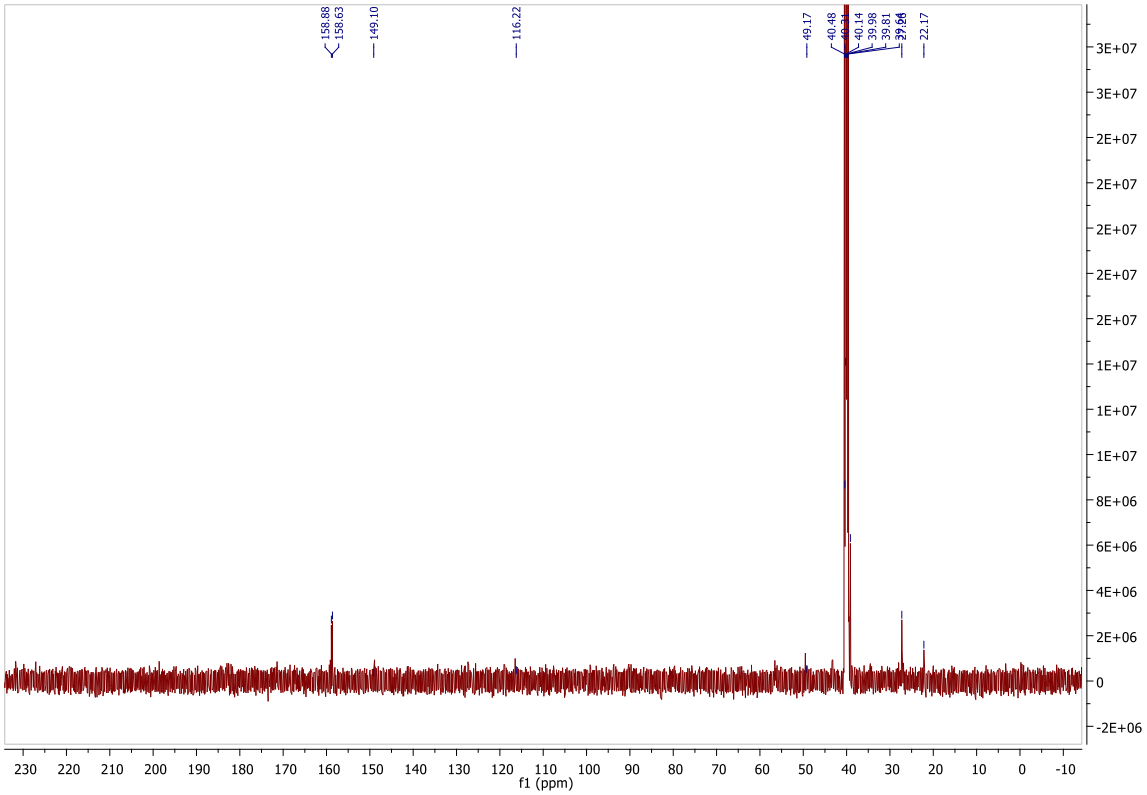

Figure A3.76: ^{13}C spectrum of **3.6 (Sq-4-Lys)** in DMSO-d_6.

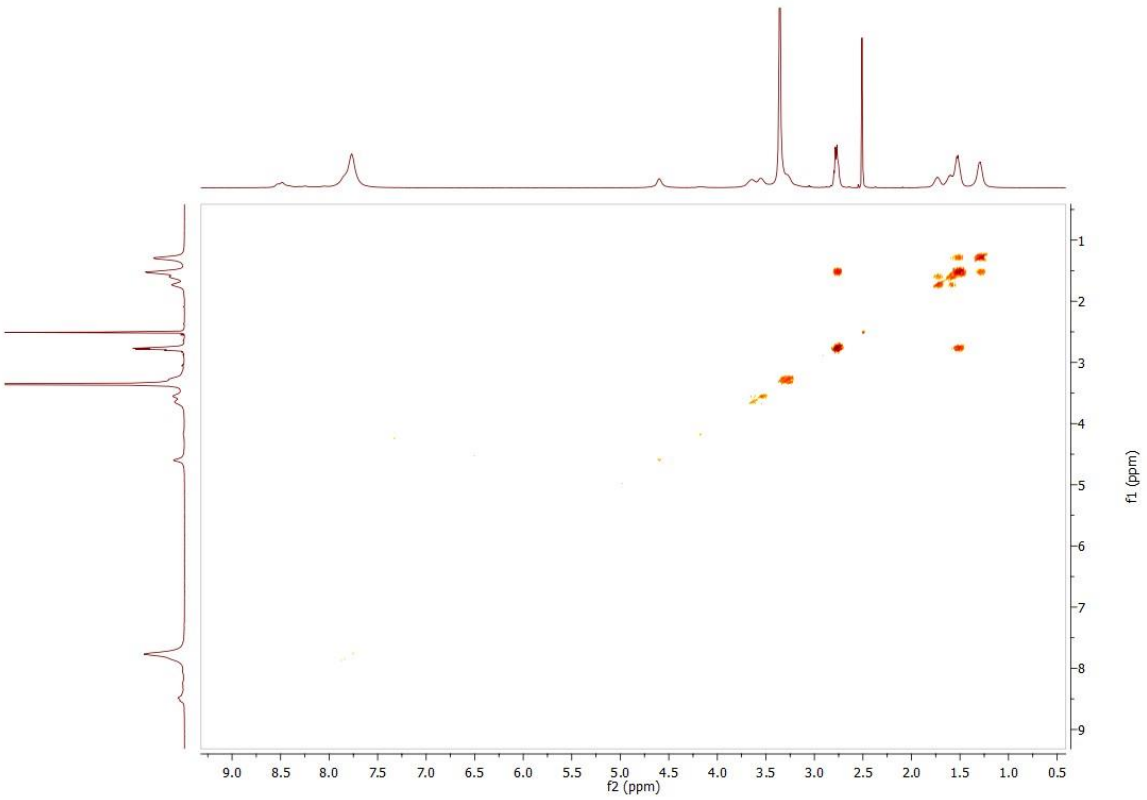

Figure A3.77: COSY spectrum of **3.6 (Sq-4-Lys)** in DMSO-d_6.

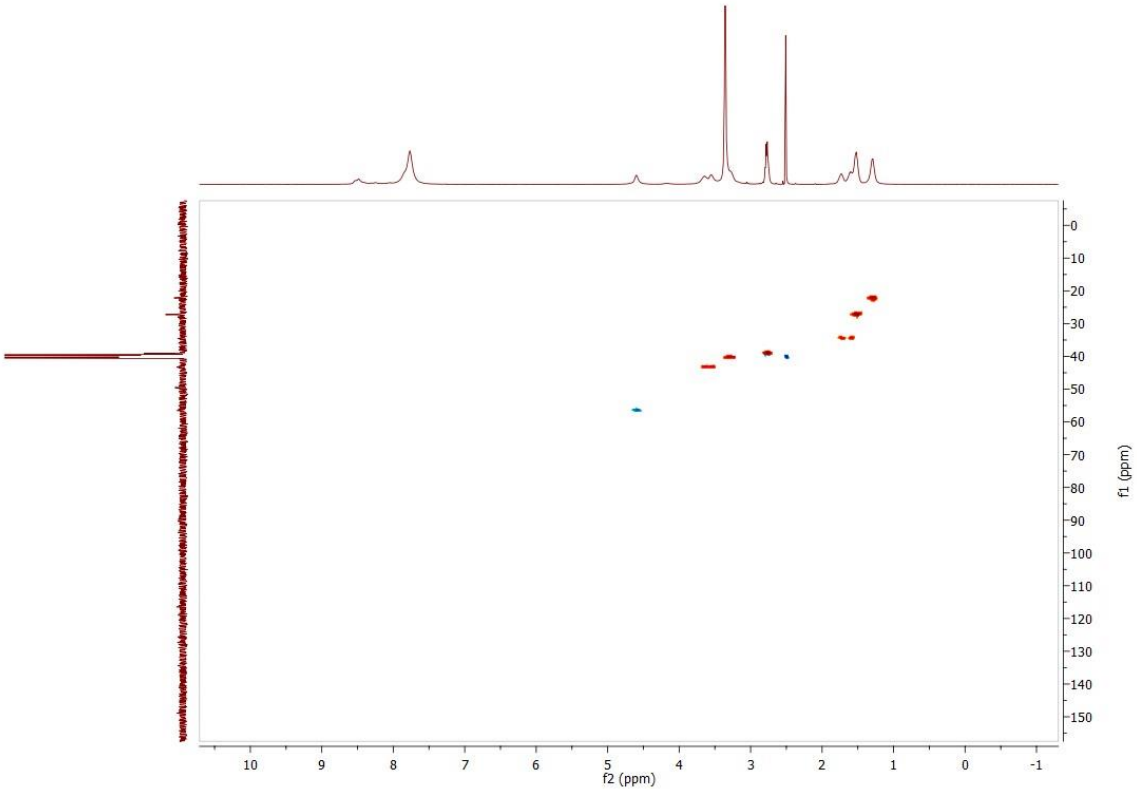

Figure A3.78: HSQC spectrum of **3.6 (Sq-4-Lys)** in DMSO-d_6.

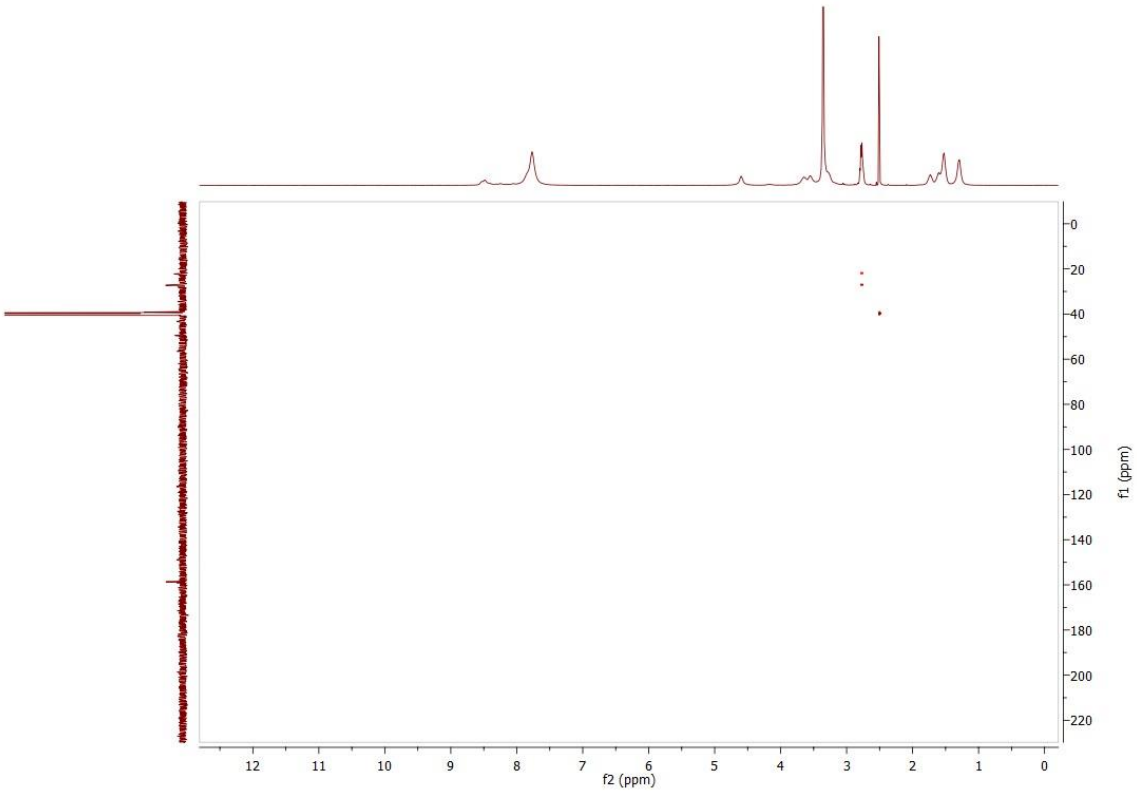

Figure A3.79: HMBC spectrum of **3.6 (Sq-4-Lys)** in DMSO-d_6.

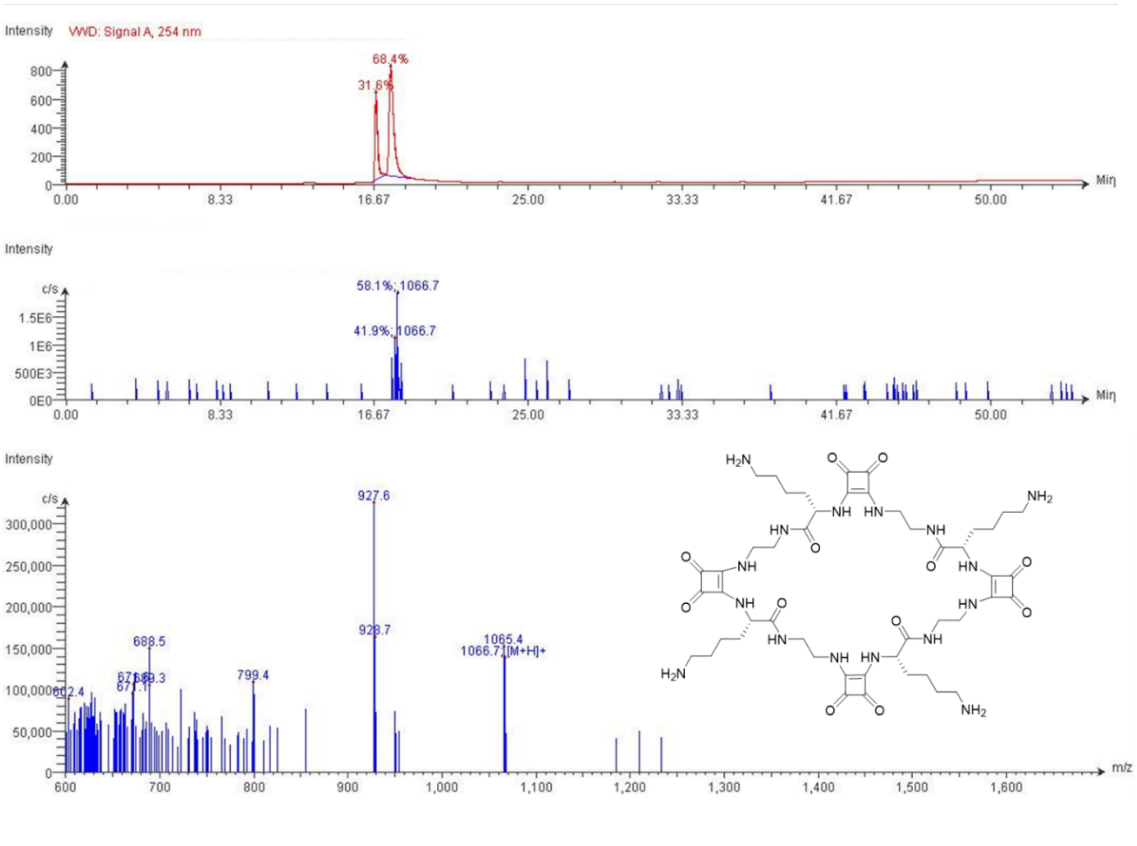

Figure A3.80: LC-MS data for **3.6 (Sq-4-Lys)**.

Compound Table

Compound Label	RT (min)	Observed mass (m/z)	Neutral observed mass (Da)	Theoretical mass (Da)	Mass error (ppm)	Isotope match score (%)
Cpd 1: C48 H72 N16 O12	0.74	1087.5396	1064.5493	1064.5516	-2.12	79.10

Mass errors of between -5.00 and 5.00 ppm with isotope match scores above 60% are considered confirmation of molecular formulae

Figure: Full range view of Compound spectra and potential adducts.

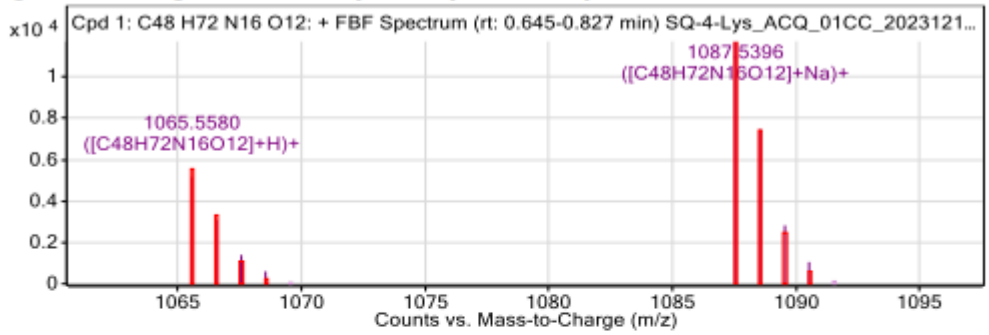

Figure: Zoomed Compound spectra view
(red boxes indicating expected theoretical isotope spacing and abundance)

Compound isotope peak List

m/z	z	Abund	Formula	Ion
1065.5580	1	5149.1	C48H72N16O12	(M+H)+
1066.5611	1	3086.4	C48H72N16O12	(M+H)+
1067.5625	1	1393.3	C48H72N16O12	(M+H)+
1068.5421	1	601.2	C48H72N16O12	(M+H)+
1087.5396	1	11701.8	C48H72N16O12	(M+Na)+
1088.5427	1	7451.3	C48H72N16O12	(M+Na)+
1089.5450	1	2820.8	C48H72N16O12	(M+Na)+
1090.5222	1	1051.0	C48H72N16O12	(M+Na)+

Figure A3.81: HRMS data for **3.6 (Sq-4-Lys)**.

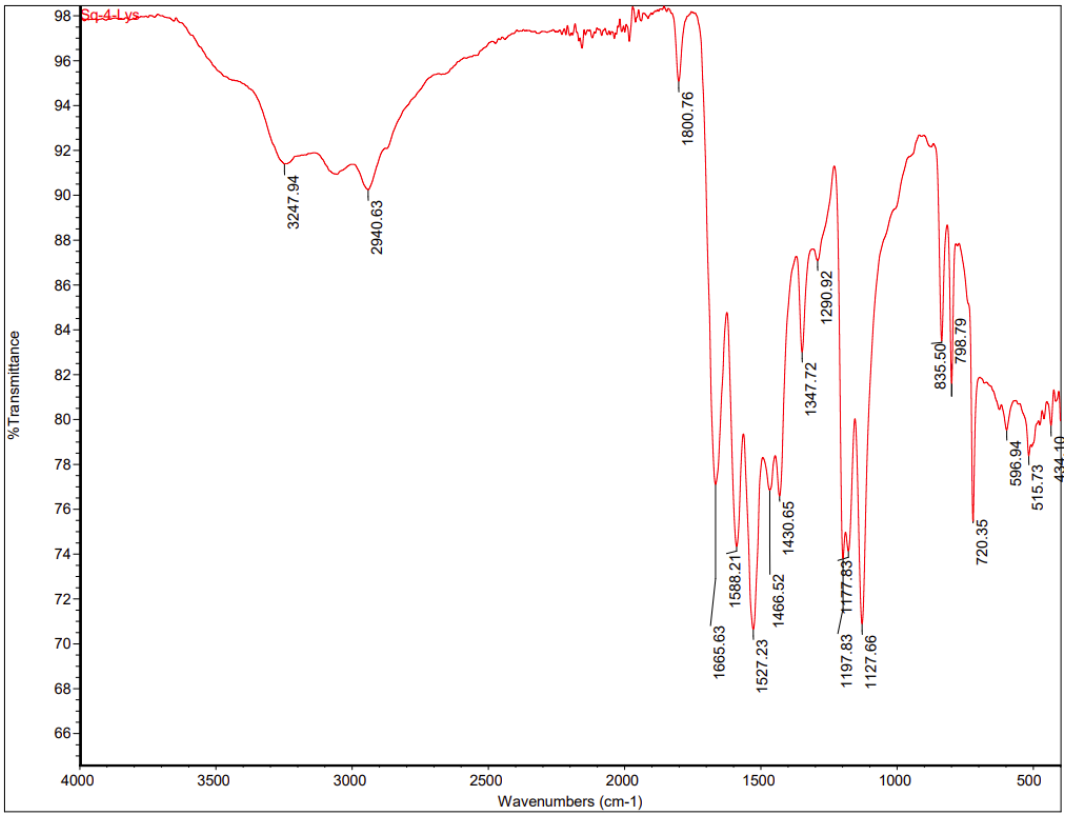

Figure A3.82: IR Spectrum of **3.6 (Sq-4-Lys)**.

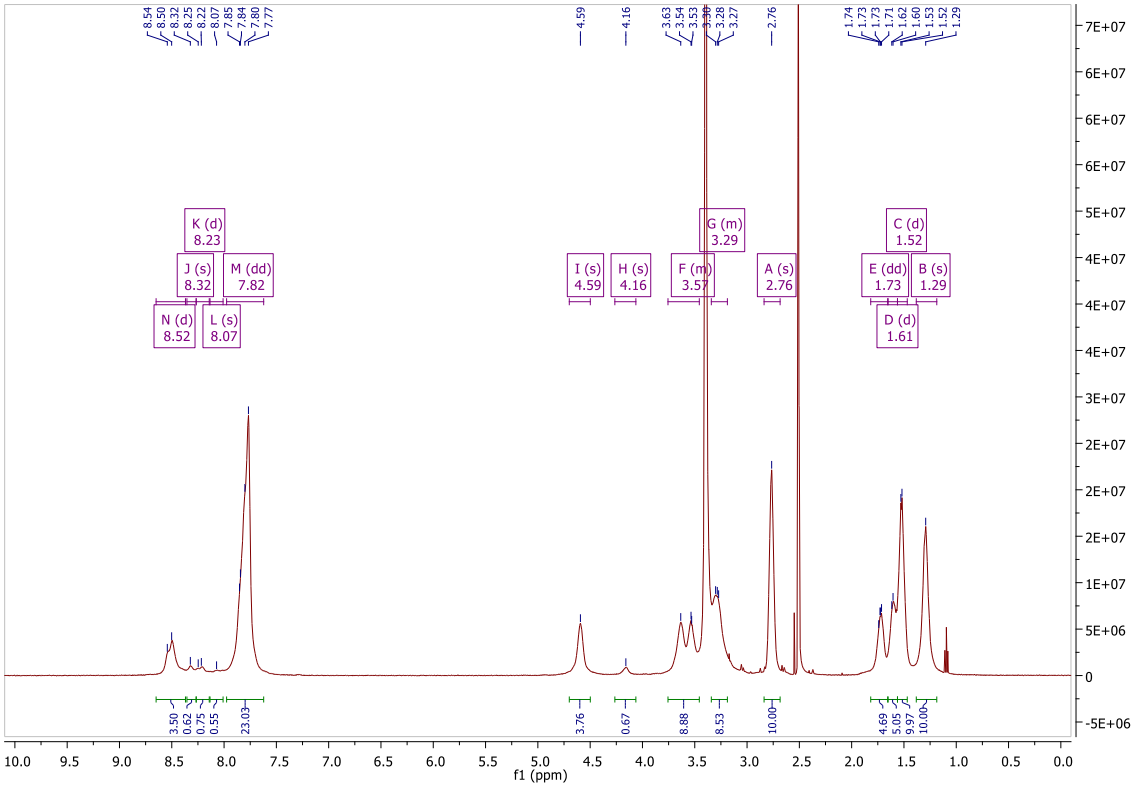

Figure A3.83: ^{1}H spectrum of **3.7 (Sq-5-Lys)** in DMSO-d_6.

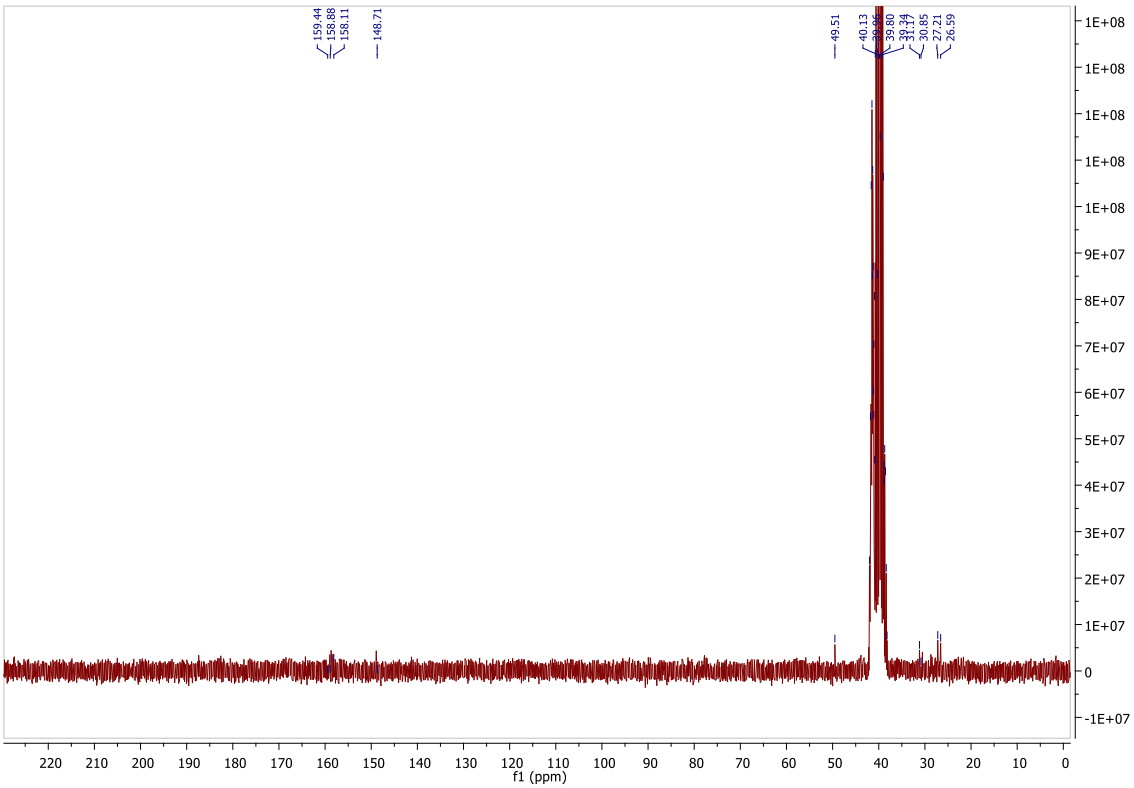

Figure A3.84: ^{13}C spectrum of **3.7 (Sq-5-Lys)** in DMSO-d_6.

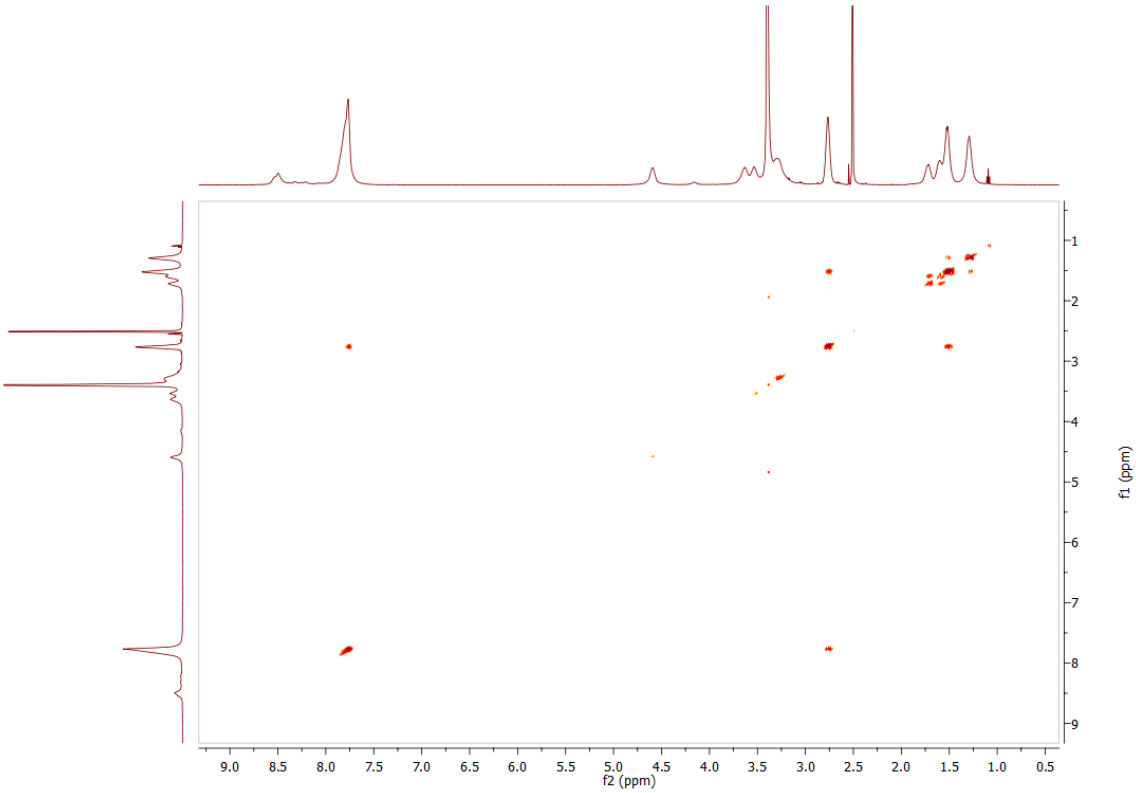

Figure A3.85: COSY spectrum of **3.7 (Sq-5-Lys)** in DMSO-d_6.

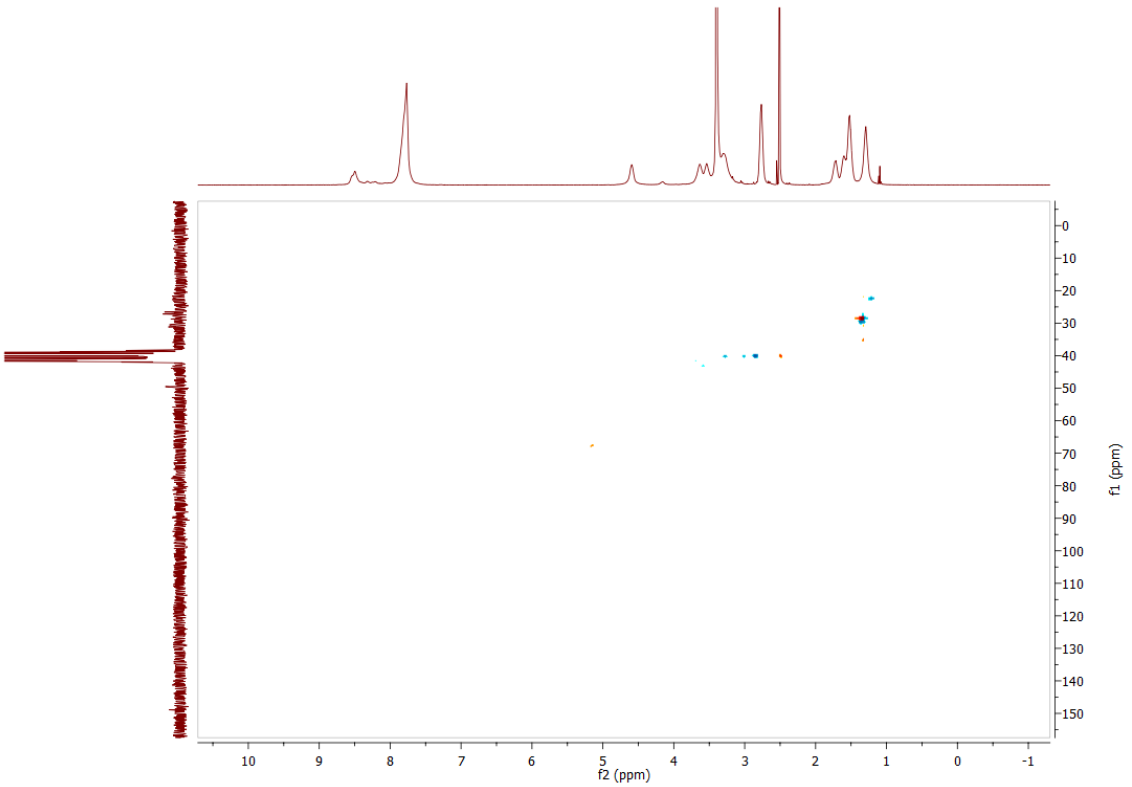

Figure A3.86: HSQC spectrum of **3.7 (Sq-5-Lys)** in DMSO-d_6.

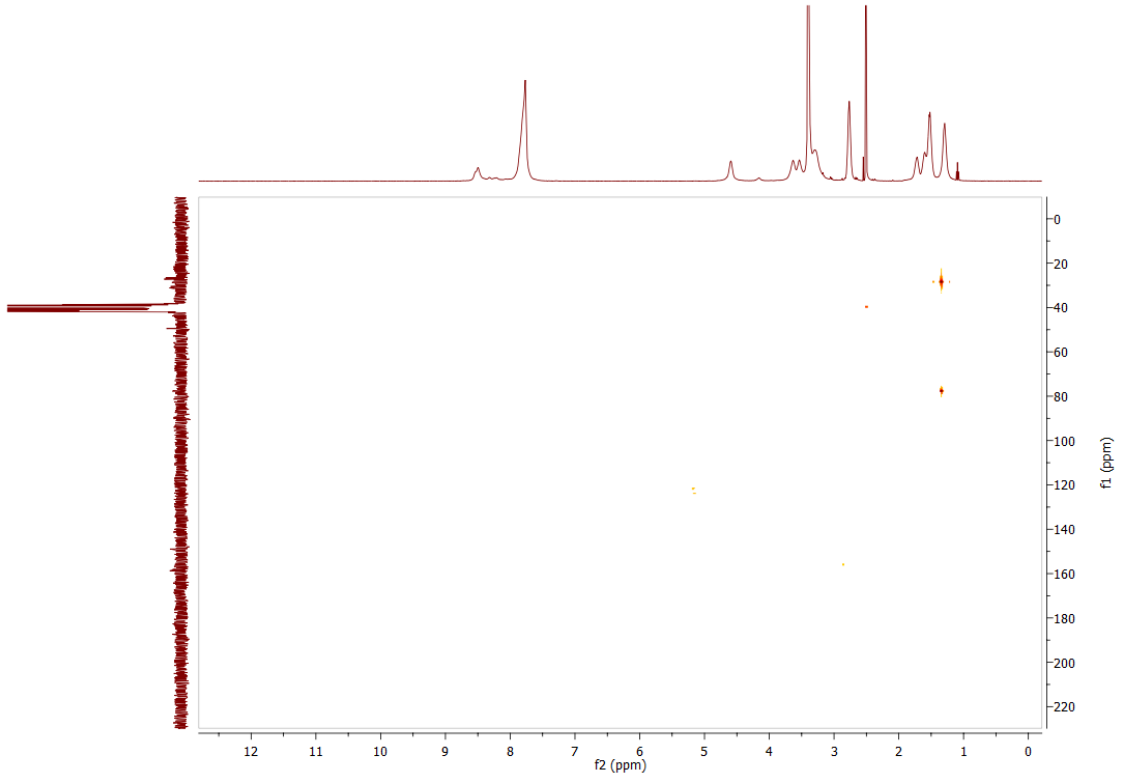

Figure A3.87: HMBC spectrum of **3.7 (Sq-5-Lys)** in DMSO-d_6.

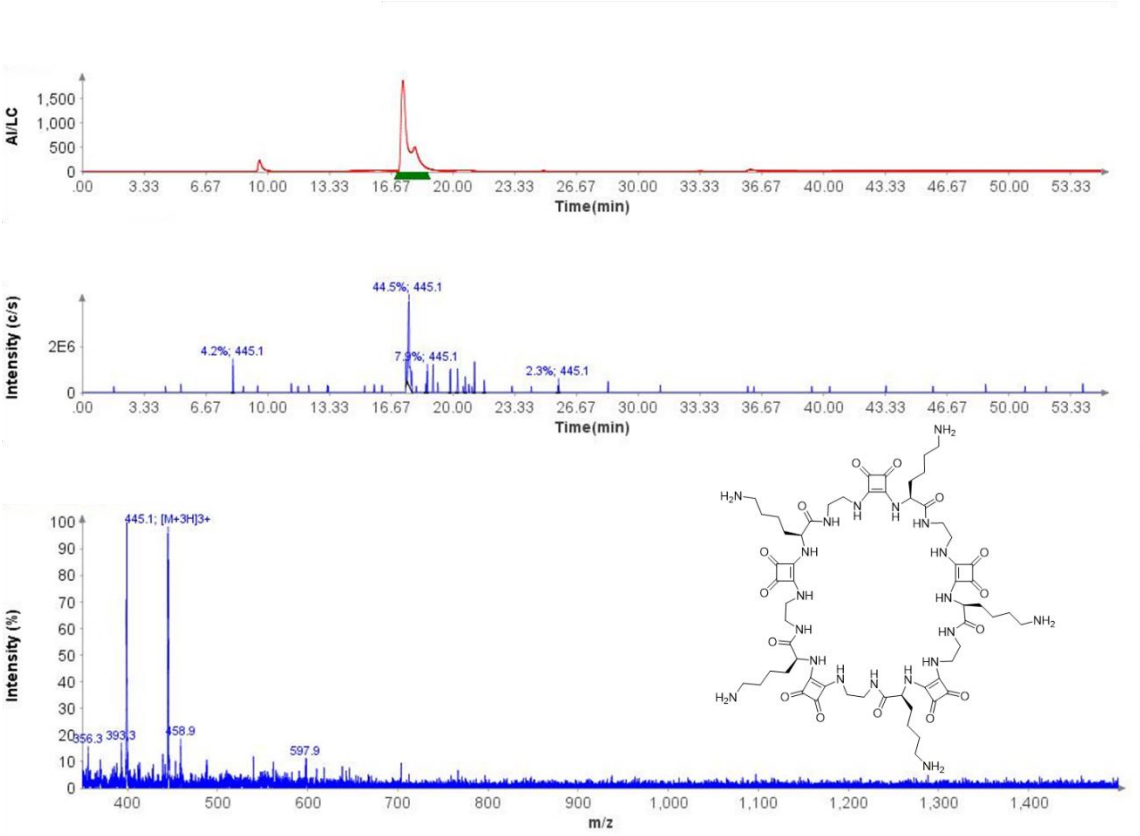

Figure A3.88: LC-MS data for **3.7 (Sq-5-Lys)**.

Compound Table

Compound Label	RT (min)	Observed mass (m/z)	Neutral observed mass (Da)	Theoretical mass (Da)	Mass error (ppm)	Isotope match score (%)
Cpd 1: C60 H90 N20 O15	0.74	1331.6957	1330.6870	1330.6895	-1.81	82.59

Mass errors of between -5.00 and 5.00 ppm with isotope match scores above 60% are considered confirmation of molecular formulae

Figure: Full range view of Compound spectra and potential adducts.

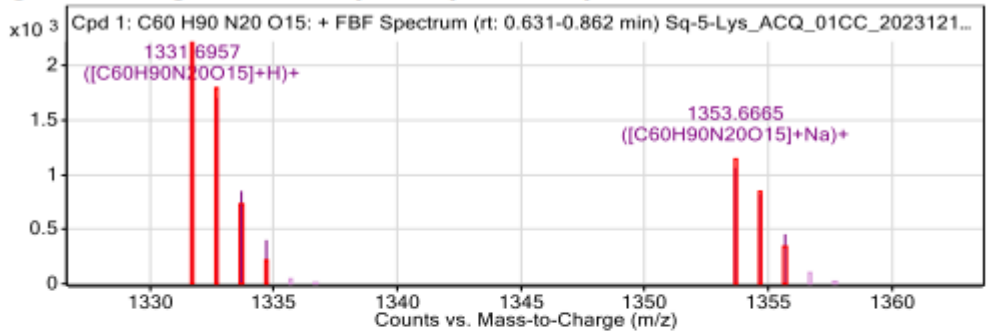

Figure: Zoomed Compound spectra view
(red boxes indicating expected theoretical isotope spacing and abundance)

Compound isotope peak List

m/z	z	Abund	Formula	Ion
1331.6957	1	2218.9	C60H90N20O15	(M+H)+
1332.6973	1	1703.4	C60H90N20O15	(M+H)+
1333.7003	1	850.4	C60H90N20O15	(M+H)+
1334.7113	1	401.0	C60H90N20O15	(M+H)+
1353.6665	1	1062.2	C60H90N20O15	(M+Na)+
1354.6813	1	817.5	C60H90N20O15	(M+Na)+
1355.6840	1	454.4	C60H90N20O15	(M+Na)+

Figure A3.89: HRMS data for **3.7 (Sq-5-Lys)**.

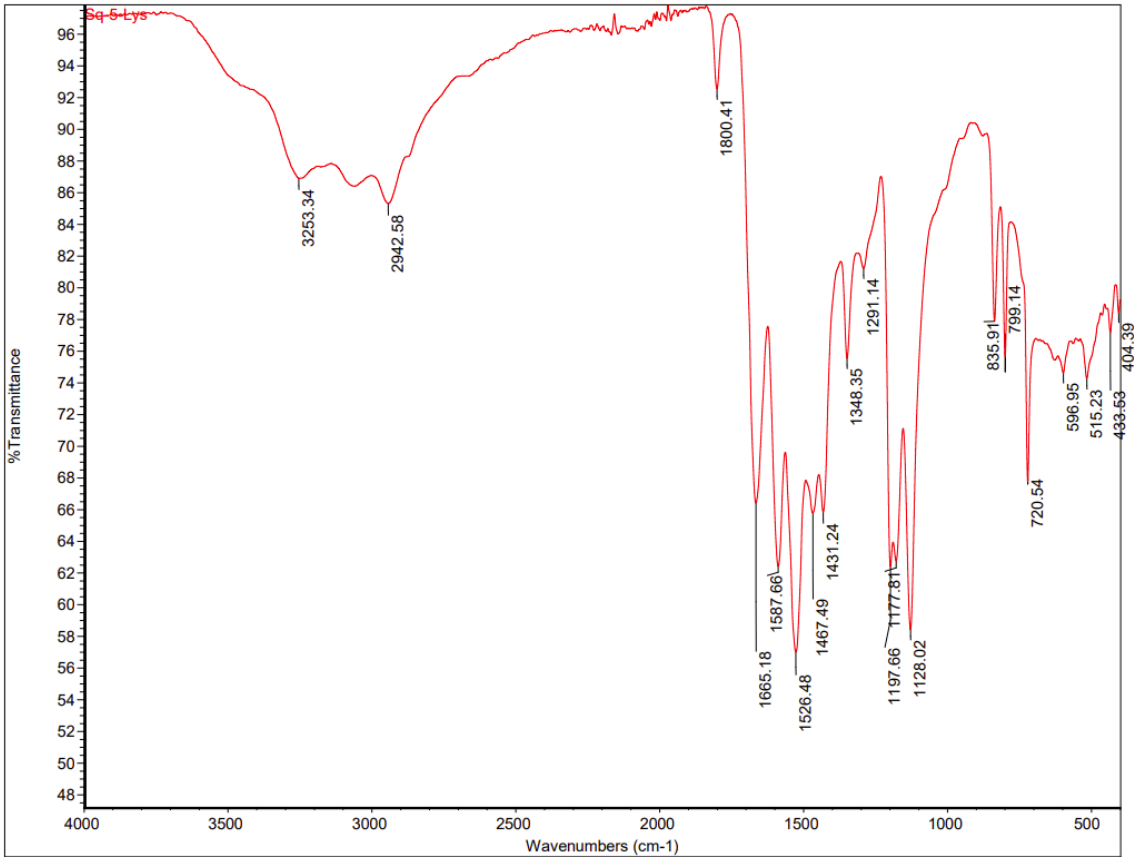

Figure A3.90: IR Spectrum of **3.7 (Sq-5-Lys)**.

Chapter 4 – Supplementary Characterisation Data

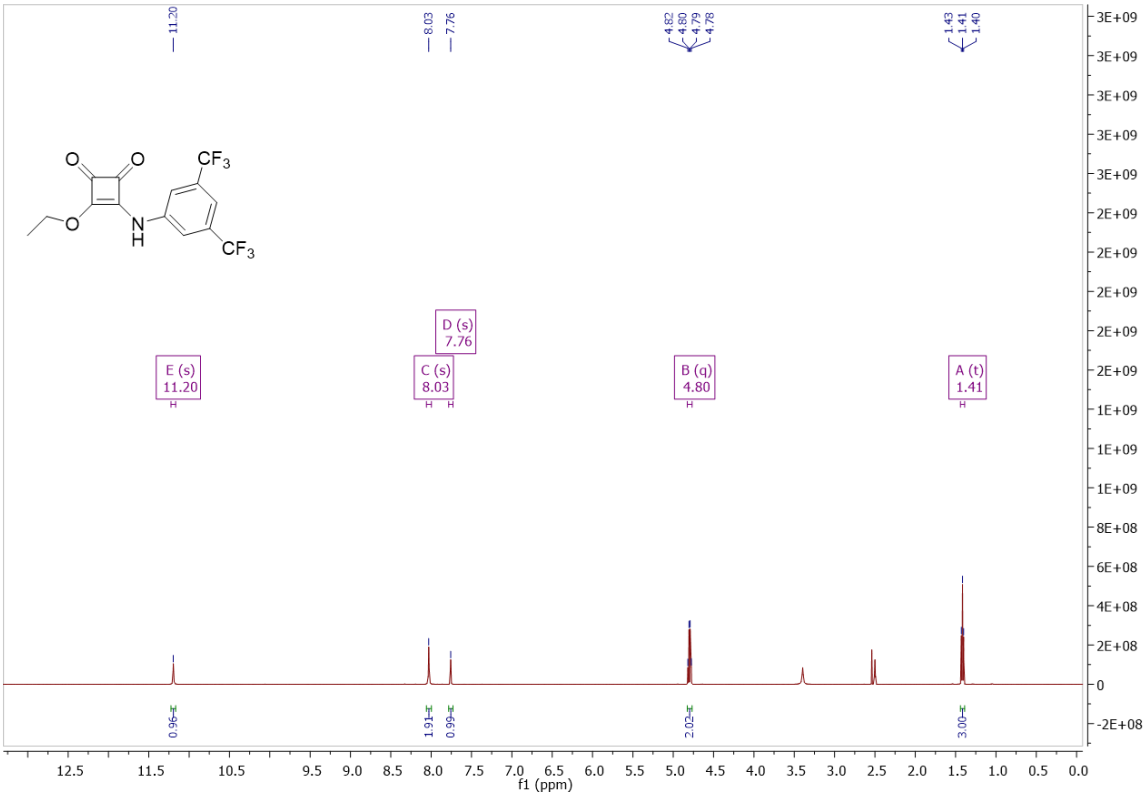

Figure A4.1: ^{1}H spectrum of **SqBisCF$_3$** in DMSO-d$_6$.

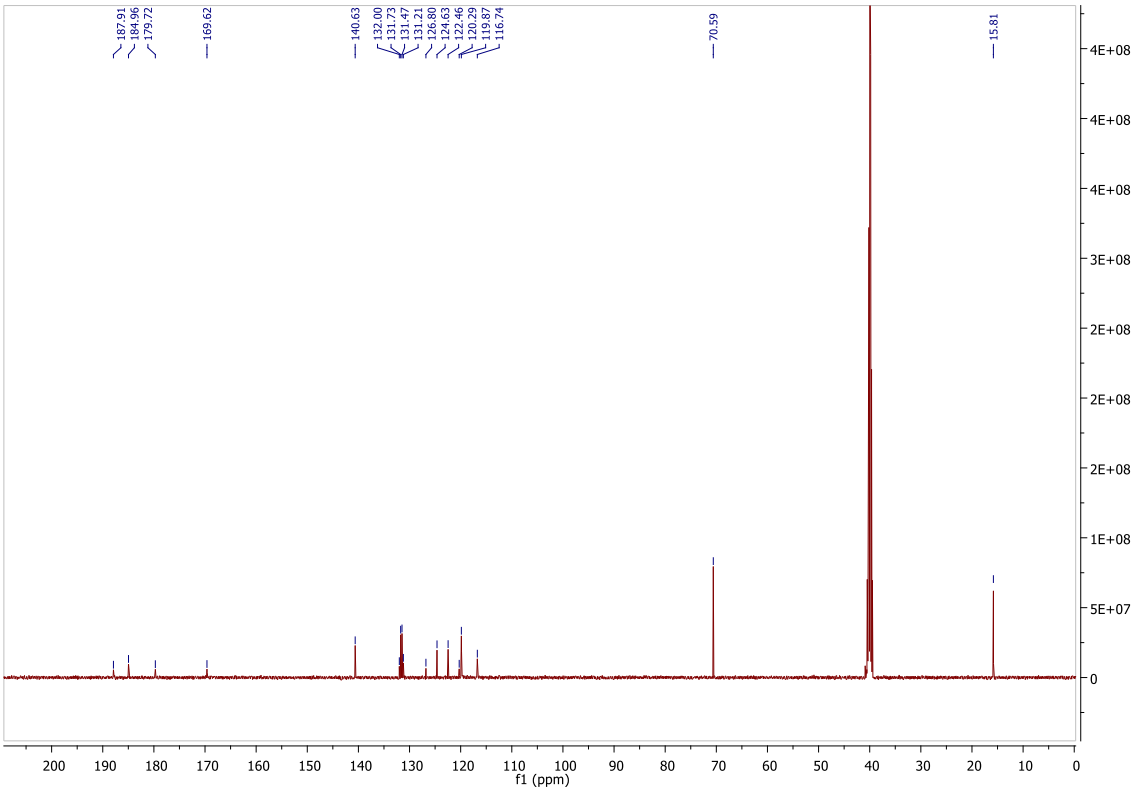

Figure A4.2: ^{13}C spectrum of **SqBisCF$_3$** in DMSO-d$_6$.

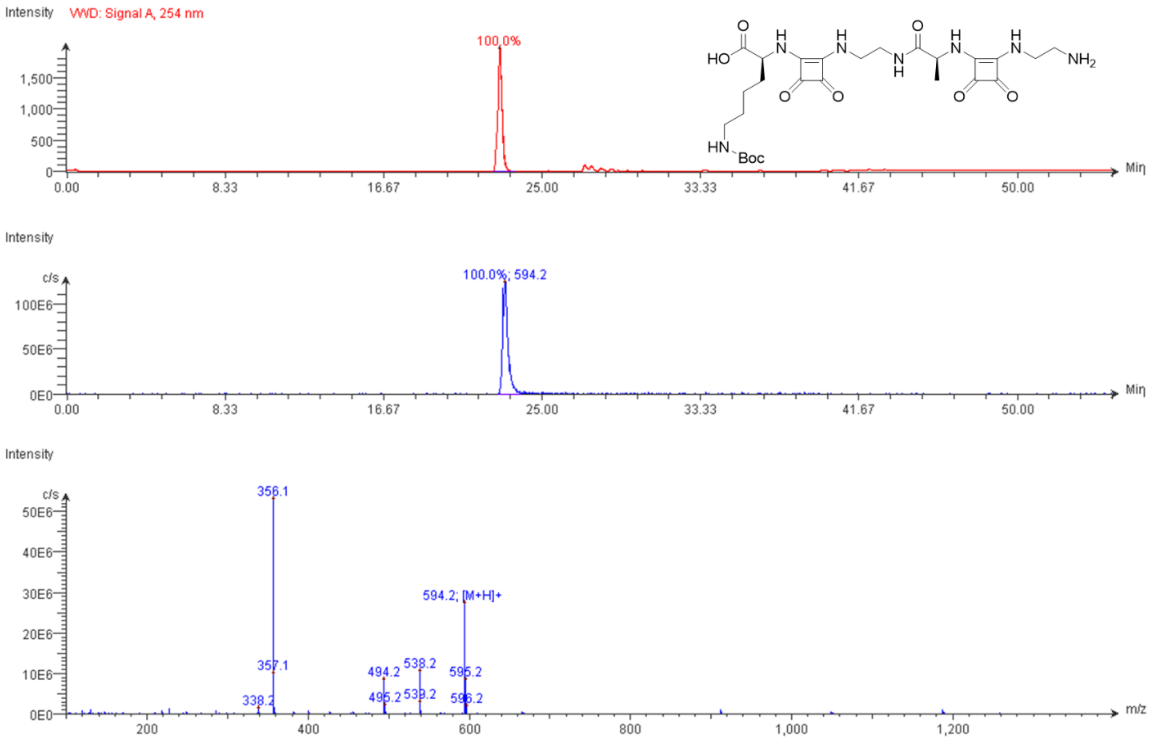

Figure A4.3: LC-MS data for **ASq-2-Ala-Lys(Boc)**.

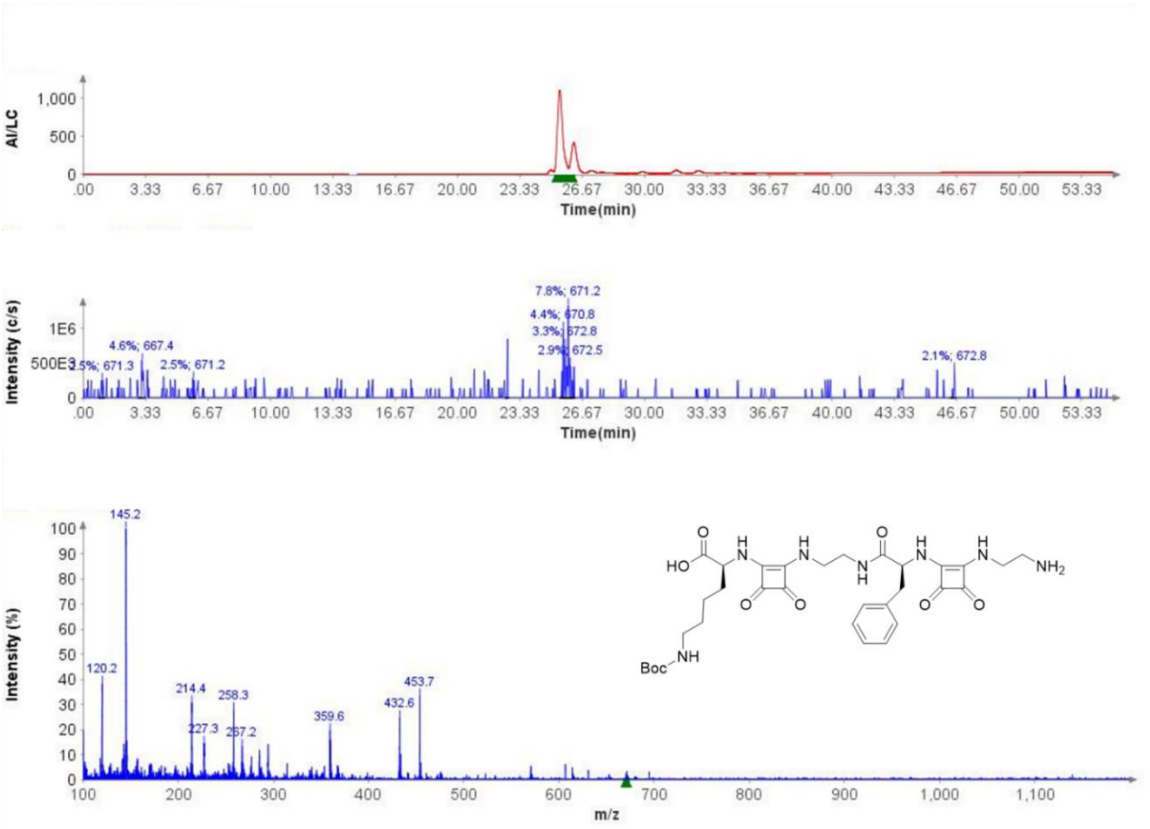

Figure A4.4: LC-MS data for **ASq-2-Phe-Lys(Boc).**

Compound Table

Compound Label	RT (min)	Observed mass (m/z)	Neutral observed mass (Da)	Theoretical mass (Da)	Mass error (ppm)	Isotope match score (%)
Cpd 1: C32 H43 N7 O9	0.69	670.3199	669.3125	669.3122	0.41	99.69

Figure: Extracted ion chromatogram (EIC) of compound.

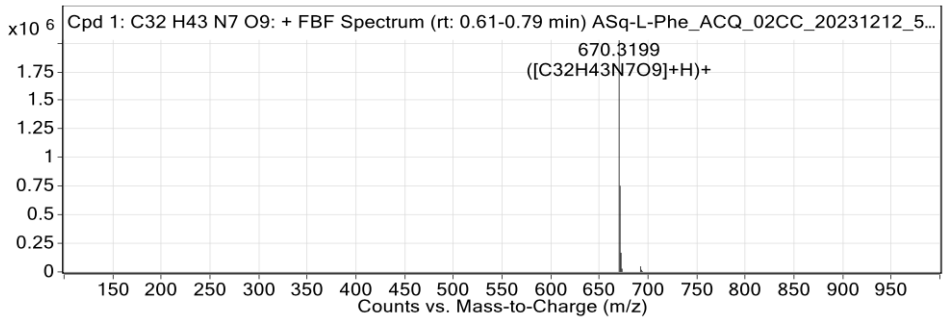

Figure: Full range view of Compound spectra and potential adducts.

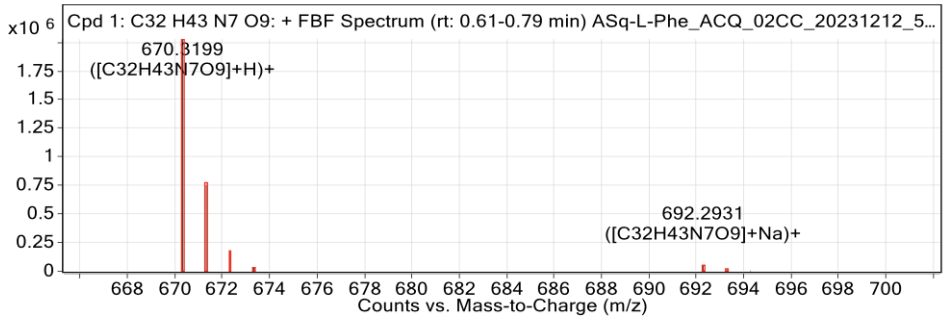

Figure: Zoomed Compound spectra view
(red boxes indicating expected theoretical isotope spacing and abundance)

Compound isotope peak List

m/z	z	Abund	Formula	Ion
670.3199	1	2027732.1	C32H43N7O9	(M+H)+
671.3231	1	753473.8	C32H43N7O9	(M+H)+
672.3259	1	167766.7	C32H43N7O9	(M+H)+
673.3278	1	28644.3	C32H43N7O9	(M+H)+
692.2931	1	48974.2	C32H43N7O9	(M+Na)+
693.2968	1	18453.3	C32H43N7O9	(M+Na)+
694.2955	1	5423.9	C32H43N7O9	(M+Na)+

Figure A4.5: HRMS data for **ASq-2-Phe-Lys(Boc).**

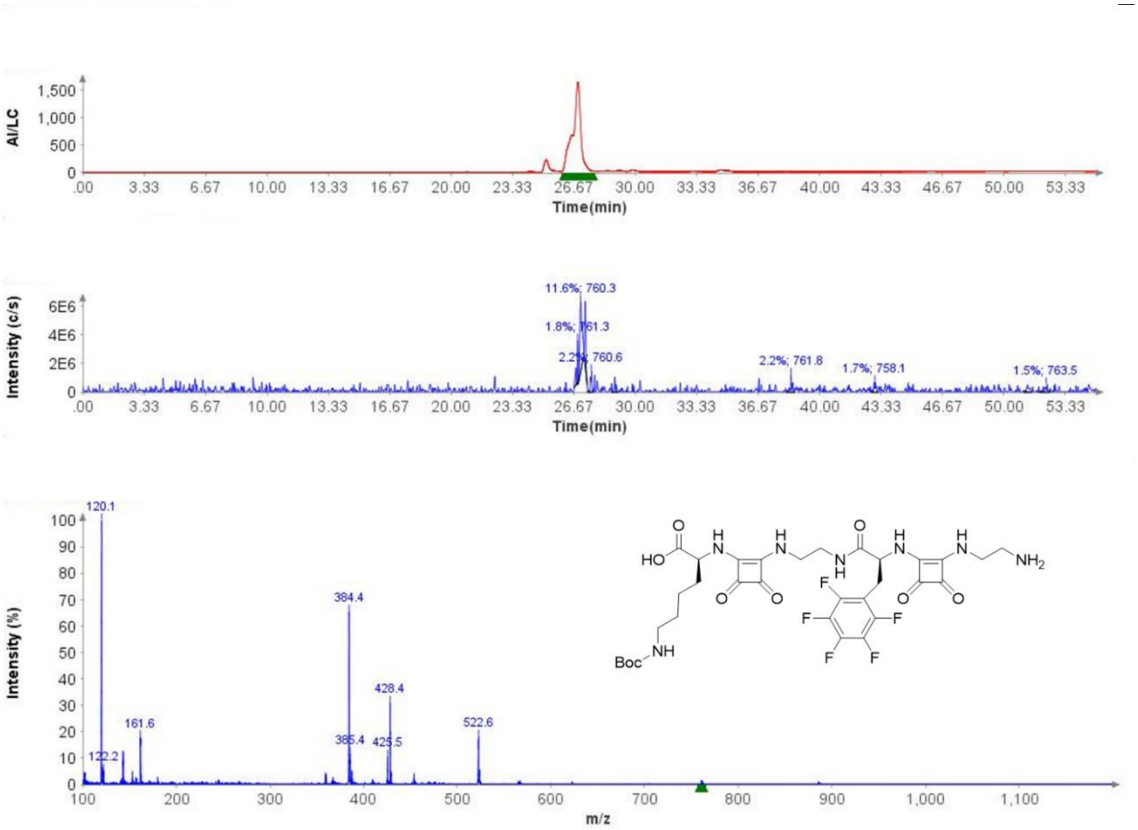

Figure A4.6: LC-MS data for **ASq-2-F_5Phe-Lys(Boc)**.

Compound Table

Compound Label	RT (min)	Observed mass (m/z)	Neutral observed mass (Da)	Theoretical mass (Da)	Mass error (ppm)	Isotope match score (%)
Cpd 1: C32 H38 F5 N7 O9	0.70	760.2729	759.2657	759.2651	0.79	99.64

Figure: Extracted ion chromatogram (EIC) of compound.

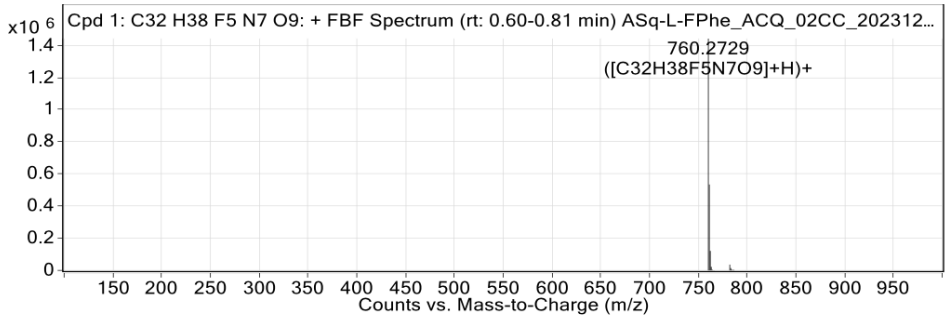

Figure: Full range view of Compound spectra and potential adducts.

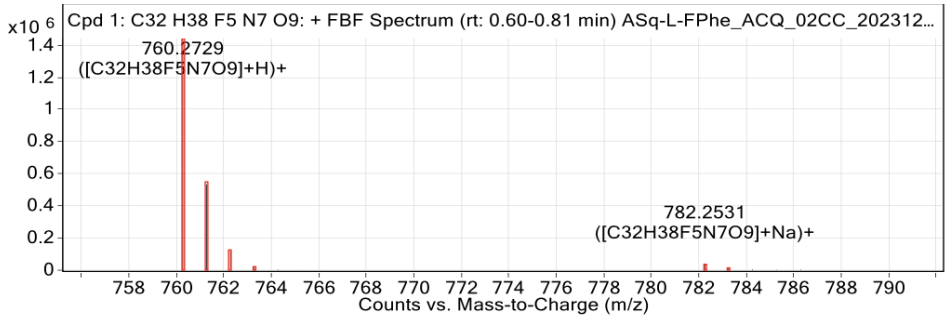

Figure: Zoomed Compound spectra view
(red boxes indicating expected theoretical isotope spacing and abundance)

Compound isotope peak List

m/z	z	Abund	Formula	Ion
760.2729	1	1442240.1	C32H38F5N7O9	(M+H)+
761.2762	1	534153.9	C32H38F5N7O9	(M+H)+
762.2787	1	121179.5	C32H38F5N7O9	(M+H)+
763.2804	1	21871.2	C32H38F5N7O9	(M+H)+
764.2794	1	3814.3	C32H38F5N7O9	(M+H)+
782.2531	1	35795.4	C32H38F5N7O9	(M+Na)+
783.2560	1	14272.1	C32H38F5N7O9	(M+Na)+
784.2562	1	4637.7	C32H38F5N7O9	(M+Na)+
785.2796	1	2017.3	C32H38F5N7O9	(M+Na)+
786.2964	1	3041.8	C32H38F5N7O9	(M+Na)+

Figure A4.7: HRMS data for **ASq-2-F_5Phe-Lys(Boc).**

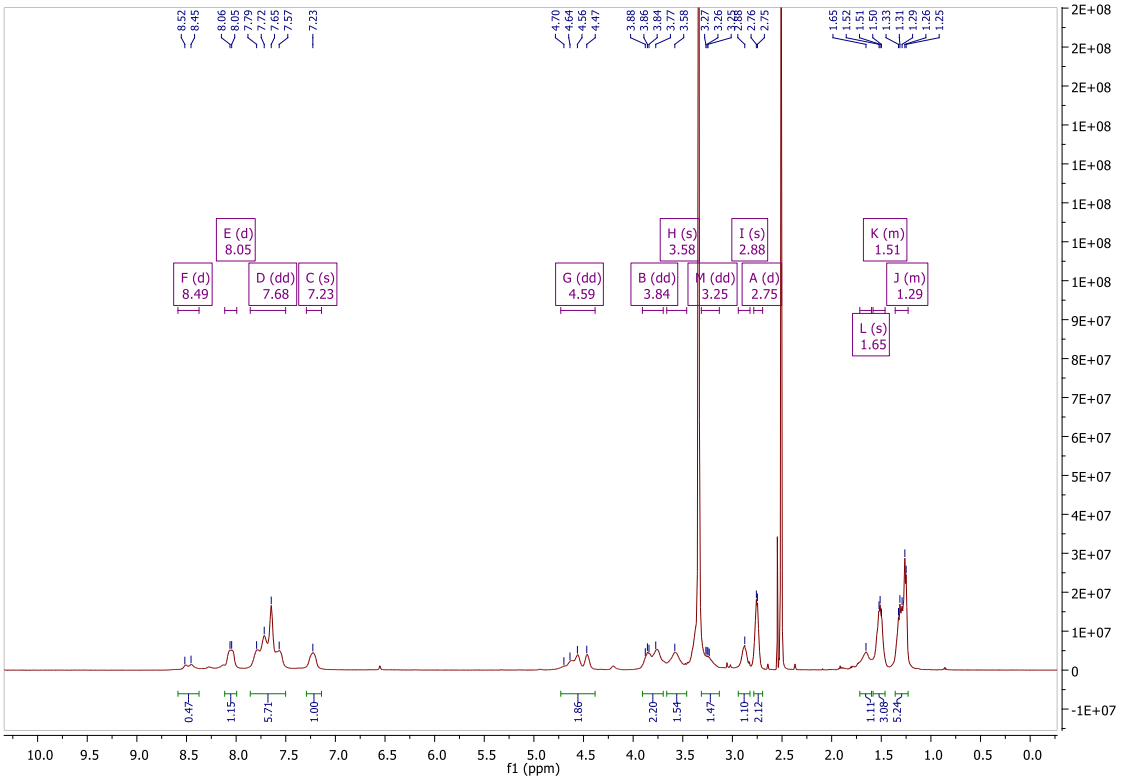

Figure A4.8: ^{1}H NMR Spectrum of **4.16 (Sq-2-Ala-Lys)** in DMSO-d_6.

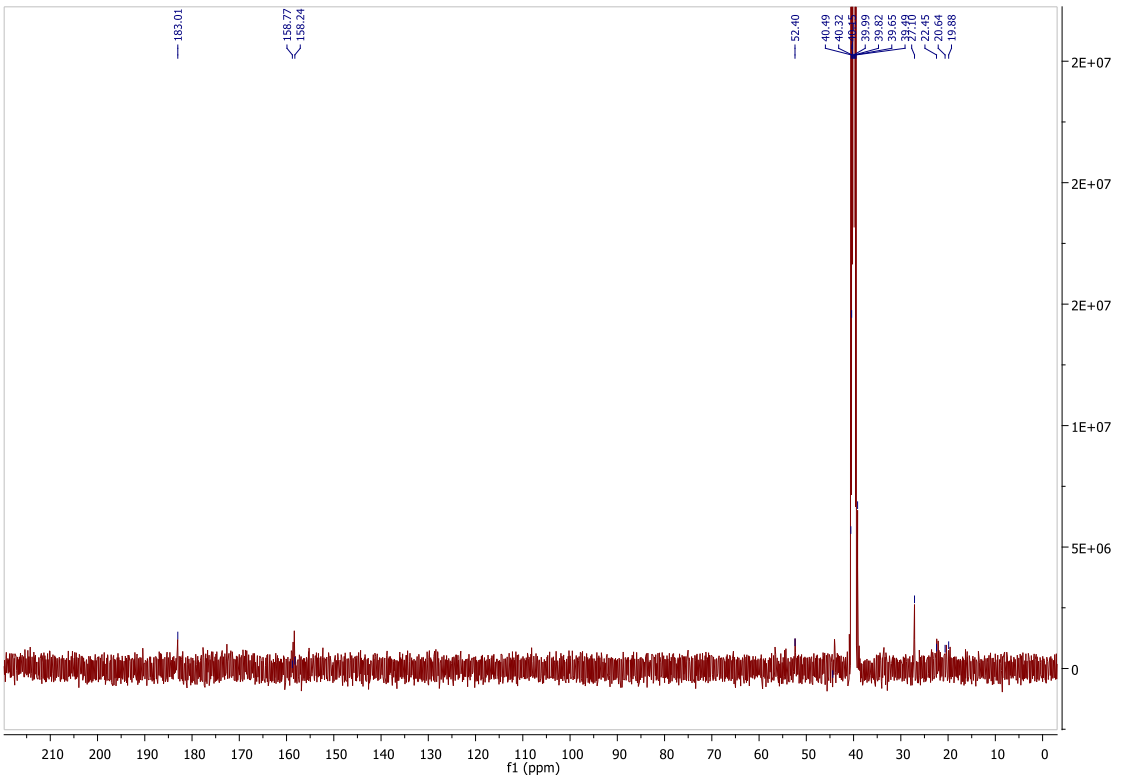

Figure A4.9: ^{13}C NMR Spectrum of **4.16 (Sq-2-Ala-Lys)** in DMSO-d_6.

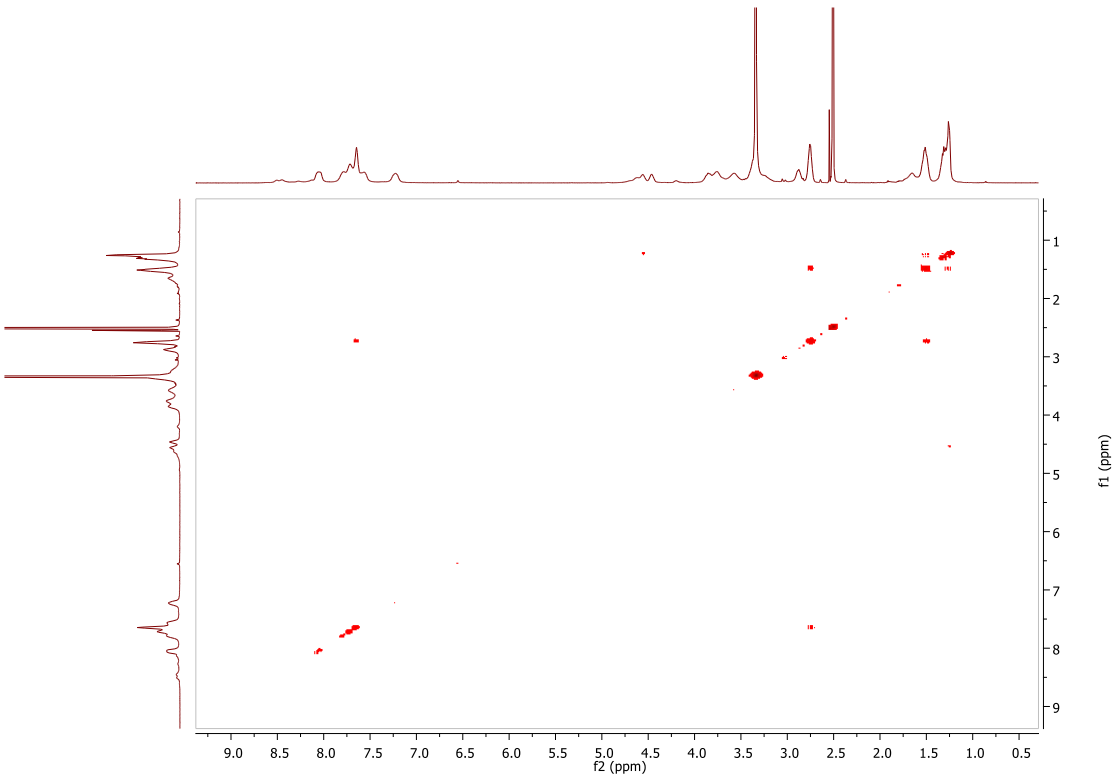

Figure A4.10: COSY Spectrum of **4.16 (Sq-2-Ala-Lys)** in DMSO-d_6.

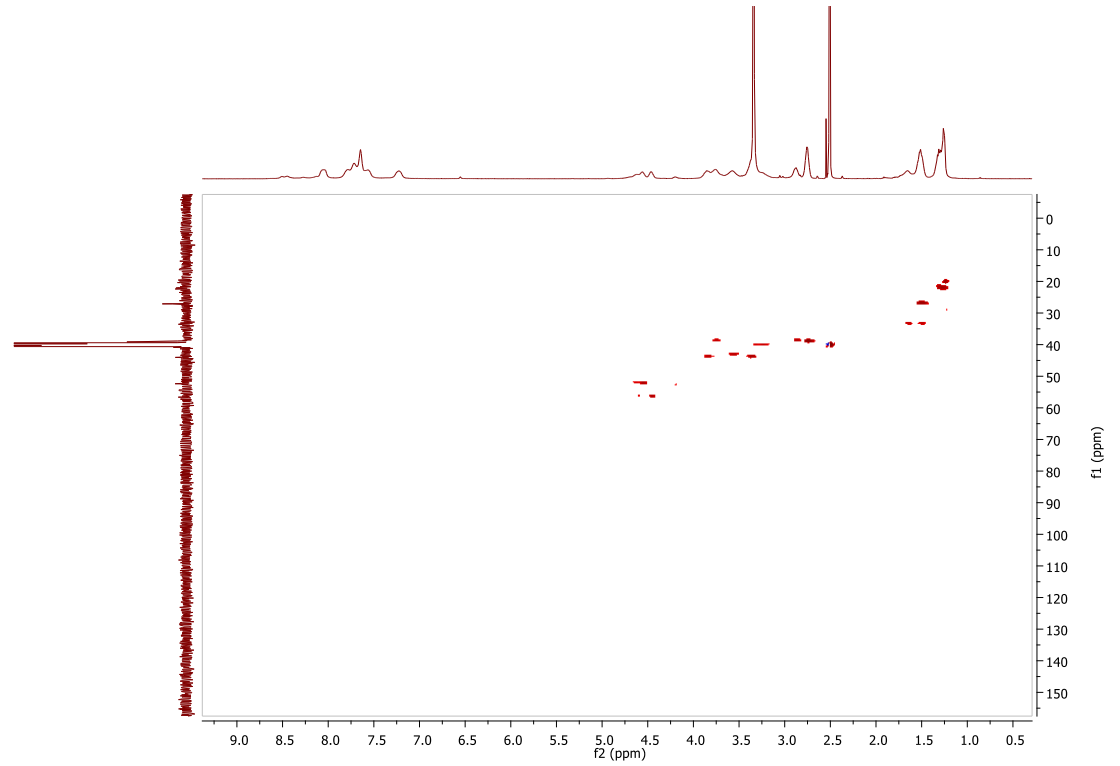

Figure A4.11: HSQC Spectrum of **4.16 (Sq-2-Ala-Lys)** in DMSO-d_6.

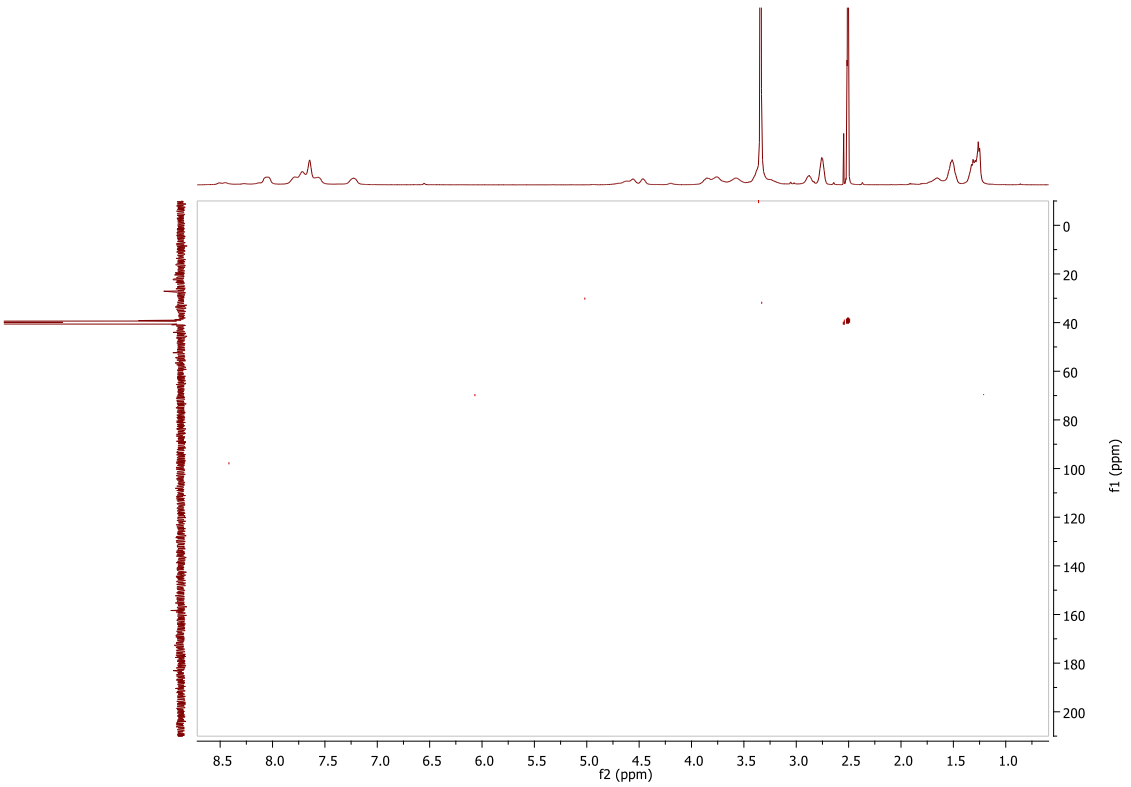

Figure A4.12: HMBC Spectrum of **4.16 (Sq-2-Ala-Lys)** in DMSO-d_6.

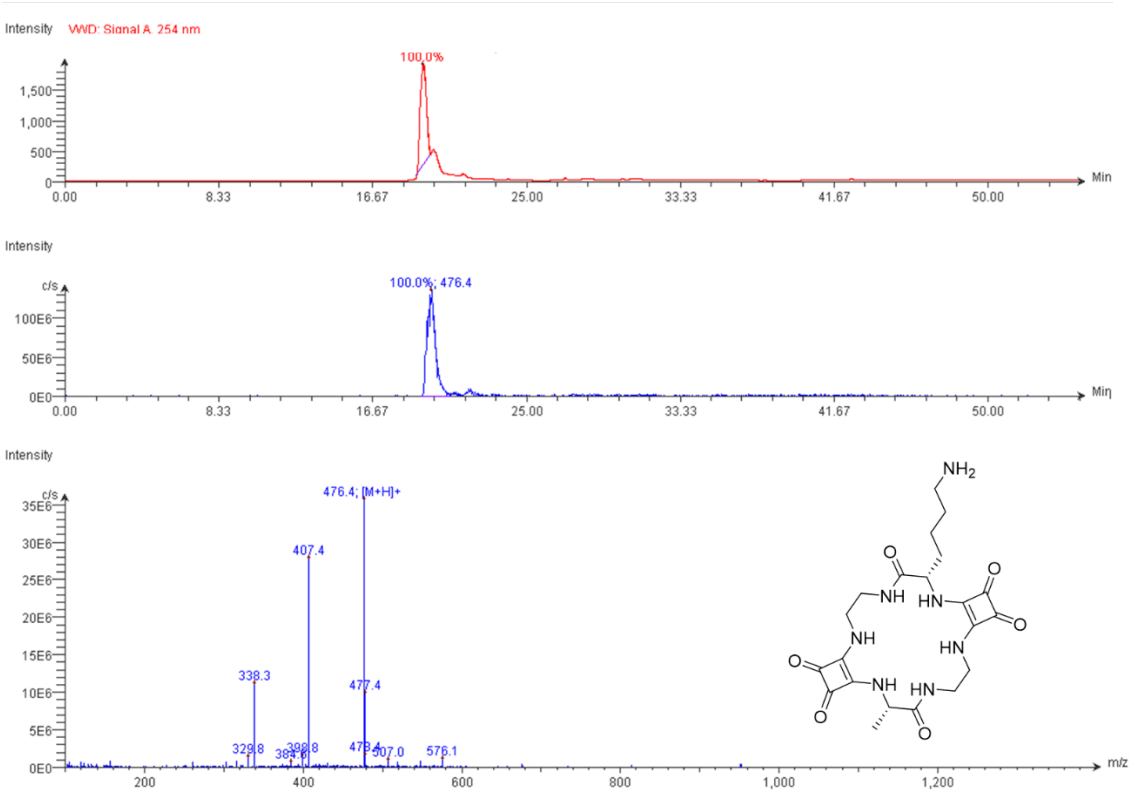

Figure A4.13: LC-MS data for **4.16 (Sq-2-Ala-Lys)**.

Compound Table

Compound Label	RT (min)	Observed mass (m/z)	Neutral observed mass (Da)	Theoretical mass (Da)	Mass error (ppm)	Isotope match score (%)
Cpd 1: C21 H29 N7 O6	0.59	476.2252	475.2179	475.2179	0.03	99.00

Figure: Full range view of Compound spectra and potential adducts.

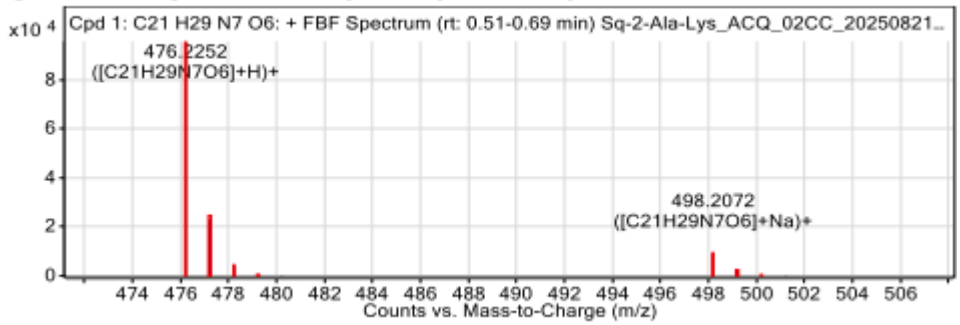

Figure: Zoomed Compound spectra view
(red boxes indicating expected theoretical isotope spacing and abundance)

Compound isotope peak List

m/z	z	Abund	Formula	Ion
476.2252	1	95789.2	C21H29N7O6	(M+H)+
477.2279	1	23142.9	C21H29N7O6	(M+H)+
478.2298	1	3954.9	C21H29N7O6	(M+H)+
479.2366	1	595.0	C21H29N7O6	(M+H)+
480.2404	1	161.7	C21H29N7O6	(M+H)+
498.2072	1	9157.7	C21H29N7O6	(M+Na)+
499.2101	1	2386.3	C21H29N7O6	(M+Na)+
500.2114	1	429.0	C21H29N7O6	(M+Na)+
501.2404	1	141.5	C21H29N7O6	(M+Na)+

Figure A4.14: HRMS data for **4.16 (Sq-2-Ala-Lys)**.

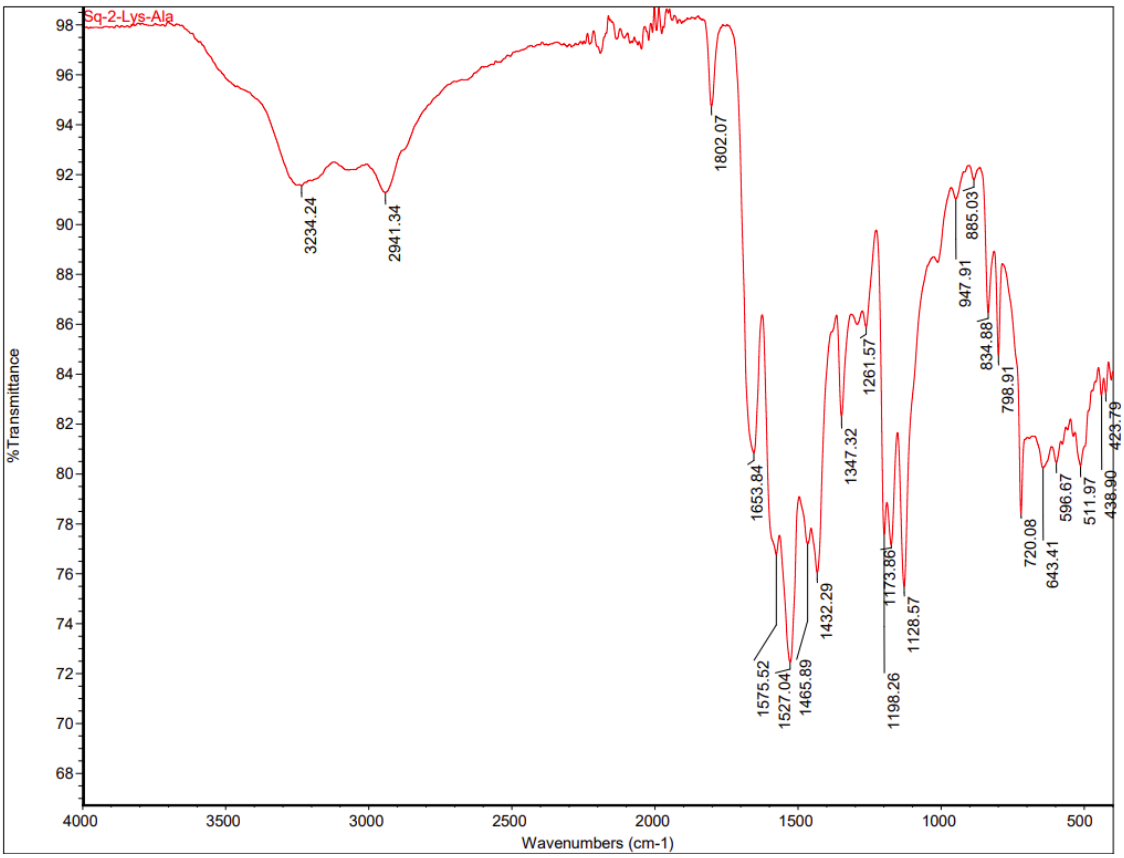

Figure A4.15: IR Spectrum of **4.16 (Sq-2-Ala-Lys)**.

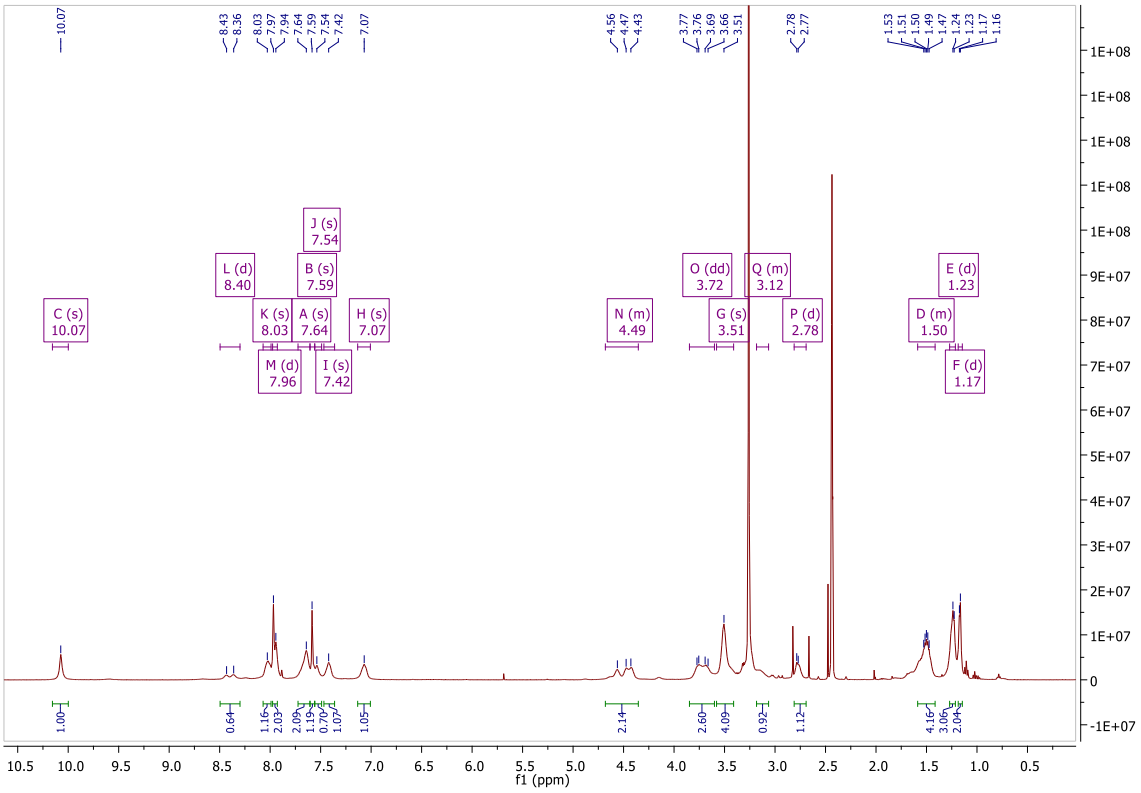

Figure A4.16: ^{1}H NMR Spectrum of **4.17 (Sq-2-Ala-Lys(SqBisCF$_3$))** in DMSO-d$_6$.

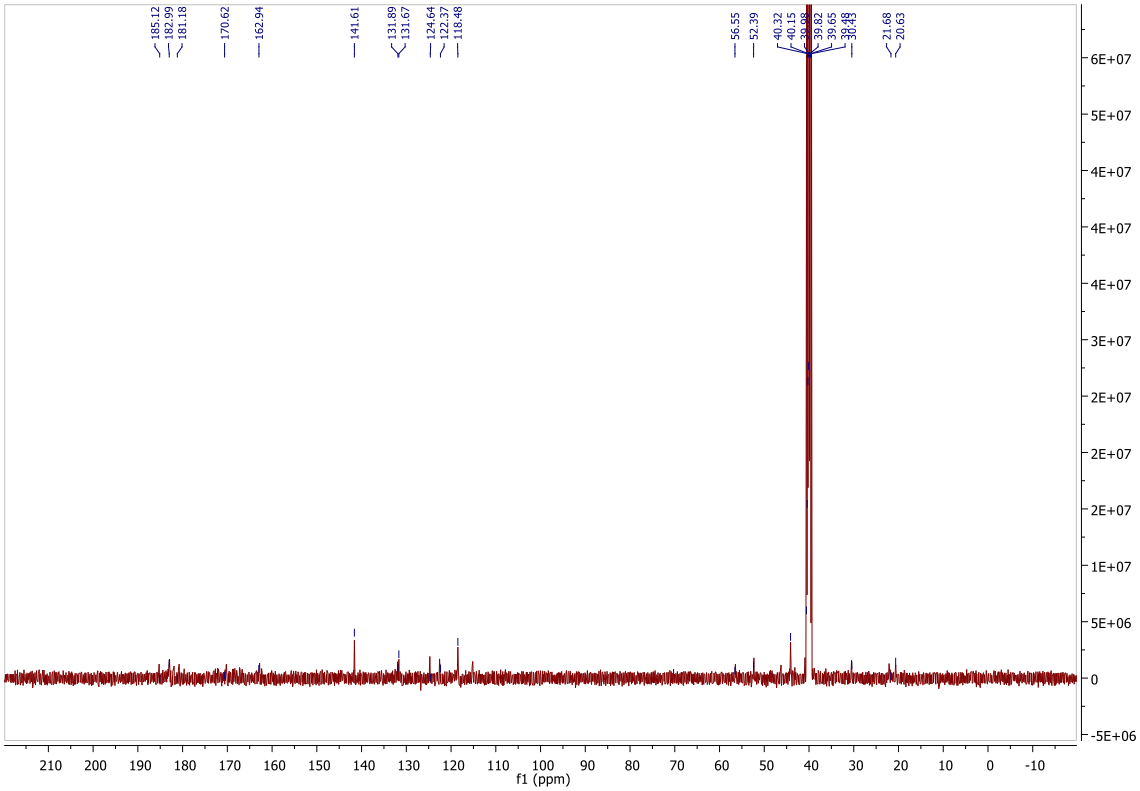

Figure A4.17: ^{13}C NMR Spectrum of **4.17 (Sq-2-Ala-Lys(SqBisCF$_3$))** in DMSO-d$_6$.

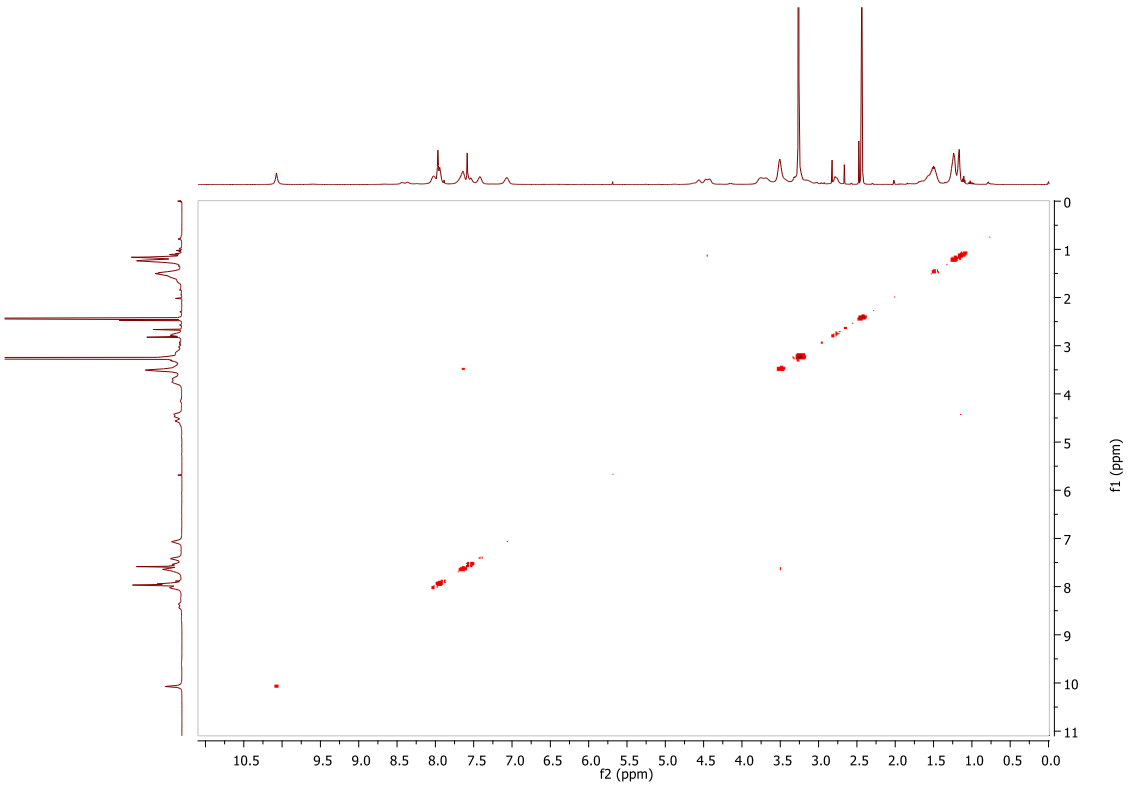

Figure A4.18: COSY Spectrum of **4.17 (Sq-2-Ala-Lys(SqBisCF$_3$))** in DMSO-d$_6$.

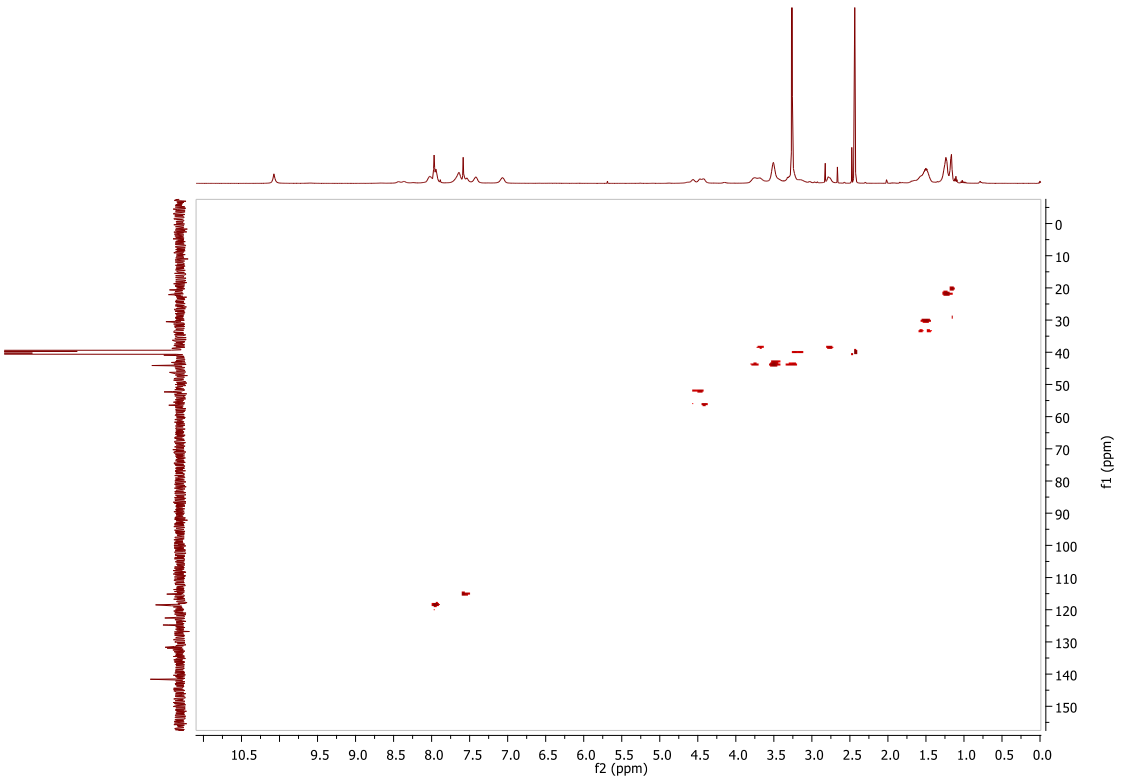

Figure A4.19: HSQC Spectrum of **4.17 (Sq-2-Ala-Lys(SqBisCF$_3$))** in DMSO-d$_6$.

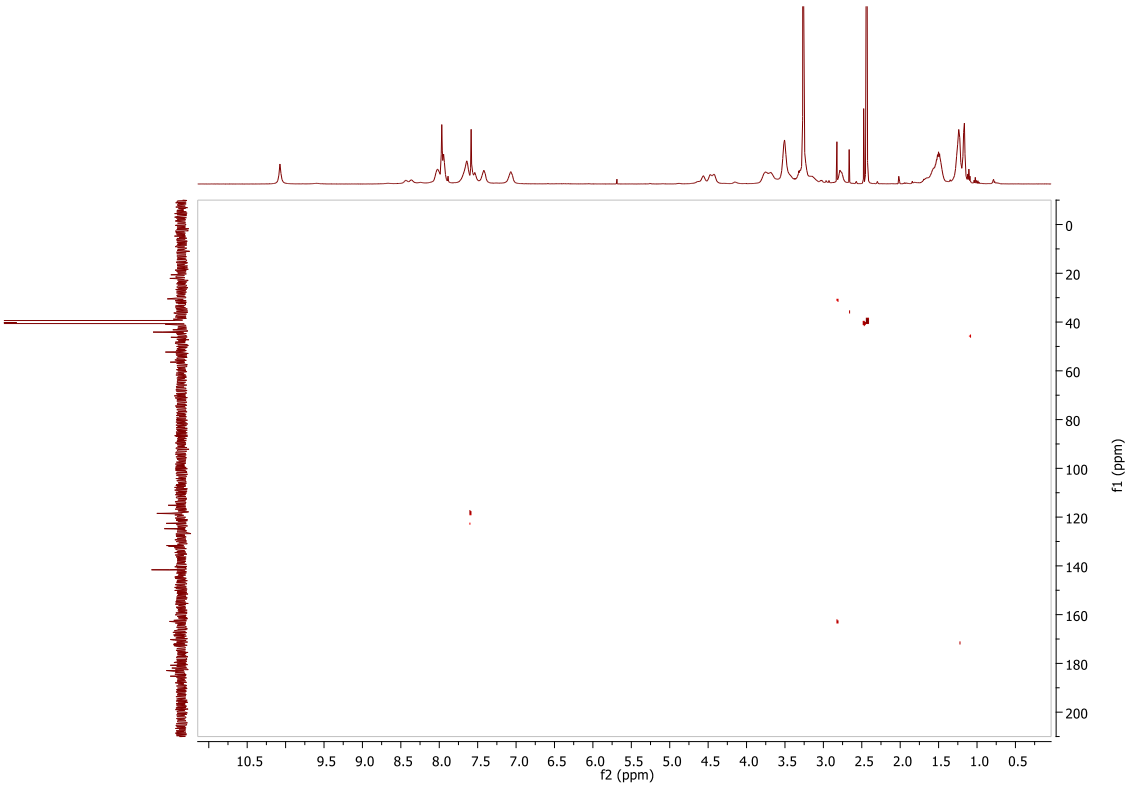

Figure A4.20: HMBC Spectrum of **4.17 (Sq-2-Ala-Lys(SqBisCF$_3$))** in DMSO-d$_6$.

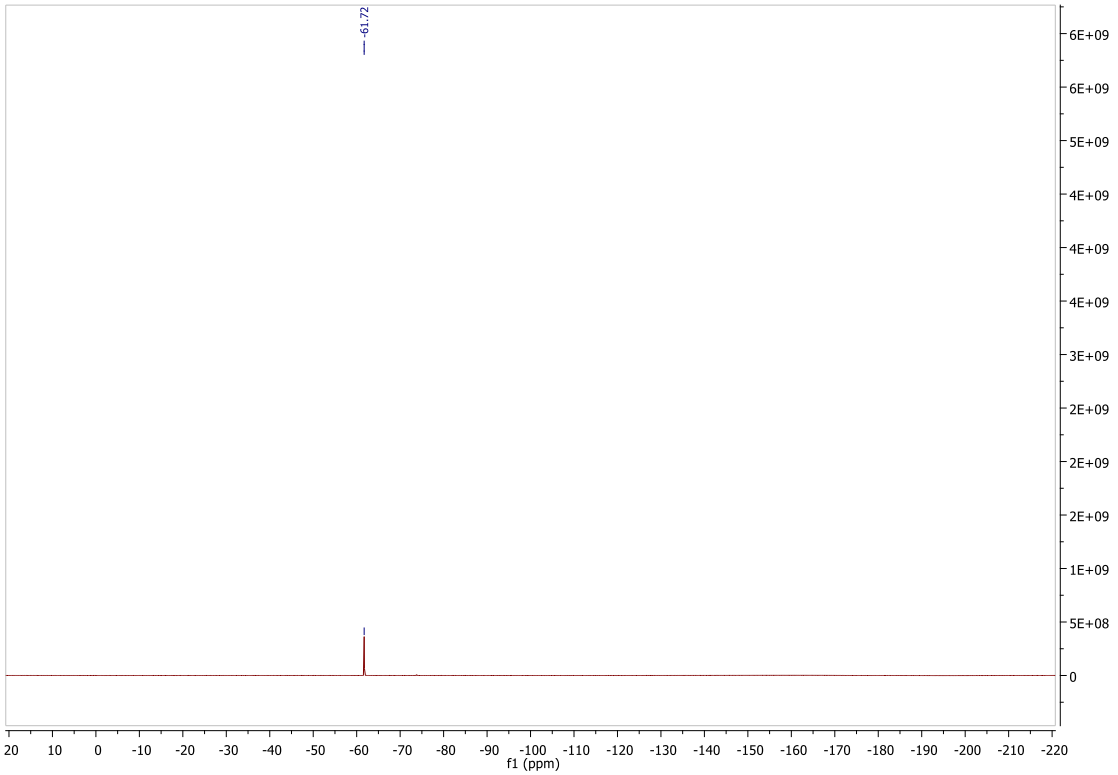

Figure A4.21: ^{19}F NMR Spectrum of **4.17 (Sq-2-Ala-Lys(SqBisCF$_3$))** in DMSO-d$_6$.

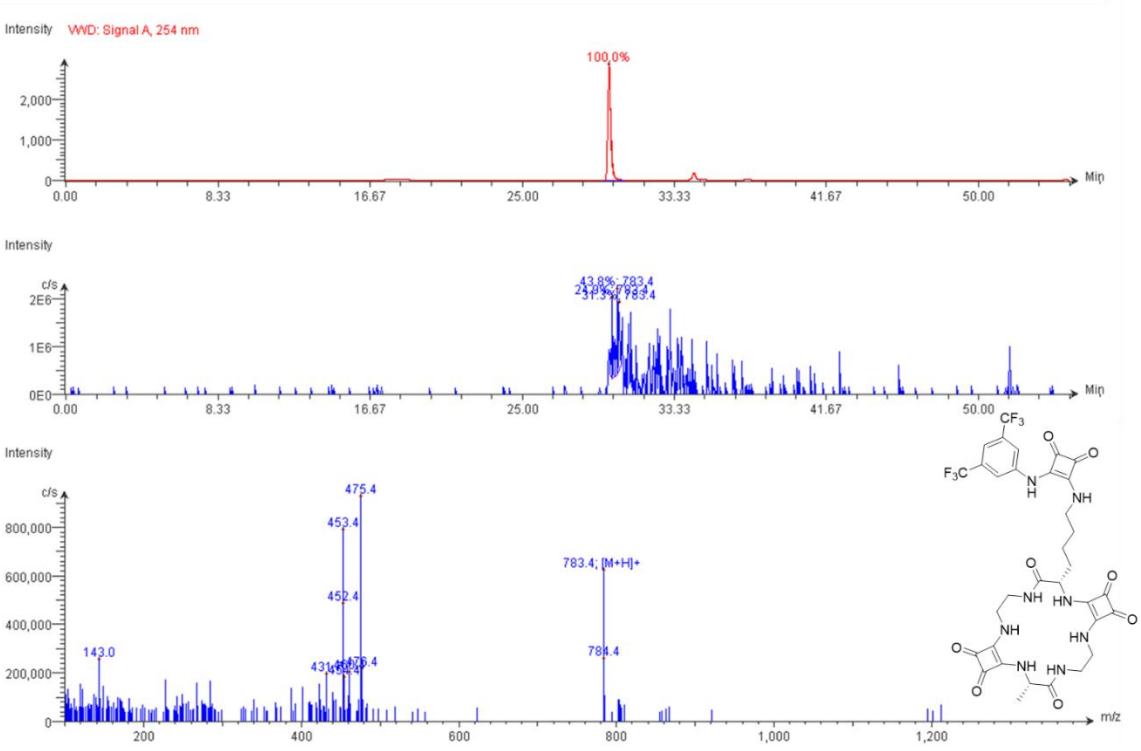

Figure A4.22: LC-MS data for **4.17 (Sq-2-Ala-Lys(SqBisCF$_3$))**.

Compound Table

Compound Label	RT (min)	Observed mass (m/z)	Neutral observed mass (Da)	Theoretical mass (Da)	Mass error (ppm)	Isotope match score (%)
Cpd 1: C33 H32 F6 N8 O8	0.75	783.2313	782.2240	782.2247	-0.89	99.29

Figure: Extracted ion chromatogram (EIC) of compound.

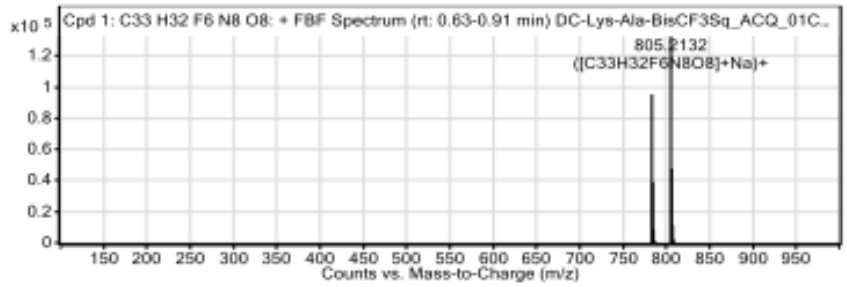

Figure: Full range view of Compound spectra and potential adducts.

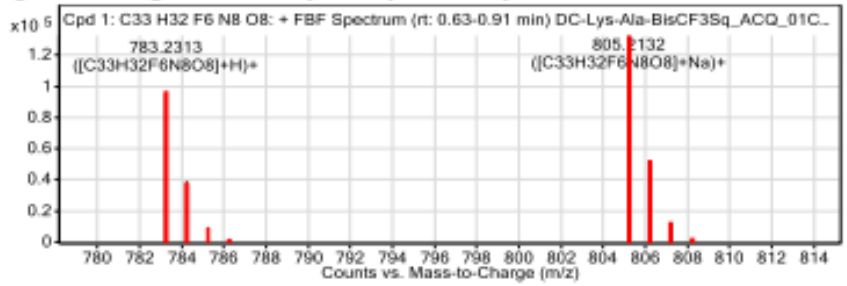

Figure: Zoomed Compound spectra view
(red boxes indicating expected theoretical isotope spacing and abundance)

Compound isotope peak List

m/z	z	Abund	Formula	Ion
783.2313	1	95321.2	C33H32F6N8O8	(M+H)+
784.2343	1	38979.7	C33H32F6N8O8	(M+H)+
785.2368	1	8456.3	C33H32F6N8O8	(M+H)+
786.2393	1	1630.6	C33H32F6N8O8	(M+H)+
805.2132	1	132568.7	C33H32F6N8O8	(M+Na)+
806.2161	1	47838.8	C33H32F6N8O8	(M+Na)+
807.2188	1	11348.2	C33H32F6N8O8	(M+Na)+
808.2213	1	2174.9	C33H32F6N8O8	(M+Na)+

Figure A4.23: HRMS data for **4.17 (Sq-2-Ala-Lys(SqBisCF$_3$))**.

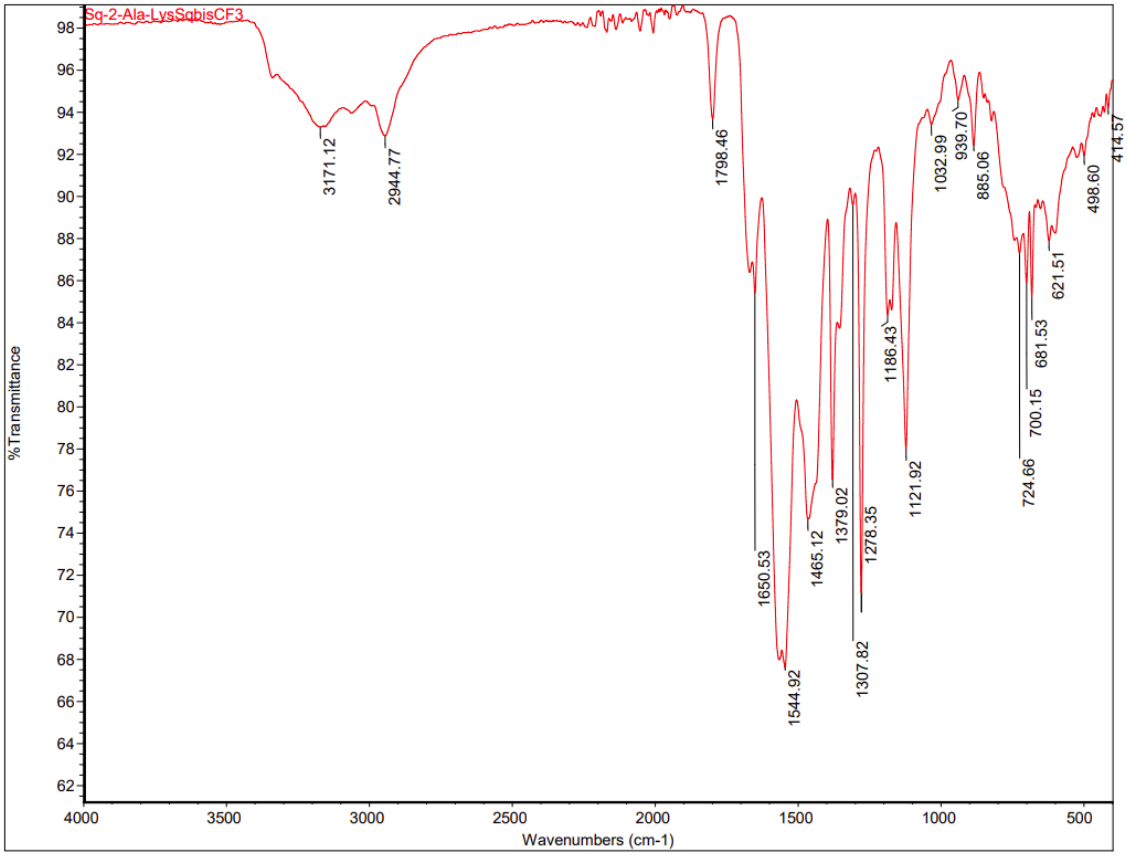

Figure A4.24: IR Spectrum of **4.17 (Sq-2-Ala-Lys(SqBisCF$_3$))**.

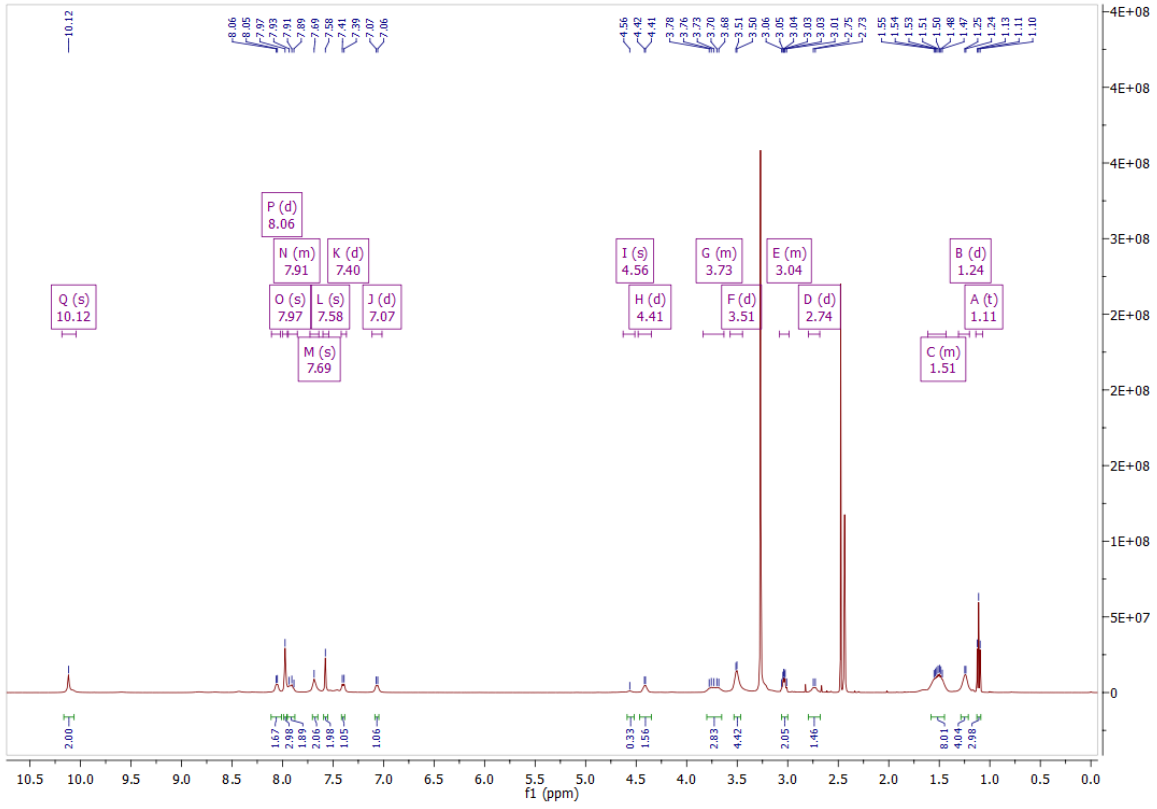

Figure A4.25: ^{1}H NMR Spectrum of **4.18 (Sq-2-Lys(SqBisCF$_3$))** in DMSO-d$_6$.

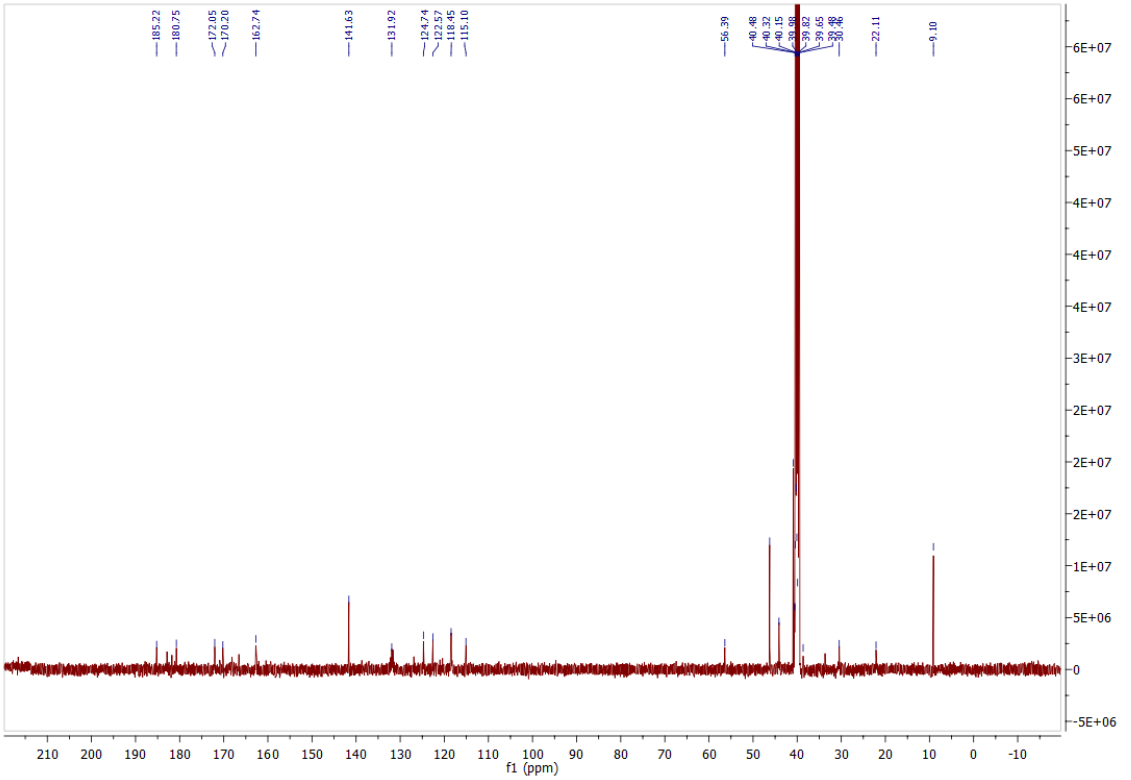

Figure A4.26: ^{13}C NMR Spectrum of **Sq-2-Lys(SqBisCF$_3$) 4.18 (Sq-2-Lys(SqBisCF$_3$))** in DMSO-d$_6$.

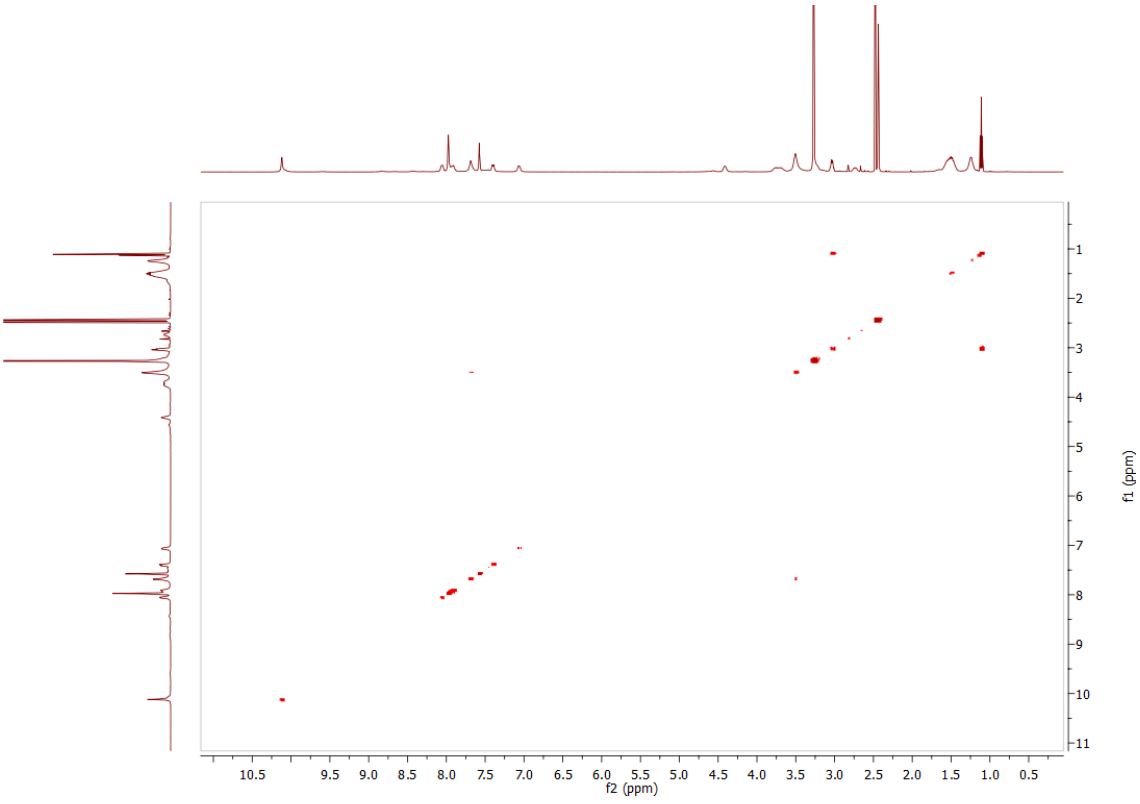

Figure A4.27: COSY Spectrum of **4.18 (Sq-2-Lys(SqBisCF$_3$))** in DMSO-d$_6$.

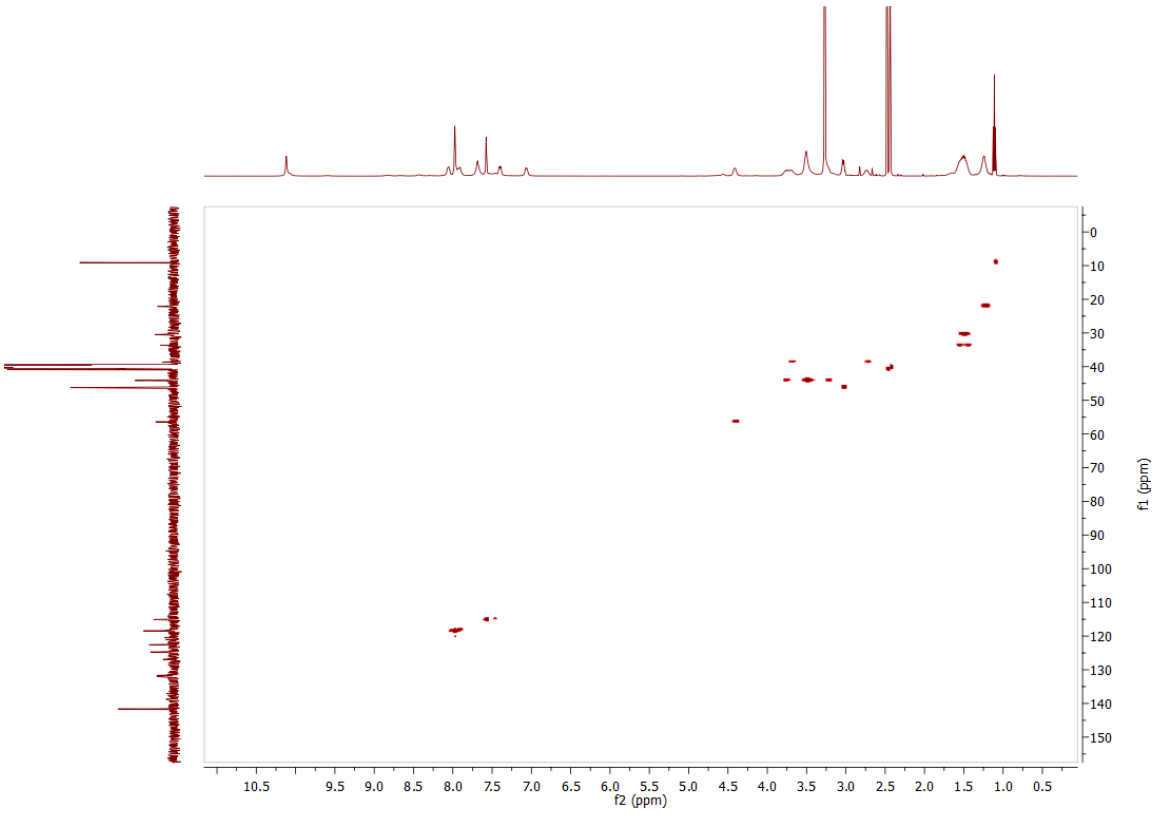

Figure A4.28: HSQC Spectrum of **4.18 (Sq-2-Lys(SqBisCF$_3$))** in DMSO-d$_6$.

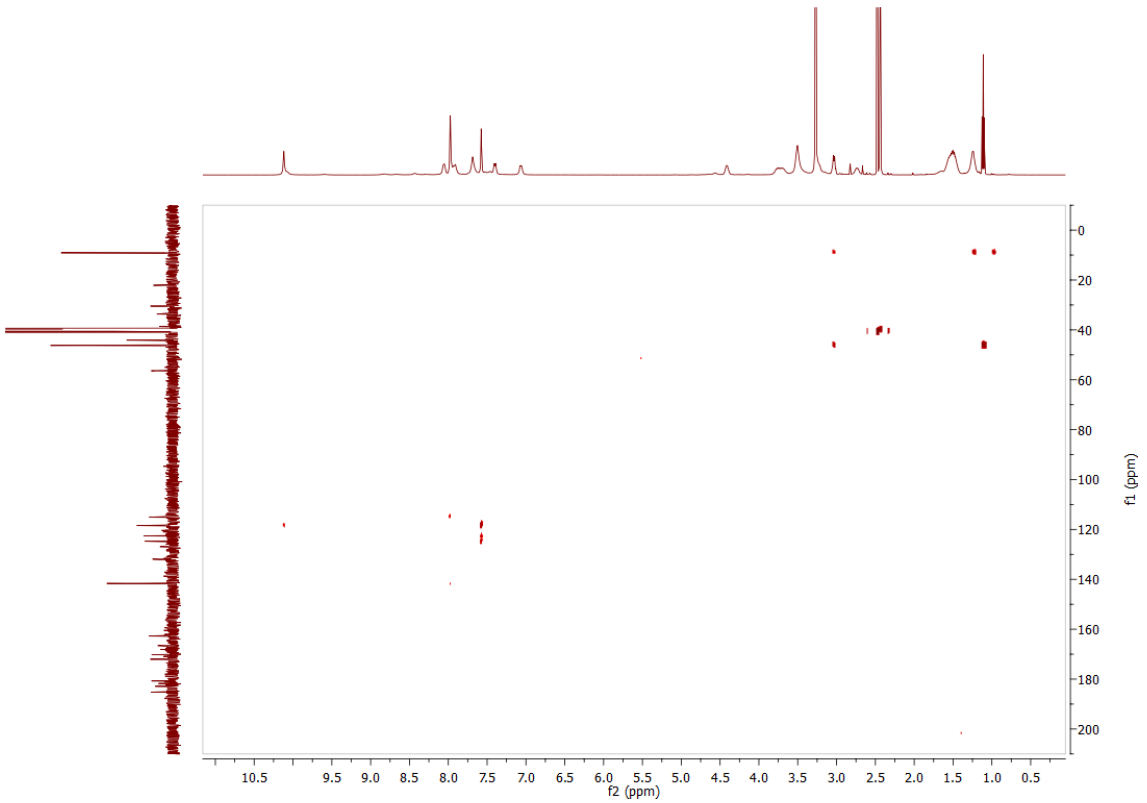

Figure A4.29: HMBC Spectrum of **4.18 (Sq-2-Lys(SqBisCF$_3$))** in DMSO-d$_6$.

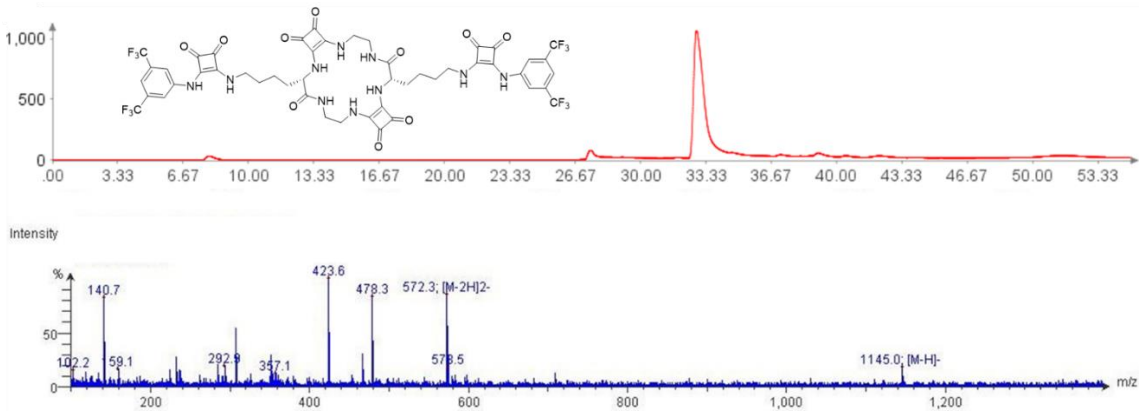

Figure A4.30: LCMS data for **4.18 (Sq-2-Lys(SqBisCF$_3$))**.

Compound Table

Compound Label	RT (min)	Observed mass (m/z)	Neutral observed mass (Da)	Theoretical mass (Da)	Mass error (ppm)	Isotope match score (%)
Cpd 1: C48 H42 F12 N10 O10	0.89	1169.2770	1146.2879	1146.2894	-1.33	99.59

Figure: Full range view of Compound spectra and potential adducts.

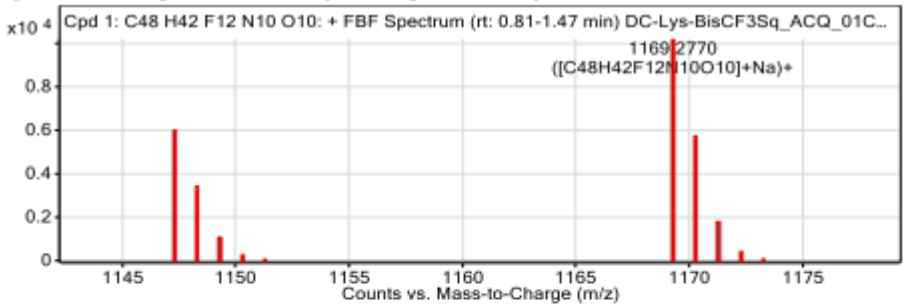

Figure: Zoomed Compound spectra view
(red boxes indicating expected theoretical isotope spacing and abundance)

Compound isotope peak List

m/z	z	Abund	Formula	Ion
1147.2953	1	6013.9	C48H42F12N10O10	(M+H)+
1148.2984	1	3217.1	C48H42F12N10O10	(M+H)+
1149.3012	1	1112.8	C48H42F12N10O10	(M+H)+
1150.3035	1	228.1	C48H42F12N10O10	(M+H)+
1151.2978	1	73.9	C48H42F12N10O10	(M+H)+
1169.2770	1	10209.1	C48H42F12N10O10	(M+Na)+
1170.2801	1	5613.5	C48H42F12N10O10	(M+Na)+
1171.2829	1	1729.9	C48H42F12N10O10	(M+Na)+
1172.2842	1	432.0	C48H42F12N10O10	(M+Na)+
1173.2804	1	113.0	C48H42F12N10O10	(M+Na)+

Figure A4.31: HRMS data for **4.18 (Sq-2-Lys(SqBisCF$_3$))**.

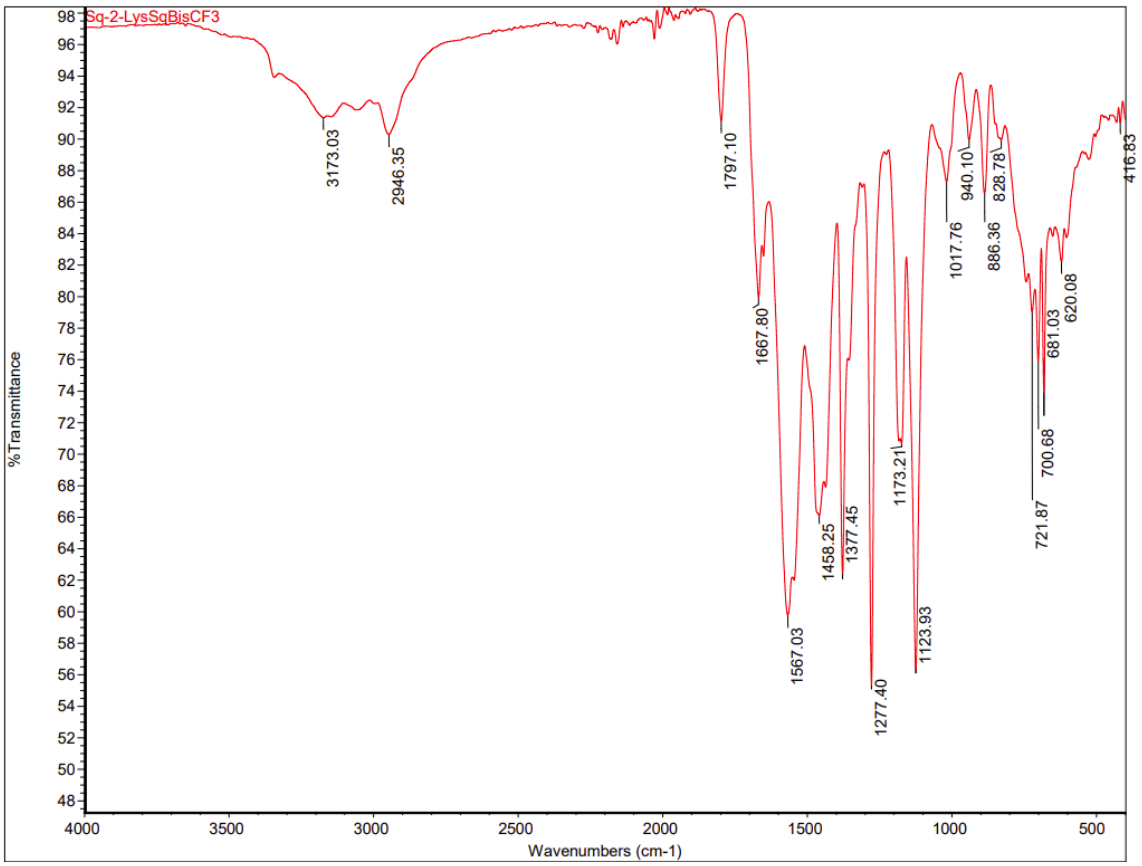

Figure A4.32: IR Spectrum of **4.18 (Sq-2-Lys(SqBisCF$_3$))**.

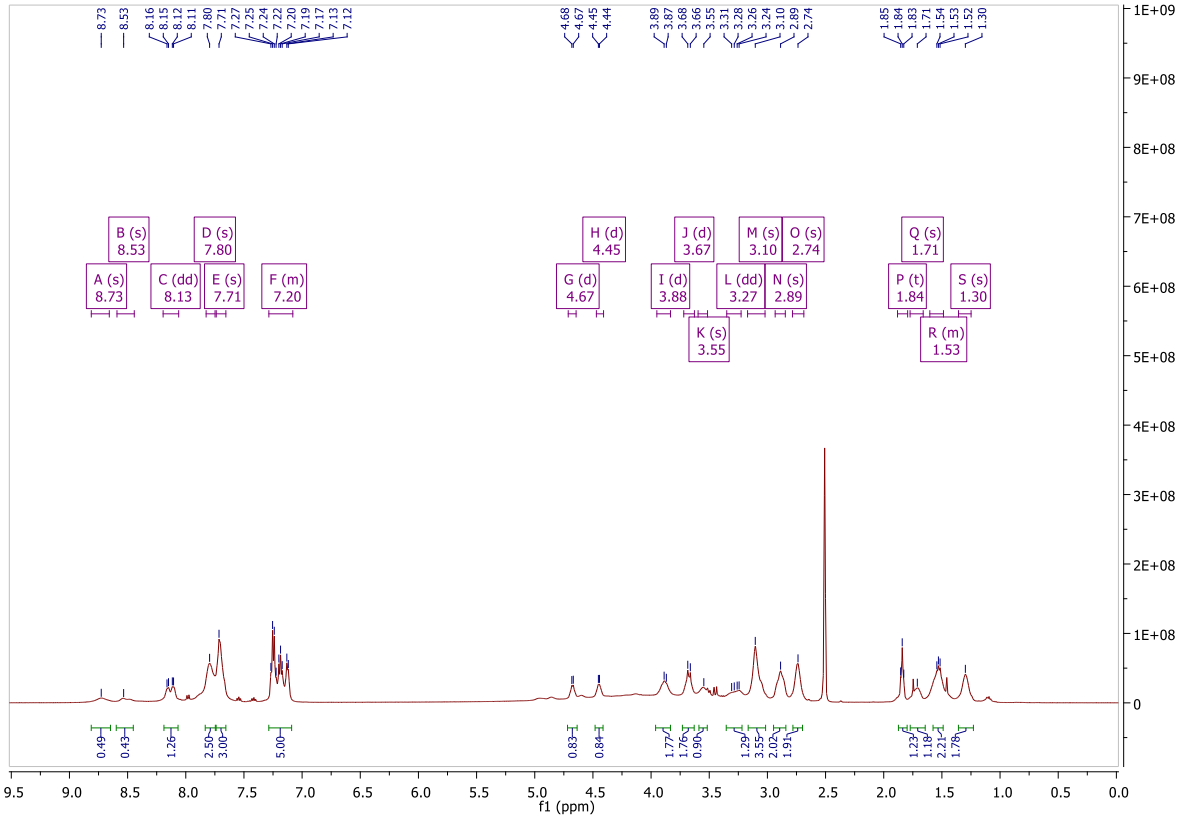

Figure A4.33: ^{1}H NMR Spectrum of **4.19 (Sq-2-Phe-Lys)** in DMSO-d_6.

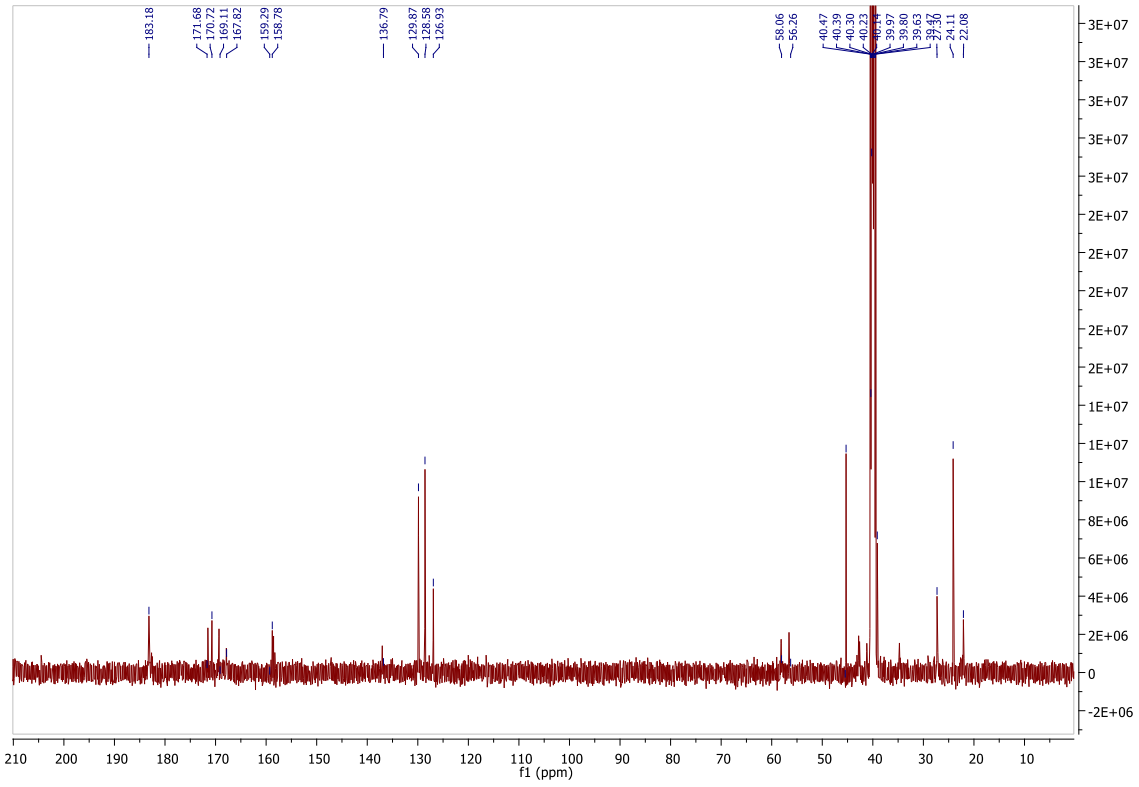

Figure A4.34: ^{13}C NMR Spectrum of **4.19 (Sq-2-Phe-Lys)** in DMSO-d_6.

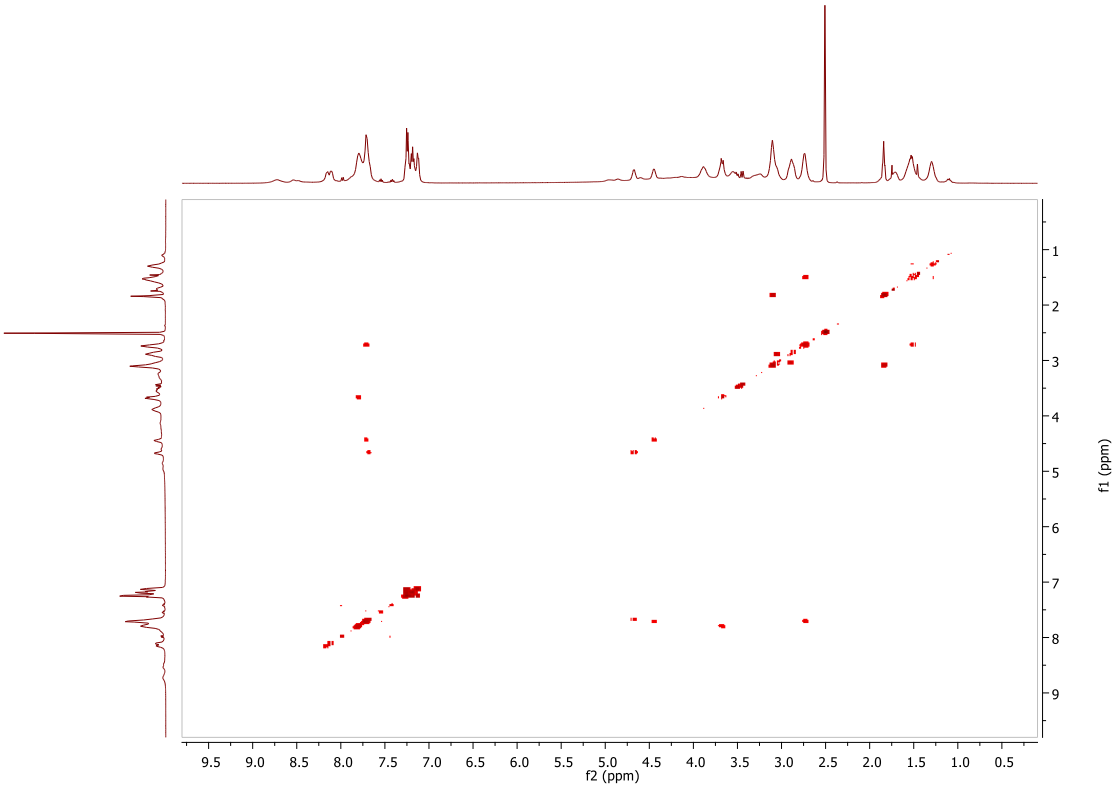

Figure A4.35: COSY Spectrum of **4.19 (Sq-2-Phe-Lys)** in DMSO-d_6.

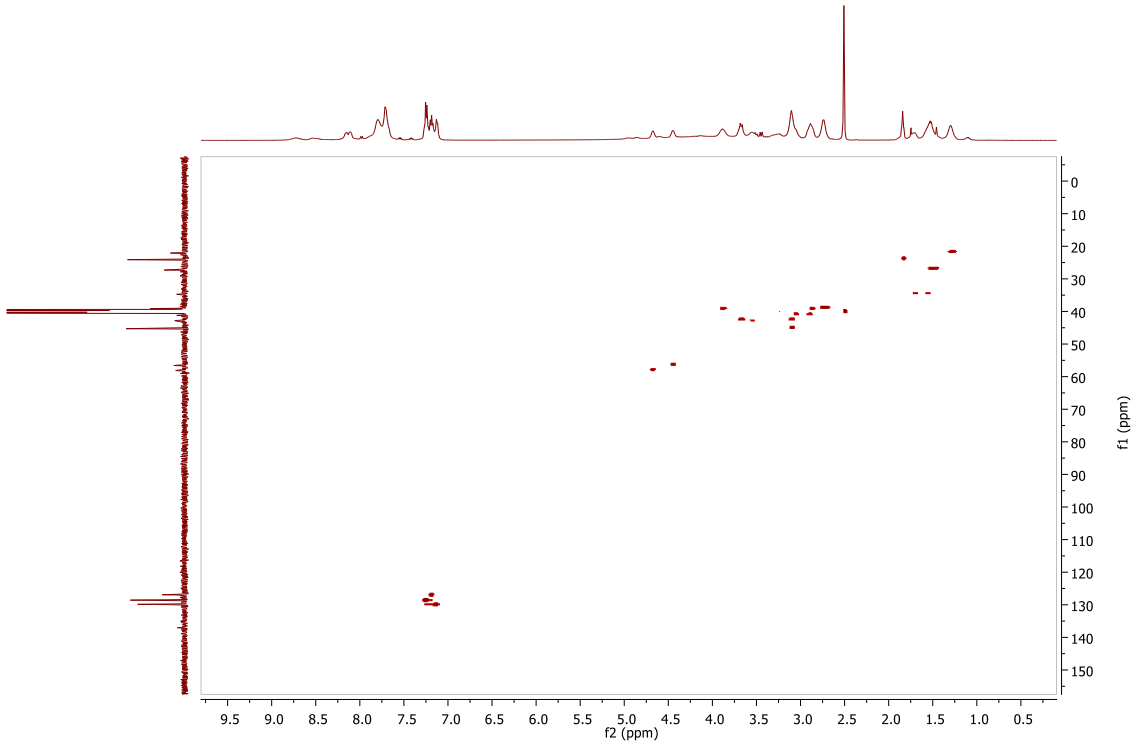

Figure A4.36: HSQC Spectrum of **4.19 (Sq-2-Phe-Lys)** in DMSO-d_6.

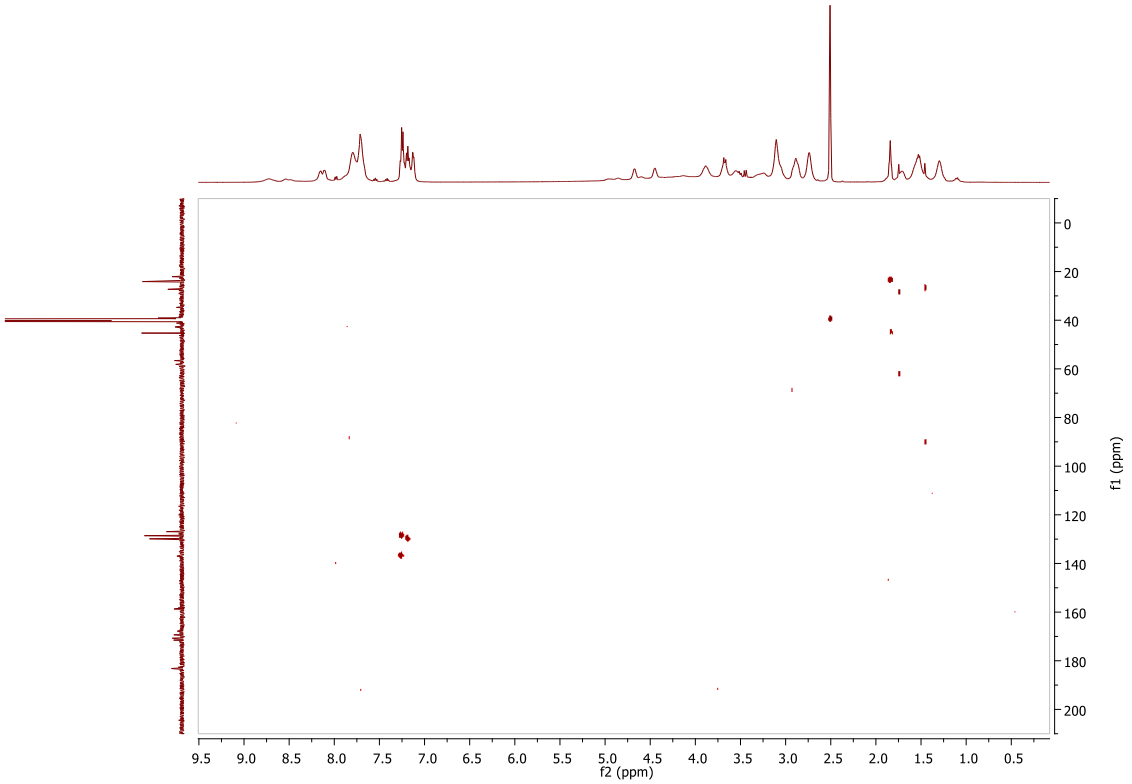

Figure A4.37: HMBC **4.19 (Sq-2-Phe-Lys)** in DMSO-d_6.

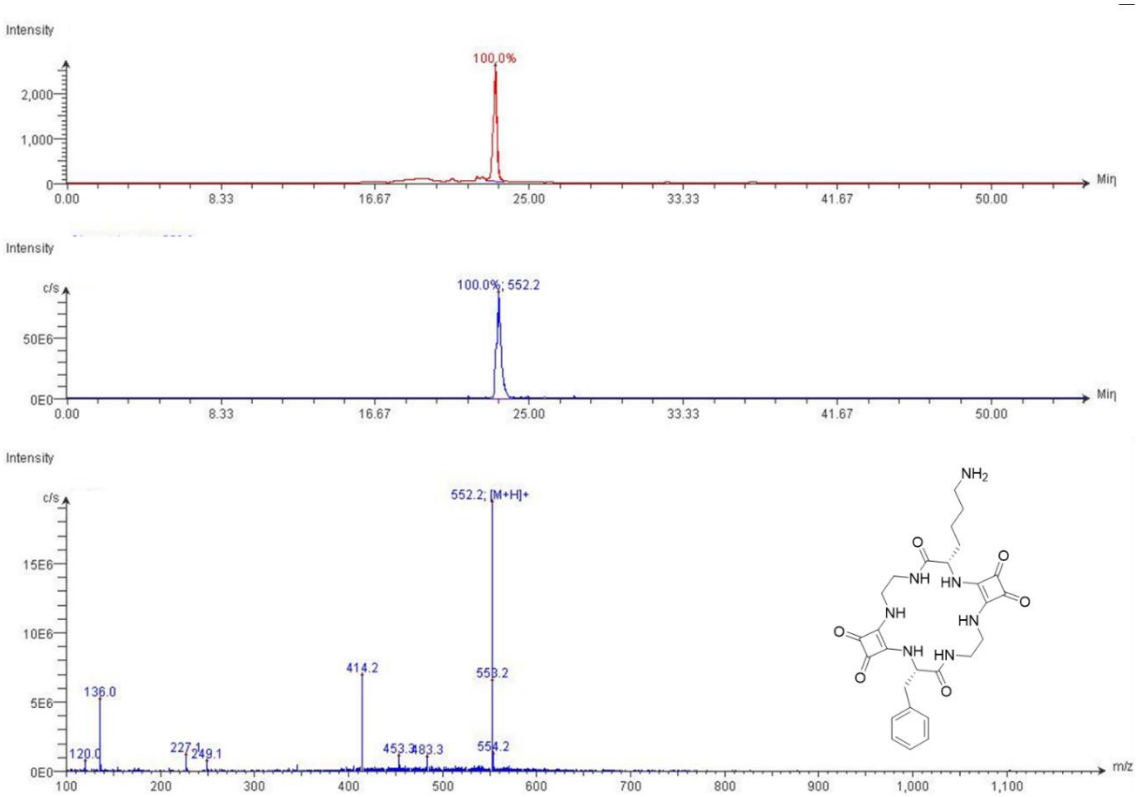

Figure A4.38: LCMS data for **4.19 (Sq-2-Phe-Lys)**.

Compound Table

Compound Label	RT (min)	Observed mass (m/z)	Neutral observed mass (Da)	Theoretical mass (Da)	Mass error (ppm)	Isotope match score (%)
Cpd 1: C27 H33 N7 O6	0.69	552.2566	551.2495	551.2492	0.49	99.16

Figure: Extracted ion chromatogram (EIC) of compound.

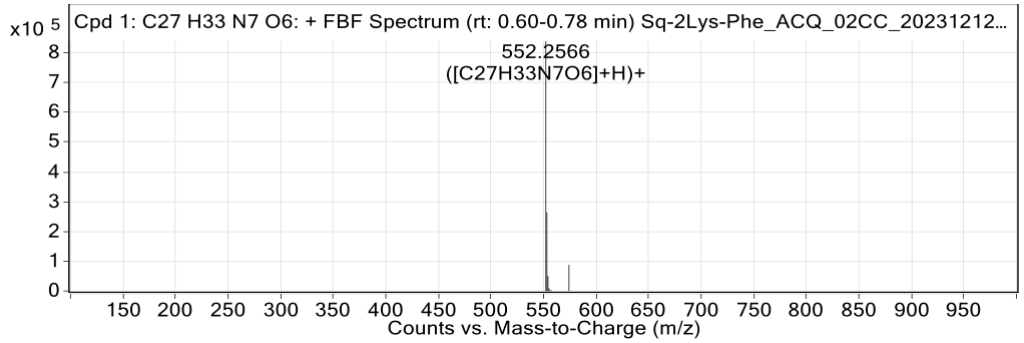

Figure: Full range view of Compound spectra and potential adducts.

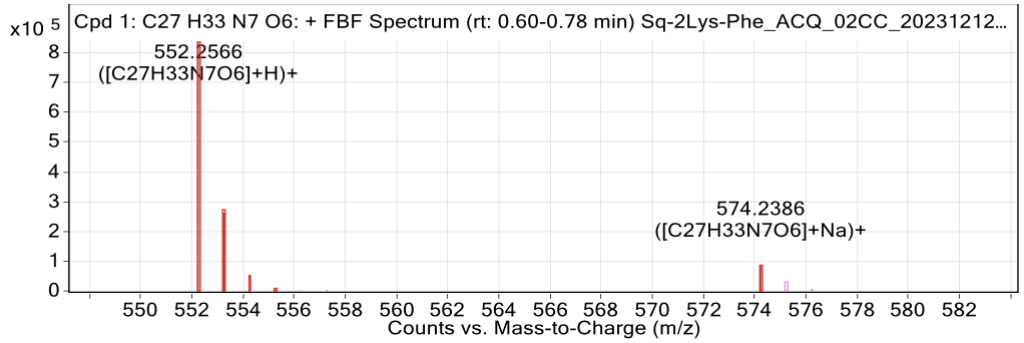

Figure: Zoomed Compound spectra view
(red boxes indicating expected theoretical isotope spacing and abundance)

Compound isotope peak List

m/z	z	Abund	Formula	Ion
552.2566	1	838988.8	C27H33N7O6	(M+H)+
553.2600	1	263759.0	C27H33N7O6	(M+H)+
554.2621	1	50503.8	C27H33N7O6	(M+H)+
555.2683	1	8553.1	C27H33N7O6	(M+H)+
556.2752	1	1576.0	C27H33N7O6	(M+H)+
557.2896	1	2641.5	C27H33N7O6	(M+H)+
574.2386	1	87917.3	C27H33N7O6	(M+Na)+

Figure A4.39: HRMS data for **4.19 (Sq-2-Phe-Lys)**.

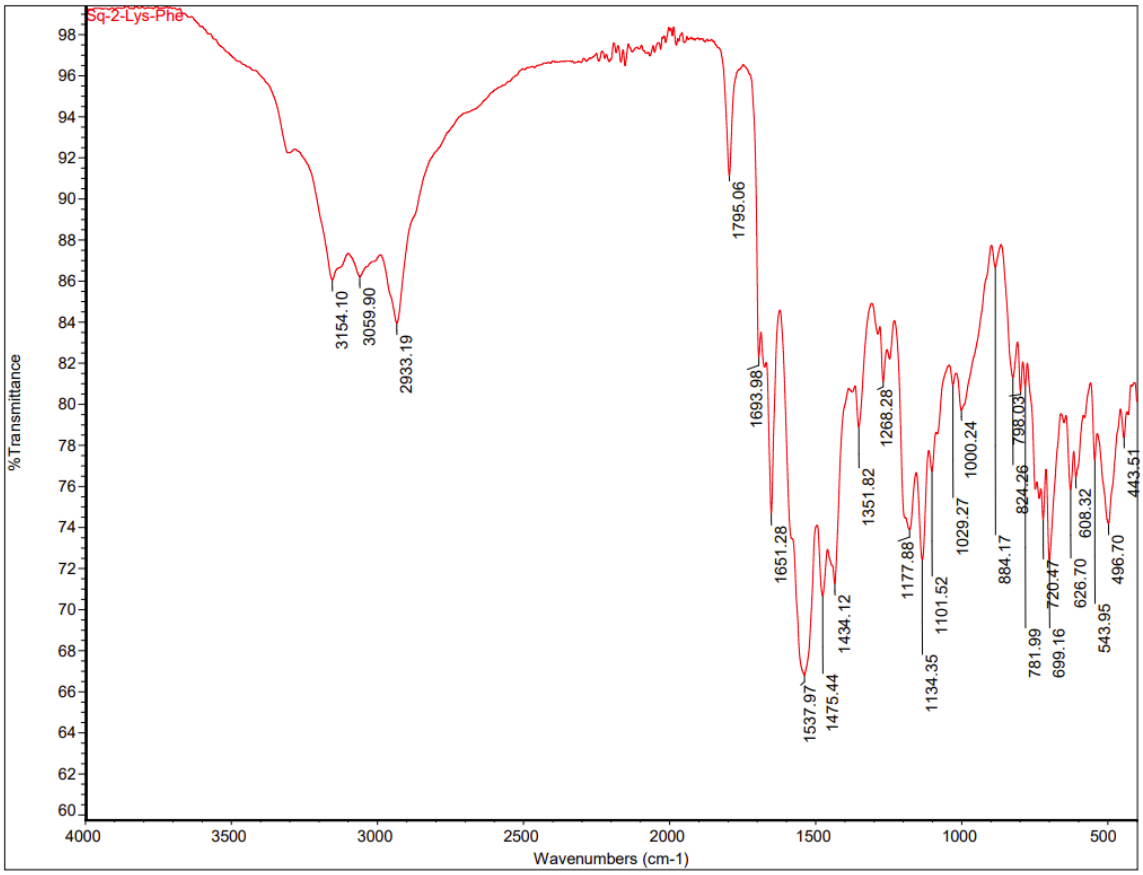

Figure A4.40: IR Spectrum of **4.19 (Sq-2-Phe-Lys)**.

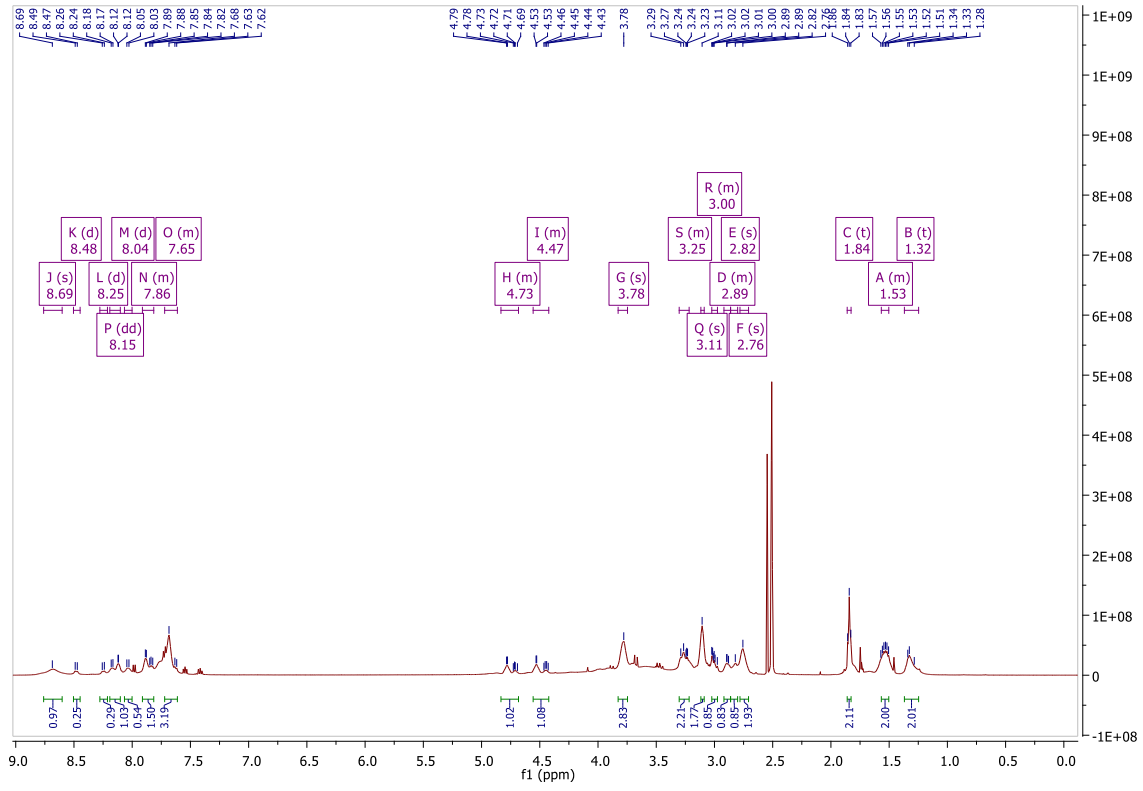

Figure A4.41: ^{1}H NMR Spectrum of **4.20 (Sq-2-F$_5$Phe-Lys)** in DMSO-d$_6$.

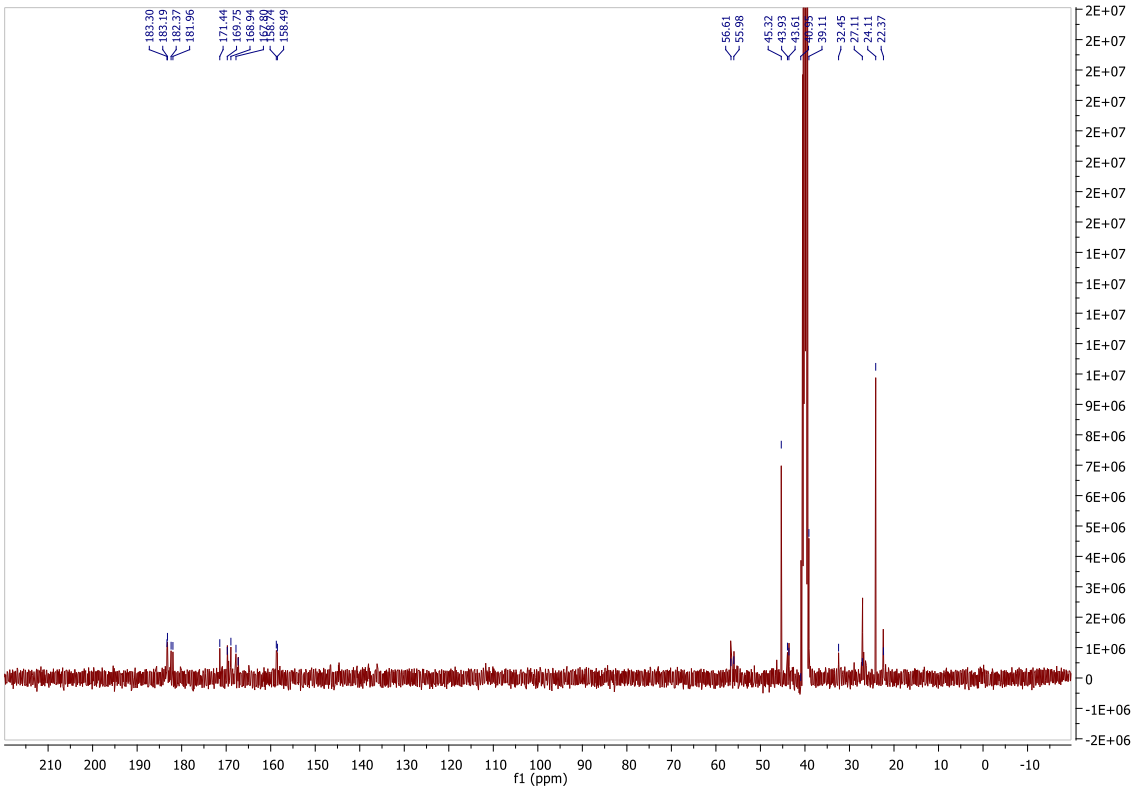

Figure A4.42: ^{13}C NMR Spectrum of **4.20 (Sq-2-F$_5$Phe-Lys)** in DMSO-d$_6$.

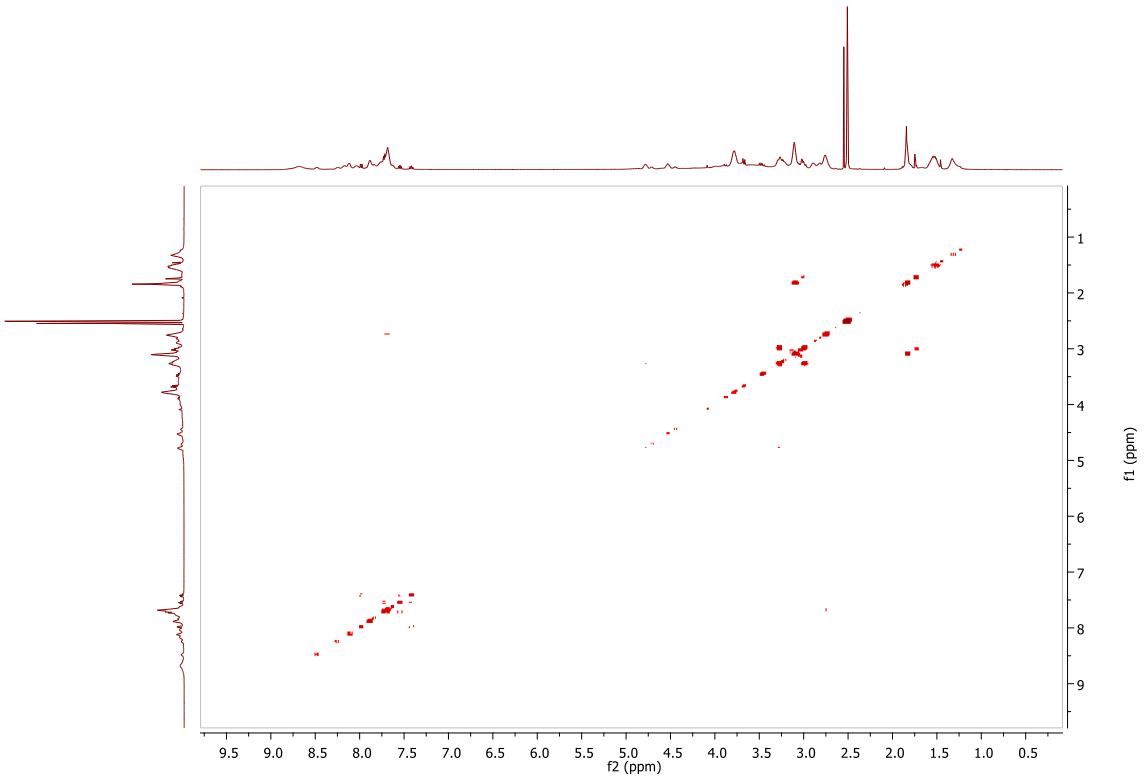

Figure A4.43: COSY Spectrum of **4.20 (Sq-2-F$_5$Phe-Lys)** in DMSO-d$_6$.

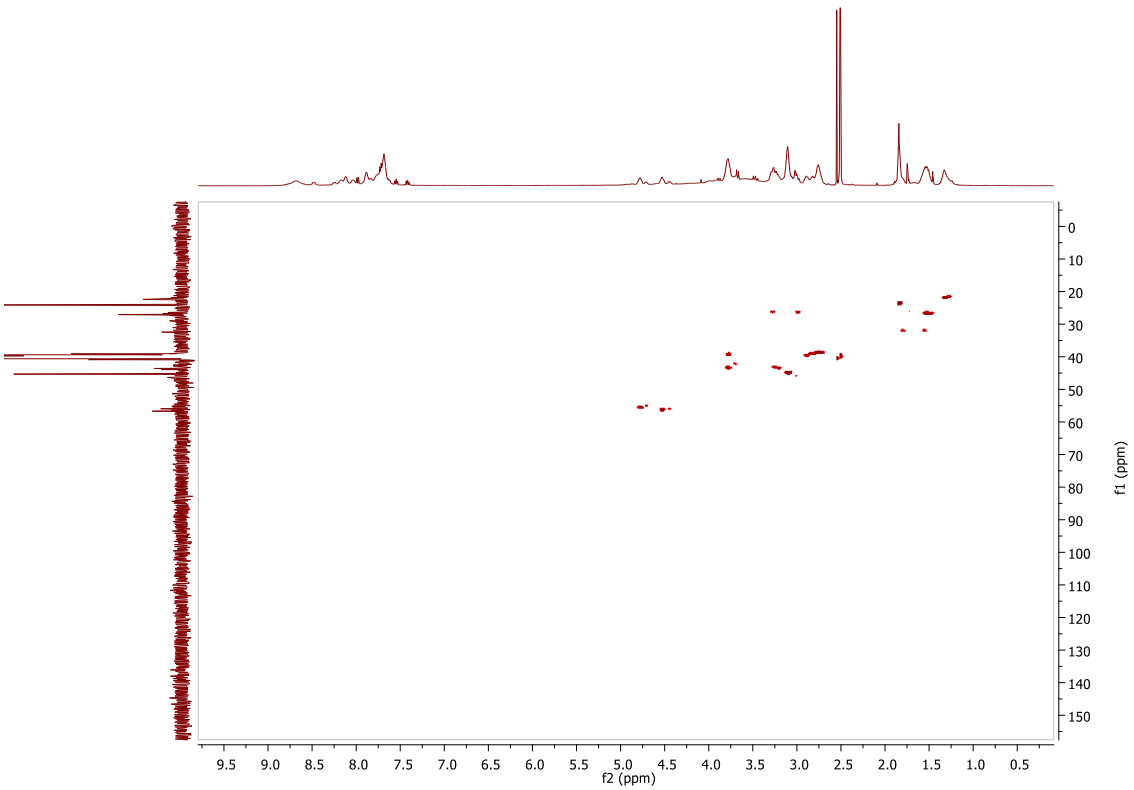

Figure A4.44: HSQC Spectrum of **4.20 (Sq-2-F_5Phe-Lys)** in DMSO-d_6.

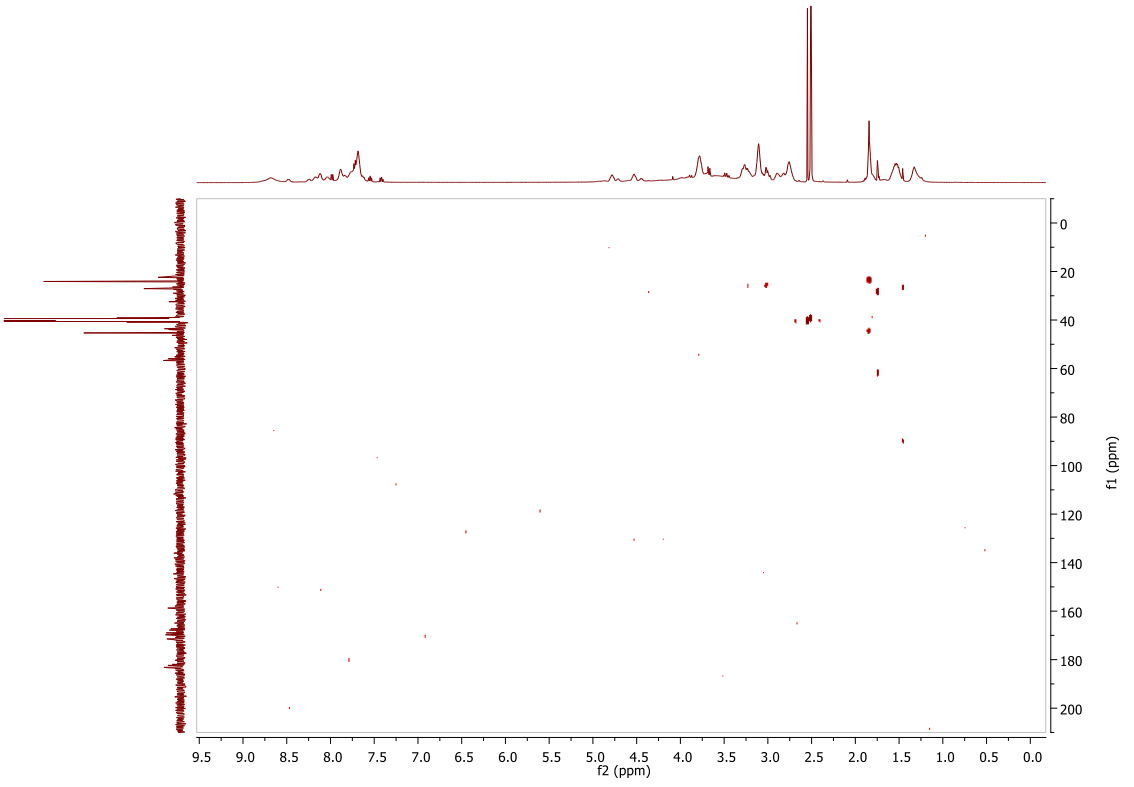

Figure A4.45: HMBC Spectrum of **4.20 (Sq-2-F_5Phe-Lys)** in DMSO-d_6.

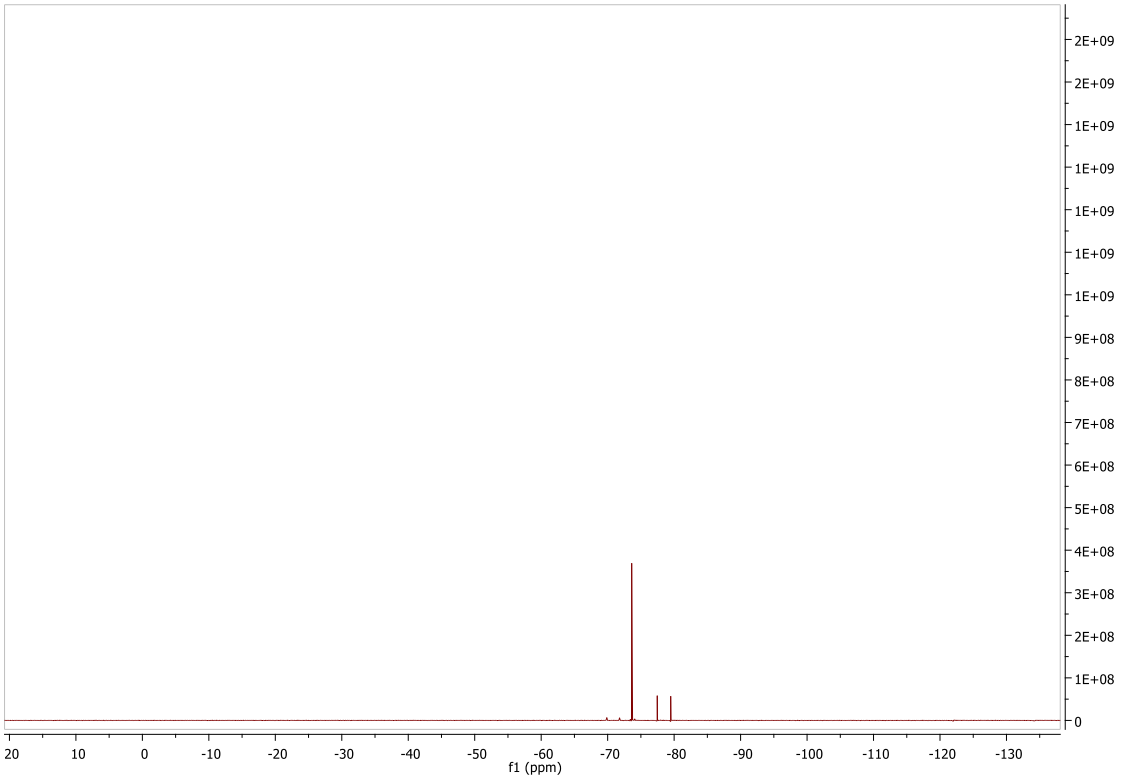

Figure A4.46: ^{19}F NMR Spectrum of **4.20 (Sq-2-F$_5$Phe-Lys)** in DMSO-d$_6$.

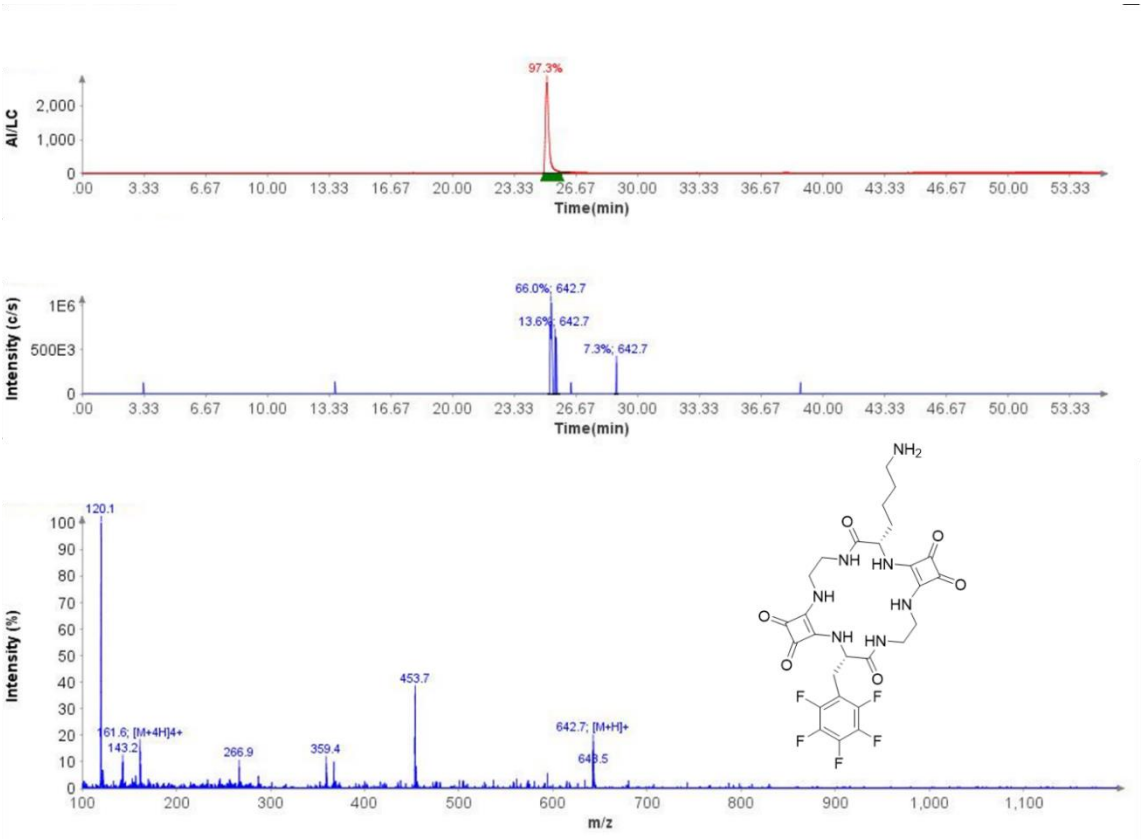

Figure A4.47: LC-MS data for **4.20 (Sq-2-F$_5$Phe-Lys)**.

Compound Table

Compound Label	RT (min)	Observed mass (m/z)	Neutral observed mass (Da)	Theoretical mass (Da)	Mass error (ppm)	Isotope match score (%)
Cpd 1: C27 H28 F5 N7 O6	0.67	642.2097	641.2023	641.2021	0.28	99.40

Figure: Extracted ion chromatogram (EIC) of compound.

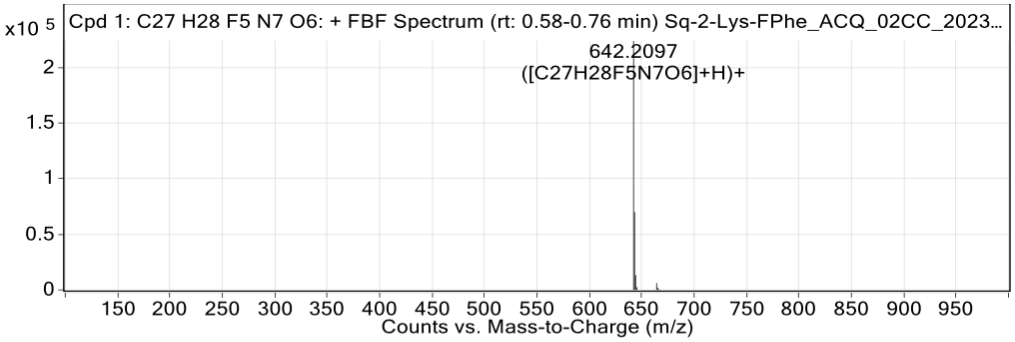

Figure: Full range view of Compound spectra and potential adducts.

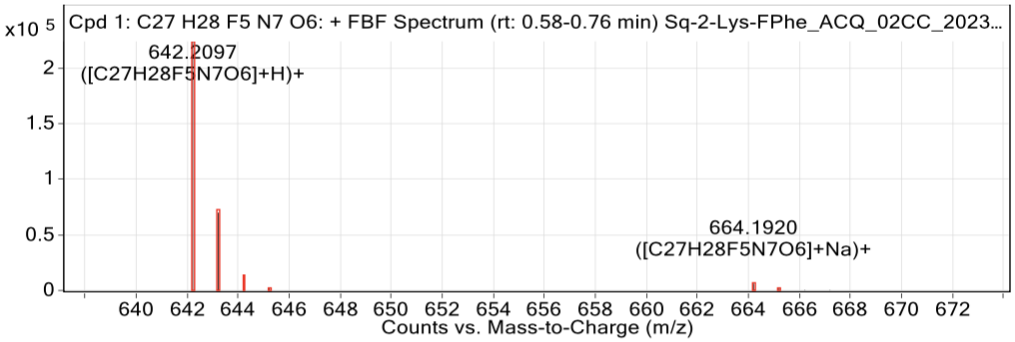

Figure: Zoomed Compound spectra view
(red boxes indicating expected theoretical isotope spacing and abundance)

Compound isotope peak List

m/z	z	Abund	Formula	Ion
642.2097	1	224201.6	C27H28F5N7O6	(M+H)+
643.2122	1	70041.4	C27H28F5N7O6	(M+H)+
644.2143	1	13229.7	C27H28F5N7O6	(M+H)+
645.2169	1	2461.3	C27H28F5N7O6	(M+H)+
664.1920	1	6159.8	C27H28F5N7O6	(M+Na)+
665.1954	1	2012.5	C27H28F5N7O6	(M+Na)+
666.2082	1	404.3	C27H28F5N7O6	(M+Na)+
667.1899	1	325.5	C27H28F5N7O6	(M+Na)+

Figure A4.48: HRMS data for **4.20 (Sq-2-F_5Phe-Lys)**.

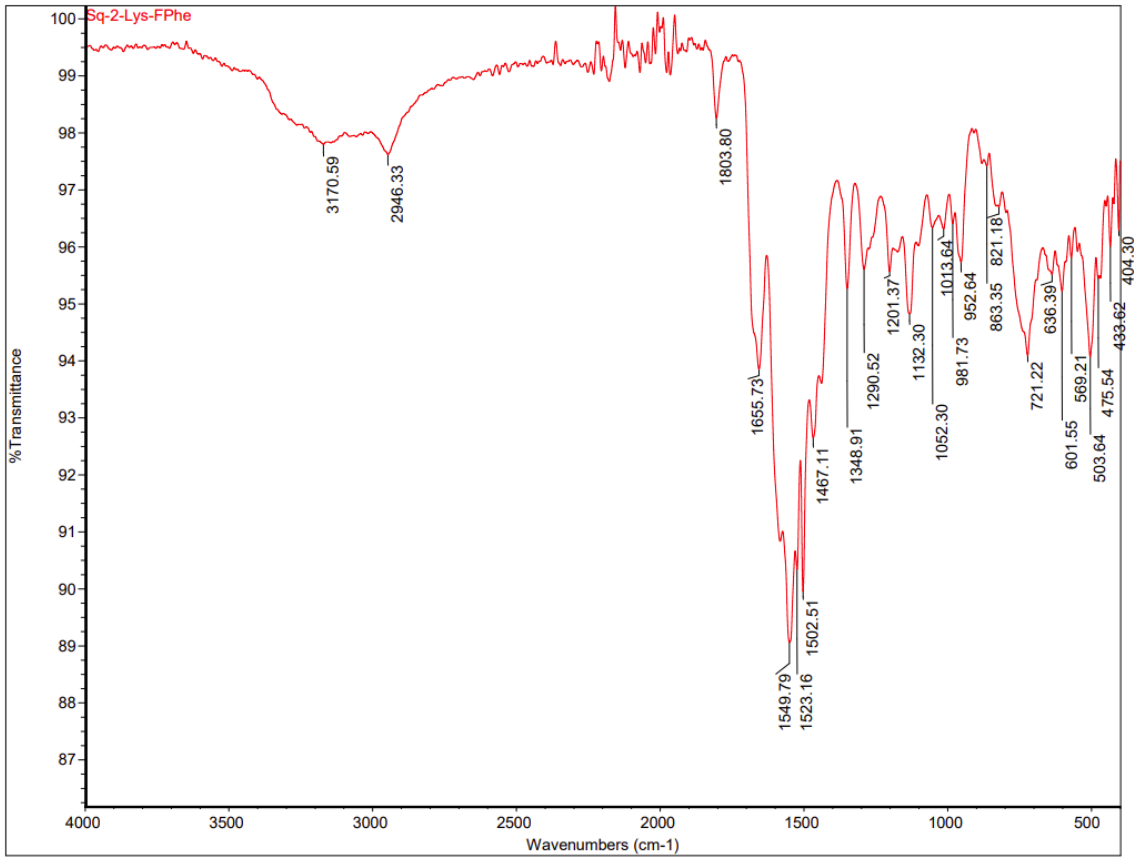

Figure A4.49: IR Spectrum of **4.20 (Sq-2-F_5Phe-Lys)**.

Chapter 4 – ^{1}H NMR Anion Binding Data

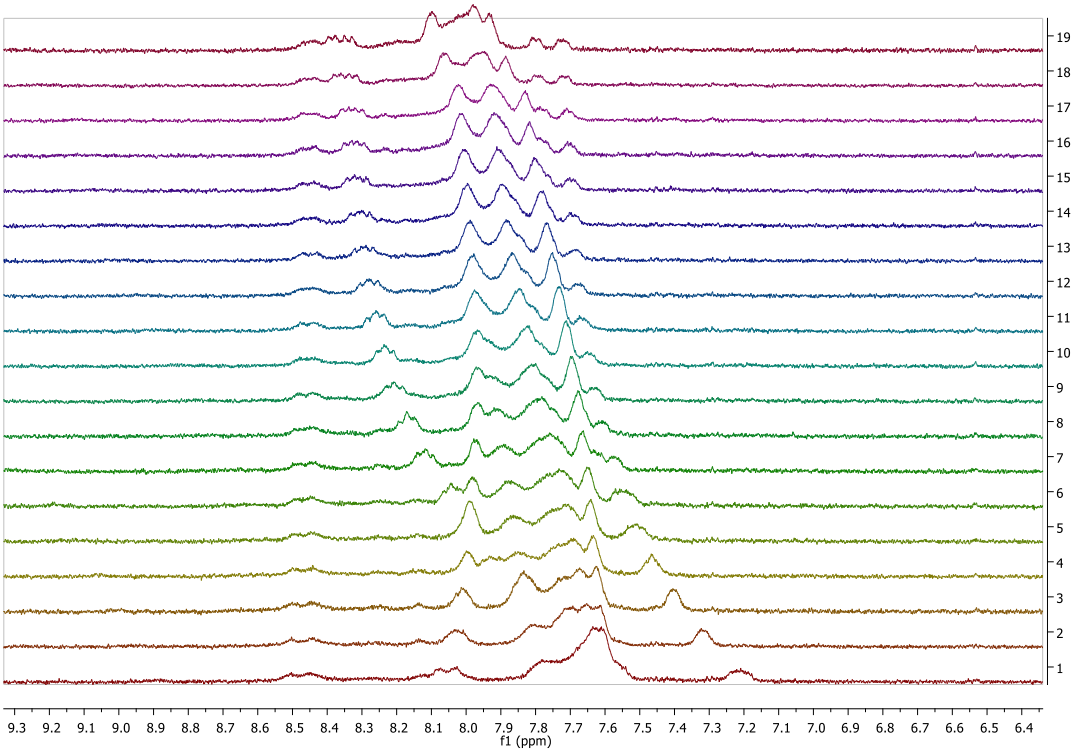

Figure A4.50: ^{1}H NMR Titration spectrum of **4.16 (Sq-2-Ala-Lys)** against TBACl (0 – 20 eq.) in DMSO-d_6.

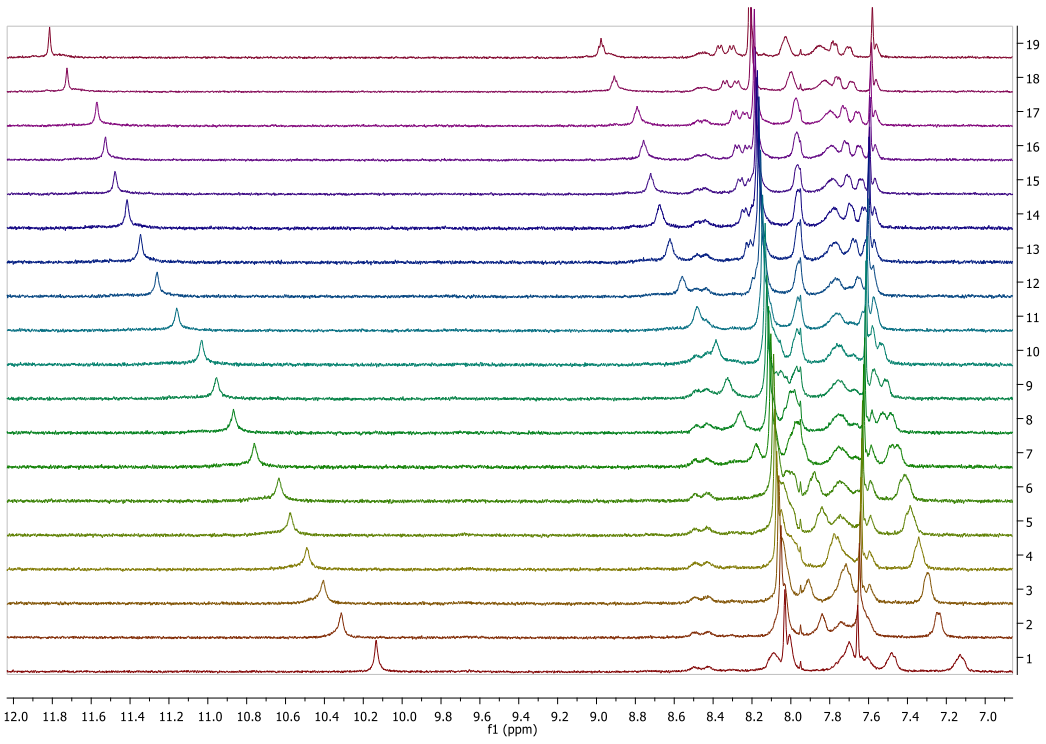

Figure A4.51: ^{1}H NMR Titration spectrum of **4.17 (Sq-2-Ala-Lys(SqBisCF_3))** against TBACl (0 – 20 eq.) in DMSO-d_6.

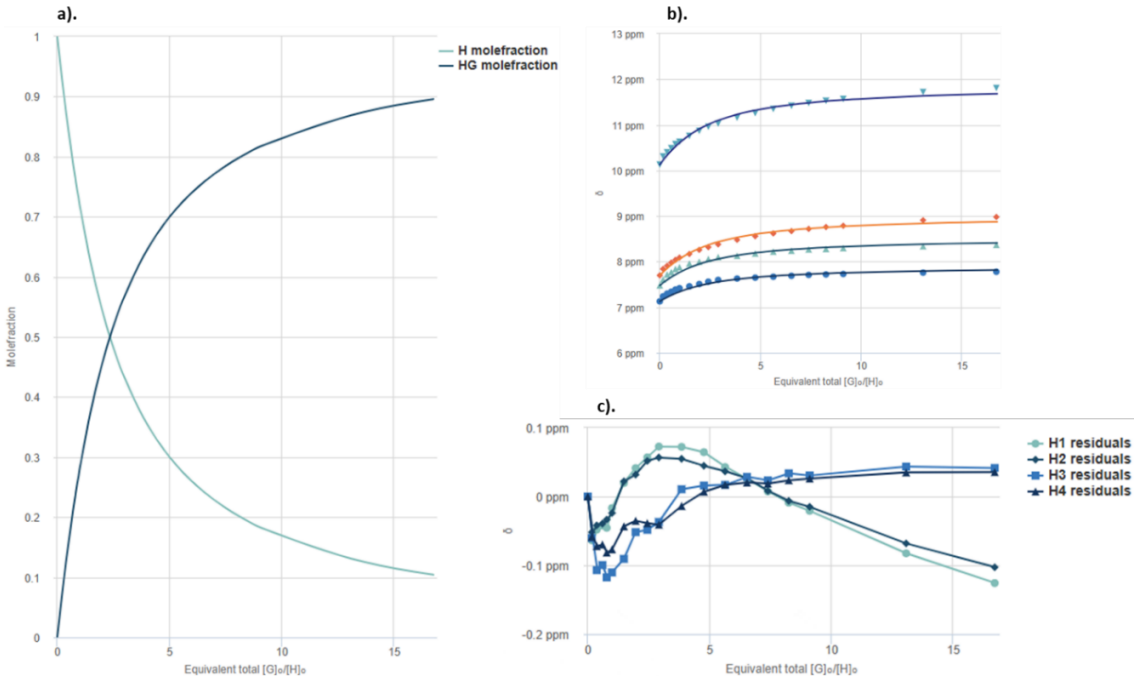

Figure A4.52: a). Mole fraction plot of Host vs Host:guest fraction with increasing guest concentration for **4.17. b).** Fitting binding isotherms of compound **4.17 (Sq-2-Ala-Lys(SqBisCF$_3$))** with TBACl in DMSO-d$_6$ at 298 K, showing the changes in chemical shifts for the squaramide NH protons fitted to the 2:1 binding model (K_a = 217 M^{-1}). **c).** Residuals plot of **4.17**.

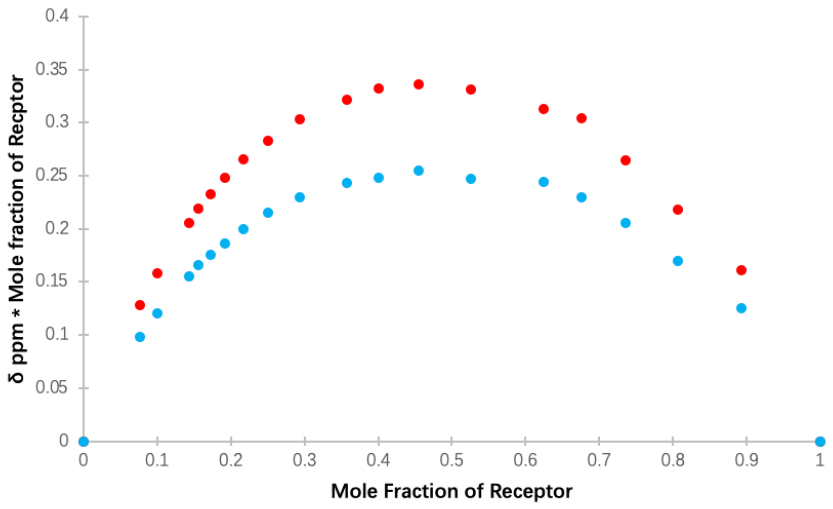

Figure A4.53: Jobs plot of the aryl squaramide NH's of compound **4.17 (Sq-2-Ala-Lys(SqBisCF$_3$))** with TBACl in DMSO-d$_6$

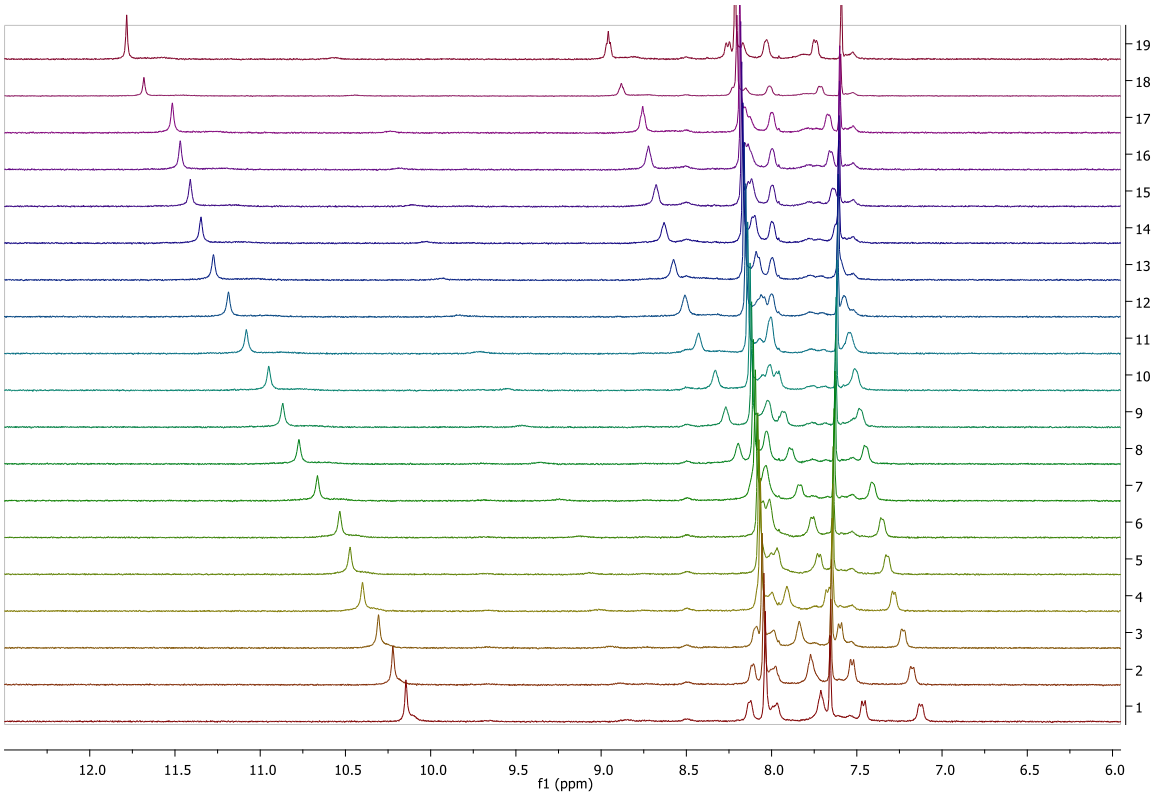

Figure A4.54: ^{1}H NMR Titration spectrum of **4.18 (Sq-2-Lys(SqBisCF$_3$))** against TBACl (0 – 20 eq.) in DMSO-d$_6$.

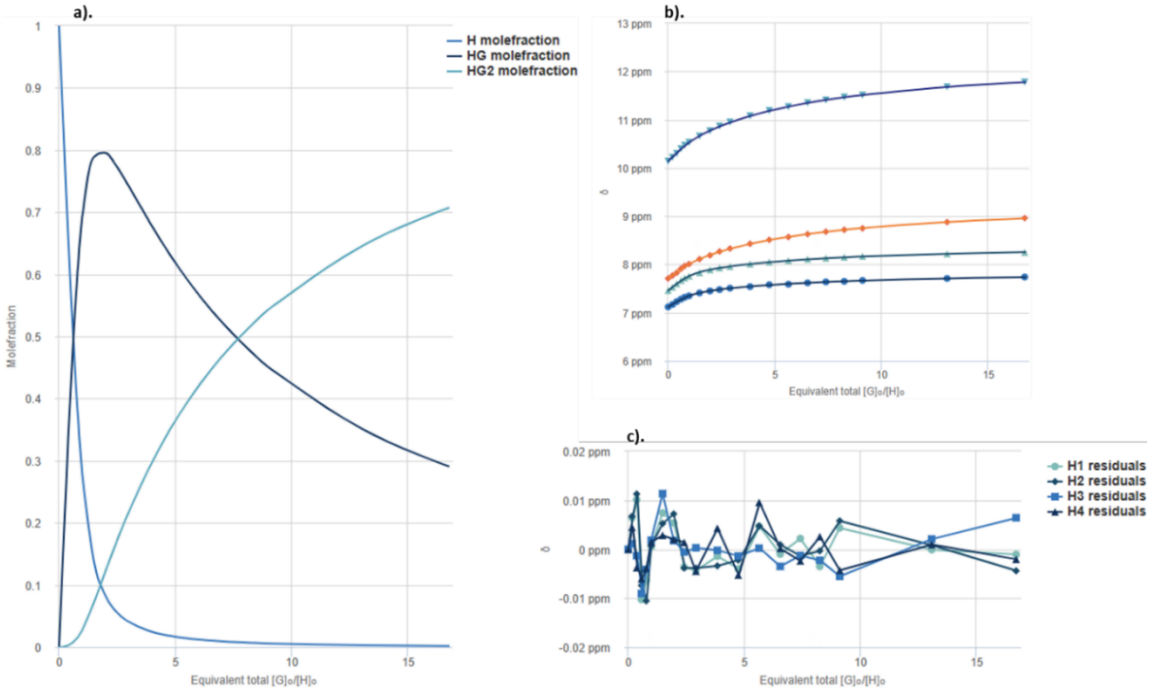

Figure A4.55: a). Mole fraction plot of Host vs Host:guest fraction with increasing guest concentration for **4.18. b).** Fitting binding isotherms of compound **4.18 (Sq-2-Lys(SqBisCF$_3$))** with TBACl in DMSO-d$_6$ at 298 K, showing the changes in chemical shifts for the squaramide NH protons fitted to the 2:1 binding model (K_{11} = 4 x10^3 M^{-1}) and (K_{12} = 64 M^{-1}). **c).** Residuals plot of **4.18**.

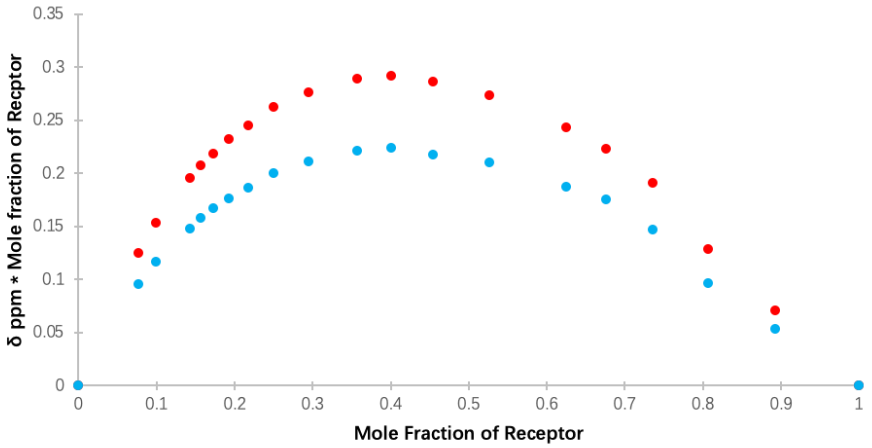

Figure A4.56: Jobs plot of the aryl squaramide NH's of compound **4.18 (Sq-2-Lys(SqBisCF$_3$))** with TBACl in DMSO-d$_6$

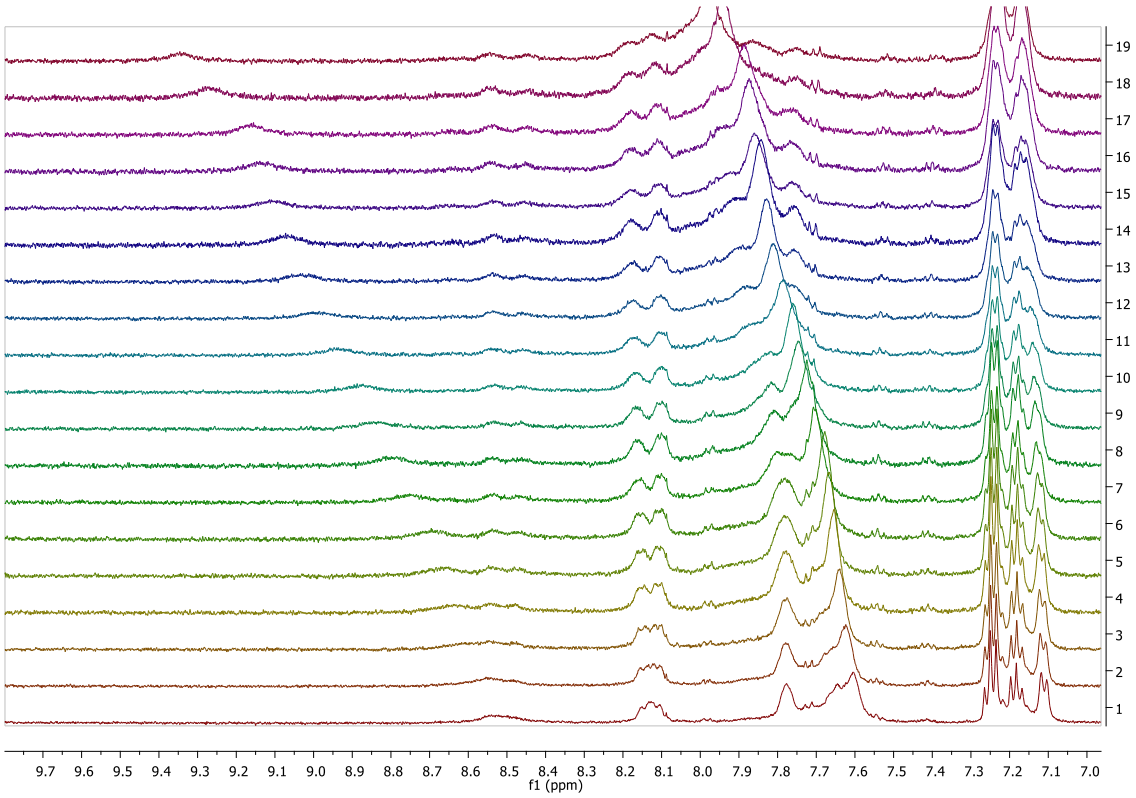

Figure A4.57: ^{1}H NMR Titration spectrum of **4.19 (Sq-2-Phe-Lys)** against TBACl (0 – 20 eq.) in DMSO-d$_6$.

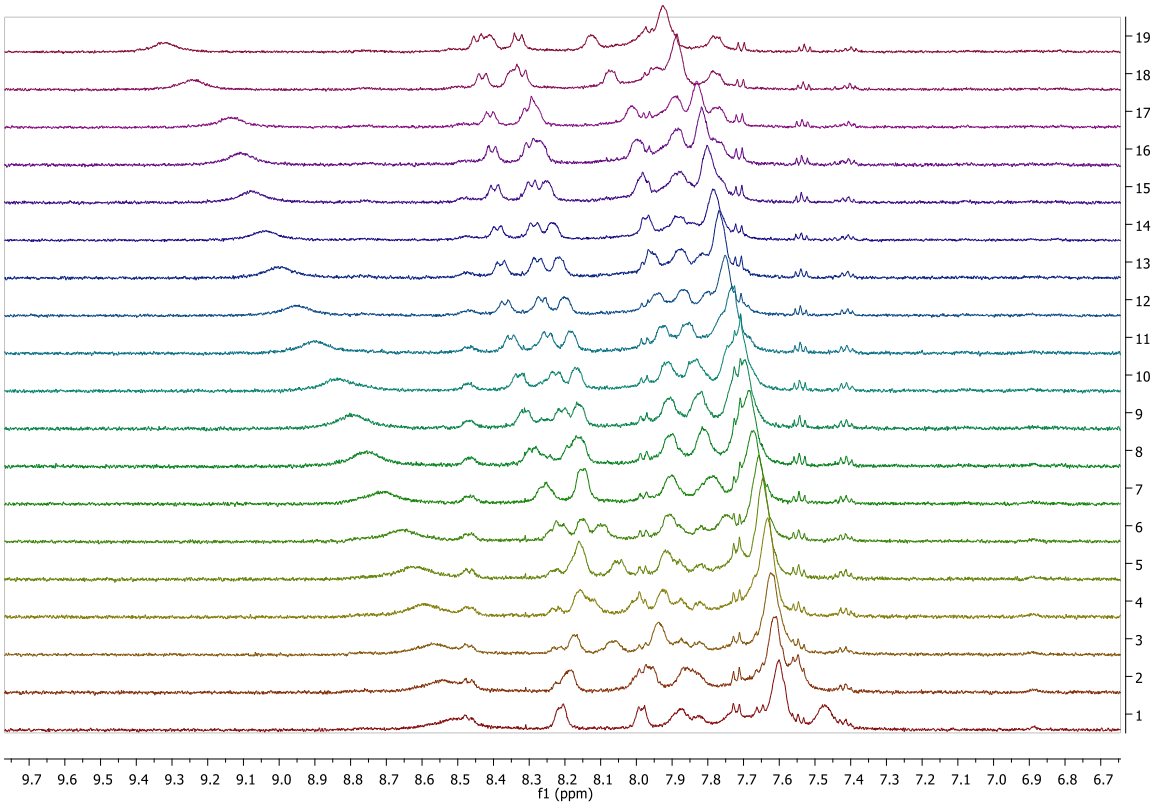

Figure A4.58: ^{1}H NMR Titration spectrum of **4.20 (Sq-2-F$_5$Phe-Lys)** against TBACl (0 – 20 eq.) in DMSO-d$_6$.

Chapter 4 – Anion Transport Data

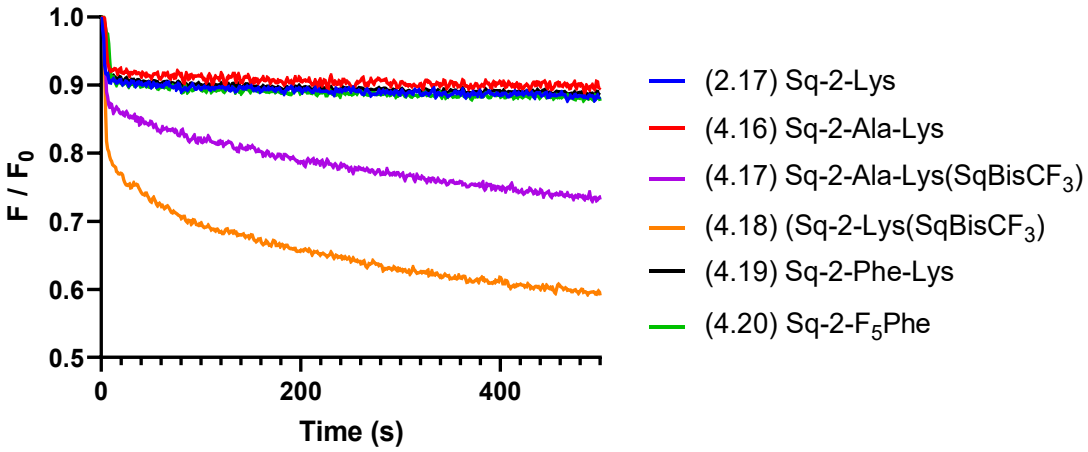

Figure A4.59: Normalised lucigenin fluorescence (F/F_0) as a function of time for liposomes subjected to external NaCl addition in the presence of receptors **2.17**, and **4.16 - 4.20** at 30μM.

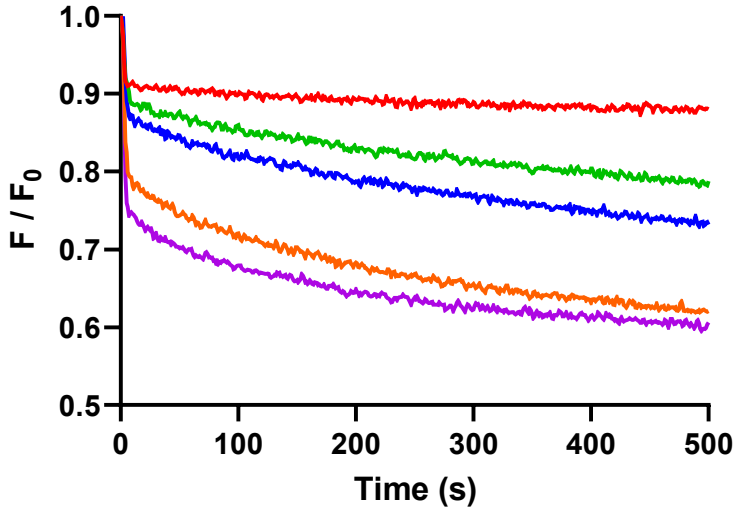

Figure A4.60: Normalised lucigenin fluorescence (F/F_0) as a function of time for liposomes (225 mM $NaNO_3$, 0.8 mM lucigenin) subjected to external NaCl addition in the presence of **(4.17) Sq-2-Ala-Lys(SqBisCF$_3$)** at varying concentrations (10 – 50 µM)

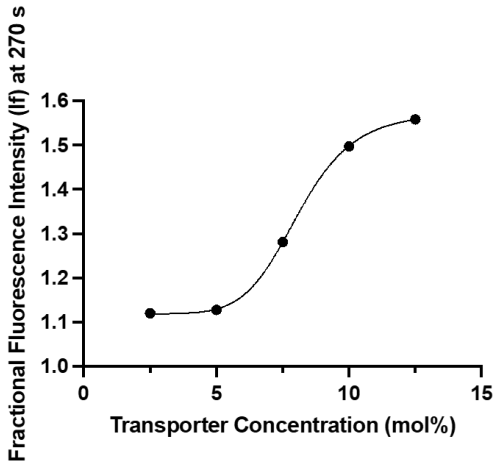

[Agonist] vs. response --
Variable slope (four parameters)

Best-fit values	
Bottom	1.119
Hillslope	7.665
Top	1.574
EC50	8.103
logEC50	0.9087
Span	0.4550
95% CI (profile likelihood)	
Bottom	1.091 to 1.144
Hillslope	4.994 to 13.26
Top	1.527 to 1.650
EC50	7.686 to 8.717
logEC50	0.8857 to 0.9404
Goodness of Fit	
Degrees of Freedom	1
R squared	1.000
Sum of Squares	6.965e-006
Sy.x	0.002639
Constraints	
EC50	EC50 > 0
Number of points	
# of X values	5
# Y values analyzed	5

Figure A4.61: Dose–response plot of fractional fluorescence intensity at 270 s versus **(4.17) Sq-2-Ala-Lys(SqBisCF$_3$)** concentration.

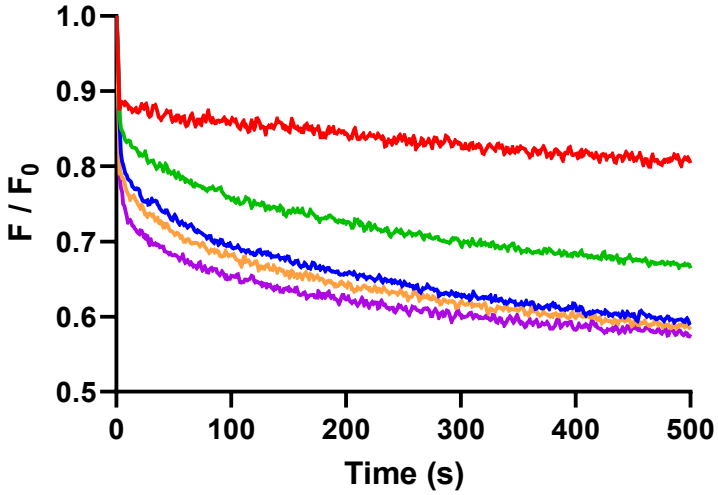

Figure A4.62: Normalised lucigenin fluorescence (F/F_0) as a function of time for liposomes (225 mM $NaNO_3$, 0.8 mM lucigenin) subjected to external NaCl addition in the presence of **(4.18) Sq-2-Lys(SqBisCF$_3$)** at varying concentrations (10 – 50 µM)

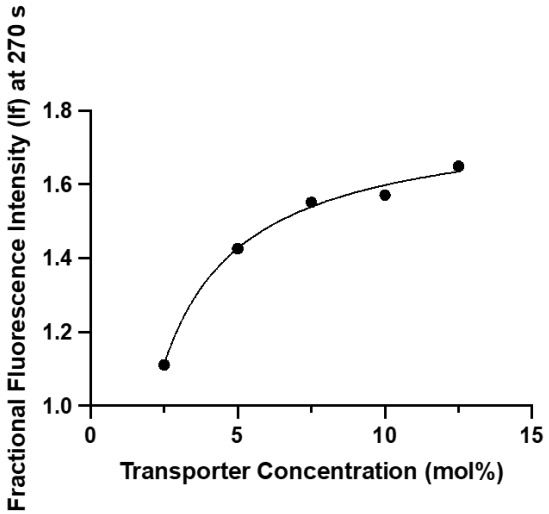

Bottom	1.000
Hillslope	2.787
Top	1.652
EC50	4.028
logEC50	0.6051
Span	0.6518
95% CI (profile likelihood)	
	??? to 1.67
Bottom	1
Hillslope	???
	1.241 to 1.
Top	671
EC50	???
logEC50	???
Goodness of Fit	
Degrees of Freedom	1
R squared	0.9863
Sum of Squares	0.002477
Sy.x	0.04977
Constraints	
Bottom	Bottom > 1
EC50	EC50 > 0
Number of points	
# of X values	5
# Y values analyzed	5

Figure A4.63: Dose–response plot of fractional fluorescence intensity at 270 s versus **(4.18) Sq-2-Lys(SqBisCF$_3$)** concentration.

Chapter 5 – Supplementary Characterisation Data

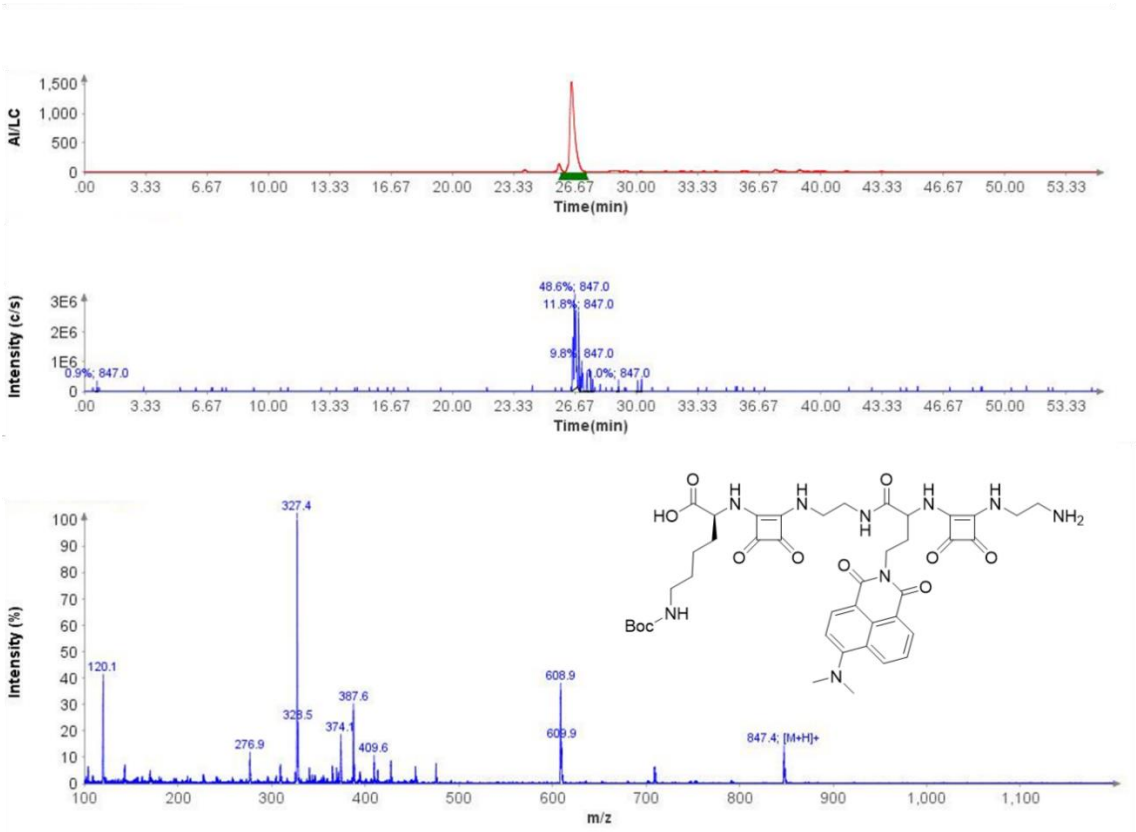

Figure A5.1: LC-MS data for **ASq-2-Lys(Boc)-Naph**.

Compound Table

Compound Label	RT (min)	Observed mass (m/z)	Neutral observed mass (Da)	Theoretical mass (Da)	Mass error (ppm)	Isotope match score (%)
Cpd 1: C41 H51 N9 O11	0.75	846.3776	845.3704	845.3708	-0.51	99.83

Figure: Extracted ion chromatogram (EIC) of compound.

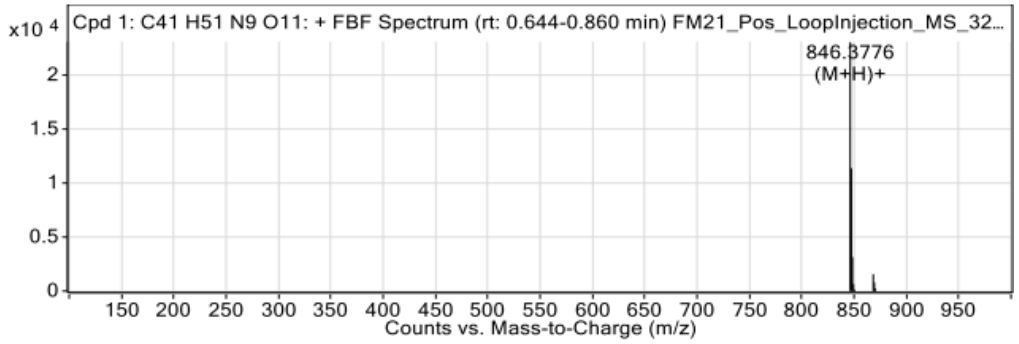

Figure: Full range view of Compound spectra and potential adducts.

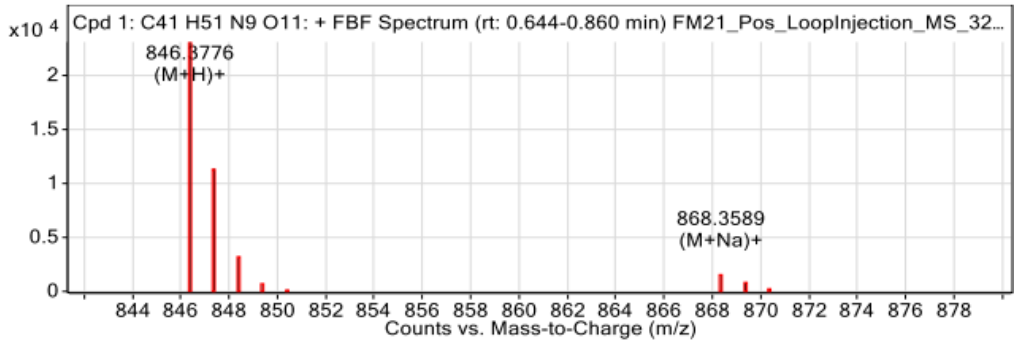

Figure: Zoomed Compound spectra view
(red boxes indicating expected theoretical isotope spacing and abundance)

Compound isotope peak List

m/z	z	Abund	Ion
846.3776	1	23057.9	(M+H)+
847.3808	1	11353.6	(M+H)+
848.3831	1	3131.6	(M+H)+
849.3862	1	651.2	(M+H)+
850.3922	1	137.0	(M+H)+
868.3589	1	1557.8	(M+Na)+
869.3622	1	800.5	(M+Na)+
870.3668	1	238.1	(M+Na)+

Figure A5.2: HRMS data for **ASq-2-Lys(Boc)-Naph**.

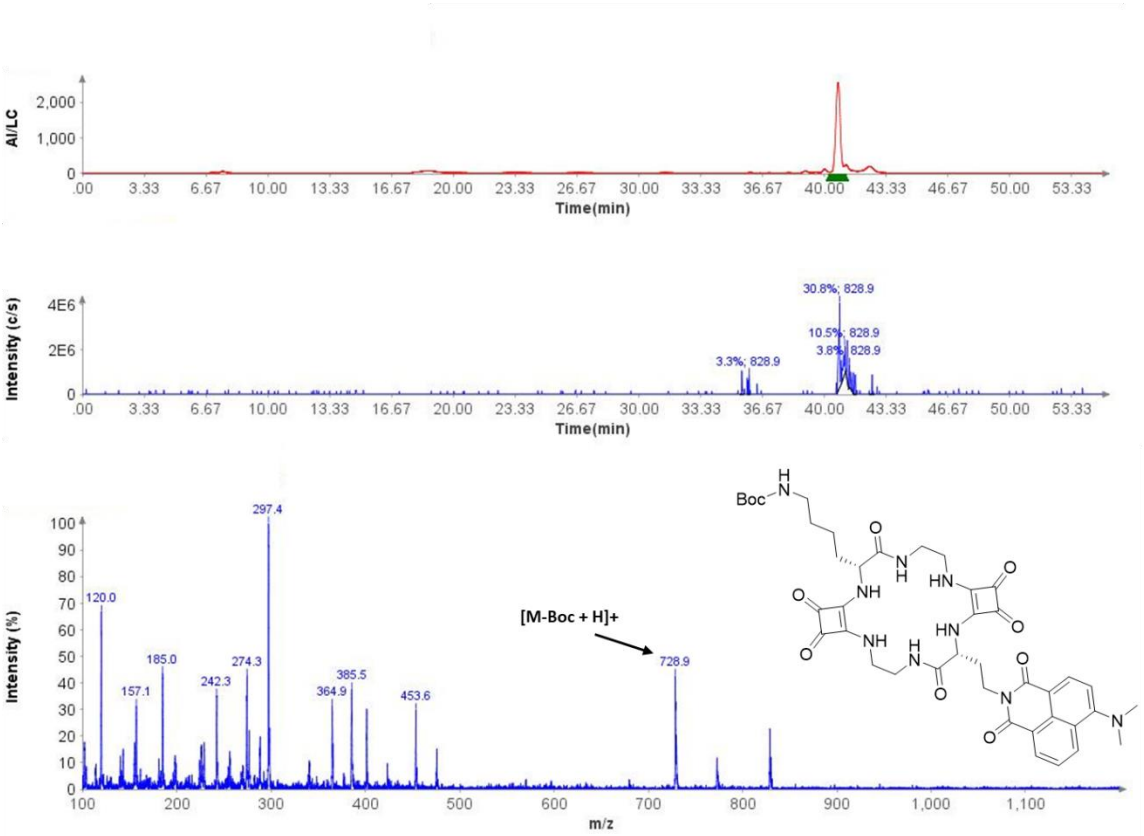

Figure A5.3: LC-MS data for **Sq-2-Lys(Boc)-Naph**.

Compound Table

Compound Label	RT (min)	Observed mass (m/z)	Neutral observed mass (Da)	Theoretical mass (Da)	Mass error (ppm)	Isotope match score (%)
Cpd 1: C41 H49 N9 O10	0.75	828.3668	827.3597	827.3602	-0.65	95.70

Figure: Extracted ion chromatogram (EIC) of compound.

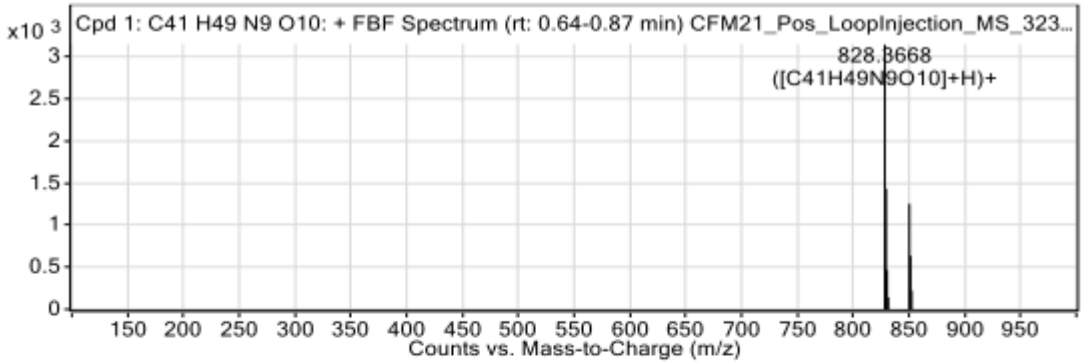

Figure: Full range view of Compound spectra and potential adducts.

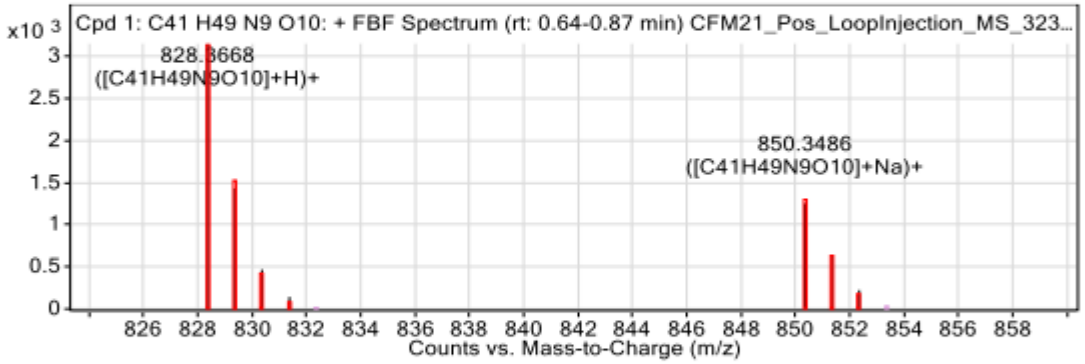

Figure: Zoomed Compound spectra view
(red boxes indicating expected theoretical isotope spacing and abundance)

Compound isotope peak List

m/z	z	Abund	Formula	Ion
828.3668	1	3150.0	C41H49N9O10	(M+H)+
829.3701	1	1433.2	C41H49N9O10	(M+H)+
830.3728	1	466.5	C41H49N9O10	(M+H)+
831.3815	1	141.7	C41H49N9O10	(M+H)+
850.3486	1	1252.9	C41H49N9O10	(M+Na)+
851.3518	1	635.0	C41H49N9O10	(M+Na)+
852.3545	1	223.6	C41H49N9O10	(M+Na)+

Figure A5.4: HRMS data for **Sq-2-Lys(Boc)-Naph**.

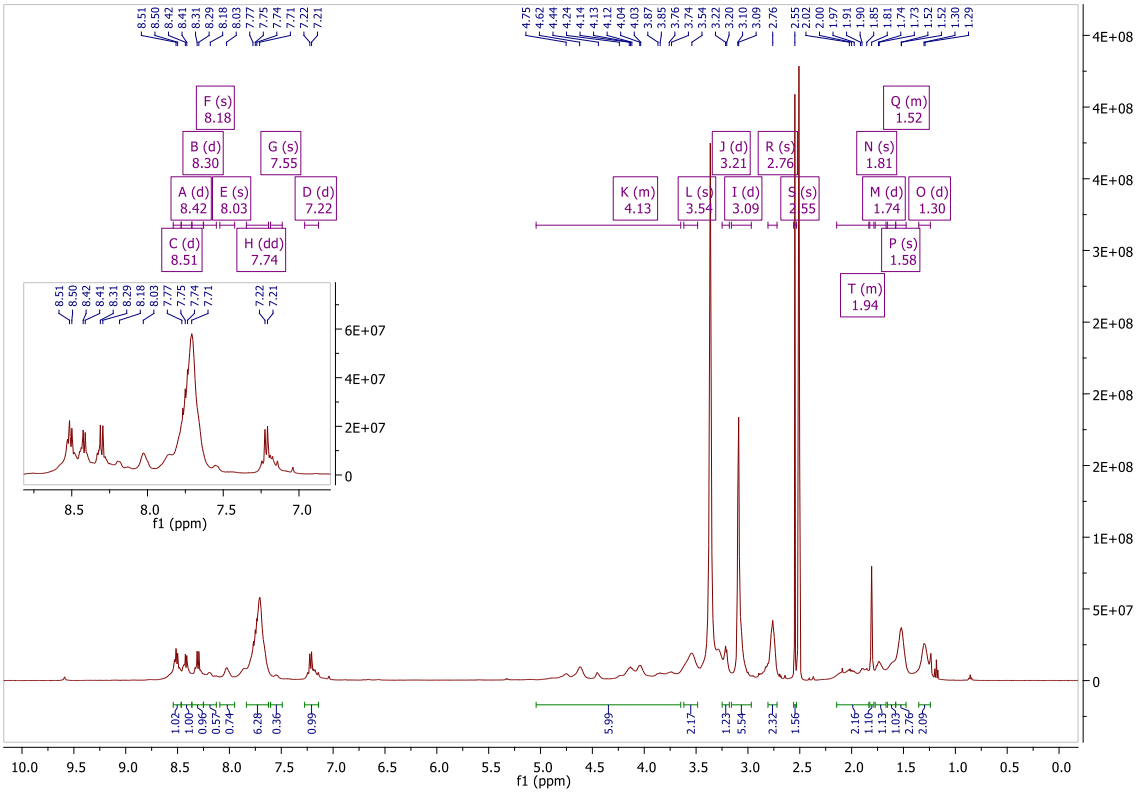

Figure A5.5: ^{1}H NMR spectrum of **(5.12) Sq-2-Lys-Naph** in DMSO-d_6

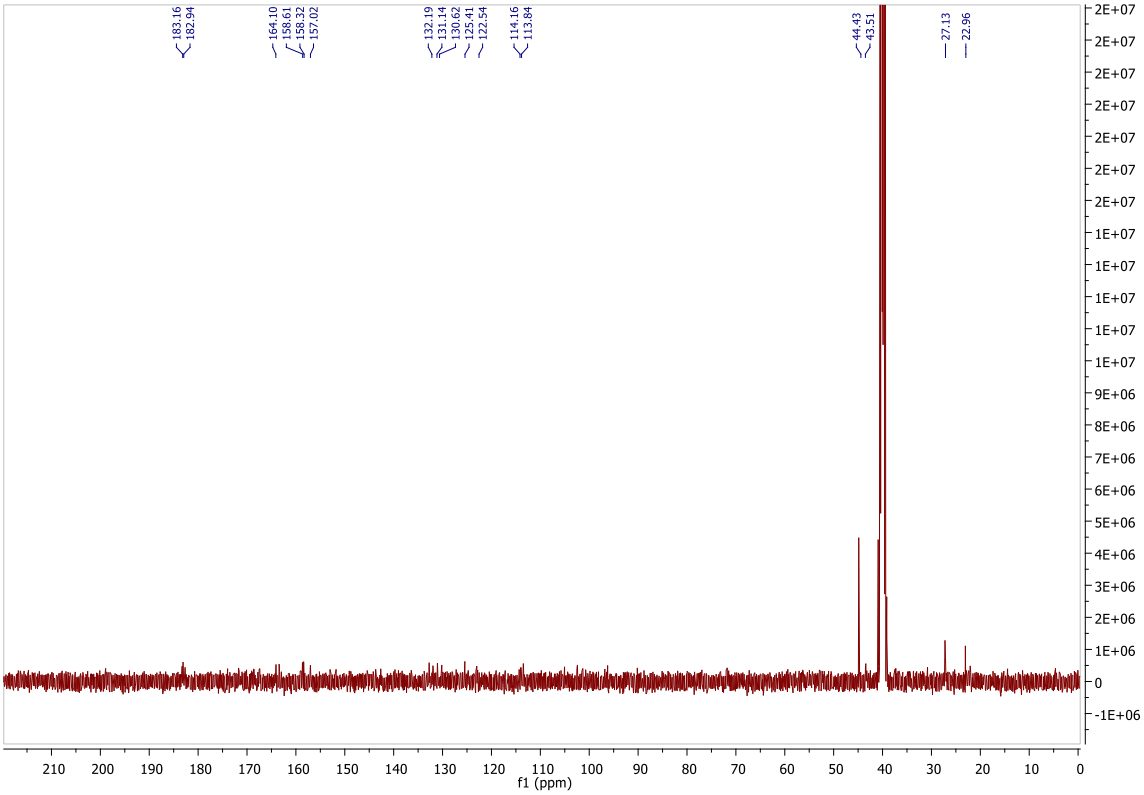

Figure A5.6: ^{13}C NMR spectrum of **(5.12) Sq-2-Lys-Naph** in DMSO-d_6

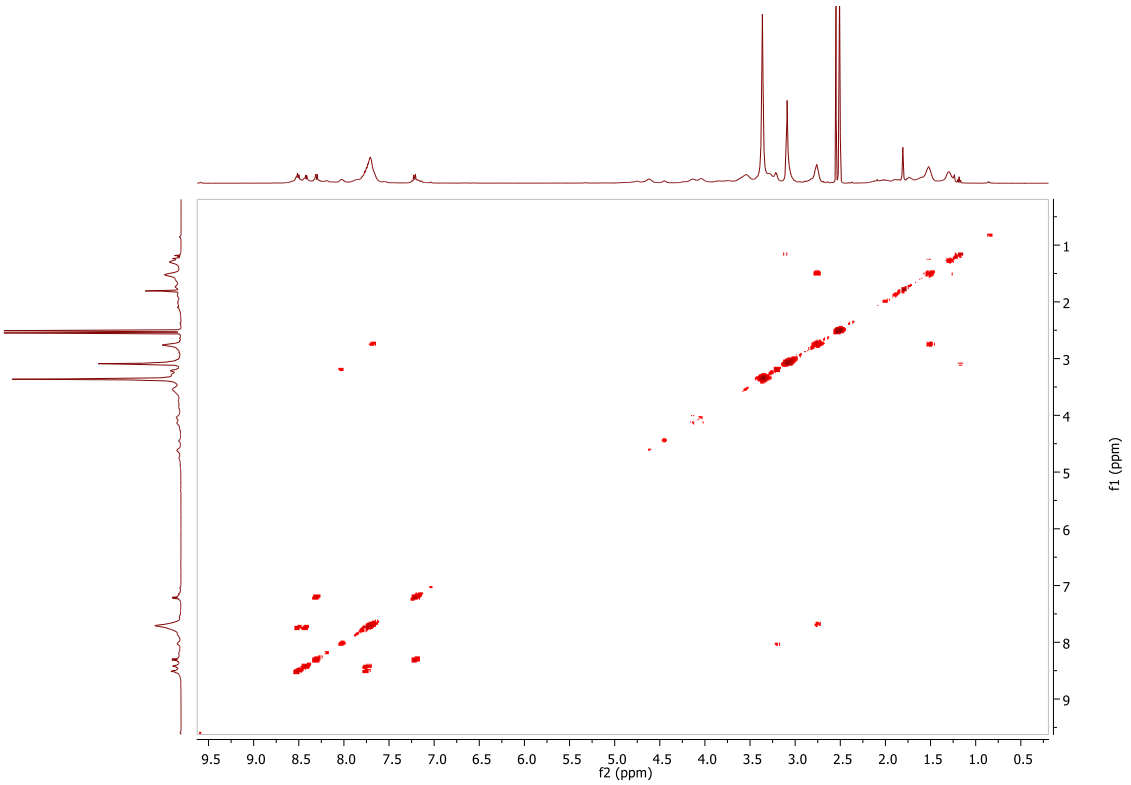

Figure A5.7: COSY spectrum of **(5.12) Sq-2-Lys-Naph** in DMSO-d_6

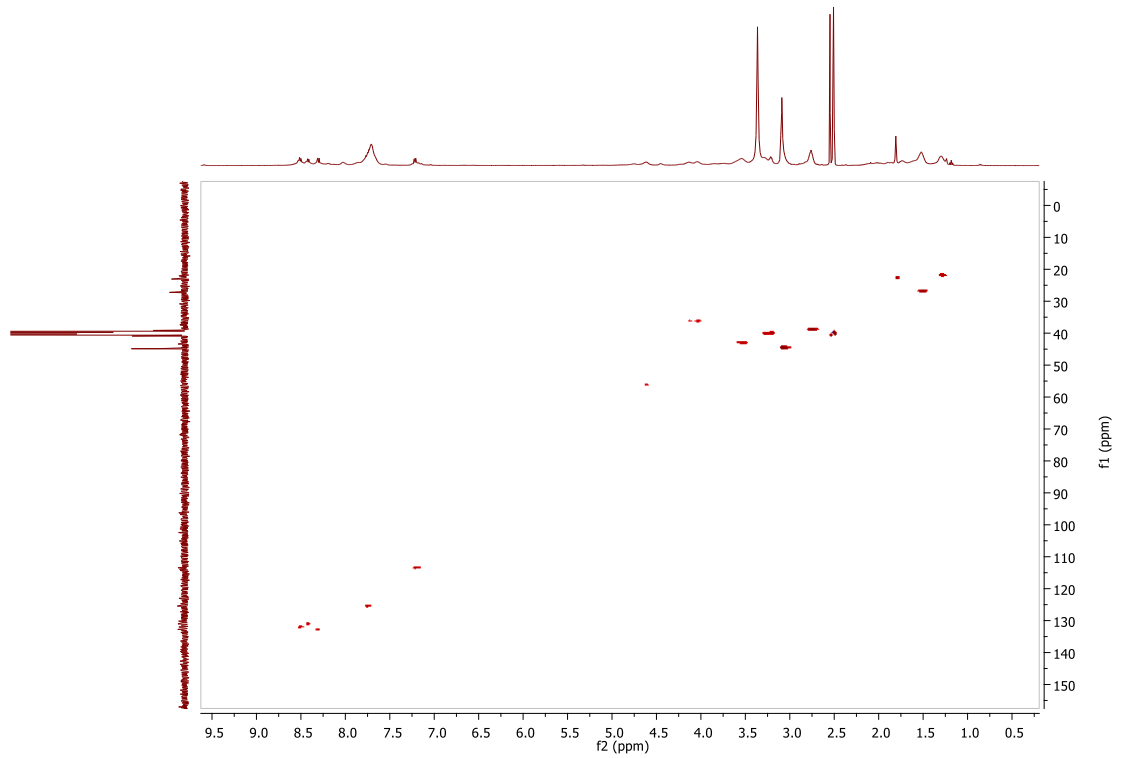

Figure A5.8: HSQC spectrum of **(5.12) Sq-2-Lys-Naph** in DMSO-d_6

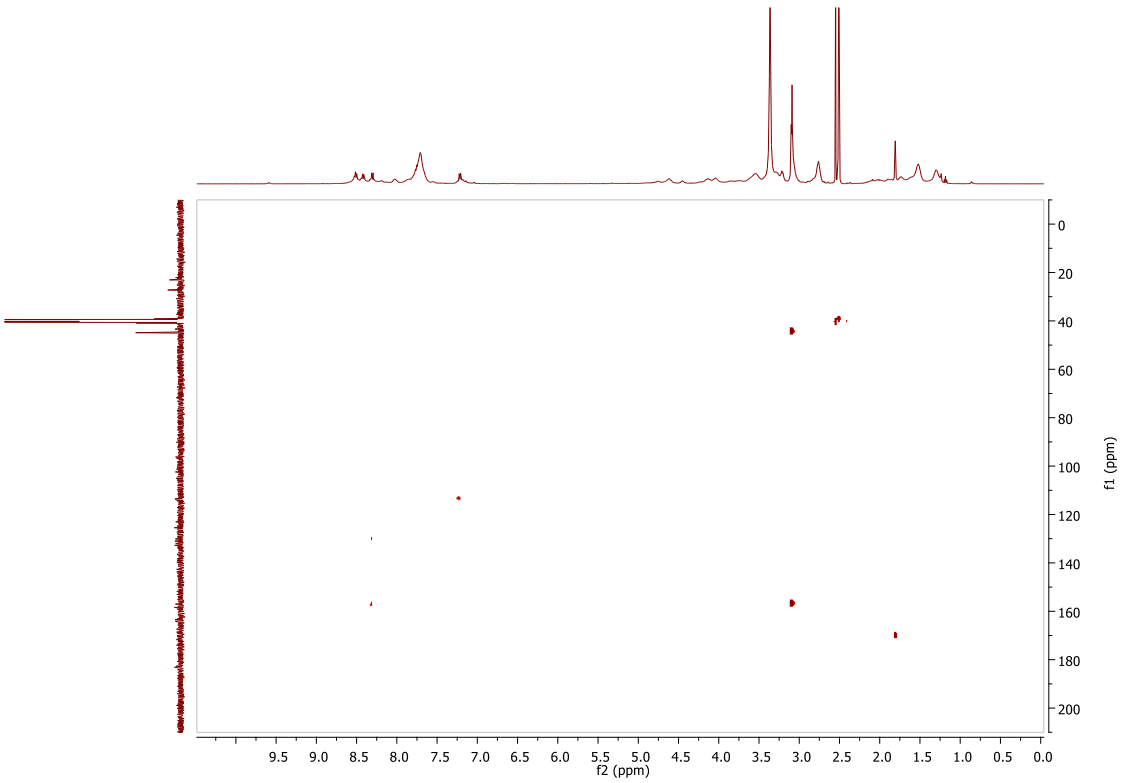

Figure A5.9: HMBC spectrum of **(5.12) Sq-2-Lys-Naph** in DMSO-d_6

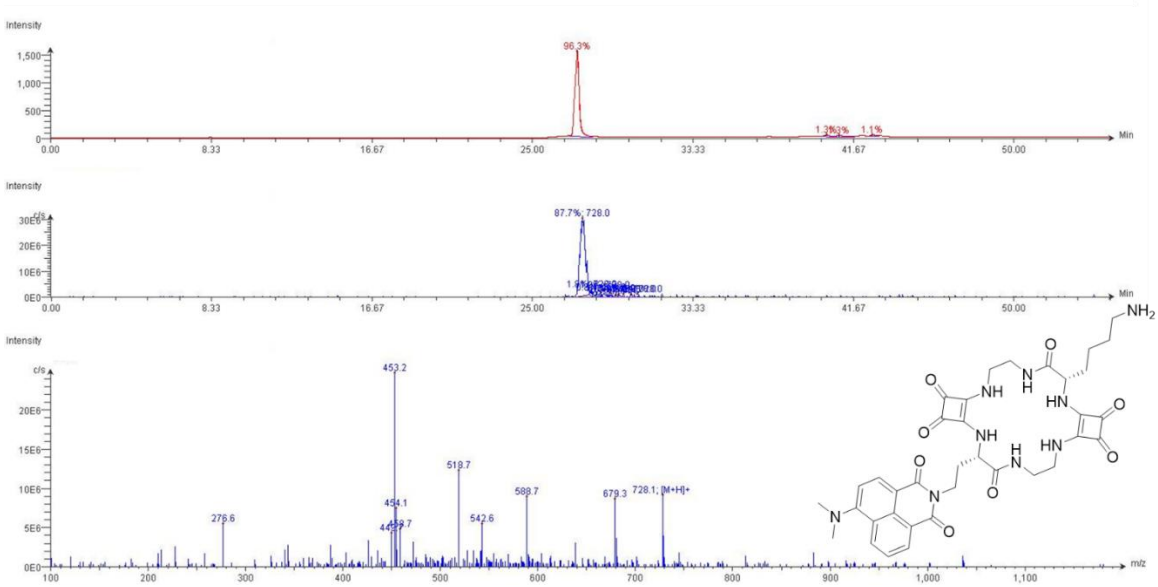

Figure A5.10: LC-MS data for **(5.12) Sq-2-Lys-Naph**.

Compound Table

Compound Label	RT (min)	Observed mass (m/z)	Neutral observed mass (Da)	Theoretical mass (Da)	Mass error (ppm)	Isotope match score (%)
Cpd 1: C36 H41 N9 O8	0.74	728.3151	727.3080	727.3078	0.27	99.85

Figure: Extracted ion chromatogram (EIC) of compound.

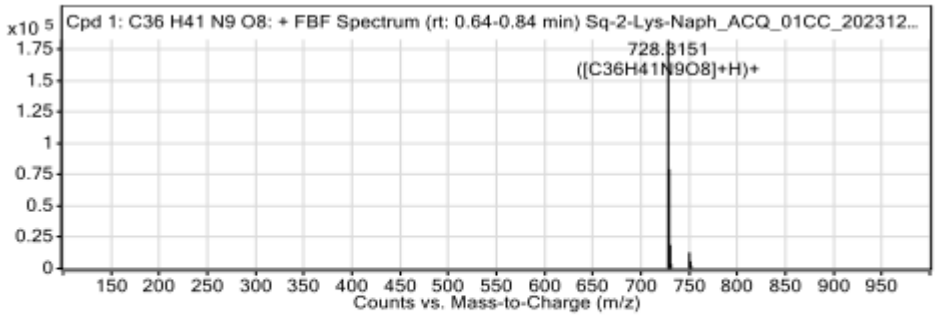

Figure: Full range view of Compound spectra and potential adducts.

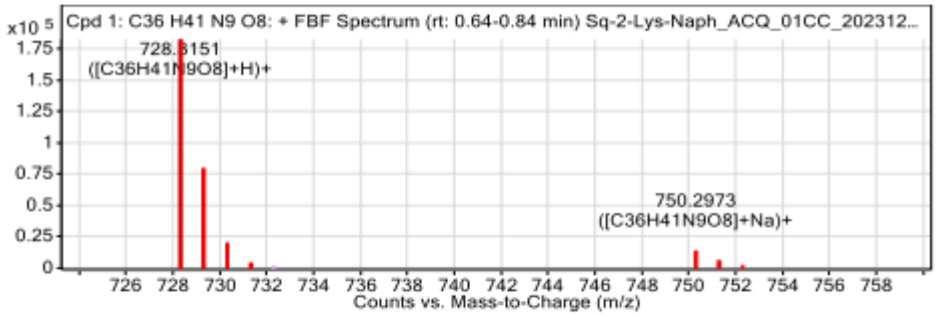

Figure: Zoomed Compound spectra view
(red boxes indicating expected theoretical isotope spacing and abundance)

Compound isotope peak List

m/z	z	Abund	Formula	Ion
728.3151	1	182839.5	C36H41N9O8	(M+H)+
729.3180	1	79394.4	C36H41N9O8	(M+H)+
730.3208	1	18892.8	C36H41N9O8	(M+H)+
731.3243	1	3636.1	C36H41N9O8	(M+H)+
750.2973	1	12883.5	C36H41N9O8	(M+Na)+
751.3020	1	5823.2	C36H41N9O8	(M+Na)+
752.3169	1	2020.0	C36H41N9O8	(M+Na)+

Figure A5.11: HRMS data for **(5.12) Sq-2-Lys-Naph**.

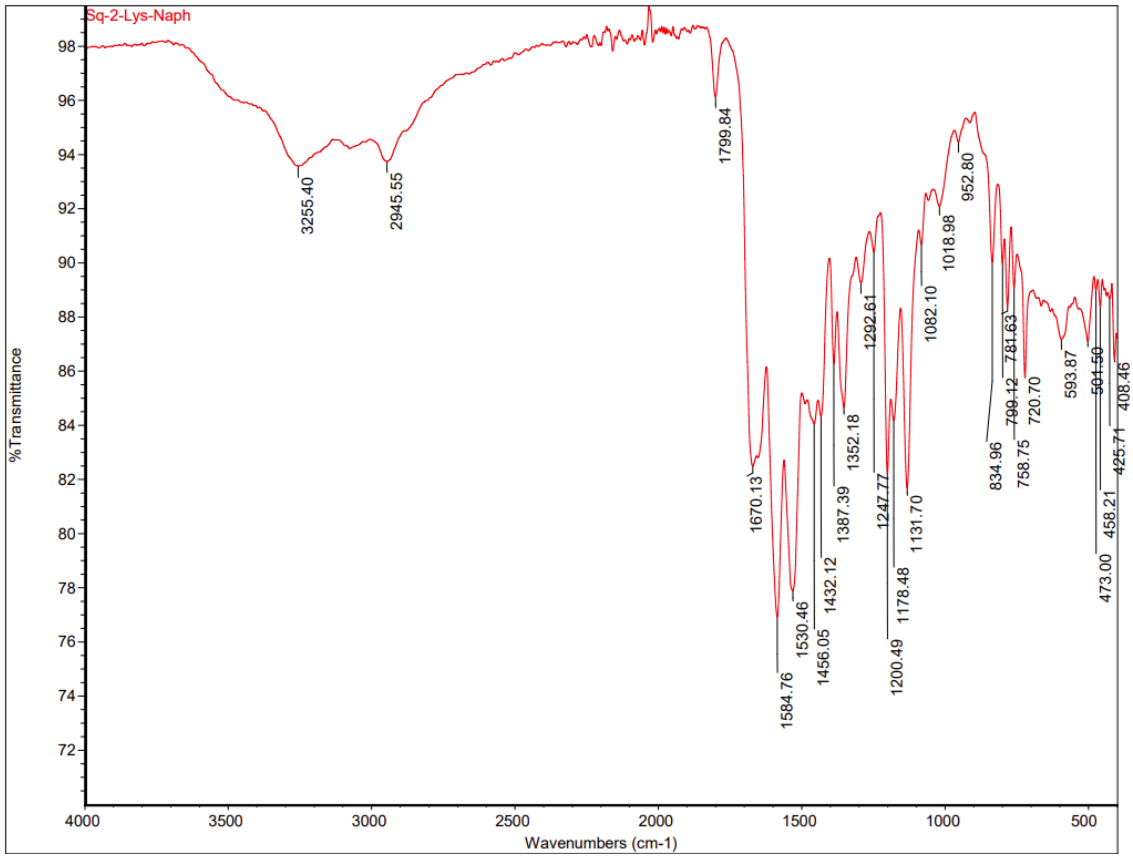

Figure A5.12: IR Spectrum of **(5.12) Sq-2-Lys-Naph**.

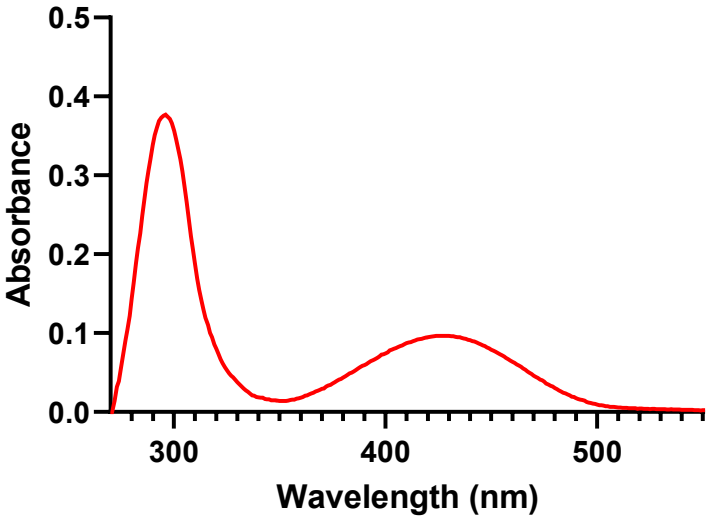

Figure A5.13: UV-Vis spectra of **(5.12) Sq-2-Lys-Naph** (30 µM) in a DMSO solution.

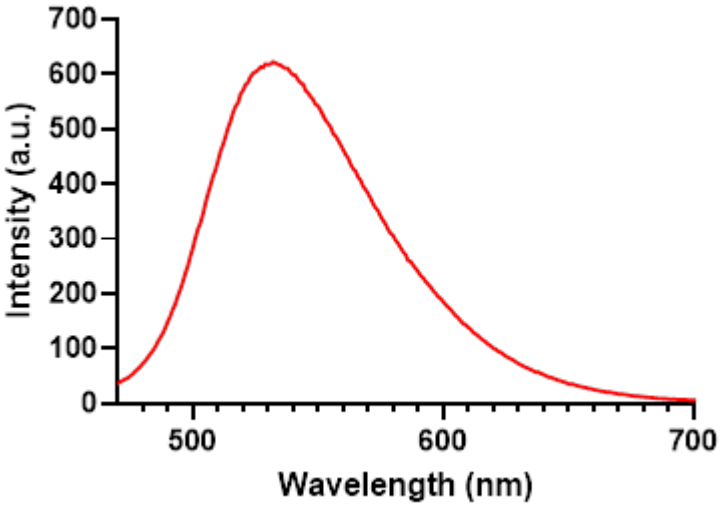

Figure A5.14: Fluorescence spectra of **(5.12) Sq-2-Lys-Naph** (30 µM) in a DMSO solution.

Chapter 5 – Fluorescence Spectroscopic Anion Sensing Data

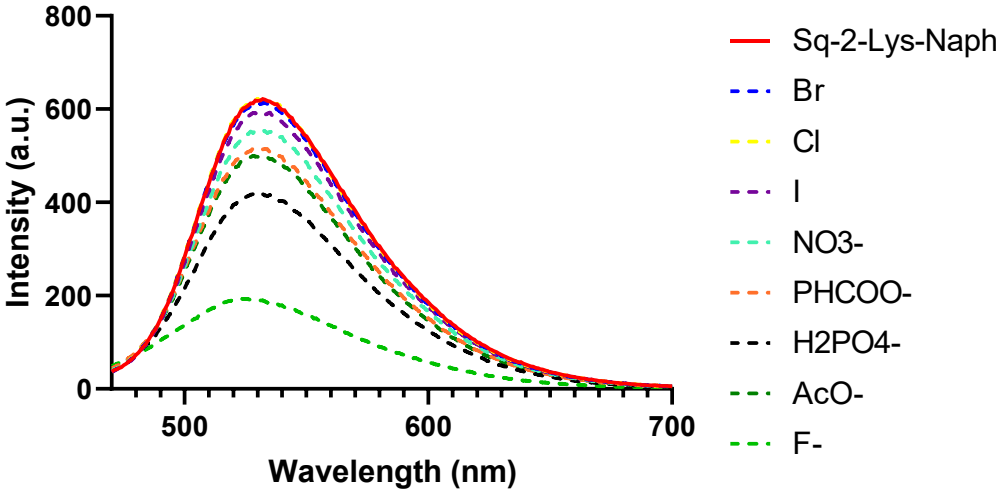

Figure A5.15: Fluorescent spectra of **(5.12) Sq-2-Lys-Naph** (30 µM λ_{ex} = 270 nm) in the presence of 40 equivalents of various anions in a DMSO solution.

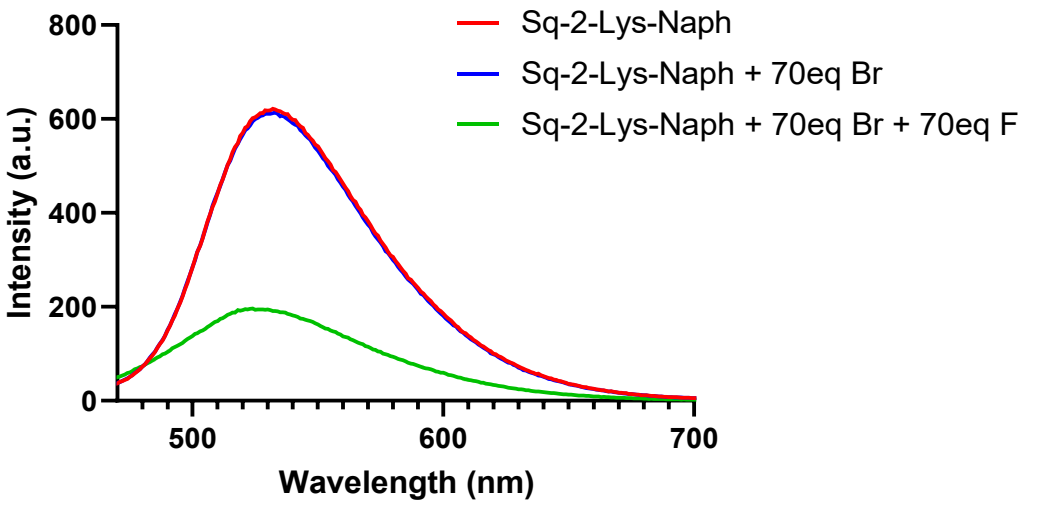

Figure A5.16: Fluorescent spectra of **(5.12) Sq-2-Lys-Naph** (30 µM λ_{ex} = 270 nm) in the presence of 70 equivalents of TBABr and TBAF in a DMSO solution.

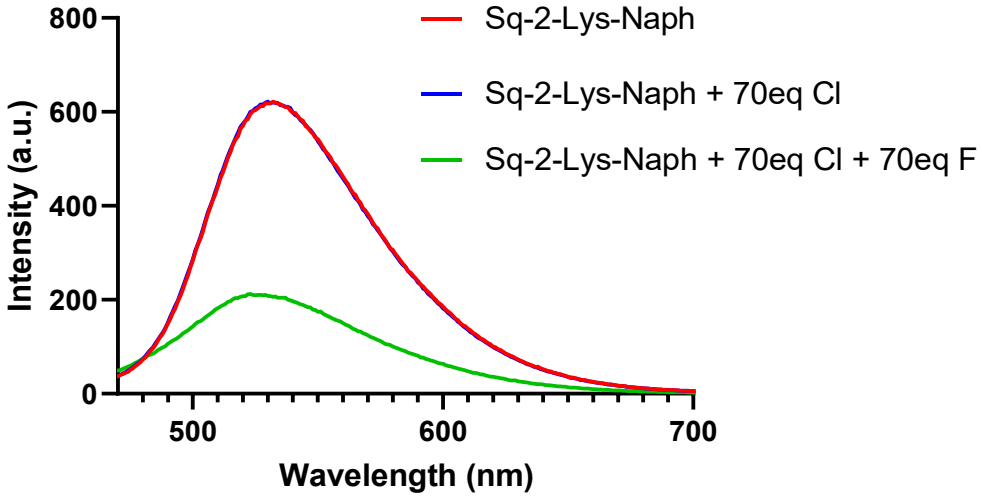

Figure A5.17: Fluorescent spectra of **(5.12) Sq-2-Lys-Naph** (30 µM λ_{ex} = 270 nm) in the presence of 70 equivalents of TBACl and TBAF in a DMSO solution.

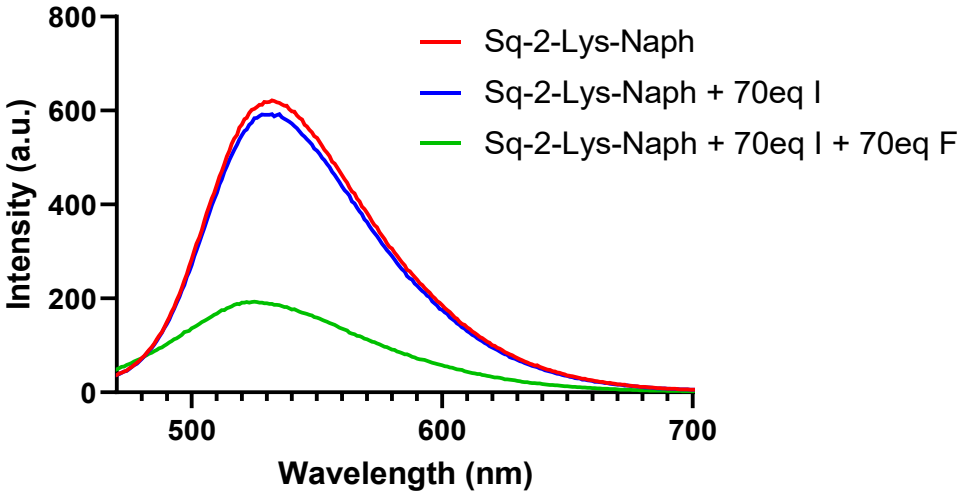

Figure A5.18: Fluorescent spectra of **(5.12) Sq-2-Lys-Naph** (30 µM λ_{ex} = 270 nm) in the presence of 70 equivalents of TBAI and TBAF in a DMSO solution.

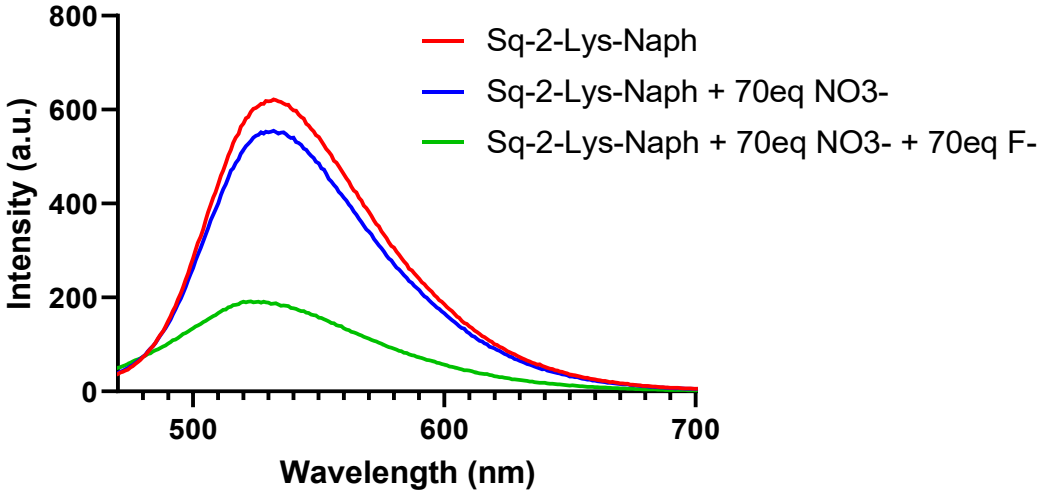

Figure A5.19: Fluorescent spectra of **(5.12) Sq-2-Lys-Naph** (30 µM λ_{ex} = 270 nm) in the presence of 70 equivalents of $TBANO_3$ and TBAF in a DMSO solution.

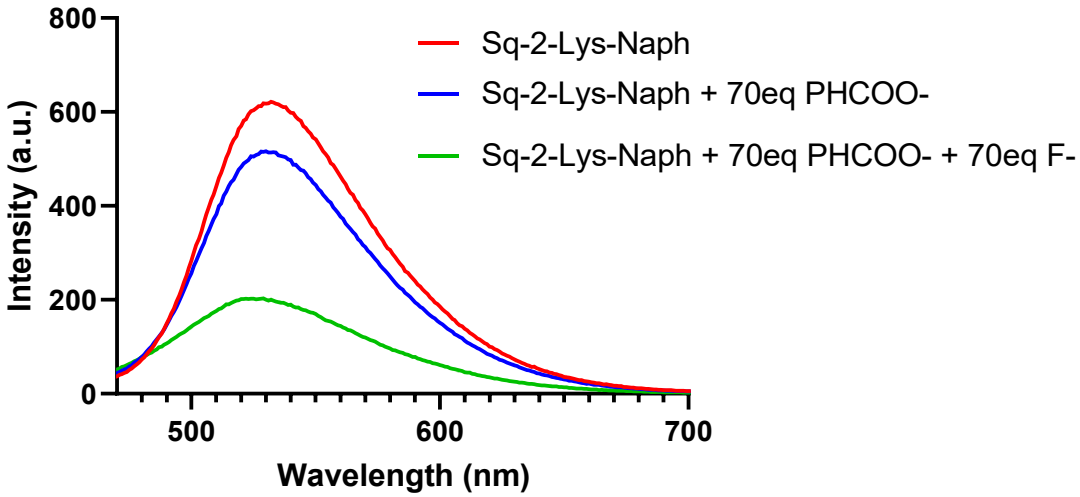

Figure A5.20: Fluorescent spectra of **(5.12) Sq-2-Lys-Naph** (30 µM λ_{ex} = 270 nm) in the presence of 70 equivalents of TBAPHCOO and TBAF in a DMSO solution.

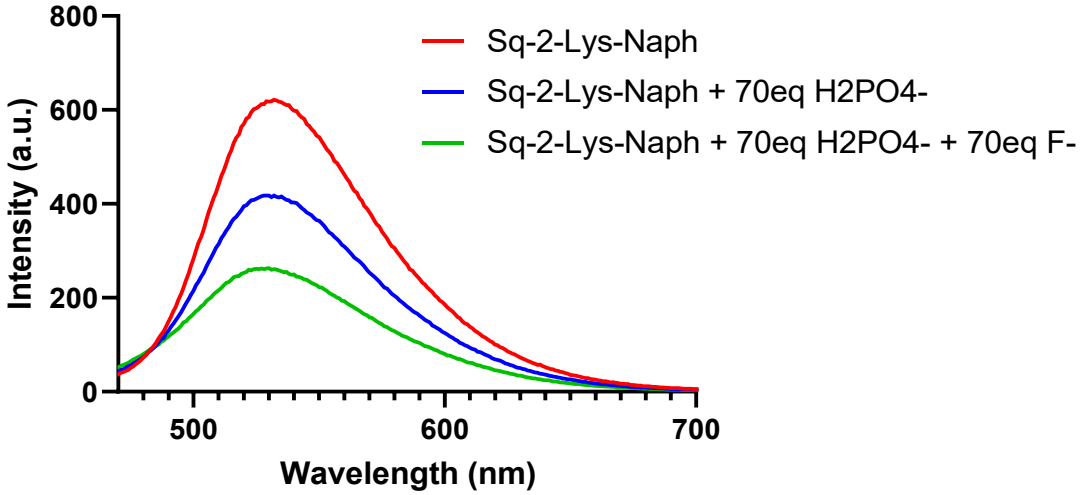

Figure A5.21: Fluorescent spectra of **(5.12) Sq-2-Lys-Naph** (30 µM λ_{ex} = 270 nm) in the presence of 70 equivalents of $TBAH_2PO_4$ and TBAF in a DMSO solution.

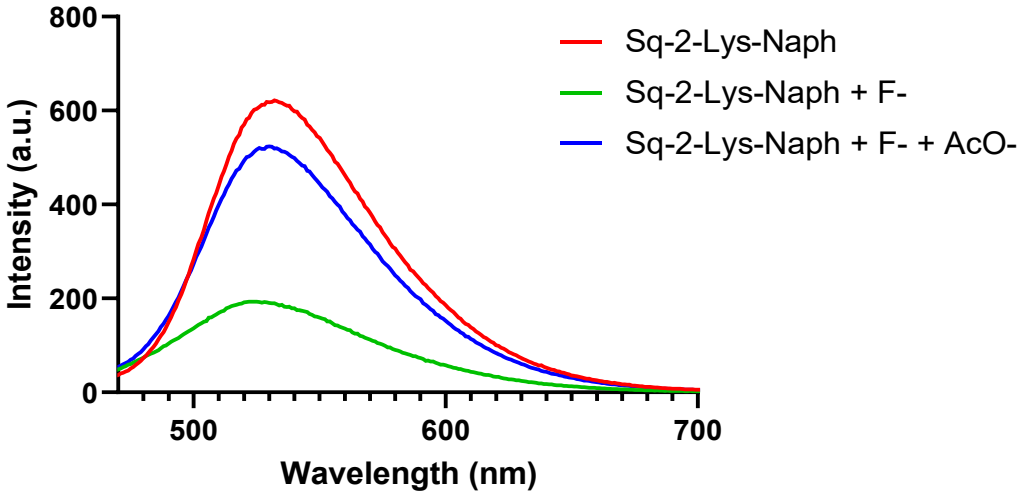

Figure A5.22: Fluorescent spectra of **(5.12) Sq-2-Lys-Naph** (30 µM λ_{ex} = 270 nm) in the presence of 70 equivalents of TBAAcO and TBAF in a DMSO solution.

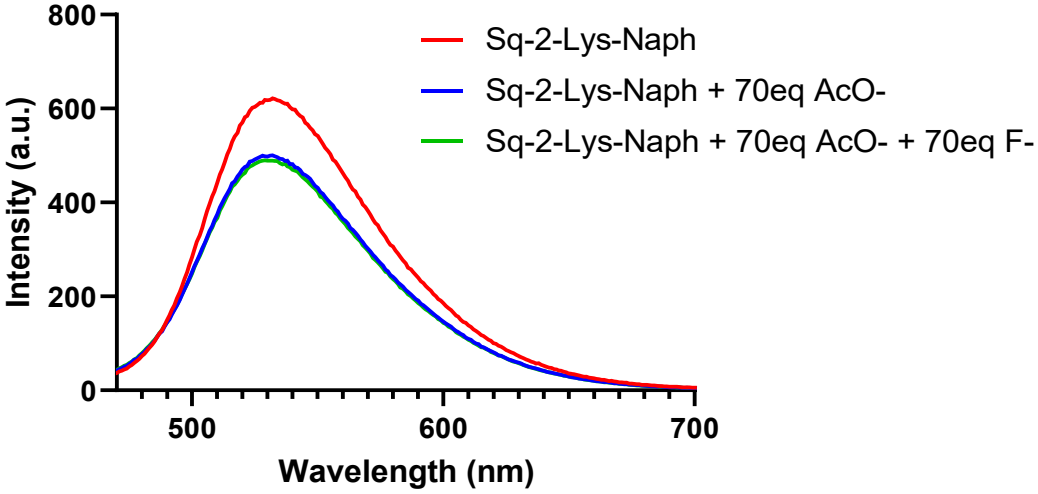

Figure A5.23: Fluorescent spectra of **(5.12) Sq-2-Lys-Naph** (30 µM λ_{ex} = 270 nm) in the presence of 70 equivalents of TBAAcO and TBAF in a DMSO solution.

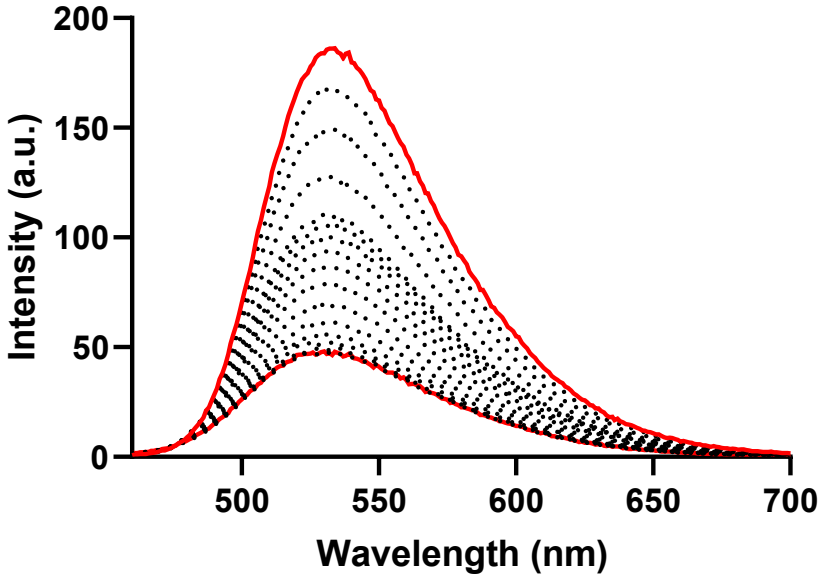

Figure A5.24: Fluorescent spectra of **(5.12) Sq-2-Lys-Naph** (10 µM λ_{ex} = 270 nm) in the presence of 0 - 80 equivalents of TBAF in a DMSO solution.

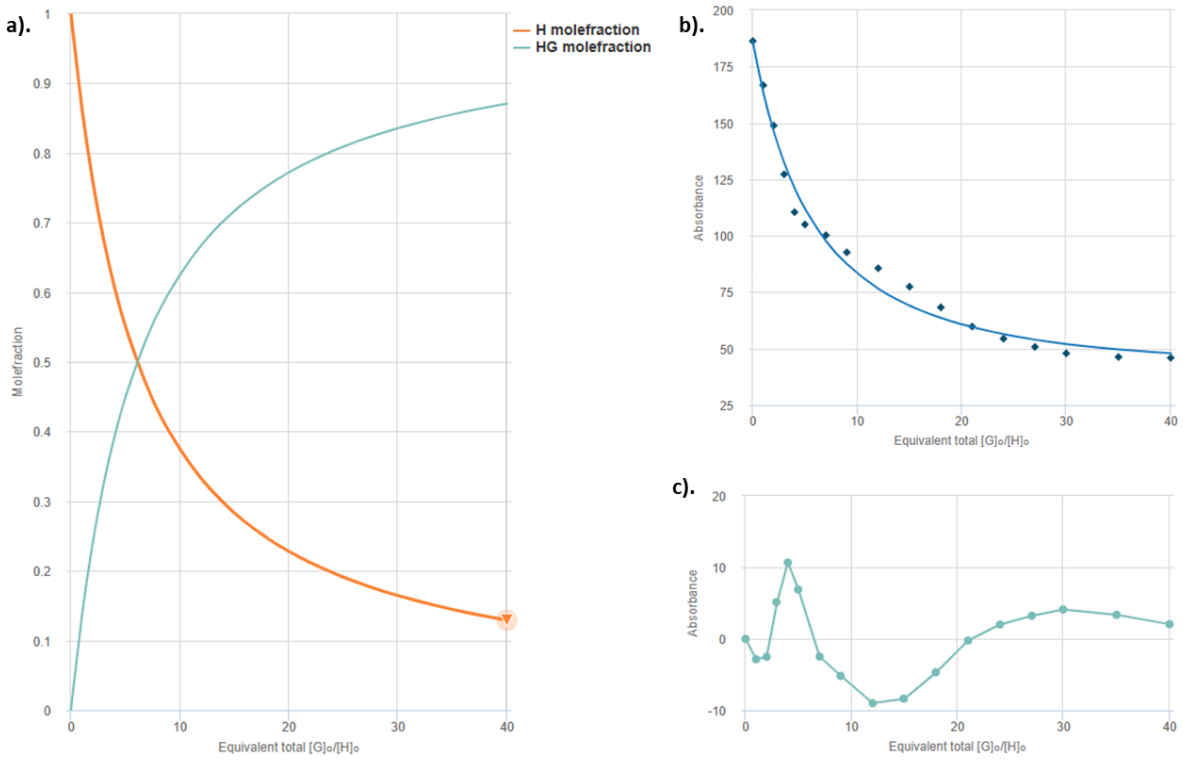

Figure A5.25: a). Mole fraction plot of Host vs Host:guest fraction with increasing guest concentration for **5.12. b).** Fitting binding isotherms of compound **5.12** with TBAF in DMSO, showing the changes in absrobance, fitted to the 1:1 binding model (K_a = 622 M^{-1}). **c).** Residuals plot of **5.12**.

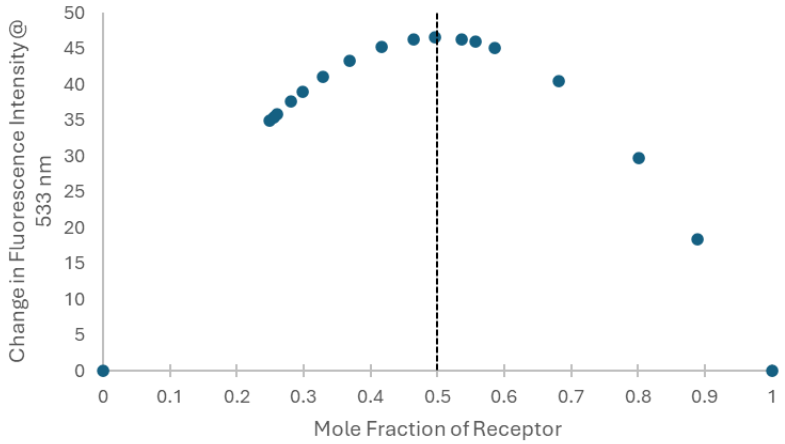

Figure A5.26: Jobs plot of compound **(5.12) Sq-2-Lys-Naph)** with TBAFl in DMSO.

Chapter 5 – ^{1}H NMR Anion Binding Data

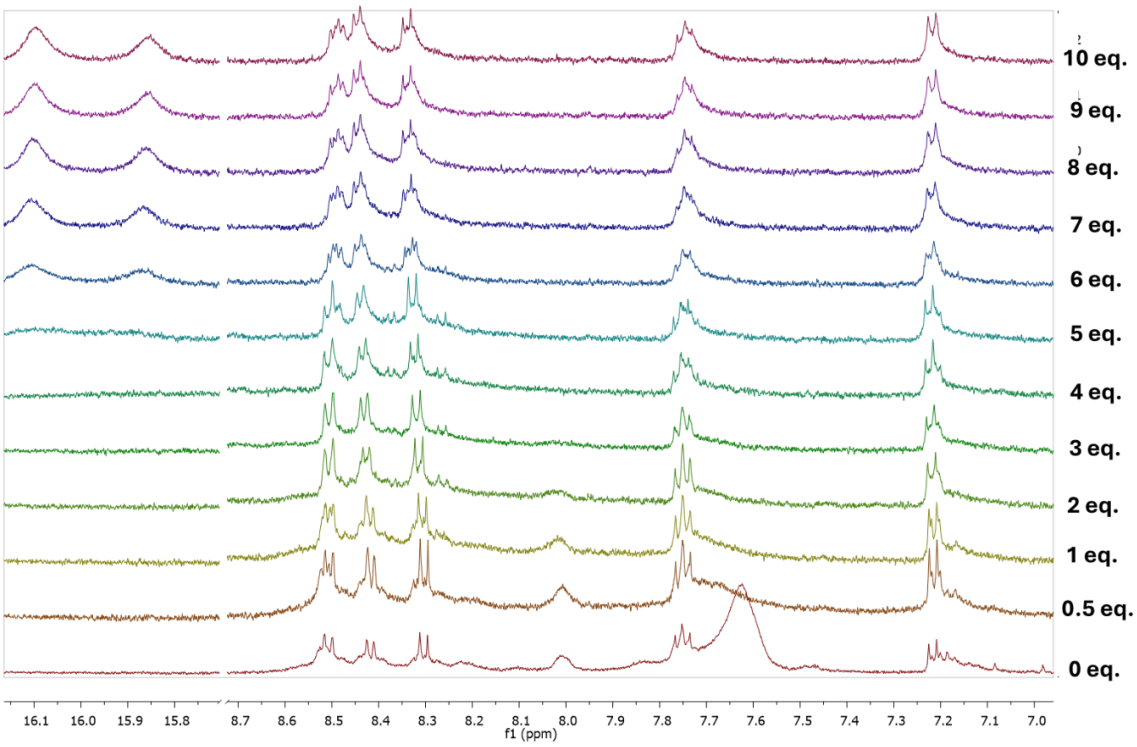

Figure A5.27: Partial ^{1}H NMR titration spectra of **(5.12) Sq-2-Lys-Naph** (2.5 mM) with increasing concentrations of TBAF in DMSO-d_6.

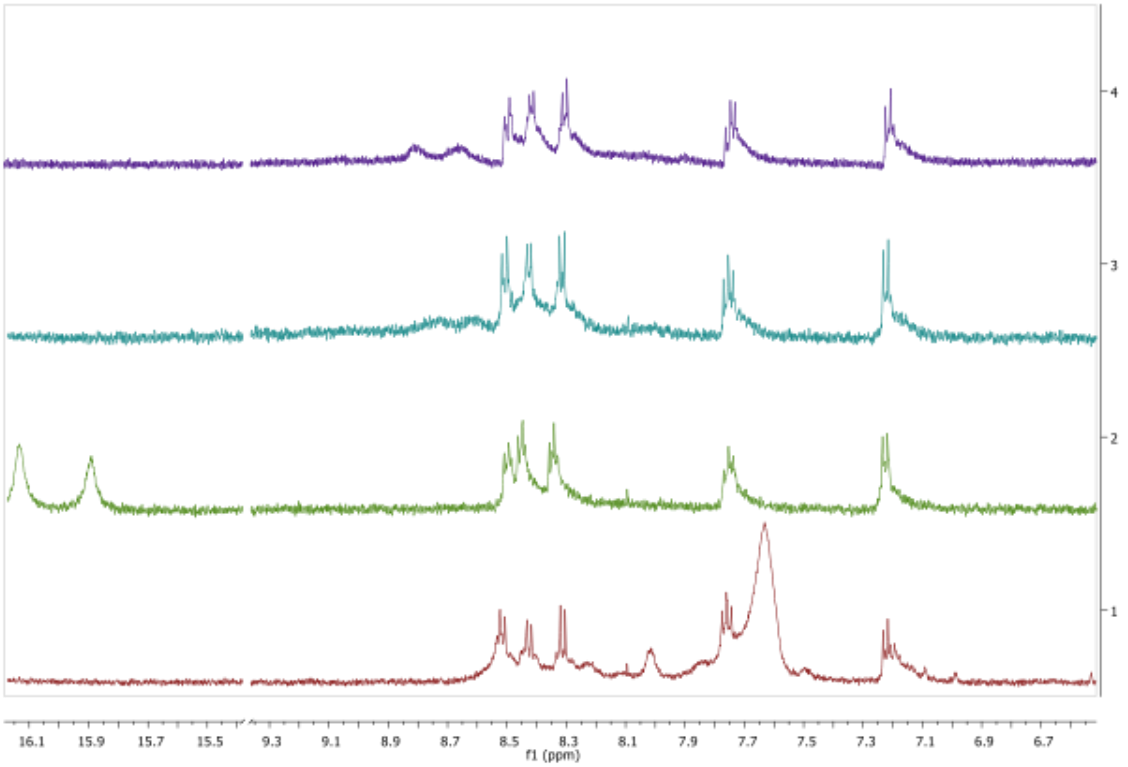

Figure A5.28: Partial ^{1}H NMR titration spectra of **(5.12) Sq-2-Lys-Naph** (2.5 mM) in DMSO-d_6 with (red) 0 equiv. of anion, (green) 5 equiv. of F^-, and (blue) 5 equiv. of F^- and 10 equiv. of AcO^-, and (purple) 10 equiv. of AcO.

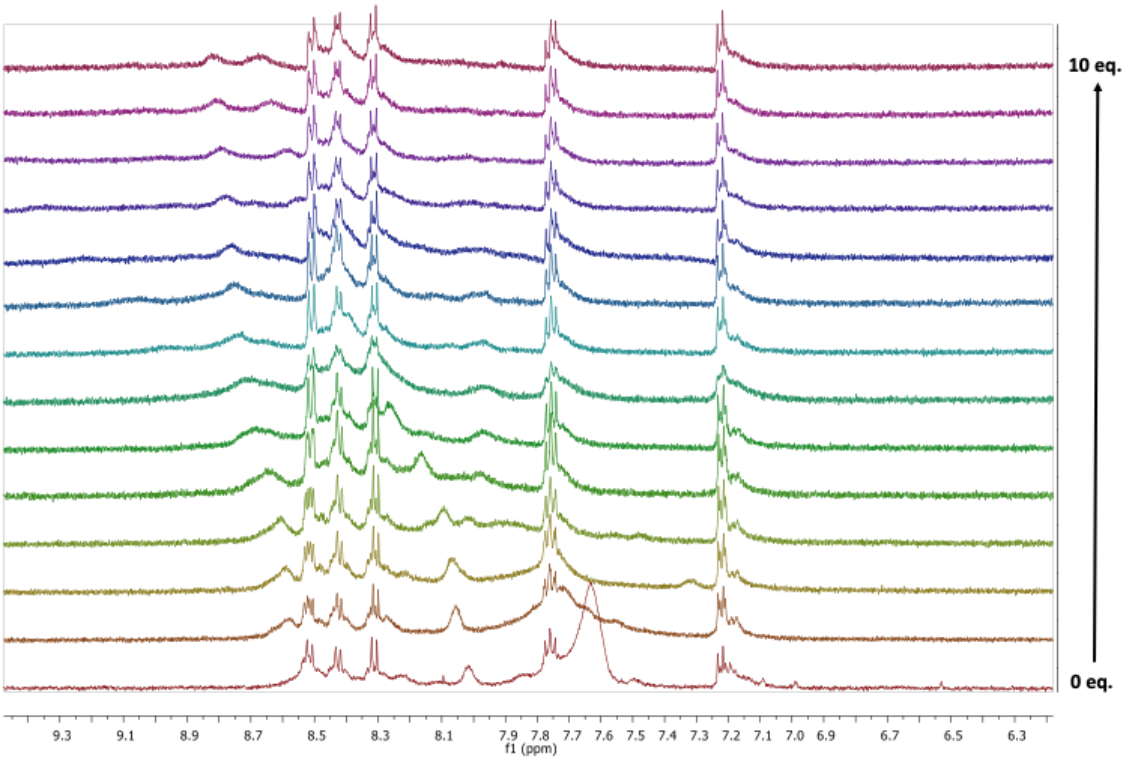

Figure A5.29: Partial ^{1}H NMR titration spectra of **Sq-2-Lys-Naph** (2.5 mM) in DMSO-d_6 with increasing concentrations of TBAAcO.

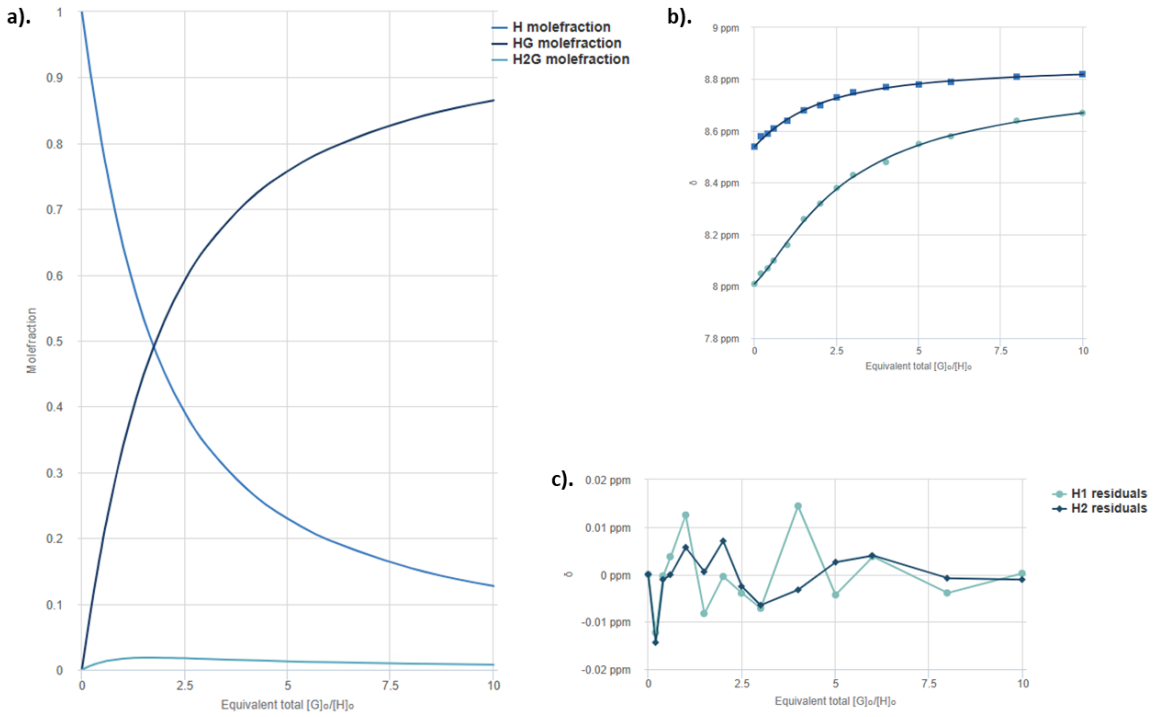

Figure A5.30: a). Mole fraction plot of Host vs Host:guest fraction with increasing guest concentration for **5.12. b).** Fitting binding isotherms of compound **5.12** with TBAAcO in DMSO-d_6 at 298 K, showing the changes in chemical shifts for the NH protons fitted to the 2:1 binding model (K_{11} = 327 M^{-1}), (K_{21} = 15 M^{-1}). **c).** Residuals plot of **5.12**.

“Every new beginning comes from some other beginning’s end”

- Seneca